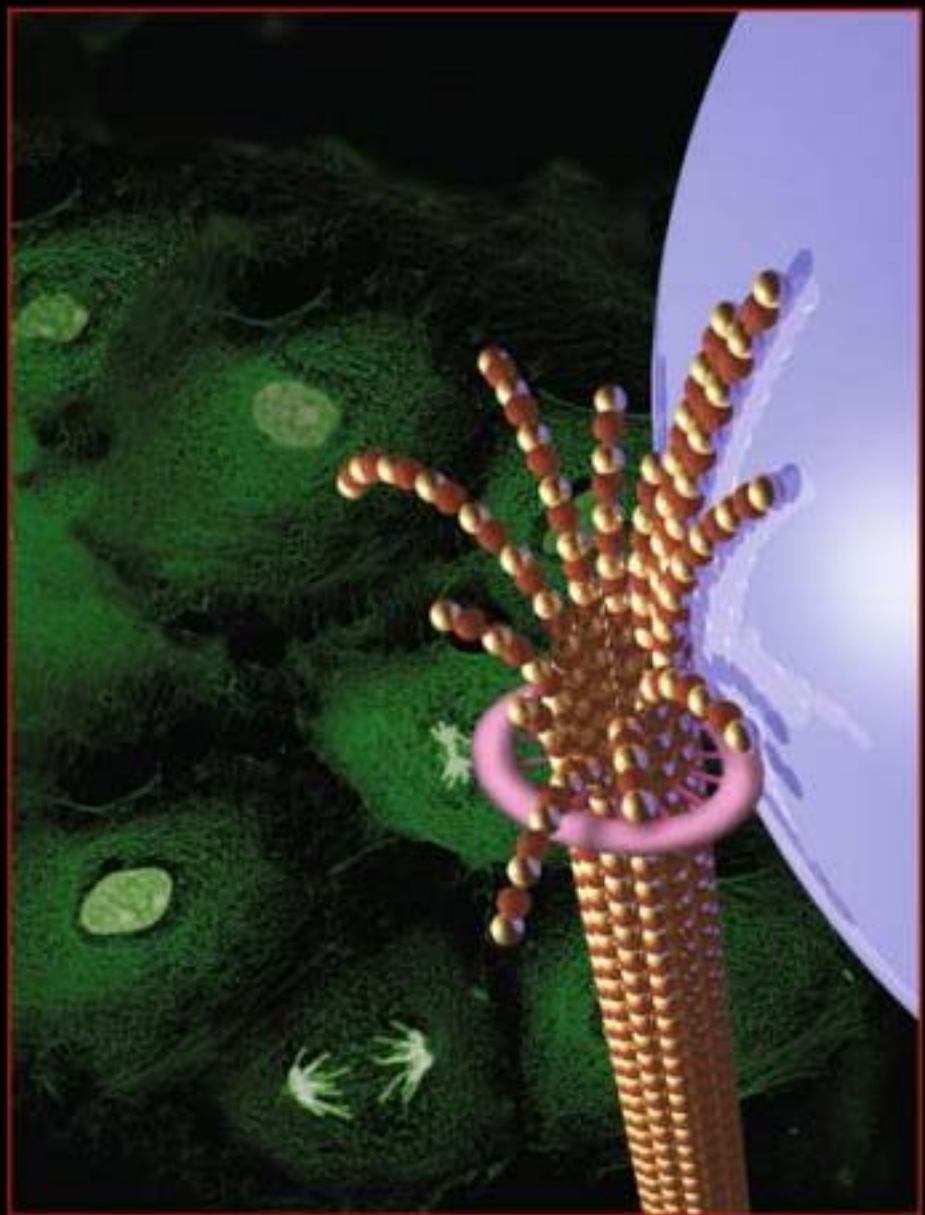


Methods in Cell Biology • Volume 95

MICROTUBULES, *IN VITRO*



Edited by

John J. Correia and Leslie Wilson



Series Editors

Leslie Wilson

Department of Molecular, Cellular and Developmental Biology
University of California
Santa Barbara, California

Paul Matsudaira

Department of Biological Sciences
National University of Singapore
Singapore

Methods in Cell Biology

VOLUME 95

Microtubules, in vitro

Edited by

Leslie Wilson

Department of Molecular, Cellular and Developmental Biology
University of California
Santa Barbara, California

John J. Correia

Department of Biochemistry
University of Mississippi Medical Center
Jackson, Mississippi



AMSTERDAM • BOSTON • HEIDELBERG • LONDON
NEW YORK • OXFORD • PARIS • SAN DIEGO
SAN FRANCISCO • SINGAPORE • SYDNEY • TOKYO
Academic Press is an imprint of Elsevier



Academic Press is an imprint of Elsevier
30 Corporate Drive, Suite 400, Burlington, MA 01803, USA
525 B Street, Suite 1900, San Diego, CA 92101-4495, USA
32, Jamestown Road, London NW1 7BY, UK
Linacre House, Jordan Hill, Oxford OX2 8DP, UK

First edition 2010

Copyright © 2010 Elsevier Inc. All rights reserved

No part of this publication may be reproduced, stored in a retrieval system
or transmitted in any form or by any means electronic, mechanical, photocopying,
recording or otherwise without the prior written permission of the publisher

Permissions may be sought directly from Elsevier's Science & Technology Rights
Department in Oxford, UK: phone (+44) (0) 1865 843830; fax (+44) (0) 1865 853333;
email: permissions@elsevier.com. Alternatively you can submit your request online by
visiting the Elsevier web site at <http://elsevier.com/locate/permissions>, and selecting
Obtaining permission to use Elsevier material

Notice

No responsibility is assumed by the publisher for any injury and/or damage to persons
or property as a matter of products liability, negligence or otherwise, or from any use
or operation of any methods, products, instructions or ideas contained in the material
herein. Because of rapid advances in the medical sciences, in particular, independent
verification of diagnoses and drug dosages should be made

ISBN-978-0-12-374815-7

ISSN: 0091-679X

For information on all Academic Press publications
visit our website at elsevierdirect.com

Printed and bound in USA
10 11 12 13 10 9 8 7 6 5 4 3 2 1

Working together to grow
libraries in developing countries

www.elsevier.com | www.bookaid.org | www.sabre.org

ELSEVIER BOOK AID International Sabre Foundation

CONTRIBUTORS

Numbers in parentheses indicate the pages on which the authors' contributions begin.

Elisabeth Adjadj (407), Institut National de la Santé et de la Recherche Médicale (INSERM), UMR829; Université Evry-Val d'Essonne; Laboratoire Structure-Activité des Biomolécules Normales et Pathologiques, INSERM – UEVE UMR U829, Evry 91025, France

José M. Andreu (353), Centro de Investigaciones Biológicas, CSIC, Madrid 28040, Spain

Ruth Hogue Angeletti (105), Laboratory of Macromolecular Analysis and Proteomics, Albert Einstein College of Medicine, Bronx, New York 10461

Charles L. Asbury (641), Department of Physiology and Biophysics, University of Washington, Seattle, Washington 98195

Ana B. Asenjo (505), Department of Physiology and Biophysics, Albert Einstein College of Medicine, Bronx, New York 10461

Fazly I. Ataullakhhanov (657), National Research Centre for Hematology, Moscow 125167, Russia, Department of Physics, Moscow State University, Moscow 119992, Russia, and Center for Theoretical Problems of Physicochemical Pharmacology, RAS, Moscow 119991, Russia

J. Avila (59), Centro de Biología Molecular (CSIC-UAM), Universidad Autónoma de Madrid, 28049 Cantoblanco, Madrid, Spain

Isabel Barasoain (353), Centro de Investigaciones Biológicas, CSIC, Madrid 28040, Spain

Pascale Barbier (449), CRO2, U911 Inserm, Aix-Marseille Université, 27 Bd Jean Moulin, 13385 Marseille Cedex 05, France

Adrian Begaye (391), Laboratory of Integrative and Medical Biophysics, National Institute of Child Health and Human Development, National Institutes of Health, Bethesda, Maryland

Bhabatark Bhattacharyya (301), Department of Biochemistry, Bose Institute, Kolkata 700 054, India

Peter Bieling (555), Cell Biology and Biophysics Unit, European Molecular Biology Laboratory, Meyerhofstrasse 1, 69117 Heidelberg, Germany

Volker Bormuth (221, 247), Max Planck Institute of Molecular Cell Biology and Genetics, 01307 Dresden, Germany

Corina Bräuer (247), Max Planck Institute of Molecular Cell Biology and Genetics, 01307 Dresden, Germany

Gary J. Brouhard (221), Department of Biology, McGill University, Montréal, Québec, Canada H3A 1B1

Berta Burd (105), Laboratory of Macromolecular Analysis and Proteomics, Albert Einstein College of Medicine, Bronx, New York 10461

Gerardo Carranza (59), Departamento de Biología Molecular, Facultad de Medicina, IFIMAV-Universidad de Cantabria, 39011 Santander, Spain

Raquel Castaño (59), Departamento de Biología Molecular, Facultad de Medicina, IFIMAV-Universidad de Cantabria, 39011 Santander, Spain

Blake D. Charlebois (207), Department of Biomedical Engineering, University of Michigan, Ann Arbor, Michigan 48109

Marie-Jeanne Clément (407), Institut National de la Santé et de la Recherche Médicale (INSERM), UMR829; Université Evry-Val d'Essonne; Laboratoire Structure-Activité des Biomolécules Normales et Pathologiques, INSERM – UEVE UMR U829, Evry 91025, France

Daniel N. Cohen (221), Medical Scientist Training Program, Vanderbilt University, Nashville, Tennessee 37232

Jeremy Cooper (641), Research Engineer, Applied Precision, Inc. Issaquah, WA 98027

Anthony Cormier (373), Laboratoire d'Enzymologie et Biochimie Structurales (LEBS), CNRS UPR3082, 91198 Gif sur Yvette, France, and Department of Molecular and Cell Biology, University of California, Berkeley, California 94720-3202

John J. Correia (47, 275), Department of Biochemistry, University of Mississippi Medical Center, Jackson, Mississippi 39216

Patrick A. Curmi (157, 407), Laboratoire Structure-Activité des Biomolécules Normales et Pathologiques, INSERM – UEVE UMR U829, Evry 91025, France

Ashley Davis (331), Cytoskeleton, Inc., 1830 South Acoma Street, Denver, Colorado 80223

Trisha N. Davis (641), Department of Biochemistry, University of Washington, Seattle, Washington 98195

François Devred (449), CRO2, U911 Inserm, Aix-Marseille Université, 27 Bd Jean Moulin, 13385 Marseille Cedex, 05, France

J. Fernando Díaz (353), Centro de Investigaciones Biológicas, CSIC, Madrid 28040, Spain

Stefan Diez (221, 247), Max Planck Institute of Molecular Cell Biology and Genetics, 01307 Dresden, Germany

Ram Dixit (521, 543), Department of Biology, Washington University, St. Louis, Missouri 63130

Marileen Dogterom (617), FOM Institute for Atomic and Molecular Physics (AMOLF), 1098 SG Amsterdam, The Netherlands

Mónica López Fanarraga (59), Departamento de Biología Molecular, Facultad de Medicina, IFIMAV-Universidad de Cantabria, 39011 Santander, Spain

Stuart C. Feinstein (481), Neuroscience Research Institute and Department of Molecular, Cellular and Developmental Biology, University of California, Santa Barbara, California 931067

Ernst-Ludwig Florin (601), Center for Nonlinear Dynamics, University of Texas at Austin, Austin, Texas 78712

Anthony Frankfurter (33), Department of Biology, University of Virginia, Charlottesville, Virginia 22904

Claire T. Friel (221), Max Planck Institute of Molecular Cell Biology and Genetics, 01307 Dresden, Germany

Christopher Gell (221), Max Planck Institute of Molecular Cell Biology and Genetics, 01307 Dresden, Germany

Daniel R. Gestaut (641), Department of Biochemistry, University of Washington, Seattle, Washington 98195

Benoît Gigant (373), Laboratoire d'Enzymologie et Biochimie Structurales (LEBS), CNRS UPR3082, 91198 Gif sur Yvette, France

Holly V. Goodson (175), Department of Chemistry and Biochemistry, The Center for the Study of Biocomplexity, University of Notre Dame, Notre Dame, Indiana 46556

Ivan V. Gregoretti (175), National Institute of Diabetes and Digestive and Kidney Diseases, National Institutes of Health, Bethesda, Maryland 20892

Ekaterina L. Grishchuk (657), Department of Physiology, University of Pennsylvania School of Medicine, Philadelphia, PA 19104

Loic Hamon (157), Laboratoire Structure-Activité des Biomolécules Normales et Pathologiques, INSERM – UEVE UMR U829, Evry 91025, France

Jonne Helenius (221), Biotechnology Center (BIOTEC), TU Dresden, 01307 Dresden, Germany

Christian Hentrich (555), Cell Biology and Biophysics Unit, European Molecular Biology Laboratory, Meyerhofstrasse 1, 69117 Heidelberg, Germany

Laree Hiser (47), School of Nursing, University of Mississippi Medical Center, Jackson, Mississippi 39216

Susan Band Horwitz (105), Department of Molecular Pharmacology, Albert Einstein College of Medicine, Bronx, New York 10461

Jonathon Howard (221, 247), Max Planck Institute of Molecular Cell Biology and Genetics, 01307 Dresden, Germany

Alan J. Hunt (207), Department of Biomedical Engineering, University of Michigan, Ann Arbor, Michigan 48109, and Center for Ultrafast Optical Science, University of Michigan, Ann Arbor, Michigan 48109

Leonid Ionov (247), Max Planck Institute of Molecular Cell Biology and Genetics, 01307 Dresden, Germany

Mary Ann Jordan (289), Department of Molecular, Cellular, and Developmental Biology, The Neuroscience Research Institute, University of California, Santa Barbara, California 93106

Sonia Kapoor (301), Department of Biosciences and Bioengineering, Indian Institute of Technology Bombay, Mumbai 400076, India

Jacob Kerssemakers (247), Kavli Institute of Nanoscience, Delft University of Technology, 2628 CJ Delft, The Netherlands

Erkan Kiris (481), TRUE Research Foundation, National Cancer Institute, Frederick, Maryland 21702

Marcel Knossow (373), Laboratoire d'Enzymologie et Biochimie Structurales (LEBS), CNRS UPR3082, 91198 Gif sur Yvette, France

Till Korten (247), Max Planck Institute of Molecular Cell Biology and Genetics, 01307 Dresden, Germany

Liedewij Laan (617), FOM Institute for Atomic and Molecular Physics (AMOLF), 1098 SG Amsterdam, The Netherlands

Daniel Lafitte (449), CRO2, U911 Inserm, Aix-Marseille Université, 27 Bd Jean Moulin, 13385 Marseille Cedex, 05, France

Isabelle Landrieu (449), CNRS-UMR 8576 UGSF-IFR 147, Université des Sciences et Technologies de Lille 1, 59655 Villeneuve d'Ascq Cedex, France

Cecile Leduc (247), Centre de Physique Moléculaire Optique et Hertzienne, Université Bordeaux 1, CNRS (UMR 5798), 33405 Talence cedex, France

Guy Lippens (449), CNRS-UMR 8576 UGSF-IFR 147, Université des Sciences et Technologies de Lille 1, 59655 Villeneuve d'Ascq Cedex, France

Sharon Lobert (47), School of Nursing and Department of Biochemistry, University of Mississippi Medical Center, Jackson, Mississippi 39216

Manu Lopus (189), Department of Molecular, Cellular, and Developmental Biology, The Neuroscience Research Institute, University of California, Santa Barbara, California 93106

Sarah Martinez (331), Cytoskeleton, Inc., 1830 South Acoma Street, Denver, Colorado 80223

Kim Middleton (331), Cytoskeleton, Inc., 1830 South Acoma Street, Denver, Colorado 80223

Herbert P. Miller (3), Department of Molecular, Cellular, and Developmental Biology, The Neuroscience Research Institute, University of California, Santa Barbara, California 93106

Leah M. Miller (105), Laboratory of Macromolecular Analysis and Proteomics, Albert Einstein College of Medicine, Bronx, New York 10461

Leonid A. Mirny (583), Harvard-MIT Division of Health Sciences and Technology, and Department of Physics, Massachusetts Institute of Technology, Cambridge, Massachusetts 02139

Naomi S. Morrissette (17), Department of Molecular Biology and Biochemistry, University of California, Irvine, California 92697

Daniel J. Needleman (583), Molecular and Cellular Biology, School of Engineering and Applied Sciences, FAS Center for Systems Biology, Harvard University, Cambridge, Massachusetts 02138

Daniel Nelson (331), Cytoskeleton, Inc., 1830 South Acoma Street, Denver, Colorado 80223

Bert Nitzsche (221, 247), Max Planck Institute of Molecular Cell Biology and Genetics, 01307 Dresden, Germany

Eva Nogales (129), Department of Molecular and Cell Biology, University of California, Berkeley, California 94720-3220, Howard Hughes Medical Institute, Berkeley, California 94720-3220, and Life Science Division, Lawrence Berkeley National Laboratory, Berkeley, California 94720-3220

Sofia Nolasco (59), Departamento de Biología Molecular, Facultad de Medicina, IFIMAV-Universidad de Cantabria, 39011 Santander, Spain, and Instituto Gulbenkian de Ciência, 2781-901 Oeiras, Portugal

Francesco Pampaloni (601), Cell Biology and Biophysics Unit, European Molecular Biology Laboratory, 69117 Heidelberg, Germany

Dulal Panda (301), Department of Biosciences and Bioengineering, Indian Institute of Technology Bombay, Mumbai 400 076, India

David Pastré (157), Laboratoire Structure-Activité des Biomolécules Normales et Pathologiques, INSERM – UEVE UMR U829, Evry 91025, France

Erwin J.G. Peterman (505), Department of Physics and Astronomy and Laser Centre, VU University, Amsterdam, NL 1081HV, The Netherlands

Heike Petzold (221), Max Planck Institute of Molecular Cell Biology and Genetics, 01307 Dresden, Germany

Vincent Peyrot (449), CRO2, U911 Inserm, Aix-Marseille Université, 27 Bd Jean Moulin, 13385 Marseille Cedex, 05, France

Jacob Piehler (555), Department of Biophysics, University of Osnabrück, Barbarastrasse 11, 49076 Osnabrück, Germany

Vincent H. Ramey (129), Life Science Division, Lawrence Berkeley National Laboratory, Berkeley, California 94720-3220, and Biophysics Graduate Program, University of California, Berkeley, California 94720-3220

Virginie Redeker (77), Laboratoire d'Enzymologie et Biochimie Structurales, CNRS, 91198 Gif-sur-Yvette cedex, France

Jan Ribbe (221), Max Planck Institute of Molecular Cell Biology and Genetics, 01307 Dresden, Germany

Jennifer L. Ross (521, 543), Department of Physics, University of Massachusetts Amherst, Amherst, Massachusetts 01003

Felix Ruhnau (247), Max Planck Institute of Molecular Cell Biology and Genetics, 01307 Dresden, Germany

Dan L. Sackett (17, 391), Laboratory of Integrative and Medical Biophysics, Program in Physical Biology, Eunice Kennedy Shriver National Institute of Child Health and Human Development, National Institutes of Health, Bethesda, Maryland 20892

Philippe Savarin (407), Institut National de la Santé et de la Recherche Médicale (INSERM), UMR829; Université Evry-Val d'Essonne; Laboratoire Structure-Activité des Biomolécules Normales et Pathologiques, Evry 91025, France

Erik Schäffer (221), Biotechnology Center (BIOTEC), TU Dresden, 01307 Dresden, Germany

Henry T. Schek III (207), Director of Engineering, 89 North, Burlington, Vermont 05401

Jennifer A. Smith (289), Department of Molecular, Cellular, and Developmental Biology, The Neuroscience Research Institute, University of California, Santa Barbara, California 93106

André Sobel (407), Institut National de la Santé et de la Recherche Médicale (INSERM), UMR839; UPMC Université Paris 06; Institut du Fer à Moulin, Paris F-75005, France

Hernando Sosa (505), Department of Physiology and Biophysics, Albert Einstein College of Medicine, Bronx, New York 10461

Anthony J. Spano (33), Department of Biology, University of Virginia, Charlottesville, Virginia 22904

Jeffrey H. Stear (221), Institute für Biologie, Humboldt Universität zu Berlin, 10115 Berlin, Germany

Thomas Surrey (555), Cell Biology and Biophysics Unit, European Molecular Biology Laboratory, Meyerhofstrasse 1, 69117 Heidelberg, Germany

Katja M. Taute (601), Center for Nonlinear Dynamics, University of Texas at Austin, Austin, Texas 78712

Ivo A. Tellez (555), Cell Biology and Biophysics Unit, European Molecular Biology Laboratory, Meyerhofstrasse 1, 69117 Heidelberg, Germany

Flavio Toma (407), Institut National de la Santé et de la Recherche Médicale (INSERM), UMR829; Université Evry-Val d'Essonne; Laboratoire Structure-Activité des Biomolécules Normales et Pathologiques, INSERM – UEVE UMR U829, Evry 91025, France

Anastasiya Trushko (221), Max Planck Institute of Molecular Cell Biology and Genetics, 01307 Dresden, Germany

Vladimir Varga (221), Max Planck Institute of Molecular Cell Biology and Genetics, 01307 Dresden, Germany

Donovan Ventimiglia (481), The Rockefeller University, New York, New York 10065

Pascal Verdier-Pinard (105), INSERM UMR 911, CRO2, Aix Marseille Université, 13385 Marseille Cedex 05, France

Chunguang Wang (373), Institute of Protein Research, Tongji University, Shanghai 200092, China

Hong-Wei Wang (129), Department of Molecular Biophysics and Biochemistry, Yale University, New Haven, Connecticut 06520-8024

Karl A. Werbovetz (17), Division of Medicinal Chemistry and Pharmacognosy, The Ohio State University, Columbus, Ohio 43210

Per O. Widlund (221), Max Planck Institute of Molecular Cell Biology and Genetics, 01307 Dresden, Germany

Leslie Wilson (3,189), Department of Molecular, Cellular, and Developmental Biology, The Neuroscience Research Institute, University of California, Santa Barbara, California 93106

Linda Wordeman (641), Department of Physiology and Biophysics, University of Washington, Seattle, Washington 98195

Hui Xiao (105), Laboratory of Macromolecular Analysis and Proteomics, Albert Einstein College of Medicine, Bronx, New York 10461

Mythili Yenjerla (189), Department of Molecular, Cellular, and Developmental Biology, The Neuroscience Research Institute, University of California, Santa Barbara, California 93106

J.C. Zabala (59), Departamento de Biología Molecular, Facultad de Medicina, IFIMAV-Universidad de Cantabria, 39011 Santander, Spain

Marija Zanic (221), Max Planck Institute of Molecular Cell Biology and Genetics, 01307 Dresden, Germany

PREFACE

It has been almost 30 years since the first Methods in Cell Biology volumes that contained methods for analysis of tubulin and microtubules were published. These were two volumes on The Cytoskeleton, edited by Les Wilson, covering the entire cytoskeleton field, which at the time was a relatively new emerging area of cell biology. Volume 24, Part A of the two-part series, focused on the isolation and characterization of cytoskeletal proteins. Of the 24 chapters, 18 were on microtubules; 5 on purification methods, 6 more on length distributions, polarity, assembly kinetics, and tubulin flux measurements, 3 on tyrosination, tubulin tyrosine ligase reactions, and only 2 on dynein. The nontubulin methods chapters covered actin, myosin, and intermediate filament purification and characterization, with 2 chapters on actin assembly measurements. The second volume, Part B, was Volume 25 and focused on biological systems and *in vitro* models. Of the 18 chapters, 1 discussed axonal transport, 1 discussed microtubule mediated motility of sperm flagella, 2 were on the role of microtubules in secretion and intracellular transport, 3 discussed mitotic spindles and mitosis in either PtK1 cells, sea urchin eggs, or *Aspergillus nidulans*, and 1 described electron microscopic methods for visualizing microtubules in spindles. The remaining methods chapters focused on actin-based systems with only one chapter devoted to intermediate filaments in muscle. While most of the chapters in the earlier volumes are classics and remain extremely useful today, so much has happened since then. At the time these volumes were assembled and published, dynamic instability had not yet been described, kinesin had not been isolated, video-enhanced differential interference contrast microscopy had not yet been developed, laser trap methods were just being discovered, and the three-dimensional (3D) structure of tubulin and microtubules was a distant dream. As advanced as the state of knowledge on microtubules was at that time, a continuous wave of new discoveries, dominated by the advancement of single-molecule methods and high-resolution techniques and their application to new families of remarkable motor proteins and microtubule-associated proteins (MAPs), has emerged that has sent the microtubule field into unimagined directions.

Here, with a focus on analysis of purified (*in vitro*) systems, 33 groups of experts have written state-of-the-art methods chapters that reflect many of the advances that have taken place in the analysis of tubulin and microtubules and their functions that have occurred in the subsequent 28 years. Volume 95, Microtubules, *In Vitro*, is organized into five sections. Section 1, on Isolation, Biochemistry, and Characterization of Antibodies and Isotypes, consists of seven chapters on tubulin isolation, β -tubulin antibody production and characterization methods, PCR methods for tubulin isotypes and MAPs, and native electrophoresis methods together with two chapters on mass spectroscopy, C-terminal posttranslational modifications, and tubulin proteomics. Section 2, Microtubule Structure and Dynamics, consists of seven chapters on cyro-electron microscopic- and atomic

force microscopic imaging of microtubules, analysis of microtubule dynamic instability at steady state, and at nanometer resolution, single-molecule imaging of microtubule dynamics and kinesin motors, and mathematical modeling of microtubule dynamics. Section 3 (Drugs) includes seven chapters on methods for measuring drug binding to tubulin and to microtubules. Section 4 (Interactions with Motors and MAPs) includes seven methods chapters useful for studying MAP tubulin interactions. These include analysis by nuclear magnetic resonance spectroscopy, isothermal titration calorimetry (ITC), fluorescence, total internal reflection fluorescence (TIRF), fluorescence polarization microscopy (FPM), and the methods for functionalizing the surfaces for these measurements. Finally, Section 5 (Functional Extracts and Force Measurements) includes five chapters describing methods for performing dynamics measurements in functional extracts, for extracting mechanical properties from thermal fluctuations of microtubules, for measuring force at dynamic microtubule ends, and for reconstructing kinetochore complexes and measuring the associated forces.

This volume in part reflects the continuing importance of tubulin and microtubule biochemistry and the emergence of modern physical methods for studying molecular interactions including immunological and PCR techniques. It also reflects the critical importance of antimitotic drugs as drugs for treatment of cancer and as tools in cell and molecular biology, and the development of assays to study them, especially at high resolution. While the antimitotic field is currently dominated by the drug discovery biotechnology and questions about biomarkers and clinical outcomes (see the recent volume edited by Tito Fojo, *The Role of Microtubules in Cell Biology, Neurobiology and Oncology*), the assays described here play a major role in drug development and in our understanding of the microtubule cytoskeleton. Recent advances in cryo-electron microscopy, nuclear magnetic resonance spectroscopy, atomic force microscopy, and proteomic methodology are driving detailed studies into the structure and function of microtubule-based systems. The single-molecule imaging and the techniques that allow nanometer and 3D-nanometer resolution, microtubule plus end tip tracking, and detailed structural pictures of kinesin motility clearly play a major role in the new experimental approaches described in this volume. The merging of single-molecule nanotechnology with high-resolution imaging has significantly changed the questions we can ask and the way microtubule structure, function, and regulation can be analyzed. While this volume is not meant to be all inclusive, it does bring together the breath of biochemical, physical, structural, dynamic, microscopic, and nanomolecular techniques that are now available for study of the microtubule cytoskeleton with purified microtubule systems. An accompanying *Methods in Cell Biology* volume that will be published later this year, *Microtubules, In Vivo*, edited by Lynne Cassimeris and Phong Tran, will focus on analysis of microtubule function in living cells.

We wish to thank all the authors for their contributions and the immense effort they put into making this volume an overwhelming success. Their willingness to contribute to this project has been essential. (To those authors who were unable to meet the deadline for this volume, we anticipate assembling a follow-up volume on microtubules *in vitro* to this volume). We especially want to thank Tara Hoey, Zoe Kruze, and Narmada Thangavelu at Elsevier for their support and organizational skills

throughout this long and seemingly endless process. Finally, we thank our colleagues, collaborators, and families, who only politely harassed us when we seemed to be distracted from our other more noble pursuits.

John (Jack) Correia

Department of Biochemistry

University of Mississippi Medical Center

Jackson, MS

Leslie Wilson

Department of Molecular, Cellular and Developmental Biology

University of California

Santa Barbara, CA

SECTION I

Isolation and Biochemistry of Tubulin and Characterization of Antibodies and Isotypes

CHAPTER 1

Preparation of Microtubule Protein and Purified Tubulin from Bovine Brain by Cycles of Assembly and Disassembly and Phosphocellulose Chromatography

Herbert P. Miller and Leslie Wilson

Department of Molecular, Cellular, and Developmental Biology and The Neuroscience Research Institute, University of California, Santa Barbara, California 93106

- I. Introduction
- II. Protocols
 - A. Optimal Starting Material and Initial Processing
 - B. Protocol for Purification of Microtubule Protein (Tubulin Plus Microtubule-Associated Proteins) in the Absence of Glycerol
 - C. Protocol for Purification of Tubulin from Microtubule Protein by Phosphocellulose Column Chromatography
 - D. Characteristics and Polymerization Properties of Purified Proteins
- III. Buffer Compositions
- IV. Concluding Comments

Acknowledgments

References

I. Introduction

Tubulin can be purified from a number of nonmammalian and mammalian nonneural sources (e.g., Farrell, 1982; Detrich and Wilson, 1983; Newton *et al.*, 2002; Bellocq *et al.*, 2005), but for most applications mammalian brain is the most commonly used starting material (Borisy *et al.*, 1975; Lee and Timasheff, 1975; Asnes and Wilson, 1979; Murphy, 1982; Williams and Lee, 1982; Sloboda and Belfi, 1998; Andreu, 2007). There are several important reasons that mammalian brain is so highly favored. First, the tubulin concentration in brain is very high, especially in

brains from young animals (Bamburg *et al.*, 1973). Second, microtubules from mammalian brain readily assemble at 30–37°C and quickly depolymerize at cold temperature (0–4°C), facilitating purification by straight forward alternating cycles of warm temperature polymerization and cold temperature depolymerization. Third, mammalian brain contains a high content of assembly-promoting/stabilizing microtubule-associated proteins (MAPs) such as MAP2 and tau. These MAPs, which are mainly found in large amounts in the axonal and dendritic processes of neurons, strongly promote microtubule nucleation and elongation and reduce the critical tubulin concentration required for self-assembly. Beginning with fresh brains from cows, pigs, chickens, goats, mice, rats (or other mammals), and especially from young animals, one can obtain tens of milligrams of assembly-competent microtubule protein (MTP) and purified tubulin in 6–10 h.

Solvents such as glycerol or dimethylsulfoxide (DMSO), and drugs like taxol, strongly promote microtubule polymerization, and a number of purification protocols based upon alternating cycles of warm assembly and cold disassembly have been developed over the years in which such solvents or taxol are added to promote polymerization. While the use of these agents increases the yields of tubulin, because of the high MAP content, purification of tubulin from brain tissue by cycles of assembly and disassembly is very efficient in the absence of such agents as long as the concentration of tubulin present during the assembly reaction is well above the critical tubulin concentration required for polymerization in the presence of the MAPs (~0.3–0.7 mg/ml). This is easy to accomplish simply by careful adjustment of the buffer volume when resuspending microtubules assembled during the preceding cycle into cold depolymerizing buffer (see below).

Also depending upon the application, the use of assembly-promoting solvents or assembly-promoting agents could present important disadvantages. The most important is that they modify the polymerization, treadmilling, and dynamic instability behaviors of microtubules and can mask the activities of drug molecules or specific MAPs that one would like to study (e.g., Schlistra *et al.*, 1991; Panda *et al.*, 1999). Thus, if protocols that involve assembly in assembly-promoting agents are used, it is critical to ensure that all of the agents are completely removed in order to study the effects of modulating proteins or drugs—a procedure that takes additional time and could result in some degradation of the tubulin. Here we present an efficient high yield and relatively easy protocol for purification of MTP (tubulin plus stabilizing MAPs, consisting of ~70–75% tubulin and 25–30% MAPs) and, subsequently, for purifying tubulin from the MTP, in the absence of assembly-promoting solvents.

===== II. Protocols

A. Optimal Starting Material and Initial Processing

1. Freshness of Brains: Age and Sex of the Animals

The yield of polymerization-competent tubulin is highly dependent upon the freshness of the brain tissue, which is difficult to control. We obtain bovine brains at a commercial slaughter house from Mr. Ramero Carlos of Manning Beef LLC, in Pico Rivera, CA, which is about a 3-h drive from our laboratory. There is a complex and somewhat time-consuming process defined by law that slaughter houses must

follow, which affects brain freshness. As a rule, when cattle arrive at the slaughter house they are first inspected to ensure good health. Animals are then filed onto a killing floor where they are rendered unconscious with a captive bolt pistol fired against the forehead centered just above the eyes. The jugular vein and carotid artery are then cut to drain the blood. Although head removal from the carcass is one of the initial steps in the slaughtering process, the brain cannot be removed from the head until the rest of the carcass has been inspected. First the internal organs are excised and inspected for parasites or disease. Then the tongue is taken and the glands around the head are examined. Only after the carcass passes inspection can the brain be removed from the head. We must arrange to obtain the brains in advance. [Murphy \(1982\)](#) has reported the half-time for loss of tubulin polymerization activity from death of the animal until brain removal to be approximately 19 min. So this process should be carried out quickly. We always request that removal of the brain from the skull be carried out as rapidly as possible—a process that under good conditions takes 20–30 min from the time of kill. The brain is immediately separated into two approximately 125 g hemispheres that are individually placed in plastic sealable bags and buried in ice. This reduces the time to chill the brain to $\sim 0^{\circ}\text{C}$ and greatly increases the half-time for loss of assembly competence. We have obtained good yields of assembly-competent tubulin from brains that were quickly buried in ice and kept on ice for as long as 5 h after slaughter.

We have found that cow brains yield only one-third the amount of assembly-competent MTP as steer brains. Thus we try to obtain steer brains. Perhaps most important is the age of the animals. Dairy cows at the slaughter house we use are usually 5–7 years old. On the other hand steers, which are raised primarily for beef, are usually no more than 2 years old when slaughtered. Since we have found that young heifers yield similar amounts of assembly-competent protein as steers, it seems that the age of the animal is much more important than the gender, with younger being better. Bulls, like cows, are usually older animals when sent to slaughter and also yield less MTP per gram of fresh brain tissue than steers. Thus, it is best to obtain brains from young steers.

2. Condition of the Brains

An important factor that influences the yield of MTP is the condition of the brains. Because the animals are initially stunned with a pistol fired against the forehead, the skull is usually shattered at the point of impact, sending fragments of bone deep into portions of the brain. This results in localized hemorrhage and damage to the surrounding brain tissue (perhaps due to protease activity), which in our experience reduces yields. Thus, we remove all damaged brain tissue as soon as possible.

3. Removal of the Meninges

We also have found that the yield of assembly-competent tubulin is greatly increased by removing the meninges and free-flowing and coagulated blood. We do this as quickly as possible at the slaughter house. The presence of blood and blood clots seems to reduce yields. Removal of the meninges also facilitates homogenization of the brain tissue. We remove the meninges with blunt tipped forceps. It is important to handle the brain tissue as gingerly as possible during the process to

minimize tissue damage, to minimize the amount of blood forced into the interstitial spaces of the tissue, and to minimize the presence of free-flowing and coagulated blood prior to homogenization.

4. Processing Speed and Optimal Cycling Temperatures

Once the brain is homogenized (see below) it is important to isolate the tubulin and associated proteins as quickly as possible. The tubulin degrades rapidly once the brain is homogenized even at 0°C and each successive polymerization cycle removes proteases and other degradative activities. It is important to keep in mind that all steps (except for warm temperature polymerization) should be carried out at 0°C with 1 mM GTP and 1 mM Mg⁺⁺ present. It is also important that soluble free calcium is removed with EGTA and that the pH is maintained in a narrow range. We use 30°C to polymerize MTP rather than 37°C. Polymerization is robust at 30°C and experience has shown that recovery of assembly-competent tubulin drops off dramatically as the temperature rises above 37°C. There can be as much as a 5°C variation in temperature above the set point on centrifuges that use a friction-based heating system. In general superspeed centrifuges use a refrigeration unit to cool the chamber and thus the rotor, but rely on friction from the movement of air to heat the chamber and rotor. Temperature is maintained by balancing refrigerated cooling and friction-generated heating. By contrast, most ultracentrifuges are equipped with both heating and cooling units. It is important to confirm the temperature of samples and adjust the centrifuge controls accordingly.

B. Protocol for Purification of Microtubule Protein (Tubulin Plus Microtubule-Associated Proteins) in the Absence of Glycerol

While the protocol has been considerably fine-tuned and standardized, the basic protocol for isolating microtubules by temperature-dependent cycles of assembly and disassembly in the absence of glycerol remains similar to the protocols that were first introduced (Borisy *et al.*, 1975; Asnes and Wilson, 1979; Murphy, 1982). The procedure we describe here is a modification of the [Asnes and Wilson procedure \(1979\)](#). It should work well with some modifications for purification of MTP and tubulin from any brain source. Purification of tubulin from cultured cells or other sources that contain much less tubulin than brain presents special problems that will not be described here (see [Farrell, 1982](#); [Detrich and Wilson, 1983](#); [Newton *et al.*, 2002](#); [Bellocq *et al.*, 2005](#)). A flowchart documenting the purification protocol is shown in [Fig. 1](#).

1. Preparation of the Crude Brain Extract (CBE)

We usually begin with two steer brains, weighing a total of between 400 and 600 g. Processing this quantity of tissue requires the equivalent of six Sorvall refrigerated superspeed centrifuges. For example Sorvall RC5B Plus centrifuges equipped with SS-34 rotors work well for the initial purification steps. It is convenient the day before carrying out the purification to prepare two buffers. The first is one 1 l of homogenizing buffer, L-GNPEM buffer, consisting of 100 mM sodium glutamate, 20 mM sodium phosphate, 1 mM EGTA, and 0.5 mM MgCl₂, pH 6.85,

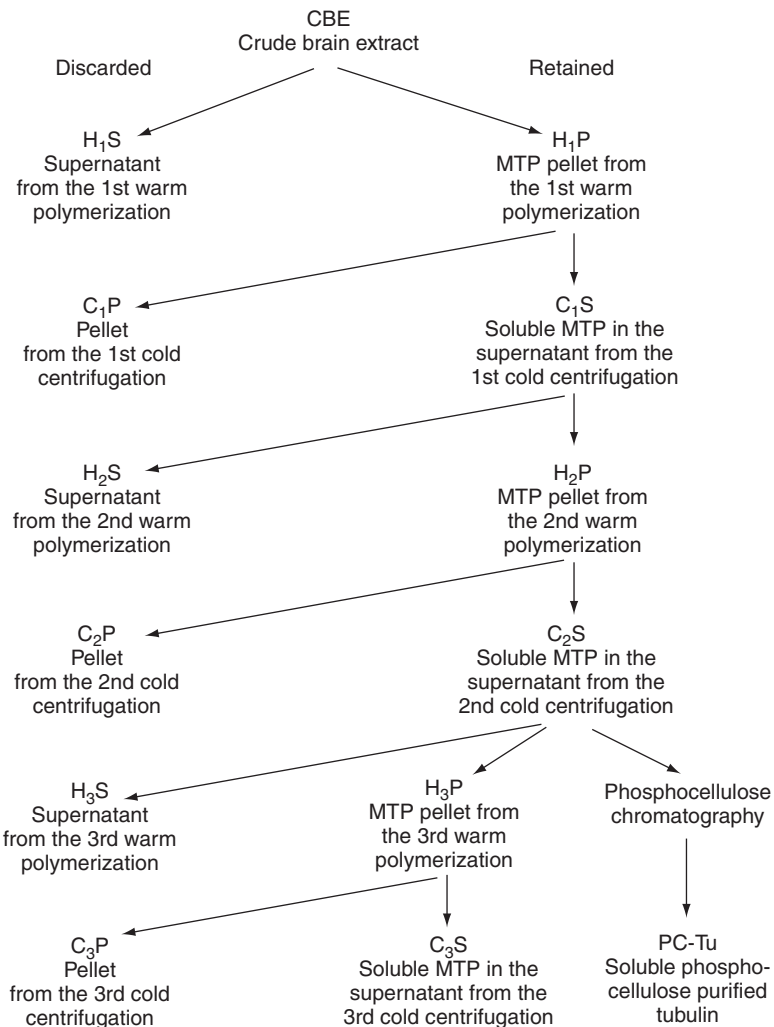


Fig. 1 Flowchart illustrating the steps in the purification of microtubule protein and phosphocellulose-purified tubulin.

and the second is 250 ml of the same buffer at pH 6.75. Both buffers should be refrigerated. Beginning at the slaughter house, the meninges, superficial blood vessels, and blood clots are removed and each brain hemisphere is placed in a separate plastic bag and buried in ice for transport back to the laboratory (see above). Once back at the laboratory, add 1 mM dithiothreitol (DTT) to one l of L-GNPEM buffer, pH 6.85. This buffer will be used to blend the brains. Brains are initially blended in a Waring Commercial Blender at a ratio of 1.5 ml of buffer per gram of wet brain weight at low speed for 30 s. Next, the blended brains are homogenized by using one pass in a motor-driven Teflon pestle/glass homogenizer (Kimble-Chase, Vinland, NJ) operated at the maximum speed (we use a Tri R Stir R motor). Next, the brain homogenate is centrifuged at 32,500 \times g (average RCF) for 40 min at 4°C

(we use 50-ml centrifuge tubes). The supernatant, now called the crude brain extract or CBE (Fig. 1), is collected in a liter graduated cylinder to measure the volume and serve as the polymerization vessel.

2. First Polymerization and Depolymerization Cycle

The appropriate amount of GTP is first added in dry form to the CBE at a final concentration of 2.5 mM. Next, the CBE is warmed to 30°C and incubated in a water bath for 30 min to polymerize the MTP into microtubules. We use a 20-gal aquarium with a Fisher Isotemp immersion circulator for all warm incubations. This is followed by centrifugation at 45,000 \times g for 30 min at 30°C again using 50-ml centrifuge tubes to obtain microtubule pellets (the H₁P). It is important to note the total volume of the warm supernatant, now called the H₁S, which is then discarded.

Next the H₁P microtubule pellets are resuspended in 10% of the volume of the H₁S into cold L-GNPEM buffer, pH 6.75. The suspended microtubules are then homogenized with three passes in a 15-ml glass pestle “A”/glass tissue homogenizer (we prefer the Kontes K885300-0015) and incubated on ice for 40 min to fully depolymerize the microtubules. The solubilized H₁P fraction is then centrifuged at 45,000 \times g for 45 min at 4°C to clarify it and remove any particulate debris. Next the clarified supernatant, the C₁S, is collected and retained and the C₁P pellet is discarded (Fig. 1).

3. Second Polymerization Cycle

First, 2.5 mM GTP from a stock solution of 100 mM GTP is added to the C₁S, which is then incubated for 30 min at 30°C. The C₁S, now a suspension of microtubules, is centrifuged at 45,000 \times g for 60 min at 30°C. The H₂S is decanted and the volume is noted before it is discarded. At this point, the H₂P can be quick-frozen (see below) in liquid nitrogen and stored as pellets in a -70°C ultracold freezer until further purification or processing is convenient. As a rule, this will be ~8–9 h after beginning to prepare the CBE. The H₂P can either be taken through another cycle of assembly/disassembly to obtain a clean MAP-rich tubulin preparation or be subjected to phosphocellulose chromatography (see below) to prepare MAP-free purified tubulin, often called PC-Tubulin (Pc-Tu), for use in experiments.

4. Third Purification Cycle

We often use MTP that has been processed through three cycles of warm assembly and cold disassembly. This third cycle involves centrifuging through 50% sucrose cushions to remove any proteins that do not adhere to the microtubules. The third cycling process is similar to the two previous cycles with the following modifications. The frozen H₂P pellets are quickly thawed by initially placing the tubes containing the pellets in a beaker of room temperature water, followed by cooling the tubes on ice. The thawed H₂P pellets are then suspended in L-GNPEM buffer, pH 6.75, using one-third the volume of the former H₂S, homogenized with three passes in a 15-ml glass pestle “A”/glass tissue homogenizer, and incubated on ice for 20 min to fully depolymerize the microtubules. The solubilized H₂P solution is then centrifuged to clarify it at 105,000 \times g (average RCF) for 1 h at

4°C. This centrifugation step and the subsequent centrifugation step require a refrigerated ultracentrifuge. We use a Beckman/Coulter Optima L-90 ultracentrifuge with a type 70.1 Ti rotor.

The C₂S supernatant is removed and 2.5 mM GTP is added. The solution is then incubated for 30 min at 30°C to polymerize the microtubules. A 50% sucrose solution (w/v) in L-GNPEM buffer, pH 6.75, is warmed to 30°C. Five milliliters of this solution is dispensed into 10-ml Oakridge centrifuge tubes, and 1 ml of the polymerized microtubule suspension is layered on top of the 50% sucrose cushion. Microtubules are centrifuged through the sucrose cushion at 150,000 \times g for 2 h at 30°C to collect microtubule pellets. The supernatant, now called the H₃S, is aspirated, as is the subnatant of 50% sucrose. This will leave a translucent MTP pellet, called the H₃P (Fig. 1), at the bottom of the tube.

The H₃P is resuspended at 0°C in a small volume of PEM buffer, consisting of 100 mM PIPES, 1 mM EGTA, and 1 mM MgSO₄, pH 6.8, such that the protein concentration is between 5 and 10 mg/ml. The suspension is then Dounce homogenized with three passes in a 7-ml glass pestle “A”/glass tissue homogenizer (Kontes K885300-0007) and incubated on ice for 20 min to depolymerize the microtubules. The solubilized MTP from the H₃P is then centrifuged at 45,000 \times g for 20 min at 4°C. The supernatant containing the solubilized MTP is removed (now called the C₃S), and 100 μ M GTP is added. The MAP-rich MTP concentration is measured and the solution is drop-frozen in liquid nitrogen (see below). In our experience, the C₃S MTP solution can be stored as frozen beads in an ultracold freezer at -70°C for at least 1 year without noticeable loss of assembly competence.

5. Preparation of Frozen Beads

We prepare frozen beads as follows. Four tri-corner polypropylene beakers (250 ml), which are easily held for decanting the liquid nitrogen, are each completely filled with liquid nitrogen. Using a Pasteur pipette, one drop of MTP solution is added per beaker, alternating the beakers, allowing each bead to freeze before another drop is added. The liquid nitrogen is decanted and discarded and the frozen beads are placed into 50-ml plastic tubes for storage. The average bead volume with this procedure is \sim 32 μ l.

C. Protocol for Purification of Tubulin from Microtubule Protein by Phosphocellulose Column Chromatography

An alternative to the third cycle for purification of MTP (tubulin plus MAPs) is to purify tubulin devoid of MAPs beginning with the C₂S using phosphocellulose column chromatography. A similar procedure is also described by Ross and Dixit in this volume. Prepare the C₂S as described earlier. However, instead of dissolving the H₂P in L-GNPEM buffer with one-third the volume of the H₂S, resuspend the microtubule pellet in one-tenth the volume of the previous H₂S using PEM₅₀ buffer, which is composed of 50 mM PIPES, 1 mM EGTA, and 1 mM MgSO₄, pH 6.8. The supernatant (C₂S) from the ultracentrifugation run is retained and supplemented with 100 μ M GTP.

1. Preparation of the Phosphocellulose

The required column volume for the procedure can be calculated in terms of ml by multiplying the total number of mg of protein in the C₂S by 0.67. The amount of dry phosphocellulose (actually cellulose phosphate, Whatman P-11) required for the column is 0.17 g dry phosphocellulose per ml settled column volume, which is stirred into 25 volumes of 0.5 M NaOH. The phosphocellulose resin is allowed to settle and the liquor containing the fines is decanted. The phosphocellulose resin is now resuspended in a large excess volume of glass-distilled water. After the resin has settled, the water is decanted. The water wash is repeated three more times. Next, the phosphocellulose resin is resuspended in 25 volumes of 0.5 M HCl. The resin is allowed to settle and the HCl solution is decanted. The resin is then washed four times with a large excess of glass-distilled water. The phosphocellulose resin is equilibrated in the buffer of choice (we use PEM₅₀ buffer). A 10× solution of PEM₅₀ buffer (consisting of 0.5 M PIPES, 1 mM EGTA, and 1 mM MgSO₄, pH 6.8), enough to cover the phosphocellulose resin to double the volume, is stirred in. After settling, the liquid is decanted and the resin is washed four times with 1× PEM₅₀ buffer. The pH of the liquor is measured after the resin has settled and compared to the pH of the buffer to ensure that the resin is equilibrated and at the correct pH.

2. Building and Developing the Column

To retain maximal assembly competence of the tubulin, the column should be run in a cold room or cold cabinet, buffers should be stored and used at 4°C, and the proteins kept on ice. For 150 mg of C₂S, we use a 2.5 × 30 cm glass Flex Column (Kontes K420401-2550) with a bed volume of 100 ml. The column is filled with the phosphocellulose resin to the 100 ml mark, and 250 ml of PEM₅₀ buffer + 100 μM GTP (PEM₅₀G buffer) is passed through the column as the final step in the equilibration process. The pH of the filtrate is checked after it has passed through the column and compared to the pH of the buffer. Equilibration is continued until the pH of the emerging filtrate is the same as the starting buffer. The buffer on top of the column is drained to the top of the resin bed, being careful not to let the column dry out. The C₂S is loaded onto the top of the phosphocellulose resin bed and allowed to flow completely into the resin bed. Six to ten milliliters of PEM₅₀G buffer is layered on top of the resin bed, a reservoir with 175 ml of PEM₅₀G buffer is attached to the column, and the column is developed, collecting 2–3 ml fractions. The phosphocellulose-purified tubulin (PC-Tu) will begin to elute from the column around 40 ml and should be completely eluted from the column by 100 ml (Fig. 2). The protein-containing fractions consisting of pure PC-Tu are pooled, placed on ice, and concentrated from approximately 1.5–2 mg/ml to 7–10 mg/ml. We use an Amicon Ultra 15 Centrifugal Filter device (Millipore Corp, Billerica, MA) with a 30,000 molecular weight cut-off and a Sorvall super-speed centrifuge with an SS-34 rotor equipped with a lidless run device to concentrate the PC-Tu. The concentrated PC-Tu is collected and 100 μM GTP and 1 mM MgSO₄ are added. The PC-Tu concentration is determined and the solution is drop-frozen in liquid nitrogen (previously described). The PC-Tu can be stored as frozen beads in an ultracold freezer at –70°C for at least 1 year without loss of assembly capability. A typical elution profile is shown in Fig. 2.

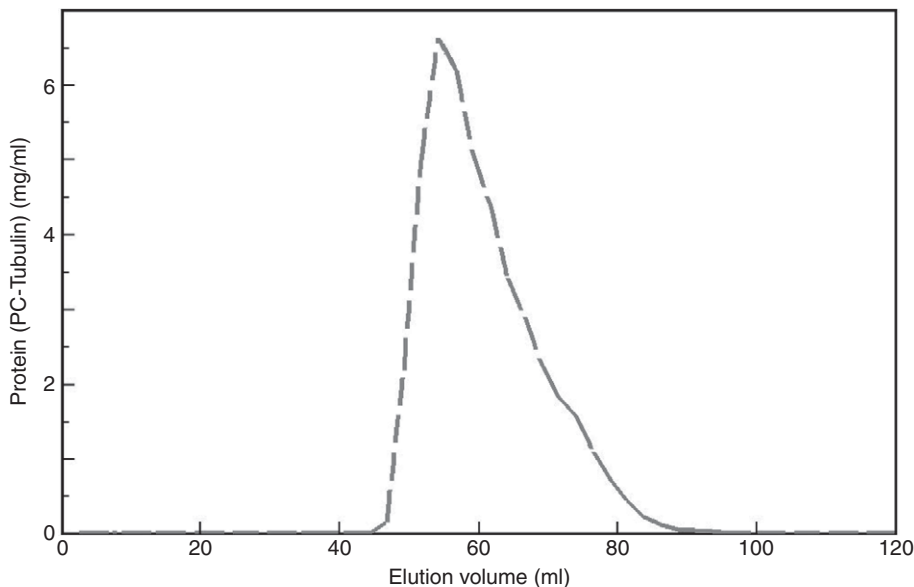


Fig. 2 Typical elution profile of tubulin from a 100-ml phosphocellulose column equilibrated in PEM50G buffer and loaded with 150 mg of microtubule protein, C₂S. Ninety-nine percent of the protein in the entire peak is tubulin.

PAGE gels showing the CBE, the MTP, and PC-Tu (α - and β -tubulin are labeled) are shown in Fig. 3. Typical yields at various steps are shown in Table I.

D. Characteristics and Polymerization Properties of Purified Proteins

The MTP, C₃S, after being stored in a -70°C freezer for 13 months, self-assembles into microtubules robustly, displaying quick self-nucleation as the temperature is raised from 0 to 30°C , followed by rapid elongation and eventual attainment of a stable polymer mass plateau (Fig. 4, solid line). As a rule, the composition is \sim 70–75% tubulin and 20–25% MAPs.

For efficient polymerization of PC-Tu (Fig. 4, dashed line), assembly should be initiated by addition of nucleating seeds. The seeds we use consist of short glycerol-/DMSO-stabilized microtubules. For the assembly curve shown in Fig. 4, we used PC-Tu that had previously been stored for 15 months in a -70°C freezer. The seeds were prepared as follows. Ten percent of the PC-Tu solution to be assembled was removed and to it was added a total of 20% glycerol and 10% DMSO. The solution was warmed to 30°C and incubated for 20–30 min to assemble microtubules. The microtubules were then sheared by passing the suspension three times through a 25-gauge needle to reduce the microtubule mean length to \sim 5 μm and to increase the microtubule number concentration. After 10 min of additional incubation to allow the microtubules to reattain a stable polymer mass steady state, the seeds were ready to nucleate microtubule polymerization. The original 10% volume of the microtubule seed suspension was then added back to the remaining 90% of the PC-Tu sample (prewarmed to 30°C) to nucleate microtubule polymerization in the remaining

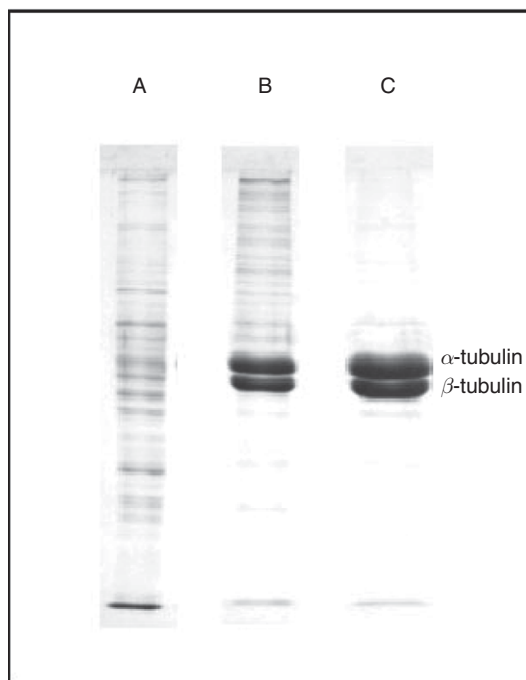


Fig. 3 SDS PAGE of crude brain extra (CBE) and purified proteins. Lane A is the CBE. Lane B is purified microtubule protein after three cycles of assembly and disassembly and passage through a sucrose cushion. Lane C is phosphocellulose-purified tubulin. Ten micrograms of protein was loaded onto each lane and the developed gel was stained with Coomassie Blue. Note the separation between α - and β -tubulin, which is accomplished by using Sigma L-5750 as the source of SDS.

Table I
Protein Yields in Typical Preparations Starting with Two Brains

Step	Protein (mg/ml)	Volume (ml)	Total protein (mg)
Wet brain weight			562,000
CBE	15.8	930	14,700
H ₁ P			980
C ₁ S	9.6	64	600
H ₂ P			360
C ₂ S	23	12	280
H ₃ P			210
C ₃ S	11	18	200
PC-Tu	11	14	150

sample. The final glycerol concentration was 2% and the final DMSO concentration was 1%. The nucleated microtubules elongated efficiently and achieved a stable polymer mass (Fig. 4, dotted line). The difference in overall absorbance between the MTP microtubule sample and the PC-Tu microtubule sample is indicative of the polymer mass and reflective of the difference in the tubulin critical concentration for assembly of the two samples.

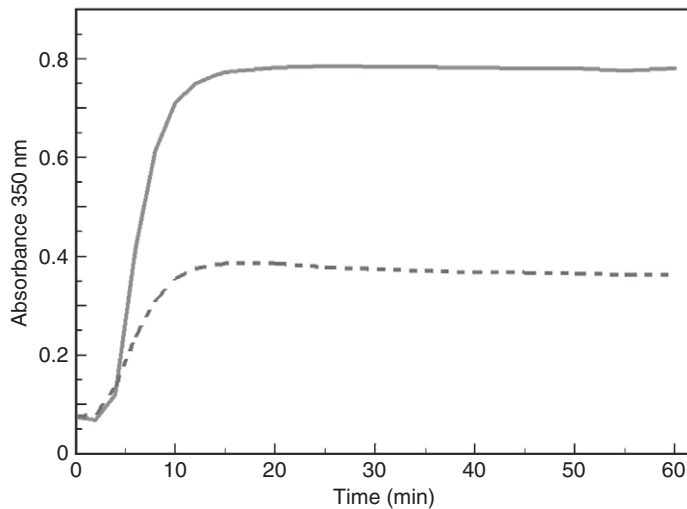


Fig. 4 Polymerization characteristics of purified proteins as determined turbidimetrically (350 nm). MTP, 19 μ M tubulin, *solid line*, and 18 μ M PC-Tu, *dashed line*. Proteins were polymerized at 30°C in PEM buffer. The MTP was self-nucleated, whereas assembly of PC-Tu was initiated by addition of microtubule nucleating seeds.

III. Buffer Compositions

L-GNPEM buffer plus DTT, pH 6.85
 100 mM sodium glutamate
 20 mM sodium phosphate
 1 mM EGTA
 0.5 mM $MgCl_2$
 1 mM DTT (added at the time of use)

L-GNEPEM buffer, pH 6.75
 100 mM sodium glutamate
 20 mM sodium phosphate
 1 mM EGTA
 0.5 mM $MgCl_2$

PEM buffer, pH 6.8
 100 mM PIPES
 1 mM EGTA
 1 mM $MgSO_4$

PEM50 buffer, pH 6.8
 50 mM PIPES
 1 mM EGTA
 1 mM $MgSO_4$

10 \times PEM50 buffer, pH 6.8
 500 mM PIPES
 1 mM EGTA
 1 mM $MgSO_4$

PEM50G buffer, pH 6.8
50 mM PIPES
1 mM EGTA
1 mM MgSO₄
100 mM GTP

IV. Concluding Comments

The methods we have described here for isolation of MTP and purified tubulin from bovine brain in the absence of assembly-promoting solvents have been used for a great many years in our laboratory. Mammalian brain has been an extremely valuable source of polymerization-competent tubulin for many experimental applications in cell and molecular biology. While the basic strategy for warm polymerization and cold depolymerization cycling has changed little, the specific steps and buffer conditions (e.g., GTP concentration, pH values to use) have been fine-tuned and refined extensively to optimize yields and purity. We have tried to be as thorough as possible in indicating critical steps and ensuring that the protocols are as simple as possible to follow. Finally, we want to emphasize that there is a considerable variation in the tubulin and MAP contents of mammalian tissues and, especially, among tissues from different eukaryotic organisms. Thus, the procedures described here may need to be substantially modified, or may not work at all, for many tissues or species.

Acknowledgments

This study was supported by USPHS Grant NS13560. Many individuals have contributed to the refinement of the protocols described here. While we are unable to cite them all, we especially want to acknowledge the contributions of Drs. Clara Asnes, Kevin Sullivan, Kevin Farrell, and Aileen Morse.

References

Andreu, J.M. (2007). Large scale purification of brain tubulin with the modified Weisenberg procedure. *Methods Mol. Med.* **137**, 17–28.

Asnes, C.F., and Wilson, L. (1979). Isolation of bovine brain microtubule protein without glycerol: Polymerization kinetics change during purification cycles. *Anal. Biochem.* **98**, 64–73.

Bamburg, J.R., Shooter, E.M., and Wilson, L. (1973). Developmental changes in microtubule protein of chick brain. *Biochemistry* **12**, 1476–1482.

Bellocq, C., Andrey-Tornare, I., Paunier Doret, A.-M., Maeder, B., Paturle, L., Job, D., Haiech, J., and Edelstein, S.J. (2005). Purification of assembly competent tubulin from *Saccharomyces cerevisiae*. *Eur. J. Biochem.* **210**, 343–349.

Borisy, G.G., Marcum, J.M., Olmsted, J.B., Murphy, D.B., and Johnson, K.A. (1975). Purification of tubulin and associated high molecular weight proteins from porcine brain and characterization of microtubule assembly *in vitro*. *Ann. N. Y. Acad. Sci.* **253**, 107–132.

Detrich, H.W., III, and Wilson, L. (1983). Purification, characterization, and assembly properties of tubulin from unfertilized eggs of the sea urchin *Strongylocentrotus purpuratus*. *Biochemistry* **22**, 2453–2462.

Farrell, K.W. (1982). Purification and reassembly of tubulin from outer doublet microtubules. *Methods Cell Biol.* **24**, 61–75.

Lee, J.C., and Timasheff, S.N. (1975). The reconstitution of microtubules from purified calf brain tubulin. *Biochemistry* **14**, 5183–5187.

Murphy, D.B. (1982). Assembly-disassembly purification and characterization of microtubule protein without glycerol. *Methods Cell Biol.* **24**, 31–50.

Newton, C.N., DeLuca, J.G., Himes, R.H., Miller, H.P., Jordan, M.A., and Wilson, L. (2002). Intrinsically slow dynamic instability of HeLa cell microtubules *in vitro*. *J. Biol. Chem.* **277**, 42456–42462.

Panda, D., Miller, H.P., and Wilson, L. (1999). Rapid treadmilling of MAP-free brain microtubules *in vitro* and its suppression by tau. *Proc. Natl. Acad. Sci. U.S.A.* **96**, 12459–12464.

Schlinstro, M.J., Bayley, P.M., and Martin, S.R. (1991). The effects of solution composition on microtubule dynamic instability. *Biochem. J.* **277**, 839–847.

Sloboda, R.D., and Belfi, L.M. (1998). Purification of tubulin and microtubule-associated proteins by membrane ion-exchange chromatography. *Protein Expr. Purif.* **13**, 205–209.

Williams, R.C., Jr., and Lee, J.C. (1982). Preparation of tubulin from brain. *Meth. Enzymol.* **85** (pt B), 376–385.

CHAPTER 2

Isolating Tubulin from Nonneural Sources

Dan L. Sackett^{*}, Karl A. Werbovetz[†], and Naomi S. Morrissette[‡]

^{*}Laboratory of Integrative and Medical Biophysics, Program in Physical Biology, Eunice Kennedy Shriver National Institute of Child Health and Human Development, National Institutes of Health, Bethesda, Maryland 20892

[†]Division of Medicinal Chemistry and Pharmacognosy, The Ohio State University, Columbus, Ohio 43210

[‡]Department of Molecular Biology and Biochemistry, University of California, Irvine, California 92697

Abstract

- I. Why Tubulin from Nonneural Sources?
- II. General Principles of Tubulin Purification
- III. Specific Properties of Distinct Nonneural Sources
 - A. Metazoan Sources (e.g., Tissue Culture Cells, Chicken Red Blood Cells)
 - B. *Tetrahymena thermophila*
 - C. Kinetoplastid Parasites (*Leishmania*, *Trypanosoma*)
 - D. *Saccharomyces cerevisiae*
 - E. Land Plants
- IV. Genetic Manipulation of Tubulin Genes
 - A. Genetic Manipulation of Tubulin Genes in *S. cerevisiae*
 - B. Genetic Manipulation of Tubulin Genes in *T. thermophila*
- V. Isolation of Tubulin: Theme and Variation
- VI. Protocol Notes
- VII. Summary
- Acknowledgments
- References

Abstract

Tubulin is a highly conserved, negatively charged protein that is found in essentially all eukaryotic cells. These properties ensure that isolation protocols successful in one system will likely work, with a few modifications, in most systems. Tubulin has been isolated most frequently from mammalian brain, and the main difference encountered in other systems versus brain is that tubulin is much less abundant in nearly all other sources than it is in brain. This means that attempting to purify

tubulin by direct polymerization from a homogenate will often fail or be quite inefficient. However, the conservation of negative charge on tubulin means that an initial ion exchange step can be used to both purify and concentrate the protein from most systems. Polymerization-competent tubulin can usually be obtained by inducing polymerization in the salt eluate from the ion exchange step. We describe protocols for this procedure and describe its application to a number of vertebrate, fungal, protozoal, and plant sources.

===== I. Why Tubulin from Nonneuronal Sources?

Although researchers have isolated tubulin from a large variety of organisms ranging from yeast to sea urchin to higher land plants, the source of pure tubulin for most biochemical assays is clearly vertebrate brain (Borisy *et al.*, 1974; Farrell and Wilson, 1978; Morejohn and Fosket, 1982). Neurons contain abundant microtubules, and cow or pig brains obtained from slaughterhouses represent an economical and straightforward source for tubulin. However, researchers may have a variety of critically important reasons to exploit tubulin purified from alternative sources. These include characterization of tubulin isoforms that are distinctly expressed in nonneuronal cells or tissues such as flagellar-specific isoforms or altered tubulin expression in cancer cells (Aoki *et al.*, 2009; Banerjee, 2002; Cucchiarelli *et al.*, 2008; Galmarini *et al.*, 2008; Kemphues *et al.*, 1979; Kimble *et al.*, 1990; Ohishi *et al.*, 2007; Rao *et al.*, 2001; Rawlings *et al.*, 1992; Shalli *et al.*, 2005; Verdier-Pinard *et al.*, 2003). Another reason is a need for a tubulin sample containing fewer isoforms and fewer posttranslational modifications (PTMs) than the notoriously complex brain tubulin (Williams *et al.*, 1999). Tubulin from cultured cell lines selected for resistance to particular drugs might be sought in order to study the binding site for the drugs (Sackett *et al.*, 1997). Moreover, there may be a need to work with tubulin from specific species to characterize small molecule activity that is specifically directed to phylogenetically restricted tubulin subsets, such as the activity of the benzimidazoles (benomyl, albendazole, and mebendazole) on helminth and fungal tubulins or the action of dinitroanilines on plant and protozoan tubulins (Gill and Lacey, 1992; Hugdahl and Morejohn, 1993; Morejohn *et al.*, 1987). Lastly, genetically tractable unicellular eukaryotes such as *Saccharomyces cerevisiae* or *Tetrahymena thermophila* can be used to express tubulins with directed mutations for characterization in biochemical assays (Callahan *et al.*, 1984; Gaertig *et al.*, 1995; Gupta *et al.*, 2003, 2002). In this chapter, we discuss alternative sources of tubulin and how to purify tubulin dimers from these other sources.

===== II. General Principles of Tubulin Purification

The principal consideration in developing a method for purifying tubulin from most nonneuronal sources is the relatively low concentration of tubulin in the cell or tissue extract, compared to that found in brain homogenate. While tubulin can be assembled directly from clarified brain homogenate, it is inefficient or impossible to use induced polymerization as a first step to purify tubulin from these alternative sources. Instead, the first step following preparation of a clarified homogenate is to

concentrate tubulin while also effecting purification without microtubule assembly. Anion exchange chromatography is well suited to both of these roles. A benefit of using chromatography to isolate and concentrate tubulin is that cells can be lysed in a much larger volume, since there is no need to maintain a critical concentration for tubulin. While the details of each step in the protocol that follows may need to be adjusted somewhat for each source material, the general methods are the same. Rather than attempting to describe one exact protocol applicable to all source materials, we will outline a general series of steps and discuss the parameters to consider when applying this general protocol to a particular situation. The essential tubulin purification protocol entails these steps:

1. *Homogenize* cells/tissues to release soluble tubulin into an appropriate buffer
2. *Clarify* the tubulin-containing extract by centrifugation
3. *Isolate* tubulin from the extract by anion exchange chromatography
4. *Concentrate* tubulin eluted from the anion exchange material
5. *Polymerize* the tubulin and pellet microtubules
6. Adjust the *tubulin concentration*, aliquot, and *store* at -80°C or lower

We will discuss each of these procedures in greater detail in Section VI.

III. Specific Properties of Distinct Nonneuronal Sources

A. Metazoan Sources (e.g., Tissue Culture Cells, Chicken Red Blood Cells)

Nonneuronal sources of metazoan tubulin have included tissue culture cells, nucleated erythrocytes, and various tissues or organs. This list includes tissues such as liver (Jennett *et al.*, 1987) and testis (Lessman, 1993); specialized cells such as human lymphocytes (Liebes *et al.*, 1980), mammalian platelets (Castle and Crawford, 1978; Ikeda and Steiner, 1978), avian erythrocytes (Murphy, 1991), surf clam oocytes (Suprenant and Rebhun, 1984), sea urchin sperm (Shelanski and Taylor, 1968); and tumor cells cultured in monolayer (Sackett *et al.*, 1997) and ascites (Doenges *et al.*, 1977). These materials can be obtained in a variety of ways, but will eventually feed into the same protocol following homogenization. In all cases, the steps needed are to obtain and wash sufficient material for the prep and efficiently disrupt the washed cells to release soluble tubulin.

Tissue culture cells are in principle a good source for tubulin since they may express isotypes or bear PTMs of specific interest in the particular cells under study (Sackett, 1995; Sackett *et al.*, 1991, 1997). The main problem with tissue culture cells as a source of tubulin is obtaining sufficient starting material. A small-scale preparation with 1 g of cells to start can yield about 0.5 mg of tubulin, which is $\sim 0.5\%$ of the total protein. To obtain the starting material, cells are grown under appropriate culturing conditions, harvested from flasks, pelleted in a centrifuge, washed once with PBS, resuspended in an equal volume of PME buffer (see below), snap frozen on dry ice, and stored at -80°C or in liquid nitrogen. A typical T₇₅ flask with a confluent (adherent) mammalian cell line can yield about 10^7 cells, and 1 g = $\sim 2 \times 10^8$ cells, so many flasks will be required for a tubulin preparation of any size. Frozen cell pellets can be accumulated until sufficient material is obtained; we found no problem keeping the pellets frozen for extended periods of time, as we

earlier found for brain tissue which had been frozen quickly and stored appropriately (Sackett *et al.*, 1991).

Red blood cells (RBCs) have been used as a source of tubulin due to the nearly single isotype nature of the protein obtained (Murphy, 1991). The original description of this isolation used chicken blood obtained at a slaughterhouse, but we have found that washed, packed RBCs from PelFreez (Rogers, AR) are a suitable alternative. These preparations are shipped so that they arrive on ice the morning after initial collection, and this time delay seems not to cause a problem.

B. *Tetrahymena thermophila*

T. thermophila is easily grown in large volumes of a simple inexpensive media (Sequestrene proteose peptone, SPP) at either room temperature or 30°C. We typically grow 6 l of culture at a time to isolate tubulin dimers; each 2-l flask contains 1 l of media and is inoculated with 30 ml of a starter culture ($\sim 2 \times 10^4$ cells/ml). Healthy growth of cultures requires good aeration (150 rpm on a rotary shaker). For optimal tubulin recovery, it is important to collect the cultures before they reach late log phase (no more than $\sim 4 \times 10^5$ cells/ml) since log phase cultures secrete tetrain, a cysteine protease that effectively degrades tubulin (Suzuki *et al.*, 1998). Pelleted *Tetrahymena* can be frozen overnight or for up to 2 months before tubulin purification (-80°C).

C. Kinetoplastid Parasites (*Leishmania*, *Trypanosoma*)

The purification of assembly-competent tubulin from *Leishmania* is simplified by the fact that tubulin constitutes an estimated 11% of the total cellular protein in the promastigote stage of this parasite (Fong and Chang, 1981). However, the large-scale growth of *Leishmania* species that are pathogenic to humans is undesirable due to biosafety concerns and because the media required for culturing these parasites to high cell densities is expensive. We have found that tubulin purified from *Leishmania tarentolae*, a species of *Leishmania* that infects reptiles rather than humans, is an attractive alternative. Higher cell densities can be achieved with *L. tarentolae* (up to 2×10^8 parasites/ml) (Morgan *et al.*, 2008; Yakovich *et al.*, 2006) compared to pathogenic species such as *Leishmania amazonensis* (up to 5×10^7 parasites/ml) (Werbovetz *et al.*, 1999). Also, *L. tarentolae* is grown in relatively inexpensive brain heart infusion medium supplemented with hemin, while culturing pathogenic *Leishmania* species to high cell densities typically requires Schneider's *Drosophila* medium containing up to 20% fetal bovine serum. The *L. tarentolae* α - and β -tubulin amino acid sequences are >98 and $>96\%$ identical to those found in pathogenic *Leishmania* species, respectively, and the susceptibility of *L. tarentolae* tubulin to antimitotic dinitroanilines is indistinguishable from that of the *L. amazonensis* protein (Yakovich *et al.*, 2006).

Cultures of *L. tarentolae* can be passed in standard T₂₅ flasks at 25°C and transferred to 2 l flasks for large-scale growth on a shaker incubator set to 125 rpm and 25°C (Yakovich *et al.*, 2006). We have not experienced decreased tubulin yields from cultures grown to late log phase and typically allow the parasites to reach this growth stage prior to harvesting the organisms by centrifugation at $1200 \times g$ and 4°C. After washing the organisms with PBS, cell pellets can be stored at -80°C until use. The purification of assembly-competent tubulin from *Trypanosoma brucei* has

been reported by MacRae and Gull (MacRae and Gull, 1990), and our isolation of tubulin from *Leishmania* species (Morgan *et al.*, 2008; Werbovetz *et al.*, 1999; Yakovich *et al.*, 2006) was based on their protocol. Since MacRae and Gull reported that *T. brucei* procyclic parasites were cultured to a density of $2\text{--}4 \times 10^7$ cells/ml in medium containing 10% serum, we speculate that it would be more challenging to conduct large-scale tubulin purification from trypanosomes.

D. *Saccharomyces cerevisiae*

Purification of tubulins from budding yeast was first accomplished in 1981 by John Kilmartin who purified assembly-competent dimers from 50 g of pelleted cells using diethylaminoethyl (DEAE)-Sephadex to isolate tubulin from other cytosolic proteins and ammonium sulfate to concentrate the column eluate (Kilmartin, 1981). These samples were assembled into microtubules for electron microscopy and used in assembly assays to assess the effects of colchicine and benomyl on tubulin polymerization. The technique was further optimized by Barnes, Louie, and Botstein, who purified *S. cerevisiae* tubulin with copurifying microtubule associated proteins (Barnes *et al.*, 1992) and by Davis *et al.*, who purified tubulin for biochemical analysis (Davis *et al.*, 1993). Himes and colleagues have purified tubulins with directed mutations for characterization *in vitro* (Gupta *et al.*, 2002, 2003) and recently, tubulin has been purified from fission yeast (*Schizosaccharomyces pombe*) for biochemical assays (des Georges *et al.*, 2008).

There are many advantages to working with yeast (genetic tractability and ease of growth); however, the yeast cell wall and the relatively low concentration of tubulin dimers in budding yeast require starting with a large amount of packed cells and working to ensure that as many cells are disrupted as is possible. Growth in rich media (yeast extract peptone dextrose, YPD) is best for tubulin purification; bulk cultures that have reached late log or stationary phase after overnight growth can be supplemented with additional 2% glucose and allowed to grow for several more hours (Gupta *et al.*, 2002). This strategy achieves the dual purpose of providing additional starting material and getting the yeast out of late log/stationary phase, where their cell walls are harder to disrupt (Mohan Gupta, personal communication). Pelleted and washed yeast is stored at 4°C overnight to destabilize the microtubules prior to tubulin purification. Researchers have purified yeast tubulin from 500 g to >2 kg of packed wet cells. This can yield ~ 5 mg pure tubulin from 500 g of packed wet cells (Gupta *et al.*, 2002, 2003). Yeast cell wall disruption can be carried out enzymatically or, for larger amounts, mechanically, using a bead beater, coffee grinder, or microfluidics device with on-going monitoring to ensure that $>95\%$ of the cells are disrupted.

E. Land Plants

Assembly-competent plant tubulin dimers were first isolated from cultured cells of Paul's Scarlet rose by Morejohn and Foskett (Morejohn and Fosket, 1982). Tubulin has also been isolated from plant tissues, but isolation of material from tissues is more problematic than isolation of tubulin from cultured cells due to polyphenol secondary metabolites which can cause protein crosslinking and compromise the quality of recovered tubulin. One strategy to reduce secondary metabolites is to use

plants grown in the dark; etiolation is associated with decreased polyphenolic production (Davies, 1972). However, the best solution is to use cultured plant cells, which are low in secondary metabolites. Cultured cells in early exponential growth are preferable since cellular proteins are being synthesized rapidly and polyphenolic compounds are at their lowest concentrations (Davies, 1972; Morejohn and Fosket, 1982). Assembly-competent plant tubulin dimers can be isolated from a variety of cultured plant cells including carrot (*Daucus carota*) (Dawson and Lloyd, 1985; Morejohn *et al.*, 1984), hibiscus (*Hibiscus rosa-sinensis*) (Morejohn *et al.*, 1984), and tobacco (*Nicotiana tabacum*) (Yadav and Filner, 1983). To maximize success, choose a nonpigmented cell culture (e.g., cells cultured in the dark or cell types that lack pigment production) and be sure the culture has a high percentage of actively dividing cells. Before starting tubulin isolation check the health of the plant culture under the microscope. Living cells have centrally located nuclei with distinct cytoplasmic strands and the cytoplasm appears smooth in texture. In contrast, dead and dying cell nuclei are appressed to the side of the cell; they lack cytoplasmic strands and the cytoplasm appears rough in texture (Richard Cyr, personal communication).

Different plant cells have diverse properties and grow at distinct rates. For example, BY2 cells (tobacco) grow quickly, requiring subculturing each week, whereas most *Arabidopsis* cultures grow more slowly and only require subculturing every other week. Cells such as carrot that have a dense cytoplasm resembling the apical meristem are superior to cells such as BY2 that have a parenchymal character (less cytoplasm and more vacuole) for protein purification since greater cytoplasm per cell provides more total protein for purification. Cells that grow faster also tend to have more recoverable tubulin. A good beginning strategy is to grow 100 ml cultures in ten 500 ml Erlenmeyer flasks to mid-log phase (e.g., 3–4 days for BY2 cells). It is possible to scale up to as many as 120 flasks for a single isolation. Plant cell collection requires porous cloth with a biased weave such as the backing material used for furniture upholstery or Miracloth (sold by Calbiochem, La Jolla, CA). Three sheets of cloth are arranged at 90° to each other to construct a collection filter which is seated into a large Erlenmeyer flask. Cells are retained by the cloth and excess culture media is removed by wringing the cloth. Isolated cells should be rinsed in ice-cold PM buffer to remove secreted factors that adversely affect protein purification. Cells from the wrung-out cloth should be weighed so that PME can be added at a ratio of 2 ml per 3 g of cells. After the suspended cells are >95% disrupted (see later), centrifuge the lysate at 4°C for 20 min at 7000 × g. Remove the floating lipid layer, collect the supernatant, and centrifuge a second time at 48,000 × g for 30 min. Skim additional floating lipids and pool the supernatant for application to a DEAE column (Richard Cyr, personal communication).

IV. Genetic Manipulation of Tubulin Genes

A. Genetic Manipulation of Tubulin Genes in *S. cerevisiae*

S. cerevisiae has been used to extensively dissect tubulin function by generation of either spontaneous or directed mutations to α-, β-, or γ-tubulin. Budding yeast has two α-tubulin genes, *TUB1* and *TUB3*, and a single β-tubulin gene, *TUB2* (Neff

et al., 1983; Schatz *et al.*, 1986a). *TUB1* and *TUB2* are essential genes, but *TUB3* can be deleted without loss of viability, although the *tub3* null has some meiotic/sporulation defects (Schatz *et al.*, 1986b). Well-established methods allow researchers to delete essential genes in *S. cerevisiae* by supplying a copy of the gene in *trans* on a nonintegrating plasmid that segregates as a minichromosome. These strains can be used to test the effects of mutant forms of the gene in the absence of the wild-type gene by performing a “plasmid shuffle” which uses positive and negative selectable markers to simultaneously select for transformation of a second plasmid that carries an altered allele and selects against the original complementing plasmid containing the wild-type allele (Boeke *et al.*, 1987; Caron *et al.*, 2001; Schatz *et al.*, 1988). If altered α - or β -tubulin alleles can be shuffled into yeast with chromosomally deleted copies of the gene, the resulting strain can be used to purify a homogeneous population of tubulin with an altered amino acid sequence.

An alternative strategy to express altered tubulins in yeast is to generate a tubulin gene replacement in diploid cells. This is accomplished by linking an altered tubulin gene to a marker which permits selection for homologous integration into one of the two copies of the tubulin gene. In the case that sporulation yields four viable haploids, the cells that bear the gene replacement as the sole source of tubulin can be isolated by tetrad dissection. These cells express a homogeneous population of tubulin bearing the directed mutation. In the case that the diploid is viable but the sporulated haploid mutant is not, mutant tubulins coexpressed with wild-type tubulin can be purified to homogeneity using an affinity tag such as a carboxy-terminal His₆ tag. Himes and colleagues used a gene replacement strategy to examine the effect of mutations to C354 of β -tubulin on microtubule dynamics (Gupta *et al.*, 2002) and to probe the binding site amino acid requirements for tubulin–taxol interactions (Gupta *et al.*, 2003). In both studies, the haploid mutant lines were viable, permitting isolation of homogeneous tubulin populations without purification away from wild-type tubulin dimers.

B. Genetic Manipulation of Tubulin Genes in *T. thermophila*

One of the original biochemical sources for tubulin is the free-living protozoan *T. thermophila*; tubulin was first purified from *Tetrahymena* in 1976 (Kuriyama, 1976). *Tetrahymena* is a ciliate, with an abundant microtubule cytoskeleton. In addition to its ease of growth and abundant tubulin, *Tetrahymena* is genetically tractable, containing a single, essential α -tubulin gene (*ATU1*) and two β -tubulin genes (*BTU1* and *BTU2*) which encode identical proteins (only one gene is essential) (Barahona *et al.*, 1988; Callahan *et al.*, 1984; Gaertig *et al.*, 1993). Due to its unusual nuclear organization and life cycle, it is possible to knock out essential genes in *Tetrahymena* and to later select for genes to complement this loss. *Tetrahymena* contains two nuclei: a “germ line” micronucleus which is a transcriptionally silent “backup” copy of the genome and a “somatic” macronucleus which contains the actively transcribed genome. When an essential gene is knocked out in the micronucleus, asexually growing cells are unaffected because they retain the expressed macronucleus copy of the gene. However, when *Tetrahymena* undergo sexual recombination, macronuclei are destroyed and new ones are reconstituted from the micronucleus after meiosis. Therefore, when *Tetrahymena* bearing an essential gene deletion in the micronucleus are forced to undergo sexual recombination, they only

survive if the missing gene is supplied in *trans* for integration into the new macro-nucleus. We have used existing α -tubulin knockout strains (Gaertig *et al.*, 1995; Hai and Gorovsky, 1997) to substitute modified α -tubulin genes in *Tetrahymena*. Modified α -tubulin genes are introduced into mating pairs using a biolistic gene gun and only *Tetrahymena* that successfully integrate this gene copy into the macronucleus survive. We have introduced directed point mutations into the *Tetrahymena* α -tubulin gene that corresponds to amino acid substitutions that are associated with dinitroaniline resistance in the protozoan parasite *Toxoplasma gondii*. The α -tubulin genes bearing these mutations both complement the α -tubulin knockout and confer dinitroaniline resistance in the transformed *Tetrahymena*. We have purified tubulin with single amino acid substitutions that confer dinitroaniline resistance for drug binding and microtubule assembly assays. Tubulin isolated from these engineered strains assembles in the presence of the dinitroaniline oryzalin, while wild-type *Tetrahymena* microtubule assembly is inhibited (N. Morissette and S. Lyons-Abbott, in preparation).

===== V. Isolation of Tubulin: Theme and Variation

You may anticipate using the following equipment:

- Centrifuge
- Water bath (37°C)
- DEAE-Sepharose column
- Peristaltic pump
- Disruption device (e.g., sonicator, microfluidics device, French Press)
- Glass wool
- Tubes, pipettes
- Ultracentrifuge tubes

Buffers for cell lysis, column chromatography, and tubulin assembly are typically simple variations on a physiological buffer (phosphate buffers, MES buffers, etc.) with additional components such as protease inhibitors, potassium chloride, and glutamate for column elution and guanosine triphosphate (GTP) and dimethylsulf-oxide (DMSO) for microtubule assembly.

You may anticipate using the following solutions:

- *PME + P buffer (PME plus protease inhibitors)*
0.1 M Pipes pH 6.9
1 mM MgCl₂
1 mM EGTA (ethylene glycol tetraacetic acid)
- *PME + P column wash buffer*
0.1 M Pipes pH 6.9
1 mM MgCl₂
1 mM EGTA
0.1 M KCl
0.25 M glutamate

If the wash buffer causes tubulin loss of the column, the KCl can be omitted and the pH adjusted to 6.5 as an alternative method of increasing wash stringency.

- *PME + P column elution buffer*
0.1 M Pipes pH 6.9
1 mM MgCl₂
1 mM EGTA
0.3 M KCl
0.75–1.0 M glutamate
- *Microtubule assembly buffer*
2 mM GTP
8% (v/v) DMSO
10 mM MgCl₂
Suspend in 1× PME

Protease inhibitors: Different cell types vary in protease content; therefore, investigators may need to optimize protease inhibitor additions for the lysis and elution buffers. We list a few considerations for specific cell types later.

- *T. thermophila* has a secreted cysteine protease (tetrain) that influences tubulin purification. Effective inhibitors include 1 mM benzamidine, 1 mM 4-(2-aminoethyl) benzenesulfonyl fluoride hydrochloride, 800 nM aprotinin, 50 μM bestatin, 15 μM E64, 10 μM pepstatin, and 25 μg/ml leupeptin.
- *S. cerevisiae* proteolysis does not appear to be a significant issue during tubulin purification. Himes and colleagues supplement lysis buffer with 2 mM phenylmethylsulfonyl fluoride (PMSF) (Gupta *et al.*, 2003).
- *Leishmania major* is known to contain genes encoding 65 cysteine proteases (Ivens *et al.*, 2005; Mottram *et al.*, 2004). In the absence of cysteine protease inhibitors, immunoblotting of *L. amazonensis* lysates prepared by sonication using an anti-α-tubulin antibody indicates the appearance of an approximately 35-kDa band in addition to the expected 50-kDa band. We therefore include 25 μg/ml leupeptin during the lysis, clarification, and chromatography phases of our purification protocol. Serine peptidases are also present in the *Leishmania* genome (Mottram *et al.*, 2004), so benzamidine (1 mM) and PMSF (0.5 mM) are used in these buffers as well.
- Plant cells have proteases and polyphenol oxidase activity which can degrade and crosslink proteins during the purification process. Reducing agents inhibit polyphenol oxidase activity: 15 mM dithiothreitol (DTT) is an effective inhibitor (Moore *et al.*, 1997). If the buffer solution turns brown during extraction (indicating polyphenol oxidase activity) add more DTT to the sample. Abundant protease inhibitors will improve the quality of the isolated tubulin: use antipain, aprotinin, chymostatin, leupeptin, and pepstatin at 10 μg/ml, BAME and TAME at 50 μg/ml, and PMSF at 1 mM. Make stocks of each using the appropriate solvents rather than the commercially available combination tablets. Keep the extraction buffer pH neutral and use Mg²⁺ and EGTA to further inhibit protease activity (Richard Cyr, personal communication).

Step 1. Homogenize cells/tissues

*Methods for disrupting cells vary extensively. Plant cells and budding yeast have cell walls that need to be efficiently broken in order to effectively obtain a cytoplasmic lysate. Protozoans such as *Tetrahymena* and the kinetoplastid parasites have much of their tubulin in stable structures such as flagella/cilia and subpellicular/corset microtubules.*

Devices and methods to disrupt specific cell types are listed below:

- Vertebrate tissues: Tissues are homogenized in 2 ml/g of PME with protease inhibitors appropriate to the particular tissue. Sonication on ice can also be quite effective. Check for the degree of cell lysis by microscopy.
- Avian erythrocytes: Sonication is the usual method of lysis. Packed erythrocytes are resuspended in 2 ml/g of PME and sonicated on ice in 30-s bursts. For volumes of greater than 100 ml, it is important to use the stub horn on the sonicator, rather than the microtip attachment. Lysis can be easily monitored by microscopy.
- *Tetrahymena* disruption: *T. thermophila* ($\sim 2 \times 10^9$ cells, 6 l of mid-log culture) are collected by centrifugation at $2500 \times g$ for 10 min at room temperature and frozen overnight at -80°C . Pellets thawed on ice are resuspended in 40 ml PME + P buffer on ice and sonicated (BioRad, Hercules, CA) with ten 30-s bursts at 25 W and a 2-min cooling interval between each burst.
- *S. cerevisiae* disruption has been carried out using coffee grinders, bead beaters, or by a microfluidics device. The cost-effective coffee grinder method disrupts a 50% slurry of yeast in buffer flash frozen into liquid nitrogen using commercially available grinders. By far the most efficient method of disruption employs a microfluidizer device to treat yeast cells 5–10 times. Disruption of $>95\%$ of the cells is essential to obtain efficient tubulin purification.
- *Leishmania* disruption: extensive sonication is required to liberate tubulin heterodimers from the stable subpellicular and flagellar microtubules present in *Leishmania*. Lysis is carried out on ice employing a probe sonicator set at full power (25 W). We use ten 30-s bursts with 2-min cooling intervals between bursts; additional rounds of sonication do not increase the yield of *Leishmania* tubulin in our experience.
- Plant cell disruption: plant cell walls from different species vary considerably in thickness and therefore may require different methods for disruption. Plant cells can be disrupted by homogenization or by using a basic blender or bead beater. Flash-frozen material can be disrupted using the coffee grinder method described for yeast. Pressure disruption using a French Press at 5000 psi consistently disrupts plant cells and is the best choice, if available. The degree of cell disruption should be monitored by microscopy; it is essential to identify conditions that result in $>90\%$ cell disruption yet leave cell nuclei intact (the presence of nucleoli separated from nuclei indicates that the disruption conditions are unnecessarily harsh). Once suitable disruption conditions are established, it is critical to work quickly and keep the sample ice cold.

Step 2. Clarify the tubulin-containing extract by centrifugation

Once cells are disrupted, the cell suspension is cooled on ice for 30 min, then centrifuged at $40,000 \times g$ for 40 min at 4– 80°C . The decanted supernatant can also be filtered through glass wool to remove particulates prior to loading onto a column for purification.

Step 3. Isolate tubulin from the extract by anion exchange chromatography

Both α - and β -tubulin subunits are slightly acidic, with isoelectric points of approximately 4.8–5.2. They are effectively bound to positively charged resins

such as DEAE-Sepharose until eluted with buffers containing a high salt concentration. *See Section VI, Note 1, for more details about this step.* The clarified homogenate is poured over a preequilibrated column of DEAE-Sepharose or equivalent and the flowthrough collected in fractions. The column is washed with 1 column volume of PME + P wash buffer and then eluted with 2 column volumes of PME+P column elution buffer, again collecting fractions. Most of the tubulin will be in the fractions corresponding to the first column volume of elution, but this should be checked by sodium dodecyl sulfate (SDS) gel. *See Section VI, Notes 2 and 3, for discussion of optimization.*

Step 4. Concentrate tubulin eluted from the anion exchange material

In order for tubulin to assemble after elution, it must be above the critical concentration. Methods to concentrate tubulin include concentration by ammonium sulfate precipitation and concentration in devices that use dialysis filter and centrifugation. For small volumes (<~50 ml) we have found that centrifugal concentrators, such as the conical devices from Pierce (Thermo Scientific, Rockford, IL), are very convenient. For larger volumes, ammonium sulfate precipitation is useful (Andreu, 2007). For this purpose, ammonium sulfate is added to 43% saturation, which is done by adding, with constant stirring on ice, 25.3 g ammonium sulfate per 100 ml solution. If the volume is not too large, the solution may be combined with a saturated solution of ammonium sulfate kept at 4–80–80°C, in the ratio of 2 volumes of saturated ammonium sulfate to 3 volumes of column eluant. In either case, the solution is allowed to stand on ice for at least 10 min after all the solid is dissolved or all of the saturated solution is added. The solution is then centrifuged for 10 min at ~20,000 \times g, the supernatant removed, and the pellet redissolved in a small volume (~2 \times the pellet volume) of 1 M sodium glutamate buffer.

Step 5. Polymerize the tubulin and pellet microtubules

Microtubule assembly from eluted tubulin is induced with GTP and DMSO. Tubulin polymerization is promoted by the sodium glutamate present in the elution buffer or resolubilization buffer. The tubulin solution is incubated at 37°C for 60 min for assembly and then spun at 50,000 \times g at 30°C for 30 min. The pelleted microtubules are resuspended in cold PME buffer (to a concentration of ~10 mg/ml or higher) and further solubilized via probe sonication (ten to thirty ~5-s bursts at 10 W). This tubulin-rich solution is incubated on ice for 30 min and then spun at 50,000 \times g at 4°C for 30 min to remove insoluble contaminants.

Step 6. Adjust the tubulin concentration, aliquot, and store at –80°C or lower

The supernatant containing heterodimeric tubulin is stored at –80°C in 50 μ l aliquots. Alternatively, the solution may conveniently be drop-frozen in liquid nitrogen and stored at –80°C or in liquid nitrogen. Tubulin concentration may be determined by UV absorbance, using extinction for native tubulin of $E_{276} = 1.16 \text{ g/(l/cm)}$, or by dilution in neutral SDS, with extinction $E_{276} = 1.07 \text{ g/(l/cm)}$ (Andreu, 2007). *See Section VI, Note 4, for information on quantifying tubulin in whole cells to assess purification efficacy.*

VI. Protocol Notes

1. For the ion exchange step, it is important that the DEAE be equilibrated and that there be sufficient column material for the preparation that is being loaded onto it. For equilibration, consult the manufacturer for specific details, but a useful general protocol is to wash the resin with 1 volume of 10× loading buffer, followed by 5 volumes of 1× loading buffer. To be certain of equilibration, one should be certain that the pH and conductivity of the final wash buffer are not changed following exposure to the resin, but we have found that this is usually not necessary. The capacity of the column should be considered. These exchangers have a rated capacity of ~50–100 mg of albumin per milliliter of settled bed. We have found that using a volume of exchanger with capacity equal to the total amount of soluble protein in the clarified homogenate is usually a good guideline. In this regard, the yield of protein differs considerably between different starting materials, but a guide is as follows: tissues yield soluble protein ~1–2% of the wet weight of tissue, while cells yield more, ~8–10% of wet weight, although for some cells such as erythrocytes, the yield is even higher, ~20% of wet weight. Finally it is worth noting that the column geometry should be short and squat, since for a given volume of exchanger, added length does not improve separation, but does significantly slow flow.
2. To optimize the prep, it is important to know that all tubulin is being absorbed from the loading solution and to know what volume of elution is sufficient to recover the bulk of tubulin. For both of these, running an SDS gel is a good first step. If the loading solution contains so many other proteins that the tubulin band is unclear, then it may be necessary to do an immunoblot. In either case, the fractions that were collected while loading allow a determination of what volume of solution could be loaded before tubulin began to “break through” in the loading phase. For the elution, it may be sufficient to take all fractions that have $OD_{280} \geq 0.1$ times the highest tube. However, it may be desirable to keep more than this in some cases. For example, the highly glutamylated species will probably be eluted later, so if these are of particular interest it may be necessary to continue to collect fractions beyond the arbitrary cutoff.
3. After the presence of tubulin in column fractions can be demonstrated by gel electrophoresis or immunoblotting, microplate assembly assays can be performed as a fast and routine method to verify the presence of assembly-competent tubulin. These assays, which involve the addition of column fractions, DMSO (to 10% v/v), and GTP (to 1 mM) to PME buffer, provide a more rapid means of identifying tubulin-rich fractions than gel electrophoresis or immunoblotting.
4. It may be useful to quantify the concentration of tubulin per cell in order to have a basic sense of its abundance in order to assess the efficiency of extraction and purification. Prepare cell lysates for your system of choice using a defined number of cells per volume SDS polyacrylamide gel electrophoresis (PAGE) loading buffer in order to be able to load total protein from a set cell number onto a protein gel. Run a dilution series of this lysate along with standards consisting of known amounts of purified tubulin. Purified tubulin at a defined concentration is available from Cytoskeleton, Inc. (Denver, CO). After resolving samples and standards by SDS PAGE blotted to a suitable membrane for immunoblot analysis,

blots should be probed with pan-specific tubulin antibody such as the 1-5-2 mouse anti- α -tubulin monoclonal antibody (available from Sigma, St. Louis MO). The relative intensity of individual samples can be quantified relative to the tubulin standards.

===== VII. Summary

Tubulins are highly conserved proteins found in all eukaryotes, and tubulin dimers from diverse organisms have similar biochemical properties such as GTPase activity, assembly and disassembly properties, and polymer structure. Historically, the bulk of the work characterizing tubulin structure and biochemistry has focused on tubulin from neural sources. Although the high degree of amino acid conservation among α - and β -tubulins allows researchers to draw parallels between vertebrate brain tubulin properties and tubulins from other sources, there are examples of differences in amino acid sequences between tubulin types that impart distinct drug sensitivities or permit specific functions such as construction of the flagellar apparatus. Moreover, in order to understand how tubulin mutations, changes in isoform levels, or PTMs affect the properties of a tubulin population, it is essential to purify tubulin from specific sources to compare its behavior to that observed with the omnipresent brain tubulin samples. The protocol and variations presented here are intended to assist researchers to develop protocols that can be optimized to purify tubulin from diverse nonneuronal sources for such studies.

Acknowledgments

NM would like to thank Mohan Gupta (University of Chicago), Richard Cyr (Pennsylvania State University), and Sally Lyons-Abbott (UCI) for information, comments, and corrections. This work was supported in part by the Intramural Research Program of the Eunice Kennedy Shriver National Institute of Child Health and Human Development, NIH (DLS), and NIH grant AI067981 (NSM).

References

Andreu, J. M. (2007). Large scale purification of brain tubulin with the modified Weisenberg procedure. *Methods Mol. Med.* **137**, 17–28.

Aoki, D., Oda, Y., Hattori, S., Taguchi, K., Ohishi, Y., Basaki, Y., Oie, S., Suzuki, N., Kono, S., Tsuneyoshi, M., Ono, M., Yanagawa, T., and Kuwano, M. (2009). Overexpression of class III beta-tubulin predicts good response to taxane-based chemotherapy in ovarian clear cell adenocarcinoma. *Clin. Cancer Res.* **15**, 1473–1480.

Banerjee, A. (2002). Increased levels of tyrosinated alpha-, beta(III)-, and beta(IV)-tubulin isotypes in paclitaxel-resistant MCF-7 breast cancer cells. *Biochem. Biophys. Res. Commun.* **293**, 598–601.

Barahona, I., Soares, H., Cyrne, L., Penque, D., Denoulet, P., and Rodrigues-Pousada, C. (1988). Sequence of one alpha- and two beta-tubulin genes of *Tetrahymena pyriformis*. Structural and functional relationships with other eukaryotic tubulin genes. *J. Mol. Biol.* **202**, 365–382.

Barnes, G., Louie, K. A., and Botstein, D. (1992). Yeast proteins associated with microtubules *in vitro* and *in vivo*. *Mol. Biol. Cell* **3**, 29–47.

Boeke, J. D., Trueheart, J., Natsoulis, G., and Fink, G. R. (1987). 5-Fluoroorotic acid as a selective agent in yeast molecular genetics. *Methods Enzymol.* **154**, 164–175.

Borisy, G. G., Olmsted, J. B., Marcum, J. M., and Allen, C. (1974). Microtubule assembly *in vitro*. *Fed. Proc. Fed. Amer. Soc. Exp. Biol.* **33**, 167–180.

Callahan, R. C., Shalke, G., and Gorovsky, M. A. (1984). Developmental rearrangements associated with a single type of expressed alpha-tubulin gene in *Tetrahymena*. *Cell* **36**, 441–445.

Caron, J. M., Vega, L. R., Fleming, J., Bishop, R., and Solomon, F. (2001). Single site alpha-tubulin mutation affects astral microtubules and nuclear positioning during anaphase in *Saccharomyces cerevisiae*: Possible role for palmitoylation of alpha-tubulin. *Mol. Biol. Cell* **12**, 2672–2687.

Castle, A. G., and Crawford, N. (1978). The subcellular distribution of [³H]-colchicine-binding activity and tubulin in pig blood platelets. *Thromb. Haemost.* **39**, 386–403.

Cucchiarelli, V., Hiser, L., Smith, H., Frankfurter, A., Spano, A., Correia, J. J., and Lobert, S. (2008). Beta-tubulin isotype classes II and V expression patterns in nonsmall cell lung carcinomas. *Cell Motil. Cytoskeleton* **65**, 675–685.

Davies, M. E. (1972). Polyphenol synthesis in cell suspension cultures of Paul's Scarlet rose. *Planta* **104**, 50–65.

Davis, A., Sage, C.R., Wilson, L., and Farrell, K. W. (1993). Purification and biochemical characterization of tubulin from the budding yeast *Saccharomyces cerevisiae*. *Biochemistry* **32**, 8823–8835.

Dawson, P. J., and Lloyd, C. W. (1985). Identification of multiple tubulins in taxol microtubules purified from carrot suspension cells. *Embo. J.* **4**, 2451–2455.

des Georges, A., Katsuki, M., Drummond, D. R., Osei, M., Cross, R. A., and Amos, L. A. (2008). Mal3, the *Schizosaccharomyces pombe* homolog of EB1, changes the microtubule lattice. *Nat. Struct. Mol. Biol.* **15**, 1102–1108.

Doenges, K. H., Nagle, B. W., Uhlmann, A., and Bryan, J. (1977). *In vitro* assembly of tubulin from nonneuronal cells (Ehrlich ascites tumor cells). *Biochemistry* **16**, 3455–3459.

Farrell, K. W., and Wilson, L. (1978). Microtubule reassembly *in vitro* of *Strongylocentrotus purpuratus* sperm tail outer doublet tubulin. *J. Mol. Biol.* **121**, 393–410.

Fong, D., and Chang, K. P. (1981). Tubulin biosynthesis in the developmental cycle of a parasitic protozoan, *Leishmania mexicana*: Changes during differentiation of motile and nonmotile stages. *Proc. Natl. Acad. Sci. U.S.A.* **78**, 7624–7628.

Gaertig, J., Cruz, M. A., Bowen, J., Gu, L., Pennock, D. G., and Gorovsky, M. A. (1995). Acetylation of lysine 40 in alpha-tubulin is not essential in *Tetrahymena thermophila*. *J. Cell Biol.* **129**, 1301–1310.

Gaertig, J., Thatcher, T. H., McGrath, K. E., Callahan, R. C., and Gorovsky, M. A. (1993). Perspectives on tubulin isotype function and evolution based on the observation that *Tetrahymena thermophila* microtubules contain a single alpha- and beta-tubulin. *Cell Motil. Cytoskeleton* **25**, 243–253.

Galmarini, C. M., Treilleux, I., Cardoso, F., Bernard-Marty, C., Durbecq, V., Gancberg, D., Bissery, M. C., Paesmans, M., Larsimont, D., Piccart, M. J., Di Leo, A., and Dumontet, C. (2008). Class III beta-tubulin isotype predicts response in advanced breast cancer patients randomly treated either with single-agent doxorubicin or docetaxel. *Clin. Cancer Res.* **14**, 4511–4516.

Gill, J. H., and Lacey, E. (1992). The kinetics of mebendazole binding to *Haemonchus contortus* tubulin. *Int. J. Parasitol.* **22**, 939–946.

Gupta, M. L., Jr., Bode, C. J., Georg, G. I., and Himes, R. H. (2003). Understanding tubulin-Taxol interactions: Mutations that impart Taxol binding to yeast tubulin. *Proc. Natl. Acad. Sci. U.S.A.* **100**, 6394–6397.

Gupta, M. L., Jr., Bode, C. J., Thrower, D. A., Pearson, C. G., Suprenant, K. A., Bloom, K. S., and Himes, R. H. (2002). beta-Tubulin C354 mutations that severely decrease microtubule dynamics do not prevent nuclear migration in yeast. *Mol. Biol. Cell* **13**, 2919–2932.

Hai, B., and Gorovsky, M. A. (1997). Germ-line knockout heterokaryons of an essential alpha-tubulin gene enable high-frequency gene replacement and a test of gene transfer from somatic to germ-line nuclei in *Tetrahymena thermophila*. *Proc. Natl. Acad. Sci. U.S.A.* **94**, 1310–1315.

Hugdahl, J. D., and Morejohn, L. C. (1993). Rapid and reversible high-affinity binding of the dinitroaniline herbicide oryzalin to tubulin from *Zea mays* L. *Plant Physiol.* **102**, 725–740.

Ikeda, Y., and Steiner, M. (1978). Sulphydryls of platelet tubulin: Their role in polymerization and colchicine binding. *Biochemistry* **17**, 3454–3459.

Ivens, A. C., Peacock, C. S., Worthey, E. A., Murphy, L., Aggarwal, G., Berriman, M., Sisk, E., Rajandream, M. A., Adlem, E., Aert, R., Anupama, A., Apostolou, Z., *et al.* (2005). The genome of the kinetoplastid parasite, *Leishmania major*. *Science* **309**, 436–442.

Jennett, R. B., Sorrell, M. F., Johnson, E. L., and Tuma, D. J. (1987). Covalent binding of acetaldehyde to tubulin: Evidence for preferential binding to the alpha-chain. *Arch. Biochem. Biophys.* **256**, 10–18.

Kemphues, K. J., Raff, R. A., Kaufman, T. C., and Raff, E. C. (1979). Mutation in a structural gene for a beta-tubulin specific to testis in *Drosophila melanogaster*. *Proc. Natl. Acad. Sci. U.S.A.* **76**, 3991–3995.

Kilmartin, J. V. (1981). Purification of yeast tubulin by self-assembly *in vitro*. *Biochemistry* **20**, 3629–3633.

Kimble, M., Dettman, R. W., and Raff, E. C. (1990). The beta 3-tubulin gene of *Drosophila melanogaster* is essential for viability and fertility. *Genetics* **126**, 991–1005.

Kuriyama, R. (1976). *In vitro* polymerization of flagellar and ciliary outer fiber tubulin into microtubules. *J. Biochem.* **80**, 153–165.

Lessman, C. A. (1993). Taxol-induced assembly of brain and testis tubulins, and ovarian follicle tubulin dynamics in the frog (genus *Rana*), *in vitro*. *Comp. Biochem. Physiol. B* **104**, 155–162.

Liebes, L. F., Fleit, H., Zucker-Franklin, D., and Silber, R. (1980). Human lymphocyte tubulin. Purification and characterization in normal and leukemic cells. *Biochim. Biophys. Acta* **633**, 245–257.

MacRae, T. H., and Gull, K. (1990). Purification and assembly *in vitro* of tubulin from *Trypanosoma brucei brucei*. *Biochem. J.* **265**, 87–93.

Moore, R. C., Zhang, M., Cassimeris, L., and Cyr, R. J. (1997). *In vitro* assembled plant microtubules exhibit a high state of dynamic instability. *Cell Motil. Cytoskeleton* **38**, 278–286.

Morejohn, L. C., Bureau, T. E., Molá-Bajer, J., Bajer, A. S., and Fosket, D. E. (1987). Oryzalin, a dinitroaniline herbicide, binds to plant tubulin and inhibits microtubule polymerization *in vitro*. *Planta* **172**, 252–264.

Morejohn, L. C., Bureau, T. E., Tocchi, L. P., and Fosket, D. E. (1984). Tubulins from different higher plant species are immunologically nonidentical and bind colchicine differentially. *Proc. Natl. Acad. Sci. U.S.A.* **81**, 1440–1444.

Morejohn, L. C., and Fosket, D. E. (1982). Higher plant tubulin identified by self-assembly into microtubules *in vitro*. *Nature* **297**, 426–428.

Morgan, R. E., Ahn, S., Nzimiro, S., Fotie, J., Phelps, M. A., Cotrill, J., Yakovich, A. J., Sackett, D. L., Dalton, J. T., and Werbovetz, K. A. (2008). Inhibitors of tubulin assembly identified through screening a compound library. *Chem. Biol. Drug Des.* **72**, 513–524.

Mottram, J. C., Coombs, G. H., and Alexander, J. (2004). Cysteine peptidases as virulence factors of *Leishmania*. *Curr. Opin. Microbiol.* **7**, 375–381.

Murphy, D. B. (1991). Purification of tubulin and tau from chicken erythrocytes: Tubulin isotypes and mechanisms of microtubule assembly. *Methods Enzymol.* **196**, 235–246.

Neff, N. F., Thomas, J. H., Grisafi, P., and Botstein, D. (1983). Isolation of the beta-tubulin gene from yeast and demonstration of its essential function *in vivo*. *Cell* **33**, 211–219.

Ohishi, Y., Oda, Y., Basaki, Y., Kobayashi, H., Wake, N., Kuwano, M., and Tsuneyoshi, M. (2007). Expression of beta-tubulin isotypes in human primary ovarian carcinoma. *Gynecol. Oncol.* **105**, 586–592.

Rao, S., Aberg, F., Nieves, E., Band Horwitz, S., and Orr, G.A. (2001). Identification by mass spectrometry of a new alpha-tubulin isotype expressed in human breast and lung carcinoma cell lines. *Biochemistry* **40**, 2096–2103.

Rawlings, D. J., Fujioka, H., Fried, M., Keister, D. B., Aikawa, M., and Kaslow, D. C. (1992). Alpha-tubulin II is a male-specific protein in *Plasmodium falciparum*. *Mol. Biochem. Parasitol.* **56**, 239–250.

Sackett, D. L. (1995). Rapid purification of tubulin from tissue and tissue culture cells using solid-phase ion exchange. *Anal. Biochem.* **228**, 343–348.

Sackett, D. L., Giannakakou, P., Poruchynsky, M., and Fojo, A. (1997). Tubulin from paclitaxel-resistant cells as a probe for novel antimicrotubule agents. *Cancer Chemother. Pharmacol.* **40**, 228–232.

Sackett, D. L., Knipling, L., and Wolff, J. (1991). Isolation of microtubule protein from mammalian brain frozen for extended periods of time. *Protein Expr. Purif.* **2**, 390–393.

Schatz, P. J., Pillus, L., Grisafi, P., Solomon, F., and Botstein, D. (1986a). Two functional alpha-tubulin genes of the yeast *Saccharomyces cerevisiae* encode divergent proteins. *Mol. Cell. Biol.* **6**, 3711–3721.

Schatz, P. J., Solomon, F., and Botstein, D. (1986b). Genetically essential and nonessential alpha-tubulin genes specify functionally interchangeable proteins. *Mol. Cell. Biol.* **6**, 3722–3733.

Schatz, P. J., Solomon, F., and Botstein, D. (1988). Isolation and characterization of conditional-lethal mutations in the TUB1 alpha-tubulin gene of the yeast *Saccharomyces cerevisiae*. *Genetics* **120**, 681–695.

Shall, K., Brown, I., Heys, S. D., and Schofield, A. C. (2005). Alterations of beta-tubulin isotypes in breast cancer cells resistant to docetaxel. *Faseb J.* **19**, 1299–1301.

Shelanski, M. L., and Taylor, E. W. (1968). Properties of the protein subunit of central-pair and outer-doublet microtubules of sea urchin flagella. *J. Cell Biol.* **38**, 304–315.

Suprenant, K. A., and Rebhun, L. I. (1984). Purification and characterization of oocyte cytoplasmic tubulin and meiotic spindle tubulin of the surf clam *Spisula solidissima*. *J. Cell Biol.* **98**, 253–266.

Suzuki, K. M., Hayashi, N., Hosoya, N., Takahashi, T., Kosaka, T., and Hosoya, H. (1998). Secretion of tetraain, a Tetrahymena cysteine protease, as a mature enzyme and its identification as a member of the cathepsin L subfamily. *Eur. J. Biochem.* **254**, 6–13.

Verdier-Pinard, P., Wang, F., Martello, L., Burd, B., Orr, G. A., and Horwitz, S. B. (2003). Analysis of tubulin isotypes and mutations from taxol-resistant cells by combined isoelectrofocusing and mass spectrometry. *Biochemistry* **42**, 5349–5357.

Werbovetz, K. A., Brendle, J. J., and Sackett, D. L. (1999). Purification, characterization, and drug susceptibility of tubulin from Leishmania. *Mol. Biochem. Parasitol.* **98**, 53–65.

Williams, R. C., Jr., Shah, C., and Sackett, D. (1999). Separation of tubulin isoforms by isoelectric focusing in immobilized pH gradient gels. *Anal. Biochem.* **275**, 265–267.

Yadav, N. S., and Filner, P. (1983). Tubulin from cultured tobacco cells: Isolation and identification based on similarities to brain tubulin. *Planta* **157**, 46–52.

Yakovich, A. J., Ragone, F. L., Alfonzo, J. D., Sackett, D. L., and Werbovetz, K. A. (2006). Leishmania tarentolae: Purification and characterization of tubulin and its suitability for antileishmanial drug screening. *Exp. Parasitol.* **114**, 289–296.

CHAPTER 3

Characterization of Anti- β -tubulin Antibodies

Anthony J. Spano and Anthony Frankfurter

Department of Biology, University of Virginia, Charlottesville, Virginia 22904

Abstract

- I. Introduction
- II. The Characterization of AA2, a Pan-specific Anti- β -tubulin Monoclonal Antibody That Reacts with All Vertebrate β -Tubulin Isotypes (Gene Products)
- III. The Characterization of Isotype-Specific β -Tubulin Monoclonal and Polyclonal Antibodies
- IV. The Characterization of Antibodies That Recognize the Glutamyl Side Chain of Glutamylated Proteins
- V. Summary

References

Abstract

Tubulin antibodies are among the most extensively used immunological reagents in basic and applied cell and molecular biology. In this chapter, we provide a brief overview of the practices and reagents developed in our laboratory during the past 25 years for characterizing anti- β -tubulin antibodies.

I. Introduction

Many of the commercially available anti- β -tubulin antibodies are marketed with minimal information regarding their specificity and the epitopes to which they bind. These shortcomings limit their utility. Here, we describe the characterization of pan-specific and isotype-specific monoclonal and polyclonal anti- β -tubulin antibodies. These antibodies have been used extensively for Western blotting, affinity purification, and immunohistochemistry. We also discuss our more recent efforts to generate and characterize monoclonal and polyclonal antibodies that specifically recognize

glutamylated tubulin. Hopefully, this overview will be useful to investigators interested in producing their own antibodies, as well as to those who depend on commercially available reagents for their research.

===== II. The Characterization of AA2, a Pan-specific Anti- β -tubulin Monoclonal Antibody That Reacts with All Vertebrate β -Tubulin Isotypes (Gene Products)

Pan-specific α - or β -tubulin antibodies are frequently used in Western blot experiments to demonstrate protein abundance relative to tubulin. They are also used extensively to illuminate changes in cell morphology and cytoskeletal organization during development, or as a result of disease, drug treatment, or genetic manipulation. These antibodies are presumed to recognize equally all of the expressed α - or β -tubulin isotypes. A recent report demonstrates that at least one of the widely used commercially available monoclonal antibodies, Tub 2.1, fails to meet this requirement (Yang *et al.*, 2009). Presently, we know of two commercially available pan-specific anti- β -tubulin mouse monoclonal antibodies whose epitopes have been partially mapped, DM1B and AA2. Both antibodies react with epitopes located within the C-terminal domain spanned by amino acids 412–430. This region is the most highly conserved in β -tubulin, in both animal and plant species (Arevalo *et al.*, 1990; Blose *et al.*, 1984; de la Vina *et al.*, 1988; Sullivan, 1988). The sequence of these 31 amino acids is entirely conserved in seven of the eight human β -tubulin isotypes, and with one exception, a conservative substitution, in seven of the eight mouse β -tubulin isotypes (Fig. 1). Only the megakaryocyte-specific class VI β -tubulin isotype (β VI) contains nonconservative substitutions in this region that appear likely to interfere with the binding of either DM1B or AA2.

DM1B was generated with native chick brain tubulin as the immunogen, whereas we generated AA2 with phosphocellulose-purified bovine brain tubulin (Blose *et al.*, 1984). When it became apparent that AA2 recognizes a highly conserved epitope present in vertebrate and nonvertebrate tubulins, we used a bovine serum albumin-conjugated synthetic peptide β (412–430) and a bacterially expressed fusion protein consisting of the maltose-binding protein (MBP) and the extended C-terminal domain of β -tubulin (400–429) to establish that the epitopes for AA2 and DM1B were located in the same region. A Western blot demonstrating the specificity of AA2 is presented in Fig. 2.

The characterization of AA2 exemplifies the procedures that we have employed to characterize isotype-specific tubulin antibodies as well as other proteins.

We use standard procedures to generate mouse monoclonal antibodies, and commercial suppliers to provide rabbit polyclonal antisera (Binder *et al.*, 1985; Caceres *et al.*, 1984). Mouse IgGs are purified from tissue culture supernatants by conventional Protein-G chromatography. Rabbit IgGs are purified first from serum proteins by Protein-A chromatography, and specific IgGs are then isolated by peptide affinity chromatography.

The mouse monoclonal antibodies and the affinity purified rabbit polyclonal antibodies are screened first by enzyme-linked immunosorbent assay (ELISA) to determine their reaction with nondenatured purified bovine or rat brain tubulin. This

Human		400	430
1	MFRRKAFLHWYTGEGMDEMEFTEAESNMNDLVSEYQQYQDATA	EEEEEDFGE	EEAEEEAA
2A	MFRRKAFLHWYTGEGMDEMEFTEAESNMNDLVSEYQQYQDATA	DEQGEF	EEEGEDEA
2B	MFRRKAFLHWYTGEGMDEMEFTEAESNMNDLVSEYQQYQDATA	DEQGEF	EEEGEDEA
3	MFRRKAFLHWYTGEGMDEMEFTEAESNMNDLVSEYQQYQDATA	EEEEGEMYED	DEESEAQGPK
4A	MFRRKAFLHWYTGEGMDEMEFTEAESNMNDLVSEYQQYQDATA	EEEGEDEAEE	EVAA
4B	MFRRKAFLHWYTGEGMDEMEFTEAESNMNDLVSEYQQYQDATA	EEEGEDEAEE	EVAA
5	MFRRKAFLHWFTGEGMDEMEFTEAESNMNDLVSEYQQYQDATA	NDGEAEFED	DEEEIDG
6	MFRRKAFVHWYTSEGMD	IN	EVTEEAEMEPEDKGH

Mouse		400	430
1	MFRRKAFLHWYTGEGMDEMEFTEAESNMNDLVSEYQQYQDATA	EEEEEDFGE	EEAEEEAA
2	MFRRKAFLHWYTGEGMDEMEFTEAESNMNDLVSEYQQYQDATA	DEQGEF	EEEGEDEA
2C	MFRRKAFLHWYTGEGMDEMEFTEAESNMNDLVSEYQQYQDATA	DEQGEF	EEEGEDEA
3	MFRRKAFLHWYTGEGMDEMEFTEAESNMNDLVSEYQQYQDATA	EEEEGEMYED	DEESEAQGPK
4	MFRRKAFLHWYTGEGMDEMEFTEAESNMNDLVSEYQQYQDATA	EEEGEDEAEE	EVAA
5	MFRRKAFLHWFTGEGMDEMEFTEAESNMNDLVSEYQQYQDATA	NDGEAEFED	DEEEINE
6	MFRRKAFVHWYTSEGMD	ISEPGEAESDIH	DLVSEYQQFODVAGLEDSEEDV

Fig. 1 An alignment of the amino acid sequences comprising the extended C-terminal domains of the eight human and eight mouse β -tubulin isotypes. Highlighted residues (gray) indicate the common domain containing the epitopes for the monoclonal antibodies AA2 and DM1B. Residues highlighted in yellow represent non-identical positions within the common domain. (See Plate no. 1 in the Color Plate Section.)

Immunoreactivity of the anti- β -tubulin monoclonal antibody AA2

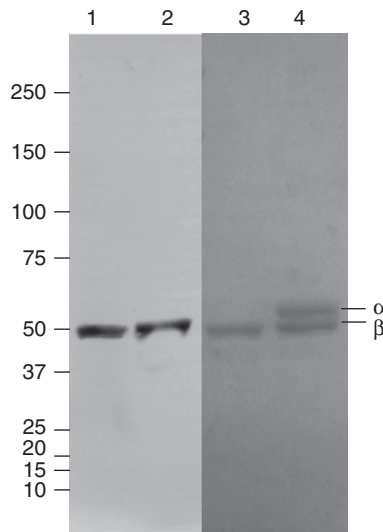


Fig. 2 The anti- β -tubulin pan-specific monoclonal antibody AA2 reacts with an epitope located within the extended C-terminal domain of β -tubulin. MBP-tubulin fusion protein (β -tubulin, amino acids 400–429) (lane 1); purified rat brain β -tubulin (lane 2). Lanes 3 and 4 are the corresponding Coomassie-stained gel bands of protein samples loaded in lanes 1 and 2, respectively.

step is obligatory. We have produced numerous antibodies that react well with the synthetic peptide used as an immunogen, but react weakly or not at all with tubulin. Following this initial screening, we probe a set of bacterially expressed MBP fusion proteins by Western blotting to more precisely determine antibody specificity. The construction of these MBP fusion proteins has been described previously (Hiser *et al.*, 2006).

III. The Characterization of Isotype-Specific β -Tubulin Monoclonal and Polyclonal Antibodies

Our laboratory has produced a number of isotype-specific β -tubulin antibodies that can be used for both biochemical analyses and immunocytochemistry (Bhattacharya *et al.*, 2008; Katsatos *et al.*, 2001; Lee *et al.*, 1990a,b; Moody *et al.*, 1996). Isotype-specific β -tubulin antibodies are in great demand. They are used to determine tubulin isotype abundance, cellular distribution, and subcellular localization during early brain development as well as to identify changes in isotype expression associated with oncogenesis and in response to drug therapy (e.g., Akasaka *et al.*, 2009; Anthony *et al.*, 2004; Arai *et al.*, 2002; Dumontet *et al.*, 2009; Gan and Kavallaris, 2008; Hayashi *et al.*, 2009; Jaglin *et al.*, 2009; Keays *et al.*, 2007; Lee *et al.*, 1990b; Miller *et al.*, 2008; Nakamura *et al.*, 2003; Saussede-Aim *et al.*, 2009; Sugita *et al.*, 2005; Terada *et al.*, 2005; Terry *et al.*, 2009; Wu *et al.*, 2009). For example, there is steadily increasing evidence that the aberrant expression of the neuronal-specific β -tubulin isotype (β III) is correlated with tumorigenesis and increased resistance to chemotherapeutic agents (e.g., Dumontet *et al.*, 2009).

With one exception, all our isotype-specific β -tubulin mouse monoclonal and rabbit polyclonal antibodies were produced with synthetic peptides conjugated to keyhole limpet hemocyanin. Each peptide was identical in sequence to all or a portion of the extreme C-terminal isotype-defining domain of one of the eight human and eight mouse β -tubulin isotypes. The amino acid sequences comprising the entire isotype-defining domains of each β -tubulin isotype (431 to the C-terminus) are shown in Fig. 1. In order to determine antibody specificity by Western blotting, dot blotting, and ELISA, we constructed a set of MBP fusion proteins in which each one of the human and the mouse β -tubulin C-terminal isotype-defining domains is represented (Hiser *et al.*, 2006). These MBP fusion proteins, approximately 45 kDa, offer several important advantages compared to synthetic peptides. They are extremely easy to purify, are highly soluble in aqueous solutions, and adhere well to a solid support. They can also be used as standards for estimating β -tubulin isotype abundance.

A complete list of the isotype-specific anti- β -tubulin monoclonal and polyclonal antibodies that we have produced is shown in Table I. On dot blots and Western blots, each of these antibodies recognizes only purified tubulin and the MBP fusion protein related to the peptide immunogen.

The anti- β II and β III antibodies were generated without any difficulty. In contrast, we have been unsuccessful in producing antibodies that are specific for either β I or β IV. Our antibodies react with both isotypes. This failure may be due to the fact that the sequences of the synthetic peptides used as immunogens are identical to the last

Table I
Immunogens Used for the Generation of β -Tubulin Isotype-Specific Antibodies

Name	S ^a	Isotype	Immunogen ^b	Reference
6B1	m	II	KLH-(C)EEEEGEDEA	Moody <i>et al.</i> (1996)
7B9	m	II	KLH-(C)EEEEGEDEA	Moody <i>et al.</i> (1996)
TTII	r	II	KLH-(C)DEQGEFEEEEGEDEA	Unpublished
TuJ1	m	III	Rat brain tubulin	Lee <i>et al.</i> (1990b)
5G8	m	III	KLH-(C)EAQGPK	Unpublished
2G10	m	III	KLH-(C)MYEDDEEESEAQGPK	Unpublished
TTIII	r	III	KLH-(C)MYEDDEEESEAQGPK	Unpublished
TTVh	r	V	KLH-(C)GGGEIDG	Bhattacharya <i>et al.</i> (2008)
TTVm	r	V	KLH-(C)GGGEINE	Bhattacharya <i>et al.</i> (2008)
6H10	m	VI	KLH-(C)DEEVTEEAEMEPEDKGH	Unpublished

^aS, species; m, mouse monoclonal; r, rabbit polyclonal.

^b(C), cysteine added for maleimide coupling. All polyclonal antibodies were affinity purified using peptide-cyanogen bromide Sepharose.

seven C-terminal amino acids for β I and β IV. These sequences are highly similar, different by a single residue. However, other investigators have been successful. Monoclonal antibodies specific for these two isotypes are commercially available (Banerjee *et al.*, 1992; Roach *et al.*, 1998).

Our first attempt to isolate an anti-human β V also resulted in failure. The immunogen was a synthetic peptide identical to the last C-terminal 20 amino acids of human β V (Fig. 1). All of the selected monoclonal antibodies not only reacted strongly with the β V MBP fusion protein, but also reacted, albeit less strongly, with the β III MBP fusion protein. An alignment of the β III and β V C-terminal isotype-defining sequences indicated that an internal sequence of seven amino acids was the most probable source of the cross-reaction (YEDDEEE/FEDEEEE).

To overcome such potential sources of cross-reaction, we devised a strategy of immunizing with truncated synthetic peptides that minimize the influence of flanking sequences on the immune response to the targeted epitope. For example, to generate specific anti-human β V and anti-mouse β V polyclonal antibodies, we used as immunogens synthetic peptides that are identical to human β V and mouse β V only at the last four C-terminal amino acids, CGGGEIDG and CGGGEINE (Bhattacharya *et al.*, 2008).

More recently, we have used this strategy of immunizing with truncated peptides that minimize the influence of flanking sequences to generate antibodies that recognize the γ -glutamyl link in glutamylated tubulin.

IV. The Characterization of Antibodies That Recognize the Glutamyl Side Chain of Glutamylated Proteins

Tubulin is a substrate for several types of evolutionarily conserved posttranslational modifications: detyrosination and retyrosination, acetylation, phosphorylation, palmitoylation, glutamylation, and glycation (Alexander *et al.*, 1991; Argarana *et al.*, 1977; 1978; Caron, 1997; Edde *et al.*, 1990; Eipper, 1972; Fukushima *et al.*,

2009; Janke *et al.*, 2005; L’Hernault and Rosenbaum, 1985; Ozols and Caron, 1997; Redeker *et al.*, 1994; Rosenbaum, 2000; Westermann and Weber, 2003). Of these posttranslational modifications, three, the detyrosination and retyrosination of α -tubulin and the glycation and glutamylation of α - and β -tubulin, are catalyzed by amino acid ligases belonging to the ATP-grasp superfamily of enzymes (Galperin and Koonin, 1997; Janke *et al.*, 2005).

Our laboratory has a longstanding interest in the glutamylation of brain tubulin (Alexander *et al.*, 1991; Redeker *et al.*, 1998, 2004). Glutamylation is a covalent, reversible modification that results in the formation of a string of glutamate residues linked through the side chain of a glutamate residue in the polypeptide backbone. The number of glutamate residues in the glutamyl side chain can vary considerably. Whereas the initial glutamate residue is added through an obligatory γ -carboxyl link, the remaining residues are added through α -carboxyl links (Redeker *et al.*, 1996). This modification was initially considered unique to tubulin; however, recent evidence indicates that a large, heterogeneous population of proteins is a substrate for glutamylation (Janke *et al.*, 2008; Regnard *et al.*, 2000). In tubulin, the target residues are located in the C-terminal isotype-defining domains. The position of the glutamylation sites in β I, II, III, and IV has been identified by mass spectrometry (Alexander *et al.*, 1991; Mary *et al.*, 1994; Redeker *et al.*, 1992; Rudiger *et al.*, 1992). β V, a minor β -tubulin isotype that is not present in neural tissue, appears to be glutamylated, but the site has not been identified (Verdier-Pinard *et al.*, 2005). The megakaryocyte-specific β -tubulin, β VI, is not a substrate for glutamylation (Rudiger and Weber, 1993). Examples of the structures of monoglutamylated and diglutamylated peptides identical in their primary sequences to the β III and β II C-terminal isotype-defining domains, respectively, are shown in Fig. 3.

The structures of mono- and di-glutamyl branched peptides

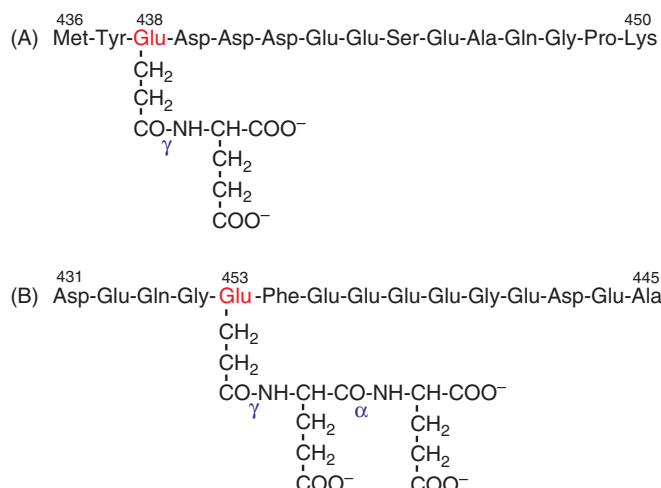


Fig. 3 The structures of a monoglutamyl and a diglutamyl branch are shown. The first glutamate in the branch is added through an obligatory γ -carboxyl peptide bond and the additional glutamate residues are added only through α -carboxyl peptide bonds. There is no evidence indicating that polyglutamylation occurs on any other amino acid. The sequence of the monoglutamylated peptide shown in (A) is identical to the C-terminal isotype-defining domain of mouse class III β -tubulin. The sequence of the diglutamylated peptide shown in (B) is identical to the C-terminal isotype-defining domain of mouse class II β -tubulin.

Of the different tubulins characterized by mass spectrometry, mammalian brain tubulin ranks as perhaps the most extensively glutamylated. More than 96% of the tubulin purified from mature rodent and bovine brain is glutamylated (D. Hunt and A. Frankfurter, unpublished observations). Compared to both adult and neonatal brain tubulin, the proportion of glutamylated tubulin subunits to nonglutamylated tubulin subunits is considerably lower in tubulin from other organs (V. Redeker and A. Frankfurter, unpublished observations). Further, during early postnatal brain development, the proportion of glutamylated α - and β -tubulin subunits increases dramatically, as does the average number of residues in the γ -glutamyl side branch (Redeker *et al.*, 2004). Since, the α - and β -tubulin isoforms expressed in brain are not glutamylated to the same extent, this developmentally regulated posttranslational modification produces in the adult brain an extremely heterogeneous population of glutamylated tubulin subunits. Because there is also evidence that tubulin subunits undergo deglutamylation, by as yet unidentified hydrolases, the process of glutamylation and deglutamylation produces a microtubule surface on which the distribution of charge and the charge density is continuously changing.

In order to facilitate the study of this unusual posttranslational modification, we have generated several antibodies that recognize the γ -glutamyl link in the glutamyl side chain. We have focused on generating antibodies that recognize the glutamylated isoforms of β II and β III, the two most abundant β -tubulin isoforms expressed in brain.

The first step in generating such antibodies is to locate the services of a competent, willing synthetic chemist, commercial or academic. The cost of this custom synthesis is considerable. Unfortunately, we have been unable to depend on a reliable source for the manufacture of glutamylated peptides. Consequently, when we locate a source, we order a greater quantity of peptide(s) than we estimate is required for a single round of antibody production and characterization. We require a quantity of peptide sufficient to immunize one to five mice (0.3–1.5 mg) or one to two rabbits (2–4 mg). Next, we require a sufficient quantity of peptides, the glutamylated peptide and a sister nonglutamylated peptide (1–2 mg per peptide), for dot blotting and ELISAs. And finally, for polyclonals, we require glutamylated peptide (5–10 mg) sufficient for purification by affinity chromatography. Upon receipt, the structures of the peptides are verified by mass spectrometry. We view this as essential because we have received a number of peptides that were incorrectly synthesized.

We have produced six specific γ -Glu antibodies, two mouse monoclonal antibodies, and four rabbit polyclonal antibodies. The sequences of the six immunogens and the six parent peptides from which the immunogens were derived are shown in **Table II**.

The following discussion focuses primarily on one reagent, a mouse monoclonal antibody, 7D2. A synthetic, monoglutamylated peptide whose primary amino acid sequence was identical to the β III C-terminal isotype-defining domain was used to generate 7D2 (**Table II**).

The antibody is an ideal research reagent. An IgG2a, it purifies by Protein-G and Protein-A affinity chromatography and is not labile at the acidic pH required for purification. 7D2 concentrates well without aggregating and can be coupled to cyanogen bromide (CNBr)-activated Sepharose without difficulty. It can be used for Western blotting, in competitive ELISAs, and for immunoaffinity purification of glutamylated proteins.

Table II
Immunogens Used for the Generation of Anti- γ -glutamyl Antibodies

Name	S ^a	Parent isotype	Immunogen ^{b,c}
TT β IIGlu	r	II	(C)GGGGE{E}F-amide
TTSG1	r	III	(C)GGYE{E}D-amide
TTSG2	r	III	(C)GGYE{EE}D-amide
TT β III β IIGlu	r	III	(C)MYE{E}DDEEESEAQGPK
7D2	m	III	(C)MYE(E)DDEEESEAQGPK
6D4	m	II	(C)DATADEQGE{E}FEEEEGEDEA

^aS, species; m, mouse monoclonal; r, rabbit polyclonal.

^b(C), cysteine added for maleimide coupling.

^c{E} or {EE}, one or two glutamate residues in side chain. All polyclonal antibodies were affinity purified using peptide-cyanogen bromide Sepharose.

The initial characterization of 7D2 was accomplished with dot blots. A dot blot demonstrating the specificity of 7D2 for the γ -glutamyl linkage is shown in Fig. 4. In this experiment, the anti- β III antibody TuJ1 was used as a control (Lee *et al.*, 1990a,b). The blot shows that TuJ1 reacts with purified brain tubulin, with the unmodified fusion protein containing approximately the last third of the β III polypeptide and with all of the β III peptides containing the last six amino acids. By contrast, 7D2 reacts only with the purified brain tubulin and with the monoglutamylated peptide. It does not react with the unmodified β III sequence in the MBP fusion protein or the other peptides.

The specificity of the antibody was established further by performing competitive ELISAs. The binding of the antibody to purified brain tubulin was determined in the presence of nonglutamylated, monoglutamylated, diglutamylated, and triglutamylated β III peptides. The results from one experiment are shown in Fig. 5.

Demonstration of the specificity of antibodies 7D2 and TuJ1

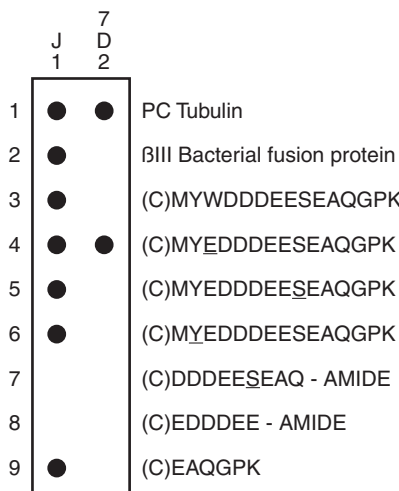


Fig. 4 The dot blot demonstrates the specificity of antibodies 7D2 and TuJ1. Underlined residues indicate posttranslational modifications. Y and S are phosphorylated, and E is monoglutamylated. The (C) represents a cysteine added for conjugation.

Competitive ELISA showing the binding of 7D2 to tubulin in the presence of glutamylated and non-glutamylated class III beta-tubulin peptides

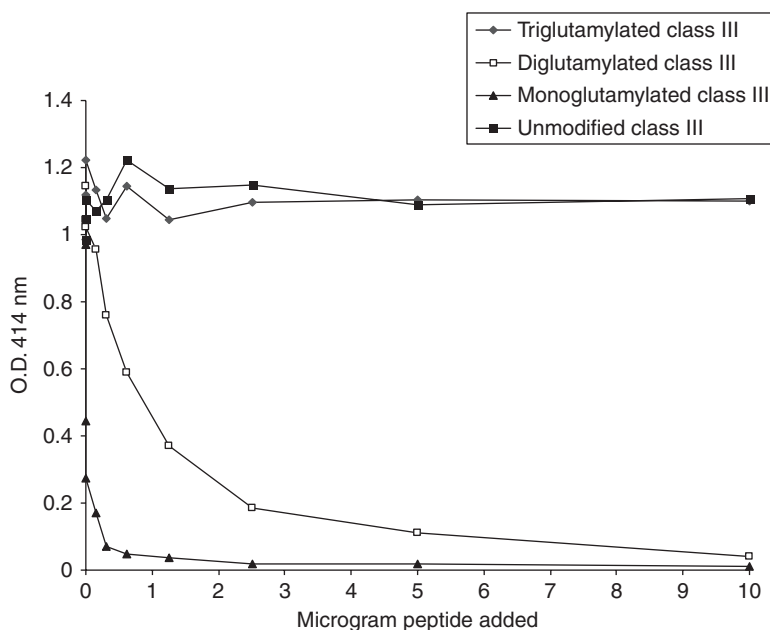


Fig. 5 A competitive enzyme-linked immunosorbent assay showing the binding of 7D2 to purified rat brain tubulin in the presence of glutamylated and nonglutamylated class III β -tubulin peptides is presented. One hundred nanograms of tubulin was adsorbed to each well of a microtiter plate. Peptides, preincubated with 7D2, were then added to each well. Horseradish peroxidase-conjugated secondary antibody was used to visualize antibody binding. Absorbance values were recorded at 414 nm, the maximum wavelength of tetramethylbenzidine reaction product.

The assay clearly demonstrates that 7D2 preferentially reacts with the monoglutamylated peptide. It binds approximately one to two orders of magnitude less efficiently to the diglutamylated peptide and does not react at all with the triglutamylated or nonglutamylated peptides.

Lastly, purified adult rat brain tubulin was passed through a column loaded with 7D2 coupled to CNBr and the retentate analyzed by mass spectrometry. The β -tubulin subunits identified were primarily monoglutamylated β III, and to a much lesser extent diglutamylated β III, validating the competitive ELISA (V. Redeker and A. Frankfurter, unpublished observations).

To determine whether 7D2 recognizes proteins other than tubulin, Western blots of whole human organ extracts were probed with the antibody. The Western blot presented in Fig. 6 demonstrates that 7D2 recognizes multiple polypeptides with masses ranging from \sim 25 to 200 kDa.

Since the β III gene is not expressed in nonneuronal tissues, it is unlikely that the immunoreactive polypeptides at \sim 50 kDa represent tubulin. The Western blot experiments confirm previous reports in which the monoclonal antibody GT335 was used to identify a large number of glutamylated polypeptides (Regnard *et al.*, 2000; van Dijk *et al.*, 2007).

7D2-Reactive glutamylated polypeptides present in extracts of human kidney, ovary, placenta and prostate

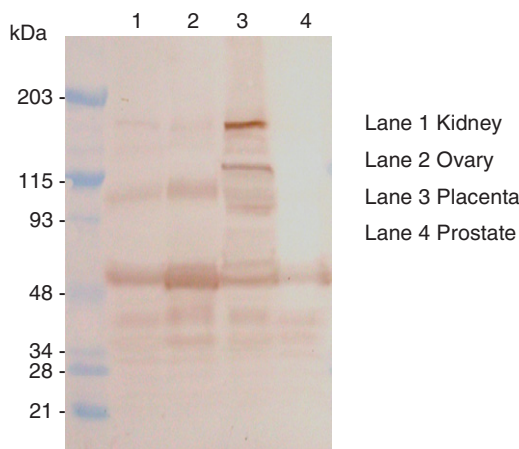


Fig. 6 A Western blot probed with 7D2 reveals multiple polypeptides with masses ranging from ~25 to 200 kDa. Since the class III β -tubulin gene is not expressed in nonneuronal tissues, the immunoreactive polypeptides at either ~50 kDa or less do not represent tubulin or tubulin proteolytic fragments.

Recently, we devised a purification scheme involving both ion exchange and immunoaffinity chromatography to isolate glutamylated polypeptides. We have had considerable success in using arginine-Sepharose chromatography to purify tubulin and tubulin C-terminal peptides for analysis by mass spectrometry (Redeker *et al.*, 1998, 2004). We extended this procedure by combining it with 7D2 immunoaffinity chromatography and have purified rat brain and rat testes nucleosome assembly proteins (NAPs) as well as other glutamylated polypeptides. The procedure involves the following steps:

1. Tubulin is removed from rat brain and rat testes soluble extracts by taxol-driven microtubule assembly followed by ultracentrifugation.
2. The tubulin-depleted supernatant is fractionated by arginine-Sepharose chromatography. Bound polypeptides are eluted with 400 mM MES pH 6.5 or 1.5 M Na glutamate, dialyzed against PBS pH 7.4, and then applied to a 7D2-Sepharose column.
3. Polypeptides are eluted from the 7D2 column with 1.2 M NaCl and then analyzed by gel electrophoresis and/or mass spectrometry.

A silver-stained gel and a companion Western blot from one experiment are shown in **Fig. 7**. The silver-stained gel shows the eluted polypeptides contained within three separate fractions. Lane 1 shows 7D2-binding rat brain polypeptides previously eluted from an arginine-Sepharose column with 400 mM MES, pH 6.5. Lane 2 shows 7D2-binding rat brain polypeptides previously eluted from an arginine-Sepharose column with 1.5 M Na glutamate, and lane 3 shows 7D2-binding rat testes polypeptides previously eluted from an arginine-Sepharose column with 1.5 M Na glutamate.

These three experiments demonstrate that in addition to tubulin, an impressive number of putative glutamylated polypeptides are present in soluble extracts of rat

Glutamylated NAPS recovered by 7D2 immunoaffinity chromatography

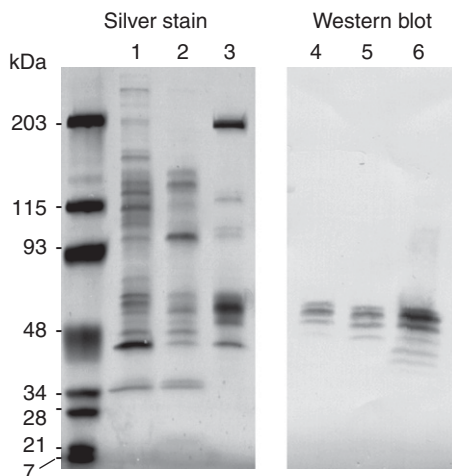


Fig. 7 The silver-stained gel shows the profiles of eluted polypeptides following three rounds of 7D2 immunoaffinity chromatography. Lane 1 shows 7D2-binding rat brain polypeptides eluted from an arginine-Sepharose column with 400 mM MES, pH 6.5. Lane 2 shows the 7D2-binding rat brain polypeptides eluted from an arginine-Sepharose column with 1.5 M Na glutamate, and lane 3 shows 7D2-binding rat testes polypeptides eluted from an arginine-Sepharose column with 1.5 M Na glutamate. These three experiments demonstrate that in addition to tubulin, an impressive number of putative glutamylated polypeptides are present in soluble extracts of rat brain and testes, and these can be captured by arginine-Sepharose and further enriched for by 7D2 immunoaffinity chromatography. The Western blot in this figure (lanes 4, 5, and 6) demonstrates that the three fractions shown in the companion silver stain contain glutamylated NAPs.

brain and testes and can be captured by arginine-Sepharose chromatography and further enriched for by 7D2 immunoaffinity chromatography. The Western blot shown in [Fig. 7](#) demonstrates that each of the three silver-stained fractions contain glutamylated NAPs. The anti-NAPs monoclonal antibody used in this experiment was a gift from [Ishimi et al. \(1985\)](#).

The identity of the other silver-stained polypeptides has not yet been established. Overall, the results from these experiments confirm an earlier study in which the monoclonal GT335 was used to capture glutamylated NAP1 and NAP2 as well as other putative glutamylated polypeptides ([Regnard et al., 2000](#)). It would be worthwhile to determine the extent to which GT335 and 7D2 capture the same polypeptides, since the primary amino acid sequences of their immunogens were different.

We are most interested in studying the three polyclonal antibodies: TT β IIglu, TTSG1, and TTSG2. Their immunogens were designed so that their primary amino acid sequences possess minimal similarity with the primary amino acid sequences of β II and β III. This was done to minimize the antigenic influence of the amino acids flanking the glutamylated site in the expectation that these antibodies would recognize a large number of glutamylated proteins. Conversely, it seems unlikely that any anti- γ -Glu antibody devoid of polypeptide context could be generated that recognizes a single glutamylated protein.

V. Summary

We have provided a brief overview of the methods and reagents developed in our laboratory for characterizing anti- β -tubulin antibodies. We have purposely not included a discussion of anti- α -tubulin antibodies. The difficulties inherent in producing and characterizing antibodies that react with individual α -tubulin isotypes and their posttranslational modifications are considerably greater than those associated with generating and characterizing β -tubulin antibodies. We also described the progress we have made in generating a small library of monoclonal and polyclonal antibodies that recognize the γ -glutamyl link in glutamylated proteins.

Without minimizing their potential utility, anti- γ -Glu antibodies should be used with considerable forethought. In view of the fact that numerous proteins appear to be targets of glutamylation, these antibodies will have to be used very carefully for immunocytochemistry. Further, caution should be used in identifying immunoreactive bands on a Western blot following one-dimensional sodium dodecyl sulfate gel electrophoresis. For example, glutamylated tubulin and NAP1 comigrate in the first dimension. Lastly, antibodies like 7D2 will be valuable in identifying glutamylated polypeptides, but they cannot be used to determine the extent of glutamylation, since the polypeptides with glutamyl side chains longer than two residues will remain undetected.

References

Akasaka, K., Maesawa, C., Shibasaki, M., Maeda, F., Takahashi, K., Akasaka, T., and Masuda, T. (2009). Loss of class III beta-tubulin induced by histone deacetylation is associated with chemosensitivity to paclitaxel in malignant melanoma cells. *J. Invest. Dermatol.* **129**, 1516–1526.

Alexander, J. E., Hunt, D. F., Lee, M. K., Shabanowitz, J., Michel, H., Berlin, S. C., MacDonald, T. L., Sundberg, R. J., Rebhun, L. I., and Frankfurter, A. (1991). Characterization of posttranslational modifications in neuron-specific class III beta-tubulin by mass spectrometry. *Proc. Natl. Acad. Sci. U.S.A.* **88**, 4685–4689.

Anthony, T. E., Klein, C., Fishell, G., and Heintz, N. (2004). Radial glia serve as neuronal progenitors in all regions of the central nervous system. *Neuron* **41**, 881–890.

Arai, K., Shibutani, M., and Matsuda, H. (2002). Distribution of the class II beta-tubulin in developmental and adult rat tissues. *Cell Motil. Cytoskeleton* **52**, 174–182.

Arevalo, M. A., Nieto, J. M., Andreu, D., and Andreu, J. M. (1990). Tubulin assembly probed with antibodies to synthetic peptides. *J. Mol. Biol.* **214**, 105–120.

Argarana, C. E., Arce, C. A., Barra, H. S., and Caputto, R. (1977). *In vivo* incorporation of [¹⁴C]tyrosine into the C-terminal position of the alpha subunit of tubulin. *Arch. Biochem. Biophys.* **180**, 264–268.

Argarana, C. E., Barra, H. S., and Caputto, R. (1978). Release of [¹⁴C]tyrosine from tubulinyl-[¹⁴C] tyrosine by brain extract. Separation of a carboxypeptidase from tubulin-tyrosine ligase. *Mol. Cell. Biochem.* **19**, 17–21.

Banerjee, A., Roach, M. C., Trcka, P., and Luduena, R. F. (1992). Preparation of a monoclonal antibody specific for the class IV isotype of beta-tubulin. Purification and assembly of alpha beta II, alpha beta III, and alpha beta IV tubulin dimers from bovine brain. *J. Biol. Chem.* **267**, 5625–5630.

Bhattacharya, R., Frankfurter, A., and Cabral, F. (2008). A minor beta-tubulin essential for mammalian cell proliferation. *Cell Motil. Cytoskeleton* **65**, 708–720.

Binder, L. I., Frankfurter, A., and Rebhun, L. I. (1985). The distribution of tau in the mammalian central nervous system. *J. Cell Biol.* **101**, 1371–1378.

Blose, S. H., Meltzer, D. I., and Feramisco, J. R. (1984). 10-nm filaments are induced to collapse in living cells microinjected with monoclonal and polyclonal antibodies against tubulin. *J. Cell Biol.* **98**, 847–858.

Caceres, A., Binder, L. I., Payne, M. R., Bender, P., Rebhun, L., and Steward, O. (1984). Differential subcellular localization of tubulin and the microtubule-associated protein MAP2 in brain tissue as revealed by immunocytochemistry with monoclonal hybridoma antibodies. *J. Neurosci.* **4**, 394–410.

Caron, J. M. (1997). Posttranslational modification of tubulin by palmitoylation: I. *In vivo* and cell-free studies. *Mol. Biol. Cell* **8**, 621–636.

de la Vina, S., Andreu, D., Medrano, F. J., Nieto, J. M., and Andreu, J. M. (1988). Tubulin structure probed with antibodies to synthetic peptides. Mapping of three major types of limited proteolysis fragments. *Biochemistry* **27**, 5352–5365.

Dumontet, C., Jordan, M. A., and Lee, F. F. (2009). Ixabepilone: Targeting betaIII-tubulin expression in taxane-resistant malignancies. *Mol. Cancer Ther.* **8**, 17–25.

Edde, B., Rossier, J., Le Caer, J. P., Desbruyeres, E., Gros, F., and Denoulet, P. (1990). Posttranslational glutamylation of alpha-tubulin. *Science* **247**, 83–85.

Eipper, B. A. (1972). Rat brain microtubule protein: Purification and determination of covalently bound phosphate and carbohydrate. *Proc. Natl. Acad. Sci. U.S.A.* **69**, 2283–2287.

Fukushima, N., Furuta, D., Hidaka, Y., Moriyama, R., and Tsujiuchi, T. (2009). Post-translational modifications of tubulin in the nervous system. *J. Neurochem.* **109**, 683–693.

Galperin, M. Y., and Koonin, E. V. (1997). A diverse superfamily of enzymes with ATP-dependent carboxylate-amine/thiol ligase activity. *Protein Sci.* **6**, 2639–2643.

Gan, P. P., and Kavallaris, M. (2008). Tubulin-targeted drug action: Functional significance of class II and class IVb beta-tubulin in vinca alkaloid sensitivity. *Cancer Res.* **68**, 9817–9824.

Hayashi, Y., Kuriyama, H., Umezawa, H., Tanaka, J., Yoshimasu, T., Furukawa, T., Tanaka, H., Kagamu, H., Gejyo, F., and Yoshizawa, H. (2009). Class III beta-tubulin expression in tumor cells is correlated with resistance to docetaxel in patients with completely resected non-small-cell lung cancer. *Intern. Med.* **48**, 203–208.

Hiser, L., Aggarwal, A., Young, R., Frankfurter, A., Spano, A., Correia, J. J., and Lobert, S. (2006). Comparison of beta-tubulin mRNA and protein levels in 12 human cancer cell lines. *Cell Motil. Cytoskeleton* **63**, 41–52.

Ishimi, Y., Sato, W., Kojima, M., Sugasawa, K., Hanaoka, F., and Yamada, M. (1985). Rapid purification of nucleosome assembly protein (AP-I) and production of monoclonal antibodies against it. *Cell Struct. Funct.* **10**, 373–382.

Jaglin, X. H., Poirier, K., Saillour, Y., Buhler, E., Tian, G., Bahi-Buisson, N., Fallet-Bianco, C., Phan-Dinh-Tuy, F., Kong, X. P., Bomont, P., Castelnau-Ptakine, L., Odent, S., et al. (2009). Mutations in the beta-tubulin gene TUBB2B result in asymmetrical polymicrogyria. *Nat. Genet.* **41**, 746–752.

Janke, C., Rogowski, K., Wloda, D., Regnard, C., Kajava, A. V., Strub, J. M., Temurak, N., van Dijk, J., Boucher, D., van Dorsselaer, A., Suryavanshi, S., Gaertig, J., et al. (2005). Tubulin polyglutamylase enzymes are members of the TTL domain protein family. *Science* **308**, 1758–1762.

Janke, C., Rogowski, K., and van Dijk, J. (2008). Polyglutamylation: A fine-regulator of protein function? ‘Protein Modifications: Beyond the usual suspects’ review series. *EMBO Rep.* **9**, 636–641.

Katsetos, C. D., Del Valle, L., Geddes, J. F., Assimakopoulou, M., Legido, A., Boyd, J. C., Balin, B., Parikh, N. A., Maraziotis, T., de Chadarevian, J. P., Varaklis, J. N., Matsas, R., et al. (2001). Aberrant localization of the neuronal class III beta-tubulin in astrocytomas. *Arch. Pathol. Lab. Med.* **125**, 613–624.

Keays, D. A., Tian, G., Poirier, K., Huang, G. J., Siebold, C., Cleak, J., Oliver, P. L., Fray, M., Harvey, R. J., Molnar, Z., Pinon, M. C., Dear, N., et al. (2007). Mutations in alpha-tubulin cause abnormal neuronal migration in mice and lissencephaly in humans. *Cell* **128**, 45–57.

Lee, M. K., Rebhun, L. I., and Frankfurter, A. (1990a). Posttranslational modification of class III beta-tubulin. *Proc. Natl. Acad. Sci. U.S.A.* **87**, 7195–7199.

Lee, M. K., Tuttle, J. B., Rebhun, L. I., Cleveland, D. W., and Frankfurter, A. (1990b). The expression and posttranslational modification of a neuron-specific beta-tubulin isotype during chick embryogenesis. *Cell Motil. Cytoskeleton* **17**, 118–132.

L’Hernault, S. W., and Rosenbaum, J. L. (1985). Chlamydomonas alpha-tubulin is posttranslationally modified by acetylation on the epsilon-amino group of a lysine. *Biochemistry* **24**, 473–478.

Mary, J., Redeker, V., Le Caer, J. P., Prome, J. C., and Rossier, J. (1994). Class I and IVa beta-tubulin isotypes expressed in adult mouse brain are glutamylated. *FEBS Lett.* **353**, 89–94.

Miller, L. M., Menthenia, A., Chatterjee, C., Verdier-Pinard, P., Novikoff, P. M., Horwitz, S. B., and Angeletti, R. H. (2008). Increased levels of a unique post-translationally modified betaIVb-tubulin isotype in liver cancer. *Biochemistry* **47**, 7572–7582.

Moody, S. A., Miller, V., Spanos, A., and Frankfurter, A. (1996). Developmental expression of a neuron-specific beta-tubulin in frog (*Xenopus laevis*): A marker for growing axons during the embryonic period. *J. Comp. Neurol.* **364**, 219–230.

Nakamura, Y., Yamamoto, M., Oda, E., Yamamoto, A., Kanemura, Y., Hara, M., Suzuki, A., Yamasaki, M., and Okano, H. (2003). Expression of tubulin beta II in neural stem/progenitor cells and radial fibers during human fetal brain development. *Lab. Invest.* **83**, 479–489.

Ozols, J., and Caron, J. M. (1997). Posttranslational modification of tubulin by palmitoylation: II. Identification of sites of palmitoylation. *Mol. Biol. Cell* **8**, 637–645.

Redeker, V., Frankfurter, A., Parker, S. K., Rossier, J., and Detrich, H. W., 3rd (2004). Posttranslational modification of brain tubulins from the Antarctic fish *Notothenia coriiceps*: Reduced C-terminal glutamylated correlates with efficient microtubule assembly at low temperature. *Biochemistry* **43**, 12265–12274.

Redeker, V., Levilliers, N., Schmitter, J. M., Le Caer, J. P., Rossier, J., Adoutte, A., and Bre, M. H. (1994). Polyglycylation of tubulin: A posttranslational modification in axonemal microtubules. *Science* **266**, 1688–1691.

Redeker, V., Melki, R., Prome, D., Le Caer, J. P., and Rossier, J. (1992). Structure of tubulin C-terminal domain obtained by subtilisin treatment. The major alpha and beta tubulin isotypes from pig brain are glutamylated. *FEBS Lett.* **313**, 185–192.

Redeker, V., Rossier, J., and Frankfurter, A. (1998). Posttranslational modifications of the C-terminus of alpha-tubulin in adult rat brain: Alpha 4 is glutamylated at two residues. *Biochemistry* **37**, 14838–14844.

Redeker, V., Rusconi, F., Mary, J., Prome, D., and Rossier, J. (1996). Structure of the C-terminal tail of alpha-tubulin: Increase of heterogeneity from newborn to adult. *J. Neurochem.* **67**, 2104–2114.

Regnard, C., Desbruyeres, E., Huet, J. C., Beauvallet, C., Pernollet, J. C., and Edde, B. (2000). Polyglutamylated of nucleosome assembly proteins. *J. Biol. Chem.* **275**, 15969–15976.

Roach, M. C., Boucher, V. L., Walss, C., Ravidin, P. M., and Luduena, R. F. (1998). Preparation of a monoclonal antibody specific for the class I isotype of beta-tubulin: The beta isotypes of tubulin differ in their cellular distributions within human tissues. *Cell Motil. Cytoskeleton* **39**, 273–285.

Rosenbaum, J. (2000). Cytoskeleton: Functions for tubulin modifications at last. *Curr. Biol.* **10**, R801–R803.

Rudiger, M., Plessman, U., Kloppel, K. D., Wehland, J., and Weber, K. (1992). Class II tubulin, the major brain beta tubulin isotype is polyglutamylated on glutamic acid residue 435. *FEBS Lett.* **308**, 101–105.

Rudiger, M., and Weber, K. (1993). Characterization of the post-translational modifications in tubulin from the marginal band of avian erythrocytes. *Eur. J. Biochem.* **218**, 107–116.

Saussede-Aim, J., Matera, E. L., Ferlini, C., and Dumontet, C. (2009). Beta3-tubulin is induced by estradiol in human breast carcinoma cells through an estrogen-receptor dependent pathway. *Cell Motil. Cytoskeleton* **66**, 378–388.

Sugita, Y., Nakamura, Y., Yamamoto, M., Oda, E., Tokunaga, O., and Shigemori, M. (2005). Expression of tubulin beta II in neuroepithelial tumors: Reflection of architectural changes in the developing human brain. *Acta Neuropathol.* **110**, 127–134.

Sullivan, K. F. (1988). Structure and utilization of tubulin isotypes. *Annu. Rev. Cell Biol.* **4**, 687–716.

Terada, N., Kidd, G. J., Kinter, M., Bjartmar, C., Moran-Jones, K., and Trapp, B. D. (2005). Beta IV tubulin is selectively expressed by oligodendrocytes in the central nervous system. *Glia* **50**, 212–222.

Terry, S., Ploussard, G., Allory, Y., Nicolaiw, N., Boissiere-Michot, F., Maille, P., Kheuang, L., Coppolani, E., Ali, A., Bibeau, F., Culin, S., Butyan, R., et al. (2009). Increased expression of class III beta-tubulin in castration-resistant human prostate cancer. *Br. J. Cancer* **101**, 951–956.

van Dijk, J., Rogowski, K., Miro, J., Lacroix, B., Edde, B., and Janke, C. (2007). A targeted multienzyme mechanism for selective microtubule polyglutamylated. *Mol. Cell.* **26**, 437–448.

Verdier-Pinard, P., Shahabi, S., Wang, F., Burd, B., Xiao, H., Goldberg, G. L., Orr, G. A., and Horwitz, S. B. (2005). Detection of human beta V-tubulin expression in epithelial cancer cell lines by tubulin proteomics. *Biochemistry* **44**, 15858–15870.

Westermann, S., and Weber, K. (2003). Post-translational modifications regulate microtubule function. *Nat. Rev. Mol. Cell Biol.* **4**, 938–947.

Wu, C., Chang, A., Smith, M. C., Won, R., Yin, X., Staigaitis, S. M., Agamanolis, D., Kidd, G. J., Miller, R. H., and Trapp, B. D. (2009). Beta4 tubulin identifies a primitive cell source for oligodendrocytes in the mammalian brain. *J. Neurosci.* **29**, 7649–7657.

Yang, H., Cabral, F., and Bhattacharya, R. (2009). Tubulin isotype specificity and identification of the epitope for antibody Tub 2.1. *Protein Eng. Des. Sel.* **22**, 625–629.

CHAPTER 4

Expression Profiling of Tubulin Isootypes and Microtubule-Interacting Proteins Using Real-Time Polymerase Chain Reaction

Sharon Lobert^{*†}, Laree Hiser^{*}, and John J. Correia[†]

^{*}School of Nursing, University of Mississippi Medical Center, Jackson, Mississippi 39216

[†]Department of Biochemistry, University of Mississippi Medical Center, Jackson, Mississippi 39216

Abstract

- I. Introduction and Rationale
- II. Methods and Materials
 - A. RNA Extraction from Cells or Tissues
 - B. cDNA Preparation
 - C. Designing Primers for qRT-PCR
 - D. Primer Preparation
 - E. Optimizing the PCR Reaction Conditions
 - F. Preparation of Standard Curve for Quantitative Real-Time RT-PCR
 - G. Comparative RT-PCR
- III. Results and Discussion
 - A. β -Tubulin Isootypes and MIPs in Human Tissues
 - B. β -Tubulin Isootypes and MIP Levels Change in Response to Drug Treatment
- IV. Summary
- References

Abstract

Real-time polymerase chain reaction (PCR) has been used for quantification of intracellular mRNA levels in cell culture and tissue samples. It is an important tool for studying antimitotic drug effects on tubulin isotype and microtubule-interacting protein levels and for measuring differences in normal and tumor tissue samples that

could have predictive or prognostic applications. Both quantitative and comparative methods are valuable approaches; however, the selection of either approach requires an understanding of their benefits and challenges. In this chapter, we provide detailed protocols for real-time PCR experiments, discuss issues to consider in selecting real-time PCR methodologies, and give examples utilizing either quantitative or comparative approaches.

===== I. Introduction and Rationale

Real-time analysis of reverse transcriptase polymerase chain reactions (RT-PCRs) is a useful tool for studying tubulin isotype and microtubule-interacting protein (MIP) mRNA levels under varying experimental conditions. We are able to measure drug effects on tubulin isotype and MIP transcription in cell culture. Quantitative or comparative RT-PCR experiments, using templates from cells grown in culture, provide insight into drug effects on transcription of specific messages over time. We can also study patterns of tubulin isotype and MIP expression in tissues, allowing us to assess potential biomarkers for disease pathology and evaluate the utility of expression profiles for predicting therapeutic outcomes (Cucchiarelli *et al.*, 2008; Dozier *et al.*, 2003; Hiser *et al.*, 2006). The methods (quantitative or comparative) are also employed to compare normal and tumor tissue samples from patients and can be used to examine the impact of chemotherapy on tubulin isotype and MIP expression profiles.

Inherent in the use of quantitative or comparative RT-PCR are different models for setting up experiments and analyzing data. There are several excellent technical guides describing RT-PCR protocols on the Stratagene (<http://www.Stratagene.com/tradeshows/feature.aspx?fpId=1>) and the Invitrogen webpages (<http://tools.Invitrogen.com/content.cfm?pageid=12257>). While there are pros and cons for the utilization of either method, some types of experiments are more readily handled by one method as opposed to the other. Issues to consider when selecting quantitative or comparative RT-PCR as the method for data collection are discussed in this chapter and data examples are provided.

===== II. Methods and Materials

A. RNA Extraction from Cells or Tissues

Total RNA that is suitable for use in expression studies may be obtained using a combination of TRIzol Reagent (Invitrogen, Carlsbad, CA) and spin columns (e.g., RNeasy kit; Qiagen, Valencia, CA). The result is a high yield of good-quality RNA.

1. Prepare 100 μ l of tissue or whole cell lysate in an RNase-free microcentrifuge tube. For tissues, start with 0.25 G or less and homogenize with mortar and pestle in liquid nitrogen. For cell culture studies, we start with about 10×10^6 cells. Cells are washed with phosphate-buffered saline (PBS), centrifuged into a pellet, and resuspended in 100 μ l PBS.

2. Add 1 ml TRIzol prewarmed to room temperature. Avoid contact with skin and breathing the vapor. Let the mixture stand at room temperature about 5 min to complete cell lysis and dissociation of nucleoprotein complexes.
3. Add 0.2 ml chloroform to the homogenate. Shake vigorously for 15 s. Do not vortex because of the possibility of RNA breakage. Allow the sample to stand at room temperature for 2–3 min.
4. Separate the aqueous and organic phases in a 1.5 ml microcentrifuge tube by centrifugation at $12,000 \times g$ for 15 min at 4°C.
5. Carefully remove aqueous phase (top) and transfer to another RNase-free tube. *It is extremely important not to get any of the material from the aqueous/organic interface; it is suggested to sacrifice aqueous material rather than risk taking this precipitate.* From this step on, work in an area that is RNase free.
6. Measure the volume of the aqueous sample. If it is more than 750 μ l, divide it equally into two tubes.
7. Slowly add an equal volume of 70% ethanol (EtOH) prepared in RNase-free water, mixing as it is added. Do this by pipeting up and down. Measure the full amount of EtOH, but expel only a little from the pipet tip before drawing up more solution. Continue this process as a way of mixing the contents of the tube at the same time you are adding the EtOH. *Slow introduction of the EtOH is important to avoid localized precipitation of RNA.*
8. Load the sample (up to 700 μ l) into an RNeasy column seated in a collection tube. Centrifuge for 30 s at $\geq 8,000 \times g$. Discard the flow-through. If the sample volume is larger than the loading capacity of the column, repeat this step until the entire sample has been passed over the column.
9. Add 350 μ l Buffer RW1 (from the RNeasy kit) onto the column and centrifuge for 15 s at $\geq 8,000 \times g$. Discard flow-through.
10. Transfer the spin column into a new collection tube (from the kit) and discard the old collection tube.
11. Add 10 μ l of DNase I stock solution to 70 μ l Buffer RDD. Mix by gentle inversion and centrifuge briefly.
12. Add the DNase I incubation mix (80 μ l) directly to RNeasy spin column membrane and place on the benchtop to incubate RT for 15 min.
13. Add 350 μ l Buffer RW1 and centrifuge for 15 s at $\geq 8,000 \times g$. Discard the flow-through.
14. Transfer the spin column into a new collection tube (from the kit) and discard the old collection tube.
15. Add 500 μ l Buffer RPE and centrifuge for 30 s at $\geq 8,000 \times g$. Discard the flow-through.
16. Add another 500 μ l Buffer RPE and centrifuge for 2 min at $\geq 8,000 \times g$.
17. Centrifuge the empty tube for 2 min more at $\geq 8,000 \times g$ to dry the column.
18. Transfer column into a 1.5-ml collection tube (with cap) and pipet 30 μ l of RNase-free water directly onto the center of the column membrane. Allow the sample to sit at room temperature for 1–2 min, and then centrifuge for 1 min at $\geq 8,000 \times g$ to elute the RNA. Yields can be improved by using warm (preheated to 98°C) RNase-free water.
19. For greater recovery of RNA, repeat the previous step using 20 μ l prewarmed RNase-free water for a total of 50 μ l RNA.

20. Measure RNA concentration spectrophotometrically (NanoDrop 1000 UV-Vis spectrophotometer; NanoDrop Technologies, Inc., Wilmington, DE): $\lambda_{260} = 15,100 \text{ M}^{-1} \text{ cm}^{-1}$.
21. Store the purified RNA at -80°C .

The RNA quality is determined using three assessments: (1) $A_{260/280}$, (2) 28S/18S ribosomal RNA ratio, and (3) the RIN (RNA integrity number). Good-quality RNA typically has a ratio of absorbance at 260/280 nm between 1.8 and 2.0 (this may be influenced by the quantity of RNA and thus the size of the peaks, with larger peaks having higher ratios than shorter peaks). We do this using the Agilent 2100 Bioanalyzer RNA chip and Agilent software (Agilent Technologies, Santa Clara, CA) according to the manufacturer's instructions. The maximum 28S/18S ribosomal RNA ratio is near 2.0 as determined using an Agilent 2100 Bioanalyzer. The RIN, ranging from 1 to 10, is determined by a proprietary formula in the Agilent 2100 Bioanalyzer software. This quantification includes factors for all RNA, including the degraded material. The optimum RIN for tracking good-quality RNA should be determined experimentally (Imbeaud *et al.*, 2005; Schroeder *et al.*, 2006). We generally consider samples as acceptable when the RIN is greater than 8.5.

B. cDNA Preparation

We use a two-step RT-PCR procedure in which cDNA is first produced and can be stored at -20°C for use in many PCR experiments. This allows us to study multiple targets from a single cDNA sample and to replicate experiments with each target. In the first step, the total RNA is treated with DNase I in solution and then, after DNase treatment, a poly (dT) primer is used in reverse transcription reactions to generate cDNA from all mRNA transcripts. We use 2 μg of total RNA, as determined by absorbance at 260 nm using a NanoDrop 1000 UV-Vis spectrophotometer (NanoDrop Technologies, Inc.) in our RT reactions. An avian myeloblastosis virus (AMV) RT (Promega Corporation, Madison, WI) is used because of its temperature stability and RNaseH activity.

1. Start with 2 μg of RNA and add RNase-free water to give a total volume of 7.5 μl in a 0.2- or 0.5-ml microcentrifuge tube.
2. Add the following in this order:
 - a. 0.5 μl of RNase OUT.
 - b. 1.0 μl 10 \times DNase I for a total of 10 μl .
 - c. 1.0 μl of DNase I for a total of 10 μl .
3. Incubate for 15 min at 25°C in thermal cycler.
4. Add 1 μl of Stop solution to end the DNase I digestion.
5. Incubate for 10 min at 70°C to disrupt secondary structure and then immediately place on ice.
6. Add 0.5 μg of poly (dT)₁₅ (2 μl of 500 $\mu\text{g}/\text{ml}$).
7. Heat to 70°C for 5 min.
8. Chill on ice for 5 min and centrifuge briefly.
 - a. While tubes are on ice, warm sodium pyrophosphate to 42°C .
9. Add the following in the order shown (Promega Corporation):
 - a. 5 μl AMV RT 5 \times reaction buffer.
 - b. 2.5 μl of 40 mM dNTP mix.

- c. 2.5 μ l of 40 mM sodium pyrophosphate.
- d. 3.0 μ l AMV RT (30 units).
- e. Bring final volume to 25 μ l with 12 μ l of nuclease-free water.
10. Incubate for 60 min at 42°C. The temperature may be altered depending on the primers used and the specificity required.
11. Add 40 μ l of RNase-free water for a total of 65 μ l. This dilutes the cDNA to prevent inhibition of the DNA polymerase in the PCR reaction.
12. Label tubes and store at -20°C.

C. Designing Primers for qRT-PCR

There are many good programs available to assist with primer design (e.g., NIH primer blast, Integrated DNA Technologies primer blast). Factors to consider when selecting the ideal primer pair include (1) projected amplicon length, (2) primer length, (3) GC content, (4) melting temperature, (5) potential hairpin formation, and (6) specificity of the primer pair. We use SYBR Green I (Invitrogen, Carlsbad, CA) as the fluorescent probe for cDNA amplification. SYBR Green I fluoresces when bound to double-stranded DNA. The amplicon length is 200–250 bp for optimal signal detection. Longer amplicons tend to reduce the amplification efficiency and increase the time necessary for the extension step. The primer lengths are limited by their potential to form secondary structure and should be 15–30 bases.

1. Aim for a melting temperature (T_m) of 60°C and 40–60% GC content. If GC content is too high, then stable structures such as hairpins may form or nonspecific binding to the target may occur; if GC content is too low, then you need a longer primer to reach the optimal T_m (which increases the chance of secondary structures and the chance of nonspecific annealing).
2. The amplicon length should be about 200–250 bp for use with SYBR Green I.
3. The specificity of the selected primer pair for the gene of interest should be assessed using the NIH Blast software (<http://blast.ncbi.nlm.nih.gov/Blast.cgi>).

D. Primer Preparation

1. A number of commercial sources for synthesis of custom DNA oligonucleotides are available. Minimal purification of primers is adequate for most PCR applications.
2. Briefly centrifuge the tube to make sure the lyophilized primer is at the bottom before opening the vial.
3. Add the appropriate amount of DNase-free water to give a final concentration of at least 100 μ M.
4. Store the solubilized oligonucleotide at -20°C.

E. Optimizing the PCR Reaction Conditions

The use of SYBR Green I for detection in real-time PCR has a cost advantage, but data are susceptible to misinterpretation because of the presence of PCR artifacts. To circumvent this problem, we carefully optimize the reaction conditions for each primer pair to minimize nonspecific products or primer dimers and to maximize yield

of the desired amplicon. Commercially available premixes (MasterAmp or FailSafe; Epicentre Biotechnologies, Madison, WI) simplify the optimization procedure.

1. Use aerosol-resistant (filtered) pipet tips to avoid cross-contamination.
2. Prepare a Master Mix to use in 12 reactions (Note: The total volume should be 37.5 μ l, enough for 12 reactions with a little left over.)

Recipe:

1 μ l	RT reaction (cDNA)
3 μ l	2 μ M forward primer (Note that the stock solution must be diluted.)
3 μ l	2 μ M reverse primer
29.5 μ l	Autoclaved nanopure water (DNase free)
1 μ l	Titanium Taq DNA polymerase (Add this last.)

3. Mix well and centrifuge briefly.
4. Label 12 0.5- μ l microcentrifuge tubes (autoclaved or nuclease free) as A–L to denote the various premixes (buffers to be tested).
5. Add 3 μ l of the appropriate 2 \times premix to each. (Note: Some of the premixes do not freeze at -20°C , while some need to be thawed.)
6. Add 3 μ l of the Master Mix to each tube. Mix well and centrifuge briefly.
7. Place the 12 microcentrifuge tubes into a thermal cycler. If a heated lid is not available, add mineral oil to the top of each reaction to prevent evaporation. (Note: Set the number of cycles. For the first attempt, 35 is a reasonable number.)

Thermal settings:

95 $^{\circ}\text{C}$ up to 1 min (to activate the Titanium Taq, a “hot-start” enzyme)
35 cycles of 95 $^{\circ}\text{C}$ up to 30 s (the denaturation step in each cycle)
68 $^{\circ}\text{C}$ up to 1 min (the annealing and extension steps)
Cool to 4 $^{\circ}\text{C}$ after 35 cycles and remain cold until manually stopped

8. Directly from the reaction tube, load 1 μ l of each reaction onto an Agilent DNA 1000 Chip to analyze the products.
9. Select the best premix to use based on the amplicon size, absence of nonspecific products, and product yield. If necessary, repeat the reactions and vary the number of cycles or the cycling conditions. It may be necessary to separate the annealing and extension steps so that a lower annealing temperature (e.g., 55 $^{\circ}\text{C}$) can be used. The extension step should then be at 72 $^{\circ}\text{C}$.
10. Identical optimized conditions will be used in the comparative or quantitative RT-PCR experiments.

F. Preparation of Standard Curve for Quantitative Real-Time RT-PCR

Quantitative RT-PCR requires a standard curve for each amplicon. To obtain the control cDNA template of a known quantity for the generation of standard curves, the specific amplicon generated in a PCR reaction is isolated from an agarose gel. Several gel extraction kits are commercially available for this purpose (e.g., CONCERTTM Rapid Gel Extraction kit; Marilgen Biosciences, Inc., Ijamsville, MD). The use of a standard curve provides information about amplification efficiency and circumvents the need to manually correct for amplification efficiencies as is

necessary when comparing amplicons generated using different primer sets. Most importantly, the use of a standard curve allows absolute quantitation of transcript levels.

1. Prepare an agarose gel with a high enough percentage (e.g., 3%) of agarose to get good resolution of the amplicon of interest. Using a buffer without EDTA may help prevent inhibition of later enzyme reactions. Wells should be large enough to accommodate the sample.
2. Load cDNA sample (PCR reaction such as done during optimization of the reaction conditions) and DNA ladder on gel. Perform electrophoresis long enough to achieve good separation of the amplicon. For a standard mini-gel in TAE (Tris-acetate-EDTA) buffer, 100 V for about 30 min is generally adequate.
3. Stain with ethidium bromide or another suitable DNA dye, identify the amplicon, and excise the band from the gel with a minimal amount of agarose.
4. Weigh the gel slice.
5. Extract the DNA according to the kit instructions. This generally involves heating the agarose slice in solubilization buffer, binding of the DNA to a filter in a spin column at high ionic strength, several wash steps, and elution of the DNA at low ionic strength. It is advisable to elute the amplicon in a minimal volume of DNase-free water (e.g., 35 μ l) to maximize the concentration. It is often possible to elute with a smaller volume of water than is recommended by the kit instructions.
6. Determine the concentration of purified cDNA spectrophotometrically: $\lambda_{260} = 15,100 \text{ M}^{-1} \text{ cm}^{-1}$.
7. Preparation of the standard curve is made from 10-fold serial dilutions of a known amount of amplicon purified from an agarose gel. Our standard curves typically have seven points which span the range 1 to 1 million copies.

As noted above, qRT-PCR data collection is initiated with a known amount of RNA, usually 2 μ g. This permits us to normalize the final data as copies per μ g of total RNA. The gene-specific primer efficiencies are obtained directly from the standard curves, and for acceptable data the calculated efficiencies are typically 90–110% (<http://www.stratagene.com/tradeshows/feature.aspx?fpId=1>). Note that comparison of absolute numbers obtained from standard curves of different genes makes the assumption that the efficiency of cDNA preparation using poly(dT) primers was equivalent for all transcripts. The data are normalized as the β -tubulin isotype or MIP mRNA copy number in the unknown sample to 1 μ g of total RNA.

Copy number calculation:

$$640 \text{ G/mol} \times \text{number of nucleotide pairs} = \text{cDNA in G/mol per amplicon}$$

$$\text{cDNA mol/L} = \text{cDNA concentration (G/L)} / \text{cDNA G/mol}$$

$$\text{Copy number/L} = \text{cDNA mol/L} \times 6.02 \times 10^{23} \text{ molecules/mol}$$

We used quantitative RT-PCR to measure β -tubulin isotypes in cancer cell lines (Hiser *et al.*, 2006), normal and tumor breast tissues (Dozier *et al.*, 2003), and normal and tumor lung tissues (Cucchiarelli *et al.*, 2008). For tissue and cell culture studies, a 96-well PCR plate is run for each primer set. Duplicate or triplicate wells for each point of the standard curve, unknown samples, and no template controls are loaded. The no template controls are essential for assessing potential contamination of

reagents or contamination that occurred during preparation of the reactions that would cause misinterpretation of the data. We carry out duplicate or triplicate experiments for each set of cell or tissue samples in order to obtain estimates of technical error. We have measured β -tubulin isotype and MIP mRNA in 40–80 tissue samples. Because data for a single β -tubulin isotype is collected across several PCR plates, we load one or more quality control samples. The quality control is a sample that has been previously studied and the mRNA amounts are known. This allows us to validate the consistency of the standard curve across several PCR plates and makes it possible to combine data sets.

G. Comparative RT-PCR

We use comparative real-time PCR for cell culture studies in which we have two to four time points for drug treatment and want to compare the response of several tubulin and MIP genes. This method requires the use of preferably two or more housekeeping genes to normalize data. β_2 -Microglobulin, hypoxanthine reductase transferase (*HPRT1*), glyceraldehyde-3 phosphate dehydrogenase (*GAPDH*), and others are suggested (<http://tools.invitrogen.com/content.cfm?pageid=12257>) as good candidate genes that are not likely to be altered by experimental conditions; however, it is important to test this for specific experimental conditions. We used both *GAPDH* and *HPRT1* in a recent study of regulation of β -tubulin and MIP gene transcription in response to paclitaxel treatment over 72 h. We found that there was little or no change in transcription of either housekeeping gene in response to drug treatment. Data normalized to *GAPDH* or *HPRT1* alone or in combination demonstrated the same overall effect.

Analysis of comparative RT-PCR data requires determination of the primer efficiency for each set of forward and reverse primers. Primer efficiencies are estimated from real-time PCR using specific primer sets with serial dilutions of cDNA (efficiency = $10^{(-1/\text{slope})} - 1$). Ten-fold serial dilution standard curves from quantitative PCR experiments give us a good estimate of the primer efficiencies for β -tubulin isotype and MIP genes. For housekeeping genes, we use two-fold serial dilutions of the template. The experiments are done in triplicate and the mean primer efficiency is determined. Our real-time PCR instrument is the Stratagene MxPro3000 (Stratagene, La Jolla, CA). The MxPro software for data analysis allows input of the primer efficiency data, and the output data are corrected for the differences in primer efficiency.

===== III. Results and Discussion

A. β -Tubulin Isotypes and MIPs in Human Tissues

We used quantitative RT-PCR to measure mRNA expression of β -tubulin isotypes and MIPs in human normal and tumor tissues. Primers were designed for each β -tubulin isotype (classes I, IIA, IIB, III, IVA, IVB, V, and VI) and for *MAP4* and *stathmin 1* (Table I).

Although β -tubulin isotype class II is considered a single isotype class based upon the carboxy-terminal protein sequence, there are two genes for this isotype (*TUBB2A*: NM_001069.2 and *TUBB2B*: NM_178012.4). In a recent study of

Table I
Human β -Tubulin Isotype and MIP Target Genes and Primers

Protein	Gene name	Accession number	Forward sequence 5'-3'	Reverse sequence 5'-3'	Amplicon length (bp)
β -I	<i>TUBB</i>	NM_178014.2	CCC CAT ACA TAC CTT GAG GCG A	GCC AAA AGG ACC TGA GCG AA	290
β -IIA	<i>TUBB2A</i>	NM_001069.2	CTC AGA TCA ATC GTG CAT CCT TAG TGA ACT TCT GT	GTA TAG ATA CCT TCA CAG ACA ATA CTG TAA TTT TTA GAG GAG TTC CAC A	167
β -IIB	<i>TUBB2B</i>	NM_178012.4	ACG GGT TAG GGA AAG CGG A	TTC CGA CAC AAA CGT TTA TGT GA	242
β -III	<i>TUBB3</i>	NM_006086.2	ATG AGG GAG ATC GTG CAC AT	CCC CTG AGC GGA CAC TGT	238
β -IVA	<i>TUBB4</i>	NM_006087.2	TCT CCG CCG CAT CTT CCA	GCT CTG G ¹ G ACA TAA TTT CCT CCT	274
β -IVB	<i>TUBB2C</i>	NM_006088.5	GCT GTT TGT CTA CTT CCT CCT GCT	CAG TTG TTC CCA GCA CCA CTC T	349
β -V	<i>TUBB6</i>	NM_032525.1	CGG G ¹ GA GGA AGC TTT TGA GGA T	CTG GGT AGA ACC CGC AAT TCT CT	244
β -VI	<i>TUBB1</i>	NM_030773.2	AGT TGT GTT GGG CTC ACA CCA	TTG CCA CAC TGG CCA ATC TGA	133
GAPDH	<i>GAPDH</i>	NM_002046.3	GCC GAG CCA CAT CGC TCA GAC ACC A	GGG ATC TCG CTC CTG GAA GAT GGT GAT GGG A	270
MAP4	<i>MAP4</i>	NM_002375.4	CCC TTT CTG AGG TAG CAG TGC CTT GTG GAG GT	CTG GCT CCC TCA TGT TCT TGG CAC AGC AGA	181
Stathmin 1	<i>STMN1</i>	NM_001145454.1	GGT GGC GGC AGG ACT TTC CTT ATC CCA GTT GAT T	TTC TCG TGC TCT CGT TTC TCA GCC AGC TGC TTC	312
P53	<i>TP53</i>	NM_000546.4	AGG CCT TGG AAC TCA AGG AT	CAA GGG TTC AAA GAC CCA AA	235
HPRT1	<i>HPRT1</i>	NM_000194.2	TGC TGA CCT GCT GGA TTA CA	CCT GAC CAA GGA AAG CAA AG	229

^a In a number of locations Inosine is inserted to break up runs of four or more Gs that might lead to unusually stable secondary structure.

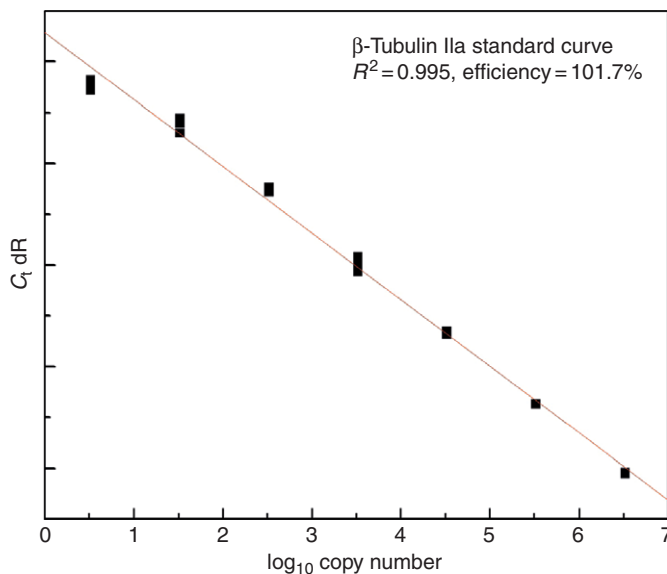


Fig. 1 Plot of real-time PCR data for β -tubulin class IIA. The standard curve is represented by closed symbols. *X*-axis: copies of mRNA; *Y*-axis: C_t (threshold cycle).

normal and non-small-cell lung carcinoma (NSCLC) samples, we showed that diseased tissues have significantly higher amounts of β -tubulin mRNA (Cucchiarelli *et al.*, 2008). Figure 1 shows real-time PCR data for β -tubulin class IIA, with data plotted as copy number versus threshold C_t (cycle at which significant product is first observed). The closed symbols represent the standard curve. From the slope of the plot, the primer efficiency is shown to be 103%. In a subset of samples, we compared β -tubulin classes IIA and IIB (Fig. 2). We found that β -tubulin class IIA was more abundant in normal lung tissues compared to β -tubulin class IIB ($p < 0.05$, Student's *t* test). Further, β -tubulin classes IIA plus IIB were significantly more abundant in NSCLC cells compared to normal lung tissues ($p < 0.05$, Student's *t* test). We also found that the ratios of β -tubulin classes II/V and *MAP4/stathmin 1* are significantly higher in NSCLC cells compared to normal lung tissues ($p < 0.05$, Student's *t* test). These data suggest that changes in expression of β -tubulin isotypes and MIPs could be biomarkers for lung pathology, and further suggested that more aggressive tumors have higher ratios of these markers; however, more study needs to be done to validate the observed trends.

B. β -Tubulin Isotypes and MIP Levels Change in Response to Drug Treatment

We used comparative real-time PCR to study changes in MIP mRNA levels in cell culture in response to paclitaxel treatment. In these experiments, MCF7 breast cancer cells, which have wild-type tumor suppressor p53, were treated with low level (400 nM) paclitaxel for 4, 8, and 24 h. Comparative real-time PCR was done using *GAPDH* and *HPRT1* as normalizing genes. This comparative PCR method allowed us to assess the cell response to drug treatment at multiple time points using two housekeeping genes on single PCR plates. The control, 0 h, sample was used as the

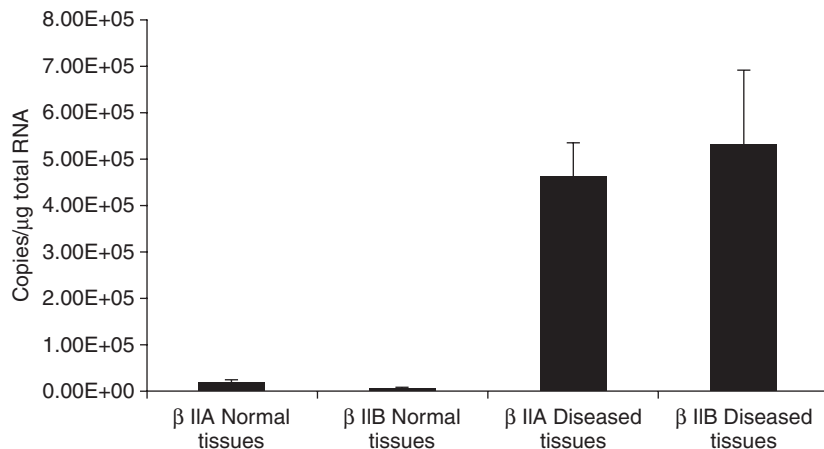


Fig. 2 Comparison of β -tubulin classes IIA and IIB mRNA in 13 normal lung and 45 NSCLC tissues with standard error of the mean.

calibrator for each gene of interest. In these experiments we measured *MAP4* and *stathmin 1* mRNA levels in response to drug treatment (Fig. 3). It has been reported that both *MAP4* and *stathmin 1* mRNA levels are regulated by *p53* (Ahn *et al.*, 1999; Zhang *et al.*, 1999). These data demonstrate a decrease in mRNA for both MIPs within 4 h of drug treatment in agreement with the reported studies. Similar results were found normalizing to *HPRT1*.

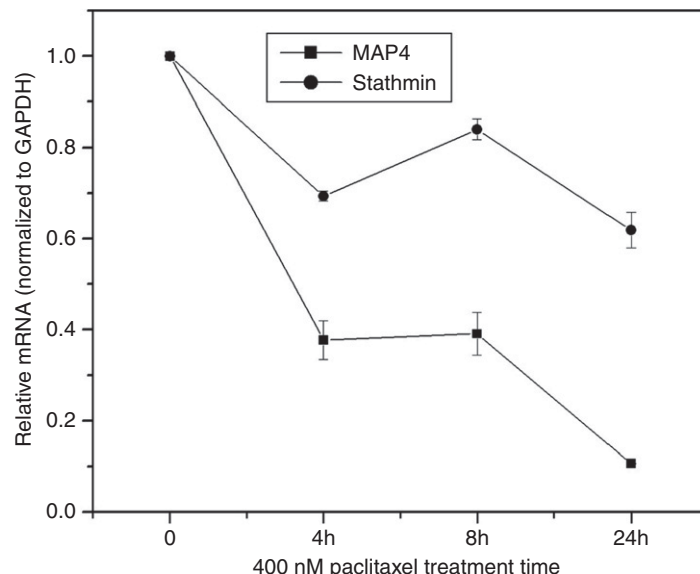


Fig. 3 Comparison of *MAP4* and *stathmin 1* mRNA in MCF7 breast cancer cells during exposure to 400 nM paclitaxel. Standard deviations were determined from two separate experimental plates.

IV. Summary

In conclusion, quantitative or comparative real-time PCR techniques are useful for studying tubulin isotypes and MIPs as potential biomarkers for cancer diagnosis and treatment selection and for investigating molecular mechanisms associated with drug treatment. It is important to select the appropriate method depending upon the research question. With good-quality initial samples, highly reproducible quantitative or comparative data can be collected. Data analysis provides insights into tubulin isotypes and MIPs as potential biomarkers and into mechanisms that underlie drug treatment and drug resistance.

References

Ahn, J., Murphy, M., Kratowicz, S., Want, A., Levine, A. J. and George, D. L. (1999). Down-regulation of the stathmin/OP18 and FKBP25 genes following p53 induction. *Oncogene* **18**, 5954–5958.

Anonymous (2007). Introduction to quantitative PCR: Methods and applications guide, Stratagene An Agilent Technologies Company, <http://www.stratagene.com/tradeshows/feature.aspx?fpId=1>

Anonymous (2008). Real-time PCR: From theory to practice, Invitrogen Corporation, <http://tools.invitrogen.com/content.cfm?pageid=12257>

Cucchiarelli, V. E., Smith, H., Hiser, L., Correia, J. J. and Lobert, S. (2008). β -Tubulin isotype classes II and V expression patterns in nonsmall lung tumors. *Cell Motil. Cytoskel.* **65**, 675–685.

Dozier, J., Hiser, L., Davis, J. A., Thomas, N. D., Tucci, M., Benghuzzi, H. A., Frankfurter, A., Correia, J. J. and Lobert, S. (2003). β Class II tubulin predominates in normal and tumor breast tissue. *Breast Cancer Res.* **5**, R157–R169.

Hiser, L., Aggarwal, A., Young, R., Spano, A., Frankfurter, A., Correia, J. J. and Lobert, S. (2006). Comparison of beta-tubulin mRNA and protein levels in twelve human cancer cell lines. *Cell Motil. Cytoskel.* **63**, 41–52.

Imbeaud, S., Graudens, E., Boulanger, V., Barlet, X., Zaborski, P., Eveno, E., Mueller, O., Schroeder, A. and Auffray, C. (2005). Towards standardization of RNA quality assessment using user-independent classifiers of microcapillary electrophoresis traces. *Nucleic Acids Res.* **33**(6), e56. doi:10.1093/nar/gni054.

Schroeder, A., Mueller, O., Stocker, S., Salowsky, R., Leiber, M., Gassmann, M., Lightfoot, S., Menzel, W., Granzow, M. and Ragg, T. (2006). The RIN: An RNA integrity number for assigning integrity values to RNA measurements. *BMC Mol. Biol.* **7**, 3. doi:10.1186/1471-2199-7-3.

Zhang, C. C., Yang, J.-M., Bash-Babula, J., White, E., Murphy, M., Levine, A. J. and Hait, W. N. (1999). DNA damage increases sensitivity to vinca alkaloids and decreases sensitivity to taxanes through p53-dependent repression of microtubule-associated protein 4. *Cancer Res.* **59**, 3663–3670.

CHAPTER 5

Nondenaturing Electrophoresis as a Tool to Investigate Tubulin Complexes

Mónica López Fanarraga^{*}, Gerardo Carranza^{*}, Raquel Castaño^{*}, Sofía Nolasco^{*,†}, J. Avila[‡], and J.C. Zabala^{*}

^{*}Departamento de Biología Molecular, Facultad de Medicina, IFIMAV-Universidad de Cantabria, 39011 Santander, Spain

[†]Instituto Gulbenkian de Ciência, 2781-901 Oeiras, Portugal

[‡]Centro de Biología Molecular (CSIC-UAM), Universidad Autónoma de Madrid, 28049 Cantoblanco, Madrid, Spain

Abstract

- I. Introduction
- II. Rationale
- III. Methods
 - A. Native Gels and Western Blotting
 - B. Analysis of Purified Tubulin: Tubulin Stability Assessed Using Nondenaturing Gels
 - C. Kinetic Analysis of Tubulin Complexes and Characterization of *In Vitro*-Synthesized Products
 - D. Isotype-Specific Antibody Analysis
 - E. 2-D Native SDS Electrophoresis
 - F. Preparation and Analysis of Subtilisin-Treated Dimers
 - G. Other Applications of Nondenaturing Electrophoresis: Stability Study of the *In Vivo* Tubulin Complexes by Native Electrophoresis
- IV. Materials
- V. Discussion
- VI. Summary
- Acknowledgments
- References

Abstract

A protein molecule may exist as a monomer, homo-oligomer, or hetero-oligomer in a multiprotein complex. One-dimensional (1-D) native electrophoresis has long been used to characterize tubulins and their complexes. In this chapter, we describe the simplest way to identify the state of aggregation of commercial or homemade tubulins for further studies based on 1-D electrophoresis under nondenaturing conditions. We present a series of detailed protocols that can be used to analyze the maturation of α - and β -tubulins and to identify the complexes formed during the folding and dimerization pathway as well as their stability.

I. Introduction

From the pioneering work of [Smithies \(1955\)](#) and [Markert and Hunter \(1959\)](#) followed by the descriptions of disk electrophoresis by Ornstein and Davis, both in 1964, electrophoresis has become one of the most effective methods for separating single macromolecules or complexes of several macromolecules according to the size and charge of the different molecular entities. To isolate single proteins, [Shapiro *et al.* \(1967\)](#) reported the use of polyacrylamide electrophoresis in the presence of the anionic detergent sodium dodecyl sulfate (SDS). In this condition, single polypeptide chains can be isolated because their fractionation depends only on the molecular weight of the polypeptide chains. These results were later confirmed by [Weber and Osborn \(1969\)](#), who showed the reliability of molecular weight determinations by dodecyl sulfate polyacrylamide gel electrophoresis (PAGE). This technique was refined by [Laemmli \(1970\)](#). Although this excellent method for protein fractionation was described mainly for the characterization of single proteins present in isolated fractions, addition of the denaturing detergent SDS makes it impossible to determine whether the proteins present interact with their neighbors or with themselves by forming multimolecular complexes of physiological relevance. Thus, alternative techniques without denaturing agents were tested with the aim of isolating and characterizing monomers, dimers, and multimolecular complexes of a protein and its associated proteins. [Zabala and Cowan \(1992\)](#) described a technique for the fractionation of monomers, dimers, and multimolecular complexes of tubulin using nondenaturing conditions. This widely used technique allows one to perform functional studies on the assembly of multimolecular protein complexes. In this chapter, we describe different applications of nondenaturing gel electrophoresis to examine the structure of tubulin complexes.

II. Rationale

Nondenaturing gel electrophoresis is used to separate proteins by retaining their higher-order structure and their interactions with other polypeptides; this is achieved by avoiding the use of denaturing agents in the gel. Unlike SDS-PAGE, in non-denaturing gel electrophoresis, the migration of proteins depends on their global shape and charge, implying that the mobility of a protein complex can vary

according to the nature of its conformation. In this kind of approach, one must remember that the electric charge of a protein, or a protein complex, depends on the composition of the electrophoresis buffer.

Although nondenaturing electrophoresis provides less resolution than does SDS-PAGE, this technique is useful because it permits the study of protein–protein and protein–ligand interactions. Native gel electrophoresis is used widely in many types of studies such as the analysis of the charge changes caused by chemical degradation, changes between the folded and unfolded conformation, formation of oligomers and aggregates, identification of individual proteins within a complex, characterization of nucleoprotein particles, and protein–protein- or protein–ligand-binding events. Native gel electrophoresis is also an excellent tool for analyzing the stability of samples, the effects of excipients, and antibody–protein complexes (Safer, 1994).

The combination of native electrophoresis and Western blotting is a powerful tool to identify the individual protein components in a complex by immunodetection. In this type of combined method, it is important to pay particular attention to negative results because the epitopes recognized by the antibodies can be unavailable in the protein complex structure. In addition, in those cases where more precise proteomic analysis of the components should be performed, nondenaturing gel electrophoresis can be complemented by a second SDS-PAGE dimension.

Two main types of native gels are used in protein electrophoresis: polyacrylamide and agarose. The concentrations of acrylamide and bisacrylamide determine the resolution range of the gel. Agarose gels are used for electrophoresis of proteins generally larger than 200 kDa.

We have developed a protocol that can be used to routinely investigate different aspects of our main research subject, tubulin, and its folding intermediates (Fig. 1). Here we describe several examples of native PAGE applications that we currently use in our studies. These include the quality analysis of purified tubulin, characterization of properly folded tubulin dimers, analysis of tubulin complex stability and assembly kinetics, and characterization of the *in vitro*-synthesized tubulin complexes. Two additional applications of the technique are also possible: the analysis of single protein components in two-dimensional (2-D) native SDS electrophoresis and analysis of the efficiency of the preparation of subtilisin-treated tubulin dimers; these additional applications show the versatility of this technique.

III. Methods

A. Native Gels and Western Blotting

Many techniques based on native electrophoresis have been developed to separate native proteins and protein complexes. Among them, blue native electrophoresis is one of the best known techniques (Wittig and Schägger, 2008; Burré *et al.*, 2009). This technique was developed initially to study membrane proteins, although it is now used more widely. Most of the native electrophoresis systems use acrylamide-gradient gels. In our system, we use a native continuous-buffer system, which allows the addition of glycerol or nonionic detergents in the buffer, although we typically do not use them. We routinely do not degas the polyacrylamide mix, but this can be done in a sidearm flask under vacuum to speed the polymerization. To prepare the

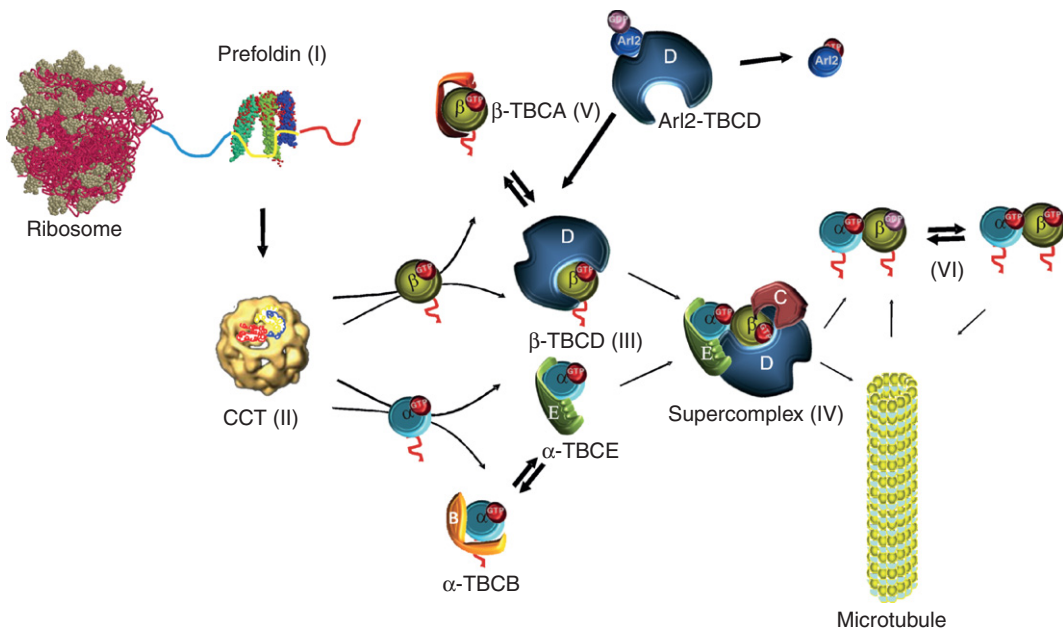


Fig. 1 Model of the tubulin-folding pathway in mammals adapted from Fanarraga *et al.* (2001, 2003). After synthesis, the tubulin polypeptides are protected by molecular chaperones that bind to prefoldin, which will next transfer these polypeptides to the cytosolic chaperonin chaperonin-containing Tcp-1. Five different tubulin-folding proteins, named tubulin cofactors, are then required in the post-chaperonin-folding pathway, which, after guanosine triphosphate hydrolysis, allows the release of the $\alpha\beta$ -heterodimer. Although recent work suggests that several cofactors are involved in the proteasome pathway, the role of these cofactors in tubulin degradation is not known completely. (See Plate no. 2 in the Color Plate Section.)

gel, we use a 75- or 100-ml Erlenmeyer flask. The polyacrylamide stock can be prepared in the laboratory, but it is more convenient to use a ready-to-use commercial solution, such as ProtoGel 30% (w/v) acrylamide and 0.8% (w/v) bisacrylamide from National Diagnostics, Hessle, England. The ProtoGel solution is mixed with 0.5 M MES, pH 6.7, 1 M MgCl₂, and 0.5 M ethylene glycol tetraacetic acid (EGTA) (Table I), and 10% (w/v) ammonium persulfate and tetramethylethylenediamine (TEMED) are then added.

All reagents and solutions must be prepared with Milli-Q-purified water or equivalent. The recipe shown in Table I is for 40 ml of solution, which is adequate for one gel measuring 14 cm \times 16 cm and 1.0 mm thick. Ten milliliters of solution is enough for two minigels measuring 7 cm \times 8 cm and 0.75 mm thick. Ammonium persulfate can be prepared and stored frozen in aliquots at -20°C, but we prefer to use it freshly made and we add TEMED just before polymerization. Pour the gel mix into the gel cast and insert the appropriate comb to allow the gel to polymerize for 30–60 min (Avila *et al.*, 2008). When running a 14 cm \times 16 cm gel, we change the buffer in the cathode chamber every 2 h. This technique can also be used to identify different polypeptides in the same complex by transferring the proteins from the native gel to nitrocellulose or a polyvinylidene fluoride membrane. Native protein transfer is performed as for conventional SDS gels, except that the native transfer

Table I
Gel Preparation

Stock solution (ml)	Final acrylamide concentration in gel (%)			
	4	5	6	7
DW	25.96	24.64	23.28	21.96
30% Acrylamide/0.8% bisacrylamide	5.32	6.64	8	9.32
0.5 M MES pH 6.7	8	8	8	8
1 M MgCl ₂	0.04	0.04	0.04	0.04
0.5 M EGTA	0.08	0.08	0.08	0.08
1 M GTP ^a	0.04	0.04	0.04	0.04
10% (w/v) APS	0.56	0.56	0.56	0.56
TEMED	0.04	0.04	0.04	0.04

APS, ammonium persulfate; DW, distilled water; EGTA, ethylene glycol tetraacetic acid; GTP, guanosine triphosphate; TEMED, tetramethylethylenediamine.

^aInclusion of GTP in the gel mix and in the running buffer was shown to be essential for preservation of the native tubulin dimer as well as some of the complexes described in Fig. 1 (Zabala and Cowan, 1992).

buffer contains no methanol. Protein transfer requires the same duration and current conditions. After the gel is run, the bands of interest can be detected with immunodetection.

B. Analysis of Purified Tubulin: Tubulin Stability Assessed Using Nondenaturing Gels

Since the 1970s, many similar methods to purify microtubule proteins including tubulins and microtubule-associated proteins have been developed and reported (reviewed recently by Avila *et al.*, 2008). Most protocols are based on the reversible assembly capacity of microtubule proteins. Although it is possible to polymerize microtubules *in vitro* in the presence of guanosine triphosphate (GTP) and at 35°C, assembly-promoting agents such as glycerol or dimethyl sulfoxide (DMSO) are often included. The quality and quantity of tubulins and other microtubule-associated proteins can be followed by SDS-PAGE analysis. However, this kind of electrophoresis does not tell us anything about the state of aggregation of these proteins and, thus, whether they are competent for microtubule assembly or interaction with other proteins. In other words, we cannot predict the amount of tubulin that becomes partially aggregated into intermediate polymerization structures and will not be competent for further experiments. In addition, we have observed that a single freezing step can cause the formation of some tubulin aggregates. To avoid these problems, we encourage the “polishing” of tubulin dimers through a gel filtration column. We routinely use Superdex-200, Superose-6, or Superose-12 columns (the column size depends on the amount to be purified), from Pharmacia GE Healthcare, Buckinghamshire, UK. GTP is often included in the column buffer for stabilization purposes, but we have found that this is not strictly required and may compromise further experiments.

Figure 2 shows a chromatogram of a gel filtration Superdex 200 PC 3.2/30 column. We used purified tubulin as described by Avila *et al.* (2008). After purification through the phosphocellulose column, tubulin is usually stored at -80°C. About 500 µg of purified tubulin at 12 µg/µl is injected in the column, which has been

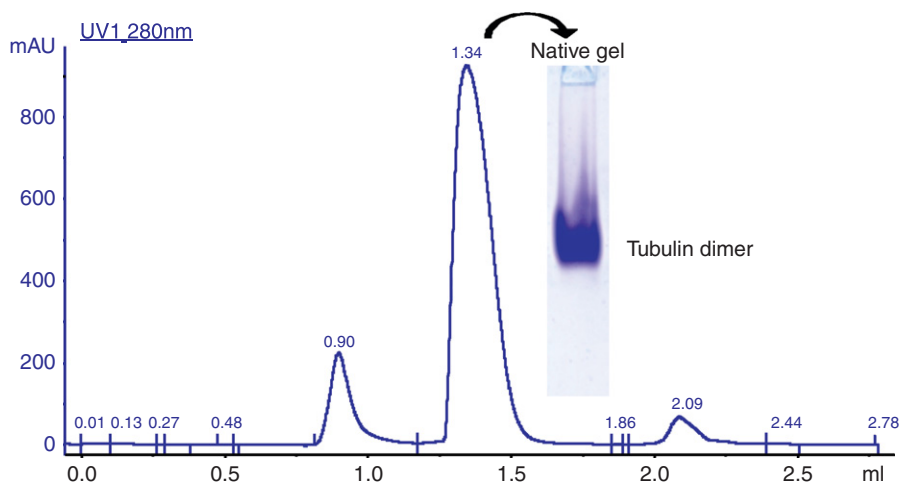


Fig. 2 Chromatographic elution profile obtained at 280 nm of absorbance from a gel filtration analysis of phosphocellulose-purified tubulin through a high-resolution Superdex 200 PC 3.2/30 column. Inset: nondenaturing gel (6% polyacrylamide) analysis of the peak corresponding to a molecular mass of 110 kDa eluted from the column. The gel has been stained with Coomassie blue.

equilibrated with buffer A (0.1 M MES buffer, pH 6.7, containing 1 mM MgCl₂, 1 mM EGTA, and 25 mM KCl). About 70–80% of the tubulin protein elutes as a homogeneous peak in the elution volume and corresponds to the size of the tubulin dimer. A proportion of tubulin may appear in the void volume of the column, suggesting the formation of large aggregates. The tubulin fractions containing dimers can be quantified using a NanoDrop spectrophotometer (Thermo Scientific, Wilmington, NC, USA) and kept on ice. About 15 µg of protein in 10 µl is then loaded onto a 6% nondenaturing minigel with native loading buffer (Avila *et al.*, 2008, this work). As shown in the inset of Fig. 2, a large band corresponding to the tubulin dimer can be observed, whereas there is no staining at the origin of the gel, revealing that all the tubulin in the peak behaves as dimers that do not aggregate.

Because tubulin has long been considered a highly unstable protein, we wanted to further understand tubulin behavior at different temperatures and at different times and after thawing and refreezing many times in the presence of different reagents such as glycerol and DMSO used routinely as coadjuvants in polymerization experiments. Aliquots of 1.25 µg/µl tubulin were diluted with buffer A, frozen, and thawed 1, 2, 4, 8, or 16 times, as indicated in Fig. 3, in the presence of 25% glycerol or 10% DMSO. These samples were frozen and thawed the same number of times before being loaded onto a 14 cm × 16 cm nondenaturing gel. The results shown in Fig. 3 (panel B) show that, although the inclusion of glycerol preserved tubulin from denaturation or aggregation when frozen and thawed up to 16 times, 50% of the total tubulin in buffer A aggregated or unfolded after eight freeze–thaw cycles and 20% after only two cycles. The effect of freezing–thawing was greatest in the presence of DMSO. After 2 freeze–thaw cycles, the result was similar at the same dilution in buffer A, but the effect was much greater after 16 cycles.

As mentioned above, it is believed that tubulin becomes unstable after several hours at 4°C. To study the effect of temperature on the unfolding and aggregation of

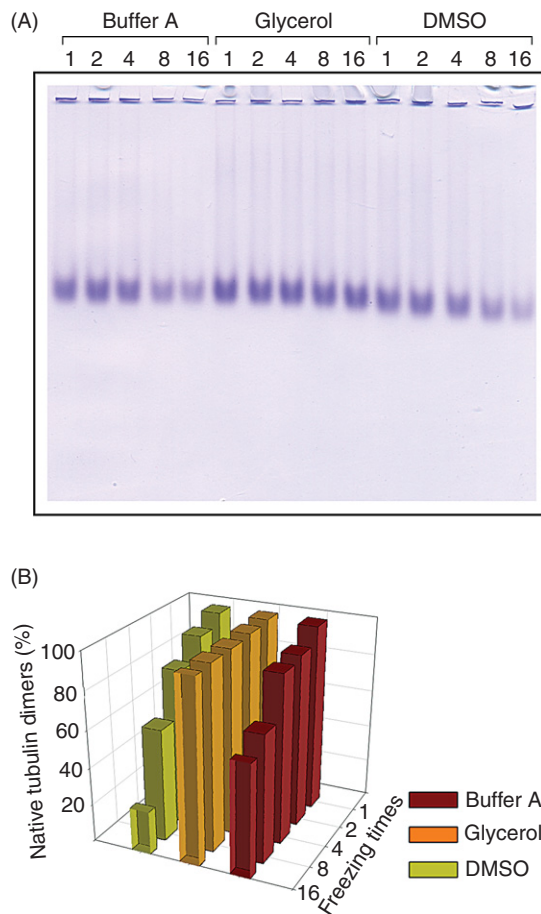


Fig. 3 (A) Nondenaturing polyacrylamide gel electrophoresis (6% polyacrylamide) of 4 μ l-purified tubulin (at 1.25 μ g/ μ l) frozen for the times indicated in the presence of buffer, 25% glycerol, or 10% dimethyl sulfoxide. The gel was stained with Coomassie blue and scanned before drying. The bands were quantified using ImageJ 1.36b (by Wayne Rasband, NIH, MD, USA) software freely available on the Internet. (B) Quantification of the percentage of tubulin heterodimers remaining. The three-dimensional bar chart was made using SigmaPlot 8.0 software (Systat Software, Richmond, CA, USA). (See Plate no. 3 in the Color Plate Section.)

the dimer, we incubated 1.25 μ g/ μ l of purified tubulin, which had already been frozen once (0 h) at 4°C and at 30°C for the times indicated in [Fig. 4](#). Aliquots were then loaded onto a 14-cm \times 16-cm nondenaturing gel (panel A) and on a 14-cm \times 16-cm denaturing SDS gel (panel B). Although at both temperatures, tubulin dimers remained stable for 8 h, the amount of tubulin dimer remaining active after 20 h of incubation declined to 65% at 4°C and 30% at 30°C (panel C). After 30 h, the percentage of folded tubulin was 44% at 4°C and 7% at 30°C. In addition, after 20 h at 30°C, the stability of tubulin was compromised because of degradation (panel B).

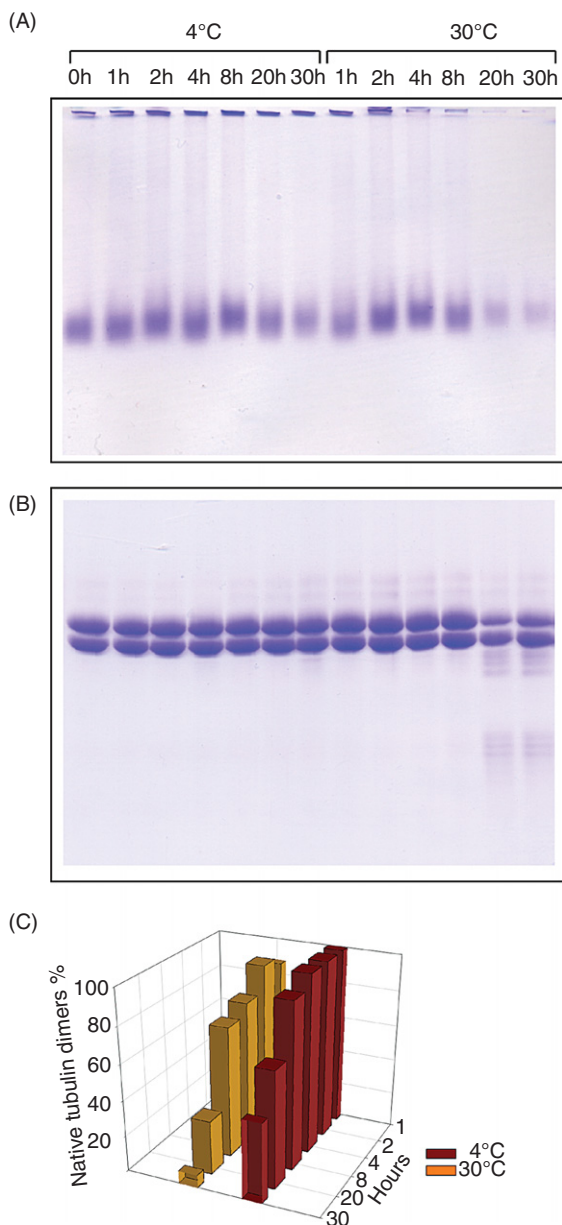


Fig. 4 Evaluation of the quality of native tubulin heterodimers by nondenaturing polyacrylamide gel electrophoresis (6% polyacrylamide). (A) Characterization of 4 μ l aliquots of purified tubulin (at 1.25 μ g/ μ l) in 100 mM MES, pH 6.7, containing 25 mM KCl, 1 mM MgCl₂, and 1 mM EGTA, incubated for the times indicated at 4 or 30°C. Incubation time is indicated in hours. (B) The same tubulin samples were loaded onto an 8.5% sodium dodecyl sulfate gel. Both gels were stained with Coomassie blue and then scanned before drying. (C) Quantification of the percentage of tubulin heterodimers remaining. The three-dimensional bar chart was made using SigmaPlot 8.0 software (Systat Software, Richmond, CA). (See Plate no. 4 in the Color Plate Section.)

C. Kinetic Analysis of Tubulin Complexes and Characterization of *In Vitro*-Synthesized Products

The correct folding of tubulins and the generation of functional $\alpha\beta$ -tubulin heterodimers require the participation of molecular chaperones such as prefoldin and chaperonin-containing Tcp-1 (CCT, Gao *et al.*, 1993; Geissler *et al.*, 1998; Vainberg *et al.*, 1998) as well as several proteins known as tubulin-folding cofactors (A–E) (reviewed in Fanarraga *et al.*, 2001, 2003; Fig. 1). Pulse–chase experiments can be used to follow the fate of newly synthesized tubulin during its folding and dimerization pathway. This system allows one to study tubulin-folding kinetics (Campo *et al.*, 1994). Full-length cDNA encoding wild-type α_6 - or β_3 -tubulin cloned into appropriate vectors was used as the template and coupled to the *in vitro* transcription and translation (Craig *et al.*, 1992) in the presence of ^{35}S -methionine for 20 min at 30°C. Figure 5 shows the analysis of a 20-min pulse with ^{35}S -methionine to allow the complete synthesis of α_6 -tubulin (panel A) and β_3 -tubulin (panel B) isotypes. After the lag period (at 0 min), synthesis of tubulin polypeptides was stopped with cold methionine and 1 mM RNase A (0.08 $\mu\text{g}/\mu\text{l}$). At the times indicated in Fig. 5, 2 μl aliquots of the *in vitro* reactions were frozen every

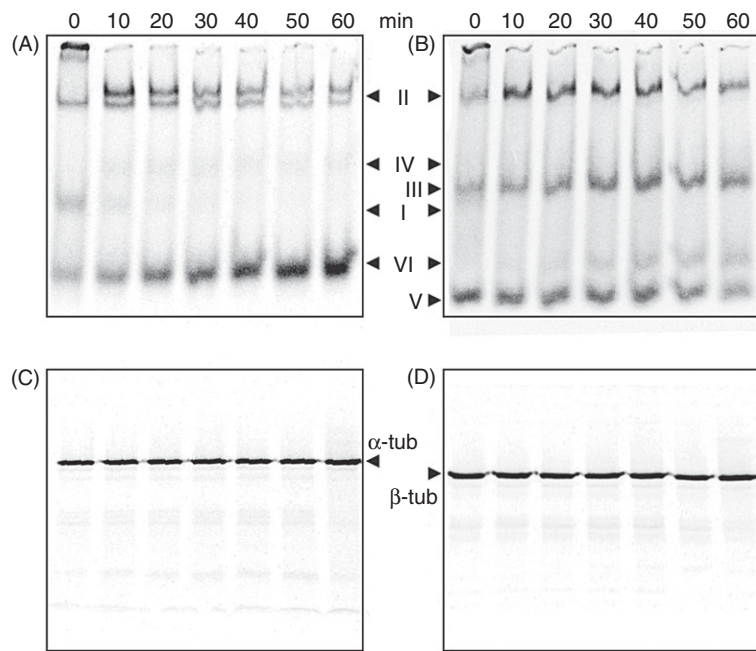


Fig. 5 Pulse–chase experiments of *in vitro*-translated tubulin isotypes. Newly synthesized α_6 -tubulin (A) and β_3 -tubulin (B) isotypes were analyzed by electrophoresis on 4.5% nondenaturing gels. Panel A shows the results of a 20 min pulse that was chased with cold methionine and RNase A and analyzed for the times indicated. Roman numerals indicate the different complexes that appeared during the *in vitro* translation of the tubulins depicted in Fig. 1 (see Section III). (C, D) The same tubulin samples run under denaturing conditions. The samples were diluted with the same volume of distilled water, 2 \times sodium dodecyl sulfate (SDS) loading buffer was added, and the samples were loaded onto an 8.5% SDS-polyacrylamide gel. Following electrophoresis, gels were fluorographed, dried, and exposed to film (Hyperfilm, GE Healthcare).

10 min on dry ice. Samples were diluted with native loading buffer and loaded onto 6% native minigels.

As stated above, native electrophoresis allows one to identify the tubulin complexes as they are formed during the tubulin-folding process. This way, completely denatured or newly synthesized tubulin enters into the prefoldin complex (I) (Vainberg *et al.*, 1998), which can be detected soon after initiation of synthesis. Prefoldin then transfers the tubulin substrate to CCT to form a binary complex (II), which appears as a band close to the origin (Fig. 5). This band containing the complex of CCT bound to tubulin was first shown to participate in tubulin biogenesis by Yaffe *et al.* (1992). For some β -tubulin isotypes such as β_3 , this band, which has a molecular mass of about 900 kDa, precedes the two other bands corresponding to complexes (III) and (IV) (Fontalba *et al.*, 1993; Tian *et al.*, 1996). One band contains cofactor D/ β -tubulin complexes (lower band) and the other contains tubulin-folding cofactor E/ α -tubulin in addition to cofactor D and β -tubulin (Fontalba *et al.*, 1993; Tian *et al.*, 1996). Finally, the two fast-migrating bands correspond to the $\alpha\beta$ -tubulin heterodimers and the tubulin-folding cofactor A (TBCA)/ β -tubulin complexes (VI) and (V), respectively (Campo *et al.*, 1994; Llosa *et al.*, 1996).

D. Isotype-Specific Antibody Analysis

Tubulins are encoded by members of multigene families and are generally highly conserved at the sequence level except for the last 15 amino acids of their C-terminus, which are markedly divergent. The conserved peptide region in vertebrates constitutes the so-called isotype-defining region of tubulins. Because native electrophoresis allows the preservation of antibody–protein complexes, this technique can also be used to evaluate biochemically the affinity of an isotype-specific antibody. Protein–antibody complexes migrate differently during electrophoresis than do unbound protein monomers, resulting in retardation of the tubulin-containing band along the gel run, and the band retardation reflects the antibody binding. Further details on this technique and a more detailed study that evaluated the affinity of two polyclonal antibodies raised against the β -tubulin isotypes, β_6 and β_2 , relative to all β -tubulin isotypes, has been published (Fanarraga *et al.*, 1998). In this particular study, six different β -tubulin isotypes were translated *in vitro* using a reticulocyte cell-free translation system in the presence of ^{35}S -methionine (as explained above). The resulting reactions containing radiolabeled newly synthesized β -tubulin protein were next incubated with the two antibodies in two separated experiments, and the products of the incubation reactions were analyzed under nondenaturing gel electrophoresis where the various molecular forms of β -tubulin were separated and characterized. Dried gels were fluorographed and showed that, although the two polyclonal antibodies recognized the β -tubulin isotypes they were raised against, the anti- β_2 -tubulin antibody appeared to be more specific than the anti- β_6 -tubulin, which also recognized the platelet-specific β_1 -tubulin isotype and resulted in a 38% reduction in radioactivity at the β_1 -tubulin monomer band (Fanarraga *et al.*, 1998).

E. 2-D Native SDS Electrophoresis

Folded α - and β -tubulins may exist as heterodimers in solution, forming microtubules or binding to the characterized tubulin-folding cofactors. Classical 2-D

electrophoresis (2-D PAGE) allows one to separate the different polypeptides present in multimolecular complexes into individual species. The first dimension uses the isoelectric point as a differential characteristic to allow separation, and the second dimension uses the size under denaturing conditions in a SDS gel. This powerful method is used mainly to separate and identify peptides or proteins in complex samples for immunological or proteomic applications. A 2-D PAGE method using a native gel for the first dimension and a denaturing gel for the second dimension allows the separation of complexes under native conditions, and the composition can then be studied by SDS-PAGE. This technique also allows the determination of the stoichiometry of the different subunits in the complex. Here we show an example of an application of this technique to study the reactions involving tubulins synthesized *in vitro*; we used this method to study the formation of the different tubulin-folding intermediates described above.

The protein complexes are fractionated in the first dimension, and the second dimension is used to analyze the quality (length) and quantity of the *in vitro*-synthesized tubulin polypeptides (Fig. 6). These results demonstrate that tubulin polypeptides are constituents of the different complexes formed and allow us to exclude artifacts caused by the synthesis of partial products. The samples were loaded onto a native 0.75-mm thick minigel (7 cm × 8 cm) as described above. After 2 h of electrophoresis, a single running lane containing the electrophoresed sample was excised with a blade on glass, loaded onto a preparative 1.5 mm thick minigel (7 cm × 8 cm), and fixed to the gel with 0.5% agarose prepared in 1× SDS-loading buffer. Electrophoresis was performed for a further 2 h at 80 V, after which the gel was dried and fluorographed as described above. As shown in Fig. 6, all bands contained full-length α_6 -tubulin (Fig. 6A and C) or β_3 -tubulin (Fig. 6B and D) polypeptides. The Roman numerals indicate the position of the bands of the different tubulin complexes represented in Fig. 1 as detected in native gels.

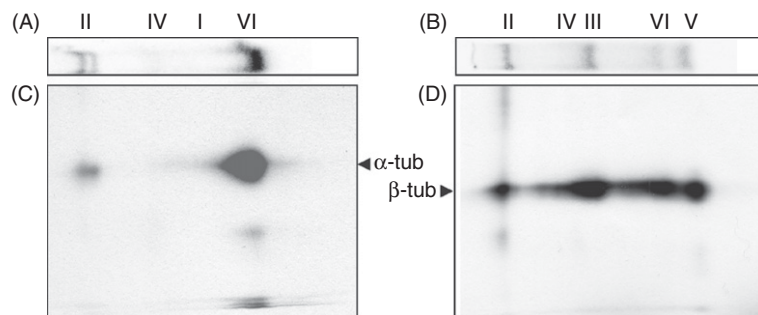


Fig. 6 Nonclassical two-dimensional native SDS-PAGE of *in vitro*-translated tubulin polypeptides. Aliquots of *in vitro*-translated α_6 - and β_3 -tubulin isotypes (A, B) incubated for 60 min at 30°C (Fig. 5) were loaded onto a 4.5% native minigel. Complete lanes containing this first dimension were excised from the gel and loaded onto an 8.5% sodium dodecyl sulfate polyacrylamide gel (C, D). After electrophoresis, the gels can be stained with Coomassie blue or fixed directly, and fluorographed. Panel C shows the second dimension for the α_6 -tubulin isotype and panel D shows the β_3 -tubulin isotype.

F. Preparation and Analysis of Subtilisin-Treated Dimers

Subtilisin cleaves tubulin subunits near the carboxy-terminus to generate two fragments. The larger fragment can coassemble into microtubules more efficiently than the whole molecule (Sacket *et al.*, 1985; Serrano *et al.*, 1984a,b). The small fragment corresponds to the highly acidic carboxy-terminus of tubulin needed for the interaction with microtubule-associated proteins and is believed to play a regulatory role in microtubule dynamics and tubulin folding (Fontalba *et al.*, 1995; Littauer *et al.*, 1986; Sacket *et al.*, 1985; Serrano *et al.*, 1984a,b; 1986). Subtilisin can be used to digest soluble tubulin or polymerized microtubules; the amount of enzyme can be manipulated to digest one or both tubulin subunits, or at different sites on the C-terminus. This technique was used by Hertzner and Walzak (2008) to study the influence of the C-terminus and the specific geometry of tubulin in the depolymerization activity of kinesin-13. Here, we describe a general protocol to eliminate the C-terminus (40–50 residues) of both subunits in solution. These tubulin heterodimers (named “S-dimers”) can form microtubules and sheets in the presence of calcium ions (Lobert *et al.*, 1993) and are useful for studying the contribution of the C-terminus to the tubulin-folding, dimerization, and polymerization processes.

Limited proteolysis with subtilisin was performed essentially as described by Serrano *et al.* (1984a,b). Tubulin (4 mg/ml) was incubated at 25°C in 50 mM MES, pH 6.7, containing 1 mM EGTA and 0.5 mM MgCl₂ with different amounts of subtilisin (w/w) for 30 min as shown in Fig. 7A. After subtilisin digestion, the reaction was cooled to 4°C and stopped with 1 mM phenylmethylsulfonyl fluoride (PMSF) made freshly in DMSO and 1 μM aprotinin. Tubulin was repolymerized once in the presence of 1 mM GTP and 2 mM CaCl₂ for 30 min at 35°C and then

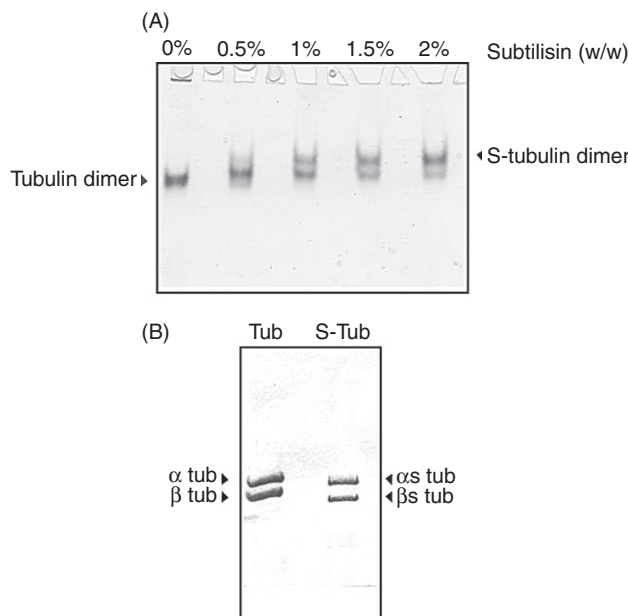


Fig. 7 (A) Monitoring the progress and efficiency of the subtilisin digestion of purified tubulin dimers using a non-denaturing polyacrylamide gel and sodium dodecyl sulfate polyacrylamide gel electrophoresis. (B) Symbols indicate the position of cow brain native tubulin dimers ($\alpha\beta$) and subtilisin-digested dimers ($\alpha_s\beta_s$).

loaded with a Pasteur pipette on a prewarmed sucrose cushion in a tube. The microtubules made of S-tubulin were next pelleted at $100,000 \times g$ for 90 min at 35°C in a Beckman TLX centrifuge and then resuspended in 100 mM MES, pH 6.7, containing 0.3 M KCl and 1 mM MgCl₂ at 4°C for 30 min to allow depolymerization. Insoluble material was removed by ultracentrifugation at $100,000 \times g$ for 20 min at 4°C. Following this procedure, the different digestion reaction products were studied by electrophoresis under native conditions (as shown in Fig. 7A) to monitor the progress and efficiency of the experiment. For this purpose, aliquots diluted to one-fifth with 25% sucrose (final concentration of 5%) made up in 50 mM MES, pH 6.7, were loaded onto a 6% nondenaturing polyacrylamide gel (Avila *et al.*, 2008, this work; Zabala and Cowan, 1992). In parallel, an aliquot of S-tubulin was also analyzed in an 8.5% SDS gel (Fig. 7B) to check that the C-terminal region of both subunits had been digested by the enzyme and that there was no contamination with native undigested tubulin after the polymerization cycle in the presence of calcium ions.

Upon electrophoresis, untreated purified brain tubulin dimers gave a single band when analyzed by electrophoresis under nondenaturing conditions (Fontalba *et al.*, 1995; Zabala and Cowan, 1992). This differed from the S-tubulin dimers, which also gave a single band (Fig. 7: $\alpha_s\beta_s$) that migrated more slowly than the corresponding wild-type tubulin heterodimer band. This difference reflects the greater negative net charge at pH 6.7 of the untreated tubulin heterodimer compared with the same protein after removal of the carboxy-terminal domain.

G. Other Applications of Nondenaturing Electrophoresis: Stability Study of the *In Vivo* Tubulin Complexes by Native Electrophoresis

Mammalian tubulin complexes can also be examined by nondenaturing gel electrophoresis of soluble protein extracts. In this experiment, we intended to test the stability of TBCA/β-tubulin dimer in soluble protein extracts at 4°C obtained from HeLa cells, a standard tumor cell line, which were cultured in monolayers in a 5% CO₂-humidified atmosphere at 37°C in Dulbecco's modified Eagle's medium containing GlutaMAX (Invitrogen, Carlsbad, California, USA) supplemented with 10% fetal calf serum (Invitrogen) and nonessential amino acids (Invitrogen). A nearly confluent 100-mm plate of HeLa cells was rinsed twice with 5 ml of PBS and the cells were scraped into the last 5 ml of PBS and centrifuged at $500 \times g$ for 3 min in a bench centrifuge. The cell pellet was then resuspended in 100 μl of lysis buffer (0.1 M MES, pH 6.7, containing 1 mM MgCl₂, 1 mM EGTA, 0.1 mM GTP, 5 nM paclitaxel, 0.2 mM dithiothreitol, 0.1 mM PMSF, and protease inhibitor cocktail) and then lysed using a 2-ml Dounce homogenizer (20 strokes with a tight pestle). All procedures were performed at room temperature to avoid microtubule depolymerization because cold shock increases the pool of soluble tubulin heterodimers and would thus affect the amount and composition of tubulin complexes.

The cellular lysate obtained was centrifuged at $14,000 \times g$ for 30 min at 20°C in a standard bench centrifuge, and the supernatants were recovered (soluble fraction). We used native electrophoresis to investigate the stability of the TBCA/β-tubulin complex (Fig. 1, complex (V)) under different conditions. We compared 30 μg of total soluble protein fractions freshly obtained with the same extract after being kept at 4°C for 48 or 96 h. Electrophoresis was performed in a native 1.5-mm thick minigel (7 cm × 8 cm) for 2 h at 80 V, after which the proteins were transferred to a

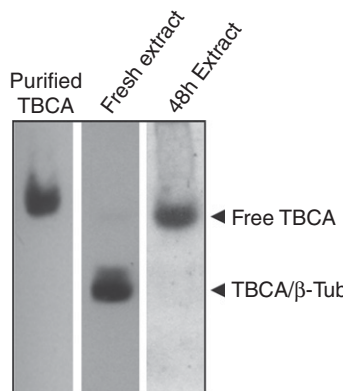


Fig. 8 Analysis of the tubulin-folding cofactor A (TBCA)/ β -tubulin complex stability at 4°C. A total of 30 μ g of freshly obtained soluble protein extract prepared from HeLa cells was compared with the same extract after 48 h storage at 4°C using nondenaturing gel electrophoresis (6%) and TBCA detection by Western blotting. This study reveals that the TBCA/ β -tubulin complex disassembles after storage.

nitrocellulose membrane for Western blotting. Immunodetection was performed using a rabbit polyclonal antiserum against TBCA (1:5000), which has been characterized broadly (Llosa *et al.*, 1996). Figure 8 shows clearly that the TBCA/ β -tubulin complex was present in the fresh extract but absent in extracts stored at 4°C for 48 h, indicating that this complex is not stable under these conditions.

IV. Materials

- Gel solutions (Table I)
- Protein sample to be analyzed
- 4 \times loading buffer
- Electrophoresis equipment (we use Mini-PROTEAN from Bio-Rad Laboratories Inc, Hercules, California, USA and 0.75-mm spacers or sturdier vertical slab units from Amersham Biosciences, GE Healthcare)
- 0.5 M MES pH 6.7 (53.3 g MES monohydrate dissolved in 400 ml water, titrated to pH 6.7 with KOH or NaOH, and adjusted to a final volume of 500 ml)
- 1 M MgCl₂
- 0.5 M EGTA [19 g EGTA–ethylene glycol-bis-(2-aminoethyl)-N,N,N',N'-tetraacetic acid dissolved in 80 ml water, titrated to pH 8 with KOH or NaOH, and adjusted to a final volume of 100 ml]
- Electrophoresis (running) buffer (0.1 M MES-KOH or MES-NaOH, pH 6.7, 1 mM MgCl₂, 1 mM EGTA, diluted in 700 ml water, 160 ml 0.5 M MES, 800 μ l 1 M MgCl₂, and 1.6 ml 0.5 M EGTA, and adjusted to a final volume of 800 ml)
- 10 \times transfer buffer [15.13 g Tris (250 mM) and 72.067 g glycine (1.92 M) dissolved in pure water and adjusted to a final volume of 500 mls]
- 1 M GTP (1.5 ml distilled H₂O, 1 g Na₂GTP); bring to final volume of 1.91 ml with H₂O; do not allow to stand at room temperature or at 4°C, but aliquot in small volumes and store at -70°C immediately

- Rabbit reticulocyte lysates from Promega, Madison, USA
- ^{35}S -methionine ($>1000\text{ Ci}/\text{mmol}$) from Amersham Biosciences, GE Healthcare
- Antibodies against the protein of interest; in this work, we raise antibodies to tubulin cofactors in our laboratory

===== V. Discussion

A main problem in denaturing gel electrophoresis is that it cannot be used to study protein–protein interactions. These interactions can occur in specific cell locations or at a specific time, and studying these interactions could contribute to understanding further the cellular processes involving tubulin. We have reviewed the use of a nondenaturing electrophoresis technique complemented with the well-known SDS denaturing electrophoresis. The various applications of this technique mentioned could complement gel filtration analysis to identify different types of protein complexes formed during the tubulin-folding and tubulin-assembly process. This technique allows one to determine the stability of some of the complexes that participate in tubulin biogenesis and has been used extensively in the study of the folding process of actin and other proteins that also require specific molecular chaperones. We also show how native electrophoresis is useful for the study of tubulin complexes that are present inside the cell before purification. This would allow one to study these complexes inside the cell or a tissue under different conditions and would represent an important tool to study the physiologic roles of tubulin and other proteins.

===== VI. Summary

One of the main purposes of this technique is to provide an easy way to investigate tubulin complexes in a way that is relevant both physiologically (i.e., complexes with other proteins) and biochemically (i.e., protein aggregates). Among others, we have presented results to show how to proceed when we want to know if a tubulin solution is competent for polymerization studies or for interaction studies with proteins of interest. We have also shown how this type of electrophoresis can be used to study the electrophoretic changes resulting from the removal of the carboxyl terminus of this protein, how a particular tubulin complex disassembles with time, and how one might take advantage of the properties of this system to investigate the quality of isotype specificity of a determined antibody. We believe native electrophoresis is a fundamental tool for modern proteomic studies.

Acknowledgments

This work was supported by grants from the Consolider-Ingenio Spanish Ministry of Education and Science (Centrosome-3D and BFU2007-64882) and the Instituto de Formación e Investigación Marques de Valdecilla (IFIMAV). We also thank Begoña Ubilla for technical help.

References

Avila J., Soares H., Fanarraga M. L., and Zabala J. C. (2008). Isolation of microtubules and microtubule proteins. *Curr. Protoc. Cell Biol.* Chapter 3, Unit 3.29.

Burré J., Wittig I., and Schägger H. (2009). Non-classical 2-D electrophoresis. *Methods Mol. Biol.* **564**, 33–57.

Campo R., Fontalba A., Sanchez L. M., and Zabala J. C. (1994). A 14 kDa release factor is involved in GTP-dependent β -tubulin folding. *FEBS Lett.* **353**, 162–166.

Craig D., Howell M. T., Gibbs C. L., Hunt T., and Jackson R. J. (1992). Plasmid cDNA-directed-protein synthesis in a coupled transcription-translation system. *Nucleic Acids Res.* **20**, 4987–4995.

Davis, B. J. (1964). Disc electrophoresis. II. Method and application to human serum proteins. *Ann. N. Y. Acad. Sci.* **121**, 404–427.

Fanarraga M. L., Aloria K., Avila J., and Zabala J. C. (1998). Characterization of tubulin isotype-specific antibodies by electrophoretic mobility shift assay. *Biotechniques* **25**, 940–942.

Fanarraga M. L., Avila J., Guasch A., Coll M., and Zabala J. C. (2001). Post-chaperonin tubulin folding cofactors and their role in Microtubule dynamics. *J. Struct. Biol.* **135**, 219–229.

Fanarraga, M. L., Abad X., Kortazar D., Bellido J., Villegas J. C., and Zabala J. C. (2003). Structure and function of the mammalian tubulin folding cofactors. In “Recent Research Developments in Biochemistry” (S. G., Pandalai, ed.) Vol. 4, pp. 575–587. Research Signpost, Trivandrum – 695023, Kerala, India.

Fontalba, A., Paciucci, R., Avila, J., and Zabala, J. C. (1993). Incorporation of tubulin subunits into dimers requires GTP hydrolysis. *J. Cell. Sci.* **106**, 627–632.

Fontalba, A., Avila, J., and Zabala, J. C. (1995). β -tubulin folding is modulated by the isotype-specific carboxy-terminal domain. *J. Mol. Biol.* **246**, 628–636.

Gao, Y., Vainberg, I. E., Chow, R. L., and Cowan, N. J. (1993). Two cofactors and cytoplasmic chaperonin are required for the folding of α - and β -tubulin. *Mol. Cell. Biol.* **13**, 2478–2485.

Geissler, S., Siegers, K., and Schiebel, E. (1998). A novel protein complex promoting formation of functional alpha- and gamma-tubulin. *EMBO J.* **17**, 952–966.

Hertzer, K. M., and Walczak, C. E. (2008). The C-termini of tubulin and the specific geometry of tubulin substrates influence the depolymerization activity of MCAK. *Cell Cycle* **7**, 2727–2737.

Laemmli, U. K. (1970). Cleavage of structural proteins during the assembly of the head of bacteriophage T4. *Nature* **227**, 680–685.

Littauer, U. Z., Giveon, D., Thierauf, M., Ginzburg, I., and Ponstingl, H. (1986). Common and distinct tubulin binding sites for microtubule-associated proteins. *Proc. Natl. Acad. Sci. U. S. A.* **83**, 7162–7166.

Llosa, M., Aloria, K., Campo, R., Padilla, R., Avila, J., Sanchez-Pulido, L. and Zabala, J. C. (1996). The β -tubulin monomer release factor (p14) has homology with a region of the DnaJ protein. *FEBS Lett.* **397**, 283–289.

Lobert, S., Hennington, B. S. and Correia, J. J. (1993). Multiple sites for subtilisin cleavage of tubulin: effects of divalent cations. *Cell Motil. Cytoskel.* **25**, 282–297.

Markert, C. L. and Hunter, R. L. (1959). The distribution of esterases in mouse tissues. *J. Histochem. Cytochem.* **7**, 42–49.

Ornstein, L. (1964). Disc electrophoresis. I. Background and theory. *Ann. N. Y. Acad. Sci.* **121**, 321–349.

Safer, D. (1994). Nondenaturing polyacrylamide gel electrophoresis NPAGE as a method for studying protein interactions. In “Cell Biology: A Laboratory Handbook” (J. E. Celis, ed.) Vol. 3, pp. 218–221. Academic Press, Inc., San Diego, CA.

Sackett, D. L., Bhattacharyya, B. and Wolff, J. (1985). Tubulin subunit carboxyl termini determine polymerization efficiency. *J. Biol. Chem.* **260**, 43–45.

Serrano, L., Avila, J., and Maccioni, R. B. (1984a). Controlled proteolysis of tubulin by subtilisin: localization of the site for MAP2 interaction. *Biochemistry* **23**, 4675–4681.

Serrano, L., de la Torre, J., Maccioni, R. B., and Avila, J. (1984b). Involvement of the carboxyl-terminal domain of tubulin in the regulation of its assembly. *Proc. Natl. Acad. Sci. U.S.A.* **81**, 5989–5993.

Serrano, L., Wandosell, F., de la Torre, J., and Avila, J. (1986). Proteolytic modification of tubulin. *Methods Enzymol.* **134**, 179–190.

Shapiro, A. L., Vinuela, E., and Maizel, J. V., Jr. (1967). Molecular weight estimation of polypeptide chains by electrophoresis in SDS-polyacrylamide gels. *Biochem. Biophys. Res. Commun.* **28**, 815–820.

Smithies, O. (1955). Zone electrophoresis in starch gels: Group variations in the serum proteins of normal human adults. *Biochem. J.* **61**, 629–641.

Tian, G., Huang, Y., Romelaere, H., Vanderkerckhove, J., Ampe, C., and Cowan, N. J. (1996). Pathway leading to correctly folded β -tubulin. *Cell* **86**, 287–296.

Vainberg, I. E., Lewis, S. A., Rommelaere, H., Ampe, C., Vandekerckhove, J., Klein, H. L., and Cowan, N. J. (1998). Prefoldin, a chaperone that delivers unfolded proteins to cytosolic chaperonin. *Cell* **93**, 863–873.

Weber, K., and Osborn, M. (1969). The reliability of molecular weight determinations by dodecyl sulfate-polyacrylamide gel electrophoresis. *J. Biol. Chem.* **244**, 4406–4412.

Wittig, I., and Schägger, H. (2008). Features and applications of blue-native and clear-native electrophoresis. *Proteomics* **8**, 3974–3990.

Yaffe, M. B., Farr, G. W., Miklos, D., Horwich, A. L., Sternlicht, M. L., and Sternlicht, H. (1992). TCP1 complex is a molecular chaperone in tubulin biogenesis. *Nature* **358**, 245–248.

Zabala, J. C., and Cowan, N. J. (1992). Tubulin dimer formation via the release of alpha- and beta-tubulin monomers from multimolecular complexes. *Cell Motil. Cytoskel.* **3**, 222–230.

CHAPTER 6

Mass Spectrometry Analysis of C-Terminal Posttranslational Modifications of Tubulins

Virginie Redeker

Laboratoire d'Enzymologie et Biochimie Structurales, CNRS, 91198 Gif-sur-Yvette cedex, France

Abstract

- I. Introduction
 - A. Posttranslational Modifications of the Tubulin C-Terminal Isotype-Defining Domain
 - B. Contribution of Mass Spectrometry in Tubulin PTMs Analysis
- II. Methods
 - A. Tubulin and Microtubule Proteins Purification
 - B. Proteolytic Cleavage and Production of the C-Terminal Isotype-Defining Peptides
 - C. Purification of C-Terminal Peptides
 - D. MALDI-MS Analysis of C-Terminal Peptides
 - E. Structural Characterization of Polymodifications
- III. Results and Discussion
 - A. The Tubulin C-Terminal Peptide Mass Fingerprinting Method
 - B. Posttranslational Polyglycation of Axonemal Tubulins from *Paramecium* Cilia
 - C. Posttranslational Polyglutamylation of Brain Tubulins
 - D. Changes in PTMs Consecutively to Polymodification Site Mutations
- IV. Conclusion
- Acknowledgments
- References

Abstract

In mammalian brain and ciliary axonemes from ciliates, α - and β -tubulins exhibit an extraordinary heterogeneity due to a combination of multigene family expression and numerous posttranslational modifications (PTMs). The combination of several PTMs located in the C-terminal tail of tubulins plays a major role in this important polymorphism of tubulin: polyglutamylation, polyglycation, detyrosination,

tyrosination, removal of the penultimate glutamate residue, and phosphorylation. In order to document the relationship and functions of these PTMs, we have developed a tubulin C-terminal Peptide Mass Fingerprinting (PMF) method. Using simplified microtubule proteins and tubulin C-terminal peptides purifications, direct matrix-assisted laser desorption ionization (MALDI) mass spectrometry (MS) analysis can generate a complete picture of all tubulin isotype-specific C-terminal peptides together with their respective PTMs. This chapter will illustrate the capability of this approach to compare tubulin isoform compositions and document the changes in PTMs between samples with different tubulin assembly properties or consecutively to inactivation of modification sites or modification enzymes. Complementary MS-based approaches useful to document the structure of the highly heterogeneous posttranslational polymodifications will also be presented.

===== I. Introduction

Microtubules are involved in the regulation of various cellular functions such as cell division, cell motility, intracellular trafficking, and maintenance of cell shape. The building block of microtubules is a α -/ β -tubulin heterodimer characterized by an extraordinary heterogeneity due to differential expression of multigene families (Sullivan, 1988) and to numerous posttranslational modifications (PTMs) (Westermann and Weber, 2003). In higher vertebrates, highly similar proteins, encoded by eight α -tubulins and seven β -tubulin genes (Khodiyar *et al.*, 2007), are differentially distributed in tissues (Sullivan, 1988). These proteins, referred to as isotypes, differ from each other by their C-terminal amino-acid sequences located within the last 15 residues (Sullivan, 1988), referred to as isotype-defining domains (Table I). Except acetylation on Lys40 of α -tubulin (LeDizet and Piperno, 1987), palmitoylation on Cys376 of α -tubulin (Ozols and Caron, 1997), and one phosphorylation site on Ser172 of β -tubulins (Fourest-Lievin *et al.*, 2006), most of the PTMs are concentrated in the C-terminal isotype-defining domain of α - and β -tubulins. This region is extensively modified by several PTMs including phosphorylation of β III, tyrosination, detyrosination, subsequent elimination of the penultimate glutamate residue of α -tubulin after detyrosination, and polyglutamylated and polyglycylated, as summarized in Table II (Gaertig and Wloga, 2008; Ludueña, 1998; Verhey and Gaertig, 2007; Westermann and Weber, 2003). This highly flexible C-terminal domain is located at the outer surface of the microtubule lattice (Nogales *et al.*, 1998) where it is accessible to multiple intermolecular interactions: it is involved in divalent cation binding and interaction with microtubule-associated proteins (MAPs) regulating structural or dynamic properties of microtubules (Bonnet *et al.*, 2001; Boucher *et al.*, 1994; Larcher *et al.*, 1996; Mejillano and Himes, 1991; Roll-Mecak and Vale, 2008; Skiniotis *et al.*, 2004; Wang and Sheetz, 2000).

A. Posttranslational Modifications of the Tubulin C-Terminal Isotype-Defining Domain

Phosphorylation of β -tubulin has been described on Ser444 and Tyr437 of β III-tubulin (Alexander *et al.*, 1991) and Ser441 of β VI-tubulin (Rüdiger and Weber, 1993). Detyrosination consists in the removal of the gene-encoded C-terminal tyrosine of α -tubulin and results in the formation of Glu-tubulin,

Table I
Mammalian Tubulin Isotypes

Tubulin isotype name (alternative name) ^a	Rodent Gene (UniProtKB Accession)	C-terminal sequence ^b	Mass of C-terminal LysC peptide ^c
α 1A (α 1)	Tuba1a (P68370)	⁴⁰¹ KRAFVHWYVGEGMEEGEFSEAREDMAALE K DYEEVGVD ³⁹¹ SVEGE ⁴⁴⁸ EEGEEY ⁴⁵¹	2350.2892
α 1B (α 2)	Tuba1b (Q6P9V9)	⁴⁰¹ KRAFVHWYVGEGMEEGEFSEAREDMAALE K DYEEVGVD ³⁹¹ SVEGE ⁴⁴⁸ EEGEEY ⁴⁵¹	2350.2892
α 1C (α 6)	Tuba1c (Q6AYZ1)	⁴⁰¹ KRAFVHWYVGEGMEEGEFSEAREDMAALE K DYEEVGADSAEGDDEGEEY ⁴⁴⁹	2079.9584
α 3A (α 3)	Tuba3a (Q68FR8)	⁴⁰¹ KRAFVHWYVGEGMEEGEFSEARED ³⁹¹ LAALE K DYEEVGVD ³⁹¹ SVEAE ⁴⁴⁸ EEGEEY ⁴⁵⁰	2249.2271
α 3B (α 7)	Tuba3b (Q68FR8)	⁴⁰¹ KRAFVHWYVGEGMEEGEFSEARED ³⁹¹ LAALE K DYEEVGVD ³⁹¹ SVEAE ⁴⁴⁸ EEGEEY ⁴⁵⁰	2249.2271
α 4A (α 4)	Tuba4a (Q5XIF6)	⁴⁰¹ 1KRAFVHWYVGEGMEEGEFSEAREDMAALE K DYEEVGIDSYEDEDEGEE ⁴⁴⁸	2123.0243
α 8 (α 8)	Tuba8 (Q6AY56)	⁴⁰¹ KRAFVHWYVGEGMEEGEFSEARED ³⁹¹ LAALE K DYEEVGTD ³⁹¹ SFEEENE ⁴⁴⁹ EEGEEF	2255.1904
α -like3	Tubal3 (B9EJS3)	⁴⁰¹ KFDL ³⁹¹ MYAKKAFLHWY ⁴⁴⁹ ITEGMELGEFVEARED ³⁹¹ LAALE K DYEEVG ⁴⁴⁹ LSF	1059.1242
β 1 (β 5)	Tubb5 (P69897)	³⁹¹ RKAFLHWY ⁴⁴⁹ TGEGMDEM ³⁹¹ EFTEAESNMNDLVSEYQQYQDATAEEEEDFGEEAE ⁴⁴⁹ EEA	6077.3028
β II (β 2A) beta-2A chain	Tubb2a, Tubb2b (P85108, Q3KRE8)	³⁹¹ RKAFLHWY ⁴⁴⁹ TGEGMDEM ³⁹¹ EFTEAESNMNDLVSEYQQYQDATADEQGEFEEEGEDEA ⁴⁴⁵	6177.3802
β III (β 4)	Tubb3 (Q4QRB4)	³⁹¹ RKAFLHWY ⁴⁴⁹ TGEGMDEM ³⁹¹ EFTEAESNMNDLVSEYQQYQDATAEEEGEMYEDDDEESEAQGPK ⁴⁵⁰	6752.0378
β IVa (β 4)	Tubb4 (B4F7C2)	³⁹¹ RKAFLHWY ⁴⁴⁹ TGEGMDEM ³⁹¹ EFTEAESNMNDLVSEYQQYQDATAEEGEFEEAEEEVA ⁴⁴⁴	6061.3470
β IVb (β 2C)	Tubb2c (Q6P9T8)	³⁹¹ RKAFLHWY ⁴⁴⁹ TGEGMDEM ³⁹¹ EFTEAESNMNDLVSEYQQYQDATAEEEGEEFEEAEEEVA ⁴⁴⁵	6190.4633
β V (β 6)	Tubb6 (Q4QQV0)	³⁹¹ RKAFLHWFT ⁴⁴⁹ TGEGMDEM ³⁹¹ EFTEAESNMNDLVSEYQQYQDATVNDGE ⁴⁴⁷ EEAFEDEEINE	6460.7097
β VI	Tubb1 (A2AQ07)	³⁹¹ RRAFVHWY ⁴⁴⁹ TSEGMDISEFGAEASDIHDLVSEYQQFQDVRAGLEDSEEDV ⁴⁴⁹ EEAEV ⁴⁴⁹ EAEDKD ⁴⁵¹ H	

Sequences of rodent tubulin isotypes are presented. Human tubulin isotypes are given in reference [Verdier-Pinard *et al.* \(2009\)](#).

^aThe nomenclature of α -tubulin is based on a recent revision ([Khodiyar *et al.*, 2007](#)), and β -tubulin isotype names are from [Sullivan *et al.* \(1988\)](#). The tubulin isotype names generally used until recently are indicated in parenthesis.

^bThe first amino-acid residue has been chosen arbitrarily.

^cMass corresponds to the calculated average $[M + H]$ average mass of the LysC C-terminal peptides. The Lysine residue involved in the LysC cleavage is in bold.

Table II
Tubulin PTMs Identified on Mammalian Tubulins

PTMs	Description	Mass change (amu) ^a	Sites
Acetylation	Addition of acetyl group on α -tubulin	+42.04	Lys40 of α 1A/B (LeDizet and Piperno, 1987)
Phosphorylation	Addition of phosphate	+79.98	Ser444 and Tyr437 of β III (Alexander <i>et al.</i>, 1991) Ser441 of β VI (Rüdiger and Weber, 1993) and Ser172 (Fourest-Lieuvin <i>et al.</i>, 2006)
Detyrosination $\Delta 2$	Removal of the C-terminal tyrosine Removal of the penultimate glutamate from detyrosinated α -tubulin	-163.18 -292.29	C-terminus of α 1A/B (Argarana <i>et al.</i>, 1978), α 4 (Redeker <i>et al.</i>, 1998) C-terminus (Paturle-Lafanechère <i>et al.</i>, 1991 ; Redeker <i>et al.</i>, 1996 ; Rüdiger <i>et al.</i>, 1992)
Δ EA	Removal of the C-terminal alanine and the penultimate valine from β -tubulin	-170.2	Class β IVb (Miller <i>et al.</i>, 2008)
Glutamylation	Addition of one or multiple glutamate as a side chain on α - and β -tubulins. Multiples sites possible. Up to 12–20 additional glutamates.	+129.11	Glu445 of α 1A/B (Eddé <i>et al.</i>, 1990), Glu443 and Glu 445 of α 4A (Redeker <i>et al.</i>, 1998), Glu441 of β I (Mary <i>et al.</i>, 1994), Glu435 of β II (Redeker <i>et al.</i>, 1992 ; Rüdiger <i>et al.</i>, 1992), Glu438 of β III (Alexander <i>et al.</i>, 1991), Glu433 of β IVa (Mary <i>et al.</i>, 1994)
Glycation	Addition of one or more glycines as a side chain on α - and β -tubulins. Multiple sites possible. Up to 30–40 additional glycines	+57.05	Glu445 of α 3A/B, Glu437 of β IV (Rüdiger <i>et al.</i>, 1995)
Palmitoylation	Addition of palmitate on α -tubulin	+238.41	Cys376 of α -tubulin (Ozols and Caron, 1997)

^a Mass changes correspond to average masses.

corresponding to α -tubulin with a glutamate residue as new C-terminus (Hallak *et al.*, 1977). The reverse tyrosination reaction, catalyzed by tubulin tyrosine ligase (TTL), adds a tyrosine residue to the C-terminus of α Glu-tubulin (Ersfeld *et al.*, 1993). Both modifications occur sequentially and generate the detyrosination/tyrosination cycle (Wehland and Weber, 1987). Removal of the penultimate glutamate leads to the formation of $\Delta 2$ -tubulin (Paturle-Lafanechère *et al.*, 1991) then removed from the tyrosination/detyrosination cycle (Rüdiger *et al.*, 1994). Recently, Miller *et al.* (2008) have described a similar PTM on β IV-tubulin from liver tissues of hepatocellular carcinoma where the two C-terminal residues (valine and alanine) can be removed by an unknown carboxypeptidase, resulting in Δ VA-tubulin. Polyglutamylation and poly-glycylation are two unusual polymeric modifications, or polymodifications, identified in the C-terminal tail of most α - and β -tubulins. Polyglutamylation and polyglycylation correspond to the sequential addition of, respectively, glutamate (Alexander *et al.*, 1991; Eddé *et al.*, 1990) or glycine residues (Redeker *et al.*, 1994) onto a lateral chain of one or more specific glutamates of the primary sequence of tubulins. Both of them increase substantially the heterogeneity of tubulins. In the case of polyglutamylation, up to 12 additional glutamate residues have been detected on single or multiple modification sites in brain tubulins (Alexander *et al.*, 1991; Mary *et al.*, 1994; 1996; Redeker *et al.*, 1992; 1998; Rüdiger *et al.*, 1992; 1995; Weber *et al.*, 1997), whereas the basal apparatus of the green flagellate *Spermatozopsis similis* contains more than 17 additional glutamate residues (Geimer *et al.*, 1997). Polyglutamylation is abundant in neurons, centrioles, basal bodies, axonemes of cilia and flagella, and mitotic spindle (Audebert *et al.*, 1993; Bobiniec *et al.*, 1998; Bré *et al.*, 1994; Kann *et al.*, 2003; Lechtreck and Geimer, 2000; Plessmann *et al.*, 2004; Wolff *et al.*, 1982). Polyglycylation consists in the addition of 3–34 glycine residues on multiple glutamate residues from the primary sequence (Redeker *et al.*, 1994; Rüdiger *et al.*, 1995; Vinh *et al.*, 1997; 1999; Weber *et al.*, 1997). Polyglycylation is abundant in axonemal structures of cilia and spermatozoa of many species (Bré *et al.*, 1996).

Most of these PTMs are reversible and can act as switches, either individually or in concert, for a fine regulation of microtubule functions within the cell. Recent experimental results have suggested that tubulin modifications are involved in the regulation of interaction with MAPs and modulation of stability and/or structure of microtubules (Gaertig and Wloga, 2008; Hammond *et al.*, 2008; Ludueña, 1998; Westermann and Weber, 2003). Antibody-based approaches designed to inhibit possible intermolecular interactions have suggested a possible role for both polymodification in stabilization of microtubule structures and regulation of ciliary beating (Bobiniec *et al.*, 1998; Bré *et al.*, 1996; Gagnon *et al.*, 1996; Million *et al.*, 1999). Recently, functional studies of both polymodifications have been greatly facilitated by the identification of different TTL-like enzymes (TTLLs) such as glutamate or glycine ligases with specific substrate preferences and either a predominant chain-initiating or a chain elongation activity (Ikegami *et al.*, 2006; Janke *et al.*, 2005; 2008; Regnard *et al.*, 1999; Rogowski *et al.*, 2009; van Dijk *et al.*, 2007; Wloga *et al.*, 2009).

B. Contribution of Mass Spectrometry in Tubulin PTMs Analysis

In order to document the functional specificity of tubulin isotypes expression and tubulin PTMs, it is important to have access to a complete map of tubulin isoform composition. However, the extraordinary heterogeneity of tubulin isoforms found in

some tissues, cells, or structures makes it challenging to characterize qualitatively and quantitatively the tubulin isoforms distribution. For years, tubulin heterogeneity has been addressed by isoelectric focusing (IEF) or two-dimensional (2D) gel electrophoresis (Alexander *et al.*, 1991; Eddé *et al.*, 1989; 1991; Redeker *et al.*, 1992; Verdier-Pinard *et al.*, 2009; Williams *et al.*, 1999; Wolff *et al.*, 1982). However, in very complex tubulin samples, the combination of differential isotype expression and multiple PTMs generates very complex electrophoretic profiles, even in high-resolution IEF or 2D gel electrophoresis in which multiple tubulin isoforms may have very close pI or/and molecular masses, and thus co-migrate (Verdier-Pinard *et al.*, 2009; Williams *et al.*, 1999). Although polyglutamylation and polyglycation were initially brought to light, respectively, by [³H] acetate posttranslational labeling of tubulin (Eddé *et al.*, 1990; 1991) and specific axonemal antibodies together with 2D gel electrophoresis (Adoutte *et al.*, 1991), the identification of the nature of these PTMs came from MS (Alexander *et al.*, 1991; Eddé *et al.*, 1990; Redeker *et al.*, 1994). In some tissues or organelles, as brain and cilia, these polymodifications result in an incredible number of distinct tubulin isoforms often impossible to resolve in a single protein spot on a 2D gel electrophoresis. Rapidly, MS has demonstrated its importance in the determination of the molecular composition of tubulin isoforms. Tubulin isoform can be analyzed by direct mass measurement of entire tubulins using liquid chromatography (LC)-MS (Verdier-Pinard *et al.*, 2003; 2005). However, when the heterogeneity of the sample is too high, as it is for brain or axonemal tubulins, this approach has limitations due to protein mass overlaps and lack in resolution of classical MS techniques. For heterogeneous tubulin samples, tubulin heterogeneity has to be characterized at the peptide level. Peptide MS profiling is an appropriate tool not only to characterize tubulin isotypes expression and multiple PTMs, but also to detect new isotypes (Rao *et al.*, 2001; Redeker *et al.*, 1998; 2004; 2005; Verdier-Pinard *et al.*, 2005) or new PTMs (Verdier-Pinard *et al.*, 2009, Redeker and Vinh, unpublished data).

In order to elucidate tubulin isoform composition in different tissues and cell extracts, we have developed a MS-based method that offers a complete picture of the molecular heterogeneity of tubulins. Using this tubulin C-terminal Peptide Mass Fingerprinting (PMF), both the tubulin isotype composition and the nature and the level of several PTMs can be rapidly characterized. When the tubulin sequences are known, this type of analysis can be rapidly achieved. When the tubulin sequence is unknown, sequence information is necessary for validation. We will describe the methodology and illustrate its capacity to analyze tubulin isoform composition and changes. We will also present how this approach can be completed in order to characterize the structure of polymodified tubulin peptides.

===== II. Methods

A. Tubulin and Microtubule Proteins Purification

Tubulin represents up to 20% of soluble proteins in brain, but only 3–5% of total proteins in most cells. Thus, most but not all tubulin purification procedures (see Chapter 1 by Miller and Wilson and Chapter 2 by Sackett *et al.*, this volume) are adapted to both the abundance of tubulin in the cells or tissues to analyze and the degree of

protein purity required. Pure brain tubulin is generally prepared from fresh tissues, by three temperature-dependent assembly/disassembly cycles according to Sh  lanski *et al.* (1973) followed by phosphocellulose chromatography (Weingarten *et al.*, 1975) in order to remove MAPs. Recently, a more rapid protocol, based on two cycles of polymerization/depolymerization in the presence of a high-molarity of piperazine-*N*, *N'*-bis-(2-ethanesulfonic acid) (PIPES) buffer, has been reported (Castoldi and Popov, 2003). Microtubule proteins can be efficiently isolated after extraction in a buffer containing NaF and vanadate to inhibit serine, threonine, and tyrosine phosphatase activity by one cycle of assembly/disassembly. After depolymerization of microtubules, tubulin can be further purified by ion chromatography, using either arginine-sepharose chromatography (Redeker *et al.*, 1998) or diethylaminoethyl (DEAE) ion-exchange chromatography (Detrich *et al.*, 1989). Purification of microtubule proteins from cytoplasm and ciliary axonemes of the ciliates *Paramecium* and *Tetrahymena* needs to be adapted to the microtubule network: cytoplasmic microtubules are recovered by centrifugation, after cold depolymerization of intracytoplasmic microtubules (Br   *et al.*, 1994) and further purified by taxol-induced assembly (Vallee and Collins, 1986), whereas axonemal tubulins are extracted from cilia as described previously (Geuens *et al.*, 1989; Xia *et al.*, 2000), and axonemal tubulin is isolated after sonication of microtubule doublets (Adoutte *et al.*, 1991). Purification of microtubule proteins from cultured cells, or nonneuronal tissues, is performed by taxol-induced polymerization of microtubules after protein extraction (Vallee and Collins, 1986). Recently, a rapid method for purification of tubulin from limited volumes of cultured cells has been reported (Fourest-Lievin *et al.*, 2006). This method preserves intact microtubule arrays during cell lysis and disassembles microtubules in a small volume of cold buffer. Microtubule proteins are further purified by one cycle of polymerization/depolymerization and a cation-exchange chromatography.

B. Proteolytic Cleavage and Production of the C-Terminal Isotype-Defining Peptides

Tubulin C-terminal peptides can be produced in-gel or in-solution by several proteolytic Sequencing Grade enzymes (Roche Diagnostics GmbH, Mannheim, Germany). Only the in-solution digestion procedures will be presented. Originally, digestion was performed with thermolysin digestion (Edd   *et al.*, 1990; Mary *et al.*, 1994; 1996; Redeker *et al.*, 1991), an endopeptidase with a broad cleavage-specificity (Matsubara, 1966). Subtilisin, an unspecific enzyme used in mild conditions, can specifically release tubulin S and the C-terminal peptides (Redeker *et al.*, 1992; R  diger *et al.*, 1992). But endoproteinases with specific cleavage sites in conserved sequences of the tubulin C-terminal domain are now preferred, because they generate C-terminal peptides of similar length for most tubulin isotypes. Endoproteinase AspN specifically hydrolyzes peptide bonds at the N-terminal side of aspartate and cysteine residues (Hagmann *et al.*, 1995), and with a 2,000-fold lower velocity at glutamate residues. Reducing the enzyme-to-substrate ratio and the incubation time avoids cleavage at glutamate residues and produces α - and β -tubulin C-terminal peptides beginning at Asp431 and Asp427, respectively, when the digestion was complete, and longer α -tubulin peptides beginning at Asp424 for incomplete digestions. AspN digestion was carried out in 50 mM Tris-HCl, pH 8.0, with a 1/400 enzyme/substrate ratio (w/w) for less than 6 h at 36  C (Redeker *et al.*, 1994). Trypsin specifically hydrolyzes proteins at the carboxylic side of arginine and lysine

residues, whereas endoproteinase LysC cleaves only after lysine residues. These enzymes produce C-terminal peptides resulting from α -tubulin cleavage at the lysine residue between position 430 and 436, and at Lys392 for all β -tubulins except class β VI. With both enzymes, digestion is performed for 18 h at 37°C by incubation in 25 mM Tris-HCl, pH 8.5, at an enzyme-to-tubulin ratio of 1:100 (w/w) (Redeker *et al.*, 2004). Enzymatic digestions are stopped either by addition of concentrated trifluoroacetic acid (TFA) at a final concentration of 1% or by heating at 100°C for 5 min. Cyanogen bromide (CNBr) cleaves efficiently at the carboxylic side of methionine residues and releases tubulin C-terminal peptides of 20–30 residues for both α - and β -tubulins (Alexander *et al.*, 1991; Rao *et al.*, 2001; Rüdiger *et al.*, 1995; Weber *et al.*, 1997). Tubulin C-terminal peptides released by these different cleavages have unique masses between 1000 and 8000 Da, which makes possible direct MS analysis of tubulin C-terminal peptides from different tissues, cell lines, or organelles.

C. Purification of C-Terminal Peptides

Initially, high-resolution purification of acidic C-terminal peptides obtained by in-solution digestions of tubulins was achieved by a 2D high-performance liquid chromatography (HPLC) separation: proteolytic peptides are first separated by anion-exchange chromatography and acidic peptides are further purified by reversed-phase chromatography as described previously (Eddé *et al.*, 1990; Mary *et al.*, 1994; 1996; Redeker *et al.*, 1992; 1994). However, in order to obtain a complete tubulin C-terminal PMF, purification of an acidic C-terminal peptide pool is preferred. This purification can be performed very efficiently and rapidly using arginine–sepharose chromatography (Redeker *et al.*, 1998; 2004; 2005). This dipolar ion-exchanger has been previously used for fractionation of transfer ribonucleic acid and exhibits properties similar to those of DEAE-Sephadex (Lacey and Snowdon, 1990). Typically, approximately 100 μ g of protein digest is loaded onto 200 μ l of arginine–sepharose. After equilibration of the column in 25 mM 2-(*N*-morpholino)ethanesulfonic acid (MES)/NaOH (pH 6.7), microtubule protein digests are loaded and the column is washed by a step elution of 25, 100, and 200 mM MES/NaOH (pH 6.7). Acidic tubulin C-terminal peptides are eluted with 25 mM MES/NaOH (pH 6.7) containing 2.5 M NaCl. Before MS, the entire acidic peptide pool is desalted on either a C18 Sep-Pak cartridge (Millipore, Bedford, MA) or miniaturized reversed-phase separation systems (Zip-Tip, Millipore, Bedford, MA). Desalting is performed by washing with 0.1% TFA in deionized water and peptides are eluted with 80% acetonitrile and 0.1% TFA in deionized water. Peptides can be concentrated using a speed-vaccum system. Low abundant peptide identification needs further separation of the peptide pool using a high-resolution reversed-phase HPLC with a C18 reversed phase column (classically: C18, 5 μ m, 220 \times 2.1 mm) (Redeker *et al.*, 1992; 1994; 1998; Redeker *et al.*, 2004). This chromatography provides a good separation of the isotype-specific C-terminal peptides. Peptides elution is performed at a flow rate of 200 μ l/min with a gradient of solvent A (0.1% TFA in deionized water) and solvent B (80% acetonitrile and 0.09% TFA in deionized water). The slope of the gradient is comprised between 1 and 0.2% and adapted to the complexity of the sample. For very low abundant tubulin samples, higher sensitivity can be obtained using nano-liquid chromatography systems.

D. MALDI-MS Analysis of C-Terminal Peptides

Mass spectra were acquired in either positive or negative ion mode with a MALDI mass spectrometer. Long α -tubulin peptides generated by AspN or long β -tubulin peptides released by LysC digestion give a good signal in positive mode, whereas β -tubulin and short α -tubulin peptides give a better signal-to-noise ratio in negative mode because of their high acidity (Redeker *et al.*, 1998; 2004). Indeed, in the last 15 amino-acid residues of tubulin, acidity is remarkably high because 50–70% of the residues are glutamate or aspartate residues. This acidity is further increased by acidic PTMs such as glutamylation or phosphorylation. Typically, a MALDI time-of-flight (MALDI-TOF) mass spectrometer equipped with a delayed extraction device (Voyager DE-STR; PerSeptive Biosystems, Inc., Framingham, MA) was used in either the reflectron or the linear mode, for short and long peptides, respectively, or for higher resolution or sensitivity, respectively (Redeker *et al.*, 2004; 2005; van Dijk *et al.*, 2007). Now, MALDI-TOF-TOF mass spectrometers with higher resolution and sensitivity present the advantage of providing sequence information by fragmentation of the same sample without absolute need of a new sample preparation (Miller *et al.*, 2008). Before deposition onto the MALDI target, the sample was mixed 1:1 (v:v) with a saturated solution of either sinapinic acid (3,5-dimethoxy-4-hydroxicinnamic acid, Aldrich, St. Louis, MO) in 30% acetonitrile and 0.1% aqueous TFA or 2,5-dihydroxybenzoic acid (DHB, Aldrich, St. Louis, MO) in 0.1% aqueous TFA. Either sinapinic acid or DHB was used as matrix for analysis of short C-terminal peptides, whereas sinapinic acid was preferred for long LysC β -tubulin peptides. For short acidic AspN tubulin peptides, a thin layer preparation of the sample in the presence of α -cyano-4-hydroxycinnamic acid (Sigma Chemical, St. Louis, MO) and nitrocellulose gave optimized signal-to-noise ratios in MS and MS/MS (Vinh *et al.*, 1997). Calibration was performed as previously described (Redeker *et al.*, 2004). A complete PMF of both α - and β -tubulin C-terminal tails was obtained by direct MALDI-MS of the C-terminal peptide pools using the purification strategy described in Fig. 1. Interestingly, β -tubulin peptides generated after LysC digestion have high masses (comprised between 6000 and 8000) and can be analyzed directly from the tubulin digest, after mixing of the sample with an equal volume of 1% TFA before addition of the matrix. Peptide identity and PTMs were determined by comparison of exact experimental masses to the theoretical masses of tubulin isotype C-terminal peptides or by additional sequence information.

E. Structural Characterization of Polymodifications

1. Edman Sequencing

N-terminal sequencing of peptides using automated Edman degradation, for example with a Procise pulsed-liquid protein sequencer (Applied Biosystems, Foster City, CA), provides an unambiguously amino-acid sequence necessary not only for the identification of isotype-defining peptides but also for the localization of modified residues (Eddé *et al.*, 1990). For polyglutamylated or polyglycylated peptides, the position of the modified residues could be identified because at the corresponding cycle no phenylthiodantoin was detected (PTH-Glu). This gap in the sequence strongly supported the presence of a modified glutamate residue, the corresponding PTH derivative being either retained on the filter of the sequencer or excluded from the separating range of the PTH-aa analyzer

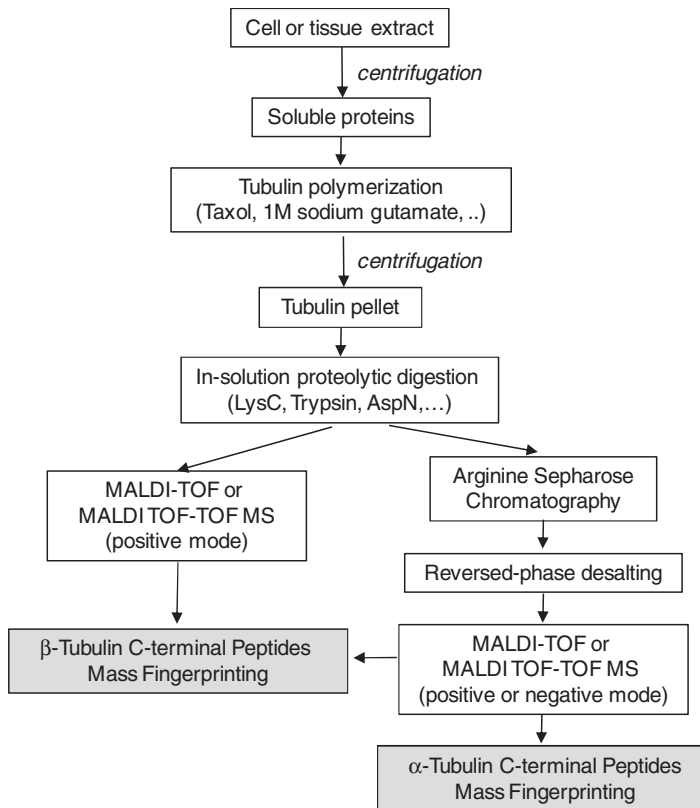


Fig. 1 α - and β -tubulin C-terminal Peptides Mass Fingerprinting Strategy. The experimental conditions are described in the Methods section.

(Eddé *et al.*, 1990). Although Edman sequencing has been used initially, modification sites are now generally identified using tandem mass spectrometry (MS/MS).

2. Tandem Mass Spectrometry

MS/MS was used in C-terminal tubulin peptide characterization, either for classical peptide identification (Alexander *et al.*, 1991; Miller *et al.*, 2008) or for structural characterization of post-translationally modified peptides (Vinh *et al.*, 1997; 1999). Different instrumental configuration may be used: MALDI instruments as MALDI-TOF in the post-source decay/collision-induced dissociation (PSD/CID) mode (Vinh *et al.*, 1997; 1999) or more recent MALDI-TOF-TOF instruments (Miller *et al.*, 2008), or nano-electrospray ionization (nanoESI) coupled to a tandem mass analyzer monitored with collision-activated dissociation (CAD) as, for example, in a Q-TOF instrument (Vinh *et al.*, 1999).

For fragmentation experiments performed on a MALDI instrument in positive and PSD/CID mode, with argon as collision gas, an optimized thin-layer sample preparation with α -cyano-4-hydroxycinnamic acid and nitrocellulose significantly improved the detection of the acidic tubulin C-terminal peptides (Vinh *et al.*, 1997). With the nanoESI Q-TOF (Micromass UK Ltd., Manchester, UK) hybrid

quadrupole orthogonal acceleration TOF tandem mass spectrometer, collision gas was argon and collision energy was set at 30 eV (Vinh *et al.*, 1999). The signal-to-noise ratio could be improved by dilution of the peptides with twice their volume of methanol/1% aqueous formic acid 1:1 (v/v) prior to introduction into the mass spectrometer in order to neutralize the negative effect of TFA on the ionization process of peptides.

Structural analysis of the polyglutamylated peptides using MS/MS is more difficult because the lateral polyglutamate chain readily fragments. N-terminal derivatization of the tubulin C-terminal peptides with TMPP ((*N*-succinimidylloxycarbonylmethyl)tris-(2,4,6-trimethoxyphenyl)phosphonium bromide) can improve MS/MS fragmentation of polyglutamylated peptides (Vinh, 1999).

3. Optimized Reversed-Phase HPLC

In the case of polyglutamylation, the first additional glutamate residue must be linked to the γ -carboxyl group of a glutamate residue from the amino-acid sequence (Eddé *et al.*, 1990). However additional glutamate residues can then be attached through amide bonds to the α - or γ -carboxyl groups of the preceeding unit. The exact structure of polyglutamylation, i.e., the nature of the linkage connecting the second and third additional glutamyl residues, was determined using optimized reversed-phase chromatography and comparison of the retention times with synthetic peptides. Seven peptides corresponding to each structural possibility of the bi- and triglutamylated C-terminal α -tubulin peptides were synthesized (Redeker *et al.*, 1991; 1996). The reversed-phase column (RP18 spheri 5, 220 \times 2.1 mm, 5 μ m, BrownleeTM, Perkin Elmer, Waltham, MA) was eluted at pH 3.0, 15°C, and 200 μ l/min. Before injection, fractions were acidified to pH 3 with TFA. After injection, solvent B2 was maintained at 1% for 15 min before starting a linear gradient from 10 to 25% of B2 in 75 min. Solvent A2 was deionized water, and solvent B2 was 80% acetonitrile in water. Both solvents were acidified to pH 3.0 with TFA. By comparison of the retention times of tubulin C-terminal peptides with those of standard peptides, the mode of linkage connecting the second and third glutamate residues was characterized (Redeker *et al.*, 1991; 1996).

III. Results and Discussion

A. The Tubulin C-Terminal Peptide Mass Fingerprinting Method

Tubulin isoform heterogeneity can be resolved in two separate bands by 1D SDS-PAGE or in many tubulin isoform bands or spots by high-resolution IEF separation or 2D gel electrophoresis (Verdier-Pinard *et al.*, 2009). After on-membrane or in-gel cleavage or enzymatic digestion of tubulin bands, each tubulin isotype can be identified by subsequent MS (Miller *et al.*, 2008; Rao *et al.*, 2001; Rüdiger *et al.*, 1995; Verdier-Pinard *et al.*, 2003; 2003). In order to minimize loss of peptides and obtain a tubulin C-terminal peptide pool as complete as possible, we have performed an in-solution digestion of microtubule proteins and optimized a peptide purification procedure compatible with direct MALDI-MS. The isolation of the C-terminal isotype-defining peptides from microtubule proteins is at the heart of MS-based

analysis of tubulin isoforms across phyla, tissues, cells, and organelles (Alexander *et al.*, 1991; Eddé *et al.*, 1990; Mary *et al.*, 1994; 1996; Redeker *et al.*, 2004; 1994; Redeker *et al.*, 2005; 1992; Redeker *et al.*, 1998; Rüdiger *et al.*, 1992; Rüdiger and Weber, 1993; Verdier-Pinard *et al.*, 2005; 2003; Vinh *et al.*, 1999; 1997). Enzymatic digestion of α - and β -tubulin with specific endoproteases such as LysC, trypsin, AspN, or CNBr chemical cleavage releases these tubulin C-terminal peptides that can be purified rapidly by arginine–sepharose chromatography before MS. This tubulin C-terminal PMF method, summarized in Fig. 1, provides for a complete picture of expressed tubulin isotypes and their C-terminal PTMs, even from extremely heterogeneous tubulin preparations.

In this method, three steps in the sample preparation of proteins and peptides were critical. First, tubulin was purified using only one cycle of depolymerization/polymerization. Second, tubulin digestion was preferentially performed using endoprotease LysC or trypsin in order to produce two peptides pools: one with C-terminal α -tubulin peptides with unique masses comprised between 2,000 and 4,000 Da and one with larger C-terminal β -tubulin peptides with masses between 6,000 and 8,000 Da. Third, tubulin C-terminal peptides were purified using a step gradient elution on an arginine–sepharose chromatography. The amino-acid sequence of the peptides can be identified by exact mass measurement or by amino-acid sequence information obtained either by MS/MS or by Edman degradation. When the masses of the tubulin C-terminal peptides are unique and in an appropriate mass range, direct MS analysis is possible. Posttranslationally modified peptides are typically detected with series of ions separated by specific mass differences: for example 57 Da for glycation, 129 Da for glutamylation, 163 Da for tyrosylation, and 80 Da for phosphorylation. Thanks to this tubulin C-terminal PMF method, the first biochemical characterization of the $\alpha4A$ -tubulin isotype was achieved (Redeker *et al.*, 1998). This direct MS analysis of complete tubulin C-terminal peptide pools offers also the possibility to perform a quantitative comparison between glutamylation or glycation levels of a given C-terminal peptide because neither glutamylation nor glycation significantly modifies the ionization efficiencies or the retention time on reversed-phase chromatography. However, isotype-defining peptides may have different ionization efficiencies. We have for example observed that tyrosinated tubulin peptides give a signal twice higher than the same peptide in its nontyrosinated form. Thus, it is not possible to quantify isotypes in one individual sample or between biological samples using this approach only. Additional strategies, using for example labeled synthetic peptides, need to be implemented (Miller *et al.*, 2008).

Although mass fingerprinting of C-terminal peptide pools is an efficient method to compare the heterogeneity of different tubulin isoforms, the detection of low abundant peptides from low abundant tubulins can be inhibited by ion suppression signal phenomenon due to an active competition in desorption with other peptides. This phenomenon, increased in complex peptide mixtures, has been observed in ESI-MS (Sun *et al.*, 2005) but also in MALDI-MS (Mock *et al.*, 1992). This phenomenon, of importance when analyzing complex tubulin samples, may underestimate some tubulin isotypes (Verdier-Pinard *et al.*, 2009). In order to detect low abundant peptides, the complexity of the peptide mixture needs to be reduced using a high-resolution reversed-phase HPLC separation with classical C18 reversed-phase separations as those described in the Methods section. Peptides of interest can also be affinity purified using antibodies directed against specific PTMs or isotype-defining

peptides in order to capture and further characterize specific populations of tubulin C-terminal peptides (Rüdiger *et al.*, 1999). A similar approach has been efficiently used to identify glutamylation and phosphorylation of β III-tubulin from bovine brain (Alexander *et al.*, 1991).

B. Posttranslational Polyglycylation of Axonemal Tubulins from *Paramecium* Cilia

1. Tubulin C-Terminal PMF of *Paramecium* Axonemal Tubulin

Polyglycylation was initially identified on axonemal tubulin from *Paramecium* cilia (Redeker *et al.*, 1994). Analysis of tubulin C-terminal peptides of *Paramecium* was undertaken in order to identify the PTMs occurring on ciliary axonemal tubulin recognized by a specific antibody (Adoutte *et al.*, 1991). Acidic peptides were purified by a high-resolution 2D HPLC separation as described in the Methods section. MS analysis of the isolated fractions revealed mass increments of 57 Da, corresponding to the mass of a glycine residue, and identified peptides bearing up to 34 additional glycine residues (Redeker *et al.*, 1994). Several years later, in order to compare the distribution of PTMs on the C-terminal peptides of *Paramecium* and *Tetrahymena*, we performed a tubulin C-terminal PMF (Redeker *et al.*, 2005). Figure 2 presents the MALDI mass spectra obtained for the C-terminal peptide pools isolated from axonemal α - and β -tubulin from *Paramecium*. Interestingly, this analysis revealed the nature and the level of PTMs for each expressed tubulin isotype. From these data, it was possible to unambiguously conclude that the predominant α - and β -tubulin isoforms are the hexaglycylated one. With the tubulin C-terminal PMF method, we detected a maximum of 20 additional glycine residues, whereas 34 were detected previously after 2D high-resolution chromatography (Redeker *et al.*, 1994). This example illustrates the ion suppression signal phenomenon observed for low abundant peptides or for peptides with low ionization efficiency, which require additional high-resolution reversed-phase HPLC separation as described previously.

2. Structural Analysis of Polyglycylation

In order to document the overall structure of the polymodifications, it is important to identify the position and the number of the modification sites. One unique modification site would involve the presence of a very long lateral chain. With multiple modifications sites, the C-terminal tail of tubulin would more or less resemble to a “brush” with multiple polyglycine chains exposed at the outer surface of the microtubule lattice. These two structures would involve different steric hindrance and thus regulate differently protein–protein interactions occurring in the C-terminal tail of tubulins. Identification of modification sites is also of key importance if one wants to examine the functional role of polyglycylation by inactivation of modification sites.

Nowadays, modification sites are generally identified by MS/MS. Although Edman degradation gives generally an unambiguous amino-acid sequence and indicates clearly the position of modified amino-acid residues, it requires pure peptide samples in relatively high amounts (1–10 pmoles). With polyglutamylated peptides, we have observed a gap at the position of the modified glutamate residues

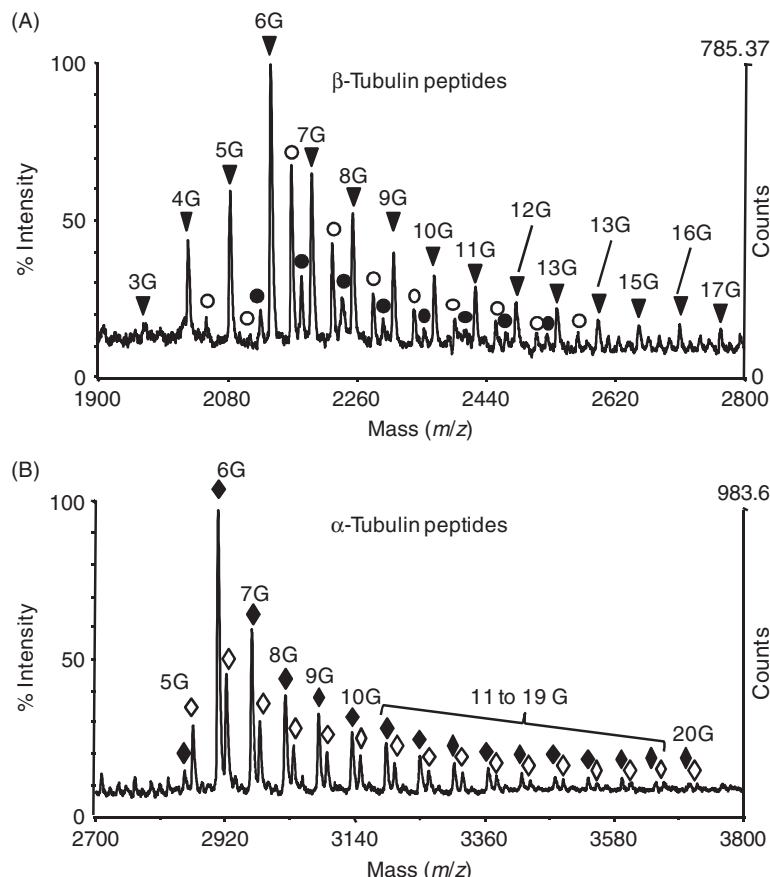


Fig. 2 C-terminal Peptide Mass Fingerprinting of β - and α -axonemal tubulin from *Paramecium* cilia. MALDI-TOF MS analysis of the C-terminal peptides released after AspN digestion of tubulin and purified as indicated in Fig. 1. (A) C-terminal peptides from β -tubulin (closed triangle) together with C-terminal peptides from short α 1- and α 2-tubulin beginning at Asp431 (open and closed circle, respectively) are observed. The difference between the theoretical mass and each of the experimental masses corresponded to multiple of 57 Da, the mass of one glycine residue. The predominant β -tubulin peptide is hexaglycylated and β -tubulin peptides with 3–17 additional glycine residues are detected. (B) C-terminal peptides from α 1 (closed diamond) and α 2 (open diamond) tubulin corresponding to long α -tubulin peptides beginning at Asp424 are observed. The predominant α -tubulin peptides are also hexaglycylated and α -tubulin peptides with 5–20 additional glycine residues are detected.

(Eddé *et al.*, 1990; Mary *et al.*, 1994; Redeker *et al.*, 1992; 1998) and we have been able to identify two modification sites in the α 4A-tubulin isotype. With polyglycylated peptides, we have not been able to identify any amino-acid residue after the first modified glutamate residue. Thus, in the β -tubulin C-peptide of *Paramecium* (427 DATAEEEGEFEEEGEQ 442), none of the last six residues was identified by Edman degradation (Redeker *et al.*, 1994). But it was not clear if this was the consequence of a very long polyglycine chains, or the presence of multiple modification sites. This was answered using MS/MS, which is capable of providing sequence information even in very complex peptide mixtures, or with very low amount of sample (fmole range), and a considerably reduced time of analysis.

Structural characterization of polyglycation of β -tubulin from *Paramecium* has been performed by MS/MS: both the number of additional glycine residues for each tubulin isoform and the structure of each level of polyglycation have been determined. The level of polyglycation of a peptide is defined by the total number of glycine residues posttranslationally added. The structure of a level is given by the location of the modified glutamate residues and by the extent of modification of each modified residue. Initially, the localization of the modification sites within a peptide sequence was performed by MS/MS on a MALDI-TOF instrument using PSD and CID (Kaufmann *et al.*, 1994; Kosaka *et al.*, 1995). This spontaneous or activated fragmentation has been well described with a specific nomenclature (Biemann, 1990). Sample preparation, ionization, and fragmentation were optimized on synthetic peptides designed to match different possible biological structures (same C-terminal sequence, different glycation sites and levels of glycation) (Vinh *et al.*, 1997). These acidic peptides, with pIs ranging from 2.5 to 3, readily form adducts with sodium and potassium ions and require optimized sample preparation to obtain a good signal-to-noise ratio. The thin-layer preparation in the presence of α -cyano-4-hydroxycinnamic acid and nitrocellulose gave the best results. Fragmentation rules for posttranslational polyglycylated peptides were established from the fragmentation pattern of synthetic peptide with the linear sequence $^{427}\text{DATAEEE-GEFEEEGEQ}^{442}$: glycylated residues behaved like nonmodified residues, and the peptides fragment regularly and form major fragments of b- and y-type ions with negligible side-chain fragmentation (Vinh *et al.*, 1999). The high-energy collision rules were extended to the low-energy fragmentation obtained with nanoESI quadrupole-TOF (nanoESI Q-TOF) MS, which is capable of fragmenting rapidly peptides in complex peptide mixtures at the sub-picomole level (Fig. 3). However, MALDI in the CID mode provides interesting low-mass signature ions (Fig. 3), corresponding to glycylated glutamate residue fragments and indicating the length of the polyglycine chain that is bound to the modified glutamate residue (Vinh *et al.*, 1999). All these rules were applied to the structural elucidation of a hexaglycylated peptide from a *Paramecium* β -tubulin. Polyglycation was identified on the last four glutamate residues (Glu^{437} , Glu^{438} , Glu^{439} , and Glu^{441}) within a single tubulin molecule, independently of the total number of additional glycine residues (Fig. 3). The results indicated that polyglycation is a multisite polymodification. Interestingly, genetic experiments in *Tetrahymena*, aimed to mutate several modification sites individually, also demonstrated that polyglycation was a multisite polymodification: on β -tubulin, mutation of four glutamate residues was lethal whereas mutation of three sites contributed to several cellular disorganizations (Xia *et al.*, 2000).

C. Posttranslational Polyglutamylation of Brain Tubulins

1. Changes in MPTs of Brain Tubulin During Development

We have characterized changes in tubulin heterogeneity, i.e., both isotype expression and PTMs, between neonatal and adult brain tubulins, using microtubule proteins only cycled once and α - and β -tubulin C-terminal peptide PFM. We have observed that α 1A/B-, β I-, β II-, and β III-tubulin isotypes are expressed in neonatal rat brain, while α 4A and β IV isotypes are expressed later during brain development and are detected only in adult brains, as presented in Fig. 4. For α 4A-tubulin

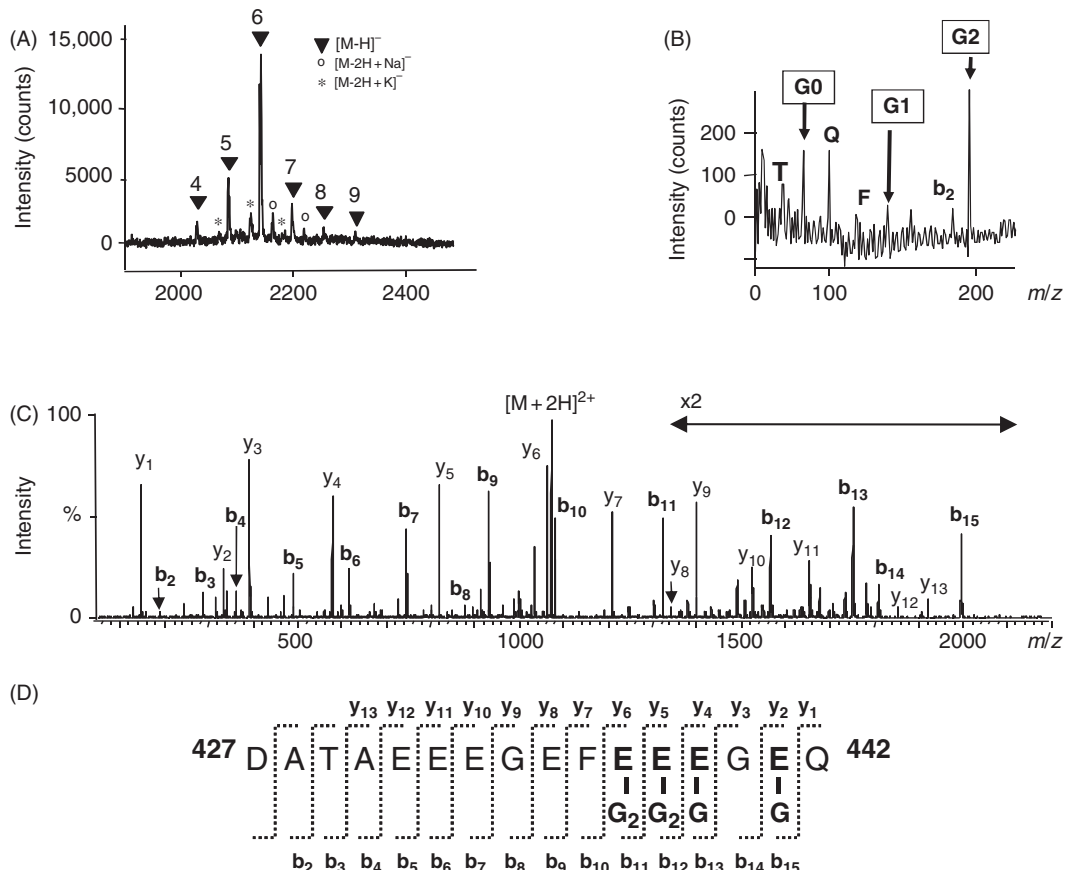


Fig. 3 Structural characterization of glyetylated β -tubulin C-terminal peptides. (A) MALDI-TOF spectra of predominant polyglyetylated C-terminal peptides of cytoplasmic *Paramecium* tubulin. Cytoplasmic tubulin is glyetylated by the addition of four to nine additional glycine residues, the hexaglyetylated form being the most abundant one. Structural characterization of this peptide using tandem mass spectrometry (MS/MS) is illustrated in (B) and (C). (B) Using MALDI-TOF PSD/CID fragmentation, signature fragment ions observed in the low mass range indicate the level of glutamylation in the peptides. These low-mass fragments denoted with G (for glycine), followed by the number of additional glycine in the fragment, indicate the level of glyetylation of one single site, and correspond to internal fragments. The fragment G1 corresponds to the fragmentation of one glutamate residue modified by one glycine residue, whereas G1 corresponds to the fragmentation of one glutamate residue modified by two glycine residues. (C) Using nanoESI Q-TOF with collision-activated dissociation (CAD), the MS/MS exhibits a regular and relatively complete fragmentation pattern, producing b- and y-type ions, and gives information on the whole sequence. (D) Sequence and localization of the modifications sites deduced from the MS/MS spectrum (C) and validated with low-mass range information from (B). These data show that four glutamate residues are modified by the posttranslational addition of glycine residues. (Data are presented with permission of Joëlle Vinh.)

expressed at the adult stage, we have also detected high levels of glutamylation of the protein predominantly nontyrosinated (Redeker *et al.*, 1994). Interestingly, $\alpha 4A$ -tubulin protein has never been detected before, and is not always observed using similar approaches (Rao *et al.*, 2001). This might be explained by the use of different tubulin purification procedures. Using only one microtubule

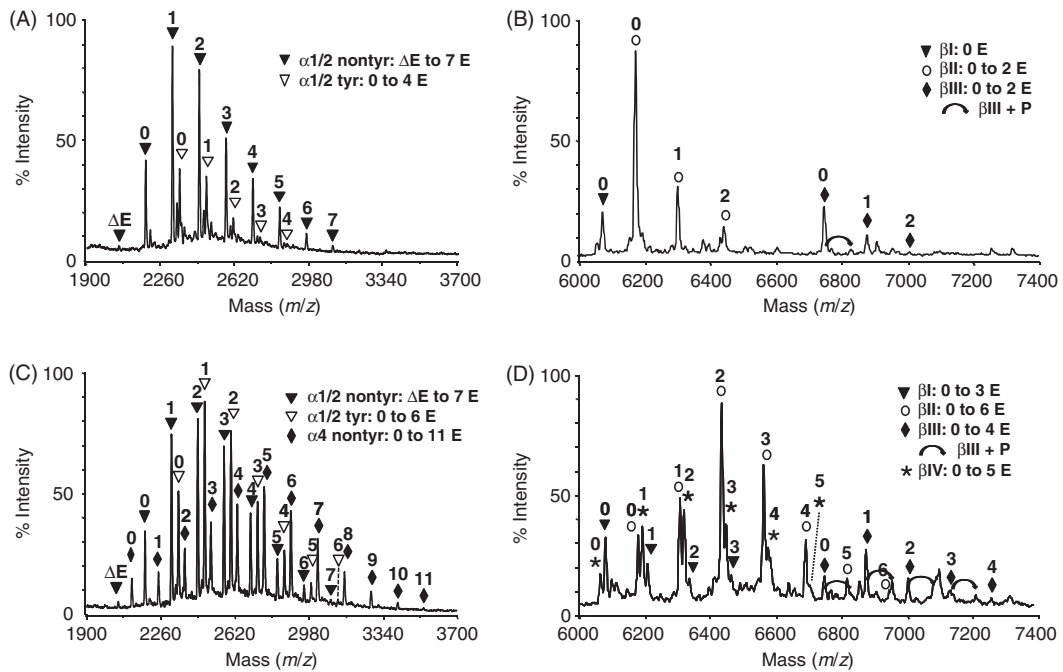


Fig. 4 C-terminal Peptide Mass Fingerprinting of α - and β -tubulin from neonatal and adult rat brain—MALDI mass spectra of the C-terminal peptides of α -tubulins (A and C) and β -tubulins (B and D) from neonatal (A and B) and adult (C and D) rat brain. Peptides were generated by LysC digestion of tubulin and purified as described in Fig. 1. C-terminal peptides of β -tubulin were analyzed directly after LysC digestion in positive mode. C-terminal peptides of α -tubulin were analyzed after arginine–sepharose chromatography in negative mode. The identification of each tubulin C-terminal peptide was made by comparison of the known amino-acid sequence and the experimental masses. The presence of additional glutamate residues corresponds to mass increments of 129 Da. (Data are presented with permission of Anthony Frankfurter.)

polymerization/depolymerization cycle, and in-solution digestion of microtubule proteins, the sample preparation minimizes loss of tubulins that would be less efficiently cycled, or tubulin C-terminal peptides that would be less efficiently extracted from the gels. From the tubulin C-terminal PMF, changes in α -tubulin polyglutamylation are discrete for α 1A/B-tubulin already highly glutamylated in neonatal brain tubulin. However, during development, a significant increase of polyglutamylation is observed for β -tubulins: nonglutamylated tubulin isoforms are predominant in neonatal animals, whereas mono-, bi-, and triglutamylated forms are predominant in adults (Fig. 4). In neonatal β II- and β III-tubulins, a maximum of two additional glutamates are observed, while in adult, β I-, β II-, β III-, and β IV-tubulins bear, respectively, up to three, six, four, and five additional glutamates. The acidity of the C-terminal tail of β III-tubulin is further increased during development by phosphorylation.

Similar observations have been made previously using 2D gel electrophoresis to analyze quantitatively and qualitatively changes in polyglutamylation of α - and β -tubulins during neuronal differentiation in cell culture (Audebert *et al.*, 1993). These data have shown that glutamylation of α -tubulin is already abundant in very

young neurons: protein spots corresponding to one to six additional glutamate residues were observed with no significant change during cell differentiation. For β -tubulin, glutamylation was detected at very low levels in young neurons and accumulated during differentiation. However, many tubulin isoforms cannot be easily isolated in single protein spots. Thus, speculation of the number of additional glutamate residues for one individual isotype becomes difficult. Interestingly, changes in glutamylation during post-natal development occur concomitantly with increased microtubule stability (Solomon, 1992) and might be involved in the regulation of MAPs binding during development. It has been proposed that polyglutamylation, which results in an increase in negative charges within the C-terminus, may facilitate MAPs binding (Bonnet *et al.*, 2001; Boucher *et al.*, 1994; Larcher *et al.*, 1996). *In vitro* studies using blot overlay studies and antibodies specific to glutamylation have suggested that the length of the polyglutamyl chain may modulate interaction with structural and motor MAPs, such as Tau, MAP1B, and MAP2 (Bonnet *et al.*, 2001; Boucher *et al.*, 1994; Larcher *et al.*, 1996). Interestingly, MAPs including MAP1, MAP2, and Tau accumulate during neuronal differentiation (Larcher *et al.*, 1992). These changes could be related to change in flexibility of young neurons with growing neurites to more stable mature neurons with long and stabilized neurites.

2. Structural Analysis of Polyglutamylation

Position of the glutamylated residue can be determined by peptide sequencing using Edman degradation (Eddé *et al.*, 1990). Structural analysis of the polyglutamylated peptides using MS/MS is more difficult than for polyglycylated peptides because of the high acidity of glutamate residues and because this modification readily fragments, as observed for phosphorylation (Boersema *et al.*, 2009). MS/MS fragmentation of polyglutamylated peptides can be considerably improved by N-terminal derivatization of tubulin C-terminal peptides using TMPP. This derivatization introduces a fixed charge on the N-terminal of peptides and orientates fragmentation and detection toward N-terminal fragment ion series (Huang *et al.*, 1997). This derivatization has been shown to facilitate the identification of glutamylation sites within the fragmentation mass spectra of short glutamylated α -tubulin peptides (Vinh, 1999). However, TMPP derivatization introduces a mass increment of 573.56 Da which may deserve an efficient peptide fragmentation of some high-mass peptides. Fragmentation of glutamylated peptides would probably be significantly improved using electron transfer dissociation (ETD) or electron capture dissociation (ECD) as has been observed for phosphorylation (Boersema *et al.*, 2009). Characterization of the lateral glutamate chains by MS/MS is still a challenging question.

This question has been addressed using an optimized reversed-phase separation and synthetic peptides mimicking all possible structures of lateral chains for bi- and triglutamylated peptides. The first additional glutamate residue must be linked to the γ -carboxyl group of a glutamate residue of the primary sequence (Redeker *et al.*, 1991), whereas the additional glutamate residues could then be attached through amide bonds to the α - or γ -carboxyl groups of the preceding residue. In optimized reversed-phase separation conditions at pH 3 and 15°C, peptides bearing free α -COOH groups elute before the peptides with free γ -COOH, as confirmed with

synthetic bi- and triglutamylated peptides. At pH 3 the α -COOH is the only group which is ionized to a large extent because of the difference in the pKa values of the α -COOH (pKa, 2.1) and γ -COOH (pKa 4.2) groups. By comparison with the retention times of standard peptides, we have determined that the second and third additional glutamate residues are linked through α -bond structures in neonatal as well as in adult brain tubulin (Redeker *et al.*, 1991; 1996). Thus, glutamylases have to initiate the addition of the first glutamate residue to the γ -carboxyl group of a specific glutamate from the primary sequence and then elongate the glutamate chain by addition of glutamate residues via α -carboxyl peptide bonds. Recently, a gene family coding for TTLLs containing a catalytic domain homologous to TTL but carrying out tubulin glutamylation was identified (Janke *et al.*, 2005; 2008; van Dijk *et al.*, 2007). This structural similarity reveals a common catalytic property in that both of them catalyze the addition of an amino acid to a glutamate residue in the isotype-defining C-terminal domain (Ersfeld *et al.*, 1993). Among the identified TTLL glutamylases, some have a predominant chain initiating activity, whereas others present an important chain elongating activity (van Dijk *et al.*, 2007). Using this optimized reversed-phase separation, we have observed that α -tubulins from adult brain present an increased level of heterogeneity, essentially attributed to the posttranslational excision of the penultimate glutamate residue, which generates the $\Delta 2$ - α -tubulin and renders tubulin nontyrosinatable (Redeker *et al.*, 1996). The increase in $\Delta 2$ - α -tubulin was not clearly observed in the tubulin C-terminal PMF because the mass difference coincided with the mass difference observed for glutamylation.

3. Role of MPTs in Cold Stability of Antarctic Fish Brain Tubulins

Interestingly, microtubule assembly from Antarctic fish tubulins is efficient at low temperatures (-2 to $+2^{\circ}\text{C}$), whereas mammalian tubulins depolymerize in these conditions. In order to document the possible role of posttranslational glutamylation of fish tubulins in the cold adaptation of microtubule assembly, we have characterized α - and β -tubulin C-terminal peptides from *Notothenia coriiceps* brain microtubule proteins using the PMF method (Redeker *et al.*, 2004). Comparison of tubulin glutamylation between cold-adapted fish brain tubulin and neonatal and adult rat brain tubulins has shown that fish brain tubulins are glutamylated differently (Redeker *et al.*, 2004). In cold-adapted fish brain, α -tubulins are more heterogeneous than in mammalian brains: nine fish α -tubulin isoforms were detected among which nonglutamylated isoforms were more abundant than glutamylated ones. However, the maximal side-chain lengths of fish α -tubulins were generally longer than those of adult rat brain α -tubulins. The number of β -isoforms observed in fish brain is lower and similar to that of the adult fish brain tubulins: four fish β -tubulin isoforms were detected, among which the nonglutamylated isoforms were the most abundant forms and the maximal glutamyl side-chain length was shorter than that observed for mammalian brain β -tubulins. The PMF approach has also revealed high level of nontyrosinated α -tubulins further trimmed by elimination of one or two C-terminal glutamate residues. When comparing the isoform distribution of brain tubulins from *Notothenia coriiceps* and mammals, we can conclude that fish tubulins present glutamylation levels similar to that of neonatal rat brain. We have proposed that

changes in tubulin glutamylation could act synergistically with unique residue substitutions in the primary structures of Antarctic fish tubulins (Detrich *et al.*, 2000; Redeker *et al.*, 2004).

D. Changes in PTMs Consecutively to Polymodification Site Mutations

In cilia and flagella, C-terminal tubulin sequences and polymodifications play an important role in the proper organization and motility of axonemal structures (Fackenthal *et al.*, 1993). In order to document the effect of C-terminal polymodifications, Gaertig's group (Thazhath *et al.*, 2002; 2004; Xia *et al.*, 2000) has produced a number of α - and β -tubulin variants, in *Tetrahymena thermophilus*, with multiple substitutions of predicted modification sites by aspartate or alanine residues, in order to inactivate the glyylation sites. In *Paramecium*, MS/MS analysis has established that several consecutive glutamate residues are glycosylated within or near the "axoneme motif" of both α - and β -tubulins (Vinh *et al.*, 1999). Tubulin variants with triple substitutions, of adjacent glutamate (E) by aspartate (D) or alanine (A) residues, on homologous amino acid of *Tetrahymena* β -tubulin were further analyzed (β EDDD⁴⁴⁰ and β EAAA⁴⁴⁰) (Redeker *et al.*, 2005; Xia *et al.*, 2000). These variants exhibit slower growth and motility than wild type (WT) and present important ultra-structural defects in their axonemes (Thazhath *et al.*, 2004; 2002; Xia *et al.*, 2000). Transmission electron microscopy revealed cilia with severe defects in the axonemal doublets. In a subpopulation of cilia from β EAAA⁴⁴⁰ and β EDDD⁴⁴⁰ mutants, cross-sections of axonemes showed that some B-tubules of nine peripheral doublets were open. And an electron-dense material was observed in the space between the outer doublets and the ciliary membrane. The effect of modification site inactivation on the composition of the PTMs of axonemal tubulin was analyzed with the tubulin C-terminal PMF method. Tubulin C-terminal PMF of WT *Tetrahymena* axonemes indicated that the two closely related ciliates *Tetrahymena* and *Paramecium* present extraordinary differences in their PTMs in accordance with immunoblotting (Redeker *et al.*, 2005): in contrast to *Paramecium* axonemal tubulin, *Tetrahymena* axonemal tubulin is not only glycosylated but also highly glutamylated, with up to 11 additional glutamate residues detected on α -tubulin, and only *Tetrahymena* α -tubulin is deetyrosinated. This result raises the question of the structure of the lateral chains posttranslationally added to tubulin when glutamylation and glyylation coexist in one unique tubulin molecule. We can make the hypothesis of either distinct modification sites for each of these two polymodifications or lateral chains containing both glutamate and glycine residues. Similar observations have been made in flagella of sea urchin spermatozoa, in which one molecule of α -tubulin can be simultaneously glycosylated and glutamylated (Mary *et al.*, 1996).

Changes in PTMs of the *Tetrahymena* mutants were analyzed using the tubulin C-terminal PMF method. Compared to the WT, tubulins from the β EAAA⁴⁴⁰ variant display a very significant loss of polymodifications. The predominant β -tubulin isoform is monoglycosylated in the mutant, whereas it is tetraglycosylated in the WT. Thus, the β -tubulin subunit of β EAAA⁴⁴⁰ exhibits a significant reduction in the level of glyylation. Ion series corresponding to α -tubulin C-terminal peptides indicate that the predominant α -tubulin isoform in the mutant is deetyrosinated and nonpolymodified (Fig. 5). The other ions of the series correspond to additions of one to eight glycine residues to the C-terminal deetyrosinated α -tubulin peptide starting at

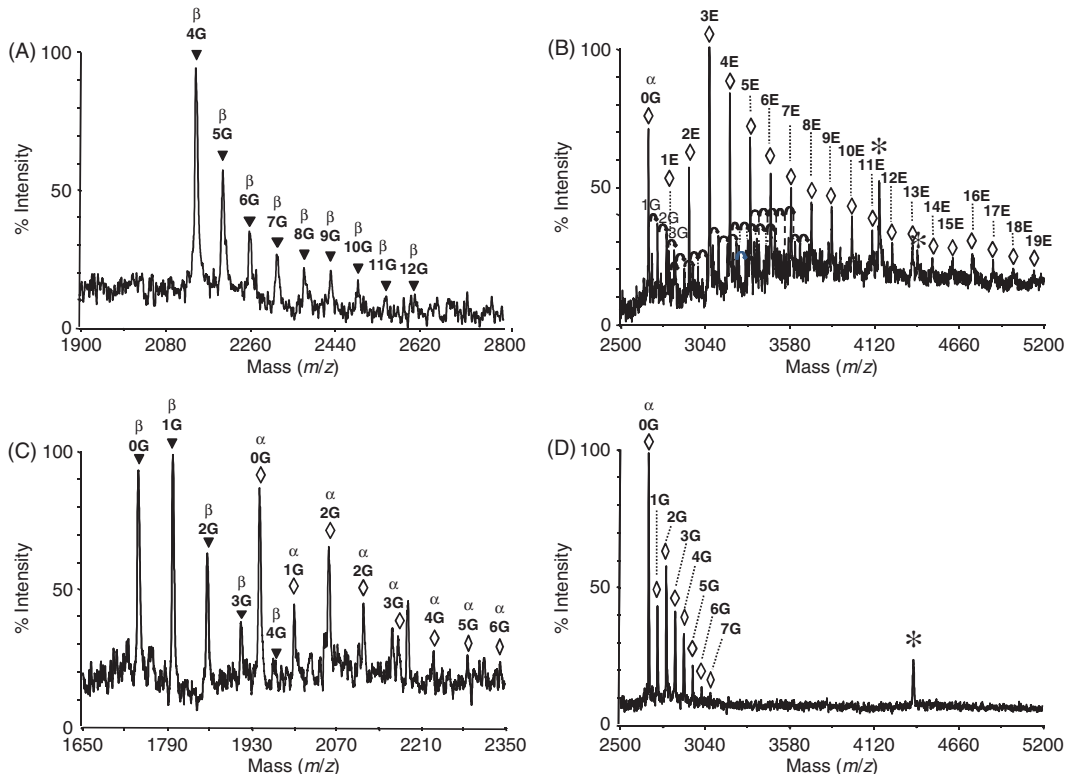


Fig. 5 C-terminal Peptide Mass Fingerprinting of α - and β -axonemal tubulin from WT and β EAAA⁴⁴⁰ *Tetrahymena* cilia—MALDI mass spectra of the C-terminal peptides of β -tubulins (A and C) and α -tubulins (B and D) from WT (A and B) and β EAAA⁴⁴⁰ (C and D) *Tetrahymena* cilia. Peptides were generated by AspN digestion of tubulin, purified as described in Fig. 1 and analyzed after arginine–sepharose chromatography. (A) C-terminal peptides of WT β -tubulin starting at residue Asp427 were detected, with 4–12 additional glycine residues and a predominant tetraglycylated form. (B) C-terminal peptides of WT α -tubulin starting at residue Asp424 were detected. This axonemal α -tubulin is predominantly glutamylated: with 1–19 additional glutamate residues detected in the PMF spectrum and the triglutamylated peptide being the most abundant one. Additional glyylation levels are also detected and indicated by curved and closed arrows in the MS spectrum. (C) C-terminal peptides of β EAAA⁴⁴⁰ β -tubulin starting at residue Asp427 were detected (closed arrows) with zero to four additional glycine residues, and the predominant peptides correspond to the nonmodified form. Additionally short α -tubulin peptides (open diamonds) starting at Asp431 were detected. These peptides were also predominantly nonmodified and present one to six additional glycine residues. (D) C-terminal peptides of β EAAA⁴⁴⁰ α -tubulin starting at residue Asp424 were detected. This axonemal α -tubulin is glycosylated by the addition of one to seven additional glycine residues and the predominant form is nonmodified. Stars correspond to internal tubulin peptides. Peptides were analyzed in positive mode. (Data are presented with permission of Jacek Gaertig.)

residue Asp424. No glutamylated peptides are detected in the α -tubulin subunit peptides pool, as observed also for the β EDDD⁴⁴⁰ mutant, whereas in the WT *Tetrahymena* the most abundant α -tubulin isoforms are predominantly polyglutamylated with up to 11 additional glutamate residues and less abundant α -tubulins are also glycosylated with up to six additional glycine residues. Thus, the α -tubulin subunit of β EAAA⁴⁴⁰ presents a strong reduction in glutamylated peptides. These results suggested a strong influence of the β -tubulin mutations on the distribution of posttranslational modifications in the

nonmutated α -tubulin subunit. Similar changes were observed with the β EDDD⁴⁴⁰ mutant, except that low levels of glutamylation could be detected for β -tubulin C-terminal peptides (Redeker *et al.*, 2005). A higher incidence of axonemal defects observed in β EAAA⁴⁴⁰, compared with β EDDD⁴⁴⁰, might be correlated with a more severe deficiency in both polymodifications, on the intact α -tubulin but also at a lower extent on the β -tubulin. These results strengthen the idea that the β -subunit is critical for the addition of polymodifications on both α - and β -tubulins. The observation that the level of the polymeric modifications are affected in both the mutated and nonmutated subunits has suggested the existence of a cross-talk among PTMs between α - and β -tubulin subunits that may affect the total level of PTMs on the microtubule. This cross-talk between α - and β -subunits could be mediated by a competition for the modifying enzymes, a participation of the nonmodified subunit as an enzyme-binding site, or indirect effects mediated by the polymer dynamics. From the complete MS profiling of tubulin PTMs, the deep ultrastructural analysis, and the physiological consequences on growth and motility of these mutants, it has been concluded that polyglycylation and/or polyglutamylation may stabilize the B-subfiber of outer doublets and regulate intraflagellar transport (Redeker *et al.*, 2005). These data suggest an important role of polymodifications in assembly of axonemal microtubules and axonemal motility (Gaertig and Wloga, 2008).

IV. Conclusion

We have made an overview of the methods that can be used in combination with MS to characterize tubulin PTMs in mammalian or nonmammalian tissues as well as in eukaryotic cell structures. Among these, the tubulin C-terminal PMF method yields relatively rapidly a complete picture of the molecular heterogeneity of tubulin isoforms, including qualitative isotype expression and characterization of PTMs of each isotype, from specific tissues, cells, or structures. These data show that due to the presence of multiple isotypes, multiple modifications, polymodifications, and multiple modification sites, the heterogeneity of some tubulin samples might be extraordinarily high. For such highly heterogeneous tubulin samples, determination of the mass of entire tubulins by LC-MS, as reported previously (Verdier-Pinard *et al.*, 2003), is challenging.

Since cross-talk between tubulin subunits have been observed, MS-based fingerprinting of tubulin isoforms will undoubtedly be necessary to assist the interpretation of functional or structural changes observed consecutively to modification site mutations and overexpression or inactivation of the enzymes involved in the addition or elimination of the polymeric side chains. Future analysis of inactivation experiments of modification sites or modification enzymes in combination with comparative proteomics using the tubulin C-terminal PMF method will contribute to document how each PTM of tubulin regulates microtubule-based functions in cells.

One limitation of this approach comes from the ion suppression phenomenon observed in MS for some peptides presenting low ionization properties or low abundance in highly complex peptide samples. This can be unraveled with high-resolution reversed-phase separation. In order to facilitate detection of low abundant isoforms in low abundant tubulin samples, future development will include the use of miniaturized chromatographic separations. Additionally, the development of a robust

absolute quantification method of tubulin isotypes would permit to go deeper in the analysis of tubulin isoform changes between biological samples. A quantitative proteomic approach using isotopically labeled synthetic peptides (Fenselau, 2007) as previously reported with ¹⁵N-labeled synthetic peptides (Miller *et al.*, 2008) should be favored. Finally, optimization of other “tubulin proteomics” approaches targeting less well-characterized PTMs of tubulins as for example phosphorylation of β -tubulin (Alexander *et al.*, 1991; Fourest-Lievin *et al.*, 2006) or C-terminal proteolysis (Miller *et al.*, 2008; Redeker *et al.*, 2004) would contribute to document how they regulate microtubule functions.

Acknowledgments

This work was supported by the Centre National de la Recherche Scientifique (CNRS) and the Institut National de la Santé et de la Recherche Médicale (INSERM). I am grateful to all the collaborators for making the described work possible and for their helpful discussions, with a special thank to J. Rossier, J. P. Le Caer, J. Vinh, J. Mary, J. M. Schmitter, J. C. Promé, A. Frankfurter, H. W. Detrich, R. Melki, J. Gaertig, M. H. Bré, N. Levilliers and A. Adoutte.

References

Adoutte, A., Delgado, P., Fleury, A., Levilliers, N., Lainé, M. C., Marty, M. C., Boisvieux-Ulrich, E., and Sandoz, D. (1991). Microtubule diversity in ciliated cells: Evidence for its generation by post-translational modification in the axonemes of Paramecium and quail oviduct cells. *Biol. Cell* **71**, 227–245.

Alexander, J. E., Hunt, D. F., Lee, M. K., Shabanowitz, J., Michel, H., Berlin, S. C., MacDonald, T. L., Sundberg, R. J., Rebhun, L. I., and Frankfurter, A. (1991). Characterization of posttranslational modifications in neuron-specific class III β -tubulin by mass spectrometry. *Proc. Natl. Acad. Sci. USA* **88**, 4685–4689.

Argarana, C. E., Barra, H. S., and Caputto, R. (1978). Release of [¹⁴C]tyrosine from tubulinyl-[¹⁴C] tyrosine by brain extract. Separation of a carboxypeptidase from tubulin-tyrosine ligase. *Mol. Cell Biochem.* **19**, 17–21.

Audebert, S., Desbruyères, E., Gruszczynski, C., Koulakoff, A., Gros, F., Denoulet, P., and Eddé, B. (1993). Reversible polyglutamylation of alpha- and beta-tubulin and microtubule dynamics in mouse brain neurons. *Mol. Biol. Cell* **4**, 615–626.

Biemann, K. (1990). Appendix 5. Nomenclature for peptide fragment ions (positive ions). *Meth. Enzymol.* **193**, 886–887.

Bobiniec, Y., Khodjakov, A., Mir, L. M., Rieder, C. L., Eddé, B., and Bornens, M. (1998). Centriole disassembly in vivo and its effect on centrosome structure and function in vertebrate cells. *J. Cell Biol.* **143**, 1575–1589.

Boersema, P. J., Mohammed, S., and Heck, A. J. (2009). Phosphopeptide fragmentation and analysis by mass spectrometry. *J. Mass Spectrom.* **44**, 861–878.

Bonnet, C., Boucher, D., Lazereg, S., Pedrotti, B., Islam, K., Denoulet, P., and Larcher, J. C. (2001). Differential binding regulation of microtubule-associated proteins MAP1A, MAP1B, and MAP2 by tubulin polyglutamylation. *J. Biol. Chem.* **276**, 12839–12848.

Boucher, D., Larcher, J. C., Gros, F., and Denoulet, P. (1994). Polyglutamylation of tubulin as a progressive regulator of in vitro interactions between the microtubule-associated protein Tau and tubulin. *Biochemistry* **33**, 12471–12477.

Bré, M. H., de Néchaud, B., Wolff, A., and Fleury, A. (1994). Glutamylated tubulin probed in ciliates with the monoclonal antibody GT335. *Cell Motil. Cytoskel.* **27**, 337–349.

Bré, M. H., Redeker, V., Quibell, M., Darmanaden-Delorme, J., Bressac, C., Cosson, J., Huitorel, P., Schmitter, J. M., Rossier, J., Johnson, T., Adoutte, A., and Levilliers, N. (1996). Axonemal tubulin polyglycylation probed with two monoclonal antibodies: Widespread evolutionary distribution, appearance during spermatozoan maturation and possible function in motility. *J. Cell Sci.* **109**, 727–738.

Castoldi, M., and Popov, A. V. (2003). Purification of brain tubulin through two cycles of polymerization-depolymerization in a high-molarity buffer. *Protein Expr. Purif.* **32**, 83–88.

Detrich, H. W., III, Johnson, K. A., and Marchese-Ragona, S. P. (1989). Polymerization of Antarctic fish tubulins at low temperatures: Energetic aspects. *Biochemistry* **28**, 10085–10093.

Detrich, H. W., III, Parker, S. K., Williams, R. C., Jr., Nogales, E., and Downing, K. H. (2000). Cold adaptation of microtubule assembly and dynamics. Structural interpretation of primary sequence changes present in the alpha- and beta-tubulins of Antarctic fishes. *J. Biol. Chem.* **275**, 37038–37047.

Eddé, B., Denoulet, P., De Néchaud, B., Koulakoff, A., Verwald-Netter, Y., and Gros, F. (1989). Posttranslational modifications of tubulin in cultured mouse brain neurons and astroglia. *Biol. Cell* **65**, 109–117.

Eddé, B., Rossier, J., Le Caer, J. P., Berwald-Netter, Y., Koulakoff, A., Gros, F., and Denoulet, P. (1991). A combination of posttranslational modifications is responsible for the production of neuronal alpha-tubulin heterogeneity. *J. Cell Biochem.* **46**, 134–142.

Eddé, B., Rossier, J., Le Caer, J. P., Desbruyères, E., Gros, F., and Denoulet, P. (1990). Posttranslational glutamylation of alpha-tubulin. *Science* **247**, 83–84.

Ersfeld, K., Wehland, J., Plessmann, U., Dodemont, H., Gerke, V., and Weber, K. (1993). Characterization of the tubulin-tyrosine ligase. *J. Cell Biol.* **120**, 725–732.

Fackenthal, J. D., Turner, F. R., and Raff, E. C. (1993). Issue-specific microtubule functions in Drosophila spermatogenesis require the beta 2-tubulin isotype-specific carboxy terminus. *Dev. Biol.* **158**, 213–227.

Fenselau, C. J. (2007). A review of quantitative methods for proteomic studies. *J. Chromatogr. B Anal. Technol. Biomed. Life Sci.* **855**, 14–20.

Fourest-Lieuvin, A., Peris, L., Gache, V., Garcia-Saez, I., Juillan-Binard, C., Lantez, V., and Job, D. (2006). Microtubule regulation in mitosis: Tubulin phosphorylation by the cyclin-dependent kinase *Mol. Biol. Cell* **17**, 1041–1050.

Gaertig, J., and Wloda, D. (2008). Ciliary tubulin and its post-translational modifications. *Curr. Top. Dev. Biol.* **85**, 83–113.

Gagnon, C., White, D., Cossion, J., Huitorel, P., Edde, B., Desbruyères, E., Paturle-Lafanechère, L., Multigner, L., Job, D., and Cibert, C. (1996). The polyglutamylated lateral chain of alpha-tubulin plays a key role in flagellar motility. *J. Cell Sci.* **109**, 1545–1553.

Geimer, S., Teltenkötter, A., Plessmann, U., Weber, K., and Lechtreck, K. F. (1997). Purification and characterization of basal apparatuses from a flagellate green alga. *Cell Motil. Cytoskel.* **37**, 72–85.

Geuens, G., Hill, A. M., Levilliers, N., Adoutte, A., and DeBrabander, M. (1989). Microtubule dynamics investigated by microinjection of Paramecium axonemal tubulin: Lack of nucleation but proximal assembly of microtubules at the kinetochore during prometaphase. *J. Cell Biol.* **108**, 939–953.

Hagmann, M. L., Geuss, U., Fischer, S., and Kresse, G. B. (1995). Peptidyl-Asp metalloendopeptidase. *Meth. Enzymol.* **248**, 782–787.

Hallak, M. E., Rodriguez, J. A., Barra, H. S., and Caputto, R. (1977). Release of tyrosine from tyrosinated tubulin. Some common factors that affect this process and the assembly of tubulin. *FEBS Lett.* **73**, 147–150.

Hammond, J. W., Cai, D., and Verhey, K. J. (2008). Tubulin modifications and their cellular functions. *Curr. Opin. Cell Biol.* **20**, 71–76.

Huang, Z. H., Wu, J., Roth, K. D.W., Yang, Y., Gage, D. A., and Watson, J. T. (1997). A picomole-scale method for charge derivatization of peptides for sequence analysis by mass spectrometry. *Anal. Chem.* **66**, 137–144.

Ikegami, K., Mukai, M., Tsuchida, J., Heier, R. L., Macgregor, G. R., and Setou, M. (2006). TTLL7 is a mammalian beta-tubulin polyglutamylase required for growth of MAP2-positive neurites. *J. Biol. Chem.* **281**, 30707–30716.

Janke, C., Rogowski, K., and van Dijk, J. (2008). Polyglutamylation: A fine-regulator of protein function? ‘Protein Modifications: Beyond the usual suspects’ review series. *EMBO Rep.* **9**, 636–641.

Janke, C., Rogowski, K., Wloda, D., Regnard, C., Kajava, A. V., Strub, J. M., Temurak, N., van Dijk, J., Boucher, D., van Dorsselaer, A., Suryavanshi, S., Gaertig, J., et al. (2005). Tubulin polyglutamylase enzymes are members of the TTL domain protein family. *Science* **308**, 1758–1762.

Kann, M. L., Soues, S., Levilliers, N., and Fouquet, J. P. (2003). Glutamylated tubulin: Diversity of expression and distribution of isoforms. *Cell Motil. Cytoskel.* **55**, 14–25.

Kaufmann, R., Kirsch, D., and Spengler, B. (1994). Mass spectrometric sequencing of linear peptides by product-ion analysis in a reflectron time-of-flight mass spectrometer using matrix-assisted laser desorption ionization. *Int. J. Mass Spectrom. Ion Process.* **131**, 355.

Khodiyar, V. K., Maltais, L. J., Sneddon, K. M., Smith, J. R., Shimoyama, M., Cabral, F., Dumontet, C., Dutcher, S. K., Harvey, R. J., Lafanechère, L., Murray, J. M., Nogales, E., et al. (2007). A revised nomenclature for the human and rodent α -tubulin gene family. *Genomics* **90**, 285–289.

Kosaka, T., Ishikawa, T., and Kinoshita, T. (1995). Collisionally-activated dissociation spectra of linear peptides in matrix-assisted laser desorption/ionization time-of-flight mass spectrometry. *Rapid. Commun. Mass Spectrom.* **9**, 1342–1344.

Lacey, E., and Snowdon, K. L. (1990). Isolation of mammalian brain tubulin by amino-activated gel chromatography. *J. Chromatogr.* **525**, 71–84.

Larcher, J. C., Boucher, D., Ginzburg, I., Gros, F., and Denoulet, P. (1992). Heterogeneity of tau proteins during mouse brain development and differentiation of cultured neurons. *Dev. Biol.* **154**, 195–204.

Larcher, J. C., Boucher, D., Lazereg, S., Gros, F., and Denoulet, P. (1996). Interaction of kinesin motor domains with a- and b-tubulin subunits at a tau-independent binding site. Regulation by polyglutamylation. *J. Biol. Chem.* **271**, 22217–22214.

Lechtreck, K. F., and Geimer, S. (2000). Distribution of polyglutamylated tubulin in the flagellar apparatus of green flagellates. *Cell Motil. Cytoskel.* **47**, 219–235.

LeDizet, M., and Piperno, G. (1987). Identification of an acetylation site of Chlamydomonas α -tubulin. *Proc. Natl. Acad. Sci. USA* **84**, 5720–5724.

Ludueña, R. F. (1998). Multiple forms of tubulin: Different gene products and covalent modifications. *Int. Rev. Cytol.* **178**, 207–275.

Mary, J., Redeker, V., Le Caer, J. P., Prome, J. C., and Rossier, J. (1994). Class I and IVa beta tubulin isotypes expressed in adult mouse brain are glutamylated. *FEBS Lett.* **353**, 89–94.

Mary, J., Redeker, V., Le Caer, J. P., Rossier, J., and Schmitter, J. (1996). Posttranslational modifications in the C-terminal tail of axonemal tubulin from sea urchin sperm. *J. Biol. Chem.* **271**, 9928–9933.

Matsubara, H. (1966). Observations on the specificity of thermolysin with synthetic peptides. *Biochem. Biophys. Res. Commun.* **24**, 427–340.

Mejillano, M. R., and Himes, R. H. (1991). Assembly properties of tubulin after carboxyl group modification. *J. Biol. Chem.* **266**, 657–664.

Miller, L. M., Mentheña, A., Chatterjee, C., Verdier-Pinard, P., Novikoff, P. M., Horwitz, S. B., and Angeletti, R. H. (2008). Increased levels of a unique post-translationally modified β IVb-tubulin isotype in liver cancer. *Biochemistry* **47**, 7572–7582.

Million, K., Larcher, J., Laoukili, J., Bourguignon, D., Marano, F., and Tournier, F. (1999). Polyglutamylation and polyglycation of alpha- and beta-tubulins during in vitro ciliated cell differentiation of human respiratory epithelial cells. *J. Cell Sci.* **112**, 4357–4366.

Mock, K. K., Sutton, C. W., and Cottrell, J. S. (1992). Sample immobilization protocols for matrix-assisted laser-desorption mass spectrometry. *Rapid. Commun. Mass Spectrom.* **6**, 233–238.

Nogales, E., Wolf, S. G., and Downing, K. H. (1998). Structure of the alpha beta tubulin dimer by electron crystallography. *Nature* **391**, 199–203.

Ozols, J., and Caron, J. M. (1997). Posttranslational modification of tubulin by palmitoylation: II. Identification of sites of palmitoylation. *Caron. Mol. Biol. Cell* **8**, 637–645.

Paturle-Lafanechère, L., Eddé, B., Denoulet, P., Van Dorsselaer, A., Mazarguil, H., Le Caer, J. P., Wehland, J., and Job, D. (1991). Characterization of a major brain tubulin variant which cannot be tyrosinated. *Biochemistry* **30**, 10523–10528.

Plessmann, U., Reiter-Owona, I., and Lechtreck, K. F. (2004). Posttranslational modifications of alpha-tubulin of *Toxoplasma gondii*. *Parasitol. Res.* **94**, 386–389.

Rao, S., Aberg, F., Nieves, E., Band Horwitz, S., and Orr, G. A. (2001). Identification by mass spectrometry of a new a-tubulin isotype expressed in human breast and lung carcinoma cell lines. *Biochemistry* **40**, 2096–2103.

Redeker, V., Frankfurter, A., Parker, S. K., Rossier, J., and Detrich, H. W., III (2004). Posttranslational modification of brain tubulins from the Antarctic fish *Notothenia coriiceps*: Reduced C-terminal glutamylated correlates with efficient microtubule assembly at low temperature. *Biochemistry* **43**, 12265–12274.

Redeker, V., Le Caer, J. P., Rossier, J., and Prome, J. C. (1991). Structure of the polyglutamyl side chain posttranslationally added to alpha-tubulin. *J. Biol. Chem.* **266**, 23461–23466.

Redeker, V., Levilliers, N., Schmitter, J. M., Le Caer, J. P., Rossier, J., Adoutte, A., and Bre, M. H. (1994). Polyglycation of tubulin: A posttranslational modification in axonemal microtubules. *Science* **266**, 1688–1691.

Redeker, V., Levilliers, N., Vinolo, E., Rossier, J., Jaillard, D., Burnette, D., Gaertig, J., and Bre, M. H. (2005). Mutations of tubulin glycation sites reveal cross-talk between the C termini of alpha- and beta-tubulin and affect the ciliary matrix in *Tetrahymena*. *J. Biol. Chem.* **280**, 596–606.

Redeker, V., Melki, R., Prome, D., Le Caer, J. P., and Rossier, J. (1992). Structure of tubulin C-terminal domain obtained by subtilisin treatment. The major alpha and beta tubulin isotypes from pig brain are glutamylated. *FEBS Lett.* **313**, 185–192.

Redeker, V., Rossier, J., and Frankfurter, A. (1998). Posttranslational modifications of the C-terminus of alpha-tubulin in adult rat brain: Alpha4 is glutamylated at two residues. *Biochemistry* **37**, 14838–14844.

Redeker, V., Rusconi, F., Mary, J., Prome, D., and Rossier, J. (1996). Structure of the C-terminal tail of α -tubulin: Increase of heterogeneity from newborn to adult. *J. Neurochem.* **67**, 2104–2114.

Regnard, C., Desbruyeres, E., Denoulet, P., and Edde, B. (1999). Tubulin polyglutamylase: Isozymic variants and regulation during the cell cycle in HeLa cells. *J. Cell Sci.* **112**, 4281–4289.

Rogowski, K., Juge, F., van Dijk, J., Wloga, D., Strub, J. M., Levilliers, N., Thomas, D., Bré, M. H., Van Dorsselaer, A., Gaertig, J., and Janke, C. (2009). Evolutionary divergence of enzymatic mechanisms for posttranslational polyglycation. *Cell* **137**, 1076–1087.

Roll-Mecak, A., and Vale, R. D. (2008). Structural basis of microtubule severing by the hereditary spastic paraplegia protein spastin. *Nature* **451**, 363–367.

Rüdiger, M., Carl, U. D., Chakraborty, T., Roepstorff, P., and Wehland, J. (1999). Affinity mass spectrometry-based approaches for the analysis of protein-protein interaction and complex mixtures of peptide-ligands. *Anal. Biochem.* **275**, 162–170.

Rüdiger, M., Plessman, U., Klöppel, K. D., Wehland, J., and Weber, K. (1992). Class II tubulin, the major brain β tubulin isotype is polyglutamylated on glutamic acid residue 435. *FEBS Lett.* **308**, 101–105.

Rüdiger, M., Plessmann, U., Rüdiger, A. H., and Weber, K. (1995). Beta tubulin of bull sperm is polyglycylated. *FEBS Lett.* **364**, 147–151.

Rüdiger, M., and Weber, K. (1993). Characterization of the post-translational modifications in tubulin from the marginal band of avian erythrocytes. *Eur. J. Biochem.* **218**, 107–116.

Rüdiger, M., Wehland, J., and Weber, K. (1994). The carboxy-terminal peptide of detyrosinated α tubulin provides a minimal system to study the substrate specificity of tubulin-tyrosine ligase. *Eur. J. Biochem.* **220**, 309–320.

Shélanski, M. L., Gaskin, F., and Cantor, C. R. (1973). Microtubule assembly in the absence of added nucleotides. *Proc. Nat. Acad. Sci. USA* **70**, 765–768.

Skiniotis, G., Cochran, J. C., Müller, J., Mandelkow, E., Gilbert, S. P., and Hoenger, A. (2004). Modulation of kinesin binding by the C-termini of tubulin. *EMBO J.* **23**, 989–999.

Solomon, F. (1992). Neuronal cytoskeleton and growth. *Curr. Opin. Neurobiol.* **2**, 613–617.

Sullivan, K. F. (1988). Structure and utilization of tubulin isotypes. *Annu. Rev. Cell Biol.* **4**, 687–716.

Sun, W., Wu, S., Wang, X., Zheng, D., and Gao, Y. (2005). An analysis of protein abundance suppression in data dependent liquid chromatography and tandem mass spectrometry with tryptic peptide mixtures of five known protein. *Eur. J. Mass Spectrom.* **11**, 575–580.

Thazhath, R., Jerka-Dziadosz, M., Duan, J., Wloga, D., Gorovsky, M. A., Frankel, J., and Gaertig, J. (2004). Cell context-specific effects of the beta-tubulin glycation domain on assembly and size of microtubular organelles. *Mol. Biol. Cell* **15**, 4136–4147.

Thazhath, R., Liu, C., and Gaertig, J. (2002). Polyglycation domain of beta-tubulin maintains axonemal architecture and affects cytokinesis in Tetrahymena. *Nat. Cell Biol.* **4**, 256–259.

Vallee, R. B., and Collins, C. A. (1986). Purification of microtubules and microtubule-associated proteins from sea urchin eggs and cultured mammalian cells using taxol, and use of exogenous taxol-stabilized brain microtubules for purifying microtubule-associated proteins. *Meth. Enzymol.* **134**, 116–127.

van Dijk, J., Rogowski, K., Miro, J., Lacroix, B., Edde, B., and Janke, C. (2007). A targeted multienzyme mechanism for selective microtubule polyglutamyltion. *Mol. Cell* **26**, 437–448.

Verdier-Pinard, P., Pasquier, E., Xiao, H., Burd, B., Villard, C., Lafitte, D., Miller, L. M., Angeletti, R. H., Horwitz, S. B., and Braguer, D. (2009). Tubulin proteomics: Towards breaking the code. *Anal. Biochem.* **384**, 197–206.

Verdier-Pinard, P., Shahabi, S., Wang, F., Burd, B., Xiao, H., Goldberg, G. L., Orr, G. A., and Horwitz, S. B. (2005). Detection of human bV-tubulin expression in epithelial cancer cell lines by tubulin proteomics. *Biochemistry* **44**, 15858–15870.

Verdier-Pinard, P., Wang, F., Burd, B., Angeletti, R. H., Horwitz, S. B., and Orr, G. A. (2003). Direct analysis of tubulin expression in cancer cell lines by electrospray ionization mass spectrometry. *Biochemistry* **42**, 12019–12027.

Verdier-Pinard, P., Wang, F., Martello, L., Burd, B., Orr, G. A., and Horwitz, S. B. (2003). Analysis of tubulin isotypes and mutations from taxol-resistant cells by combined isoelectrofocusing and mass spectrometry. *Biochemistry* **42**, 5349–5357.

Verhey, K. J., and Gaertig, J. (2007). The tubulin code. *Cell Cycle* **6**, 2152–2160.

Vinh, J. (1999). Etude et caractérisation structurale de modifications post-traductionnelles de la tubuline par spectrométrie de masse. Thesis, Université Pierre et Marie Curie, Université Paris 6, 14 April 1999.

Vinh, J., Langridge, J. I., Bre, M. H., Levilliers, N., Redeker, V., Loyaux, D., and Rossier, J. (1999). Structural characterization by tandem mass spectrometry of the posttranslational polyglycylation of tubulin. *Biochemistry* **38**, 3133–3139.

Vinh, J., Loyaux, D., Redeker, V., and Rossier, J. (1997). Sequencing branched peptides with CID/PSD MALDI-TOF in the low-picomole range: Application to the structural study of the posttranslational polyglycylation of tubulin. *Anal. Chem.* **69**, 3979–3985.

Wang, Z., and Sheetz, M. P. (2000). The C-terminus of tubulin increases cytoplasmic dynein and kinesin processivity. *Biophys J.* **78**, 1955–1964.

Weber, K., Schneider, A., Westermann, S., Müller, N., and Plessmann, U. (1997). Posttranslational modifications of alpha- and beta-tubulin in Giardia lamblia, an ancient eukaryote. *FEBS Lett.* **419**, 87–91.

Wehland, J., and Weber, K. (1987). Turnover of the carboxy-terminal tyrosine of a-tubulin and means of reaching elevated levels of detyrosination in living cells. *J. Cell Sci.* **88**, 185–203.

Weingarten, M. D., Lockwood, A. H., Hwo, S. Y., and Kirshner, M. W. (1975). A protein factor essential for microtubule assembly. *Proc. Nat. Acad. Sci. USA* **72**, 1858–1862.

Westermann, S., and Weber, K. (2003). Post-translational modifications regulate microtubule function. *Nat. Rev. Mol. Cell Biol.* **4**, 938–947.

Williams, R. C., Jr., Shah, C., and Sackett, D. (1999). Separation of tubulin isoforms by isoelectric focusing in immobilized pH gradient gels. *Anal. Biochem.* **275**, 265–267.

Wloga, D., Webster, D. M., Rogowski, K., Bré, M. H., Levilliers, N., Jerka-Dziadosz, M., Janke, C., Dougan, S. T., and Gaertig, J. (2009). TTLL3 is a tubulin glycine ligase that regulates the assembly of cilia. *Dev. Cell* **16**, 867–876.

Wolff, A., Denoulet, P., and Jeantet, C. (1982). High level of tubulin microheterogeneity in the mouse brain. *Neurosci. Lett.* **31**, 323–328.

Xia, L., Hai, B., Gao, Y., Burnette, D., Thazhath, R., Duan, J., Bré, M. H., Levilliers, N., Gorovsky, M. A., and Gaertig, J. (2000). Polyglycylation of tubulin is essential and affects cell motility and division in Tetrahymena thermophila. *J. Cell Biol.* **149**, 1097–1106.

CHAPTER 7

Methods in Tubulin Proteomics

**Leah M. Miller^{*}, Hui Xiao^{*}, Berta Burd^{*}, Susan Band Horwitz[†],
Ruth Hogue Angeletti^{*}, and Pascal Verdier-Pinard[‡]**

^{*}Laboratory of Macromolecular Analysis and Proteomics, Albert Einstein College of Medicine, Bronx, New York 10461

[†]Department of Molecular Pharmacology, Albert Einstein College of Medicine, Bronx, New York 10461

[‡]INSERM UMR 911, CRO2, Aix Marseille Université, 13385 Marseille Cedex 05, France

Abstract

I. Introduction

II. Methods

- A. Taxol-Based Isolation of Tubulin from Cell or Tissue Extracts
- B. Electrophoretic Separation of Tubulin Isotypes and Posttranslational Modifications
- C. Identification of Tubulin Isotypes and Posttranslational Modifications
- D. Analysis of Intact Tubulins by Electrospray Ionization Mass Spectrometry
- E. Relative Quantitation of Tubulin Isotypes
- F. Microtubule Interactions with Drugs and MAPs

III. Summary

Acknowledgments

References

Abstract

New analytical methods are needed for the successful outcome of experiments aimed at characterizing mechanisms of microtubule dynamics and at understanding the effects of drugs on microtubules. The identification of tubulin isotypes and of regions of the microtubule involved in drug interactions has been advanced by proteomic methodologies. The diversity of tubulin sequences and posttranslational modifications (PTMs) can generate a complex mixture of heterodimers with unique molecular dynamics driving specific functions. Mass spectrometry (MS)-based approaches have been developed, and in combination with chromatographic and/or electrophoretic separation of tubulin polypeptides or peptides, they have contributed to our understanding of tubulin proteomics. We present protocols that we have used

for the analysis of tubulin isotypes and PTMs present in tubulin isolated from cells in culture or tissues and for the identification of tubulin regions altered by microtubule-stabilizing agents. Tubulin proteomics complements structural and computer modeling information for a high-resolution view of microtubule dynamics and its alteration by drugs. These methodologies will help in providing insights into tubulin isotype-specific functions and in the design of drugs targeting either all tubulin heterodimers indiscriminately or only those containing specific isotypes.

===== I. Introduction

In most laboratories, the tubulin that is used in *in vitro* assays is isolated from mammalian brains. This tubulin is usually obtained by cycles of polymerization/depolymerization of microtubules, and when necessary, microtubule-associated proteins (MAPs) are removed either by ion-exchange chromatography or by polymerization of microtubules in high-salt buffers (Andreu, 2007; Castoldi and Popov, 2003; Gaskin and Roychowdhury, 1986; Hamel and Lin, 1981, Hamel and Lin, 1984; Lee, 1982; Murphy and Hiebsch, 1979; Shelanski *et al.*, 1973; Williams and Lee, 1982). The yield and purity of these preparations are assessed by sodium dodecyl sulfate polyacrylamide gel electrophoresis (SDS-PAGE) and Coomassie blue staining, and the functionality of isolated tubulin is checked for its ability to polymerize using turbidimetry- or pelleting-based assays (Gaskin *et al.*, 1975).

Brain tubulin is composed of several α -tubulin (α 1A, α 1B) and β -tubulin (β I, β II, β III, β IVa) isotypes and is highly posttranslationally modified, notably by polyglutamylation, glycation, phosphorylation, acetylation, detyrosination, and/or loss of the last two amino-acid residues (Luduena, 1998; Verhey and Gaertig, 2007). Even though most cell lines studied may express several tubulin isotypes (α 1B, α 1C, α 4A; β I, β IVb, β III, β V, β II), the bulk of the tubulin pool is not posttranslationally modified (Verdier-Pinard *et al.*, 2009). The ratio between β -tubulin isotypes is very different in cell lines than in preparations of brain tubulin. For instance, β I-tubulin is the major β -tubulin isotype in cell lines (Verdier-Pinard *et al.*, 2009), whereas it is the minor one in brain where β II tubulin is the most abundant (Banerjee *et al.*, 1992).

It is not proven one way or another that results from *in vitro* experiments with purified tubulin or tubulin after reconstitution with associated proteins would be systematically different, if one uses brain tubulin versus tubulin from cells in culture. Nevertheless, some differences have been noted over the years indicating that tubulin isotype composition may determine microtubule dynamics, protein association to the microtubule lattice, and drug-binding parameters (Banerjee *et al.*, 1990; Derry *et al.*, 1997; Lu and Luduena, 1994; Newton *et al.*, 2002; Panda *et al.*, 1994). Therefore, it is useful to analyze the content in tubulin preparations from nonneuronal tissues and cells in culture (Bellocq *et al.*, 1992; Farrell, 1982; Fourest-Lievin, 2006; Kilmartin, 1981; MacRae and Gull, 1990; Macrae and Luduena, 1984; Maekawa and Sakai, 1978; Morejohn and Fosket, 1982; Murphy, 1991; Rudiger and Weber, 1993; Verdier-Pinard *et al.*, 2009; Weatherbee *et al.*, 1980). This analysis may help investigators in refining the interpretation of the data from their *in vitro* assays.

Working with tubulin from nonneuronal origin can be advantageous because its lower complexity facilitates the analysis of data [see the example of hydrogen-/deuterium-exchange mass spectrometry (HDX-MS) in the chapter] or aids in the

discovery of microtubule-interacting drugs that are more active on tumor tissues and induce less neurological side effects. Immunoaffinity purification of tubulin fractions enriched in a particular isotype has been carried out for brain tubulin (Derry *et al.*, 1997; Lu and Luduena, 1994; Paturle *et al.*, 1989). In this case, or in any other tubulin fractionation process prior to *in vitro* assays, tubulin proteomics can assess the quality of these fractions. Ultimately, the MS-based methods for tubulin analysis presented in this chapter are also valuable in the characterization of antitubulin antibody specificity (Verdier-Pinard *et al.*, 2009). Such validated antibodies allow straightforward and high-throughput analysis of tubulin-containing samples. Nevertheless, MS-based relative and absolute quantification are accurate on a much larger dynamic range than antibody-based detection systems. Furthermore, analysis of tubulin by MS may reveal novel forms of tubulin, for which no validated antibodies are available, as well as provide detailed characterization of tubulin posttranslational modifications (PTMs), including the exact number of glutamate residues added in a polyglutamylation modification, which can not be directly determined with antibodies.

We present protocols that we have implemented for tubulin purification from cell lines and tissues, for MS-based analysis of isolated tubulin, and for deciphering the binding sites of microtubule-stabilizing drugs and how these drugs affect tubulin molecular dynamics.

II. Methods

A. Taxol-Based Isolation of Tubulin from Cell or Tissue Extracts

One way to purify tubulin from nonneuronal sources is to take advantage of the microtubule-promoting and microtubule-stabilizing properties of Taxol. By lowering the critical tubulin concentration for assembly, this method allows the isolation of tubulin from 1 mg of total protein. Typically, Taxol [reducing the critical concentration of pure tubulin by 10-fold from 1–2 mg/ml to 0.1–0.2 mg/ml in the presence of guanosine triphosphate (GTP)] combined with the presence of MAPs induces tubulin assembly below 0.1 mg/ml. This approach was first implemented by Vallee *et al.* (Vallee, 1982) and has been applied since on a wide array of biological material. We adapted the method to cancer cell lines in culture and we also described a modified version that gave better results on murine tissues (Miller *et al.*, 2008; Verdier-Pinard *et al.*, 2005; Verdier-Pinard *et al.*, 2003a,b).

1. Materials

Cell lines were maintained in the recommended culture medium supplemented with 10% heat-inactivated foetal bovine serum in the presence of 5% CO₂. All animal studies were conducted under protocols approved by the Animal Care and Use Committee of Albert Einstein College of Medicine in accordance with National Institute of Health guidelines. For all surgical procedures, animals were anesthetized using isoflurane gas and were killed with a lethal dose of CO₂ (10–15 psi). Taxol was provided by the Drug Development Branch of the National Cancer Institute (Bethesda, MD), dissolved in dimethylsulfoxide (DMSO), and kept as a 1 mM

stock solution at -20°C . Protease inhibitor cocktail was from Roche Applied Science (Indianapolis, IN). All other chemicals were purchased from Sigma-Aldrich (St Louis, MO). We used a TLA-100.3 rotor from Beckman Coulter (Brea, CA) for all ultracentrifugation with teflon adaptors for 1.5-ml microfuge allomer tubes, but other fixed-angle rotors and thick-wall polycarbonate tubes can be used.

2. Protocols

a. Protocol 1.

1. Depending on the cell line, 7–10 100-mm petri dishes at 80% confluence or 250 ml of exponentially growing cells in suspension yield enough tubulin material for each of the different analytical techniques described. Adherent cells are washed once with 10 ml of phosphate-buffered saline (PBS) per dish, scraped in 1 ml of PBS per dish, and pooled in a 15-ml conical tube marked with 0.1 ml graduation below 1 ml to facilitate the evaluation of the volume of packed cells after centrifugation at $1200\times g$.
2. PBS is completely removed and pellets of 0.3–0.4 ml of packed cells are typically obtained. Cells are resuspended by adding 1.5-fold the volume of packed cells (450–600 μl) of MME buffer.
3. At this stage, the cell suspensions can be frozen in liquid nitrogen in cryotubes or kept in the 15-ml conical tubes, flash frozen in liquid nitrogen, and stored at -70°C . Note that tubulin is sensitive to denaturation and liquid nitrogen is preferred for long period of storage.
4. If frozen, cell suspensions are rapidly thawed and kept on ice. If in cryotubes, cell suspensions are transferred to 15-ml conical tubes. A protease inhibitor cocktail from a 10-fold stock solution in MME buffer (75–100 μl) and 1 mM dithiothreitol (DTT) are added.
5. The 15-ml tube is placed in a beaker containing ice and water. The cell suspension is sonicated with a microtip probe (Branson, Danbury, CT), (duty cycle: 20, output cycle: 3) seven times for 30 s with 30 s rest intervals on melted ice.
6. The cell lysate is transferred to centrifuge tubes and spun at $120,000\times g$ (Beckman TL100 centrifuge for 1 h at 4°C). Note that a whitish layer of lipids may appear at the surface of the supernatant at the end of centrifugation and should not be transferred; usually, tilting the tube while slowly pipetting out the supernatant deposits most of this layer on the wall of the centrifuge tube. The cytosolic supernatant (SI) is transferred to 1.5-ml tubes, and the DNA and cell debris pellets (PI) are discarded.
7. Cytosolic supernatants are incubated for 20 min at 37°C in the presence of 10 μM Taxol and 1 mM GTP.
8. Contamination of the microtubule pellet by non-copelleting components is prevented by cautiously layering the reaction mixture on a 0.1-ml cushion containing 5% sucrose (can be increased to 20%), 10 μM Taxol, and 1 mM GTP. Samples are centrifuged at $80,000\times g$ (Beckman TL100) for 30 min at 37°C .
9. After sequential removal of the supernatant and sucrose cushion, microtubule pellets (PII) are washed with 0.1 ml of warm MME buffer and resuspended in 0.1 ml of MME buffer containing 0.35 M NaCl and 10 μM Taxol on ice. Note

that this last washing step with salt is optional, because tubulin is separated by either electrophoresis or liquid chromatography from most of the other proteins associated with the Taxol-stabilized microtubules.

10. After centrifugation at $80,000 \times g$ for 30 min at 37°C , microtubule pellets (PIII) are frozen on dry ice and kept at -70°C until their use.

We applied our method to mouse and rat tissue extracts, and depending on organ origin, we obtained variable results in terms of tubulin yield and separation on gels. Consequently, we implemented a modified protocol that significantly improved tubulin isolation from nonneuronal tissues.

b. Protocol 2.

1. Rat or mouse tissues are washed with cold PBS and flash frozen in liquid nitrogen and kept at -70°C until use. The frozen tissue is crushed in a mortar and pestle in the presence of liquid nitrogen until it is reduced to a powder.
2. One volume of tissue powder is resuspended in 1.5 volume of MES/glutamate buffer [0.1 M 2-(*N*-morpholino)ethanesulfonic acid (pH 6.8), 0.5 mM MgCl₂, 1 mM EGTA, and 1 M glutamate]. Protease inhibitor cocktail from a 10-fold stock solution in MES/glutamate buffer and 1 mM DTT are added.
3. The suspension was sonicated (Ultrasonics, duty cycle: 20, output cycle: 3) five times for 10 s with 30 s rest intervals on melted ice.
4. Sample is spun at $30,000 \times g$ (Beckman TL100) at 4°C for 15 min to remove cell debris. The supernatant is then centrifuged at $120,000 \times g$ at 4°C for 1 h.
5. The clarified supernatant is transferred to new tubes and 20 μM Taxol and 1 mM GTP are added prior to a 30-min incubation at 37°C .
6. Sample is layered on a 100 μl cushion containing 20% sucrose in MES/glutamate buffer and 20 μM Taxol, and spun at $30,000 \times g$ for 30 min at 37°C .
7. The Taxol–microtubule pellet is resuspended in 30 μl of MES/glutamate buffer containing 0.35 M NaCl and 20 μM Taxol, and incubated for 10 min at 37°C .
8. Microtubules are pelleted by centrifugation at $30,000 \times g$ for 30 min at 37°C , flash frozen in liquid nitrogen, and stored at -80°C .

3. Discussion

The Taxol-based purification of tubulin can be monitored by SDS-PAGE and Western blot analyses using a pan α - or β -tubulin antibody and pure bovine brain tubulin as a standard. It could be argued that this method for isolation of tubulins may exclude some forms of tubulin that would poorly assemble in the presence of Taxol. This is unlikely because the Taxol concentration used is about 10-times higher than the lowest *K_a* measured for Taxol–tubulin binding, and we did not observe a specific loss of a particular tubulin isotype during the procedure. Obviously, if some tubulin does not assemble in the presence of superstoichiometric concentrations of Taxol, it is likely that it represents a pool of tubulin that is not competent to assemble. Such a pool may co-purify with assembly competent tubulin from extracts using ion-exchange chromatography (Sackett, 1995; Sloboda and Belfi, 1998). Note that purification of tubulin by cycles of assembly–disassembly excludes tubulin species incorporated in cold-stable microtubules (Detrich and Overton, 1986; Pirollet *et al.*, 1983; Williams *et al.*, 1985). Because of the high

stability of Taxol–microtubules, our protocols cannot be used to isolate tubulin for subsequent *in vitro* assays, but is suitable for the analysis of the tubulin content in a cell line or tissue that will be used as a source of soluble and functional tubulin, or in diluted tubulin-containing fractions. The glutamate that is added in protocol 2 provides favorable conditions for tubulin assembly in high salt that removes MAPs and contaminants from the microtubule pellets (Hamel and Lin, 1981; Sackett, 1995). The MES/glutamate buffer was not used to prepare cell line extracts but could be an alternative to the MME buffer used in protocol 1.

B. Electrophoretic Separation of Tubulin Isotypes and Posttranslational Modifications

Electrophoresis is an effective method to separate tubulin isotypes for further analysis. For some experiments, it is necessary only to separate α - and β -tubulin from one another. However, since α - and β -tubulins are of similar molecular weight (~50 kDa), some modifications to the Lamelli method must be made in order to separate the subunits by SDS-PAGE. It has been demonstrated that a mixture containing SDS as well as longer chain alkyl sulfates is best for separation of α - from β -tubulin (Best *et al.*, 1981; Stephens, 1998). In the case of mammalian tubulin, the α -tubulin subunit will run at an apparent higher molecular weight than the β -subunit. Isoelectric focusing (IEF) can be employed for high-resolution separation of individual tubulin isotypes. The tubulin isotypes have distinct isoelectric points (pIs) (Table I) that fall within a narrow pI range which makes them amenable to separation by high-resolution IEF. The β -tubulin isotypes have predicted pIs from 4.77 to 5.05, with the majority of β -tubulin isotypes pIs falling between 4.77 and 4.79. The α -tubulins have more basic pIs in the range of 4.94–4.98, except for α -like 3, which has a predicted pI of 5.68. PTMs, such as glutamylation and phosphorylation, which add a negative charge to the tubulin isotype, shift the modified isotype to a slightly more acidic pI. Conversely, removal of the C-terminal tyrosine and also the penultimate glutamic acid from α -tubulin shifts the isotype to a slightly higher pI. As described below, commercially available narrow-range immobilized pH gradient (IPG) gels can be employed for high-resolution separation of tubulin isotypes and their PTMs. An example of the separation of tubulin isotypes by high-resolution IEF is shown in Fig. 1A.

1. Materials

Narrow-range IPG gels and ampholyte-containing buffer can be obtained from GE Healthcare Life Sciences (Piscataway, NJ) or Bio-Rad (Hercules, CA). We obtained the maximal resolution using 24-cm gels from GE Healthcare Life Sciences (Piscataway, NJ) with a linear gradient from pH 4.5 to 5.5 (Verdier-Pinard *et al.*, 2005; Verdier-Pinard *et al.*, 2003b). Unfortunately, this pH range is no longer available from this company, and alternatively, we are now using 24-cm gel strips with a linear pH gradient from 4.7 to 5.9 or 3.9 to 5.1 from Bio-Rad (Hercules, CA) or a 24-cm gel strip with a nonlinear pH gradient of 3.0–5.6 from GE Healthcare Life Sciences. An Ettan IPGphor II IEF system, also from GE Healthcare Life Sciences, was used for IEF. The IEF gels are stained with Pierce GelCode Blue Stain (Rockford, IL). All other chemicals were obtained from Sigma-Aldrich (St. Louis, MO). Images of the gels were obtained on a Microtek ScanMaker 9800 XL (Carson, CA).

Table I
Characteristics of Human Tubulin Isotypes

Tubulin Isotype ^a	Gene	Accession number	pI	Protein mass (Da) ^b	Mass (Da) of CNBr C-terminal peptide ^c	CNBr C-terminal peptide
α1A	TUBA1A	NP_006000	4.94	50135.6	2860.19	AALEKDYEEVGVD\$VEGE\$EEGEEY
α1B	TUBA1B	NP_006073	4.94	50151.6	2860.19 ¹	AALEKDYEEVGVD\$VEGE\$EEGEEY
α1C	TUBA1C	NP_116093	4.96	49895.3	2590.04	AALEKDYEEVGADSADGEDEGEEY
α4A	TUBA4A	NP_005991	4.95	49924.4	2633.07	AALEKDYEEVGIDSYEDDEGECEE
α3C	TUBA3C	NP_005992	4.98	49959.6	4150.77	EEGEFSEAREDLALEKDYEEVGVD\$VEAEAEEGEEY
α3D	TUBA3D	NP_525125	4.98	49959.6	4150.77	EEGEFSEAREDLALEKDYEEVGVD\$VEAEAEEGEEY
α3E	TUBA3E	NP_997195	4.97	49916.6	4090.71	EEGEFSEAREDLALEKDYEEVGVD\$VEAEAEEGEEY
α8	TUBA8	NP_061816	4.94	50093.6	4156.72	EEGEFSEAREDLALEKDYEEVGTD\$FEEENE\$EEF
α-like 3	TUBAL3	NP_079079	5.68	49908.7	3058.40	EEAEFL\$EAREDLAALERD\$YEEVAQSF
βI	TUBB	NP_821133	4.78	49670.8	3366.33	NDLVSEYQQYQDATAEEEDFGEEAEAAA
βII	TUBB2B	NP_821080	4.78	49953.1	3466.36	NDLVSEYQQYQDATADEQGEFEEE\$EDEA
βIII	TUBB3	NP_006077	4.83	50432.7	1624.64	YEDDEESEAQGPK
βIVa	TUBB4	NP_006078	4.78	49585.8	3350.38	NDLVSEYQQYQDATAEEGEFEEEAEAAA
βIVb	TUBB2C	NP_006079	4.79	49831.0	3479.42	NDLVSEYQQYQDATAEEGEFEEEAEAAA
βV	TUBB6	NP_115914	4.77	49857.1	3551.41	NDLVSEYQQYQDATA\$GEEAFEDEEEIDG
βVI	TUBB1	NP_110400	5.05	50326.9	810.35	EPEDK\$H

^a α-Tubulin nomenclature reflects the revised nomenclature for the α-tubulin gene family (Khodiyar, V. K., *et al.* *Genomics*, 2007, **90**, 285–289).

^b Protein mass is the average mass.

^c CNBr peptide mass is reported as the monoisotopic neutral mass.

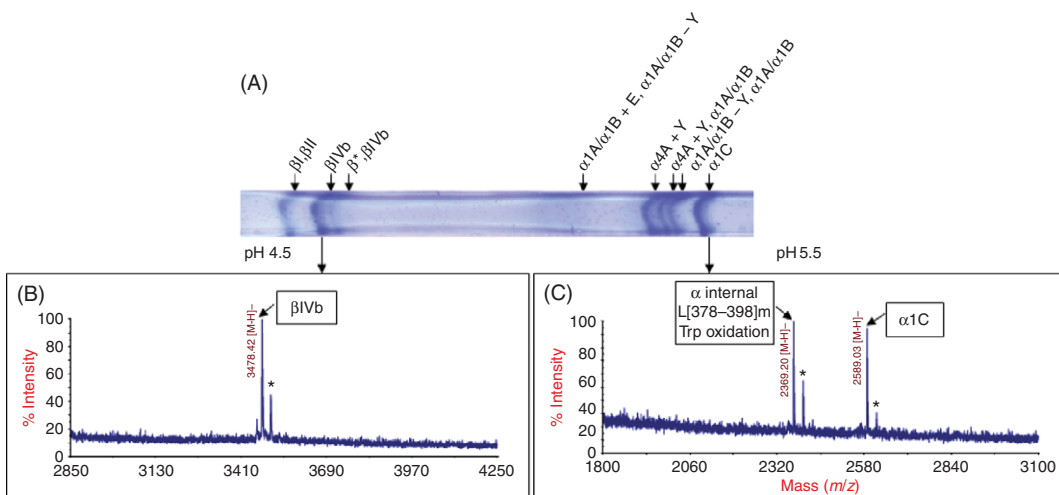


Fig. 1 Combination of isoelectric focusing and MALDI-TOF MS analysis of CNBr C-terminal tubulin peptides. (A) Region of a 24-cm pH 4.5–5.5 IPG strip containing all tubulin isotypes from a tubulin pellet of a normal rat liver. Eight bands were excised from the gel as indicated by the arrows and cleaved with CNBr. The isotype(s) observed in each band is listed above the gel. “*” represents a novel IVb posttranslational modification identified in the rat (Miller *et al.*, 2008). The CNBr C-terminal peptides for α 1A and α 1B isotypes have the same mass and cannot be distinguished from one another. A “+E” indicates glutamylated and “=Y” indicates tyrosination/detyrosination. (B) Mass spectrum obtained after CNBr cleavage of band indicated by the arrow. IVb was observed in this band. The * indicates a +28 Da peak which is due to formylation. (C) Mass spectrum obtained after CNBr cleavage of the band indicated by the arrow. The α 1C isotype was observed in this band along with an internal α -tubulin peptide. The “*” indicates a +28 Da peak which is due to formylation.

2. Protocol

1. Taxol-stabilized microtubule pellets (previous protocols) should be thoroughly resuspended in 500 μ l of solubilization buffer containing 7 M urea, 2 M thiourea, 4% 3-[3-(cholamidopropyl)dimethylammonio]-1-propanesulfonate, 0.5% Triton X-100, 0.5% ampholyte-containing buffer, 20 mM DTT, and a small amount of bromophenol blue. A solution containing everything except the ampholytes, DTT, and bromophenol blue can be prepared ahead of time and stored at -20°C for 6 months. The ampholyte-containing buffer should be in the same pI range as the IPG gel.
2. The sample is spread out evenly at the bottom of the IPG strip holder. The volume of sample must be adapted to the length of the gel strip (e.g., 450 μ l for a 24-cm GE Healthcare gel strip; note that for a long IEF running time, the volume is increased by 10 μ l). The IPG strip is then placed in the holder with the gel-side down in contact with the sample and electrodes and the “+”-pointed end toward the pointed end of the strip holder. The entire IPG gel is covered with mineral oil.
3. For a narrow-range 24-cm gel the typical running parameters include a 12-h rehydration step at 50 V and 20°C. After this active rehydration of the gel, the protein is separated with a program including 1 h at 500 V, 1 h at 1000 V, and the final step of 8 h and 15 min at 8000 V. The 24-cm IPG gels typically run for a total of 65,000 Vh. These parameters should be adjusted following the manufacturer’s instructions for the specific length of the gel.

- Following electrophoresis, the excess oil is carefully removed from the gel by blotting onto a KimWipe and the gel is fixed for 30 min in a 20% (w/v) trichloroacetic acid. Following the fixation step, the gel is washed in ddH₂O for 30 min and then stained with Coomassie blue for 1.5–2 h. The gel is then destained overnight.
- After sufficient destaining a high-resolution image of the gel is obtained for documentation prior to further processing using a flatbed scanner.

Note: It is important to ensure that all gels are kept free of contaminants, such as keratins, which can interfere with downstream MS analysis. Therefore, one should always wear gloves when handling the gel and thoroughly clean sample tubes before use.

3. Discussion

This method can be used to detect as little as 0.5 µg protein and can resolve isotypes differing in pI by 0.01 units. Typically >15 µg total tubulin pellet is loaded onto the gels. Gels have been successfully stained with other stains, including GE Healthcare Deep Purple fluorescent stain following manufacturer's protocols and acid violet 17 (Williams *et al.*, 1999). Fluorescent staining can be used to visualize small amounts of tubulin protein, which may not be detected by MS.

C. Identification of Tubulin Isotypes and Posttranslational Modifications

MS is an ideal tool for the characterization of tubulin isotypes and PTMs since each isotype has a unique amino-acid sequence and PTMs result in mass differences to the tubulin isotypes (Table II) (Verdier-Pinard *et al.*, 2009). Most tubulin isotype analysis involves cleavage of the protein into smaller peptides which are more amenable to mass spectrometric characterization. However, some MS work has been done on intact tubulin. In our laboratory, we have developed MS-based methods for the characterization of tubulin isotypes at the peptide and the protein levels and both are discussed below.

1. Protocols

a. Cyanogen Bromide Cleavage. Cyanogen bromide (CNBr) cleaves C-terminal to methionine—a cleavage which typically results in larger peptides than enzymatic cleavage since methionine is less commonly incorporated into proteins. CNBr cleaves α-tubulin into ~11 peptides ranging in size from 1,300 to 13,000 Da and β-tubulin into ~18 peptides in the range of 345–8,000 Da. The C-terminal region of both α- and β-tubulins contain a methionine within the last 40 residues which, when

Table II
Tubulin posttranslational modifications, mass changes, and location

Modification	Δm	Location
Tyrosination/detyrosination	±163.06 Da	C-terminal tail, α-tubulin
Δ2-Tubulin	−292.10 Da	C-terminal tail, α-tubulin
Glutamylation	+129.04 Da	C-terminal tail, α- and β-tubulin
Glycylation	+57.02 Da	C-terminal tail, α- and β-tubulin
Acetylation	+42.01 Da	α-Tubulin (Lys40)
Phosphorylation	+79.97 Da	β-Tubulin (Ser441/444)

cleaved with CNBr, results in unique isotype identifying peptides from 800 to 4,150 Da, which is an ideal mass range for characterization by MS.

1. Bands containing tubulin should be cut from the gel. If cutting bands from a plastic-backed IEF gel, use a GeneCatcher (Gel Company, San Francisco, CA) gel excision tip (or similar tip) to cut the band. Place the tip above the band, press down firmly, and then slide the tip along the plastic backing parallel to the other bands. This separates the gel from the backing without disrupting adjacent tubulin bands.
2. Destain the gel pieces in 150 μ l 50% acetonitrile in water at 37°C with shaking for 30 min. Repeat this step until the complete removal of the color from the gel. Evaporate the solvent and dry the bands in a SpeedVac concentrator.
3. Rehydrate the gel pieces in 100 μ l of CNBr cleavage solution (100 mg/ml CNBr in 70% formic acid). Note that this step should be done in a chemical fume hood. Also, it is important to use fresh formic acid of the highest purity to avoid formylation adducts (+28 Da) on the peptides. Alternatively, the cleavage can be performed in 70% trifluoroacetic acid (TFA) to avoid the formylation of peptides.
4. The cleavage is then allowed to proceed overnight (~16–20 h) at room temperature in the dark.
5. Following the overnight cleavage, the CNBr solution is removed from the tube and placed in a clean tube and vacuum dried.
6. The dried peptides are resuspended in 100 μ l of 50% acetonitrile containing 0.3% TFA and again vacuum dried.
7. The previous wash step (step 6) is repeated, but with 50 μ l of 50% acetonitrile containing 0.3% TFA.
8. The washed peptides are resuspended in 10 μ l of H₂O containing 0.1% TFA and purified on a C18 ZipTip following the manufacturer's suggested protocol.

b. Enzymatic Digestion. While the majority of diversity of tubulin isotypes is contained within the C-terminal region, there are sequence differences throughout the entire primary sequence. Also, some PTMs, such as acetylation at Lys40 in α -tubulin, and sequence mutations have been detected outside of the C-terminal region. Enzymatic digestion typically results in smaller peptides (less than 5000 Da) that can be readily analyzed by matrix-assisted laser desorption ionization time-of-flight MS (MALDI-TOF MS), thereby providing greater sequence coverage than CNBr cleavage for tubulin isotypes.

1. The bands containing tubulin as seen by Coomassie blue staining should be cut from the gel.
2. Destain each band with 300 μ l of a solution of 200 mM ammonium bicarbonate/50% acetonitrile at pH 8.9. After vortexing, incubate at 37°C for 30 min with shaking. Centrifuge and remove the solution. Repeat this step until a complete loss of color is achieved.
3. Add 300 μ l 100% acetonitrile to the gel band. Vortex the tube and then sonicate for 30 s. Remove the solution and dry the gel band in a SpeedVac concentrator until completely dry.
4. Rehydrate the gel piece in 300 μ l 10 mM DTT in 0.1 M ammonium bicarbonate and incubate at 56°C for 45 min to reduce all disulfide bonds. Cool the tubes to room temperature for 5 min and remove the excess solvent. Note: Whereas the C-terminal

peptides do not contain cysteine, the internal tubulin peptides may contain cysteine residues and therefore reduction and alkylation steps are included in this protocol.

5. Cysteines are alkylated by adding 300 μ l of freshly made 55 mM iodoacetamide in 0.1 M ammonium bicarbonate to the gel piece. The tube is then incubated for 30 min at room temperature in the dark, after which the excess solvent is removed.
6. Add 300 μ l of a solution containing 1:1 acetonitrile:200 mM ammonium bicarbonate pH 8.9 to the gel band. Vortex and then sonicate the sample for 30 s. Centrifuge and remove the excess solution. Repeat this step.
7. Dry the gel by adding 300 μ l of 100% acetonitrile. Vortex and then sonicate for 30 s. Remove the solution and dry the gel band in a SpeedVac concentrator.
8. Prepare a solution of trypsin in ammonium bicarbonate (25 ng/ μ l trypsin in 50 mM ammonium bicarbonate pH 8.9). Add 20 μ l trypsin solution to the dried gel piece. Gently mix and centrifuge briefly. Incubate on ice for 45 min.
9. Remove excess trypsin solution (if any) and add 50 μ l of digestion buffer (50 mM ammonium bicarbonate, pH 8.9). Note: A digestion enhancer, such as ProteaseMAX surfactant (Promega, Madison, WI), can be added at this point to increase digestion efficiency. This may result in enhanced signal for higher molecular weight peptides.
10. Digest at 37°C with shaking for 18 h.
11. Add 1% TFA to a final concentration of 0.1% to stop the digestion.
12. The peptides are then purified on a C18 ZipTip following manufacturer's instructions.

c. Combined Fragmentation. Combining enzymatic digestion and chemical cleavage of tubulin may result in the highest sequence coverage since the smaller peptides should all be easily released from the gel. This combination of cleavage techniques can also be used to achieve localization of PTMs when tandem MS (MS/MS) data cannot be obtained.

1. Follow the trypsin digest protocol above through step 10.
2. Dry the gel pieces in a SpeedVac concentrator.
3. Wash and dehydrate twice by addition of 100 μ l of acetonitrile followed by drying by SpeedVac concentrator.
4. Add 25 μ l of CNBr cleavage solution (100 mg/ml CNBr in 70% TFA) to the gel pieces. Incubate in dark for 14 h.
5. Collect the supernatant.
6. Extract the peptides twice by sonication for 5 min in 30 μ l of 60% acetonitrile, 1% TFA, and 0.1% octyl- β -D-glucopyranoside (OBG). Pool the extraction with supernatant obtained in step 5. The OBG is added to enhance the extraction of larger peptides from the gel.
7. Dry or concentrate the pooled peptide solution in a SpeedVac concentrator.

d. MALDI-TOF Mass Spectrometry. Matrix-assisted laser desorption ionization (MALDI) coupled to a time-of-flight MS (TOF MS) provides the high sensitivity and mass accuracy required for the analysis of peptides derived from enzymatic or chemical cleavage of tubulin isotypes. Furthermore, peptides harboring PTMs such as tyrosination/detyrosination and glutamylation have a unique mass shift that allows for confident assignment of these tubulin-specific modifications by MS. Sequence information and PTM localization can also be obtained by performing MS/MS on

tandem TOF instruments (MALDI-TOF/TOF). Examples of MALDI mass spectra of tubulin C-terminal peptides generated by CNBr cleavage are shown in Fig. 1 B and C.

1. The ZipTip purified peptides are mixed 1:1 with a matrix solution containing 5 mg/ml α -cyano-4-hydroxycinnamic acid in 50% acetonitrile with 0.1% TFA. This peptide/matrix mix is then spotted onto a MALDI target. Traditionally, sinapinic acid is recommended for negative ion mode MS, but we have found that α -cyano-4-hydroxycinnamic acid works equally well in negative and positive ion mode and therefore use it for all MALDI experiments.
2. The C-terminal peptides generated by CNBr cleavage are highly acidic and are best analyzed in negative ion mode (Jai-nhuknan and Cassady, 1998). However, in order to obtain the highest sequence coverage, both negative and positive ion mode spectra should be acquired. Since some of the C-terminal peptides are >4000 Da, it is important to ensure that the mass range covered in each spectrum is well above this to account for potential PTMs.
3. For enzymatic digestion, positive ion mode typically provides the best signal for all peptides. Be certain that the m/z range is sufficient to account for any PTMs that may occur.
4. In order to assign the peptides obtained via cleavage, a list of theoretical tubulin peptides specific for the enzyme or CNBr cleavage needs to be generated. Since most programs do not include the tubulin PTMs (detyrosination, glutamylation, glycation), it is necessary to add these masses manually to each of the potential modification sites.

D. Analysis of Intact Tubulins by Electrospray Ionization Mass Spectrometry

A complementary approach to tubulin peptide analysis, as discussed above, is the study of intact tubulin proteins. Analysis of the intact proteins provides a direct method to determine the tubulin isotype composition and PTMs of a sample. Also, some sequence mutations that result in a mass shift may be detected by this method. While the cleavage of the protein into peptides is more amenable to routine mass spectrometric analysis, measuring the intact protein mass allows for identification of mass changes that lie outside of the C-terminus which may not be detected at the peptide level.

1. Protocol

1. Dissolve purified microtubule pellets (~ 10 μ g) in 20 μ l of 70% formic acid and load onto a 1.0×150 mm C3 column with a flow rate of 50 μ l/min. The mobile phases employed are 5% acetonitrile containing 0.1% FA (solvent A) and 95% (v/v) acetonitrile containing 0.1% FA (solvent B).
2. Wash the sample for 45 min. in 5% solvent B and then use the following gradient to separate the tubulin isotypes: 5–30% B in 3 min., 30–45% B in 15 min., 45–55% B in 120 min., 55–75% B in 15 min., 75–95% B in 5 min., 95–5% B in 5 min.
3. The eluent from the column is directly coupled to an electrospray ionization (ESI) MS. Operate the MS in normal MS scan mode and detect ions in the m/z range of 600–1800.
4. The resulting mass spectra are deconvoluted to obtain the molecular weight for each tubulin species. When assigning tubulin isotypes based on intact mass measurements, it is important to bear in mind any potential PTMs and how they can shift the mass of each isotype.

5. In order to obtain more detailed information about the tubulin isotypes, the column effluent flow can be split and a portion of the high-performance liquid chromatography (HPLC) eluent collected for trypsin or CNBr cleavage. Reduce the volume of the fractions to ~10 μ l by vacuum drying and then follow the procedures above to cleave the protein into peptides.

2. Discussion

We have employed LCQ quadrupole ion trap and LTQ linear ion trap MS_{ss} (ThermoFinnigan, Riviera Beach, FL) for the intact analysis of tubulin, but any ESI-MS can be used. With the LCQ, we were able to determine the masses of the tubulin isotypes within 10 Da, and with the LTQ, we measure masses within 5 Da of the predicted values. We have used C4 columns to separate tubulin isotypes, but find that C3 columns typically provide better performance.

E. Relative Quantitation of Tubulin Isotypes

The quantitation of specific tubulin isotypes is commonly achieved by Western blot analysis with isotype-specific antibodies. However, validated antibodies are not available for all tubulin isotypes. MS-based methods can be employed for the relative quantitation of known tubulin isotypes as well as any novel tubulin forms or PTMs. While an extensive discussion of these methods is out of the scope of this chapter, we provide a brief overview of a couple of methods below and list a few references to which one can refer for detailed protocols.

One method that has been successfully employed for tubulin quantitation in cell lines is stable isotope labeling by amino acids in cell culture (SILAC) (Ong *et al.*, 2002; Ong and Mann, 2007). With SILAC, one cell line is grown in media lacking an essential amino acid and is supplemented with the same “heavy” amino acid that is labeled with 2 H, 15 N, or 14 C. This cell line is then mixed in an equal amount with a control cell line grown in normal, nonlabeled media. Incorporation of the heavy amino acid into proteins generates a mass shift from the unlabeled version. The ratio of the heavy to the light version of the peptides can then be determined by comparing peak intensities in the mass spectrum. Using this method we were able to measure the relative levels of β -tubulin isotypes between an ovarian (Hey) and a lung (A549) cancer cell line (Verdier-Pinard *et al.*, 2005).

Since not all samples can be directly labeled with heavy isotopes as described above, an alternative strategy must be used for quantitation. In our laboratory, we developed a method that employed two 15 N-labeled standards for relative quantitation of tubulin isotypes in tissue samples (Miller *et al.*, 2008). The first 15 N-labeled peptide was common to all β -tubulin isotypes observed in the experiment, and the second 15 N-labeled peptide was specific for the C-terminal CNBr peptide for the β -tubulin isotype that was quantitated. The tubulin sample was run on SDS-PAGE and the band containing all tubulin isotypes was cut from the gel. The same amount of a stock solution containing both of the 15 N-labeled peptides was added to each sample before CNBr cleavage, which was performed as described in protocol 3.1. Following cleavage with CNBr, the samples were analyzed in negative and positive ion mode MALDI-TOF/TOF. The ratio of the sample to the 15 N-labeled standard was determined for both the C-terminal peptide and the internal peptide by comparing the intensity of the isotopes in the mass spectrum. The internal peptide was used

to standardize the amount of β -tubulin in each sample. After normalizing all the samples, the relative amount of the isotype-specific C-terminal peptide could be determined across the different samples. With this methodology, it is important to synthesize peptides that will be equivalent to those generated by CNBr cleavage. Therefore, for internal peptides it may be necessary to add a couple of extra residues past the methionine so that the homoserine lactone is generated upon CNBr cleavage. Also, before synthesizing the internal standards, it is important to determine which internal peptides are detected in each cleavage reaction and if they are common to all observed isotypes. This method can be used to quantitate the relative amount of any α - or β -tubulin isotype. Alternatively, but following these principles, a label-free approach for tubulin isotype quantitation has been recently described (Winefield *et al.*, 2009).

F. Microtubule Interactions with Drugs and MAPs

1. Hydrogen–Deuterium Exchange

HDX-MS has emerged as a rapid and powerful experimental tool to investigate many aspects of protein architecture/dynamics including (1) determining both the sites of ligand binding and associated conformational changes, (2) mapping the contact sites between proteins, and (3) investigating the effects of single-point mutations or of amino-acid substitutions in isotypes on the regional and global dynamics of a protein (Chik and Schriemer, 2003; Stokasimov and Rubenstein, 2009; Wang *et al.*, 1998a,b, 2000; Wang *et al.*, 2001). This technology provides us with an avenue to obtain crucial knowledge of tubulin structure/dynamics that is not available from other biophysical methods (Bennett *et al.*, 2009; Huzil *et al.*, 2008; Xiao *et al.*, 2006).

a. Materials. Tubulin isolated from the marginal bands of chicken erythrocytes by the method of Murphy (Murphy, 1991) was selected for the HDX method to study interactions between tubulin and its stabilizing drugs. Chicken erythrocyte tubulin contains a single α - and β -isotype, α 1 and β VI, whose amino-acid sequences are 95% and 84% identical to their human orthologs, respectively. Purity was 99% as evaluated by SDS/PAGE and Coomassie staining, and isotype content was checked by high-resolution IEF (Verdier-Pinard *et al.*, 2005; Verdier-Pinard *et al.*, 2003b). The tubulin stock solution at 15 mg/ml was stored at -80°C . Pepsin was purchased from Sigma-Aldrich, D_2O (99.9%) from Cambridge Isotope Laboratories (Andover, MA), TFA from Applied Biosystems (Foster City, CA), and acetonitrile from Fisher Scientific (Pittsburgh, PA). Guanosine diphosphate (GDP) and GTP were purchased from Roche Applied Science (Indianapolis, IN). All other chemicals were of highest grade commercially available from Sigma-Aldrich. Guanosine-5'-[$(\alpha\beta)$ -methylene] triphosphate (GMPCPP) was purchased from Jena Bioscience (Jena, Germany).

b. Protocols.

a.1. Hydrogen–Deuterium Exchange (HDX) in Tubulin.

1. All tubulin samples are clarified by centrifugation at $100,000\times g$ at 4°C for 10 min before assembly.
2. For GTP- or GMPCPP-induced assembly, tubulin is incubated at 6.0 mg/ml (10 times the critical concentration for assembly) in MEM buffer (0.1 M 2-morpholinoethane sulfonic acid/1 mM EGTA/0.5 mM MgCl_2 , pH 6.9) at 37°C in the presence of 1 mM GTP or GMPCPP for 30 min.

3. For drug-binding experiments, Taxol and discodermolide (or other drugs) are added in three increments of increasing concentrations (10 μ M, 100 μ M, and 1 mM), and allowed to incubate for 10 min after the first two additions and 15 min after the last one.
4. GDP–tubulin dimers are prepared in the same MEM buffer, by inducing polymerization into microtubules (hydrolysis of GTP to GDP in most heterodimers) at 37°C and resuspension of microtubules in cold buffer containing 1 mM GDP (depolymerization of microtubules). The solution containing tubulin–GDP dimers is incubated at room temperature for 30 min.
5. HDX on tubulin was initiated by diluting each sample 20-fold in 0.1 M deuterated MEM buffer, pH 6.9 at 37°C. Exchange was allowed to proceed for certain time, e.g., 5, 10, 20, 30, and 60 min, after which point the aliquot exchange solutions were quenched with equal volumes of prechilled 0.5 M ammonium phosphate buffer (pH 2.5, 0°C). To minimize the back exchange during HPLC, the solvent precooling coil, static mixing tee, Rheodyne injector, and column were immersed in an ice bath.
6. For global HDX, 7 μ l of quenched reaction mixture is injected onto a 1.0 mm ID \times 50 mm C4 column (Waters Inc., Milford, MA). After desalting with 5% of solvent B [95% (v/v) acetonitrile containing 0.2% FA and 0.01% TFA] for 5 min, intact tubulin is eluted with a 2-min gradient composed of 5–95% solvent B. The effluent is directly delivered to the LTQ MS (Thermo Scientific, Waltham, MA) for mass analysis.
7. For local HDX, 5 μ l of pepsin solution is added into the quenched exchange aliquot (pepsin:protein is 1:1 molar ratio). After 5 min digestion, 20 μ l of chilled digest is injected onto a 1.0 mm ID \times 50 mm C-8 column (Waters Inc.). It should be noted that denaturant guanidinium hydrochloride (1.5 M–6 M) and reducing agent tris (2-carboxyethyl)phosphine (2.5 mM) can be added to optimize pepsin digestion.
8. Allowing a 5-min desalting with 5% solvent B, the peptic peptides are eluted with a 0.5-min gradient from 5 to 10% solvent B, followed by an 8-min gradient from 10 to 50% solvent B. The 50 μ l/min nonsplit effluent is delivered into a LTQ MS (Thermo Electron Corporation) or Fourier transform ion cyclotron resonance (FTICR) MS.

a.2. Data Analysis.

1. The peptides are identified by a combination of accurate masses and MS/MS, first with nondeuterated buffer. The extent of the deuterium incorporation of each peptic peptide is determined by MS from the centroid mass difference between deuterated and nondeuterated samples. The effect of deuterium gain or loss does not need to be taken into account when comparing the difference between distinct forms of tubulins under identical conditions.
2. Typically, triplicates are performed in HDX experiments. Average changes in deuterium incorporation (Δ HDX) \pm standard deviations are determined from these three separate experiments.

Peptides that exhibit significant changes in deuterium incorporation are mapped onto the tubulin dimer structure and onto a structure of a chicken erythrocyte microtubule protofilament pair previously constructed in our laboratory.

c. Discussion. Tubulin isolated from chicken erythrocytes is composed of only one α - and one β -tubulin isotype, i.e., α 1 and β VI. PTMs to erythrocytes are minimal; the α -isotype is almost completely deetyrosinated, while ~10% of the β -isotype is phosphorylated on Ser441 in the C-terminal domain (Rudiger and

Weber, 1993). These characteristics of chicken erythrocyte tubulin make it ideal to study using MS as it eliminates any ambiguity in the assignment of measured masses and potential conformational differences between different tubulin isotypes. Nevertheless, it could be argued that visualizing the average conformation changes rather than those occurring specifically for a given tubulin heterodimer is also important. Such analysis of a more complex mixture of tubulin can actually be facilitated by primary results on a unique tubulin heterodimer. GMPCPP, the nonhydrolysable analog of GTP, produces much more stable microtubules than GTP does. This GMPCPP mode of stabilization still needs to be elucidated using a proper control, but Taxol or other drug-specific effects can be accurately assessed against GMPCPP-stabilized microtubules.

2. Analysis of Photoaffinity-Labeled Microtubules

Photoaffinity labeling is a powerful method to determine the binding site of drugs such as Taxol on microtubules. Direct binding of the natural drug Taxol was not successful due to the low extent of photoincorporation of the drug. To improve the photoincorporation, Taxol analogs, [³H]3'-(*p*-azidobenzamido)Taxol, [³H]2-(*m*-azidobenzoyl)Taxol, and [³H]7-BzDC-Taxol, were used to photolabel microtubules. These three analogs were found to label the microtubules on β -tubulin, each at a distinct site on the microtubule. [³H]3'-(*p*-azidobenzamido)-Taxol photolabels the N-terminal 31 amino acids of β -tubulin, [³H]2-(*m*-azidobenzoyl)Taxol photolabels the peptide β 217–233, and [³H]7-BzDC-Taxol cross-links to Arg282 of β -tubulin (Rao *et al.*, 1999; Rao *et al.*, 1994; Rao *et al.*, 1995). Similarly, an analog of discodermolide, C19-[³H]BPC-discodermolide, was located at a binding site on β -tubulin at peptide 355–359 (Xia *et al.*, 2006).

a. Materials. Microtubule protein (MTP) is purified from calf brain by two cycles of temperature-dependent assembly–disassembly. The concentration of tubulin in MTP is based on a tubulin content of 85%. MTP (final concentration 1.0–1.5 mg/ml) is assembled by suspending in assembly buffer consisting of 0.1 M 2(N-morpholino)-ethanesulfonic acid (MES), 1 mM ethylene glycol bis (aminoethyl)-N,N'-tetraacetic acid (EGTA), 0.5 mM MgCl₂, and 3 M glycerol, pH 6.6. Assembly at 35°C is monitored spectrophotometrically at 350 nm by following changes in the turbidity signal that are representative of polymer mass.

[³H]3'-(*p*-azidobenzamido)Taxol, [³H]2-(*m*-azidobenzoyl)Taxol, and [³H]7-BzDC-Taxol were used at a specific radioactivity of 1.7–2.8 Ci/mmol, 0.12 Ci/mmol, and 50 Ci/mmol, respectively. C19-[³H]BPC-discodermolide was used with radioactivity of 4.1 Ci/mmol.

b. Protocols.

1. Photoaffinity Labeling of Tubulins

The drug analog, for example, [³H]3'-(*p*-azidobenzamido)Taxol (10 μ M, 1.7–2.8 Ci/mmol) is added to MTP (10 μ M tubulin) in assembly buffer and incubated at 37°C for 30 min. Aliquots (250 μ l) are placed in a multiwell plate (1.7 cm in diameter), which is kept at 4°C and irradiated for 30 min at 254 nm with a Mineralight lamp (model R52G, UVP Inc., San Gabriel, CA) at a distance of 7 cm. The extent of photoincorporation is calculated, based on one drug-binding

site per dimer, by a filter-binding assay after precipitation of photolabeled tubulin with cold acetone. The photolabeled samples are analyzed on 9% SDS-PAGE gels. For fluorography, the analytical gels were stained with Coomassie R-250, destained, treated with EN³HANCE (PerkinElmer, Waltham, MA), and exposed to PerkinElmer X-Omat AR film at -70°C. Typically, it takes 1–8 days to obtain a clear image by fluorography. In the case of tubulin photolabeling, it takes as long as 30 days to obtain an optimal image of photolabeled tubulin due to the low extent of photoincorporation.

2. Purification of Radiolabeled β -Tubulin

Gel-Based Separation. For the purification of β -tubulin, preparative SDS-PAGE gels (9%, 3 mm) are immersed in ice-cold 20 mM KCl for 5 min to visualize the α - and β -tubulin subunits. The β -tubulin band is excised, washed six to eight times with H₂O, and electroeluted for 16 h with an electroeluter (model 422, Bio-Rad, Richmond, CA) at 10 mA per electroelution tube. The recovery of β -tubulin is between 60 and 80%. SDS is removed from electroeluted β -tubulin using Extracti-gel D (Pierce, Rockford, IL), and the eluate is treated with trichloroacetic acid (final concentration 12% w/v) to precipitate β -tubulin and remove SDS. The precipitate is washed twice with ice-cold acetone to remove residual trichloroacetic acid. The radiolabeled β -tubulin is reduced and carboxymethylated prior to enzymatic cleavage.

HPLC-Based Separation. Acetone precipitation is performed on photolabeled tubulin to remove free unbound drug (1 vol of protein solution plus 4 vol of cold acetone, -20°C, overnight). Samples are then denatured with guanidine hydrochloride, and the cysteine residues are first reduced with 5 mM DTT and then carboxymethylated with 55 mM iodoacetamide. α - and β -tubulin subunits are separated by reverse-phase HPLC on an Aquapore BU-300 (220 × 2.1 mm) C4 column using an HP1090 liquid chromatography station. The protein is eluted with a linear acetonitrile 0.1% TFA gradient (25–55% over 60 min) at a flow rate of 200 μ l/min. Fractions are collected every minute. The elution of α - and β -tubulin subunits is monitored by Western blot. Fractions containing radiolabeled protein are detected with fluorography. Radioactive fractions are collected and dried by SpeedVac concentrator.

Note: An old HPLC system was used here since these experiments are using radiolabeled material. The SpeedVac concentrator, the gel apparatus, and MS equipment should be used cautiously.

3. Different Enzymatic Digestions or Chemical Cleavage of Purified Radiolabeled β -Tubulin

Subtilisin Digestion. Subtilisin is added at a 500:1 (w/w) ratio of protein: enzyme. After digestion for 1 and 12 h, reactions are stopped with 2 mM phenylmethylsulfonyl fluoride. Samples are resolved by SDS-PAGE on a 9% gel followed by fluorography.

Asp-N and Arg-C Enzyme Digestion of β -Tubulin. Samples are digested with either Asp-N or Arg-C (protein:enzyme 100:1, w/w) for 6, 12, or 18 h at 37°C according to the manufacturer's instructions (Roche Applied Bioscience). The digestion buffer for Asp-N was 50 mM sodium phosphate, pH 8.0, containing 1 M urea. Arg-C digestion buffer was 90 mM Tris-HCl, pH 7.5, 8.5 mM CaCl₂, 5 mM DTT, 0.5 mM EDTA, and 1 M urea. Digestion products were resolved on a 10–20% Tricine gel and subjected to fluorography.

Trypsin Digestion. The radioactive β -tubulin is dried and dissolved in 50 mM NH_4HCO_3 , 1 mM CaCl_2 , and 1 M urea, and then treated with trypsin (enzyme: protein w/w 1:40) for 24–48 h at 25°C.

Formic Acid Cleavage. Photolabeled β -tubulins (10–15 nmol) are dissolved in 400 μl of 75% formic acid and incubated at 37°C. After 72–96 h, formic acid is removed by evaporation in a SpeedVac concentrator (Savant, Holbrook, NY). The residues are washed twice with H_2O and dried afterwards in SpeedVac concentrator. The formic acid cleavage products are separated on 17.5% SDS-PAGE gels with 0.1 M Tris, 0.1 M Tricine, and 0.1% SDS as the cathode buffer TM and visualized by fluorography.

CNBr Cleavage. β -Tubulin is dissolved in 400 μl of 70% formic acid containing 20 mg CNBr and incubated at 37°C for 48 h. The formic acid is evaporated in a SpeedVac concentrator and the sample is washed twice with water and dried. Samples are resolved by SDS-PAGE on a 15% gel followed by fluorography.

4. Determination of Peptide Mass and Sequence of the Radiolabeled Peptide from Formic-Acid-Cleaved Photolabeled β -Tubulin

Formic acid is known to cleave preferentially Asp-Pro bonds. Because β -tubulin contains two such linkages at positions 31–32 and 304–305, complete formic acid cleavage of β -tubulin will result in three distinct peptide fragments consisting of amino acids 1–31 (A1, $M_r = \sim 3500$), 32–304 (A2, $M_r = \sim 31,000$), and 305–445 (A3, $M_r = \sim 16,000$). Besides SDS-PAGE analysis of these fragments, two alternative methods have also been used for the analysis.

Following formic acid cleavage of photolabeled β -tubulin, the protein is reduced and alkylated. The sample is centrifuged through a Centricon-10 (Amicon, Danvers, MA) microconcentrator and the filtrate is purified by reversed-phase (RP)-HPLC on an Aquapore RP-300 (Applied Biosystems, San Jose, CA) (2.1 \times 220 mm) C-8 column using an HP1090 liquid chromatograph. The peptides are eluted with a linear gradient (1%/min) of $\text{H}_2\text{O}/0.1\%$ TFA and acetonitrile/0.1% TFA at a flow rate of 200 $\mu\text{l}/\text{min}$. The fraction containing the major UV absorbing (214 nm) material, which is also the major peak of radioactivity, is collected and concentrated in a SpeedVac concentrator. The sample is ionized by electrospray on a PE-Sciex API-III (Ontario, Canada) mass analyzer and the monoisotopic mass of the sample measured. The measured mass of the sample is obtained from the different charge states. Peptide sequence can be obtained by sequencing on an Applied Biosystems 477A sequencer or by MS/MS.

5. Analysis of other Enzymatic Digests

Peptides resulting from the digestions are diluted with an equal volume of 6 M guanidine HCl and chromatographed on an Aquapore RP-300 C-8 column (2.1 \times 220 mm) using an HP1090 liquid chromatograph. The peptides are eluted with a linear gradient A from 80% H_2O , 0.1% TFA and 20% acetonitrile, 0.1% TFA to 30% H_2O , 0.1% TFA and 70% acetonitrile, and 0.1% TFA in 50 min at a flow rate of 0.2 ml/min. Fractions are collected every minute and tested for radioactivity. The radioactive fraction is further purified by C-8 reverse phase HPLC and eluted with a linear gradient B from 70% H_2O , 0.1% TFA and 30% acetonitrile, 0.1% TFA to 50% H_2O , 0.1% TFA and 50% acetonitrile, and 0.1% TFA in 60 min. Amino-acid sequence of these radioactive fractions can be obtained using Applied Biosystems 477A sequencer. The sequence can also be obtained using MS/MS.

c. Discussion. The most difficult part of this method is to design analogs of microtubule-stabilizing drugs. These analogs must be able to label microtubules with a sufficiently high extent of photoincorporation and maintain biological activity. It is also difficult to detect the photolabeled peptides due to the relatively low degree of photoincorporation. Liquid scintillators such as EN³HANCE (Dupont NEN) is necessary to improve the sensitivity of the fluorography. MS/MS may not provide sufficient sequence information for large peptides such as for peptides 32–304 and 305–445 generated by formic acid. Combination of various enzymatic digestions will give better results for sequence information of the radiolabeled peptides. For instance, CNBr cleavage followed by trypsin digestion yields smaller peptides that are easily sequenced by MS/MS compared to CNBr cleavage alone.

III. Summary

The molecular pharmacology studies describing the localization of drug-binding sites and/or the effect of such binding on tubulin molecular dynamics and those focusing on *in vitro* function of microtubules are mostly performed with brain tubulin. As we stated in the introduction, this is mainly for practical reasons and therefore tubulin proteomics in terms of the analysis of tubulin isotype composition may not appear that crucial for most investigators, whereas in terms of the identification of which region(s) of tubulin is affected by a drug, i.e., its binding site and allosteric effects, it seems more obvious. We claim that it is actually beneficial to perform experiments with nonneuronal sources of tubulin, because they may be more physiologically and pharmacologically representative of tubulin composition encountered in epithelial cells for instance. In this context, experimental design benefits from the analysis of tubulin content based on MS.

We presented protocols that may be used for analyzing the content of such tubulin preparations, and those relative to drug-binding experiments can be also applied to any tubulin. In nonneuronal tubulins, if the diversity of tubulins constituting dynamic microtubules is likely to be reduced, it is still often a mixture of isotypes. Data from HDX-MS and photolabeling experiments with microtubule interacting agents and a mixture of tubulin sequences may be complex to analyze and interpret. Even if the major species, such as β II-tubulin in brain tubulin and β I-tubulin in most nonneuronal sources, do generate the bulk of statistically significant information, the amount of β IVa- or IVb-tubulin is generally not negligible.

Among the still open questions on tubulin function and pharmacology are the differences in molecular dynamics and drug binding between tubulin isotypes. Besides computer-driven modeling (Keskin *et al.*, 2002; Tuszyński *et al.*, 2006), experimental insights into these isotype-specific functions will be necessary and would require working with homogeneous heterodimer preparations. High-throughput screening of human cell lines, amenable to mid-/large-scale production, using validated antibody arrays would identify appropriate sources for the preparation of monoisotype tubulin heterodimers. Indeed, cell-free systems for the biosynthesis of such tubulin heterodimers have been implemented (Shah *et al.*, 2001). Confirmation for assembly competence using Taxol and for homogeneity by MS can be assessed using our protocols.

Acknowledgments

This work has been supported by NIH grants CA077263 and CA124898, the National Foundation for Cancer Research (S.B.H.), NIH grant R33CA101150 (R.H.A.), and NIH grant CA125923 (L.M.M.).

References

Andreu, J. M. (2007). Large scale purification of brain tubulin with the modified Weisenberg procedure. *Methods Mol. Med.* **137**, 17–28.

Banerjee, A., Roach, M. C., Trcka, P., and Luduena, R. F. (1990). Increased microtubule assembly in bovine brain tubulin lacking the type III isotype of beta-tubulin. *J. Biol. Chem.* **265**(3), 1794–1799.

Banerjee, A., Roach, M. C., Trcka, P., and Luduena, R. F. (1992). Preparation of a monoclonal antibody specific for the class IV isotype of beta-tubulin. Purification and assembly of alpha beta II, alpha beta III, and alpha beta IV tubulin dimers from bovine brain. *J. Biol. Chem.* **267**(8), 5625–5630.

Bellocq, C., Andrey-Tornare, I., Paunier Doret, A. M., et al. (1992). Purification of assembly-competent tubulin from *Saccharomyces cerevisiae*. *Eur. J. Biochem.* **210**(1), 343–349.

Bennett, M. J., Chik, J. K., Slysz, G. W., et al. (2009). Structural mass spectrometry of the alphabeta-tubulin dimer supports a revised model of microtubule assembly. *Biochemistry* **48**(22), 4858–4870.

Best, D., Warr, P. J., and Gull, K. (1981). Influence of the composition of commercial sodium dodecyl sulfate preparations on the separation of alpha- and beta-tubulin during polyacrylamide gel electrophoresis. *Anal. Biochem.* **114**(2), 281–284.

Castoldi, M., and Popov, A. V. (2003). Purification of brain tubulin through two cycles of polymerization-depolymerization in a high-molarity buffer. *Protein Expr. Purif.* **32**(1), 83–88.

Chik, J. K., and Schriemer, D. C. (2003). Hydrogen/deuterium exchange mass spectrometry of actin in various biochemical contexts. *J. Mol. Biol.* **334**(3), 373–385.

Derry, W. B., Wilson, L., Khan, I. A., Luduena, R. F., and Jordan, M. A. (1997). Taxol differentially modulates the dynamics of microtubules assembled from unfractionated and purified beta-tubulin isotypes. *Biochemistry* **36**(12), 3554–3562.

Detrich, H. W., 3rd, and Overton, S. A. (1986). Heterogeneity and structure of brain tubulins from cold-adapted Antarctic fishes. Comparison to brain tubulins from a temperate fish and a mammal. *J. Biol. Chem.* **261**(23), 10922–10930.

Farrell, K. W. (1982). Isolation of tubulin from nonneuronal sources. *Methods Enzymol.* **85**(Pt B), 385–393.

Fourest-Lieuvin, A. (2006). Purification of tubulin from limited volumes of cultured cells. *Protein Expr. Purif.* **45**(1), 183–190.

Gaskin, F., Cantor, C. R., and Shelanski, M. L. (1975). Biochemical studies on the *in vitro* assembly and disassembly of microtubules. *Ann. N. Y. Acad. Sci.* **30**(253), 133–146.

Gaskin, F., and Roychowdhury, S. (1986). Purification of tubulin by fast-performance liquid chromatography. *Ann. N. Y. Acad. Sci.* **466**, 622–625.

Hamel, E., and Lin, C. M. (1981). Glutamate-induced polymerization of tubulin: characteristics of the reaction and application to the large-scale purification of tubulin. *Arch. Biochem. Biophys.* **209**(1), 29–40.

Hamel, E., and Lin, C. M. (1984). Separation of active tubulin and microtubule-associated proteins by ultracentrifugation and isolation of a component causing the formation of microtubule bundles. *Biochemistry* **23**(18), 4173–4184.

Huzil, J. T., Chik, J. K., Slysz, G. W., et al. (2008). A unique mode of microtubule stabilization induced by peloruside A. *J. Mol. Biol.* **378**(5), 1016–1030.

Jai-nhuknan, J., and Cassady, C. J. (1998). Negative ion postsource decay time-of-flight mass spectrometry of peptides containing acidic amino acid residues. *Anal. Chem.* **70**(24), 5122–5128.

Keskin, O., Durell, S. R., Bahar, I., Jernigan, R. L., and Covell, D. G. (2002). Relating molecular flexibility to function: a case study of tubulin. *Biophys. J.* **83**(2), 663–680.

Kilmartin, J. V. (1981). Purification of yeast tubulin by self-assembly *in vitro*. *Biochemistry* **20**(12), 3629–3633.

Lee, J. C. (1982). Purification and chemical properties of brain tubulin. *Methods Cell. Biol.* **24**, 9–30.

Lu, Q., and Luduena, R. F. (1994). *In vitro* analysis of microtubule assembly of isotypically pure tubulin dimers. Intrinsic differences in the assembly properties of alpha beta II, alpha beta III, and alpha beta IV tubulin dimers in the absence of microtubule-associated proteins. *J. Biol. Chem.* **269**(3), 2041–2047.

Luduena, R. F. (1998). Multiple forms of tubulin: different gene products and covalent modifications. *Int. Rev. Cytol.* **178**, 207–275.

MacRae, T. H., and Gull, K. (1990). Purification and assembly *in vitro* of tubulin from *Trypanosoma brucei brucei*. *Biochem. J.* **265**(1), 87–93.

Macrae, T. H., and Luduena, R. F. (1984). Developmental and comparative aspects of brine shrimp tubulin. *Biochem. J.* **219**(1), 137–148.

Maekawa, S., and Sakai, H. (1978). Characterization and *in vitro* polymerization of *Tetrahymena* tubulin. *J. Biochem.* **83**(4), 1065–1075.

Miller, L. M., Menthena, A., Chatterjee, C., Verdier-Pinard, P., Novikoff, P. M., Horwitz, S. B., and Angeletti, R. H. (2008). Increased levels of a unique post-translationally modified betaIVb-tubulin isotype in liver cancer. *Biochemistry* **47**(28), 7572–7582.

Morejohn, L. C., and Fosket, D. E. (1982). Higher plant tubulin identified by self-assembly into microtubules *in vitro*. *Nature* **297**(5865), 426–428.

Murphy, D. B. (1991). Purification of tubulin and tau from chicken erythrocytes: tubulin isotypes and mechanisms of microtubule assembly. *Methods Enzymol.* **196**, 235–246.

Murphy, D. B., and Hiebsch, R. R. (1979). Purification of microtubule protein from beef brain and comparison of the assembly requirements for neuronal microtubules isolated from beef and hog. *Anal. Biochem.* **96**(1), 225–235.

Newton, C. N., DeLuca, J. G., Himes, R. H., Miller, H. P., Jordan, M. A., and Wilson, L. (2002). Intrinsically slow dynamic instability of HeLa cell microtubules *in vitro*. *J. Biol. Chem.* **277**(45), 42456–42462.

Ong, S. E., Blagoev, B., Kratchmarova, I., et al. (2002). Stable isotope labeling by amino acids in cell culture, SILAC, as a simple and accurate approach to expression proteomics. *Mol. Cell. Proteomics* **1**(5), 376–386.

Ong, S. E., and Mann, M. (2007). Stable isotope labeling by amino acids in cell culture for quantitative proteomics. *Methods Mol. Biol.* **359**, 37–52.

Panda, D., Miller, H. P., Banerjee, A., Luduena, R. F., and Wilson, L. (1994). Microtubule dynamics *in vitro* are regulated by the tubulin isotype composition. *Proc. Natl. Acad. Sci. U. S. A.* **91**(24), 11358–11362.

Paturle, L., Wehland, J., Margolis, R. L., and Job, D. (1989). Complete separation of tyrosinated, deetyrosinated, and nontyrosinatable brain tubulin subpopulations using affinity chromatography. *Biochemistry* **28**(6), 2698–2704.

Pirollet, F., Job, D., Fischer, E. H., and Margolis, R. L. (1983). Purification and characterization of sheep brain cold-stable microtubules. *Proc. Natl. Acad. Sci. U. S. A.* **80**(6), 1560–1564.

Rao, S., He, L., Chakravarty, S., Ojima, I., Orr, G. A., and Horwitz, S. B. (1999). Characterization of the Taxol binding site on the microtubule. Identification of Arg(282) in beta-tubulin as the site of photoincorporation of a 7-benzophenone analogue of Taxol. *J. Biol. Chem.* **274**(53), 37990–37994.

Rao, S., Krauss, N. E., Heerding, J. M., et al. (1994). 3'-(p-azidobenzamido)taxol photolabels the N-terminal 31 amino acids of beta-tubulin. *J. Biol. Chem.* **269**(5), 3132–3134.

Rao, S., Orr, G. A., Chaudhary, A. G., Kingston, D. G., and Horwitz, S. B. (1995). Characterization of the taxol binding site on the microtubule. 2-(m-Azidobenzoyl)taxol photolabels a peptide (amino acids 217–231) of beta-tubulin. *J. Biol. Chem.* **270**(35), 20235–20238.

Rudiger, M., and Weber, K. (1993). Characterization of the post-translational modifications in tubulin from the marginal band of avian erythrocytes. *Eur. J. Biochem.* **218**(1), 107–116.

Sackett, D. L. (1995). Rapid purification of tubulin from tissue and tissue culture cells using solid-phase ion exchange. *Anal. Biochem.* **228**(2), 343–348.

Shah, C., Xu, C. Z., Vickers, J., and Williams, R. (2001). Properties of microtubules assembled from mammalian tubulin synthesized in *Escherichia coli*. *Biochemistry* **40**(15), 4844–4852.

Shelanski, M. L., Gaskin, F., and Cantor, C. R. (1973). Microtubule assembly in the absence of added nucleotides. *Proc. Natl. Acad. Sci. U. S. A.* **70**(3), 765–768.

Sloboda, R. D., and Belfi, L. M. (1998). Purification of tubulin and microtubule-associated proteins by membrane ion-exchange chromatography. *Protein Expr. Purif.* **13**(2), 205–209.

Stephens, R. E. (1998). Electrophoretic resolution of tubulin and tektin subunits by differential interaction with long-chain alkyl sulfates. *Anal. Biochem.* **265**(2), 356–360.

Stokasimov, E., and Rubenstein, P. A. (2009). Actin isoform specific conformational differences observed with HD exchange and mass spectrometry. *J. Biol. Chem.* **284**(37), 25421–25430.

Tuszynski, J. A., Carpenter, E. J., Huzil, J. T., Malinski, W., Luchko, T., and Luduena, R. F. (2006). The evolution of the structure of tubulin and its potential consequences for the role and function of microtubules in cells and embryos. *Int. J. Dev. Biol.* **50**(2–3), 341–358.

Vallee, R. B. (1982). A taxol-dependent procedure for the isolation of microtubules and microtubule-associated proteins (MAPs). *J. Cell Biol.* **92**(2), 435–442.

Verdier-Pinard, P., Pasquier, E., Xiao, H., et al. (2009). Tubulin proteomics: towards breaking the code. *Anal. Biochem.* **384**(2), 197–206.

Verdier-Pinard, P., Shahabi, S., Wang, F., et al. (2005). Detection of human betaV-tubulin expression in epithelial cancer cell lines by tubulin proteomics. *Biochemistry* **44**(48), 15858–15870.

Verdier-Pinard, P., Wang, F., Burd, B., Angeletti, R. H., Horwitz, S. B., and Orr, G. A. (2003a). Direct analysis of tubulin expression in cancer cell lines by electrospray ionization mass spectrometry. *Biochemistry* **42**(41), 12019–12027.

Verdier-Pinard, P., Wang, F., Martello, L., Burd, B., Orr, G. A., and Horwitz, S. B. (2003b). Analysis of tubulin isotypes and mutations from taxol-resistant cells by combined isoelectrofocusing and mass spectrometry. *Biochemistry* **42**(18), 5349–5357.

Verhey, K. J., and Gaertig, J. (2007). The tubulin code. *Cell Cycle.* **6**(17), 2152–2160.

Wang, L., Li, Y., Abildgaard, F., Markley, J. L., and Yan, H. (1998a). NMR solution structure of type II human cellular retinoic acid binding protein: implications for ligand binding. *Biochemistry* **37**(37), 12727–12736.

Wang, F., Li, W., Emmett, M. R., et al. (1998b). Conformational and dynamic changes of *Yersinia* protein tyrosine phosphatase induced by ligand binding and active site mutation and revealed by H/D exchange and electrospray ionization Fourier transform ion cyclotron resonance mass spectrometry. *Biochemistry* **37**(44), 15289–15299.

Wang, F., Miles, R. W., Kicska, G., Nieves, E., Schramm, V. L., and Angeletti, R. H. (2000). Immucillin-H binding to purine nucleoside phosphorylase reduces dynamic solvent exchange. *Protein Sci.* **9**(9), 1660–1668.

Wang, F., Shi, W., Nieves, E., Angeletti, R. H., Schramm, V. L., and Grubmeyer, C. (2001). A transition-state analogue reduces protein dynamics in hypoxanthine-guanine phosphoribosyltransferase. *Biochemistry* **40**(27), 8043–8054.

Weatherbee, J. A., Luffig, R. B., and Weihing, R. R. (1980). Purification and reconstitution of HeLa cell microtubules. *Biochemistry* **19**(17), 4116–4123.

Williams, R. C., Jr., Correia, J. J., and DeVries, A. L. (1985). Formation of microtubules at low temperature by tubulin from Antarctic fish. *Biochemistry* **24**(11), 2790–2798.

Williams, R. C., Jr., and Lee, J. C. (1982). Preparation of tubulin from brain. *Methods Enzymol.* **85**(Pt B), 376–385.

Williams, R. C., Jr., Shah, C., and Sackett, D. (1999). Separation of tubulin isoforms by isoelectric focusing in immobilized pH gradient gels. *Anal. Biochem.* **275**(2), 265–267.

Winefield, R. D., Williams, T. D., and Himes, R. H. (2009). A label-free mass spectrometry method for the quantification of protein isotypes. *Anal. Biochem.* **395**(2), 217–223.

Xia, S., Kenesky, C. S., Rucker, P. V., Smith, A. B., 3rd, Orr, G. A., and Horwitz, S. B. (2006). A photoaffinity analogue of discodermolide specifically labels a peptide in beta-tubulin. *Biochemistry* **45**(39), 11762–11775.

Xiao, H., Verdier-Pinard, P., Fernandez-Fuentes, N., et al. (2006). Insights into the mechanism of microtubule stabilization by Taxol. *Proc. Natl. Acad. Sci. U. S.A.* **103**(27), 10166–10173.

SECTION II

Microtubule Structure and Dynamics

CHAPTER 8

Cryo-EM Studies of Microtubule Structural Intermediates and Kinetochore–Microtubule Interactions

Eva Nogales ^{*,†,‡}, Vincent H. Ramey ^{‡,§}, and Hong-Wei Wang [¶]

^{*}Department of Molecular and Cell Biology, University of California, Berkeley, California 94720-3220

[†]Howard Hughes Medical Institute, Berkeley, California 94720-3220

[‡]Life Sciences Division, Lawrence Berkeley National Laboratory, Berkeley, California 94720-3220

[§]Biophysics Graduate Program, University of California, Berkeley, California 94720-3220

[¶]Department of Molecular Biophysics and Biochemistry, Yale University, New Haven, Connecticut 06520-8024

Abstract

I. Introduction

A. Microtubule Dynamics: Assembly and Disassembly Intermediates and Nucleotide Versus Lattice Effects

B. Microtubule–Kinetochore Interactions: The Yeast Dam1 Complex

II. Rationale

A. Proposed Structure of the Microtubule Disassembly Intermediate: Depolymerizer-Free GDP–Tubulin

B. GTP–Tubulin Structure in an Assembly Intermediate—Before Microtubule Closure and Protofilament Straightening

C. Structure of Dam1 Double Spirals to Describe the Oligomeric State of the Complex Around Microtubules

III. Methods

A. GDP–Tubulin Helical Tubes

B. GMPCPP–Tubulin Helical Ribbons and Tubes

C. Microtubule–Dam1 Kinetochore Complex Assemblies

IV. Discussion

A. Biological Relevance of Stabilized Tubulin Structures as Intermediates

B. Biological Relevance of Dam1 Spirals and Rings

V. Summary

Acknowledgments

References

Abstract

The existence of structural intermediates in the processes of microtubule assembly and disassembly, and their relationship with the nucleotide state of tubulin, have been the subject of significant study and recent controversy. The first part of this chapter describes experiments and methods designed to characterize, using cryo-electron microscopy (cryo-EM) and image analysis, the structure of stabilized tubulin assemblies that we propose mimic the growth and shortening states at microtubule ends. We further put forward the idea that these intermediates have important biological functions, especially during cellular processes where the dynamic character of microtubules is essential. One such process is the attachment of spindle microtubules to kinetochores in eukaryotic cell division. The second part of this chapter is consequently dedicated to studies of the yeast Dam1 kinetochore complex and its interaction with microtubules. This complex is essential for accurate chromosome segregation and is an important target of the Aurora B spindle checkpoint kinase. The Dam1 complex self-assembles in a microtubule-dependent manner into rings and spirals. The rings are able to track microtubule-depolymerizing ends against a load and in a highly processive manner, an essential property for their function *in vivo*. We describe the experimental *in vitro* protocols to produce biologically relevant self-assembled structures of Dam1 around microtubules and their structural characterization by cryo-EM.

I. Introduction

A. Microtubule Dynamics: Assembly and Disassembly Intermediates and Nucleotide Versus Lattice Effects

As key cytoskeleton components of eukaryotic cells, microtubules play important roles in many cellular processes, including intracellular transport, cell motility, meiosis, and mitosis. In the microtubule, $\alpha\beta$ -tubulin heterodimers bind head to tail into protofilaments, and about 13 protofilaments associate in parallel giving rise to a polar cylindrical polymer. Microtubules can switch stochastically between growing and shrinking phases, a phenomenon known as dynamic instability (Mitchison and Kirschner, 1984). This dynamic character is essential to microtubule function, as evidenced by the large number of natural compounds that bind tubulin, alter dynamics, and result in mitotic arrest (Downing, 2000; Jordan, 2002).

Dynamic instability is an intrinsic property of tubulin observable in purified preparations of this protein and based on the binding, hydrolysis, and exchange of nucleotide. The electron crystallography structure of tubulin assembled into protofilaments (Nogales *et al.*, 1998b; Lowe *et al.*, 2001) has been very useful in explaining the different exchangeability of the nucleotides in α - and β -tubulin, as well as the polymerization-induced hydrolysis of the exchangeable, E-site nucleotide (Nogales, 2000; Nogales *et al.*, 1998a). The N-terminal, nucleotide-binding domain of each tubulin monomer is directly involved in polymerization contacts and is connected through the core H7 helix to a smaller, intermediate domain that is also involved in polymerization. The C-terminal domain includes

two antiparallel helices that define the protofilament crest on the outside of the microtubule (Nogales *et al.*, 1998b), while the last, acidic residues are disordered and form a cloud of negative charge around the microtubule. The nonexchangeable, N-site guanosine triphosphate (GTP) in the α -subunit is buried at the monomer–monomer interface within the dimer, while the exchangeable nucleotide at the E-site in β -tubulin sits on the exposed surface of the dimer. The microtubule polymerization process results in the burial of this E-site nucleotide at the newly formed interface within a protofilament, making it nonexchangeable and exposing it to catalytic residues in α -tubulin that promote hydrolysis. Following polymerization the E-site nucleotide is both hydrolyzed and becomes nonexchangeable. This means that the microtubule body is made of guanosine diphosphate (GDP)–tubulin subunits, a structure that is energetically unstable. In the GTP cap model, the microtubule structure is proposed to be stabilized by a layer of GTP–tubulin subunits at the ends that still retain their GTP (Mitchison and Kirschner, 1984; Fig. 1, top center). When this cap is lost the microtubule rapidly depolymerizes (Fig. 1, top left).

While the formation of the longitudinal interdimer contact in a protofilament is required for GTP hydrolysis, hydrolysis in turn is likely to affect the longitudinal interface, the strength of lateral contacts between protofilaments, and the overall structure of the protofilaments. Indeed, cryo-electron microscopy (cryo-EM) studies of depolymerizing microtubules show protofilaments peeling from the ends into ring-like structures (Mandelkow *et al.*, 1991), similar to those observed from the self-assembly of GDP-containing tubulin dimers (see Nogales *et al.*, 2003 for a

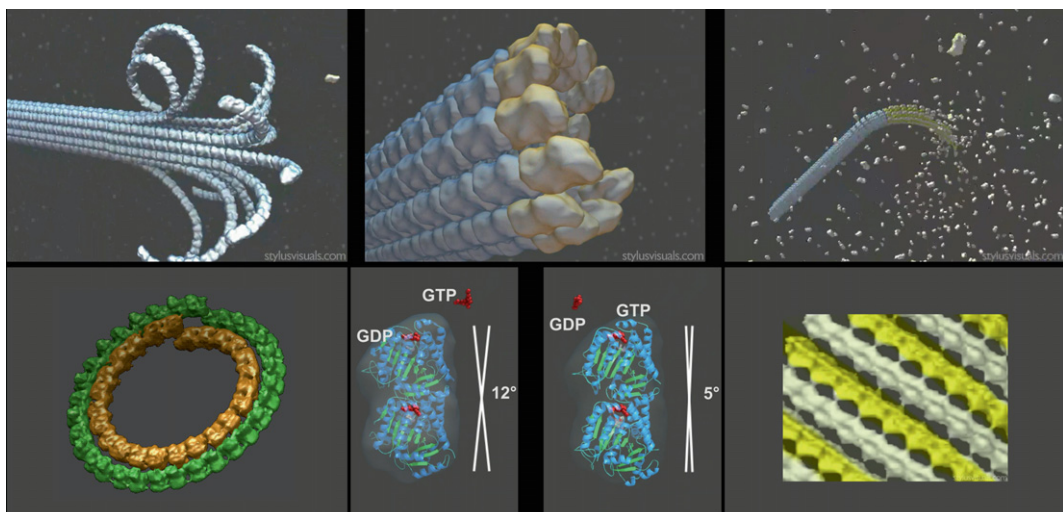


Fig. 1 Structural view of microtubule dynamics, disassembly, and assembly intermediates, and nucleotide state of tubulin. Upper panels are schematics of three distinct states for microtubules: shrinkage (left), growth (right), and minimal guanosine triphosphate (GTP) cap (center). Lower panels are the experimental cryo-electron microscopy structures for stabilized mimics of the disassembly (left) and assembly intermediates (right), and the tubulin dimer structures for guanosine diphosphate-bound and GTP-bound tubulin outside the context of the microtubule lattice (center). Adapted from Figs. 1 and 2 in Nogales and Wang (2006). (See Plate no. 5 in the Color Plate Section.)

review; [Fig. 1](#), left top). Within the body of the microtubule, GDP subunits are locked in a straight, “GTP-like” conformation due to the structural constraints imposed by the microtubule lattice ([Melki *et al.*, 1989](#)), for as long as there is a GTP cap ([Fig. 1](#), top center). Thus, the energy released by GTP hydrolysis is “stored” within the lattice as structural strain ([Caplow *et al.*, 1994](#)). The model proposes that when the GTP cap is lost, rapid depolymerization occurs, likely by weakening of lateral contacts at the ends, and the consequent release of the constrained GDP subunits into their curved, lower energy, conformational state ([Melki *et al.*, 1989](#)). GDP–tubulin rings can be observed as microtubule depolymerization products ([Bordas *et al.*, 1983](#); [Mandelkow *et al.*, 1991](#)) or can be formed from GDP–tubulin as *de novo* double rings that have been energetically well characterized ([Frigon and Timasheff, 1975](#); [Howard and Timasheff, 1986](#)).

Two alternative tubulin structures, corresponding to two different assembly states of the protein, are available at atomic resolution. The first one is that of tubulin in a polymerized, straight protofilament and bound to the stabilizer taxol obtained by electron crystallography of zinc-induced tubulin sheets ([Lowe *et al.*, 2001](#); [Nogales *et al.*, 1998b](#)). Docking of this atomic structure of the protofilament into a cryo-EM reconstruction of the microtubule ([Li *et al.*, 2002](#); [Nogales *et al.*, 1999](#)) confirmed that the electron crystallography structure corresponds very closely to that in the microtubule and thus represent the bona-fide structure of a “polymerized” tubulin. The second tubulin structure is in a curved conformation, bound to the cellular depolymerizer RB3 (a homologue of stathmin/Op18) and microtubule-destabilizing ligands (colchicine, podophyllotoxin, or vinblastine) ([Gigant *et al.*, 2000, 2005](#); [Ravelli *et al.*, 2004](#)). There is a kink between the two dimers bound to the RB3 fragment, and an indistinguishable kink between monomers within each dimer. The tubulin monomer conformation is different from that in the straight protofilament: there is a rotation of the intermediate domain with respect to the N-terminal domain, as well as a displacement along the dimer axis of the core helix H7.

Depolymerizing factors such as RB3/stathmin are likely to have effects beyond the sequestration of the GDP state of tubulin, so the tubulin structural features observed under those conditions could result from a combination of the nucleotide state and factor binding. To elucidate the structure of GDP–tubulin free of the effect of depolymerizers, we stabilized a polymer of tubulin bound to GDP formed by tight winding of a double spiral where every turn corresponds to a slightly open double-layer ring. While not lacking challenge, this polymer was a good sample for cryo-EM and image reconstruction that allowed us to obtain a structure of the low-energy state of GDP-bound tubulin ([Fig. 1](#), bottom left). Our study showed that irrespective of whether bound or unbound by a depolymerizer, the bending of the intra- and interdimer interfaces in the free GDP–tubulin protofilament is incompatible with the formation of lateral contacts in microtubules. So, how can binding of GTP result in the “straightening” of protofilaments observed in microtubules? An important question to address is whether tubulin structure is defined purely by nucleotide state (now an old concept), purely by lattice contact, or by a combination of both (the case we advocate) ([Fig. 1](#), bottom center).

Andreu and coworkers ([Buey *et al.*, 2006](#)), using arguments based mostly on the properties of FtsZ, the bacterial tubulin homolog, whose conformation appears totally insensitive to nucleotide content based on a number of X-ray crystal structures, and more recently Agard and colleagues ([Rice *et al.*, 2008](#)) based on SAXS experiments and drug-binding properties, as well as the structure of γ -tubulin ([Aldaz *et al.*, 2005](#)), have

proposed that nucleotide has no effect on tubulin conformation. The latter explained the different self-assembly properties of the two nucleotide states of tubulin based purely on differences in affinity between subunits due to the presence or absence of the γ -phosphate at the dimer–dimer interface. Incorporation into a microtubule lattice would subsequently result in the straightening of the tubulin dimer. On the other hand, Hyman *et al.* had provided experimental arguments to show that even out of the context of a microtubule lattice, tubulin bound to GTP analogue guanylyl-($\alpha\beta$)-methylene-diphosphonate (GMPCPP) (a nonhydrolyzable GTP analog) is “less curved” than its GDP-bound counterpart (Müller-Reichert *et al.*, 1998). In these experiments the depolymerizing products of GDP- and GTP-containing microtubules showed peels of significantly different curvature. Recent data from AFM visualization of individual protofilaments have further supported this idea (Elie-Caille *et al.*, 2007). Our own EM studies of the GMPCPP-bound tubulin polymer described below (Fig. 1, bottom right) agree with the Hyman reports and led us to propose the following model: the exchange of GDP for GTP in the $\alpha\beta$ -tubulin dimer results in a change from a more kinked to a smoothly curved conformation and allows for the association of protofilaments into assembly intermediates with lateral contacts that prime closure into a cylinder (Nogales and Wang, 2006; Fig. 1, top right). This closure results in the final straightening of the dimer. The two-step straightening was in fact first suggested by the studies of Chrétien and colleagues about a decade ago. They showed that under conditions of fast tubulin assembly, growth occurs via open sheets at the ends of microtubules that later close into a cylinder (Chrétien *et al.*, 1995). This mechanism, involving both a nucleotide and a lattice effect, may not be present in tubulin isoforms such as γ -tubulin or bacterial homologues that do not form cylindrical polymers, are monomeric, and/or do not exhibit dynamic behavior.

B. Microtubule–Kinetochore Interactions: The Yeast Dam1 Complex

The fundamental property of living systems is their ability to consume resources from their environment in order to reproduce, heritably passing on their genetic program to their offspring. At the level of an individual cell, the irreducible unit of self-replicating life, this propagation occurs through cell division. The problem of delivering exactly one copy of each chromosome to each daughter cell may need to be solved an enormous number of times over the course of an organism’s lifetime; errors in this process lead to aneuploidy, which can result in cell transformation (King, 2008).

The kinetochore is a network of protein complexes which assembles on centromeric chromatin to act as the connection point between the chromosomes and the microtubules that segregate them into daughter cells (Cheeseman and Desai, 2008; Westermann *et al.*, 2007). This complex machinery is involved in a multitude of functions during mitosis. A most essential function is to couple chromosome movement to microtubule depolymerization. Once all chromosomes are correctly bioriented, they must be pulled apart into daughter cells. After the spindle checkpoint has been satisfied, the anaphase-promoting complex triggers the destruction of the condensin complexes which tether sister chromatids together (Cheeseman and Desai, 2008; Westermann *et al.*, 2007). Then, by a process that does not require motor activity (Koshland *et al.*, 1988), kinetochores allow chromosomes to track the depolymerizing ends of microtubules, which are the primary site of force generation. Thus, it is thought that the energy stored in the microtubule lattice and released during depolymerization

as individual protofilaments splay outward and can be harnessed by the kinetochore machinery to produce movement (Koshland *et al.*, 1988).

The molecular mechanisms by which chromosomes attach to kinetochores, how this attachment is monitored by the cell, and how it is maintained as mitosis progresses have remained a great mystery since the first live movies of the mitotic process. For budding yeast, where this feat has to be achieved with a single microtubule attachment per kinetochore, a full part list of kinetochore proteins has emerged in recent years. The first report on Dam1 complex subunits and their requirement in mitotic spindle function appeared a decade ago. Drubin and coworkers identified Duo1p as a protein that contributed to aspects of spindle function sensed by the spindle checkpoint (Hofmann *et al.*, 1998). Dam1p was identified by two hybrid studies as a Duo1p interacting protein and shown to bind directly to microtubules. Soon after, Winey and colleagues (Jones *et al.*, 1999) reported the identification of the *Dam1* gene in a genetic screen that showed it to be involved in spindle integrity and localized to the spindle microtubules and likely to the kinetochore. Major breakthroughs in the next few years were the identification of the rest of the Dam1 complex components (Cheeseman *et al.*, 2001a,b; Enquist-Newman *et al.*, 2001; Janke *et al.*, 2002) and its functional interaction with the checkpoint kinase Ipl1 (Cheeseman *et al.*, 2002; Kang *et al.*, 2001; Shang *et al.*, 2003).

The initial genetic and biochemical studies showed the ten-subunit Dam1 complex to be essential for regulated microtubule–kinetochore attachment. But it has been during the last 4 years, following the expression of the ten Dam1 complex subunits in bacteria by the Harrison Lab, Harvard Medical School (Miranda *et al.*, 2005), that structural and biophysical studies of the interaction of the Dam1 complex with microtubules have become tractable. The first electron microscopy visualization studies of the complex proved most illuminating and exciting by showing the microtubule-induced assembly of Dam1 into rings and spirals (Miranda *et al.*, 2005; Westermann *et al.*, 2005; Fig. 2, left panels). A ring structure seemed an ideal coupler for the energy released during microtubule depolymerization due to protofilament peeling that follows GTP hydrolysis. Indeed, the novel ring–microtubule interaction allows the rings to diffuse on the microtubule and, during microtubule disassembly, to move processively following the depolymerizing end (Westermann *et al.*, 2006). The energy for processive movement comes from the conformational change in tubulin during microtubule depolymerization (Nogales and Wang, 2006). Therefore, this ring structure is able to track the depolymerizing ends of microtubules (as during anaphase), without requiring energy of its own (Fig. 2, right). These data and concepts have captivated the minds of structural biologist and mitosis cell biologists (Salmon, 2005). The last section in this chapter deals with structural studies of the two self-assembly forms of Dam1 so far visualized by electron microscopy.

II. Rationale

A. Proposed Structure of the Microtubule Disassembly Intermediate: Depolymerizer-Free GDP–Tubulin

The curved protofilament peels at the end of shortening microtubules constitute a structural intermediate in the disassembly process, where GDP–tubulin is in its relaxed state, clearly distinct from its constraint state in the body of microtubule

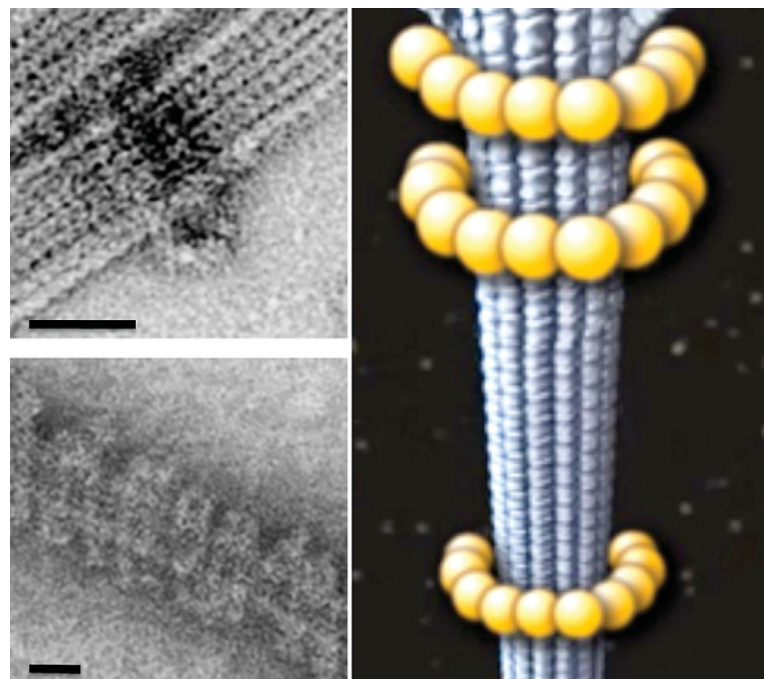


Fig. 2 Dam1 complex self-assembly around microtubules. Electron microscopy images of a Dam1 ring (top left) and double spiral (bottom left) around microtubules. Schematic representation of the Dam1 ring around a microtubule (right). Scale bars correspond to 25 nm. (See Plate no. 6 in the Color Plate Section.)

wall. Such a GDP–tubulin state can be sequestered by microtubule depolymerizers such as RB3/stathmin, colchicine, and vinblastine. The binding of these factors to GDP–tubulin, however, may have additional structural effects that go beyond that determined by the nucleotide state itself. Using the fact that high concentrations of divalent cations (which are known to stabilize tubulin assembly, likely by shielding the negative charge in tubulin as microtubule-associated proteins do in the cell), we were able to form stable tubular assemblies of GDP–tubulin in which ring closure does not occur and the protofilaments turn in a tight, double-layer helix (Fig. 3, left). The formation of such polymer does not need any depolymerizer and appears to recapitulate the shape of the horn-like protofilament structures at depolymerizing microtubule ends. Thus, this well-ordered assembly serves as an ideal sample for the structural characterization by cryo-EM of an unconstrained, GDP-bound tubulin in the absence of depolymerizing factors or drugs. Helical reconstruction of such assemblies ultimately allowed us to describe the structure of the protofilaments in this nucleotide state (Fig. 1, bottom left). This structure showed, for the first time, distinctive intra- and interdimer interactions and thus a distinction between the GTP and GDP interfaces. While both interfaces are kinked, the bending angle is clearly different, and one interface is dramatically more flexible than the other (we originally proposed that the GDP interface was more flexible than the GTP-containing intra-dimer contact, but the alternative possibility cannot be discarded from our data and is supported by recent studies; [Bennett *et al.*, 2009](#)). This is in contrast with the

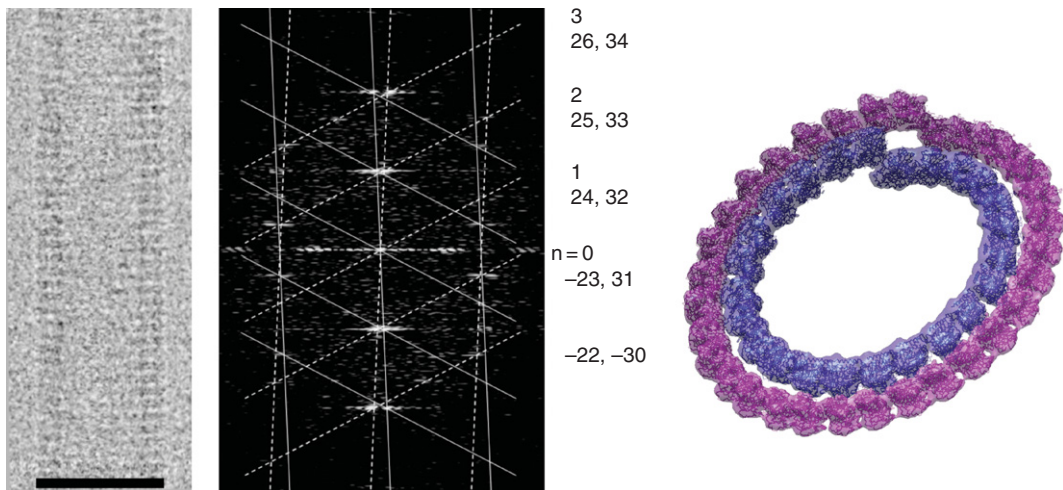


Fig. 3 Double-layered guanosine diphosphate (GDP)-tubulin tubes. Cryo-electron microscopy image of a 32/24 double-layered GDP-tubulin tube (left) and its diffraction pattern (center). The pattern was indexed for the near and far side of the helix (solid and dashed lattice, respectively). The indexing indicates severe Bessel overlap of the two layers of helices on all the layer lines (Bessel orders for the inner and outer layer, respectively, are shown on the right). Docking of the tubulin crystal structure into one turn each of the inner and outer layer. Scale bar in left panel corresponds to 50 nm. (See Plate no. 7 in the Color Plate Section.)

RB3-bound tubulin structure where both interfaces were indistinguishable. The small rearrangement seen at the intradimer interface in RB3-bound tubulin may be due to the presence of colchicine at the site (Ravelli *et al.*, 2004). In fact, early studies of colchicine binding interpreted the two-step binding of this drug as due to the induction of a conformational change in the tubulin dimer structure (Andreu *et al.*, 1991). On the other hand, it is possible that the interdimer interface gets locked into an “intradimer-like” state due to the RB3 alpha helix that runs along the surface of both dimers (Ravelli *et al.*, 2004). The EM and X-ray studies showed that, irrespective of the presence of a depolymerizer, the bending of the intra- and interdimer interfaces in GDP-tubulin protofilament is incompatible with the formation of the lateral contacts seen in microtubules (Fig. 1, bottom center). In Section III, we describe in detail the conditions for growth and stabilization of the double-layered helical GDP-tubulin assembly as well as the difficulties encountered and overcome in the image analysis of this tubulin polymer toward its three-dimensional (3D) structure.

B. GTP-Tubulin Structure in an Assembly Intermediate—Before Microtubule Closure and Protofilament Straightening

As has been addressed above, an important question in microtubule polymerization is whether tubulin structure is defined purely by nucleotide state (now an old concept), purely by lattice contact, or by a combination of both (the case we advocate). To reach our conclusions we studied the structure of a tubulin assembly that forms in the presence of a nonhydrolyzable GTP analog (GMPCPP) but low

temperatures, where microtubule growth is precluded. At normal assembly temperature (37°) GMPCPP gives rise to structurally normal microtubules but inhibits dynamics: the microtubules are stable. At low temperatures GTP–tubulin forms small oligomers that appear slightly curved. Increasing magnesium concentration, which generally has a stabilizing effect in all forms of tubulin assembly, results in the stabilization of these oligomers and leads to the formation of ring-like structures especially if GDP is used instead of GTP. We were thus very intrigued to see that a new polymer form of tubulin with laterally associated, slightly curved protofilaments appears at low temperatures when hydrolysis is prevented by using GMPCPP. Our initial working hypothesis was that temperature slows down tubulin interactions, without having a significant effect on the rate of hydrolysis upon the formation of interdimer tubulin contact. Thus, under low-temperature conditions little assembly occurs. When it does occur, hydrolysis quickly follows, before tubulin has a chance to make a microtubule closure and store the energy as lattice strain. If the hydrolysis step is eliminated, as in the case of GMPCPP–tubulin, the slow polymerization of GTP–tubulin (GMPCPP) can continue without the conformational change that hydrolysis would bring on tubulin. Under this simple assumption, we proposed that these assembly conditions could shed information on the process of microtubule assembly taking place before microtubule closure. Section III gives details on the process of stabilization and growth of these structures, the image analysis and the structure obtained, and how this structure together with additional experiments supports the idea that this stabilized assembly form corresponds to a GTP-specific intermediate in microtubule growth.

C. Structure of Dam1 Double Spirals to Describe the Oligomeric State of the Complex Around Microtubules

Defining the architecture of the Dam1 complex and its microtubule driven self-assembly is essential to understand the mechanisms by which Dam1 rings are able to couple processive movement to microtubule disassembly and thus contribute to the end-on attachment of chromosomes to the mitotic spindle and their segregation during anaphase. It is also crucial to determine how the assembly of the ring is regulated and how the ring attaches to other components of the kinetochore. Two assembly forms of the Dam1 complex have been observed around microtubules: a closed ring structure (Fig. 2, left top) and a double spiral where each turn of the spiral corresponds to a slightly opened ring (Fig. 2, left bottom; Fig. 6, left and center). While the first is the likely physiological oligomeric form of the complex based on the number of copies of Dam1 estimated from *in vivo* fluorescence studies (Joglekar *et al.*, 2006), the double spirals offered, in principle, the benefit of a higher ordered arrangement that would make it possible to use conventional helical reconstruction methods for its structural characterization by cryo-EM (Fig. 6). It turned out that the poor helical order of the Dam1 spirals makes this type of analysis more challenging than anticipated. We obtained the cryo-EM structure of the Dam1 spirals both by helical processing of a small, well-ordered segment (Wang *et al.*, 2007) and from poorly ordered assemblies using a new implementation of the iterative real-space helical reconstruction method (Egelman, 2000) that incorporated an intensive image classification step (Ramey *et al.*, 2009). In order to compare the structure of the complex by itself and when oligomerized around microtubules we needed to use two

alternative imaging modalities. While the preservation of the cylindrical character of the spiral Dam1 assembly around microtubules requires hydration and cryo-EM procedures, the small size of the unassembled complex makes negative stain studies the method of choice. Interestingly, our 3D reconstruction studies of the Dam1 complex before and after its oligomerization around microtubules identified a large conformational change accompanying self-assembly (Wang *et al.*, 2007). The detailed methods for obtaining the Dam1 spiral assembly around microtubules and the cryo-EM reconstruction procedures of the structure are described in the following section.

III. Methods

A. GDP-Tubulin Helical Tubes

SUMMARY: Double-layer tubes of GDP-bound tubulin can be formed when partially subtilisin-cleaved tubulin bound to GDP is incubated at 37°C for a few hours in the presence of high concentrations of manganese. Frozen-hydrated helical tubes can then be imaged by cryo-EM. The images of individual tubes can be classified into distinct helical families containing different number of subunits per turn. We describe how a 24/32 family was selected for further analysis and reconstruction using an iterative Fourier–Bessel algorithm to determine the relative orientation of multiple tube images (19 images used in the final average). Independent reconstructions for the inner and outer layer were then produced by Fourier integration using data up to 10-Å resolution.

1. Assembly of GDP-Tubulin Helical Tubes and Cryo-EM Analysis

We prepare our subtilisin-cleaved GDP-tubulin by closely following the procedures of Correia and coworkers (Lobert and Correia, 1992). Bovine brain tubulin from Cytoskeleton (Denver, CO) at a concentration of 6 mg/ml is incubated at 37°C for 30 min in cytoskeleton buffer II (CBII) buffer (80 mM PIPES, 1 mM ethylene glycol tetraacetic acid, 1 mM MgCl₂, and 10% glycerol at pH 6.8) in the presence of 2.5 mM GTP in order to form microtubules. Subtilisin (25 µg/ml) is then added for 10 min to cleave the tubulin C-termini. The reaction is quenched by adding 3.0 mM phenylmethylsulfonyl fluoride. The subtilisin-cleaved microtubules are spun down at 13.5 K rpm for 15 min on a tabletop centrifuge, washed with prewarmed CBII buffer at 37°C, and pelleted by an additional 8 min centrifugation step. The pellet is then resuspended in cold CBI buffer (CBII buffer without glycerol) to a concentration of about 10 mg/ml. After 20 min on ice all the microtubules are fully depolymerized. The solution is centrifuged at 50 K rpm for 15 min at 4°C to remove any insoluble aggregates on a TLA100 rotor using a Beckman Coulter Optima TLX centrifuge. The supernatant can then be characterized by sodium dodecyl sulfate polyacrylamide gel electrophoresis and Western blotting with antibodies against α -tubulin and β -tubulin. Following this procedure about half of β -tubulin C-termini are cleaved, while practically all α -tubulin molecules are intact. Although partial removal of the C-terminus of tubulin by subtilisin treatment is not necessary for the formation of the tubes, it has a positive effect on their crystalline order. More extensive subtilisin digestion results in more triple-layered tubes and was avoided.

To form well-ordered, double-layered tubes the GDP–tubulin prepared as above is diluted to a final concentration of 2–3 mg/ml in CBI buffer. GDP and MnCl₂ are added to the tubulin solution to give final concentrations of 2 and 20–50 mM, respectively. The solution is incubated at 37°C to promote GDP–tubulin assembly (although helical tubes can form at any temperature between 4 and 37°C). After 3–5 h incubation, the solution becomes cloudy. For cryo-EM analysis 3.5 µl of this solution is applied to a chloroform pretreated Quantifoil electron microscope grid (R1.2/1.3 Cu 400 mesh, SPI, PA) and then the grid is mounted in a Vitrobot (FEI, the Netherlands). The grid is blotted for 1.8 s at room temperature with 100% humidity and plunged into liquid ethane slush cooled by liquid nitrogen at about –170°C. The vitrified grids are then stored in liquid nitrogen until examination. In our studies, cryo-EM grids were transferred to a Gatan 626 cryo-holder (Gatan Inc., PA) and inserted into a CM200 electron microscope with a field emission gun (FEI, the Netherlands). The temperature of the grid in the microscope was maintained below –172°C during the whole process of examination and image recording. Using low-dose protocols, images of the tubular crystals of GDP–tubulin were recorded on Kodak SO-163 films at a magnification of 50,000 and acceleration voltage of 200 kV with a dose lower than 15 e[–]/Å² per picture. The defocus of the images ranged between –0.5 and –2.0 µm. In some sessions, focal pairs were taken of the same area to facilitate the classification of the tubes into different families using the higher defocus image. The films were developed and screened both by eye and by optical diffraction to remove those with astigmatism or drift. Selected films were digitized on a Nikon Super Coolscan 8000 ED scanner (Nikon, Japan) at 2000 dpi, resulting in a final pixel size of 2.54 Å. The images were transferred to the processing computer and converted from transmission to optical density using the EMAN image-processing package (Ludtke *et al.*, 1999).

2. Screening and Reconstruction of the Helical Tubes of GDP–Tubulin

In the presence of high concentration of manganese, GDP–tubulin forms well-ordered, multilayered tubular crystals. Most of them are double-layered tubes, while some are triple-layered tubes. Analysis of the diffraction patterns from images of these tubes indicates that each layer is a one-start helix corresponding to a curved tubulin protofilament. Depending on the number of tubulin subunits per turn of these helices, the tubular crystals can be classified into different families. Each tube can be assigned to a certain family based on its number of layers, the diameters of each layer in the tube (and thus the number of tubulin subunits per turn), and the parallel/antiparallel relationship among the protofilaments of different layers (whether they are parallel or antiparallel can be determined by examining the directions of tubulin end-on-view projections at the edge walls of the two layers in filtered images). For our structure analysis we focused on the most abundant family of double-layered tubes with 32/24 subunits in antiparallel protofilaments (Fig. 3, left). The double-layer character of the tubes results in systematic overlap of the Bessel terms from inner and outer layers on all the layer lines and makes it impossible to use traditional helical reconstruction methods (Fig. 3, center). An iterative Fourier–Bessel method developed in our laboratory (Wang and Nogales, 2005a) was used to determine the relative orientation of different tube images and to produce independent 3D reconstructions of the inner and outer layers of the tube.

The image of each tube is cut from the original micrograph within a box about four times wider than that of the tube itself. The in-plane curvature of the tubes is corrected using the straightening algorithm in the Phoelix package (Carragher *et al.*, 1996). After straightening the images are cut into three parts, the tube itself and two images of ice on both sides of the tube. These two images are averaged and used as the estimated background noise for resolution assessment. Each tube image is then padded into 512×4096 pixels, its Fourier transform calculated, and the power spectrum is analyzed for indexing. Layer lines are extracted from the Fourier transform of each tube up to a resolution of 8 \AA . The helical selection rule for each tube differs slightly from the others because the Z-heights of the layer lines vary in one or two reciprocal units from tube to tube. For the purpose of alignment and average, the layer lines are reassigned to a common selection rule from the average of all the tubes. The same process is followed for the noise images.

Though most of the layer lines of double-layered tubes are composed of overlapping Bessel terms with different Bessel orders from the inner and outer layers, those corresponding to the one-start helical track have the same order ($N=1, 2, 3\dots$). These layer lines, along with the equator, can be used to determine the x-shift and out-of-plane tilt of each tube. Using the same method as Amos and coworkers (Amos and Klug, 1975), the x-shift and out-of-plane tilt are calculated and corrected separately for the inner-layer helix and outer-layer helix of each tube. Tubes with out-of-plane tilt bigger than 5° are discarded. Twenty-nine images of 19 tubes (10 focal pairs) from the antiparallel 32/24 family of double-layered tubes were chosen for alignment in our analysis.

For each tube, only data within a resolution of 23 \AA are used for alignment. During the alignment cycle focal paired images are half-weighted in the process of data merging and averaging. The equator is not used for the alignment. The radial scale of each tube is also refined during the process of alignment. The iterative Fourier–Bessel alignment algorithm leads to convergence to a stable solution of the alignment parameters of each layer of each tube after a dozen iterations. The iterative alignment of our 29 images of 19 tubes converged after 10 iterations. To obtain the reconstruction of the two tubulin layers independently, the set of inner-layer and outer-layer alignment parameters are used, respectively, on the Fourier transforms of images for final averaging.

During the averaging, contrast transfer function (CTF) is also corrected. CTF parameters for each image are calculated from the diffraction spectra of the ice within the hole of each micrograph using the SPIDER TF series programs (Zhu *et al.*, 1997). In our analysis, the B factor was set roughly at 100 \AA^2 based on the above analysis. The amplitude contrast ratio was calculated to be 7% using the methodology of Toyoshima and Unwin (Toyoshima and Unwin, 1988). The alignment parameters are applied to the layer line data and the final average from all the tubes is calculated using the equation:

$$F_{\text{avg}} = \frac{\sum_{j=1}^M \text{CTF}_j F_j}{\sum_{j=1}^M |\text{CTF}_j|^2} \quad (1)$$

where M is the total image number, CTF_j is the CTF value of the j th image, F_j is the Fourier transform of the j th image, and F_{avg} is the Fourier transform of the final averaged structure.

The noise of the final reconstruction is calculated from the average of CTF-corrected noise data using the same alignment parameters and weighting factors of their corresponding tube image. The signal-to-noise ratio of every point on the layer lines of the final reconstruction is thus calculated. Only those points with signal-to-noise ratio higher than 2.0 are considered to be significant and retained in the final data set. Two final sets of Fourier averages are obtained corresponding to the inner-layer and outer-layer tubes, respectively. After Fourier–Bessel transformation and radial cutting in little g space, the real-space reconstructions of the inner-layer and outer-layer helices are calculated separately by Fourier integration using the averaged layer line data set. We have obtained reconstruction of both layers at a resolution up to 10 Å (one turn of the outer-layer reconstruction is shown in Fig. 1, bottom left panel, and one turn each of the inner and outer layers is shown in Fig. 3, right).

3. Building a Pseudo-atomic Model of GDP–Tubulin–Curved Protofilament

The atomic models of tubulin obtained by electron crystallography in a straight protofilament (1JFF.pdb) and that obtained by X-ray crystallography with tubulin bound to RB3 and colchicine (1SA0.pdb) were used in docking experiments into our 3D reconstructions of the inner and outer layer. Regions missing in the model of one monomer that have a counterpart in another (long loop in the N-terminal domain of β -tubulin; M-loop in the RB3–tubulin structures) were filled in with the available section and energy minimized using molecular dynamic procedures. This procedure is done to be able to account for most of the mass of the proteins and is not intended to produce the real structure. The atomic resolution models were fitted manually as rigid bodies into the OMAP map using the program O (Jones *et al.*, 1991). These manually fitted atomic models of tubulin were then converted into a density map, low-pass filtered to 23 Å, and threshold filtered to masks. The masks are used to segment the tubulin heterodimer densities from the inner-layer and outer-layer reconstructions, respectively. The resulting densities were compared by Fourier shell correlation, indicating that they are practically indistinguishable within a resolution of 15 Å. Helical symmetries of the two layers of tube were then applied to the docked atomic models in the asymmetric unit of the reconstruction to generate a docking of longer protofilaments using HLXBUILD program in Situs (Wriggers *et al.*, 1999; Fig. 3, right).

B. GMPCPP–Tubulin Helical Ribbons and Tubes

SUMMARY: Helical ribbons and tubes of GMPCPP-bound tubulin are obtained by incubating tubulin with this nucleotide at low temperatures (4–15°C) for several hours (up to 4 h) in the presence of high concentration of magnesium ions (8–30 mM). Frozen-hydrated helical tubes can then be imaged by cryo-EM. The images of two tubes corresponding to the same helical family were analyzed using traditional helical methods to obtain a reconstruction at 18-Å resolution.

1. Generating GMPCPP–Tubulin Ribbons and Tubes

The slowly hydrolyzable GTP analogue guanylyl-($\alpha\beta$)-methylenediphosphonate (GMPCPP) was purchased from Jena Bioscience Company, Germany. To obtain the GMPCPP-bound tubulin, bovine brain tubulin (Cytoskeleton) is incubated at 37°C for 30 min in CBII buffer supplemented with 2.5 mM GTP to form microtubules. Microtubules are pelleted, then resuspended in cold CBI buffer and allowed to depolymerize in ice for 20 min. Such a polymerization/depolymerization cycle produces pure GDP–tubulin due to the hydrolysis of GTP in the microtubule lattice. The solution is then centrifuged at 4°C to remove insoluble aggregates. GMPCPP is added to the supernatant to a final concentration of 10 mM, and the solution is incubated for 10 min on ice to allow for the exchange of GDP for GMPCPP. The GMPCPP–tubulin is diluted to 2–3 mg/ml in CBI buffer and MgCl₂ is added to a final concentration ranging from 4 to 30 mM. The solution is incubated at different temperatures: 4, 15, 25, and 37°C. At 4°C, a temperature at which GTP–tubulin is unable to polymerize into pelletable structures (small oligomers containing a few tubulin dimers are, however, present in solution for most typical tubulin buffers), GMPCPP–tubulin self-assembles slowly into helical ribbons at magnesium concentration higher than 8 mM. When concentrations of MgCl₂ as high as 20 mM are used, spiral ribbons are observed at 4°C after just 30 min of incubation. On longer incubation times the spiral ribbons become wider by addition of more protofilaments (Fig. 4, top). At higher temperatures, but lower than 20°C, the formation of spirals is faster. For incubation times longer than a couple of hours, more abundant and fast growing ribbon assemble and ultimately gain enough protofilaments to close into well-ordered helical tubular crystals of GMPCPP–tubulin. At concentration of MgCl₂ lower than 6 mM the assemblies become rare. When the incubation temperature is higher than 20°C, GMPCPP–tubulin forms mainly microtubules, irrespective of the concentration of magnesium. But when the magnesium concentration is high (20 mM), some helical ribbons can be seen coexisting with microtubules.

The most parsimonious explanation for how divalent cations promote tubulin self-assembly is the shielding of the negative charges in tubulin C-terminal tails by the ions, facilitating the coming together of tubulin subunits (Wolff, 1998). Assemblies that resemble these GMPCPP tubes have been reported for other conditions, both *in vitro* and *in vivo* (and generally referred to as “macrotubules”; Unger *et al.*, 1990), although structural details of those assemblies are lacking.

2. Overall Morphology of Ribbons and Tubes

The spiral ribbons and tubes can have various diameters. When we analyzed the curvature of the protofilaments in these assemblies by plotting pitch versus diameter (Fig. 4A), we saw that the curvature of the protofilaments is invariant, that is, the longitudinal bends that exist between tubulin subunits are well defined and of a unique value that do not change as the assemblies grow and eventually close into a tube. The spiral ribbons are composed of parallel, paired tubulin protofilaments just as described for the closed tubes. Pairing is indeed a very strong tendency for protofilaments under these assembly conditions. Even in very early stages of assembly, when protofilament lengthening is limited, small oligomers of about 5–8 dimers interact laterally, robustly, and in a paired fashion (Fig. 4, bottom), similarly to what has been previously proposed by Carlier and coworkers (Carlier *et al.*, 1997).

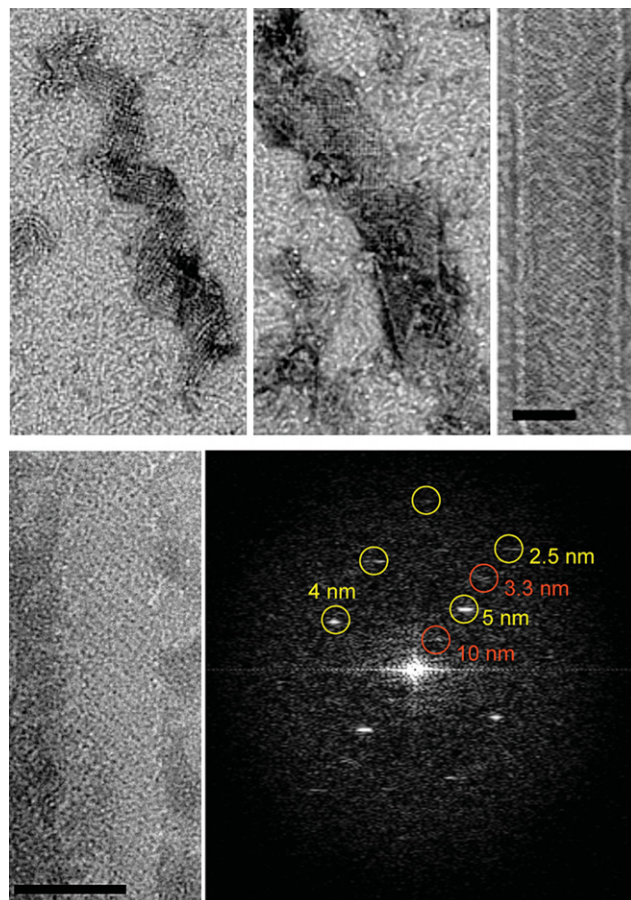


Fig. 4 Growth of GMPCPP–tubulin ribbon. Time points in the growth of GMPCPP ribbons (top). Early assemblies already show the pairing of protofilaments as shown by the presence of strong 10 nm repeats perpendicular to the protofilament axis (bottom). Scale bars correspond to 50 nm.

3. Reconstruction of GMPCPP–Tubulin Tubes and Model Building

Under the conditions described above, GMPCPP–tubulin forms open helical ribbons as well as closed well-ordered helical tubular crystals. Ribbons and tubes have similar ranges of diameter and pitch values and show the pairing of protofilaments. Samples of GMPCPP–tubulin tubes were vitrified and imaged by cryo-EM following the procedures described for the GDP–tubulin double tubes. The GMPCPP tubes have diameters that range from 500 to 600 Å and belong to different helical families. Using the best-ordered tubes belonging to the (11,–37) family, we performed helical reconstruction from two images with defocus values of 1.8 and 0.95 μ m, respectively. They were straightened, their layer lines extracted up to 12 Å, and the two Fourier transforms aligned using conventional helical reconstruction methodology. The final average was calculated by merging of the aligned Fourier transforms after CTF correction, just as was done for the GDP–tubulin tubes. This process resulted in a reconstruction of the GMPCPP–tubulin tubes with a resolution

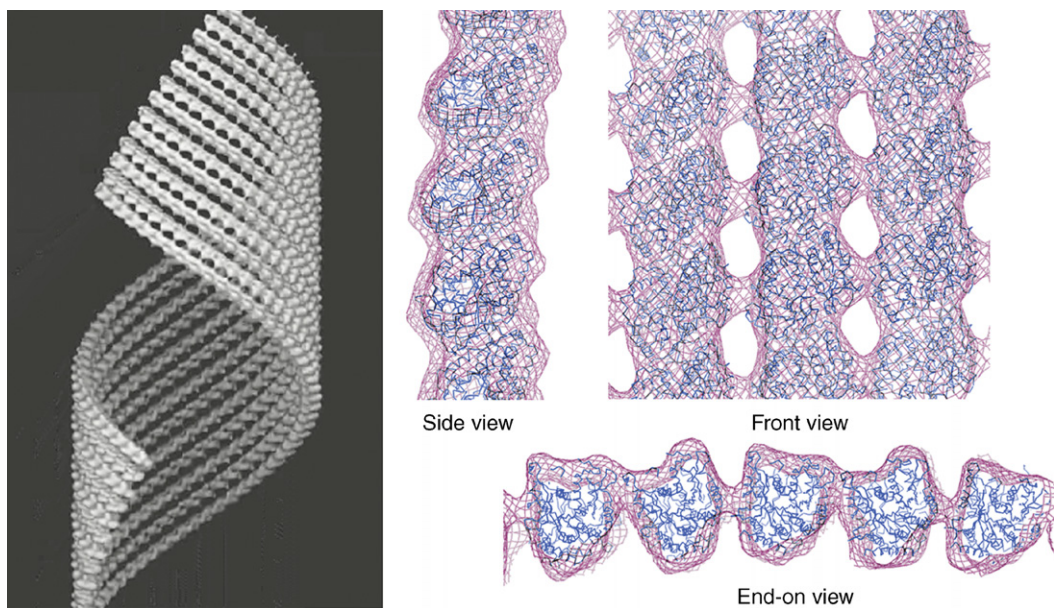


Fig. 5 Structure of GMPCPP-tubulin tubes. Three-dimensional cryo-electron microscopy reconstruction where only 10 protofilaments of the tube wall are shown (left). Docking of the crystal structure of a tubulin monomer to reproduce the tubulin lattice in this structure, shown in different views (right). The side view shows the slight outward curvature of the GMPCPP protofilament. The front view shows the striking similarity of the lateral protofilament stagger in this structure and that of microtubules. In the end-on view the pairing of protofilaments is most apparent. Right side adapted from Fig. 3c in Wang and Nogales (2005). (See Plate no. 8 in the Color Plate Section.)

of 18 Å (Fig. 5, left). The atomic model of β -tubulin (1JFF.pdb) was manually docked in the monomer densities of two adjacent protofilaments using O. The docked atomic structures were used to generate a full pseudo-atomic model for the whole density by applying helical symmetry (Fig. 5, right).

4. Direct Conversion of GMPCPP–Tubulin Tubes into Microtubules

After the formation of GMPCPP–tubulin ribbons at 15°C, increasing the temperature to 37°C resulted in the conversion of the tubes to microtubules. We visualized the samples at different time points during the 37°C incubation by negative stain EM using 2% uranyl acetate and a JEM-1200 EXII transmission microscope (JEOL, Japan). Within half an hour, the ribbons appear more open and coexist with microtubules. After incubations longer than an hour, all the ribbons have disappeared and have been substituted by microtubules.

In order to prove that the temperature-driven conversion of GMPCPP tubes into microtubules was direct, without involving a depolymerization step, we devised the following fluorescence microscopy assay. Two populations of GMPCPP–tubulin tubes with different fluorescent labels were prepared by incubation of two types of GMPCPP–tubulin mixtures (5:1 unlabeled tubulin:fluorescein–tubulin and 5:1 unlabeled tubulin:rhodamine–tubulin; fluorescence-labeled tubulins were purchased

from Cytoskeleton Inc.). The two GMPCPP tube samples were pelleted by centrifugation at 30,000 rpm for 10 min below room temperature and washed once with CBI buffer containing 15 mM magnesium to remove any free tubulin. The two pellets were resuspended and then mixed in CBI buffer with 15 mM magnesium. The mixture was incubated at 37°C for over 3 h to make sure all the helical ribbons and tubes had converted into microtubules. The incubation solution was then diluted ten times, fixed, and viewed by fluorescence microscopy with a 60× Nikon objective on a Nikon Eclipse fluorescence microscope according to the method described in Westermann *et al.* (2005). A viewing area was examined using two different filters in order to record the patterns of fluorescein-tubulin (green) and rhodamine-tubulin (red), respectively. The two patterns were then merged to show relative distributions. Images showed no overlap of the two colors, as would have been expected if the GMPCPP tubes had not depolymerized to dimers or small oligomers before microtubule formation. Interestingly, many microtubules showed adjacent green and red regions indicating annealing of the structures. As a control, the two fluorescent tubulins were mixed before any assembly, then incubated at 37°C in the presence of GMPCPP to form microtubules, fixed, and examined in the same way. In this case, the green and red images showed perfect overlap, as expected from assembly of randomly mixed tubulin dimers with the two labels (Wang and Nogales, 2005b).

C. Microtubule–Dam1 Kinetochore Complex Assemblies

SUMMARY: In the presence of microtubules, the yeast kinetochore Dam1 complex assembles into rings or helical spirals around microtubules. EM analysis of the ring revealed it to consist of 16 Dam1 complexes. Segments of well-ordered double spirals of Dam1 helical assemblies were studied by cryo-EM and helical reconstruction methods to provide the 3D structure of the assembly at a resolution of 30 Å. A new algorithm to deal with the disorder and symmetry heterogeneity of this sample has been recently developed, opening new possibilities in the characterization of the Dam1 complex, including the study of mutants or the potential to reach high-resolution reconstructions of the assemblies.

1. Preparing Ring and Spiral Assembly of Dam1 Around Microtubules

The Dam1 complex has been shown to bind more readily to microtubules made up from GMPCPP-bound tubulin (Westermann *et al.*, 2005). GMPCPP microtubules are prepared as described elsewhere (Westermann *et al.*, 2005) at a concentration of about 2 mg/ml by incubation at 37°C. For ring formation the Dam1 complex is diluted to 0.1 mg/ml concentration in microtubule-assembly CBI buffer and incubated with 0.5 mg/ml GMPCPP microtubules at room temperature for about 10 min. The sample is then negatively stained with 2% uranyl acetate and examined by EM. Rings can be readily observed around microtubules. Analysis of some end-on views of the assembly revealed a 16-fold rotational symmetry of the rings (Westermann *et al.*, 2006).

For helical spiral formation the Dam1 complex is first dialyzed against a low-salt buffer (150 mM KCl, 20 mM potassium phosphate, pH 6.8, 1 mM ethylenediaminetetraacetic acid) for 1–2 h at room temperature before addition. This room temperature dialysis in low-salt buffer, along with the high concentration of Dam1 (at least

5 mg/ml), is not necessary for ring formation but appears important in spiral formation, an effect that could be related to the existence of Dam1 oligomers in low salt prior to addition of microtubules (Westermann *et al.*, 2005). After overnight incubation, samples are applied to glow-discharged Quantifoil grids, blotted with filter paper for 1.5–2 s, and plunged into a liquid ethane slush cooled by liquid nitrogen using a Vitrobot®. Microtubules in these conditions are fully decorated with Dam1 spirals and very occasionally fragments with well-ordered assemblies can be observed.

2. Cryo-EM and Helical Reconstruction of the Dam1 Spiral Assembly Around Microtubules

The frozen-hydrated samples were transferred to a Gatan 626 cryo-holder cooled by liquid nitrogen and examined either on a Philips CM200 or on a Tecnai F20 microscope. Both microscopes are equipped with field emission guns and are operated at 200 keV. Micrographs are taken on Kodak SO163 films under low-dose mode with less than $20 \text{ e}/\text{\AA}^2$ at a magnification of 50 K. The defocus range was from -1.5 to $-3.0 \mu\text{m}$. Films are developed and scanned as described previously for single-particle negatively stained samples. The step size used was $2.54 \text{ \AA}/\text{pixel}$.

At high concentrations the Dam1 complex decorates microtubules as double spirals that show a tendency to pack tightly with time. Segments of Dam1-wrapped microtubules appearing particularly well ordered were boxed using the program BOXMRC and their power spectrum calculated using the SUPRIM package (Schroeter and Baudier, 1996; Zhou *et al.*, 1996). Out of hundreds of segments examined, two showed clear helical diffraction to resolution better than 40 \AA (Fig. 6, right). These two images not only appear particularly tightly wound but also turn out to have a tighter connection with the underlying microtubule, thus maximizing protein contacts into a more crystalline array. Most spirals appear ordered by visual inspection but do not display more than one or two layer lines, likely due to the loss of registry between adjacent turns. The handedness of the spirals was determined to be left-handed using platinum metal shadowing (Wang *et al.*, 2007).

The axial repeats of the microtubule and the Dam1 complex spirals are not a multiple of each other and this required the parallel, independent reconstruction of both structures from the same image. Analysis of two good segments using the SUPRIM image-processing package (Schroeter and Baudier, 1996) and home-modified MRC image-processing software allowed us to index both helical arrangements. While the most common arrangement of a Dam1 ring is a 16-fold symmetric ring around a 13- or 14-protofilament microtubule, the two selected images correspond to a 15-fold Dam1 spiral (14.6 unit numbers per turn, to be precise), around a 14-protofilament microtubule, and a 16-fold spiral (15.7 unit numbers per turn), around a 16-protofilament microtubule. Each particle was processed independently, and the transforms of each showed a clear two-fold symmetry with an axis perpendicular to the helical axis; that is, by changing the azimuthal angle and axial position of the phase origin, about 10 or more layer line peaks for each particle could be brought to within a few degrees of 0° or 180° , thus centering the two-fold axis. Because there are four possible locations for the two-fold axis, it is necessary to choose the same two-fold axis for both data sets. With correct choice of origin, pairs

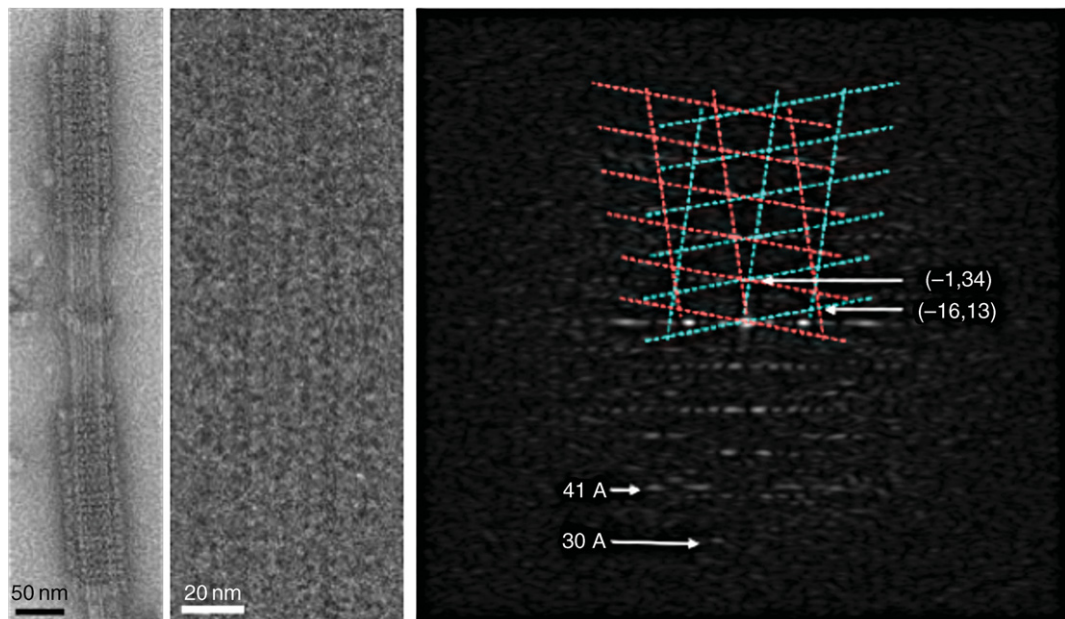


Fig. 6 Self-assembly of Dam1 complexes into double spirals around microtubules. Negative stain image (left). Cryo-electron microscopy image of a small, ordered segment of spiral (center) and its diffraction pattern (right) extending to about 30 Å resolution. The Dam1 lattice is indicated in cyan and magenta. The tubulin 41 Å repeat is indicated. (See Plate no. 9 in the Color Plate Section.)

of corresponding peaks in the two data sets are close to 0° or 180° as expected. After out-of-plane tilt correction and origin alignment, the “little *g*” data of the four sides (near and far sides for each of the two segments) are merged (DeRosier *et al.*, 1999). Only data within a resolution range below the first zero of the CTF (~35 Å for the first image and ~28 Å for the second image) are extracted for analysis and averaging. On each layer line, only data points with significant signal for amplitude and phase are maintained. Because the first segment has a larger defocus value, higher resolution layer line data arise solely from the second segment. Most of the densities are within the radii of 150–350 Å, indicating the radial separation of the Dam1 complex density from the microtubule density. After removal in little *g* space of the low radii data that corresponds to the microtubule density (Wang and Nogales, 2005a), two-fold symmetry is applied on the merged layer lines and a 3D map of the Dam1 complex assembly is obtained by Fourier–Bessel reconstruction of the averaged layer lines. The microtubule layer lines are treated similarly but separately to calculate the 3D map of the 16-protofilament microtubule in the center of the second segment. Summation of the two 3D maps results in a final 3D map of the Dam1 spiral with 15.7 units per turn around a 16-protofilament microtubule (Fig. 7).

3. Development of New Image Analysis Methodology

At saturating concentrations the Dam1 complex forms tightly packed spirals around microtubules, with each turn corresponding very closely to a slightly skewed

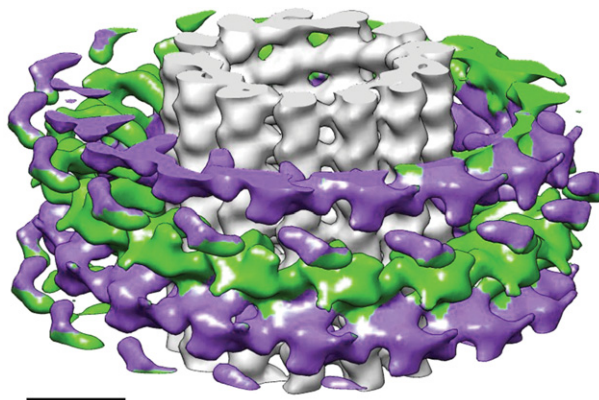


Fig. 7 Cryo-electron microscopy reconstruction of the Dam1 double spiral around microtubules. The spirals run antiparallel (each shown in two distinct colors) and the resulting lack of polarity of the Dam1 assembly stands in contrast with the polar character of the underlying microtubule. Scale bar corresponds to 100 nm. (See Plate no. 10 in the Color Plate Section.)

ring (or lock-washer). This helical arrangement has the potential to aid structural analysis, by both concentrating the complexes and aligning them. However, as described above, the Dam1 spirals formed around microtubules very rarely sustain the type of long-range helical order required for conventional helical reconstruction methodology (e.g., kinesin; Amos and Hirose, 1997; Arnal *et al.*, 1996; Sosa and Milligan, 1996). Out of hundreds of filaments examined, only two showed clear helical diffraction to a resolution better than 40 Å. A possibility to overcome this pitfall is to use the single-particle helical reconstruction approach developed by Egelman (Egelman, 2000). Ideally we would like to utilize the helical order retained at the level of single turns to avoid this limitation and robustly study this sample. Conventional Fourier–Bessel methods cannot operate on short helical stretches, due to extreme layer line broadening and lack of signal, while the normal single-particle approaches need further modification to deal with the symmetry mismatch between Dam1 and microtubule assemblies to efficiently separate the two parts during the reconstruction.

We have recently developed an approach (Ramey *et al.*, 2009) that overcomes these difficulties in studying Dam1 structure by removing the microtubule from each short segment and then applying two-dimensional image alignment and classification techniques to sort the assembly turn by turn into homogeneous classes, with no assumptions made about the symmetries present or amount of disorder. Inspection of class averages allows us to determine the number of symmetries present and to estimate what helical parameters to use in their reconstruction. Implementation of our method yielded a 30 Å reconstruction of the Dam1 complex in very good agreement with the previous reconstruction by traditional Fourier–Bessel methods (Fig. 8). Importantly, the new structure was obtained using helical segments that were too short for traditional methods and had been discarded in our previous study. This method has general applicability to many other microtubule-associated proteins that assemble around microtubules.

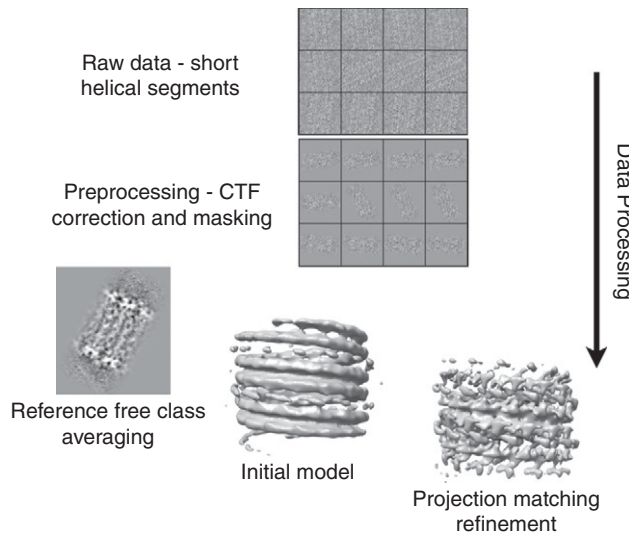


Fig. 8 Schematic overview of the single-particle approach utilized for the analysis of Dam1 spirals. Helical segments are boxed, preprocessed to remove the microtubule, and then aligned and classified to reduce heterogeneity. Two-dimensional averages can then be used to estimate helical symmetry and create an initial model for refinement by single-particle methods (adapted from Fig. 5 in Ramey *et al.*, 2009).

IV. Discussion

A. Biological Relevance of Stabilized Tubulin Structures as Intermediates

Our cryo-EM reconstruction of the high- Mg^{2+} , GMPCC-bound, cold-stabilized structures (which we will refer to as “ribbons”) (Fig. 5) showed protofilaments to be slightly and smoothly curved, with apparent, indistinguishable intra- and interdimer kinks between tubulin monomers (Wang and Nogales, 2005b). Most importantly, the structure showed the presence of alternating lateral contacts between protofilaments that otherwise preserved the precise stagger between protofilaments seen in the microtubule. This meant that the structures would be able to convert into microtubules without the need of longitudinal sliding between protofilaments, but by a rotation around a surface of the tubulin dimer. Interestingly, this surface is as or even more conserved than the final interface involved in the stable microtubule lateral contacts (Fygenson *et al.*, 2004), suggesting its likely relevance in microtubule function. It is important to mention that this type of arrangement, or at least one involving alternative lateral contacts without longitudinal displacements between protofilaments, could have been deduced directly from the extended sheets observed by Chretien and colleagues at the growing end of microtubules, unless extreme deformability is otherwise hypothesized for the tubulin subunit.

Thus, the polymer observed under our conditions has the potential to structurally correspond to the sheet structure proposed as a structural intermediate in microtubule growth. However, many aberrant tubulin polymers have been observed over the years, which reflects tubulin’s extreme tendency to polymerize and (importantly) the plasticity of the polymerization process, but which does not necessarily correspond to any structure of functional relevance (see a recent

review about the structural plasticity in tubulin and actin; [Kueh and Mitchison, 2009](#)). In all those cases, the polymers formed had to be depolymerized down to individual dimers before a microtubule could be formed with the same subunits upon changing polymerization conditions. We proposed that if our structure could directly convert into microtubules, without them breaking down into individual subunits in the process, this behavior would, once again, be in agreement with the idea that our structure corresponds to an early state in microtubule assembly. Our fluorescence microscopy experiments proved that the conversion from ribbons to microtubules is direct. So our ribbon structures have a protofilament arrangement that can explain the sheet structure of Chretien and coworkers, and they convert directly into microtubules, as those sheets do, involving rolling of the lateral interface over a highly conserved region on the protofilament surface. This led us to propose that our ribbon structure is a good model for the early stages of microtubule assembly.

On the other hand, the GDP–tubulin tube represents the structural intermediate during disassembly of microtubules. Within the body of the microtubule, GDP subunits are locked in a straight, “GTP-like” conformation due to the structural constraints imposed by the microtubule lattice ([Melki *et al.*, 1989](#)), for as long as there is a GTP cap. Thus, the energy of GTP hydrolysis is “stored” within the lattice as structural strain ([Caplow *et al.*, 1994](#)). The model proposes that when the GTP cap is lost, rapid depolymerization occurs by conversion into the low-energy, curved GDP state.

A number of computational simulations have been generated based on existing experimental data ([Janosi *et al.*, 2002](#); [Molodtsov *et al.*, 2005](#); [Tuszynski *et al.*, 2005](#); [Vanburen *et al.*, 2005](#)). With some common simplifications, such as assuming GTP–tubulin to be in a straight conformation, GDP–tubulin favoring a curved conformation, and the microtubule wall having elastic properties, they all reach the same conclusion: that the energy released from GTP hydrolysis becomes constrained lattice energy in the microtubule body and that this energy drives microtubule depolymerization and generates force that may perform work, like pulling a kinetochore along the microtubule. Simulations suggest that the mechanical stress is at a minimum at the connection between the GTP cap and the body of the microtubule and that only a couple layers of GTP–tubulin are sufficient to stabilize the microtubule ([Molodtsov *et al.*, 2005](#)). A metastable intermediate state is also predicted and suggests a mechanism for rescue (the process of switching from a shrinking to a growing phase; [Janosi *et al.*, 2002](#); [Vanburen *et al.*, 2005](#)). More elaborate simulation studies will now be possible following new knowledge of the structure of depolymerized GDP–tubulin and the process of GTP–tubulin assembly.

The elastic energy stored in the microtubule wall is released during its disassembly. A question is where this energy goes and what it is for. Work from McIntosh group showed that the frayed end of a depolymerizing microtubule can generate enough force to push a load to the opposite end of the microtubule ([Grishchuk *et al.*, 2005](#)). The discovery of the Dam1 ring complex has given further biological relevance to the curved GDP–tubulin protofilaments at the microtubule end as the potential generators of the processive and directional movement of Dam1 with depolymerizing microtubules ([Nogales and Wang, 2006](#); [Westermann *et al.*, 2006](#)).

B. Biological Relevance of Dam1 Spirals and Rings

The flexible, electrostatic interaction between the mismatched symmetries of Dam1 and the microtubule suggested that a Dam1 ring would be able to diffuse along the microtubule lattice by switching stochastically from one set of E-hooks to another. The implications for kinetochore function are considerable and have led to experiments that showed how the rings were capable, not only of one-dimensional diffusion on the microtubule lattice but also of tracking depolymerizing microtubule ends, with high processivity and without energy consumption of their own (Westermann *et al.*, 2006). In the model put forward, Dam1 ring structures interact with the microtubule via flexible elements and lack a footprint on the microtubule lattice, allowing for diffusion that becomes biased and unidirectional when the microtubule depolymerizes (Nogales and Wang, 2006; Westermann *et al.*, 2006). Robust connection of the depolymerizing spindle microtubule to the kinetochore requires a highly processive and mobile attachment. There is currently disagreement about whether this is accomplished by the Dam1 complex through a biased diffusion or forced walk mechanism (Grishchuk *et al.*, 2008; Westermann *et al.*, 2006).

An encircling ring is clearly an attractive model for processivity and a solution evolution has found for tracking another linear substrate, DNA. However, some of the required properties of Dam1 at the kinetochore have been recapitulated *in vitro* by nonencircling oligomers or single complexes, pointing to the idea that a ring may not be necessary for function (Gestaut *et al.*, 2008; Grishchuk *et al.*, 2008; see Chapter 33 by Grishchuk and Ataullakhanov, this volume). On the other hand, fluorescence data have put the number of Dam1 complexes at the budding kinetochore at 16–20 (Joglekar *et al.*, 2006), in agreement with the number seen in a single ring. Using Dam1-coated beads, Asbury *et al.* (2006) showed that the complex could follow both growing and shrinking microtubule ends. The attachments made between the beads and the microtubule were load-bearing, and sliding experiments indicated that Dam1 was forming a ring that saw growing and shrinking ends as barriers. Interestingly, the presence of the bead at microtubule ends had no apparent effect on microtubule dynamics. However, Ashbury and coworkers went on to show that applying tension to the bead against the direction of microtubule depolymerization decreased catastrophe frequency, slowed shortening, and increased rescue frequency. The authors noted the compatibility of a ring model with the force-dependent changes in dynamic parameters they observed: the ring would transmit tension to the peels at the end of depolymerizing microtubules and tend to straighten them, resulting in a microtubule-stabilizing effect. The dependency of microtubule stabilization on tension also agrees well with the idea of multiple weak binding sites for the ring: weak attachments would allow for diffusion and by themselves have little effect on disassembly parameters. However, the ring would be able to affect the stability of the microtubule when force is exerted through it against the depolymerizing direction. These concepts, however, had already been put into question. Davis and coworkers developed a fluorescence-based assay to measure Dam1–microtubule affinity with high sensitivity at extremely low concentrations of tubulin (Gestaut *et al.*, 2008). They reported values 30-fold greater than previously described (in the nanomolar range). Furthermore, single-molecule experiments showed that at low concentrations of Dam1, where only short oligomers, 1–4 copies in size are formed, this complex is able to follow both assembling and disassembling microtubule ends, although with reduced processivity.

The issue of the oligomerization state of Dam1 and its functional relevance has been further analyzed by McIntosh and coworkers (Grishchuk *et al.*, 2008). Based on fluorescence assays they proposed that Dam1 ring oligomers are unable to diffuse but able to track depolymerizing ends. Smaller oligomers diffuse with rates inversely proportional to their sizes. Interestingly, they also found that single rings are able to track microtubule ends, but not larger assemblies. While the presence of one tracking ring reduces the depolymerization rate, its encountering a second ring results in halting of the depolymerization process until one of the rings disassembles, most likely the one in contact with the microtubule edge. These results are reminiscent of the effect of force on depolymerization speed and rescue rates in the bead experiments of Asbury and coworkers. Experiments by McIntosh and coworkers using Dam1-coated beads show two very different behaviors depending on whether soluble Dam1 complexes were also available in solution. Without soluble Dam1 the beads bound only to the GMPCCP section of microtubules (a region that would mimic the stabilizing GTP cap at growing microtubule ends). These beads increased the depolymerization rate with increasing Dam1 bead decoration and tracked depolymerizing ends by rolling, rather than sliding of the beads. The authors interpret these results as a lack of ring formation and thus postulate two distinct mechanisms for end tracking by rings and small oligomers.

It is interesting to note that phosphomimetic mutants, which are impaired for ring formation but are able to track depolymerizing microtubule ends *in vitro* (Gestaut *et al.*, 2008), are, however, deleterious *in vivo*, where they result in chromosome loss (Cheeseman *et al.*, 2002). It is thus likely that smaller oligomers, while retaining some of the functional properties of the rings, are deficient in a cellular context.

===== V. Summary

Dynamic instability is essential for microtubule function, specially during mitosis. This chapter deals with studies aimed at understanding the coupling of microtubule assembly and disassembly to the nucleotide state of tubulin, and the existence and relevance of structural intermediates important in both processes. We describe the details of both the stabilization of assemblies that mimic these intermediates and the structural characterization of these assemblies using cryo-EM and image analysis. The robust and regulated engagement of highly dynamic spindle microtubules with chromosomes during mitosis involves the interaction of microtubules with kinetochore components. To begin to shed light on this important process we have studied the yeast Dam1 kinetochore complex. Using electron microscopy and image analysis we have defined the structure of this complex and its microtubule-induced self-assembly into rings and spirals. Our structural studies of these two self-assembly systems, which are exquisitely coupled during mitosis, are important for our molecular understanding of the mitotic process, and together with other functional assays, are giving us a first glimpse at a molecular mechanism essential in the life cycle of all cells.

Acknowledgments

We are in debt with all our collaborators in the studies of microtubule structure and dynamics and kinetochore complexes over the years. We are thankful to Greg Alushin for his insight into the mitotic

process and to members of the Nogales lab for inspiration and technical knowhow. This work was funded by grants from the National Institutes of Health and the Agouron Foundation. EN is a Howard Hughes Medical Institute Investigator.

References

Aldaz, H., Rice, L. M., Stearns, T. and Agard, D. A. (2005). Insights into microtubule nucleation from the crystal structure of human gamma-tubulin. *Nature* **435**, 523–527.

Amos, L., and Hirose, K. (1997). The structure of microtubule-motor complexes. *Curr. Biol.* **9**, 4–11.

Amos, L. A., and Klug, A. (1975). Three-dimensional image reconstructions of the contractile tail of T4 bacteriophage. *J. Mol. Biol.* **99**, 51–64.

Andreu, J. M., Gorbunoff, M. J., Medrano, F. J., Rossi, M., and Timasheff, S. N. (1991). Mechanism of colchicine binding to tubulin. Tolerance of substituents in ring C' of biphenyl analogues. *Biochemistry* **30**, 3777–3786.

Arnal, I., Metoz, F., DeBonis, S., and Wade, R. H. (1996). Three-dimensional structure of functional motor proteins on microtubules. *Curr. Biol.* **6**, 1265–1270.

Asbury, C. L., Gestaut, D. R., Powers, A. F., Franck, A. D., and Davis, T. N. (2006). The Dam1 kinetochore complex harnesses microtubule dynamics to produce force and movement. *Proc. Natl. Acad. Sci. USA* **103**, 9873–9878.

Bennett, M. J., Chik, J., Slysz, G. W., Luchko, T., Tuszyński, J., Sackett, D. L., and Schriemer, D. C. (2009). Structural mass spectrometry of the alpha beta-tubulin dimer supports a revised model of microtubule assembly. *Biochemistry* **48**, 4858–4870.

Bordas, J., Mandelkow, E. M., and Mandelkow, E. (1983). Stages of tubulin assembly and disassembly studied by time-resolved synchrotron X-ray scattering. *J. Mol. Biol.* **164**, 89–135.

Buey, R. M., Diaz, J. F., and Andreu, J. M. (2006). The nucleotide switch of tubulin and microtubule assembly: A polymerization-driven structural change. *Biochemistry* **45**, 5933–5938.

Caplow, M., Ruhlen, R. L., and Shanks, J. (1994). The free energy of hydrolysis of a microtubule-bound nucleotide triphosphate is near zero: All of the free energy for hydrolysis is stored in the microtubule lattice. *J. Cell Biol.* **127**, 779–788.

Carlier, M. -F., Didry, D., and Pantaloni, D. (1997). Hydrolysis of GTP associated with the formation of tubulin oligomers is involved in microtubule nucleation. *Biophys. J.* **73**, 418–427.

Carragher, B., Whittaker, M., and Milligan, R. A. (1996). Helical processing using PHOELIX. *J. Struct. Biol.* **116**, 107–112.

Cheeseman, I. M., Anderson, S., Jwa, M., Green, E. M., Kang, J., Yates, J. R., III, Chan, C. S., Drubin, D. G., and Barnes, G. (2002). Phospho-regulation of kinetochore-microtubule attachments by the Aurora kinase Ipl1p. *Cell* **111**, 163–172.

Cheeseman, I. M., Brew, C., Wolyniak, M., Desai, A., Anderson, S., Muster, N., Yates, J. R., Huffaker, T. C., Drubin, D. G., and Barnes, G. (2001a). Implication of a novel multiprotein Dam1p complex in outer kinetochore function. *J. Cell Biol.* **155**, 1137–1145.

Cheeseman, I. M., and Desai, A. (2008). Molecular architecture of the kinetochore-microtubule interface. *Nat. Rev. Mol. Cell Biol.* **9**, 33–46.

Cheeseman, I. M., Enquist-Newman, M., Muller-Reichert, T., Drubin, D. G., and Barnes, G. (2001b). Mitotic spindle integrity and kinetochore function linked by the Duo1p/Dam1p complex. *J. Cell Biol.* **152**, 197–212.

Chrétien, D., Fuller, S. D., and Karsenti, E. (1995). Structure of growing microtubule ends: Two-dimensional sheets close into tubes at variable rates. *J. Cell Biol.* **129**, 1311–1328.

DeRosier, D., Stokes, D. L., and Darst, S. A. (1999). Averaging data derived from images of helical structures with different symmetries. *J. Mol. Biol.* **289**, 159–165.

Downing, K. H. (2000). Structural basis for the interaction of tubulin with proteins and drugs that affect microtubule dynamics. *Annu. Rev. Cell Dev. Biol.* **16**, 89–111.

Egelman, E. H. (2000). A robust algorithm for the reconstruction of helical filaments using single-particle methods. *Ultramicroscopy* **85**, 225–234.

Elie-Caille, C., Severin, F., Helenius, J., Howard, J., Muller, D. J., and Hyman, A. A. (2007). Straight GDP-tubulin protofilaments form in the presence of taxol. *Curr. Biol.* **17**, 1765–1770.

Enquist-Newman, M., Cheeseman, I. M., Van Goor, D., Drubin, D. G., Meluh, P. B., and Barnes, G. (2001). Dad1p, third component of the Duo1p/Dam1p complex involved in kinetochore function and mitotic spindle integrity. *Mol. Biol. Cell* **12**, 2601–2613.

Frigon, R. P., and Timasheff, S. N. (1975). Magnesium-induced self-association of calf brain tubulin. *I. Stoichiometry. Biochemistry* **14**, 4559–4566.

Fygenson, D., Needleman, D., and Sneppen, K. (2004). Variability-based sequence alignment identifies residues responsible for functional differences in α and β tubulin. *Protein Sci.* **13**, 25–31.

Gestaut, D. R., Graczyk, B., Cooper, J., Widlund, P. O., Zelter, A., Wordeman, L., Asbury, C. L., and Davis, T. N. (2008). Phosphoregulation and depolymerization-driven movement of the Dam1 complex do not require ring formation. *Nat. Cell Biol.* **10**, 407–414.

Gigant, B., Curmi, P. A., Martin-Barbey, C., Charbaut, E., Lachkar, S., Lebeau, L., Siavoshian, S., Sobel, A., and Knossow, M. (2000). The 4 angstrom X-ray structure of a tubulin: Stathmin-like domain complex. *Cell* **102**, 809–816.

Gigant, B., Wang, C., Ravelli, R. B., Roussi, F., Steinmetz, M. O., Curmi, P. A., Sobel, A., and Knossow, M. (2005). Structural basis for the regulation of tubulin by vinblastine. *Nature* **435**, 519–522.

Grishchuk, E. L., Molodtsov, M. I., Ataullakhanov, F. I., and McIntosh, J. R. (2005). Force production by disassembling microtubules. *Nature* **438**, 384–388.

Grishchuk, E. L., Spiridonov, I. S., Volkov, V. A., Efremov, A., Westermann, S., Drubin, D., Barnes, G., Ataullakhanov, F. I., and McIntosh, J. R. (2008). Different assemblies of the DAM1 complex follow shortening microtubules by distinct mechanisms. *Proc. Natl. Acad. Sci. USA* **105**, 6918–6923.

Hofmann, C., Cheeseman, I. M., Goode, B. L., McDonald, K. L., Barnes, G., and Drubin, D. G. (1998). *Saccharomyces cerevisiae* Duo1p and Dam1p, novel proteins involved in mitotic spindle function. *J. Cell Biol.* **143**, 1029–1040.

Howard, W. D., and Timasheff, S. N. (1986). GDP state of tubulin: Stabilization of double rings. *Biochemistry* **25**, 8292–8300.

Janke, C., Ortiz, J., Tanaka, T. U., Lechner, J., and Schiebel, E. (2002). Four new subunits of the Dam1-Duo1 complex reveal novel functions in sister kinetochore biorientation. *Embo J.* **21**, 181–193.

Janosi, I. M., Chretien, D., and Flyvbjerg, H. (2002). Structural microtubule cap: Stability, catastrophe, rescue, and third state. *Biophys. J.* **V83**, 1317–1330.

Joglekar, A. P., Bouck, D. C., Molk, J. N., Bloom, K. S., and Salmon, E. D. (2006). Molecular architecture of a kinetochore-microtubule attachment site. *Nat. Cell Biol.* **8**, 581–585.

Jones, M. H., Bachant, J. B., Castillo, A. R., Giddings, T. H., Jr., and Winey, M. (1999). Yeast Dam1p is required to maintain spindle integrity during mitosis and interacts with the Mps1p kinase. *Mol. Biol. Cell* **10**, 2377–2391.

Jones, T. A., Zou, J. -Y., Cowan, S. W., and Kjelgaard, M. (1991). Improved methods of building protein models in electron density maps and the location of errors in these models. *Acta Cryst. A* **47**, 110–119.

Jordan, M. A. (2002). Mechanism of action of antitumor drugs that interact with microtubules and tubulin. *Curr. Med. Chem. Anti-Cancer Agents* **2**, 1–17.

Kang, J. -S., Cheeseman, I. M., Kallstrom, G., Velmurugan, S., Barnes, G., and Chan, C. S.M. (2001). Functional cooperation of Dam1, Ipl1, and the inner centromere protein (INCENP) related protein Sli15 during chromosome segregation. *J. Cell Biol.* **155**, 763–774.

King, R. W. (2008). When 2+2=5: The origins and fates of aneuploid and tetraploid cells. *Biochim. Biophys. Acta* **1786**, 4–14.

Koshland, D. E., Mitchison, T. J., and Kirschner, M. W. (1988). Polewards chromosome movement driven by microtubule depolymerization in vitro. *Nature* **331**, 499–504.

Kueh, H. Y., and Mitchison, T. J. (2009). Structural plasticity in actin and tubulin polymer dynamics. *Science* **325**, 960–963.

Li, H., DeRosier, D., Nogales, E., and Downing, K. H. (2002). Structure of the microtubule at 8 Å resolution. *Structure* **10**, 1317–1328.

Lober, S., and Correia, J. (1992). Subtilisin cleavage of tubulin heterodimers and polymers. *Arch. Bioch. Biophys.* **296**, 152–160.

Lowe, J., Li, H., Downing, K. H., and Nogales, E. (2001). Refined structure of alpha beta-tubulin at 3.5 Å resolution. *J. Mol. Biol.* **V313**, 1045–1057.

Ludtke, S. J., Baldwin, P. R., and Chiu, W. (1999). EMAN: Semiautomated software for high-resolution single-particle reconstructions. *J. Struct. Biol.* **128**, 82–97.

Mandelkow, E. -M., Mandelkow, E., and Milligan, R. A. (1991). Microtubules dynamics and microtubules caps: A time-resolved cryo-electron microscopy study. *J. Cell Biol.* **114**, 977–991.

Melki, R., Carlier, M. F., Pantaloni, D., and Timasheff, S. N. (1989). Cold depolymerization of microtubules to double rings: Geometric stabilization of assemblies. *Biochemistry* **28**, 9143–9152.

Miranda, J. J., De Wulf, P., Sorger, P. K., and Harrison, S. C. (2005). The yeast DASH complex forms closed rings on microtubules. *Nat. Struct. Mol. Biol.* **12**, 138–143.

Mitchison, T., and Kirschner, M. (1984). Dynamic instability of microtubule growth. *Nature* **312**, 237–242.

Molodtsov, M. I., Ermakova, E. A., Shnol, E. E., Grishchuk, E. L., McIntosh, J. R., and Ataullakhanov, F. I. (2005). A molecular-mechanical model of the microtubule. *Biophys. J.* **88**, 3167–3179.

Müller-Reichert, T., Chrétien, D., Severin, F., and Hyman, A. A. (1998). Structural changes at microtubule ends accompanying GTP hydrolysis: Information from a slowly hydrolyzable analogue of GTP, guanylyl (α,β)-methylene-diphosphonate. *Proc. Natl. Acad. Sci. USA* **95**, 3661–3666.

Nogales, E. (2000). Structural insights into microtubule function. *Ann. Rev. Biochem.* **69**, 277–302.

Nogales, E., Downing, K. H., Amos, L. A., and Löwe, J. (1998a). Tubulin and FtsZ form a distinct family of GTPases. *Nat. Struct. Biol.* **5**, 451–458.

Nogales, E., and Wang, H. W. (2006). Structural intermediates in microtubule assembly and disassembly: How and why? *Curr. Opin. Cell Biol.* **18**, 179–184.

Nogales, E., Wang, H. W., and Niederstrasser, H. (2003). Tubulin rings: Which way do they curve? *Curr. Opin. Struct. Biol.* **13**, 256–261.

Nogales, E., Whittaker, M., Milligan, R. A., and Downing, K. H. (1999). High resolution structure of the microtubule. *Cell* **96**, 79–88.

Nogales, E., Wolf, S. G., and Downing, K. H. (1998b). Structure of the $\alpha\beta$ tubulin dimer by electron crystallography. *Nature* **391**, 199–203.

Ramey, V. H., Wang, H. W., and Nogales, E. (2009). Ab initio reconstruction of helical samples with heterogeneity, disorder and coexisting symmetries. *J. Struct. Biol.* **167**(2), 97–105.

Ravelli, R. B., Gigant, B., Curmi, P. A., Jourdain, I., Lachkar, S., Sobel, A., and Knossow, M. (2004). Insight into tubulin regulation from a complex with colchicine and a stathmin-like domain. *Nature* **428**, 198–202.

Rice, L. M., Montabana, E. A., and Agard, D. A. (2008). The lattice as allosteric effector: Structural studies of alphabeta- and gamma-tubulin clarify the role of GTP in microtubule assembly. *Proc. Natl. Acad. Sci. USA* **105**, 5378–5383.

Salmon, E. D. (2005). Microtubules: A ring for the depolymerization motor. *Curr. Biol.* **15**, R299–R302.

Schroeter, J. P., and Bretaudiere, J. P. (1996). SUPRIM: Easily modified image processing software. *J. Struct. Biol.* **116**, 131–137.

Shang, C., Hazbun, T. R., Cheeseman, I. M., Aranda, J., Fields, S., Drubin, D. G., and Barnes, G. (2003). Kinetochore protein interactions and their regulation by the Aurora kinase Ipl1p. *Mol. Biol. Cell* **14**, 3342–3355.

Sosa, H., and Milligan, R. A. (1996). Three-dimensional structure of ncd-decorated microtubules obtained by a back-projection method. *J. Mol. Biol.* **260**, 743–755.

Toyoshima, C., and Unwin, N. (1988). Contrast transfer for frozen-hydrated specimens: Determination from pairs of defocused images. *Ultramicroscopy* **25**, 279–291.

Tuszynski, J. A., Luchko, T., Portet, S., and Dixon, J. M. (2005). Anisotropic elastic properties of microtubules. *Eur. Phys. J. E Soft Matter* **17**, 29–35.

Unger, E., Böhm, J. K., and Vater, W. (1990). Structural diversity and dynamics of microtubules and polymorphic tubulin assemblies. *Electron. Microsc. Rev.* **3**, 355–395.

Vanburen, V., Cassimeris, L., and Odde, D. J. (2005). A mechanochemical model of microtubule structure and self-assembly kinetics. *Biophys. J.* **89**, 2911–2926.

Wang, H. W., and Nogales, E. (2005a). An iterative Fourier-Bessel algorithm for reconstruction of helical structures with severe Bessel overlap. *J. Struct. Biol.* **149**, 65–78.

Wang, H. W., and Nogales, E. (2005b). Nucleotide-dependent bending flexibility of tubulin regulates microtubule assembly. *Nature* **435**, 911–915.

Wang, H. W., Ramey, V. H., Westermann, S., Leschziner, A. E., Welburn, J. P., Nakajima, Y., Drubin, D. G., Barnes, G., and Nogales, E. (2007). Architecture of the Dam1 kinetochore ring complex and implications for microtubule-driven assembly and force-coupling mechanisms. *Nat. Struct. Mol. Biol.* **14**, 721–726.

Westermann, S., Avila-Sakar, A., Wang, H. W., Niederstrasser, H., Wong, J., Drubin, D. G., Nogales, E., and Barnes, G. (2005). Formation of a dynamic kinetochore–microtubule interface through assembly of the Dam1 ring complex. *Mol. Cell* **17**, 277–290.

Westermann, S., Drubin, D. G., and Barnes, G. (2007). Structures and functions of yeast kinetochore complexes. *Annu. Rev. Biochem.* **76**, 563–591.

Westermann, S., Wang, H. W., Avila-Sakar, A., Drubin, D. G., Nogales, E., and Barnes, G. (2006). The Dam1 kinetochore ring complex moves processively on depolymerizing microtubule ends. *Nature* **440**, 565–569.

Wolff, J. (1998). Promotion of microtubule assembly by oligocations: Cooperativity between charged groups. *Biochemistry* **37**, 10722–10729.

Wriggers, W., Milligan, R. A., and McCammon, J. A. (1999). Situs: A package for docking crystal structures into low-resolution maps from electron microscopy. *J. Struct. Biol.* **125**, 185–195.

Zhou, Z. H., Hardt, S., Wang, B., Sherman, M. B., Jakana, J., and Chiu, W. (1996). CTF determination of images of ice-embedded single particles using a graphics interface. *J. Struct. Biol.* **116**, 216–222.

Zhu, J., Penczek, P. A., Schröder, R., and Frank, J. (1997). Three-dimensional reconstruction with contrast transfer function correction from energy-filtered cryoelectron micrographs: Procedure and application to the 70S *Escherichia coli* ribosome. *J. Struct. Biol.* **118**, 197–219.

CHAPTER 9

High-Resolution Imaging of Microtubules and Cytoskeleton Structures by Atomic Force Microscopy

Loic Hamon, Patrick A. Curmi, and David Pastré

Laboratoire Structure-Activité des Biomolécules Normales et Pathologiques, INSERM – UEVE UMR U829, Evry 91025, France

Abstract

- I. Introduction to AFM Imaging of Biomolecules
- II. Rationale
- III. AFM Principle and Operation Mode
 - A. Principle of AFM
 - B. Biomolecules Imaging
- IV. Practical Aspects of Microtubules Adsorption on Surface and AFM Imaging
 - A. Material for AFM Imaging
 - B. Material and Methods for Microtubule Assembly
 - C. Substrate for Microtubule Imaging
 - D. Buffer Conditions for Microtubule Adsorption on Mica
 - E. Practical Aspects of AFM Imaging of Microtubules
- V. AFM Imaging in Air of Microtubule
 - A. Control of the Tubulin Purity
 - B. Evidence of Microtubule Structural Changes
 - C. Intermediate Structures
- VI. AFM Imaging in Air of Tubulin or Microtubule:Protein Interactions
 - A. Example of Detection of the Interaction Between Tubulin or Microtubules with Protein
 - B. Binding of mRNA to Microtubules Mediated by YB-1
- VII. Conclusion
- References

Abstract

Atomic force microscopy (AFM), which combines a nanometer-scale resolution and a unique capacity to image biomolecular interactions in liquid environment, is a promising tool for the investigation of biological samples. In contrast with nucleic acids and nucleoprotein complexes, for which AFM is now of common use and participates in the recent advances in the knowledge of DNA-related biomolecular processes, AFM investigations of cytoskeleton structures and especially microtubules remain rare. The most critical step to observe biomolecules using AFM is the spreading of the biological material on a flat surface. This issue is now better documented concerning DNA but a lot remains to be done concerning microtubules. This is a prerequisite to further document this issue for a proper and large use of AFM to study cytoskeleton structures. We present here an overview of the various procedures previously used to spread microtubules on a flat surface and advance an easy-to-use and efficient experimental protocol for microtubule imaging by AFM in air. We show application of this protocol to observe intermediate structures of microtubule assembly without using any stabilizing agent and the observation of more complex systems like proteins or messenger ribonucleoprotein particles in interaction with microtubules.

I. Introduction to AFM Imaging of Biomolecules

The atomic force microscope is a member of the family of scanning probe microscopes which has grown steadily since the invention of the scanning tunneling microscope by Binning and Rohrer (Binnig *et al.*, 1986). In comparison with other techniques like electron microscopy, atomic force microscopy (AFM) presents unique advantage for the observation of biomolecules. AFM allows a three-dimensional imaging with molecular resolution and, in addition, experiments can be realized under aqueous environments thus allowing the investigations of biological samples in near native conditions and the tracking of biological processes in real time. Thanks to these advantages, many AFM studies have been performed on biological materials over the two past decades, and AFM imaging has further increased the knowledge in many areas of molecular biology. Most of the works using AFM have been concentrated on nucleic acids, especially DNA (Bustamante *et al.*, 1992), RNA (Lyubchenko *et al.*, 1992), DNA:proteins interactions (Kasas *et al.*, 1997), and other biomolecules like two-dimensional crystals of membrane proteins (Hoh and Schoenenberger, 1994). AFM observations of single cytoskeleton structures like actin filaments (Fritz, 1995a) or microtubules (Fritz, 1995b) have been achieved a few years after and remain rare in comparison. The few AFM studies on microtubules have dealt with microtubule structures and polymorphic assemblies (Vater *et al.*, 1995), structural properties of microtubules polymerized with a slowly hydrolyzable analogue of guanosine triphosphate (GTP) (Munson *et al.*, 2007), microtubule interactions with partners like tau (Makrides *et al.*, 2003; Schaap *et al.*, 2007; Vandebroek *et al.*, 2006), kinesin (Ando *et al.*, 2003; Kacher *et al.*, 2000), YB-1 (Chernov *et al.*, 2008b), and messenger ribonucleoprotein particle

(mRNP) (Chernov *et al.*, 2008a). The capacity of AFM to provide useful information on microtubules and their interactions with various partners does not need further proofs. However, it appears that among the published works there are significant variations concerning the imaging medium (air or liquid) and the type of surfaces on which biomolecules are adsorbed prior to AFM imaging (bare or pretreated mica, glass, silicon, grafted substrate, etc.). It is obvious that the influences of both substrate and buffer composition remain to be tackled. In addition, through the literature on this topic, microtubule stabilization may appear to be necessary for AFM imaging, due to the systematic use of microtubule-stabilizing agents (taxol and/or glutaraldehyde). In the case of highly dynamical structures like microtubules which interact with various partners (proteins, drugs), the choice of the experimental conditions (substrate, buffer composition, microtubule stabilization) is problematic since it can preclude the observation of underlying biomolecular processes. We thus propose here to detail the experimental conditions which may vary in function of the objectives of the experiments.

II. Rationale

In a first part, we briefly remind the principle of AFM and the various operating modes used to image biomolecules in air or in liquid. The second part is devoted to the variety of substrates and surface treatments which can be used to image microtubules. Among the substrates, mica, the most popular one for biomolecules, appears to be also the most suitable for microtubule imaging. We also detail the buffer composition to be used to spread microtubules on mica. Indeed, the adsorption of biomolecules on mica is orchestrated by multivalent counterions and can require a specific buffer composition. Furthermore, microtubules imaging by AFM presents some characteristics inherent to the significant microtubule height (AFM tip convolution), its fragile cylindrical structure which can collapse or open up, and the surface influence on the microtubule assembly.

Finally, we highlight some useful applications of microtubule imaging by AFM ranging from the simplest one, when AFM provides a useful control of tubulin functionality, to more complex investigations regarding the observation of microtubules in interaction with partners. In each case, the experimental conditions are defined with respect to the context of the study.

III. AFM Principle and Operation Mode

A. Principle of AFM

AFM uses as probe an extremely sharp tip (on the order of a few nanometer) to scan a sample surface. The tip is mounted at the very end of a flexible cantilever, the position of which, while scanning over the surface sample, can be recorded as an image. The scanning of the AFM tip over the surface requires its fine control using a piezoelectric ceramic that expands or contracts in the presence of a voltage gradient, leading to a high-precision three-dimensional positioning. The interaction forces between the tip and the surface are detected with angstrom resolution by an

optical lever which operates by reflecting a laser beam off the top of the cantilever. The reflected laser beam strikes a position-sensitive photodetector consisting of four photodiodes organized side-by-side. The difference between the signals of the four quadrant photodiodes indicates the position of the laser spot on the detector and thus the angular deflection of the cantilever. If the tip is scanned over the sample surface then the deflection of the cantilever can be recorded as an image which reflects the three-dimensional sample surface.

The total scan area can reach a few thousands of square micrometers and varies with the piezoelectric ceramic used. The resolution of AFM depends mainly on the sharpness of the tip which can be currently manufactured with a radius of few tens of nanometers. An atomic resolution is easily obtained for hard and small objects but for soft objects like biological samples the problem becomes tricky due to the forces exerted by the tip during imaging which causes deformation of the sample. In this case, the lateral resolution of AFM decreases to a few nanometers whereas the vertical resolution remains two orders of magnitude or better, i.e., within the angstrom range.

An AFM image can be obtained using three different operating modes: contact, noncontact, and intermittent-contact modes.

- In the contact mode, the AFM cantilever touches the sample surface. The resulting tip deflection is then fixed during the X - Y -dimensional scan by adjusting the Z extension of the piezoelectric ceramic and the AFM image is generated by plotting the Z position of the cantilever as a function of the X - Y position. This mode is not really adequate for biomolecule imaging. Indeed, the pressure exerted by the tip on the sample generates high lateral forces, which reduce the lateral resolution, compress soft biological samples, and may drag biomolecules over the surface.
- In the noncontact mode, the tip is mechanically oscillating at a frequency close to its resonance frequency. This mode uses long-ranged attraction force between the surface and the AFM tip to scan the surface sample without contact. Since biological samples have no particular electric or magnetic properties, a feedback using long-ranged force is not possible under normal atmospheric pressure, which precludes its use for biomolecule imaging.
- In the intermittent-contact mode, the cantilever is also oscillating near its resonance frequency but the tip is now touching the surface intermittently which results in a reduction of the oscillation amplitude. This amplitude is then maintained constant during the scan by adjusting the Z position of the piezoelectric ceramic and the AFM image captured in this mode is generated in a similar way as in the contact mode. Intermittent contact is less aggressive for the sample than the contact mode and thus particularly suitable to improve the resolution of AFM images of biological samples.

B. Biomolecules Imaging

1. Imaging in Liquids

AFM requires here the use of a liquid cell which encloses both the cantilever and the biological sample. The major advantages of imaging in liquid are the perspective to visualize the dynamical structural changes and interactions

between biological partners in near physiological conditions. Furthermore, the liquid environment allows the use of flexible cantilevers due to the absence of capillary forces. The interacting forces between the biomolecules and the tip are thus minimized which leads to a minor deformation of the sample and higher scan rates than in air. In spite of its undeniable advantages, the AFM studies of biomolecules in liquid are not of current use because the adsorption of biomolecules on surface is challenging to observe dynamical processes, especially because the AFM tip tends to drag biomolecules if they are not firmly attached on the substrate. Moreover, as biomolecular interactions generally occur in a millisecond timescale, the image acquisition time which ranges from 30 s to few minutes per frame depending on the scan area is too long to capture these processes at sufficient time resolution. To speed up the scan rate, recent instrumental developments have led to promising AFM prototypes which can capture images within few hundred of milliseconds and weak tip–sample interaction forces (Ando *et al.*, 2008). These developments have been especially focused on increasing the resonant frequency of cantilevers which now reaches ~3.5 MHz in air and ~1.2 MHz in water. These values are orders of magnitude higher than those of typical silica cantilevers used in AFM.

2. Imaging in Air

AFM imaging in air is less demanding than in liquid. In addition, it can provide relevant information on biomolecule structures or complex interactions at higher resolutions than in liquid because molecules are fixed on the surface after the drying step and cannot be dragged by the AFM tip during the scan. Macromolecules are first allowed to interact in solution and then a small volume of the sample (typically 10 μ L) is deposited on mica. The sample can be incubated for up to few minutes in order to allow the biomolecule diffusion and their spreading on the surface. However, short incubation times are generally preferred because the probability that a biological complex undergoes an irreversible dissociation increases for long incubation times, as reported for DNA:protein complexes (Sorel *et al.*, 2006). Then a rinsing step with purified water removes buffer component and avoids the crystallization of salts on the surface. However, it can also induce the release of the biomolecules from the surface. To prevent this, prior rinsing, biomolecules are immobilized on the surface with fixation buffer solution like 0.02% w/v uranyl acetate (Revet and Fourcade, 1998). Indeed, it has been shown for DNA, and this is also valid for microtubules, that uranyl acetate provides a strong fixation of previously adsorbed molecules.

IV. Practical Aspects of Microtubules Adsorption on Surface and AFM Imaging

A. Material for AFM Imaging

Imaging was performed in Tapping ModeTM with a multimodeTM AFM (Veeco, Santa Barbara, CA) operating with a nanoscope IIIaTM controller. We used Olympus (Hamburg, Germany) silicon cantilever AC160TS with nominal spring constants

between 36 and 75 N/m and resonant frequency of about 300 kHz. All images were collected at a scan frequency of 1.5 Hz and a resolution of 512×512 pixels. A first- or second-order polynomial function was used to remove the background slope.

B. Material and Methods for Microtubule Assembly

Tubulin is purified from sheep brain as previously described (Castoldi and Popov, 2003). Before use, tubulin stock is thawed and an additional cycle of polymerization is performed. Tubulin samples are prepared as follows: tubulin at desired concentrations (from 20 to 40 μ M) is incubated in polymerization buffer (50 mM MES-KOH, pH 6.8, 50 mM KCl, 5 mM MgCl₂, 20% glycerol) for 10 min on ice. Then, GTP is added to 1 mM final and the mixture immediately transferred to 37°C for 15 min.

C. Substrate for Microtubule Imaging

AFM imaging of microtubules requires their adsorption and immobilization on biocompatible and flat surfaces. Glass, mica, gold, and silicon surfaces have been used to noncovalently or covalently immobilize biomolecules (Wagner, 1998). The most popular substrate in this respect is muscovite mica, a highly negatively charged surface. Weak electrostatic attachment to mica of negatively charged biomolecules such as microtubules or DNA is obtained by adding multivalent cations (Hansma and Laney, 1996). The mechanism of anionic biomolecule adsorption has been recently attributed to the sharing of multivalent counterions between mica and the anionic polymers (DNA, microtubule, etc.) (Pastré *et al.*, 2006).

An electrostatic attraction of biomolecules onto mica is simple and does not require major surface functionalization steps. It also presents two other major advantages. First, the adsorption strength can be modulated by varying the concentration of multivalent cations in the buffer. Second, as the adsorption is mediated by counterions, biomolecules are not directly interacting with the surface which preserves their accessibility to partners.

Nevertheless, other methods to adsorb microtubules on a substrate for AFM imaging have been developed. They consist in chemical modifications of the mineral substrate which could lead to a charge inversion. For example, mica pretreatment in a solution containing 10 mM NiCl₂ allows Ni²⁺ ions to strongly bind the mica surface and thus provides positive charges for biomolecule adsorption. However, such a surface treatment can affect biological sample conformation as observed for actin (Costa *et al.*, 2004). Other treatments include two-dimensional organosilane polymers formed by condensation of 3-aminopropyl-triethoxysilane, which adsorb readily to mica and reverse the charge through their protonated amino groups at neutral pH, cationic lipid bilayer (Kacher *et al.*, 2000), and amino-derivatized substrate activated with glutaraldehyde to immobilize microtubules via their native amino groups (Vinckier *et al.*, 1995). The major drawback is that such surfaces lead inexorably to a decrease of resolution due to the softness and/or the roughness of the substrate. Consequently, we preferred to use bare mica since it combines atomic flatness and tunable adsorption conditions.

D. Buffer Conditions for Microtubule Adsorption on Mica

Biomolecule adsorption on bare mica is obtained by raising sufficiently the multivalent cation concentration of the buffer. Multivalent cations compensate for the effect of monovalent salts which cannot contribute to the attraction force between the biomolecule and the mica surface. For example, in the case of DNA, 5 mM MgCl₂ is sufficient to induce DNA adsorption on mica in the presence of 50 mM NaCl. The global surface charge density of microtubules is lower than that of DNA, which may lower the attraction to mica since the higher the charge density the higher the adsorption strength. However, the negative charges of tubulin are concentrated on the C-terminal tails leading to a local charge density comparable to that of DNA. As the C-terminal domains are oriented outward the microtubule wall, the C-terminal tails can serve as anchors to allow the microtubule adsorption on mica. We thus determined that the presence of 5 mM of MgCl₂ in the polymerization buffer is sufficient for microtubule adsorption on freshly cleaved mica.

1. Protocol for Microtubule Imaging in Air

After microtubules assembly in the polymerization buffer at 37°C, a 10 µL aliquot is deposited on mica and incubated for typically 20 s, which allows the diffusion of microtubules on the surface and their adsorption. The mica surface is then plunged for 30 s in uranyl acetate solution (0.02% w/v) for microtubule fixation on the substrate. Finally, the sample is rinsed with pure water (Millipore) and dried with a filter paper. It is worth pointing out that the process of deposition should be as quick as possible since microtubules are highly temperature sensitive. For microtubule imaging in air, the scan rate of the tip can vary between 1.5 and 2 Hz per line according to the scan area, larger area being scanned with a lower rate. For example, the scan frequency should be decreased down to 0.6 Hz to maintain a sufficient resolution for a 10 × 10 µm² area. Consequently, the time required for scanning this area reaches 20 min if there are 512 lines per frame.

As AFM is generally used to image isolated biomolecules, the concentration of material in the sample for deposition is very low, typically less than 1 µM for proteins. Above these concentrations, the surface density of biomolecules becomes very high and crowded which precludes high-resolution imaging. However, biopolymers like microtubules require a high concentration of building block to assemble above a threshold called the critical concentration (Cc). A first possibility consists in the dilution of the sample after microtubule assembly but this requires the prior stabilization of microtubules for example by taxol. Consequently, microtubules are not imaged in their native conformation. A second possibility is to decrease the time of incubation of the sample on mica to limit the amount of biological material adsorbed on the surface. This approach is risky since microtubules are large structures which diffuse slowly in the viscous polymerization buffer containing generally a high concentration of glycerol (20% under our conditions). Consequently, the adsorption process will select free tubulin and small microtubules at the expense of long microtubules, which may result in an image which is not representative of the composition of the sample. We, however, prefer to deposit the sample without any dilution during a sufficiently long time to allow the adsorption of the majority of microtubule (between 20 s and 1 min). As the surface coverage by proteins is high under such conditions, we search for and image lower surface densities areas.

2. Protocol for Microtubule Imaging in Liquid

AFM imaging in liquid requires a higher sample volume, typically 200 μL and thus a higher quantity of microtubules. Tubulin is assembled in polymerization buffer containing 20 μM taxol for microtubule stabilization. Microtubules are then pelleted at 25,000 $\times g$ for 10 min at 37°C to remove nonpolymerized tubulin. The supernatant is discarded and the pellet is gently resuspended in a starting volume of polymerization buffer containing 10 μM taxol and 0.2% glutaraldehyde for 30 min to prevent the opening up of microtubules during adsorption on surface. Microtubule-stabilized sample (20 μL) is deposited on mica surface and placed in the liquid cell. The liquid cell is then filled with 100 μL of buffer (50 mM MES-KOH, pH 6.8, 50 mM KCl, 5 mM MgCl₂). It is worth pointing out that unpolymerized tubulin should be removed by centrifugation before microtubule adsorption on mica. Indeed, its presence in the sample leads to its accumulation on the surface which alters the quality of images. In addition, imaging conditions can be affected by the binding of tubulin to the AFM tip.

In practice, AFM imaging in liquid is generally performed by injecting biological samples in the cell through a thin channel. In the case of microtubules, it is not possible to use this channel without exposing microtubules to serious structural damages due to the shearing forces on their fragile macroscopic structures. It is therefore better to first apply an aliquot of the microtubule sample on mica to adsorb microtubules on the surface and then to mount the liquid cell. Finally, whereas the time of sample preparation and installation is very long when AFM imaging is performed in liquid, the scan rate could be faster than in air and could reach 6–10 Hz per line due to the lower quality factor of the vibrating cantilever in liquid than in air. Then, 30 s to 2 min per frame is sufficient for image acquisition of a 10 \times 10 μm^2 scan area.

E. Practical Aspects of AFM Imaging of Microtubules

1. Tip Convolution

As the construction of the AFM image is the result of an interaction between the tip and the sample, the convolution of the sample by the imaging tip leads to an increase of the apparent lateral dimension of the microtubule, whereas the vertical resolution is not affected (Fig. 1). This effect is more pronounced when the AFM tip becomes enlarged due to its fouling. Consequently, the true dimension of the sample can only be estimated by measuring its height, but not its width. Moreover, microtubules like all biological samples are soft material and can be deformed by the tip pressure. It is then necessary to minimize the force between the sample and the tip to preserve the physical integrity of the microtubules.

2. Microtubule Collapse on Surface

Microtubules are hollow cylinders that may collapse when imaged in air due to their adsorption on mica surface followed by the drying step. Indeed, AFM measurements in air show microtubules with heights ranging between 8 and 10 nm (Fig. 2A). Moreover, one would expect that microtubules stabilized by taxol, which reinforces the lateral interactions between tubulin protofilaments,

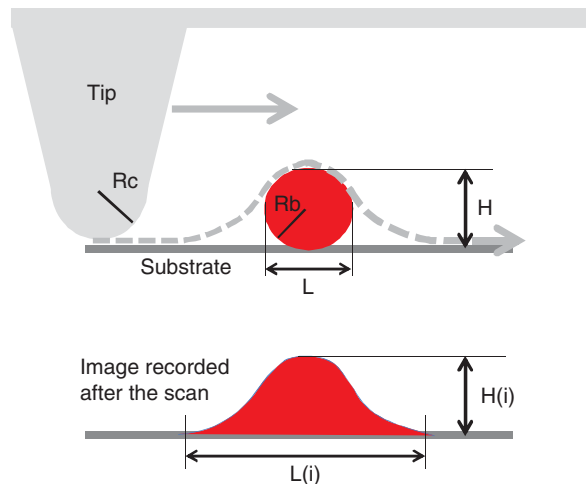


Fig. 1 The convolution of the sample (radius $R_b = 12$ nm for microtubule) by the tip (radius $R_c = 30$ nm) during the scan leads to an increase of the apparent lateral dimension of the biomolecules (compare L to $L(i)$) whereas the vertical resolution is not affected (H and $H(i)$ are relatively close).

would maintain their cylindrical structure after the drying step. Yet sections of such microtubules indicate that they also collapse and some of them open up which is not suitable for functional studies (Fig. 2B). Another way to stabilize microtubules is to use post-fixation with glutaraldehyde (0.2–0.5% v/v) but we find no significant increase of their average height whatever the glutaraldehyde concentration used. For higher glutaraldehyde concentrations or longer exposure times, the average microtubule height slightly increases but is associated with curvatures or breakages of the microtubule cylinder (Fig. 2C), which is not satisfying (Cross and Williams, 1991).

To obtain microtubules with height close to the expected 25 nm, the drying step is problematic. Indeed, only microtubules imaged in liquid have a height ranging from 18 to 22 nm (Fig. 2D) but imaging in liquid requires the use of a stabilizing agent like taxol or glutaraldehyde and these conditions result in other limitations for the exploration of microtubule:partner interaction since microtubules no longer exhibit dynamic behavior.

3. Surface Influence on Cytoskeletal Protein Assembly

As biomolecules are attracted onto mica for AFM imaging, their surface concentration can be higher than that existing in the bulk solution (Fig. 3A). In the case of tubulin or other cytoskeletal proteins like FtsZ, its prokaryote homologue, which also assembles into polymer above a C_c , it appears that the increased concentration in the surface vicinity yields conditions for polymerization even though the bulk protein concentration is lower than C_c (Fig. 3B). This surface-driven assembly necessitates the two-dimensional diffusion of proteins on mica which has been demonstrated for

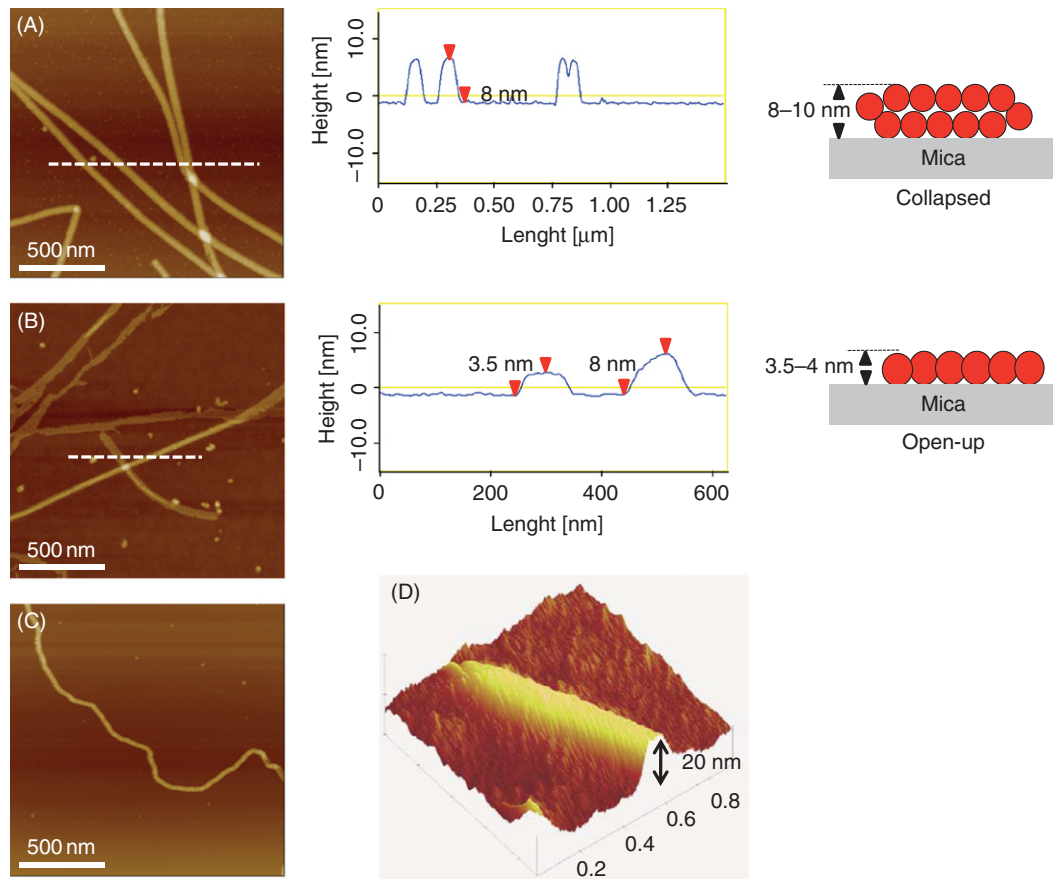


Fig. 2 Effects of microtubule adsorption on mica and drying step on microtubule structure. (A) The drying step of the sample leads to the microtubule collapse. Microtubule heights range between 8 and 10 nm. Z scale: 30 nm. (B) The stabilization of microtubules by taxol before drying does not avoid the collapse. Sometimes, taxol promotes the opening-up of the microtubule which appears as a flat sheet of protofilaments organized side-by-side. Z scale: 30 nm. (C) Post-fixing the microtubules by glutaraldehyde before drying is often used for their stabilization. If the average height slightly increases ($h = 10\text{--}12\text{ nm}$), for glutaraldehyde concentration higher than 0.5%, microtubules present abnormal bendings. Z scale: 40 nm. (D) Image of taxol-stabilized microtubules in liquid. In this case, microtubules maintain a cylindrical structure with an average height ranging from 18 to 22 nm. Z scale: 40 nm. (See Plate no. 11 in the Color Plate Section.)

tubulin protofilaments and FtsZ filaments (Hamon *et al.*, 2009) and depends on buffer composition or pretreatment of the mica surface. Indeed, if the surface pretreatment reinforces the attraction strength between the surface and the protein, the protein diffusion rate on surface decreases as well as the probability of surface assembly. Nevertheless, it is worth pointing out that only small tubulin protofilaments are produced on mica and to the best of our knowledge, this effect is unable to provoke the formation of microtubules.

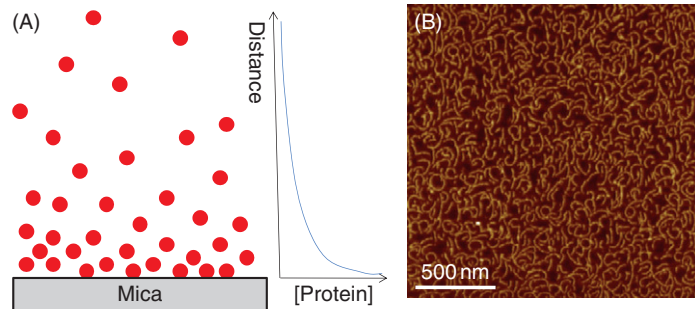


Fig. 3 Surface influence on tubulin polymerization. (A) Schematic representation of the attraction exerted by the surface on proteins which leads to an increase of protein concentration at the vicinity of the mica surface. (B) AFM image of tubulin polymerization on mica surface. Mica was incubated during 300 s in polymerization buffer containing only 80 nM tubulin. Free tubulin assembles on surface to form short protofilaments. Z scale: 10 nm.

===== V. AFM Imaging in Air of Microtubule

A. Control of the Tubulin Purity

AFM appears as a powerful quality control tool for tubulin purification and polymerization. Indeed, AFM allows one to image a microtubule sample without using a large quantity of biological material (10 μ g of tubulin is largely enough). On a large-scale image ($15 \times 15 \mu\text{m}^2$), the presence of small or large aggregates of tubulin can be easily detected, reflecting the purity of the sample.

In addition, tubulin polymerization *in vitro* is often monitored by light scattering measurements. The scattered light signal is a function of the size and the number of objects in the polymerization buffer but it is not possible to discriminate the contribution of the different families of polymers or aggregates that may be present in the sample. A straightforward method is then to image an aliquot from the sample after polymerization, which will document in a few minutes the different structures contained in the sample.

B. Evidence of Microtubule Structural Changes

Microtubules interact with numerous partners which strongly influence the kinetics of their assembly. These partners can act on the nucleation step, modify the rate of assembly, and stabilize or destabilize microtubules. For example, it has been shown recently that small cationic molecules like natural polyamines can favor microtubule nucleation and elongation via facilitated diffusion (Mechulam *et al.*, 2009). When a member of this family, spermine (small tetravalent cation), is added to the polymerization buffer at concentration higher than 300 μ M, the light scattering assembly curve reaches a plateau value higher than in the absence of this partner (Fig. 4A). A sample of the polymerization medium imaged by AFM reveals that the presence of spermine promotes the formation of microtubule bundles (Fig. 4B) attributed to an electrostatic interaction between the C-terminal domains of tubulin and the tetravalent cations. The presence of these large structures which have been

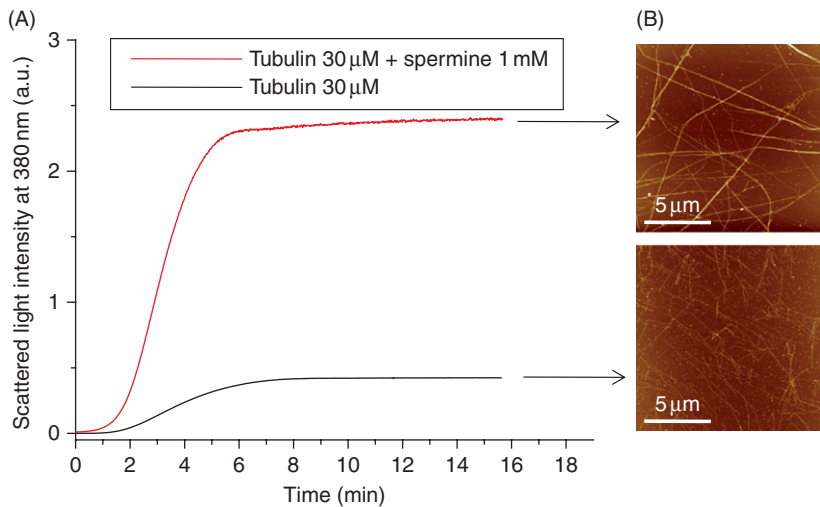


Fig. 4 Effect of spermine on the tubulin polymerization. (A) The presence of polyamine (400 μ M spermine) in the polymerization buffer strongly increases the plateau value as detected by light scattering measurements at 380 nm. (B) In the absence of spermine (bottom), microtubules displayed a normal appearance whereas microtubules formed large bundles in the presence of spermine (top), which explains the higher value of the light scattering plateau data. Z scale of each AFM image: 100 nm.

already observed by transmission electron microscopy using taxol-stabilized microtubules (Needleman *et al.*, 2004) explains the higher plateau value since their presence increases the light scattering intensity compared to isolated microtubules.

C. Intermediate Structures

The elongation rate of microtubules can be very high both *in vitro* and *in vivo*, i.e., about 10 μ m/min (Cassimeris *et al.*, 1988; Odde, 1997). This high rate of elongation is thus not compatible with the long acquisition time per frame of the AFM (larger than 30 s). Consequently, real-time imaging of the microtubule elongation process by AFM in liquid is not so far possible. However, AFM in air can provide information on the intermediate structures during microtubule assembly. To do so, one can take aliquots of the tubulin sample at very short time intervals after sample warming to promote microtubule polymerization and deposit them on mica for imaging in air. Thus, by comparison between each deposited samples, AFM users can detect different populations of intermediate structures and analyze the successive steps of assembly from the early stage of microtubule polymerization (Fig. 5A). It is worth pointing out that coexisting on the surface are different populations ranging from free tubulin, small aggregates or oligomers of various shapes, and long or short microtubules. Nevertheless, the accumulation of scanned area gives sufficient data to evidence the mean structures and their representativeness of the assembly mechanism.

Using the same approach, it is possible to capture the depolymerization intermediates by AFM. After reaching the thermodynamic equilibrium between microtubule assembly and disassembly rates, microtubules are allowed to depolymerize on

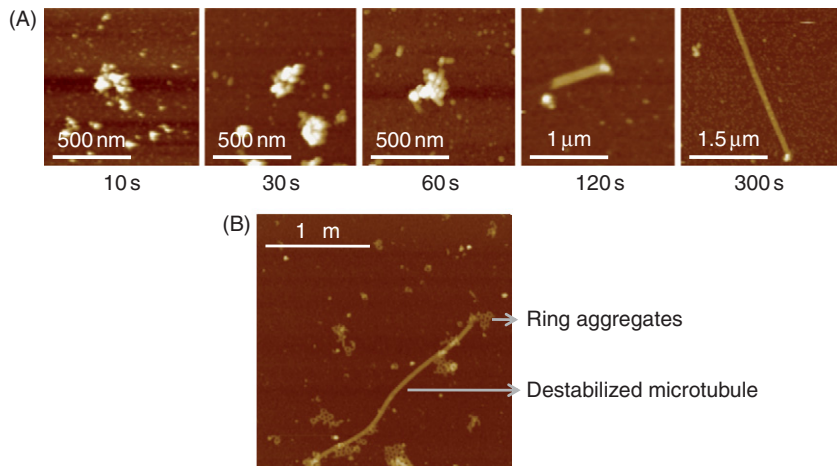


Fig. 5 (A) AFM imaging of intermediate structures of early stage of microtubule assembly. After different times of polymerization (from 10 s to 5 min), an aliquot of the polymerization buffer containing 30 μ M tubulin is deposited on mica surface and imaged after the drying step. Short microtubules emerge from tubulin aggregates. For longer times of polymerization, longer microtubules are polymerized but small aggregates are still present at their extremities. Z scale: 40 nm. (B) AFM imaging of intermediate structures at early stage of microtubule depolymerization. After microtubule polymerization, i.e., at the plateau value of the light scattering curve, the sample is deposited on ice for few seconds (30 s for this image) and an aliquot is immediately transferred on mica for AFM imaging. Destabilized microtubules are decorated by small aggregates of tubulin rings. Z scale: 40 nm.

ice for few seconds and an aliquot is rapidly deposited on mica. The resulting microtubules are then shorter and display at their extremities or along their walls small aggregates of rings (Fig. 5B), which have been already observed using cryo-electron microscopy (Mandelkow *et al.*, 1991).

These two examples of high-resolution imaging of intermediate structures show that AFM imaging in air is a promising tool to explore the mechanisms of microtubule assembly and disassembly without using complex approaches or specific sample preparations.

VI. AFM Imaging in Air of Tubulin or Microtubule:Protein Interactions

Free tubulin and microtubules are known to interact with numerous proteins like microtubule-associated proteins or molecular motor but they are also the target of many drugs which act as microtubule-stabilizing or microtubule-destabilizing agents (taxol, vinblastine, colchicine, etc.). Many experimental approaches are used to study such interactions *in vitro* but high-resolution images by AFM may provide very useful information on both the localization of the partner along the microtubule wall when visible and the impact of these partners on the microtubule structure (bending, bundling, shrinking, aspect of microtubule ends, etc.).

A. Example of Detection of the Interaction Between Tubulin or Microtubules with Protein

The protein YB-1 is involved in a wide variety of cellular processes in eukaryotic cells (Kohno *et al.*, 2003) and, recently, its interaction with tubulin and microtubules has been highlighted (Chernov *et al.*, 2008b). It has been demonstrated that YB-1 strongly favors microtubule assembly *in vitro* by inducing a shortening of the lag time in a dose-dependent manner and an increasing of the apparent rate of assembly. The binding of YB-1 to tubulin is also visualized by AFM by measuring the height of tubulin:YB-1 complexes adsorbed on surface. Particles formed when YB-1 and tubulin are incubated together prior to deposition on mica have an average height of 8 nm, whereas the height of YB-1 and tubulin alone are 0.7 and 4 nm, respectively. It indicates that YB-1 and tubulin interact and form complexes probably made of several molecules of both tubulin and YB-1. As AFM provides a Z resolution in the angstrom range, such height differences are easily detected. Furthermore, the presence of YB-1 during microtubule assembly promotes microtubule formation and reduces Cc while leaving the morphology of microtubule unaltered. Microtubules formed in the presence of YB-1 (Fig. 6B) are also significantly higher than the control ones (Fig. 6A) which could correspond to the coating of the microtubules by YB-1.

A key point when studying only the interaction between microtubules and a biological partner is that the presence of free tubulin can perturb the AFM imaging due to the formation of large complexes or aggregates of tubulin:partner. To avoid these difficulties, after microtubule assembly in presence of the partner, the sample is stabilized with taxol and centrifugated in order to discard free tubulins and small complexes or aggregates before sample deposition on mica. Nevertheless, sometimes partners form with tubulin/microtubules small complexes like tubulin rings and imaging of such intermediary structures is of great interest to decipher the role of partner in microtubule assembly. Consequently, the sample should not be centrifugated; different populations will be adsorbed on the surface as described in Section V.C. and are representative of the composition of the sample.

B. Binding of mRNA to Microtubules Mediated by YB-1

As quoted above, it has been shown recently that YB-1 can interact with microtubules but YB-1 was mainly known to interact with nucleic acids and participate in the formation of mRNPs (Anderson and Kedersha, 2006; Czaplinski and Singer, 2006). The traffic of some of these RNPs in the cytoplasm is mediated by an active transport on the cytoskeleton implying molecular motors. For a maximal efficiency of the transport owing to the frequent detachments of molecular motors from microtubules, these RNPs are thought to stay within a short distance from microtubule and cationic RNP proteins could help to keep them in the vicinity of the anionic microtubule surface. A direct evidence of this mechanism was obtained by imaging mRNPs in interaction with microtubules by AFM (Chernov *et al.*, 2008a). When a sufficient amount of YB-1 is added to a mixture of microtubules and mRNA, RNPs clearly colocalized with microtubules and clustered on microtubule walls (Fig. 6C). As the proportion of YB-1 increased, the cluster appeared larger whereas, in the absence of YB-1, no interaction between RNA and microtubule is detected, as expected for anionic mRNA and microtubules. This shows the promising potential of

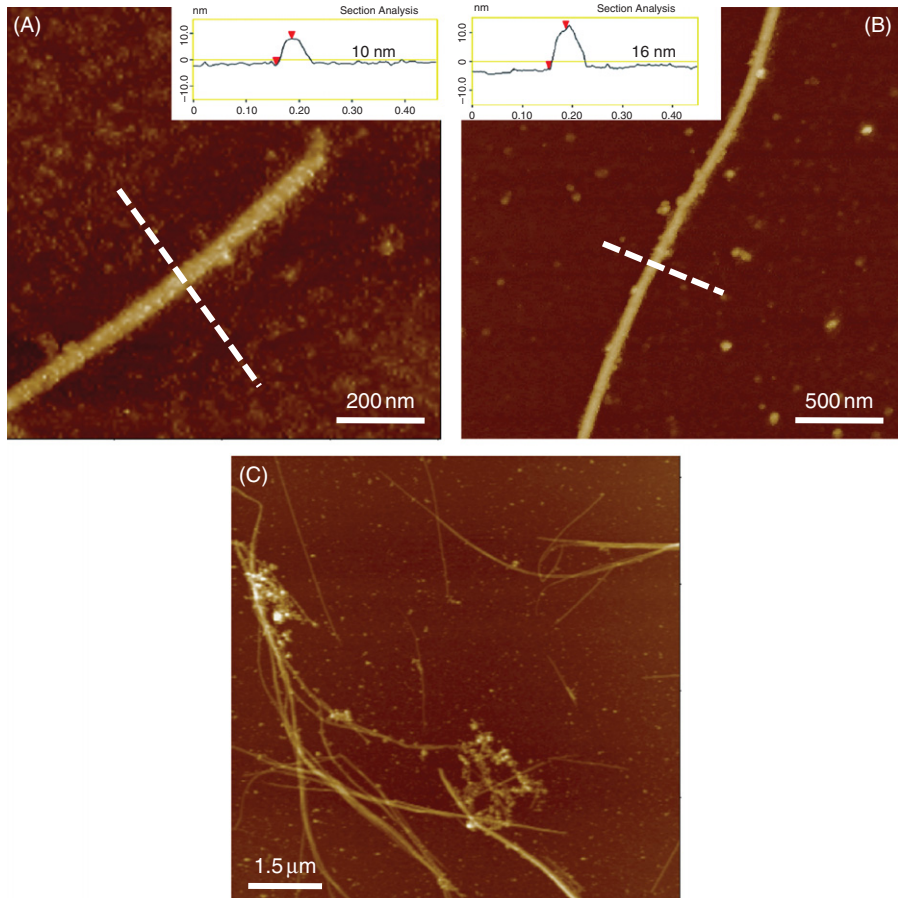


Fig. 6 AFM imaging of microtubule:protein interactions. (A) Taxol-stabilized microtubules present an average height of 10 nm. Z scale: 40 nm. (B) Microtubules assembled in the presence of YB-1 (1:1 molar ratio) and stabilized with taxol have an average height significantly higher than control (A) which could be due to the coating of the microtubule wall by YB-1. Z scale: 40 nm. (C) AFM imaging of ribonucleoprotein particle (RNP):microtubule association. 2Luc messenger ribonucleoprotein particle (5 μ g/mL) and 1.5 μ M YB-1 are first preformed in the polymerization buffer. Then preformed microtubules (20 μ M tubulin) stabilized with taxol (20 μ M) and centrifuged to remove free tubulin are added to the RNP solution. The mixture is incubated for 10 min at 37°C. RNPs clearly colocalize with microtubules and tend to cluster on microtubule walls. Z scale: 100 nm. (See Plate no. 12 in the Color Plate Section.)

AFM for the study of macromolecular assemblies on microtubules when the various partners can be easily distinguished like microtubules, rigid cylinders, long mRNA, extended coil, and YB-1, which appears as a small globule.

===== VII. Conclusion

AFM is a powerful tool to study *in vitro*-isolated biomolecules or microtubules in interaction with partners. It allows microtubule visualization at the single microtubule level and needs only few micrograms of tubulin per sample (10 times less than

a standard light scattering measurement). In less than 10 min, AFM can reveal at high resolution the molecular composition of a microtubule sample (microtubules, free tubulin, bundles, and aggregates). Due to these characteristics, AFM can be used routinely as a control method. In addition, AFM imaging allows the capture of transient states of highly dynamical microtubules like nucleus intermediates or collapsing microtubule ends. Indeed, thanks to the short time required for sample deposition and adsorption on the mica surface, AFM users can capture time lapse images of microtubule assembly or disassembly with a time resolution of less than 30 s. Moreover, the interaction between microtubules and partners can be revealed directly or indirectly by AFM due to its high sensibility in Z. For example, the local increase in height along the microtubule wall informs directly of the presence of a protein partner. The bundling and disruption of microtubules, which could be the indirect consequence of the microtubule:partner interactions, are also easily detected by AFM. Finally, one of the main strengths of biomolecule imaging by AFM is the possibility to image the sample in a liquid environment and to follow its dynamical structural changes. Nevertheless, the scan rates of actual commercial AFM are too slow to follow the mechanism of microtubule assembly at the single microtubule level in real time. In addition the presence of free tubulin coexisting with microtubules in the liquid cell during the scan remains problematic. Therefore, to image microtubules in liquid at high resolution, taxol and/or glutaraldehyde pretreatments are generally required. The captured information is then similar to that obtained by imaging the sample in air after fixation. However, in the last decade, instrumental developments have improved the reliability of the microscope and allowed faster scan rates which open new perspectives to image nonstabilized microtubules interacting with their partners in liquid.

References

Anderson, P., and Kedersha, N. (2006). RNA granules. *J. Cell Biol.* **172**, 803–808.

Ando, T., Kodera, N., Naito, Y., Kinoshita, T., Furuta, K., and Toyoshima, Y. Y. (2003). A high-speed atomic force microscope for studying biological macromolecules in action. *Chemphyschem* **4**, 1196–1202.

Ando, T., Uchihashi, T., Kodera, N., Yamamoto, D., Miyagi, A., Taniguchi, M., and Yamashita, H. (2008). High-speed AFM and nano-visualization of biomolecular processes. *Pflugers Arch* **456**, 211–225.

Binnig, G., Quate, C. F., and Gerber, C. (1986). Atomic force microscope. *Phys. Rev. Lett.* **56**, 930–933.

Bustamante, C., Vesenka, J., Tang, C. L., Rees, W., Guthold, M., and Keller, R. (1992). Circular DNA molecules imaged in air by scanning force microscopy. *Biochemistry* **31**, 22–26.

Cassimeris, L., Pryer, N. K., and Salmon, E. D. (1988). Real-time observations of microtubule dynamic instability in living cells. *J. Cell Biol.* **107**, 2223–2231.

Castoldi, M., and Popov, A. V. (2003). Purification of brain tubulin through two cycles of polymerization-depolymerization in a high-molarity buffer. *Protein Expr. Purif.* **32**, 83–88.

Chernov, K. G., Curmi, P. A., Hamon, L., Mechulam, A., Ovchinnikov, L. P., and Pastre, D. (2008a). Atomic force microscopy reveals binding of mRNA to microtubules mediated by two major mRNP proteins YB-1 and PABP. *FEBS Lett.* **582**, 2875–2881.

Chernov, K. G., Mechulam, A., Popova, N. V., Pastre, D., Nadezhina, E. S., Skabkina, O. V., Shanina, N. A., Vasiliev, V. D., Tarrade, A., Melki, J., Joshi, V., Baconnais, S., Toma, F., Ovchinnikov, L. P., and Curmi, P. A. (2008b). YB-1 promotes microtubule assembly *in vitro* through interaction with tubulin and microtubules. *BMC Biochem.* **9**, 23.

Costa, L. T., Pinto, J. R., Moraes, M. B., de Souza, G. G., Sorenson, M. M., Bisch, P. M., and Weissmuller, G. (2004). Chemical treatment of mica for atomic force microscopy can affect biological sample conformation. *Biophys. Chem.* **109**, 63–71.

Cross, A. R., and Williams, R. C., Jr. (1991). Kinky microtubules: Bending and breaking induced by fixation *in vitro* with glutaraldehyde and formaldehyde. *Cell Motil. Cytoskeleton* **20**, 272–278.

Czaplinski, K., and Singer, R. H. (2006). Pathways for mRNA localization in the cytoplasm. *Trends Biochem. Sci.* **31**, 687–693.

Fritz, M., Radmacher, M., Cleveland, J. P., Allersma, M. W., Stewart, R. J., Gieselman, R., Jamme, P., Schmidt, C. F., and Hansma, P. K. (1995a). Imaging globular and filamentous proteins in physiological buffer solutions with tapping mode atomic force microscopy. *Langmuir* **11**, 3529–3535.

Fritz, M. R., Allersma, M. W., Cleveland, J. P., Stewart, R. J., Hansma, P. K., and Schmidt, C. F. (1995b). Imaging microtubules in buffer solution using tapping mode atomic force microscopy. *Proc. SPIE* **2384**, 150–157.

Hamon, L., Panda, D., Savarin, P., Joshi, V., Bernhard, J., Mucher, E., Mechulam, A., Curmi, P. A., and Pastre, D. (2009). Mica surface promotes the assembly of cytoskeletal proteins. *Langmuir* **25**, 3331–3335.

Hansma, H. G., and Laney, D. E. (1996). DNA binding to mica correlates with cationic radius: Assay by atomic force microscopy. *Biophys. J.* **70**, 1933–1939.

Hoh, J. H., and Schoenenberger, C. A. (1994). Surface morphology and mechanical properties of MDCK monolayers by atomic force microscopy. *J. Cell Sci.* **107**(Pt 5), 1105–1114.

Kacher, C. M., Weiss, I. M., Stewart, R. J., Schmidt, C. F., Hansma, P. K., Radmacher, M., and Fritz, M. (2000). Imaging microtubules and kinesin decorated microtubules using tapping mode atomic force microscopy in fluids. *Eur. Biophys. J.* **28**, 611–620.

Kasas, S., Thomson, N. H., Smith, B. L., Hansma, H. G., Zhu, X., Guthold, M., Bustamante, C., Kool, E. T., Kashlev, M., and Hansma, P. K. (1997). Escherichia coli RNA polymerase activity observed using atomic force microscopy. *Biochemistry* **36**, 461–468.

Kohno, K., Izumi, H., Uchiumi, T., Ashizuka, M., and Kuwano, M. (2003). The pleiotropic functions of the Y-box-binding protein, YB-1. *Bioessays* **25**, 691–698.

Lyubchenko, Y. L., Jacobs, B. L., and Lindsay, S. M. (1992). Atomic force microscopy of reovirus dsRNA: A routine technique for length measurements. *Nucleic Acids Res.* **20**, 3983–3986.

Makrides, V., Shen, T. E., Bhatia, R., Smith, B. L., Thimm, J., Lal, R., and Feinstein, S. C. (2003). Microtubule-dependent oligomerization of tau. Implications for physiological tau function and tauopathies. *J. Biol. Chem.* **278**, 33298–33304.

Mandelkow, E. M., Mandelkow, E., and Milligan, R. A. (1991). Microtubule dynamics and microtubule caps: A time-resolved cryo-electron microscopy study. *J. Cell Biol.* **114**, 977–991.

Mechulam, A., Chernov, K. G., Mucher, E., Hamon, L., Curmi, P. A., and Pastre, D. (2009). Polyamine sharing between tubulin dimers favours microtubule nucleation and elongation via facilitated diffusion. *PLoS Comput. Biol.* **5**, e1000255.

Munson, K. M., Mulugeta, P. G., and Donhauser, Z. J. (2007). Enhanced mechanical stability of microtubules polymerized with a slowly hydrolyzable nucleotide analogue. *J. Phys. Chem. B* **111**, 5053–5057.

Needleman, D. J., Ojeda-Lopez, M. A., Raviv, U., Miller, H. P., Wilson, L., and Safinya, C. R. (2004). Higher-order assembly of microtubules by counterions: From hexagonal bundles to living necklaces. *Proc. Natl. Acad. Sci. U. S.A.* **101**, 16099–16103.

Odde, D. J. (1997). Estimation of the diffusion-limited rate of microtubule assembly. *Biophys. J.* **73**, 88–96.

Pastré, D., Hamon, L., Landousy, F., Sorel, I., David, M. O., Zozime, A., Le Cam, E., and Pietrement, O. (2006). Anionic polyelectrolyte adsorption on mica mediated by multivalent cations: A solution to DNA imaging by atomic force microscopy under high ionic strengths. *Langmuir* **22**, 6651–6660.

Revet, B., and Fourcade, A. (1998). Short unligated sticky ends enable the observation of circularised DNA by atomic force and electron microscopies. *Nucleic Acids Res.* **26**, 2092–2097.

Schaap, I. A., Hoffmann, B., Carrasco, C., Merkel, R., and Schmidt, C. F. (2007). Tau protein binding forms a 1 nm thick layer along protofilaments without affecting the radial elasticity of microtubules. *J. Struct. Biol.* **158**, 282–292.

Sorel, I., Pietrement, O., Hamon, L., Baconnais, S., Cam, E. L., and Pastre, D. (2006). The EcoRI-DNA complex as a model for investigating protein-DNA interactions by atomic force microscopy. *Biochemistry* **45**, 14675–14682.

Vandebroek, T., Terwel, D., Vanhelmont, T., Gysemans, M., Van Haesendonck, C., Engelborghs, Y., Winderickx, J., and Van Leuven, F. (2006). Microtubule binding and clustering of human Tau-4R and Tau-P301L proteins isolated from yeast deficient in orthologues of glycogen synthase kinase-3beta or cdk5. *J. Biol. Chem.* **281**, 25388–25397.

Vater, W., Fritzsche, W., Schaper, A., Bohm, K. J., Unger, E., and Jovin, T. M. (1995). Scanning force microscopy of microtubules and polymorphic tubulin assemblies in air and in liquid. *J. Cell Sci.* **108**(Pt 3), 1063–1069.

Vinckier, A., Heyvaert, I., D'Hoore, A., McKittrick, T., Van Haesendonck, C., Engelborghs, Y., and Hellemans, L. (1995). Immobilizing and imaging microtubules by atomic force microscopy. *Ultra-microscopy* **57**, 337–343.

Wagner, P. (1998). Immobilization strategies for biological scanning probe microscopy. *FEBS Lett.* **430**, 112–115.

CHAPTER 10

Using Computational Modeling to Understand Microtubule Dynamics: A Primer for Cell Biologists

Holly V. Goodson* and Ivan V. Gregoretti†

*Department of Chemistry and Biochemistry, The Center for the Study of Biocomplexity, University of Notre Dame, Notre Dame, Indiana 46556

†National Institute of Diabetes and Digestive and Kidney Diseases, National Institutes of Health, Bethesda, Maryland 20892

Abstract

- I. Introduction
- II. Mathematical and Computational Modeling: A Primer
 - A. Mathematical Modeling
 - B. Computational Modeling
 - C. When to Use Deterministic Versus Stochastic Models?
 - D. Other Considerations in Building and Using Models
 - E. How Can Models Provide Insight into Cell Biology?
- III. Using Modeling to Understand Microtubule Dynamics
 - A. Deterministic Models of Microtubule Behavior
 - B. Stochastic Models of Microtubule Dynamics: General Considerations
 - C. Using Stochastic Modeling to Investigate Microtubule Dynamics: Some Examples
- IV. Conclusions
- References

Abstract

Experimental cell biology, biochemistry, and structural biology have provided a wealth of information about microtubule function and mechanism, but we are reaching a limit as to what can be understood from experiment alone. Standard biochemical approaches are not sufficient to make quantitative predictions about

microtubule behavior, and they are limited in their ability to test existing conceptual models of microtubule mechanism. Because microtubules are so complex, achieving a deep understanding of microtubule behavior and mechanism will require the input of mathematical and computational modeling. However, this type of analysis can be daunting to the uninitiated. The purpose of this chapter is to provide a straightforward introduction to the various types of modeling and how they can be used to study microtubule function, dynamics, and mechanism.

===== I. Introduction

The process of microtubule assembly and disassembly has been a subject of intense investigation since tubulin was identified in the late 1960s. Cell biology textbooks now lay out clear summaries of the results of these efforts, stating that microtubules *in vivo* and *in vitro* undergo dynamic instability, that this behavior is an outcome of conformational changes associated with guanosine triphosphate (GTP) hydrolysis, and that it is functionally important for both capturing cargo and cytoskeletal remodeling. On the basis of these achievements, one might think that microtubule polymerization behavior is well understood. Surprisingly, one needs only to ask a few simple questions to realize how incomplete this understanding is. Consider, for example, an experiment where a given amount of tubulin is polymerized. How much polymer will be produced? How many microtubules will result, how long will they be, and what will be their dynamic instability parameters? How will the answers change with time? Perhaps most importantly, how will the system be altered by the presence of microtubule-binding proteins (MTBPs)?

For many of these questions, it is easy to intuitively arrive at qualitative answers: more polymer, less polymer, etc. What is missing is our ability to make *quantitative* predictions. Without these quantitative predictions, it is difficult to test the prevailing conceptual models against experiment. Moreover, even qualitative predictions become challenging in some apparently straightforward situations. For example, consider adding to an *in vitro* dynamic instability assay a MTBP that has been experimentally demonstrated to suppress catastrophe at 10 μM tubulin. What will happen to the dynamic instability parameters when the system reaches steady state? The quick response is “it will still reduce catastrophe,” but this might not be correct. A protein that reduces catastrophe will likely reduce the steady-state concentration of free tubulin. It is impossible to predict the effect of this protein on catastrophe at this new steady-state tubulin concentration. Moreover, such a protein might even have the counterintuitive effect of reducing rescue or the rate of growth simply as a result of reducing the steady-state tubulin concentration.

The classical approach to establishing these relationships would be to do more experiments. However, while experiments are essential, they will not be sufficient. For example, in the case of the catastrophe-promoting MTBP outlined above, we could measure the dynamic instability parameters at various concentrations of tubulin and MTBPs, but it quickly becomes apparent that it would be highly impractical to do enough experiments to map out the full set of relationships for even a single MTBP. Ideally, we would like to predict effects on dynamic instability from quantitative data on microtubule–MTBP interactions, but it is unclear how to

develop these relationships. Arriving at answers to these problems is difficult because a solution of dynamic microtubules is a complex *system* of many interacting parts. Standard biochemical approaches based on consideration of single interactions simply are not capable of considering these multiple interactions. To predict microtubule assembly behavior, one needs approaches capable of considering the simultaneous and interconnected nature of the various events that occur in a system of dynamic microtubules. Such system-level problems require system-level approaches, i.e., mathematical and computational modeling.

In this chapter, we will discuss how mathematical and computational modeling can be used to understand microtubule behavior, but before getting to this, we will introduce readers to the basic types of modeling and their applications. The focus here will be on helping readers develop an intuitive understanding of when and how to use these approaches; the practical aspects of writing and using the programs will be the focus of articles written elsewhere.

===== II. Mathematical and Computational Modeling: A Primer

A. Mathematical Modeling

Mathematical and computational modeling might seem to be two different approaches, but as discussed below, computational modeling is a subset of mathematical modeling. They may sound intimidating, but most cell biologists have used these approaches without realizing it. In mathematical modeling, a researcher uses equations or sets of linked equations to predict the behavior of a system. Familiar mathematical models of the physical world include $F = ma$ (force = mass \times acceleration) and $V = IR$ (voltage = current \times resistance). Of course, these two equations are now recognized as “facts,” but they started out as mathematical models of physical relationships developed through a combination of experimental data and logic, similar to the way that models of biological systems are now being derived. Equally, biochemists perform mathematical modeling when they use the Michaelis–Menten equation to analyze enzyme–substrate reactions. The Michaelis–Menten equation has been profoundly useful in predicting the rates of enzyme-catalyzed reactions as a function of substrate concentration, and it is one of the primary tools used to dissect any new enzyme-catalyzed reaction. To understand how mathematical modeling can be used in microtubule dynamics, it is worthwhile to briefly consider the Michaelis–Menten equation: $V = (k_{\text{cat}} \times E_t)[S]/(K_M + [S])$.

This equation was derived by first writing down the various chemical equations that constitute the individual steps of an enzyme-catalyzed reaction, then writing down the kinetic equations that describe these steps, and then trying to connect these differential equations into a unified expression relating reaction velocities to starting concentrations. However, as anyone will find by trying to repeat this process, it gets very complicated very quickly: when the Michaelis–Menten equation was derived, a number of assumptions were made so that the mathematics could be simplified. The details of these assumptions are not relevant here (they can be found in any biochemistry book), but what *is* relevant is to understand both that *multiple assumptions were necessary to derive this simple equation* and that

for this equation to be valid, these assumptions must be met. We will return to the issue of assumptions in modeling below, because understanding the existence and implications of the necessary assumptions is essential to utilizing any model and interpreting its results.

A key aspect of many mathematical models such as the Michaelis–Menten equation is that they are *deterministic*—given the same starting condition, they will always produce the same result. The standard equations used in introductory science courses ($F = ma$, $\Delta G = \Delta H - T\Delta S$) are all deterministic mathematical models of the system at hand. One important thing to realize about deterministic mathematical models is that they are often best utilized for studying and predicting the behavior of *large populations*, be they populations of proteins, cells, or organisms. While individual behaviors vary and are thus difficult to predict precisely, these variations average out when the population is considered as a whole, and so the behavior of the population can be predicted unambiguously. A familiar example is radioactive decay—it is impossible to know when a particular atom will disintegrate, but the behavior of a population of molecules of any radioisotope can be precisely predicted simply by knowing the half-life.

B. Computational Modeling

With computational modeling, it is obvious that a computer is employed. Sometimes, the computer is used to solve or otherwise explore deterministic mathematical models, which can get very complex when systems of linked equations are involved. Anyone who has used a curve-fitting program to plot a theoretical binding curve has used computational modeling of this type: it could be done by hand, but it would get very tiresome. Similarly, a biochemist uses computational modeling when fitting data to the Michaelis–Menten equation. Molecular dynamics are another example of deterministic modeling done with computers. In molecular dynamics simulations, the behavior of a collection of atoms (usually a macromolecule) is studied by repetitively computing Newton's equations of motion.

While it is common to use computers to analyze deterministic mathematical models, the phrase “computational modeling” often refers specifically to non-deterministic or “stochastic” modeling. A stochastic mathematical model differs from a deterministic model only in that some aspect of randomness is integrated into the equations describing the system. Instead of being deterministic, a stochastic model is *probabilistic*—the equations in the model do not dictate what will happen but the *probability* that something will happen. Because they incorporate randomness, stochastic models are often called “Monte Carlo models” in reference to the historic gambling capital. Stochastic modeling usually requires computers because it is normally necessary to run the model many times in order to examine a sufficiently large number of events. For example, we can imagine a stochastic computational model built to predict how many molecules of a rare transcription factor are bound to their targets at a given time in the nucleus of a single cell. Each time the model is run, the researcher will obtain a different answer (number of molecules). However, in running the model many times the researcher finds the distribution of answers with all the associated power of statistics.

C. When to Use Deterministic Versus Stochastic Models?

As noted above, deterministic models are good for describing the behavior of large populations of entities (e.g., the decay of a macroscopic amount of a radioisotope), while stochastic models are often better at describing the behavior of the individual entities in the system (e.g., the decay of individual atoms of the radioisotope). However, these are not hard and fast rules. Deterministic modeling is ideal when it is possible, because it gives unambiguous answers and can be very fast. However, many systems are simply too complex, too “noisy,” too sensitive, or too poorly understood for useful deterministic models to exist. In these cases, stochastic models can sometimes be used to predict the behavior of a population on the basis of the characteristics of its individual components. This can be very important when it is simply impossible to predict the population-level behavior of a system on the basis of first principles. A familiar example of a system that is unapproachable deterministically but approachable via stochastic modeling is weather forecasting (Lorenz, 1996). As explained more below, stochastic modeling is similarly important for studying microtubule dynamics.

In summary, deterministic modeling is a “top-down” approach in which one discerns the behavior of the system by considering the behavior of populations of molecules (or other entities) as they proceed through individual steps in a process. Stochastic modeling is a “bottom up” approach in which one considers the behavior of individual molecules (entities), and adds up the sum of these behaviors to get the behavior of the population. If one has sufficient understanding of a system, stochastic modeling of large numbers of individuals will converge to the same answers obtained by deterministic modeling of the population. The observation of such convergence is strong evidence that understanding is becoming deep. An example of such convergence can be found in the congruence between the conclusions of statistical mechanics and classical thermodynamics.

D. Other Considerations in Building and Using Models

In any attempt to model a biological process, it is important to use the appropriate level of detail. How does one determine the appropriate scale? Atoms? Molecules? Groups of molecules? Cells? It might seem like more detail is always better, but more detail also requires more computational power, and eventually, additional detail is irrelevant. For example, consideration of quantum mechanics will add little (other than time) to a simulation of actin polymerization in cell migration. On the other hand, insufficient detail can give very misleading results. Generally speaking, a reasonable starting point is to consider the conceptual model on which the computational model is based, then use the “units” in this model as the units of the computational model. Thus, in considering actin polymerization, the unit would be the actin monomer. By contrast, when studying the cross-linking of actin filaments, one could probably simulate actin at the level of filaments or filament segments. The level of detail (in the language of modeling, the level of “coarse-graining” or “fine-graining”) is then adjusted depending on the goals of the model, and whether in initial trials it achieves these goals. Often, as understanding of a system matures, researchers will make multiple models of the system, each at a different scale, and each specialized to address a particular question. Such “multi-scale models” can be extremely powerful in their ability to provide a predictive understanding of a system.

A closely related issue is that in any model, there are assumptions. In some models (the most useful ones), the assumptions are explicitly stated, straightforward in their implications, and biologically reasonable. For example, the Michaelis–Menten model of enzyme kinetics assumes that the system is at steady state, i.e., that the concentration of the intermediates is unchanging. This assumption was essential to simplify the math so that the equation could be derived, but it is also biologically justifiable: any biochemist knows what steady state means and how to experimentally achieve this state. Unfortunately, simplifications that are mathematically or computationally expedient often have biological implications that are hard to fathom. This difficulty can arise from the complexity of the equations or from the fact that the biological system is poorly understood. All too frequently, important assumptions are buried in math so that biologists reading about the model do not even know that they exist. These issues significantly impair the utility of a model and the validity of any conclusions drawn from it. Because relatively few individuals are able to do both the modeling work and understand the biology, modeling is often a collaborative effort. *It is the responsibility of the biologists in these efforts and in the community at large to demand that assumptions of models be both explicit and biologically justifiable.* Unfortunately, a statement that is clear to mathematicians can be opaque to biologists (ourselves included); the reverse is also true. Working through the assumptions of a model and their implications can take considerable effort and patience on both sides, but it is both necessary and ultimately rewarding.

E. How Can Models Provide Insight into Cell Biology?

Given these basic descriptions of mathematical and computational modeling, one can start to see how they can be useful in understanding biological systems. First, one can use models to test present understanding of the system. If one builds a model based on the existing knowledge, and it does not produce the observed behavior, then either there is a mistake in the model or the present understanding is wrong. In this way, the mere attempt to build a model can be informative: once simple mistakes are ruled out, such inconsistencies call for both new hypotheses and new experiments to test the hypotheses. Thus, models can be used to tune understanding and direct experiment. Second, once a reasonable model exists, it can be an excellent teaching tool for helping researchers and students gain an intuitive understanding of their system. The human mind often has trouble considering more than one variable at a time, and training intuition through experiment requires time and resources. Computer models can allow one to see in seconds the results of experiments that would be impractical or even impossible in real life. Returning to the Michaelis–Menten example, what would happen to the reaction velocity if the concentration of substrate were increased 10-fold? One might intuitively expect that it would also increase 10-fold, but work with the equation shown above quickly shows that this would be true only at low substrate concentrations: if the substrate concentration started out high ($>>K_m$), further increase in substrate concentration would have little effect. A final reason to use modeling is that once the model is sufficiently well verified, it can be used to predict behavior in biotechnological, engineering, or medical contexts. Medical examples that are currently in use range from pharmacokinetic models of drug metabolism that help doctors determine proper drug dosing (Huang *et al.*, 2009) to epidemiological models that helped determine government

response to the recent H1N1 flu outbreak (Coburn *et al.*, 2009). Computer simulations are even being used to train doctors in treating patients (Weinberg *et al.*, 2009).

In considering how to use modeling in cell biology, it is important to emphasize that there are two basic classes of models. The most familiar models are those that expect to simulate reality, i.e., to quantitatively replicate and/or predict the behavior of the living system. Such models are extremely useful, but to fully achieve this goal of quantitative recapitulation, the model needs to be both conceptually complete and mathematically accurate—it needs to incorporate all the relevant variables, it needs to have an accurate representation of the relationships between them, and it needs to have a nearly complete set of quantitative values for the various constants. Since such complete description rarely exists in biological systems more complex than protein–ligand interactions, one might argue that modeling has little place in biology until such complete descriptions are possible. However, the medical examples given above emphasize that incomplete models can have great practical utility as long as the researchers using these models are mindful of their assumptions and limitations.

In addition, there is another class of useful models, which we will call “proof of principle” models. In proof-of-principle modeling, the researcher uses his/her present understanding to put together a hypothetical set of rules governing the interactions in the system, and tests whether the set of rules *can* give rise to the behavior in question. Observation that the behavior can be achieved by these rules does not “prove” that these rules govern the real system, but it is consistent with this hypothesis; failure to achieve the behavior would be strong evidence that the set of rules is incomplete and so should be revised. Very often, models properly predict behavior under some conditions and not under others, helping to direct researchers toward the necessary improvements in the model (and thus in understanding). By iterated simulation and experimentation, understanding of the system can be expanded and matured. In a broader way, proof-of-principle simulations can also be used to design biotechnological systems that might not exist in nature but could potentially have practical applications. Recent examples include the rational design of networks of transcription regulators (Ajo-Franklin *et al.*, 2007; Elowitz and Leibler, 2000).

III. Using Modeling to Understand Microtubule Dynamics

A. Deterministic Models of Microtubule Behavior

Given the success of the Michaelis–Menten equation, it seems obvious that it would be useful to have a similar equation describing at least some basic aspects of microtubule behavior. Not surprisingly, there have been many attempts to arrive at such equations. The first attempts, made in the mid-1970s, were based on Oosawa’s analysis of the behavior of equilibrium polymers, i.e., polymers that assemble to the point where there is a thermodynamic equilibrium between polymers and the constituent subunits (Oosawa and Asakura, 1975; Oosawa and Kasai, 1962). Oosawa utilized logic similar to that used in deriving the Michaelis–Menten equation to derive a set of equations describing the relationship between the amount of starting subunit and the amount of polymer at equilibrium. His work explained the somewhat counterintuitive observation that such polymers have a “critical concentration,” which is both the concentration of subunit needed to obtain significant amounts of

polymer and the concentration of subunit present at equilibrium no matter how much subunit you start with.

These Oosawa equations, especially as reworked and interpreted by Johnson and Borisy (Johnson and Borisy, 1975, 1977; Johnson and Borisy, 1979, see also Howard, 2001), properly predicted a number of aspects of tubulin assembly, including the existence of a critical concentration, and to this day, they remain the main framework for predicting tubulin assembly. However, a key assumption of building these equations was that the polymer system was *at equilibrium*. This assumption is invalid: when a solution of tubulin and GTP assembles to a maximum, it is instead at *steady state*—even when the population of polymer has achieved a maximum and is unchanging, energy is flowing through the system in the form of GTP hydrolysis.¹ Because of this inaccuracy, the Oosawa model is very limited in its ability to describe tubulin behavior. In particular, it is inconsistent with dynamic instability and so fails to predict behavior at the level of individual polymers, but it also fails in describing some population-level attributes such as quantitative predictions of the critical concentration.

However imperfect the Oosawa model is, it has thus far proven surprisingly difficult to derive a practically useful set of equations that describe microtubule polymerization in a more accurate way. Why? The lack of success is not due to lack of effort (e.g., Flyvbjerg *et al.*, 1996; Freed, 2002; Margolin *et al.*, 2006; Mitchison and Kirschner, 1987) but to the additional complexity engendered by the nonequilibrium nature of microtubule polymerization. When attempts have been made to derive improved models, they have either been so complex or required so many simplifying assumptions (some biologically questionable) that they have been of limited utility. In summary, there are good mathematical models of equilibrium polymers, but microtubules are not equilibrium polymers, and the complexity introduced by the flow of energy through the system has thus far made it difficult to derive a more precise set of relationships for microtubule assembly from first principles and logic alone. Consideration of MTBPs makes the problem even more difficult. These observations suggest that in the near term, the greatest progress in quantitatively predicting tubulin behavior will come from stochastic models, specifically from models where distinct particles and the multiplicity of the interactions are modeled from the ground up.

B. Stochastic Models of Microtubule Dynamics: General Considerations

Because dynamic instability occurs at the level of individual microtubules, and because the transitions occur randomly, it is intuitively reasonable that stochastic models would be useful for studying dynamic instability. Indeed, it is easy to imagine making a model in which “microtubules” are modeled as simple lines that grow and shrink according to experimentally determined rates, and undergo random transitions with average frequencies that match those in experiment. However, while

¹ Many people mistakenly consider steady state and equilibrium to be equivalent because in both cases, the concentration of polymer is not changing. The easiest way to distinguish the two is to remember that living (adult) organisms are at steady state, but George Washington (dead for > 200 years) has probably achieved equilibrium. Similarly, a system of tubulin + GTP does not achieve equilibrium until all of the GTP is hydrolyzed.

such a model could be useful in studying how dynamic instability influences other processes (e.g., a researcher could vary the dynamic instability parameters to see how organelle capture is affected), it would provide little insight into dynamic instability itself because the researcher has dictated all of microtubule behavior. To study the mechanism of dynamic instability, one must make the model more “fine-grained”—more detailed—so that the standard dynamic instability behaviors emerge from the sum of more microscopic events in the model. In other words, the researcher must make a model that considers the biochemistry underlying tubulin polymerization: subunit addition and detachment, bond breaking, bond formation, and GTP hydrolysis. In such a model, as in real reactions, these biochemical processes are not governed by deterministic rate constants but by probabilities, where the rate constants we are familiar with grow out of the probabilistic behavior of individual molecules. Depending on the goals of the model, the modeler may choose to include other influences on these biochemical processes, e.g., physical strain due to the conformation of the tip (Howard, 2001), but a model incorporating these basic biochemical processes is a starting point.

One of the major challenges of making a model with this level of detail is that the kinetic constants governing the various processes are in most cases unknown. To deal with this problem, the researcher typically uses data to put limits on the possible values (e.g., the GTPase of polymerized bovine brain tubulin is faster than 0.1/s), and then lets the computer explore values within this range to find the value that best fits the data. This approach can be a powerful way not only to build a model, but also to arrive at predictions for otherwise unknown biochemical parameters. Examples where this has been done for aspects of microtubule biochemistry include [Odde, 1997](#); [VanBuren *et al.*, 2002](#). However, this approach is often not as straightforward as it sounds—in almost any reasonably detailed model of microtubule dynamics, there are too many unknown parameters to conduct an exhaustive exploration of the possible parameter space. Moreover, even if one could conduct an exhaustive search, it is likely that the results would predict ranges of values, not specific values, simply because there are too many degrees of freedom. In these cases, the researcher has to pick a set of parameter values to work with, tuning this set as more data are obtained. In these situations, it is important that the modeler differentiate (in both writing and thinking) these arbitrarily chosen or “guesstimated” parameter values from the more strongly “predicted” parameter values. It is also crucial that the modeler test different parameter sets to make sure that any conclusions derived from the model are not “parameter-specific.” Fortunately, there are many strategies to assess robustness (see [Saltelli *et al.*, 2008](#)).

Another challenge that arises when it becomes clear that “more detail” is desired is to determine the right level of detail. Even a process as simple as “binding” contains hidden complexity when it is part of tubulin polymerization: a tubulin dimer in a microtubule participates in at least four bonds with other dimers above, below, and at the two sides. Of course, these bonds themselves consist of multiple smaller scale interactions. Do you, as a modeler, decide to “coarsen” your simulation and consider binding as one event? If so, it would allow the model to run much faster, which might be necessary if the microtubules are to be modeled as part of a larger system. Or, do you add the additional detail of considering the various lateral and longitudinal bonds separately and including the multiple conformational states of the heterodimers? This type of model would be more appropriate for investigations of

the mechanism of dynamic instability, but it might be impractically slow for some applications. There is no straightforward way to answer this question. Just as wet-lab experiments usually require trial and error, it may be necessary to build multiple iterations of a model in order to determine the right level of detail.

C. Using Stochastic Modeling to Investigate Microtubule Dynamics: Some Examples

The easiest way to see how modeling can be used to understand microtubule dynamics is to discuss a few examples out of the wide array of stochastic microtubule modeling that has been performed. The existing models have tended to fall into one of three classes of detail. For the purpose of discussion, we will refer to these models here as “class 1,” “class 2,” and “class 3.” At one end of the scale are the class 1 models, in which microtubules are modeled at the level of filaments, and their behavior (transition frequencies, growth and depolymerization rates) is directly imposed (set) by the modeler. These class 1 models have been very useful for investigating the *function* of microtubule dynamics. As one example, Holy and Leibler used a class 1 model to provide evidence that one of the main purposes of microtubule dynamics is to allow microtubules to explore space (Holy and Leibler, 1994). In studying this question, they set the level of dynamics to different values, and showed that the likelihood of interaction between chromosomes and microtubules depended on having a sufficiently high rate of dynamic instability. Another example was provided by Glicksman and colleagues, who used a similar model to examine how changes in dynamic instability parameters that occur at the transitions between interphase and mitosis relate to differences between the interphase and mitotic microtubule arrays (Glicksman *et al.*, 1993). These examples highlight nicely how more detail is not necessarily better—a simple model in which the dynamics of the filaments are set by the modeler can be ideal for addressing the question at hand.

At the opposite end of the detail spectrum are what we will call the class 2 models, which investigate the *mechanism* of microtubule dynamics. These class 2 models differ from class 1 models not only in that they are more detailed (class 2 models usually work at the level of attachment and detachment of individual dimers) but also in the origin of the dynamic instability parameters: in class 2 models, the dynamic instability parameters evolve from the sum of the other events in the model instead of being set by the modeler. However, while class 2 models have in common the feature of trying to model microtubule polymerization at the level of microscopic biochemical processes, they differ, sometimes dramatically, in how they are built, both in the level of detail and in the rules and assumptions governing assembly of the modeled microtubule. For example, some models have been built under the assumption that the microtubule is a 5-start helix (Bayley *et al.*, 1989; Chen and Hill, 1985), while others have used a linear protofilament-based structure (VanBuren *et al.*, 2005, 2002). Some have assumed that GTP hydrolysis is a stochastic process governed by a rate constant (Chen and Hill, 1985; VanBuren *et al.*, 2005, 2002), while others have assumed that it is tightly coupled to assembly (Bayley *et al.*, 1989, 1990; Martin *et al.*, 1993). As one might expect, these models arrive at rather different predictions for the structure of the cap.

Remarkably, even though the models cited above differ in fundamental ways, they have been able to recapitulate aspects of dynamic instability. How is an

experimentalist supposed to decide which one of these conflicting models, if any, best reflects reality? First, since so many biochemical aspects of microtubule dynamics are as yet unknown, it is important to remember that all models of microtubule dynamics produced thus far are proof-of-principle models: they show that the given mechanism *could* give rise to behavior like dynamic instability, and what the cap *might* look like.

To proceed further in investigating which of a set of models is most likely to reflect reality, one should, as a first approach, see whether any of the models have assumptions that are inconsistent with data. For example, the original stochastic model of Hill and Chen required what are now known to be nonphysiological helical interactions between tubulin subunits (Chen and Hill, 1985). Though models with incorrect assumptions like this might have utility in some contexts, the nature of these assumptions ultimately limits their ability to provide information on the structure of the stabilizing cap or the mechanism of dynamic instability.

Then, if a model's mechanism is biochemically and structurally plausible, the next approach is to see how well its behavior fits experimental data. In thinking about this, it is important to remember that in almost any reasonably detailed model of microtubule dynamics, there will be many parameters (kinetic constants, etc.) whose values are as yet unknown and so must be "fit" (varied by the computer). The more free parameters there are, the easier it is to fit *any* model to the data.² For a model to provide convincing evidence that its mechanism has relevance to *the* mechanism, it must replicate experimental data over a range of conditions, the more the better. The observation that fundamentally different models appear to explain the existing data equally well shows that we do not yet have enough data to rule out the inconsistent models. Does this mean that modeling as yet has no utility in studying the mechanism of dynamic instability? On the contrary, it shows how important modeling is in helping to direct experiment. Resolution of the mechanism of dynamic instability will result from modelers and experimentalists getting together and iteratively going through a process of designing experiments to test the models, tuning the models to be consistent with the new data, and designing more experiments.

Thus far, we have discussed class 1 and class 2 models. The third class of models is a hybrid of the first two in that the modeler simulates a class 2 *system* of dynamic microtubules. A key aspect of a class 3 model is that in these simulations, the microtubules *compete for the same pool of tubulin*. This approach allows the modeler to investigate how characteristics of the system (e.g., the number of microtubules, presence of physical constraints, the mass of total tubulin) affect the behavior of the individual microtubules (Gregoretti *et al.*, 2006). Many people are confused about why a class 3 model would give answers different from those obtained by simply running a class 2 model multiple times. The reason is that in a class 2 model, the concentration of free tubulin is locked to a particular value, but in a class 3 model, it is free to evolve as a function of the interaction of the parts of the model. This is a fundamentally important distinction because dynamic instability parameters depend on the concentration of free tubulin.

To explain this difference more clearly, imagine the following pair of otherwise identical simulations “*a*” (class 2) and “*b*” (class 3). In both *a* and *b*, there are 100

² von Neumann may have said it best: “With four parameters I can fit an elephant, and with five I can make him wiggle his trunk.” (As cited in Dyson, 2004).

microtubules and the concentration of tubulin is initially set to 20 μM . However, in *a* the concentration remains locked at 20 μM for the entirety of the simulation (because it is a class 2 simulation), while in *b*, the microtubules compete for the common pool of tubulin, and so the concentration drops as the simulation proceeds. This distinction produces a dramatic difference in behavior: In *a*, the mass of polymer will steadily increase until the simulation is stopped because 20 μM is above the transition to unbounded growth (for a discussion of bounded vs unbounded growth, see Verde *et al.*, 1992; Gregoretti *et al.*, 2006). In *b*, the microtubules will undergo an initial burst of growth when the concentration of tubulin is high and near 20 μM , but their growth will slow as free tubulin is depleted, and it will eventually evolve to a steady state in which the mass of polymer has reached a maximum and the concentration of tubulin has fallen to the critical concentration. Consideration of this example shows why both class 2 and class 3 models are needed to investigate and understand microtubule behavior: class 2 models are appropriate for comparison to experimental situations in which the concentration of free tubulin is known, i.e., *in vitro* early pre-steady state. However, class 3 models are required to investigate any situation in which the concentration of free tubulin changes with time or as a function of the environment. Thus, class 3 models will be very important for understanding how MTBPs affect microtubules in cells or in *in vitro* experiments at steady state.

There are relatively few examples of class 3 models thus far, in part because the computational intensity needed to simulate a system of many detailed microtubules in parallel. We used a simplified class 3 model to investigate how environmental variables such as the size of the cell impact the behavior of a system of dynamic microtubules (Gregoretti *et al.*, 2006). This experience was for us a remarkable example of how modeling can improve understanding: by playing (quite literally) with the model, we were able to realize that several initially surprising behaviors of the microtubule cytoskeleton are in fact predictable outcomes of the interactions between a system of dynamic microtubules and its environment. Specific examples include the persistent growth of microtubules in interphase (this is a predictable outcome of having sufficient tubulin in a confined space), the increase in dynamics at mitosis (this is expected from the mitotic increase in nucleation), and the observation that mutations in the microtubule nucleation machinery are associated with “defects” in microtubule plus-end behavior (when the number of microtubules is reduced, the natural length of the remaining microtubules increases). Most of these conclusions are obvious in retrospect, but it was only the process of tuning our intuition through work with the models that caused us to think about these relationships. Because there are many counterintuitive aspects to systems of dynamic microtubules, we are presently designing an online version of this model so that users at remote sites can use this model to develop their own intuition. We encourage the readers to take advantage of this and other similar modeling resources as they come online.

IV. Conclusions

In this brief primer, we have attempted to provide an introduction to the main types of modeling and how they can be used to investigate microtubule mechanism and behavior. It is important that microtubule biologists familiarize themselves with

modeling because the field is nearing the limit of what can be understood by experiment alone: even a simple solution of tubulin and GTP is a complex system that cannot be predicted by standard biochemical approaches. Already, modeling has been used to address basic questions like the function of dynamic instability and the mechanism of persistent microtubule growth *in vivo*. In the near future, iterative modeling and experiment will be required to dissect the mechanism of dynamic instability and its alteration by MTBPs. Success in these efforts will require intimate collaboration between the biological and modeling communities. We hope that this chapter will provide biologists with the foundation for interpreting the modeling literature and encourage them to utilize modeling in their own work.

References

Ajo-Franklin, C. M., Drubin, D. A., Eskin, J. A., Gee, E. P., Landgraf, D., Phillips, I., and Silver, P. A. (2007). Rational design of memory in eukaryotic cells. *Genes Dev.* **21**, 2271–2276.

Bayley, P., Schilstra, M., and Martin, S. (1989). A lateral cap model of microtubule dynamic instability. *FEBS Lett.* **259**, 181–184.

Bayley, P.M., Schilstra, M. J., and Martin, S. R. (1990). Microtubule dynamic instability: Numerical simulation of microtubule transition properties using a Lateral Cap model. *J. Cell Sci.* **95**(Pt. 1), 33–48.

Chen, Y. D., and Hill, T. L. (1985). Monte Carlo study of the GTP cap in a five-start helix model of a microtubule. *Proc. Natl. Acad. Sci. U.S.A.* **82**, 1131–1135.

Coburn, B. J., Wagner, B. G., and Blower, S. (2009). Modeling influenza epidemics and pandemics: Insights into the future of swine flu (H1N1). *BMC Med.* **7**, 30.

Dyson, F. (2004). A meeting with Enrico Fermi. *Nature* **427**, 297.

Elowitz, M.B., and Leibler, S. (2000). A synthetic oscillatory network of transcriptional regulators. *Nature* **403**, 335–338.

Flyvbjerg, H., Jobs, E., and Leibler, S. (1996). Kinetics of self-assembling microtubules: An “inverse problem” in biochemistry. *Proc. Natl. Acad. Sci. U.S.A.* **93**, 5975–5979.

Freed, K. F. (2002). Analytical solution for steady-state populations in the self-assembly of microtubules from nucleating sites. *Phys. Rev. E Stat. Nonlin. Soft Matter Phys.* **66**, 061916.

Glikman, N. R., Skibbens, R. V., and Salmon, E. D. (1993). How the transition frequencies of microtubule dynamic instability (nucleation, catastrophe, and rescue) regulate microtubule dynamics in interphase and mitosis: analysis using a Monte Carlo computer simulation. *Mol. Biol. Cell* **4**, 1035–1050.

Gregoretti, I. V., Margolin, G., Alber, M. S., and Goodson, H. V. (2006). Insights into cytoskeletal behavior from computational modeling of dynamic microtubules in a cell-like environment. *J. Cell Sci.* **119**, 4781–4788.

Holy, T. E., and Leibler, S. (1994). Dynamic instability of microtubules as an efficient way to search in space. *Proc. Natl. Acad. Sci. U.S.A.* **91**, 5682–5685.

Howard, J. (2001). “Mechanics of Motor Proteins and the Cytoskeleton.” Sinauer, Sunderland, MA.

Huang, W., Lee, S. L., and Yu, L.X. (2009). Mechanistic approaches to predicting oral drug absorption. *AAPS J.* **11**, 217–224.

Johnson, K. A., and Borisy, G. G. (1975). The equilibrium assembly of microtubules *in vitro*. *Soc. Gen. Physiol. Ser.* **30**, 119–141.

Johnson, K. A., and Borisy, G. G. (1977). Kinetic analysis of microtubule self-assembly *in vitro*. *J. Mol. Biol.* **117**, 1–31.

Johnson, K. A., and Borisy, G. G. (1979). Thermodynamic analysis of microtubule self-assembly *in vitro*. *J. Mol. Biol.* **133**, 199–216.

Lorenz, E. N. (1996). “The Essence of Chaos.” University of Washington Press, Seattle, WA.

Margolin, G., Gregoretti, I. V., Goodson, H. V., and Alber, M.S. (2006). Analysis of a mesoscopic stochastic model of microtubule dynamic instability. *Phys. Rev. E Stat. Nonlin. Soft Matter Phys.* **74**, 041920.

Martin, S. R., Schilstra, M. J., and Bayley, P. M. (1993). Dynamic instability of microtubules: Monte Carlo simulation and application to different types of microtubule lattice. *Biophys. J.* **65**, 578–596.

Mitchison, T. J., and Kirschner, M. W. (1987). Some thoughts on the partitioning of tubulin between monomer and polymer under conditions of dynamic instability. *Cell Biophys.* **11**, 35–55.

Odde, D. J. (1997). Estimation of the diffusion-limited rate of microtubule assembly. *Biophys. J.* **73**, 88–96.

Oosawa, F., and Asakura, S. (1975). “Thermodynamics of the Polymerization of Protein.” Academic Press, New York.

Oosawa, F., and Kasai, M. (1962). A theory of linear and helical aggregations of macromolecules. *J. Mol. Biol.* **4**, 10–21.

Saltelli, A., Chan, K., and Scott, E.M. (eds.) (2008). “Sensitivity Analysis.” Wiley, Chichester.

VanBuren, V., Cassimeris, L., and Odde, D.J. (2005). Mechanochemical model of microtubule structure and self-assembly kinetics. *Biophys. J.* **89**, 2911–2926.

VanBuren, V., Odde, D. J., and Cassimeris, L. (2002). Estimates of lateral and longitudinal bond energies within the microtubule lattice. *Proc. Natl. Acad. Sci. U.S.A.* **99**, 6035–6040.

Verde, F., Dogterom, M., Stelzer, E., Karsenti, E., and Leibler, S. (1992). Control of microtubule dynamics and length by cyclin A- and cyclin B-dependent kinases in Xenopus egg extracts. *J. Cell Biol.* **118**, 1097–1108.

Weinberg, E. R., Auerbach, M. A., and Shah, N. B. (2009). The use of simulation for pediatric training and assessment. *Curr. Opin. Pediatr.* **21**, 282–287.

CHAPTER 11

Analysis of Dynamic Instability of Steady-State Microtubules *In Vitro* by Video-Enhanced Differential Interference Contrast Microscopy with an Appendix by Emin Oroudjev

Mythili Yenjerla, Manu Lopus, and Leslie Wilson

Department of Molecular, Cellular, and Developmental Biology, The Neuroscience Research Institute, University of California, Santa Barbara, California 93106

Abstract

- I. Introduction
- II. Method
 - A. Polymerization of Purified Tubulin to Steady State
 - B. Video-Enhanced Differential Interference Contrast Microscopy of Microtubules
 - C. Analysis of Dynamic Instability Using Software Programs
- III. Summary and Conclusion
- Acknowledgments
- References
- Appendix
 - I. Introduction
 - II. MT-LHAP and Its Features
 - III. Instructions to Use MT-LHAP
 - A. Loading the stack of images and tracking the microtubules in MT-LHAP
 - B. Importing Microtubule Tracking Data into MT-LHAP
 - C. Generation of Life-History Plots and Manual Data Analysis
 - D. Automatic Data Analysis
 - E. Post-Analysis Procedures
 - IV. Conclusion
 - References

Abstract

Microtubules are major constituents of the cytoskeleton which display dynamic properties. They exhibit dynamic instability which is defined as the stochastic switching between growing and shortening at microtubule ends. Dynamic instability plays an important role in diverse cellular functions including cell migration and mitosis. Many successful antimitotic drugs and microtubule-associated proteins (MAPs) are known to modulate microtubule dynamics, and it is important to analyze the *in vitro* dynamic instability of microtubules to study the mechanism of action of microtubule-targeted therapeutics and MAPs. In this chapter, we describe a method to analyze the *in vitro* dynamic instability of microtubules at steady state using video-enhanced differential contrast (VE-DIC) microscopy in detail. In this method, microtubules are assembled to steady state at 30°C with MAP-free tubulin in a slide chamber in the presence of GTP, using sea urchin axonemes as nucleating seeds. Images of microtubules are enhanced and recorded in real time by a video camera and an image processor connected to a DIC microscope which is maintained at 30°C. We use two software programs to track and analyze the growing and shortening of plus or minus ends of microtubules in the real-time images recorded using VE-DIC. In this chapter, we describe the instructions to use the tracking software Real Time Measurement II (RTM II) program. The instructions to use the analysis software Microtubule Life History Analysis Procedures (MT-LHAP) in Igor Pro software have been described in detail in an appendix ([Oroudjiev, 2010](#)) following this chapter.

I. Introduction

Microtubules are major constituents of the cytoskeleton in eukaryotic cells. These polymeric fibers are composed of α - and β -tubulin heterodimers arranged in a “head-to-tail” fashion. They play an important role in diverse cellular processes from maintaining structural integrity and positioning of intracellular organelles to cell migration, cell division, and transport of cellular cargo. Microtubules are highly dynamic polymers and exhibit two types of nonequilibrium dynamic behaviors, one of which is dynamic instability. Dynamic instability is the switching between growing and shortening at microtubule ends ([Mitchison and Kirschner, 1984](#)). It is often defined by four main parameters, which are the growth rate, the shortening rate, and the transition frequencies from growth to shortening and from shortening to growth. Additionally, “attenuation” or “pause,” denoting no detectable change in microtubule length, and “dynamicity,” which is a measure of the total rate of tubulin exchange at microtubule ends ([Jordan and Wilson, 2004](#)), are also used to describe dynamic instability behaviors. In the simplest model, dynamic instability can be considered to be due to the gain and loss of a short region of GTP (or GDP-Pi), called the stabilizing “GTP cap” at the microtubule ends (see reviews by [Desai and Mitchison, 1997](#); [Kueh and Mitchison, 2009](#); [Lopus *et al.*, 2009](#) for in-depth treatments of dynamic instability).

Dynamic instability of microtubules plays an important role in mitotic progression. It is critical in spindle formation and the capture, alignment, and proper segregation of chromosomes during mitosis ([Kirschner and Mitchison, 1986](#);

Kline-Smith and Walczak, 2004). Antimitotic drugs such as paclitaxel and vinblastine, which are widely used in cancer chemotherapy and inhibit or promote polymerization and depolymerization at relatively high concentrations, suppress microtubule dynamics at low concentrations without significantly changing the microtubule polymer mass (Jordan and Wilson, 2004). Even at such low concentrations, these molecules arrest cells in mitosis and induce cell death (Jordan and Wilson, 1998; Jordan and Wilson, 2004). Microtubule dynamics are also tightly regulated in terminally differentiated cells such as neurons (Dent and Kalil, 2001), and studies are underway to develop microtubule-stabilizing drugs for treating neurodegenerative disorders (Trojanowski *et al.*, 2008). Analysis of microtubule dynamic instability is very useful in studying the mechanisms of action of these microtubule-targeted drugs and also microtubule-associated proteins (MAPs) that regulate dynamics.

Dynamic instability of microtubules can be measured both in living cells and *in vitro* with microtubules assembled from purified tubulin and various drugs or regulatory proteins. In cells, dynamic instability occurs only at microtubule plus ends (the end with β -tubulin facing outward), whereas the minus ends (the end with α -tubulin facing outward) remain the same length or shorten (Sammak *et al.*, 1987). On the other hand, dynamic instability occurs at both ends of microtubules assembled *in vitro*, with the plus ends being more robust than the minus ends (Walker *et al.*, 1988). The main advantage of analyzing dynamic instability *in vitro* is that it provides mechanistic information about the specific role of different agents on microtubule dynamics in the absence of cellular MAPs. In addition, under *in vitro* conditions dynamic instability can be studied at both the ends to obtain mechanistic insight into the ways drugs or regulatory proteins affect stability at the opposite ends, although the plus ends are tracked much more often than the minus ends. In some cells such as neurons, the minus ends of microtubules are not anchored (Keating *et al.*, 1997), and therefore tracking minus ends also *in vitro* could be important when studying the role of drugs or MAPs that target microtubules in these cells. For example, stathmin, a destabilizing MAP abundant in neurons, strongly promotes the catastrophe frequency at minus ends *in vitro* and may serve in cells to destabilize microtubules whose minus ends have become dissociated from centrosomes (Manna *et al.*, 2006).

In vitro dynamic instability of microtubules is determined either at pre-steady state or at steady state. Pre-steady state refers to the early elongation phase of microtubule elongation, which occurs at high initial free tubulin concentrations and is usually measured between 2 and 10 min after initiation of polymerization. Once steady state is attained, the subunit concentration remains constant at the overall critical concentration. Microtubules usually attain steady state *in vitro* ~30–40 min after initiating polymerization using “microtubule seeds” or stabilizing agents. The dynamic instability parameters one can measure during pre-steady state conditions are mainly the rate and extent of growth because shortening events are not very frequent at high free tubulin concentration (LeBoeuf *et al.*, 2008). On the other hand, both growing and shortening parameters can be readily measured for microtubules at steady state, as is observed in cells. In our laboratory, we prefer to analyze dynamic instability at steady state, since drugs and regulatory proteins that modulate dynamics have differential effects on the various dynamic instability parameters including shortening events, which can be valuable in understanding microtubule-binding

mechanisms. For example, the synthetic halichondrin eribulin (E7389), which is thought to work by end-poisoning of microtubules, does not have any effect on shortening events at plus ends at steady state but strongly suppresses growth events (Jordan *et al.*, 2005).

Dynamic instability can be analyzed *in vitro* by recording the length changes of individual microtubules at their plus ends assembled from MAP-free tubulin in real time by using either dark-field microscopy or differential interference contrast (DIC) microscopy. Here we describe a method based upon DIC microscopy, which generates a three-dimensional (3D) shadowed image of individual microtubules. The microtubules are assembled to steady state *in vitro* at 30°C with MAP-free tubulin in a slide chamber using sea urchin axonemes as nucleating seeds. The microtubules assemble onto the nucleating seeds and can be readily distinguished from the seeds, which have a considerably larger diameter. Images of microtubules are enhanced and recorded in real time using a video camera and an image processor connected to a video-enhanced (VE)-DIC microscope. The growing and shortening of plus or minus ends of the individual microtubules in real-time videos are then tracked using Real Time Measurement II (RTM II) program and analyzed using Microtubule Life History Analysis Procedures (MT-LHAP) program (see the Appendix by Oroudjev (2010) immediately following this chapter) to obtain the dynamic instability parameters.

II. Method

A. Polymerization of Purified Tubulin to Steady State

1. Preparation of Purified Tubulin

Mammalian brain is a rich source of tubulin, and microtubules prepared from bovine brain tubulin are highly dynamic and are therefore very convenient for analyzing dynamic instability of microtubules *in vitro*. We prepare MAP-free tubulin (>0.99% pure) from microtubule protein isolated from fresh bovine brain by two cycles of polymerization and depolymerization in the absence of glycerol or other stabilizing agents. The MAPs are removed by phosphocellulose chromatography and the tubulin is drop-frozen in liquid nitrogen and stored at -70°C as described in detail in a preceding chapter (Miller and Wilson, 2010; Chapter 1, this volume). The tubulin preparation stored at -70°C can be used for about 1 year. The dynamicity should be checked by VE-DIC microscopy before proceeding with dynamic instability experiments.

2. Protocol for Preparation of Axoneme Seeds from *Strongylocentrotus purpuratus*

Polymerization of tubulin can be initiated by purified centrosomes or axonemes. We use sea urchin axonemes, which serve as excellent microtubule seed initiators for tubulin polymerization and allow easy imaging of individual microtubules. Flagellar axonemes are prepared from the sperm of sea urchin *Strongylocentrotus purpuratus* (Stephens, 1970; Farrell, 1982). Male sea urchins are cut open and the gonads are removed and placed into sea water (4°C). The gonads are minced, filtered through cheesecloth, and centrifuged at 3000 g, for 10 min at 4°C to obtain a pellet of sperm. The pellets are washed in filtered sea water

and centrifuged at 3000 g for 10 min at 4°C. All subsequent steps for preparation of axoneme seeds are carried out at 4°C.

Sperm pellets are suspended in axoneme extraction buffer (0.1 M KCl, 5 mM MgSO₄, 0.5 mM ethylenediaminetetraacetic acid (EDTA), 1 mM dithiothreitol, 10 mM Tris, pH adjusted to 7.0 using orthophosphoric acid) with 1% triton-X-100 to demembranate sperm and are homogenized. The suspension is centrifuged at 1500 g for 5 min to pellet sperm heads and membrane fragments (Bell *et al.*, 1982). The supernatant containing sperm tails is centrifuged at 47,800 g for 20 min. The homogenization and differential centrifugation are repeated with the pellet obtained at 1500 g. The pellet obtained after centrifugation at 47,800 g containing sperm tails is homogenized and centrifuged at 1500 g for 5 min. The supernatant is saved, while the pellet is resuspended in axoneme wash buffer without triton, homogenized, and re-extracted by centrifugation at 1500 g for 5 min. Both the supernatants are combined and centrifuged at 47,800 g for 10 min. The pellet is resuspended in axoneme wash buffer, homogenized in a hand homogenizer, and centrifuged again at 47,800 g for 10 min. The washing is repeated twice more and the final white pellet of axonemes is suspended in PMEM buffer [87 mM PIPES (1,4-Piperazinediethanesulfonic acid; Sigma-Aldrich, St. Louis, MO), 36 mM MES (2-(N-Morpholino)ethanesulfonic acid; Sigma-Aldrich), 1.4 mM MgCl₂, 1 mM EGTA (Ethylene glycol-bis(2-aminoethyl ether)-N,N,N',N'-tetraacetic acid Sigma-Aldrich), pH 6.8]. The suspended axonemes are observed using DIC microscope (Olympus IX71) fitted with 100× objective to dilute axonemes appropriately. The mean length of axonemes is about 2–4 μm and axonemes are diluted before use, such that there are two to three axonemes per microscopic field of view as too many axonemes can result in overlapping microtubules that may be difficult to track. The axonemes are drop-frozen as small aliquots in liquid nitrogen and stored at –70°C. The stored axonemes can be used for 1–2 years depending on the preparation, until they start to form aggregates at which time they are discarded.

3. Preparation of the Slide Chamber

A slide chamber is prepared using a standard glass microscope slide and a cover-slip that will be filled with the tubulin polymerization mixture to observe and record the growing and shortening dynamics of the microtubules. We use number 1 cover-slips to prepare the slide chambers. Number 1 coverslips are thin and give the objective more working distance between its front lens element and the coverslip outer surface for oil-immersion objectives (Salmon and Tran, 2007). The coverslips are placed in ceramic holders, washed in 50% nitric acid, nanopure water (four times), and 70% ethanol, dried at 60°C in a vacuum oven, and stored in a clean Petri dish with lens paper. The glass microscopic slides are cleaned with 70% ethanol and dried with a Kimwipe before use. The cleaned glass slide and a strip of double-sided tape are used to make the slide chamber. We use ½" or ¾" wide Scotch double-sided tape which is cut slightly longer than a coverslip. The strip is then cut in half lengthwise and pressed onto the surface of the microscopic slide parallel to the long axis of the slide. The second half of the strip is placed 2–3 mm away from the first strip and pressed onto the slide. Thin tape is preferred as it will reduce the focal drift of microtubules in the chamber. The coverslip is placed on the tape strips and pockets of air are pressed out through the chamber by rubbing on the coverslip

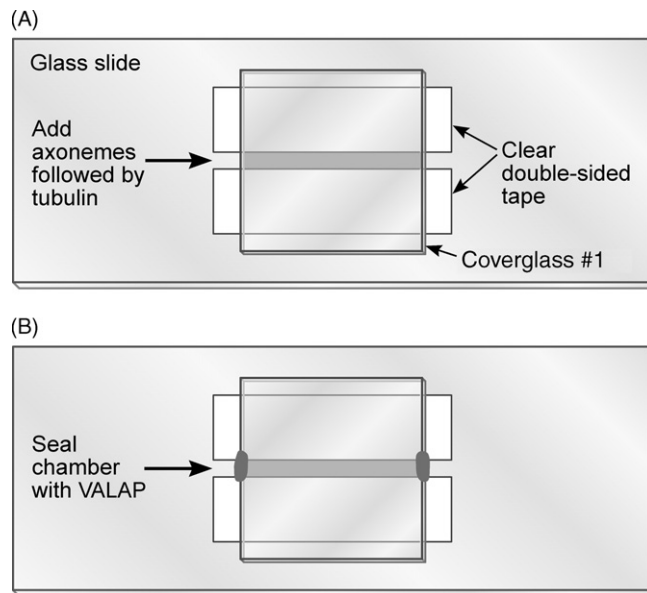


Fig. 1 (A) Microtubule slide chamber; (B) slide chamber sealed with VALAP.

firmly with a blunt object (Fig. 1A). Solutions are first flowed into the chamber and then the chamber is sealed at its edges using VALAP (equal mixture of vaseline, lanolin, and paraffin) (Fig. 1B).

4. Polymerization of Tubulin to Steady State in Slide Chambers

An aliquot of purified tubulin solution is thawed on ice and centrifuged at 12,000 g for 10 min to sediment any aggregated tubulin, which is discarded. As a rule, a final concentration of 10–15 μ M tubulin (determined by trial and error; see below) is added to 2 mM GTP and PMEM buffer (Panda *et al.*, 1995), and the solution is kept on ice. The concentration of tubulin should be adjusted after viewing the images of the microtubules on the DIC microscope so that they are of moderate length to track and not too long or overlapping. Drugs or proteins to be tested are added to this reaction mixture and compared with the appropriate vehicle control. The final pH of the polymerization mixture should be 6.8 for a (solvent) control; if otherwise, the pH of the PMEM buffer has to be readjusted until the pH of the polymerization mixture is 6.8.

Microtubules are polymerized to steady state at the ends of axoneme seeds in the slide chamber. To initiate polymerization, axoneme seeds are diluted in PMEM buffer to achieve two to three seeds per microscope field and mixed with a vortex mixer, and 5 μ l of the axoneme suspension is added to fill a slide chamber. The slide chamber is then incubated at 25°C for 5 min to allow adherence of axonemes to the slide chamber. Five microliters of PMEM buffer is added to the chamber and wicked through with a Whatman filter paper to remove unattached axonemes. Five microliters of the polymerization mixture (which can be prepared during incubation of axonemes) is then added and wicked through twice. Both ends of the chamber are sealed with a drop of melted VALAP (Fig. 1B). The chamber is then placed at 30°C

in an incubator for 30 min to polymerize the tubulin at the ends of the axoneme seeds. The microtubules grow onto the axoneme seeds and are not attached to the glass, while the axonemes remain attached to the glass. This ensures that the microtubules are free in solution, and not adhered to glass, which could affect their dynamics. After 30 min, when steady state is reached, the slide is transferred to a DIC microscope (we use an Olympus IX71, with a 100 \times objective, numerical aperture 1.4) in which the temperature of the stage is maintained at 30°C and real-time images are recorded for tip tracking. At steady state, microtubules grow slowly and shorten rapidly by reversible exchange with soluble tubulin in the chamber. The slide is discarded after 45 min as the dynamic activity of tubulin can change due to aging of protein. To study microtubule dynamics at pre-steady state, the slide is transferred to the microscope at 30°C immediately after adding the polymerization mixture to the chamber and real-time videos are recorded between 2 and 10 min. The leftover tubulin, axonemes, and GTP aliquots are discarded.

5. Factors Affecting Tubulin Polymerization and Dynamic Instability of Microtubules

The dynamic instability parameters can vary with tubulin preparations, and therefore it is best to use the same tubulin preparation for an entire study. Temperature is another important factor as even a small decrease in temperature can cause microtubule depolymerization or an increase can cause denaturation. Solvents such as dimethylsulfoxide (DMSO) which are commonly used to solubilize many drugs can suppress microtubule dynamics (<0.5% DMSO can be used to dissolve test compounds and compared with appropriate solvent control). Buffer containing PIPES (87 mM), MES (36 mM) in the presence of Mg²⁺ (1.4 mM), and EGTA (1 mM) at pH 6.8 is known to yield rapid dynamics at steady state (Panda *et al.*, 1995). However, a pH of 7.2 has also been used for studying effects of stathmin on microtubule dynamics, which is also the mean pH within the cytoplasm of cells. At this pH, stathmin is found to strongly promote the catastrophe frequency (Manna *et al.*, 2006).

B. Video-Enhanced Differential Interference Contrast Microscopy of Microtubules

Here, we briefly describe the working of a DIC microscope and the capture of live images of microtubules (see Lacey, 1989; James and Tanke, 1991; Salmon and Tran, 2007). Microtubules are about 25 nm in diameter, smaller than the diffraction limit of the DIC microscope, and cannot be seen by the eye or conventional photography (Allen *et al.*, 1981; Salmon and Tran, 2007). The images are therefore enhanced by a video camera (VE-DIC) and a real-time image processor.

1. Working Principle of DIC Microscopes

DIC microscopy is a light microscopic technique based on an interference principle involving two coherent beams of light (from the same small light source) and image contrast achieved with gradients in optical path. It produces clear optical sections of thick transparent specimens and a 3D shadowed image. DIC is also called Nomarski contrast microscopy and has two Nomarski or modified Wollaston prisms in its optical configuration, one of which has an adjustable position. In

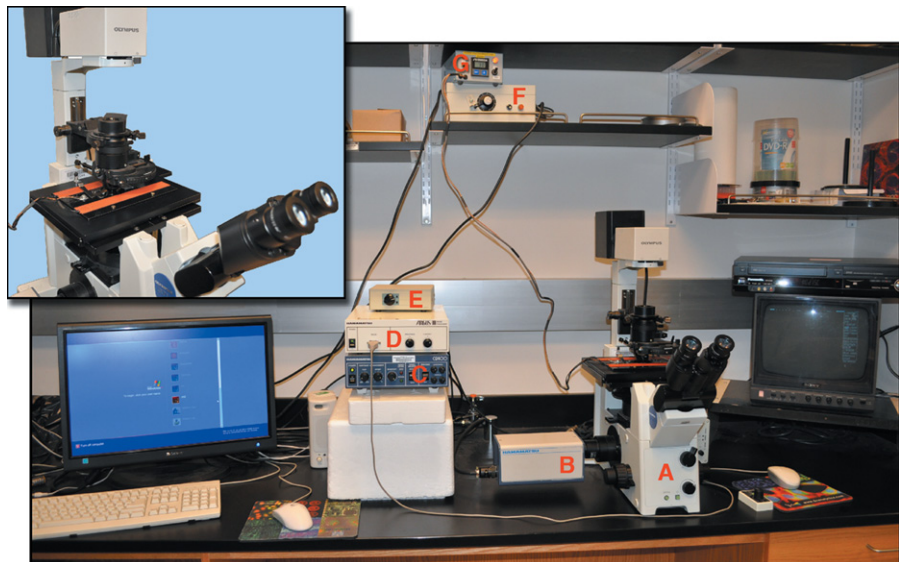


Fig. 2 Photograph of an inverted DIC microscope system connected to a TV monitor, DVD recorder, and a computer. (A) Olympus IX71, (B) Hamamatsu C2400 CCD camera, (C) Hamamatsu C2400 camera controller, (D) Hamamatsu Argus-10 image processor, (E) data switch to transfer real-time images between TV and computer, and (F and G) two parts of the heating control unit. Inset shows a DIC microscope with the stage connected to a heating element to maintain temperature at 30°C.

addition to the two Nomarski prisms, the main components of a DIC microscope include a polarizer and an analyzer. In a DIC microscope, light from the lamp first passes through a polarizer. The plane polarized light from the polarizer is split by a Nomarski prism inserted near the condenser diaphragm plane. The divergent beams pass through the condenser and are converted into two wave fronts that pass through the specimen separated laterally from each other in the wedge direction by a small amount. The two wave fronts are recombined by the objective and the second Nomarski prism. The components pass through the analyzer and undergo interference to generate an image with visible contrast based on gradients of optical length differences in the object (for a schematic illustration and description, see [Lacey, 1989](#); [James and Tanke, 1991](#); [Salmon and Tran, 2007](#)). [Figure 2](#) shows a photograph of our inverted DIC microscope connected to a computer and a TV with DVD recorder.

2. Temperature Maintenance

For recording real-time dynamics of microtubules, the stage of the microscope is maintained at a constant temperature of 30°C by a heating unit or a warm-air blower. We use a heating unit that is connected to the DIC microscope and maintains the temperature of the stage at 30°C.

3. Image Enhancement and Capture

The slide chamber is placed on the DIC microscope stage, which is maintained at 30°C. As indicated above, we use an inverted Olympus IX71, with a 100× objective and numerical aperture 1.4 (inverted microscope gives more working

distance). For our DIC microscopic system, we place a drop of immersion oil on the objective and invert the slide chamber onto the drop of oil on objective lens. We place another drop of oil on the bottom of the slide and we lower the condenser gently into oil. Care must be taken to avoid air bubbles while placing the oil as well as when filling the slide chambers with the polymerization mixture. The condenser is adjusted for Koehler illumination by centering the image of field diaphragm and the images are captured using a CCD camera. We use a Hamamatsu C2400 CCD camera. The analogue electronics in the video camera produce video contrast enhancement (Salmon and Tran, 2007). The axonemes with microtubules can be seen and brought into focus by observing on a TV monitor or a computer screen.

The images are further enhanced by a real-time digital image processor before recording (for a detailed description of image enhancement, see Salmon and Tran, 2007). We use Hamamatsu C2400 camera controller and Argus-10 image processor (Hamamatsu) (see Fig. 2) to allow background subtraction and high contrast enhancement. After the microtubules can be viewed, the image is defocused until the microtubules disappear and the background is subtracted to reduce fixed-pattern noise (Allen and Allen, 1983). After background subtraction, the image is refocused to get the final image. The best contrast in the image is obtained by adjusting the gain, brightness, and light intensity. Figure 3 shows microtubules before and after background subtraction and image enhancement.

After images are enhanced, they are recorded in real time digitally either on DVDs or on a computer. We record real-time images on a computer using Virtual Dub software (www.virtualdub.org). For real-time compression of images, we use Huffyuv-2.1.1 codec (neuron2.net/www.math.berkeley.edu/benrg/huffyuv.html). Unlike other codecs, Huffyuv-2.1.1 does not cause loss of real-time image quality. We use UYVY (YUV 4:2:2) interleaved format and a 720×480 frame size to obtain best possible resolution. Real-time videos of individual microtubules are recorded for a 10-min period for tracking. Figure 4A–F shows time-lapse images of steady-state microtubules growing and shortening within the sealed slide chamber.

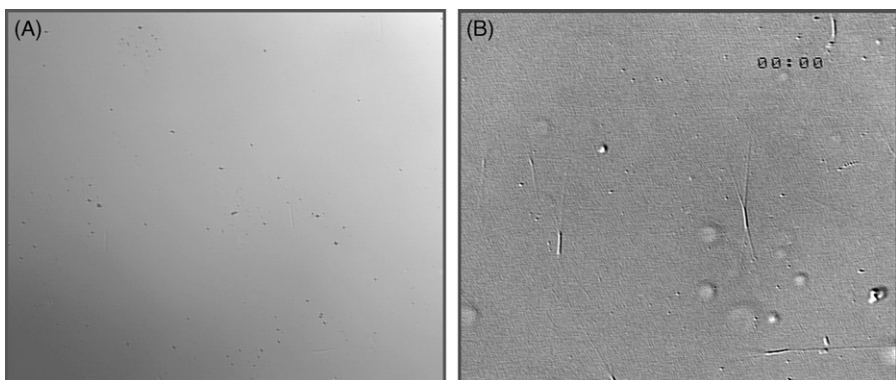


Fig. 3 (A) Microtubules before image enhancement and (B) after image enhancement.

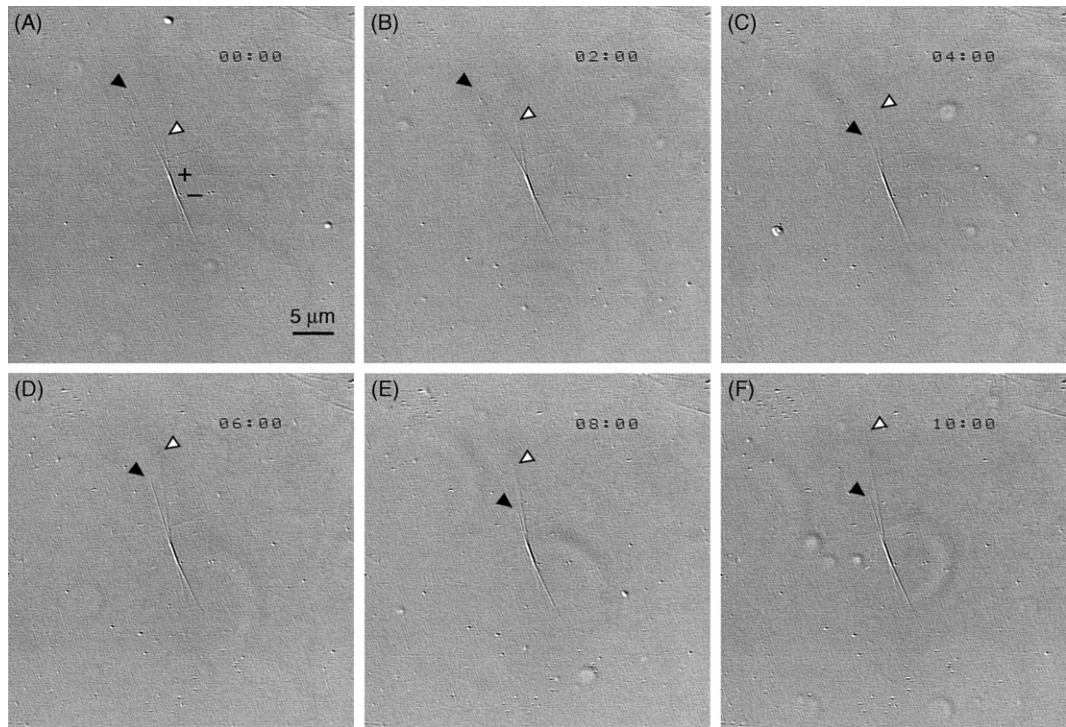


Fig. 4 Time-lapse images of microtubules showing dynamic instability of microtubules assembled *in vitro* at (A) 0, (B) 2, (C) 4, (D) 6, (E) 8, and (F) 10 min. White arrow heads show a growing microtubule and black arrow heads show a shortening microtubule at the plus end with time.

C. Analysis of Dynamic Instability Using Software Programs

1. Tracking and Analysis by RTM II and MT-LHAP Programs

Polymerization of tubulin occurs at both ends of the axoneme seeds, with microtubules assembled onto the plus ends of the seeds being more dynamic than the minus ends. Plus ends are distinguished from the minus ends based on their higher growing rates, higher catastrophes, and greater excursion lengths (Panda *et al.*, 1996; Walker *et al.*, 1988). If the microtubule ends are indistinguishable, we do not track them.

The position of an individual microtubule end (growing and shortening) in the recorded videos is tracked using an in-house software called RTM II (<http://www.igorexchange.com/project/MT-LHAP>). The recorded video is opened and played in RTM II program and tip tracking is performed by clicking on the microtubule tip with a mouse cursor manually. The juncture between the axoneme and microtubule is first fixed as the origin, and then the moving microtubule tip is tracked every 4 s for a 10 min video relative to the fixed origin during playback. Care must be taken while tracking as the microtubule ends may sometimes appear to be a little blurred, or a focal drift of microtubules in the slide chamber may occur. As a rule, we track 30 or more microtubules for each experimental condition to obtain statistically significant data. Tip tracking in RTM II software gives the X- and Y-coordinates of the moving tip of a microtubule over time in the “Click History” window.

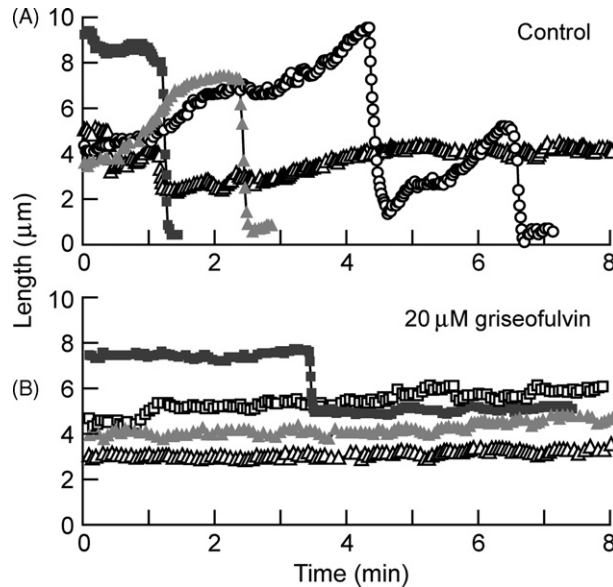


Fig. 5 Life-history plot of length changes of individual microtubules. Life-history traces at the plus ends of four individual (A) control microtubules and (B) microtubules assembled in the presence of 20 μM griseofulvin, which suppresses dynamic instability. The microtubules were assembled from purified bovine brain tubulin, and the changes in length were analyzed by using VE-DIC microscopy (from Panda *et al.*, 2005).

The X - and Y -coordinates of the moving microtubule ends obtained over time from RTM II pasted in Microsoft Excel is imported and converted to microtubule length changes using MT-LHAP (<http://www.igorexchange.com/project/MT-LHAP>) for RTM II, in-house software developed by Dr. Emin Oroudjev inside Igor Pro programming language environment (www.wavemetrics.com). MT-LHAP (see Appendix to this chapter by Oroudjev, 2010 for details) generates life-history plots with the microtubule length versus time (Fig. 5) and also generates data such as slopes denoting rates and excursion lengths for the growing and shortening intervals. The scaling factor ($\mu\text{m}/\text{pixel}$) for microtubule length is determined by measuring the pixels of 1- μm polystyrene beads using DIC microscope. The scaling factors for both X - and Y -coordinates are entered in the MT-LHAP program. All the microtubules which are tracked using RTM II are then analyzed by MT-LHAP program based on the following criteria.

2. Criteria of Analysis

The intervals of growth or shortening or pause are determined based on the following criteria which we arrived at by tracking microtubules that were stabilized using paclitaxel. These criteria are somewhat arbitrary. We consider a microtubule to be growing if its length increases by a minimum of 0.3 μm at a rate of $\geq 0.3 \mu\text{m}/\text{min}$. Shortening events are identified by a length change of at least 1 μm at a rate of $\geq 2 \mu\text{m}/\text{min}$. Microtubules that change $<0.3 \mu\text{m}/\text{min}$ over a duration of five data points are considered to be in an attenuated or paused state, neither growing nor shortening detectably. All intervals excluded from growing and shortening intervals by criteria are also included in attenuation. A catastrophe is any switch to rapid shortening, and the transition of a shortening event to a growth or attenuation event is considered as a rescue.

Table I

Effects of 5 μ M tasidotin on some dynamic instability parameters at plus ends of microtubules at steady state *in vitro* (from Ray *et al.*, 2007)

	Growth rate (μ m/min)	Shortening rate (μ m/min)	Catastrophe frequency (events/min)	Rescue frequency (events/min)	Dynamicity (μ m/min)
Control	1.7 \pm 0.8	28.4 \pm 2.0	0.5 \pm 0.01	1.8 \pm 0.2	2.3
Tasidotin	1.9 \pm 0.1	9.0 \pm 0.7	0.2 \pm 0.01	1.1 \pm 0.1	0.5

Data are mean \pm SE.

All the growing or shortening rates/lengths of microtubules tracked for a particular reaction condition (obtained using MT-LHAP program based on the criteria of analysis) are averaged to obtain the mean growing rate/length or mean shortening rate/length. Percentage of time spent in growing or shortening or in attenuation is calculated as the percentage of the value obtained by dividing the sum of all the growth or shortening or attenuation durations respectively by the total time of observation for all microtubules in a particular condition. The catastrophe frequency is calculated by dividing the number of catastrophes by the sum of total time spent growing and attenuated for all microtubules in a particular condition. The rescue frequency is calculated by dividing the total number of rescues by the time spent shortening for all microtubules in a particular condition. Dynamicity is the rate of total tubulin exchanged at a microtubule end during all growing and shortening events (Kamath *et al.*, 2006). Dynamicity is calculated as the sum of total growth lengths and total shortening lengths divided by the total time of observation for all microtubules for a particular condition. For example, results obtained for the effect of tasidotin on steady-state microtubule dynamic instability parameters are given in Table I. We express the results of the dynamic instability parameters as the mean and standard error of mean and sometimes also additionally represent life-history plots and frequency histograms.

III. Summary and Conclusion

Microtubules are highly dynamic constituents of the cytoskeleton. Their dynamic properties are tightly regulated by cellular MAPs and are modulated in a variety of ways by many microtubule-targeted drugs. Analysis of microtubule dynamic instability *in vitro* therefore becomes very important in studying the mechanism of action of MAPs or new therapeutics that act on microtubules directly or through MAPs. VE-DIC is a good imaging tool that has been successfully utilized to analyze microtubule dynamics *in vitro*. Further advancements in microscope systems that can improve the resolution and real-time imaging of microtubules and development of semi-automated or automated microtubule tracking methods that will eventually replace the manual tracking process will greatly benefit research in microtubule dynamics.

Acknowledgments

We acknowledge the support of NIH grant NS13560. We also thank Drs. Stuart C. Feinstein, Adria C. Lebeouf, and Sasha F. Levy for the RTM II program.

References

Allen, R. D., and Allen, N. S. (1983). Video-enhanced microscopy with a computer frame memory. *J Microsc.* **129**, 3–17.

Allen, R. D., Allen, N. S., and Travis, J. L. (1981). Video-enhanced contrast, differential interference contrast (AVEC-DIC) microscopy: A new method capable of analyzing microtubule-related motility in the reticulopodial network of *Allogromia laticollaris*. *Cell Motil.* **1**, 291–302.

Bell, C. W., Fraser, C., Sale, W. S., Tang, W. J., and Gibbons, I. R. (1982). Preparation and purification of dynein. In “Methods in Cell Biology” (L. Wilson, ed.), Vol. 24, pp. 373–397. Elsevier Inc., San Diego, CA.

Dent, E. W., and Kalil, K. (2001). Axon branching requires interactions between dynamic microtubules and actin filaments. *J. Neurosci.* **21**, 9757–9769.

Desai, A., and Mitchison, T. J. (1997). Microtubule polymerization dynamics. *Annu. Rev. Cell Dev. Biol.* **13**, 83–117.

Farrell, K. W. (1982). Purification and reassembly of tubulin from outer doublet microtubules. In “Methods in Cell Biology” (L. Wilson, ed.), Vol. 24, pp. 61–78. Elsevier Inc., San Diego, CA.

James, J., and Tanke, H. J. (1991). Special optical techniques of image formation. In “Biomedical Light Microscopy”, pp. 75–83. Kluwer Academic Publishers, Norwell, MA.

Jordan, M. A., Kamath, K., Manna, T., Okouneva, T., Miller, H. P., Davis, C., Littlefield, B. A., and Wilson, L. (2005). The primary antimitotic mechanism of action of the synthetic halichondrin E7389 is suppression of microtubule growth. *Mol. Cancer Ther.* **4**, 1086–1095.

Jordan, M. A., and Wilson, L. (1998). Microtubules and actin filaments: Dynamic targets for cancer chemotherapy. *Curr. Opin. Cell Biol.* **10**, 123–130.

Jordan, M. A., and Wilson, L. (2004). Microtubules as a target for anticancer drugs. *Nat. Rev. Cancer* **4**, 253–265.

Kamath, K., Okouneva, T., Larson, G., Panda, D., Wilson, L., and Jordan, M. A. (2006). 2-Methoxyestradiol suppresses microtubule dynamics and arrests mitosis without depolymerizing microtubules. *Mol. Cancer Ther.* **5**, 2225–2233.

Keating, T. J., Peloquin, J. G., Rodionov, V. I., Momcillovic, D., and Borisy, G. G. (1997). Microtubule release from the centrosome. *Proc. Natl. Acad. Sci. U.S.A.* **94**, 5078–5083.

Kirschner, M., and Mitchison, T. (1986). Beyond self-assembly: From microtubules to morphogenesis. *Cell* **45**, 329–342.

Kline-Smith, S. L., and Walczak, C. E. (2004). Mitotic spindle assembly and chromosome segregation: Refocusing on microtubule dynamics. *Mol. Cell* **15**, 317–327.

Kueh, H. Y., and Mitchison, T. J. (2009). Structural plasticity in actin and tubulin polymer dynamics. *Science* **325**, 960–963.

Lacey, A. J. (1989). Rendering transparent specimens visible by inducing contrast. In “Light Microscopy in Biology a Practical Approach” (A. J. Lacey, ed.), pp. 41–43. IRL Press, Oxford, UK.

LeBoeuf, A. C., Levy, S. F., Gaylord, M., Bhattacharya, A., Singh, A. K., Jordan, M. A., Wilson, L., and Feinstein, S. C. (2008). FTDP-17 mutations in Tau alter the regulation of microtubule dynamics: An “alternative core” model for normal and pathological Tau action. *J. Biol. Chem.* **283**, 36406–36415.

Lopus, M., Yenjerla, M., and Wilson, L. (2009). Microtubule dynamics. In “Wiley Encyclopedia of Chemical Biology” (T. P. Begley, ed.), Vol. 3, pp. 153–160. Wiley, Hoboken, NJ.

Manna, T., Thrower, D., Miller, H. P., Curmi, P., and Wilson, L. (2006). Stathmin strongly increases the minus end catastrophe frequency and induces rapid treadmilling of bovine brain microtubules at steady state *in vitro*. *J. Biol. Chem.* **281**, 2071–2078.

Margolis, R. L., and Wilson, L. (1998). Microtubule treadmilling: What goes around comes around. *Bioessays* **20**, 830–836.

Miller, H. P., and Wilson, L. (2010). Preparation of microtubule protein and purified tubulin from bovine brain by cycles of assembly and disassembly and phosphocellulose chromatography. In “Methods in Cell Biology” (J. J. Correia, and L. Wilson, eds.), Elsevier Inc., San Diego, CA. In Press.

Mitchison, T., and Kirschner, M. (1984). Dynamic instability of microtubule growth. *Nature* **312**, 237–242.

Oroudjev, E. (2010). Microtubule Life History Analysis Procedures in Igor Pro software to analyze dynamic instability of microtubules *in vitro*. In “Methods in Cell Biology” (J. J. Correia, and L. Wilson, eds.), Elsevier Inc., San Diego, CA. In Press.

Panda, D., Daijo, J. E., Jordan, M. A., and Wilson, L. (1995). Kinetic stabilization of microtubule dynamics at steady state *in vitro* by stoichiometric concentrations of tubulin-colchicine complex. *Biochemistry* **34**, 9921–9929.

Panda, D., Jordan, M. A., Chu, K. C., and Wilson, L. (1996). Differential effects of vinblastine on polymerization and dynamics at opposite microtubule ends. *J. Biol. Chem.* **271**, 29807–29812.

Panda, D., Rathinasamy, K., Santra, M. K., and Wilson, L. (2005). Kinetic suppression of microtubule dynamic instability by griseofulvin: Implications for its possible use in the treatment of cancer. *Proc. Natl. Acad. Sci. U.S.A.* **102**, 9878–9883.

Ray, A., Okouneva, T., Manna, T., Miller, H. P., Schmid, S., Arthaud, L., Luduena, R., Jordan, M. A., and Wilson, L. (2007). Mechanism of action of the microtubule-targeted antimitotic depsipeptide tasidotin (formerly ILX651) and its major metabolite tasidotin-carboxylate. *Cancer Res.* **67**, 3767–3776.

Salmon, E. D., and Tran, P. (2007). High-resolution video-enhanced differential interference contrast light microscopy. In “Methods in Cell Biology” (G. Sluder, and D. E. Wolf, eds.), Vol. 81, pp. 335–364. Elsevier Inc., San Diego, CA.

Sammak, P. J., Gorbsky, G. J., and Borisy, G. G. (1987). Microtubule dynamics *in vivo*: A test of mechanisms of turnover. *J. Cell Biol.* **104**, 395–405.

Stephens, R. E. (1970). Thermal fractionation of outer fiber doublet microtubules into A- and B-subfiber components. A- and B-tubulin. *J. Mol. Biol.* **47**, 353–363.

Trojanowski, J. Q., Duff, K., Fillit, H., Koroshetz, W., Kuret, J., Murphy, D., and Refolo, L. (2008). New directions for frontotemporal dementia drug discovery. *Alzheimers Dement.* **4**, 89–93.

Walker, R. A., O’Brien, E. T., Pryer, N. K., Soboeiro, M. F., Voter, W. A., Erickson, H. P., and Salmon, E. D. (1988). Dynamic instability of individual microtubules analyzed by video light microscopy: Rate constants and transition frequencies. *J. Cell Biol.* **107**, 1437–1448.

APPENDIX

Microtubule Life History Analysis Procedures (MT-LHAP) in Igor Pro Software to Analyze Dynamic Instability of Microtubules *In Vitro*

Emin Oroudjev

Department of Molecular, Cellular, and Developmental Biology, The Neuroscience Research Institute, University of California, Santa Barbara, California 93106

===== I. Introduction

Microtubules represent one of the major structural components of the cytoskeleton and are involved in many cellular functions such as mitosis, cytokinesis, vesicular transport, and cell motility (Jordan and Kamath 2007). As described in several chapters in this volume, microtubule dynamic instability plays an important role in many cellular functions dependent upon microtubules.

Dynamic instability of microtubules can be assessed *in vitro* by recording real-time images of the individual microtubules assembled from purified tubulin with sufficient spatial and temporal resolution and at desired experimental conditions (Yenjerla *et al.*, 2010, this chapter). The position of the microtubule end relative to a fixed point of origin is tracked, either by dedicated utility inside imaging software or by using a separate tracking software (dedicated microtubule tracking software RTM II can be downloaded together with MT-LHAP; see below). From the tracking data, microtubule life-history plots are generated as the distance from the point of origin to the microtubule end for each time frame. The life-history plot for each tracked microtubule is then used to determine and analyze the parameters of dynamic instability by using preset criteria (Yenjerla *et al.*, 2010, this chapter). We have developed a number of procedures in Igor Pro data analysis software (WaveMetrics, Inc., Lake Oswego, OR) which are combined into a single integrated bundle called “Microtubule Life History Analysis Procedures” (MT-LHAP) to generate life-history plots and to obtain the dynamic instability parameters of the microtubules. The software and some supporting files can be downloaded from IgorExchange ftp site (<http://www.igorexchange.com/project/MT-LHAP>). Here, we describe the features of MT-LHAP software and the instructions for its use.

II. MT-LHAP and Its Features

MT-LHAP was written inside Igor Pro data analysis software. It automatically generates life-history plots of the length changes of individual microtubules over time which can be further processed and analyzed for growth, shortening, or attenuation events in manual or automatic mode. It allows the investigator to expedite data processing and analysis while retaining full control over the criteria and parameters used for dynamic instability assessment. The procedures are executed via a simple graphical user interface (GUI) that allows users to run procedures without learning syntax of Igor Pro programming language. All the procedures are combined into a single integrated MT-LHAP bundle that can be downloaded along with the supporting files. Please note that in order to use MT-LHAP procedures, users should first procure and install Igor Pro software (version 6.12 is recommended but newer versions are expected to be compatible).

III. Instructions to Use MT-LHAP

MT-LHAP file should be first loaded into Igor Pro software. All functions/procedures of MT-LHAP can be then executed via buttons on a GUI panel. The user has an option to import into MT-LHAP the data obtained from the tracking software (e.g., RTM II) by using the “Load New File” button or to load a stack of time-lapse frames/images (only eight-bit tiff images supported at this time) by using “Load New Image” button and track microtubules inside MT-LHAP. Prior to loading any data or images, it is important to check and enter the correct *X* and *Y* scaling factors ($\mu\text{m}/\text{pixel}$) as they are needed to convert *X*- and *Y*-coordinates values into distances (μm). MT-LHAP can calculate microtubule length either as a distance from origin point (placed somewhere on a microtubule body) to microtubule tip or as changes in microtubule length by measuring changes in microtubule tip distances between consecutive time frames. Correspondingly, the user should select whenever he/she wants to measure changes in microtubule length as changes in origin-to-tip distances or as tip-to-tip distances (tip-to-tip method is more accurate and should be used whenever possible). For correct interpretation of the direction of microtubule growth or shortening, the vector of tip-to-tip change can deviate from the vector of origin-to-tip direction no more than 80° .

A. Loading the stack of images and tracking the microtubules in MT-LHAP

Prior to loading any stack of images, the user should select correct value for “Time Step” (i.e., time intervals between consecutive frames) to assure proper estimation of elapsed time. Loaded image will be inverted and optimized by using Igor Pro adaptive histogram normalization procedure. By changing the settings for image contrast and histogram vertical and horizontal bin sizes, the user can optimize this normalization procedure.

After the image file is loaded and processed, MT-LHAP will open three windows: “ResultsTableWave,” “LifeHistoryPlotWindow,” and “StackImage.” The user then should use the “StackImage” window to track microtubule ends. This is done first by selecting an origin point on a first frame with cursor “B” and “Record Ori Point” button and then marking the end of microtubule tip on each consecutive frame by

positioning cursor “A” over it and pressing the “Record Tip Position” button (note that stack will automatically progress to the next frame every time this button is pressed). When tracking is done, the user should transfer tracking information to the “LifeHistoryPlotWindow” window by pressing the “Life History Plot” button.

B. Importing Microtubule Tracking Data into MT-LHAP

Alternatively, MT-LHAP can import microtubule tracking data generated by a separate software via “Load New File” procedure (“Load New File” button at GUI interface) and generate a corresponding life-history plot in a “LifeHistoryPlotWindow.” At present MT-LHAP imports microtubule tracking data only from a Microsoft Excel 2003 compatible file (*.xls format) that conforms to certain conventions as described below to be correctly processed by MT-LHAP. The majority of the software used to track microtubules can export tracking results in a data file that is compatible for MT-LHAP. A sample of such a compatible data file is included in the bundle. Alternatively, a compatible data file can be produced manually by using the following guidelines: The name of the file should not exceed eight characters. All data should be placed in a worksheet #1 of the excel file. The A2, B2, and C2 cells in a excel file have to be labeled as “Elapsed_Time,” “X,” and “Y,” respectively (the X and Y represent the pixel coordinates of the microtubule tip). The A3 cell should contain the starting time point (i.e., time point for the origin point). Cells A4 and downward contain elapsed time values for the corresponding microtubule end tracking points. These numbers are then multiplied by the time coefficient to convert them into minutes. Correspondingly, time coefficient value (found on GUI interface right under “Load New File” button) should be adjusted as needed prior to data loading. The B3 and C3 cells should contain the corresponding X - and Y -coordinates of the microtubule origin point. Cells B4 and downward contain X -coordinates and cells C4 and downward contain Y -coordinates, respectively, for the microtubule ends corresponding to the elapsed time. Please note that all values for X - and Y -coordinates will be multiplied by X and Y scaling factors ($\mu\text{m}/\text{pixel}$) to convert those values into distances (μm). Users should ensure compatibility of produced files with MT-LHAP as incompatible files might generate erroneous results.

C. Generation of Life-History Plots and Manual Data Analysis

Following import of tracking data or after completion of microtubule end tracking, MT-LHAP automatically calculates the microtubule length for each time point and then constructs a life-history plot in a “LifeHistoryPlotWindow” window. The user can manually assign the life-history plot into segments of growth, shortening, or attenuation based on the criteria described earlier ([Yenjerla et al., 2010](#), this chapter). The user can evaluate the desired part of life-history plot by first positioning cursors A and B at the corresponding border points and then by using the “Probe” button on the graph window. The “Probe” procedure calculates the change in time (min) and the change in length (μm) for the marked part of the life-history plot as well as estimates the slopes of change in length over change in time, which denote the rates ($\mu\text{m}/\text{min}$). The procedure reports its calculations in the upper left corner of the graph. From the results obtained, the user should categorize the various components of the life-history plot as “growth,” “shortening,” or “attenuation” based on the preset criteria ([Yenjerla et al., 2010](#), this chapter). The “probe” procedure usually is run multiple times and cursors are moved along life-history plot line until the

user designates an event. To assign a particular event to the desired part of the life-history plot, the user then uses corresponding buttons on the graph window. For each designated “growth,” “shortening,” or “attenuation” event, the change in time (min), change in length (μm), and absolute rates ($\mu\text{m}/\text{min}$) are recorded in the “results table.” The transition to a new event such as a “catastrophe” or a “rescue” is categorized depending on the preceding event based on the preset criteria (Yenjerla *et al.*, 2010) using the corresponding buttons on the GUI panel or on the graph window. The number of “catastrophe” or “rescue” events for each microtubule is also recorded in the “results table.”

D. Automatic Data Analysis

Alternatively to the manual analysis, the user can execute an automatic analysis option by pressing the “Auto Analysis” button. MT-LHAP will analyze current life-history plot in a “LifeHistoryPlotWindow” window using standard rules (Yenjerla *et al.*, 2010) and criteria values from MT-LHAP GUI interface. Results from the last analysis (manual or automatic) can be erased from the memory by the “Undo Last Analysis” button, and analysis can be rerun either in automatic or in manual mode.

E. Post-Analysis Procedures

After the entire life-history plot is analyzed and categorized, tracking information of additional microtubules can be similarly loaded from a file or from an image stack and processed. While MT-LHAP analyzes one microtubule track at a time, analysis results for each microtubule will accumulate in the “ResultsTableWave” table for subsequent use. After all the tracking data for various microtubules are processed user should finalize calculation of all results by pressing “End Analysis” button. Recorded measurements from the “ResultsTableWave” table are transferred into the Microsoft Excel spreadsheet to determine the overall average parameters of dynamic instability as described earlier (Yenjerla *et al.*, 2010). We express the results of the dynamic instability parameters as the mean and standard error of mean and sometimes also additionally represent life-history plots and frequency histograms.

IV. Conclusion

We use MT-LHAP in an Igor Pro environment to calculate the various parameters of *in vitro* dynamic instability of microtubules. Further development of MT-LHAP by incorporating semi-automated or fully automated tracking may be beneficial.

References

- Jordan, M. A., and Kamath, K. (2007). How do microtubule-targeted drugs work? An overview. *Curr. Cancer Drug Targets* **7**, 730–742.
- Jordan, M. A., and Wilson, L. (2004). Microtubules as a target for anticancer drugs. *Nat. Rev. Cancer* **4**, 253–265.
- Kueh, H. Y., and Mitchison, T. J. (2009). Structural plasticity in actin and tubulin polymer dynamics. *Science* **325**, 960–963.
- Yenjerla, M., Lopus, M., and Wilson, L. (2010). Analysis of dynamic instability of steady state microtubules *in vitro* by video enhanced differential interference contrast microscopy. In “Methods in Cell Biology” (J. J. Correia, and L. Wilson, eds.), Elsevier Inc., San Diego, CA. In Press.

CHAPTER 12

Nanometer-Resolution Microtubule Polymerization Assays Using Optical Tweezers and Microfabricated Barriers

Blake D. Charlebois^{*}, Henry T. Schek III[†], and Alan J. Hunt^{*,‡}

^{*}Department of Biomedical Engineering, University of Michigan, Ann Arbor, Michigan 48109

[†]Director of Engineering, 89 North, Burlington, Vermont 05401

[‡]Center for Ultrafast Optical Science, University of Michigan, Ann Arbor, Michigan 48109

Abstract

- I. Introduction
- II. Rationale
- III. Methods
- IV. Materials
 - A. Buffer
 - B. Experimental Apparatus
 - C. MT Length Constraints: Applied Force and Barrier Design
 - D. Preparation of Biotinylated MT Seeds
 - E. Preparation of NeutrAvidin®-Coated Beads
- V. Discussion
 - A. Advantages of Force Clamping
 - B. Data Analysis: Bead Position Relative to Trap Center
 - C. Data Analysis: MT Length Changes
 - D. Detection Limits: Forces, Bandwidth, and Resolution
 - E. Potential Sources of Artifacts
- VI. Summary
- Acknowledgments
- References

Abstract

Microtubule (MT) polymerization dynamics, which are crucial to eukaryotic life and are the target of important anticancer agents, result from the addition and loss of 8-nm-long tubulin-dimer subunits. Addition and loss of one or a few subunits cannot

be observed at the spatiotemporal resolution of conventional microscopy, and requires development of approaches with higher resolution. Here we describe an assay in which one end of an MT abuts a barrier, and MT length changes are coupled to the movement of an optically trapped bead, the motion of which is tracked with high resolution. We detail assay execution, including preparation of the experimental chamber and orientation of the MT against the barrier. We describe design requirements for the experimental apparatus and barriers, and preparation of materials including stable, biotinylated MT seeds from which growth is initiated and NeutrAvidin®-coated beads. Finally, we discuss advantages of moving the optical trap such that it applies a constant force (force clamping), detection limits, the importance of high temporal resolution, data analysis, and potential sources of experimental artifacts.

===== I. Introduction

Microtubules (MTs) are essential to many processes in eukaryotic cells: they help orchestrate chromosome movements, organelle transport, and changes in cell morphology, and they provide mechanical support for intracellular organization. MT polymerization dynamics (Desai and Mitchison, 1997) are of great interest because rapid MT length changes allow tasks such as cytoskeletal reorganization and mitosis, and because these dynamics are the target of important anticancer drugs (Jordan and Wilson, 2004). MTs exhibit unusual polymerization dynamics: in a phenomenon termed *dynamic instability*, they alternate between phases of growth and relatively rapid shortening (Mitchison and Kirschner, 1984). This behavior, as well as its modulation by MT-associated proteins (MAPs) and MT-binding drugs, has been the subject of intensive research, yet it remains difficult to rigorously test the multiple, often conflicting models for dynamic instability. Certain principles are, however, generally accepted: dynamic instability is driven by energy released from GTP hydrolysis; after a GTP-subunit incorporates into an MT, the GTP hydrolyzes to GDP + inorganic phosphate; GDP-tubulin is less stable in the MT lattice, and a growing MT has a stabilizing cap of GTP-tubulin and a labile inner core of GDP-tubulin (Desai and Mitchison, 1997; Mitchison and Kirschner, 1984).

Most direct characterization of MT dynamics, focusing on rates of growth, shortening, and transitions between growth and shortening, has been by light microscopy (e.g., Chretien *et al.*, 1995; Dye *et al.*, 1996; Gildersleeve *et al.*, 1992; Horio and Hotani, 1986; Jordan *et al.*, 1993; Odde *et al.*, 1996; Walker *et al.*, 1988), and this approach continues to yield valuable insights into MT dynamics and their modulation (e.g., Bieling *et al.*, 2007; Brouhard *et al.*, 2008; Helenius *et al.*, 2006; Moores *et al.*, 2006; Pedigo and Williams, 2002). However, conventional light microscopy allows observation of MT length changes corresponding to the addition or loss of hundreds of subunits. At standard video rate, the temporal resolution is, at best, on the order of the time between subunit additions or losses, though recent data suggest subunit exchange is much more rapid (Schek *et al.*, 2007). Rates of growth and shortening thus represent an average over many addition or loss events. Observing one or a few such events to unequivocally determine molecular-scale details requires much higher spatiotemporal resolution.

Nanometer-resolution measurements of events resulting from MT dynamics has recently been achieved with the development of assays using optical tweezers (e.g., Asbury *et al.*, 2006; Grishchuk *et al.*, 2005; Kerssemakers *et al.*, 2006; Schek *et al.*, 2007; reviewed in Gardner *et al.*, 2008), including those in which the tweezers are used to polymerize an MT into a barrier and track MT length changes (Kerssemakers *et al.*, 2006; Schek *et al.*, 2007), yielding important new insights into MT polymerization dynamics. For instance, on short (hundreds of ms) time-scales, growth rates were directly measured to be highly variable and, even during periods of net growth, sometimes negative (Kerssemakers *et al.*, 2006; Schek *et al.*, 2007), with growth-phase shortening events that correspond to the loss of several layers of subunits (Schek *et al.*, 2007).

II. Rationale

To observe MT polymerization with sufficient spatiotemporal resolution to detect addition or loss of one or a few 8-nm subunits, MT length changes can be measured by coupling them to the movement of an object whose position can be tracked at high resolution: in this case, a bead held by optical tweezers. The MT-linked bead is trapped, and the MT is oriented such that it abuts a suitably designed barrier (Fig. 1A–C). Because MTs are relatively rigid, growth or shortening at the end of the MT abutting the barrier will result in bead movement, which can be tracked with high precision using interferometry or video processing. The trap position can be held fixed (Kerssemakers *et al.*, 2006), or it can be moved such that applied force is constant (Schek *et al.*, 2007), which is termed *force clamping*. Here we focus on our force-clamp assay (Schek *et al.*, 2007), but note advantages of other approaches (Kerssemakers *et al.*, 2006).

III. Methods

The assay entails constructing an experimental chamber, flowing in the experimental solution including NeutrAvidin®-coated beads coupled to biotinylated MT seeds (short, stable MTs from which growth can be initiated), trapping an MT-linked bead, orienting the MT against a barrier (Figs. 1 and 2), and collecting position data. Microfabrication of barriers on glass coverslips is described elsewhere (Schek and Hunt, 2005), and here we focus on execution of the assay.

A coverglass patterned with barriers microfabricated from LOR and SU-8 (MicroChem, Newton, MA) photoresist layers (Fig. 1C, Section IV) is cleaned with, in succession, methanol, ethanol, isopropanol, 0.1% sodium dodecyl sulfate (SDS), and purified water. This is incorporated into an experimental chamber using two aluminum foil spacers, each with a thin coating of vacuum grease, to position the coverglass a small distance (~70 μ m) above the slide. The foil spacers are spaced about 6 mm apart to create an experimental flow chamber with barriers on the upper surface, and open ends such that fluids may be introduced by capillary action. Thin spacing must be maintained between the coverglass and slide: because our microscope is upright, we use silica beads (Section IV), which sink to the bottom of the chamber where they must be initially trapped (Fig. 1D); however, with increasing

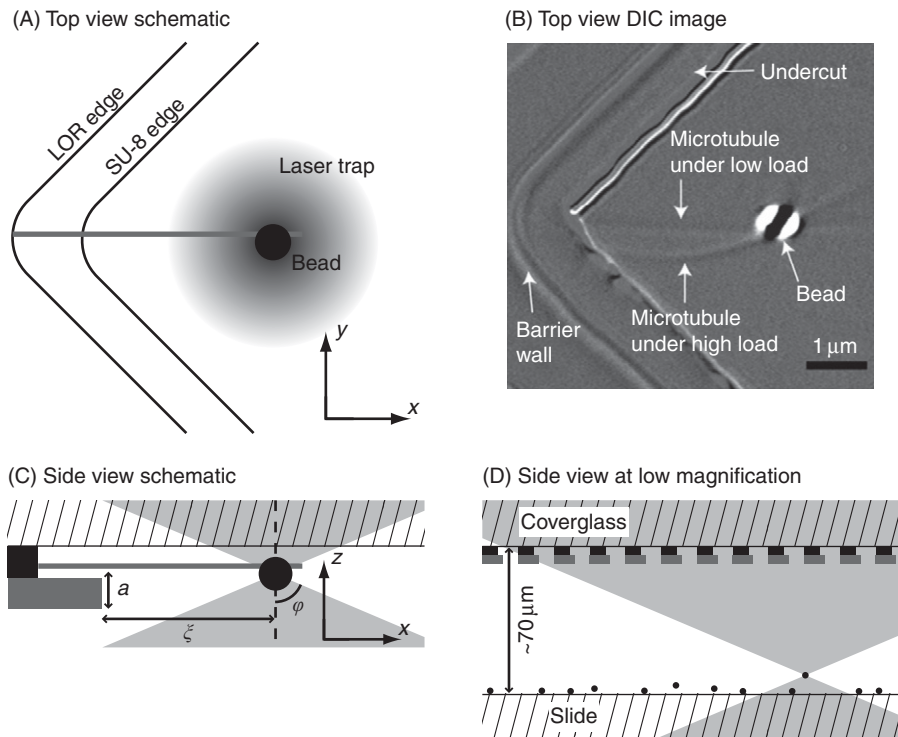


Fig. 1 Assay overview and experimental geometry. (A) Schematic top view. The microtubule (gray) tip is constrained in the y direction by the vertex of the LOR photoresist wall, which also blocks movement or growth in the negative x direction. The microtubule is pushed toward the barrier by the laser trap via the bead. A force-clamp feedback loop can move the laser trap along the x -axis such that the force on the bead is constant, in which case microtubule length changes result in corresponding trap movement. This image is after Schek *et al.* (2007), Fig. 1. (B) Differential interference contrast image corresponding to (A). An image of the microtubule when buckled is superimposed on the image of the microtubule under low load, demonstrating that the microtubule tip remains constrained over a range of forces. Reprinted from *Current Biology*, Vol. 17, Schek, Gardner, Cheng, Odde, & Hunt, “Microtubule assembly dynamics at the nanoscale” pp. 1445–1455, ©2007 with permission from Elsevier. (C) Schematic side view. The laser propagates in the negative z direction. The undercut of the LOR layer (black) allows the SU-8 layer (gray) and coverglass (hatched) to constrain the microtubule tip in the z direction. The focus of the trapping laser beam (gray triangles), which is slightly above the bead center (not shown), is a distance a above the bottom of the SU-8 layer in the z direction and a distance ξ from the SU-8 edge in the x direction. If ξ approaches $\sqrt{2}a \tan(\varphi)$ (assuming the barrier edge is 45° from the x axis), the laser will be clipped by the barrier. This image is after Schek and Hunt (2005), Fig. 1. (D) Schematic side view at lower magnification. Beads sink to the bottom of the experimental chamber, which is $\sim 70 \mu\text{m}$ below the coverglass. Positioning the trap at increasing depth impairs trapping due to spherical aberration and interference of the laser with photoresist structures.

depth, the beam profile of the trapping laser is increasingly impaired by spherical aberration and by passage through the photoresist structures that form the barriers above (Fig 1D). This can be partially remedied by patterning barriers at a reduced surface density or by increasing power of the trapping laser when searching for a bead.

Before introducing the experimental mixture, buffer is flowed into the experimental chamber, and if any areas exclude liquid this is remedied by gently pressing the coverglass. Because beads spontaneously aggregate, they are

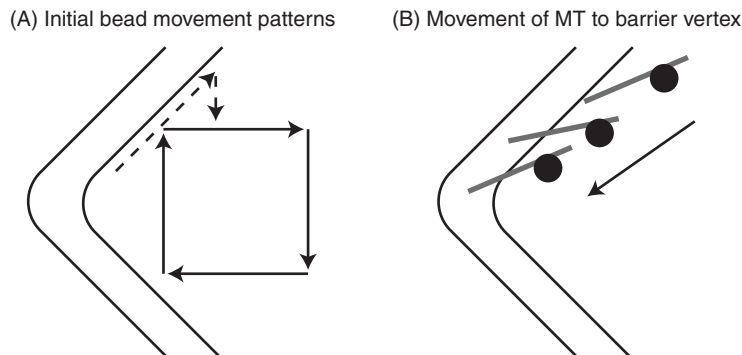


Fig. 2 Orienting an MT in the barrier. (A) Initial bead movement patterns. The bead is moved, for instance, in a square pattern (solid arrows) or along the barrier edge and then toward the center in the *y* direction (dashed arrows) to keep the MT in the focal plane and orient it as shown in (B). (B) Movement of MT into barrier vertex. The MT is maneuvered into the undercut and along the barrier edge toward the vertex. Final orientation should be similar to that of Fig. 1A.

separated by passage through a 25-G needle several times immediately before the experiment. Following this shearing, several chamber volumes of the experimental mixture (buffer, beads, stable MT seeds, free tubulin, MAPs, and MT-binding drugs as applicable) are flowed into the experimental chamber, which must then be sealed to prevent drying and drying-induced fluid flow during experiments; we use VALAP (a 1:1:1 mixture of Vaseline, lanolin, and paraffin), which is melted and brushed onto the ends of the chamber. The chamber is then quickly moved to the microscope, and a single free bead is trapped. To determine whether one or more MT seeds are attached to a given trapped bead, the bead is moved laterally relative to the buffer by moving the trap or microscope stage to bring an MT into the focal plane (the trap is positioned such that the bead is held in the imaging focal plane).

A bead with an MT seed is moved to the vicinity of a barrier and oriented appropriately (Fig. 2). The bead can be moved in a pattern (Fig. 2A) that keeps the MT in the focal plane and orients its plus end near an edge of the barrier (Fig. 2B), at which point the bead can be moved such that the MT moves into the undercut and down the barrier edge to the vertex. The MT tip must be located at the barrier vertex and constrained by the undercut (Fig. 1A–C), at which point applying the force clamp will push the MT against the barrier. From this point onward, trap movements required to maintain constant force correspond to changes in MT length.

To establish whether the plus end or the minus end is in the barrier, the growth of both ends is observed by light microscopy. If experimental conditions require a relatively low growth rate, the investigator may more easily determine MT polarity by inducing high growth at the end of an experiment by flowing in buffer with a high tubulin concentration. An alternative approach for establishing MT polarity is to substitute axonemes for seeds, as MTs preferentially grow from the plus ends of isolated axonemes. These provide tighter control over protofilament number and allow the MT to be oriented using a keyhole trap (Kerssemakers *et al.*, 2006).

IV. Materials

All chemicals are obtained from Sigma-Aldrich (St. Louis, MO) unless otherwise specified.

A. Buffer

We perform experiments in BRB-80 [80 mM pipes, 1 mM MgCl₂, 1 mM ethylene glycol tetraacetic acid (EGTA), pH 6.8]. Because MT growth (Khan and Luduena, 1991) and flexural rigidity (Mickey and Howard, 1995) are influenced by the oxidation state, we supplement the buffer with oxygen scavengers: 0.12 mg/ml catalase, 0.6 mg/ml glucose oxidase, 30 mM glucose, and 2 mM dithiothreitol. We also supplement buffer with an additional mM MgCl₂ per mM of guanine nucleotide.

B. Experimental Apparatus

The optical tweezers apparatus (Brouhard *et al.*, 2003; Schek and Hunt, 2006; Visscher and Block, 1998) should have several features. First, it should detect bead position with high spatiotemporal resolution using, for instance, back-focal-plane interferometry (BFPI) (Gittes and Schmidt, 1998a). High temporal resolution allows thermal noise to be suppressed by filtering, which improves spatial resolution (see Section V). Second, the apparatus should be able to apply a time-averaged constant force (force clamp) by moving the trap, which has several advantages (Section V), including tracking MT length changes over a larger range and minimizing the effect of force on results. Finally, it should allow simultaneous light microscopy appropriate for visualizing MTs, such as video-enhanced differential-interference contrast (VE-DIC) microscopy. For VE-DIC, contrast enhancement, background subtraction, and frame averaging can be achieved with a Hamamatsu ARGUS (Hamamatsu Photonics, Hamamatsu City, Japan) or with equivalent commercial or custom digital image acquisition and processing. The setup should ideally simultaneously process and record video at 30 Hz, allowing the user to record MT movement while observing it in real time.

C. MT Length Constraints: Applied Force and Barrier Design

The MT used for the experiment must be short enough that it will not buckle under the trapping force (Schek and Hunt, 2005). The force at which a segment of MT buckles under compression is proportional to its flexural rigidity and inversely proportional to the square of its length, and has been estimated at 2 pN for a 10-μm MT (Gittes *et al.*, 1993), though smaller values have been measured (e.g., Kikumoto *et al.*, 2006; Kurachi *et al.*, 1995). The length of MT between the bead and barrier in our experiments is generally ~5 μm.

The MT must also be long enough that the experiment can be conducted without impairing measurements of the bead position (Schek and Hunt, 2005). The geometry of both the barrier and laser beam must be considered (Fig. 1C). The laser must not pass through photoresist upstream of the trap, as this would change the beam profile, thereby introducing an error in the applied force. In the case of BFPI detection, the laser beam should not pass through photoresist downstream of the trap either, since this affects the bead position measurement. Relatively thin layers of photoresist allow the assay to be conducted with the trap closer to the barrier. The effect of

the barriers on the trap and bead detection at a given position can be determined experimentally by performing a power spectrum calibration (Gittes and Schmidt, 1998b): if the power spectrum is Lorentzian and the parameters yielded by the calibration are consistent with those obtained in the absence of barriers, then the effect of the barrier on measured bead position is negligible.

D. Preparation of Biotinylated MT Seeds

For taxol-stabilized seeds, 50 μ M tubulin and 1 mM GTP in buffer (see above) are incubated at 37°C for 25 min, brought to 10 μ M taxol, and immediately vortexed. These MTs are centrifuged (Beckman Airfuge; Beckman Coulter, Brea, CA), the supernatant is discarded, and the pellet is rinsed and resuspended in BRB-80 with 10 μ M taxol. Biotin succinimidyl ester (B1606; Invitrogen Corporation, Carlsbad, CA) is added at 1.7 mM, and the sample is incubated at 37°C for 15 min. To quench the reaction, three volumes of 400 mM glycine (in BRB-80) are added, followed by an additional 10 min of incubation. The sample is centrifuged, the supernatant is discarded, and the pellet is rinsed and resuspended in BRB-80 without taxol. It is then sheared several times through a 30-G needle. Finally, in order to deplete taxol, the seeds are centrifuged, rinsed, and resuspended two more times in buffer. The resulting seeds should be \sim 2 μ m long. The amount of free biotin in the experimental solution must be minimal, as it may compete with seeds for NeutrAvidin®-binding sites.

For guanylyl-(α,β)-methylene-diphosphonate (GMP-CPP; NU-405S; Jena Bioscience, Jena, Germany) stabilized seeds, the above protocol is altered as follows. The initial tubulin concentration is 2 μ M to reduce spontaneous MT nucleation (Hyman *et al.*, 1992). The 1 mM GTP is replaced with 0.2 mM GMP-CPP (this five-fold reduction in concentration reduces expense). Only one centrifugation is performed after shearing.

For experiments in which a relatively low polymerization rate is expected, seeds can be made longer by adjusting the shearing protocol (e.g., see Farrell *et al.*, 1987; Melki *et al.*, 1993; Williams and Rone, 1989; Yamauchi *et al.*, 1993), or short seeds can be elongated before the experiment by incubating with tubulin (pulsed if necessary). Seeds will anneal to form longer MTs over longer time periods (hours). We generally begin a day of experiments by making seeds and stop collecting data when the seed concentration and length are no longer appropriate.

E. Preparation of NeutrAvidin®-Coated Beads

A solution of \sim 0.6- μ m silica beads (SS03N; Bangs Laboratories, Fishers, IN) at 10 mg/ml in BRB-80 is sonicated and vortexed (a few minutes each), and 20 μ g/ml biotin-BSA is added, followed by 5 min of vortexing. The beads are then centrifuged. The supernatant is discarded and the pellet is rinsed three times with BRB-80 gently and without resuspension. It is then resuspended in 10 times the original volume (\sim 1 mg/ml beads) and vortexed. This solution is brought to 20 μ g/ml NeutrAvidin® (A2666, Invitrogen) and vortexed gently for 5 min. During this step, a low bead concentration reduces the chances of NeutrAvidin® binding two biotinylated beads to each other. The beads are centrifuged, the supernatant is discarded, and the pellet is rinsed and resuspended in the original volume (\sim 10 mg/ml beads). The beads are centrifuged, rinsed, and resuspended three additional times. Silica beads will slowly sediment, so when making aliquots, the beads should be mixed frequently to ensure

all aliquots have roughly the same concentration. Aliquots are flash-frozen in liquid nitrogen and stored at -80°C .

Most beads should be attached to zero, one, or occasionally two seeds, and the concentration of bead–seed complexes must be low enough to prevent the formation of networks of beads and seeds. In the experimental solution, we generally use taxol-stabilized biotinylated seeds at $\sim 1/50$ dilution and beads at $\sim 1/80$ dilution, but these quantities vary significantly.

===== V. Discussion

Here we discuss advantages of force clamping, approaches to data analysis, assessment of detection limits, and potential sources of artifacts.

A. Advantages of Force Clamping

In contrast to stationary-trap experiments, a force-clamp experiment (Finer *et al.*, 1994; Gittes and Schmidt, 1998b; Visscher and Block, 1998) uses a feedback loop in which the trap is moved in response to changes in the bead position such that the time-averaged force is constant. This offers several advantages. In a stationary-trap experiment, the MT lengthens against the barrier, pushing the bead from the trap center. Data collection terminates when the MT pushes the bead out of useable range of the trap or force becomes high enough to buckle the MT or induce a catastrophe. Also, because the force changes with bead movement, its effect on MT polymerization dynamics is variable. With force clamping, data can be collected over a much larger range of displacement because the trap moves to accommodate bead movement, and the force can be tightly controlled as an experimental variable or kept low to minimize its effect on polymerization dynamics. Also, stationary-trap data underestimates MT growth because MT displacement is partially accommodated by stretching of the bead–MT linkage. The stiffness of the bead–MT linkage must be obtained to correct this underestimation (Kerssemakers *et al.*, 2006), and this can be challenging due to nonlinear compliance and variability of compliance between bead–MT complexes (Svoboda *et al.*, 1993; Visscher and Block, 1998). Force clamping obviates the need to correct for this compliance (Visscher and Block, 1998); it maintains a constant stretch of the bead–MT linkage so that changes in bead position directly correspond to changes in MT length (Schek *et al.*, 2007).

B. Data Analysis: Bead Position Relative to Trap Center

The raw bead position data allow assessment of force-clamp performance and can allow detection of events that occur more quickly than the force clamp responds. Although the position of the bead can be detected at kHz frequencies with sub-nanometer precision using techniques such as BFPI (Gittes and Schmidt, 1998a), much of the high-frequency movement is due to thermal motion, and must be filtered to obtain a precise estimate of MT length changes. Applying a low-pass filter yields a good signal-to-noise ratio and allows examination of events occurring on a timescale longer than the reciprocal of the filter cutoff frequency (see “Detection limits”

below). To minimize phase distortion, forward–backward filtering may be appropriate (e.g., [Gustafsson, 1996](#)).

Bead position data also allow forces experienced by the bead and MT to be assessed. For instance, if the bead is subjected to a combination of thermal, Hookean, and drag (proportional to velocity) forces, the power spectrum of the bead position versus time trace will be Lorentzian and will yield spring constants and damping coefficients ([Gittes and Schmidt, 1998b](#)). In addition to allowing the stiffness of the optical trap to be verified, this type of analysis can identify artifacts resulting from, for instance, the MT becoming stuck to the barrier, or the laser beam being clipped by a barrier.

C. Data Analysis: MT Length Changes

A subunit addition will change MT length by 0–8 nm: given the 13 protofilament lattice structure of an MT, addition of a single subunit increases the MT length by at most 8 nm if the subunit adds to the leading protofilament, and various smaller amounts including no length change if the subunit adds to a lagging protofilament.

Several approaches are available for analysis of length changes. Most simply, length changes Δx and growth rates r are computed for each fixed time interval of length τ . For analysis of the distribution of Δx or r , variance may be of particular interest because the variance of MT growth rate is higher than expected from conventional linear polymer growth theory ([Oosawa, 1970](#)), and there has been substantial interest in determining the mechanism behind this (e.g., [Dye *et al.*, 1996](#); [Howard and Hyman, 2009](#); [Odde *et al.*, 1996](#); [Pedigo and Williams, 2002](#)). In cases where it is difficult to choose an appropriate timescale, τ , of interest *a priori*, analysis can be repeated for multiple values of τ ([Svoboda *et al.*, 1994](#)), an algorithm can be applied that computes growth or shortening rate using time intervals of varying length as it proceeds through the time series ([Schek *et al.*, 2007](#)), or a timescale-independent approach such as spectral analysis can be applied ([Odde *et al.*, 1996](#)). To detect repeated displacement events (e.g., steps), the distance between relatively stationary periods can be examined, for example, by forming a pairwise-distance distribution function ([Svoboda *et al.*, 1993](#)). Searches for steps must be approached cautiously however: without fundamental expectations for speed and size of steps to form a null hypothesis, it is difficult to design a statistical test to establish that a noisy data stream contains “steps,” and related errors have repeatedly plagued biophysical studies of nanoscale movements. Limits to detection of steps in noisy signals are discussed further in [Moffit *et al.* \(2008\)](#).

D. Detection Limits: Forces, Bandwidth, and Resolution

For experiment design and data interpretation, it is crucial to understand the forces to which the bead is subjected: trap, bead–MT linkage, viscous, and thermal. These forces and their implications for detection limits are discussed in detail elsewhere ([Gittes and Schmidt, 1998b](#); [Moffit *et al.*, 2008](#); [Visscher and Block, 1998](#)). Briefly, in a force-clamp assay, theoretical spatial resolution can be computed, and is predicted to improve with decreasing bead–MT linkage compliance, bead drag coefficient, and filter cutoff frequency used by the force clamp ([Gittes and Schmidt, 1998b](#)). Therefore, resolution may improve with a smaller bead, which should

decrease drag and bead–MT compliance due to bead rocking, or with higher applied force, assuming the bead–MT linkage compliance exhibits strain hardening (Svoboda *et al.*, 1993). Furthermore, high bandwidth facilitates stationary-trap or force-clamp data analysis, in which case filtering may be required to suppress thermal noise and achieve desired spatial resolution, though at the cost of lowered temporal resolution (e.g., see supplemental material accompanying Schek *et al.*, 2007). Temporal resolution is therefore determined by detector bandwidth or by the filter cutoff, and events that cannot be resolved in time will be detected with a delay or, if they do not result in a persistent displacement, will be missed or underestimated: for example, a spike caused by rapid addition and loss of subunits may not be apparent in filtered data, but still be visible in the raw high-bandwidth data.

In addition to theoretical considerations, data should be collected using a control MT in which length changes are suppressed, such as a GMP-CPP-stabilized MT without free tubulin, in order to experimentally assess detection limits and potential artifacts (Schek *et al.*, 2007).

E. Potential Sources of Artifacts

Several potential sources of artifacts should be considered.

1. An MT may become stuck to a barrier. To verify that this has not occurred, the MT should be pulled slightly (~500 nm) away from the barrier wall at the end of each experiment, and the trace should be inspected for evidence of sticking.
2. If substantial MT nucleation occurs during the experiment (this is easily observed under VE-DIC), the concentration of free tubulin may fall rapidly toward the critical concentration. Nucleation of pure GTP-tubulin is highly cooperative; the rate of nucleation is extremely sensitive to free tubulin concentration (e.g., Carlier and Pantaloni, 1978; Fygenson *et al.*, 1995; Voter and Erickson, 1984). Furthermore, nucleation is stimulated in the presence of, for instance, γ -tubulin or γ -tubulin complexes (reviewed in Job *et al.*, 2003), taxol (e.g., Schiff *et al.*, 1979), certain MAPs (e.g., Gupta *et al.*, 2009; Moores *et al.*, 2006; Slep and Vale, 2007), or a slowly-hydrolysable GTP analog such as GMP-CPP (Hyman *et al.*, 1992; Sandoval and Weber, 1980).
3. MT ends other than the one in the barrier may impair measurements. For instance, the end of the MT opposite that under investigation may strike a different wall. Also, an MT that is out of plane, and therefore not visible, may strike the barrier. Data should be inspected for signs that such events occurred (e.g., a drop in thermal movements or movement of the bead in the y direction).
4. Drift may impair measurements. Barrier movement in the x direction due to stage drift may result in underestimation or overestimation of MT growth rates. Depending on the design of the tweezers apparatus, drift in the z direction may affect trap stiffness and bead-position detection sensitivity. It may also change the zero position of the bead detection system, thereby introducing error in the applied force.
5. Small details in the shape of the barriers may cause artifactual length change measurements. With sufficient forces and appropriate barrier design, this can be addressed or avoided: this is discussed in the supplemental material accompanying Schek *et al.* (2007).

VI. Summary

We have described an assay for studying MT polymerization dynamics with high spatiotemporal resolution and discussed interpretation of the data. This technique promises to yield a wealth of insights into MT polymerization dynamics and their modulation by MAPs and MT drugs.

Acknowledgments

We thank J. Damon Hoff and Jun Cheng for fruitful discussions.

References

Asbury, C. L., Gestaut, D. R., Powers, A. F., Franck, A. D., and Davis, T. N. (2006). The Dam1 kinetochore complex harnesses microtubule dynamics to produce force and movement. *Proc. Natl. Acad. Sci. U.S.A.* **103**, 9873–9878.

Bieling, P., Laan, L., Schek, H., Munteanu, E. L., Sandblad, L., Dogterom, M., Brunner, D., and Surrey, T. (2007). Reconstitution of a microtubule plus-end tracking system in vitro. *Nature* **450**, 1100–1105.

Brouhard, G. J., Schek, H. T., and Hunt, A. J. (2003). Advanced optical tweezers for the study of cellular and molecular biomechanics. *IEEE Trans. Biomed. Eng.* **50**, 121–125.

Brouhard, G. J., Stear, J. H., Noetzel, T. L., Al Bassam, J., Kinoshita, K., Harrison, S. C., Howard, J., and Hyman, A. A. (2008). XMAP215 is a processive microtubule polymerase. *Cell* **132**, 79–88.

Carlier, M. F., and Pantaloni, D. (1978). Kinetic-analysis of cooperativity in tubulin polymerization in presence of guanosine diphosphate or triphosphate nucleotides. *Biochemistry* **17**, 1908–1915.

Chretien, D., Fuller, S. D., and Karsenti, E. (1995). Structure of growing microtubule ends – 2-dimensional sheets close into tubes at variable rates. *J. Cell Biol.* **129**, 1311–1328.

Desai, A., and Mitchison, T. J. (1997). Microtubule polymerization dynamics. *Annu. Rev. Cell Dev. Biol.* **13**, 83–117.

Dye, R. B., and Williams, R. C. (1996). Assembly of microtubules from tubulin bearing the nonhydrolyzable guanosine triphosphate analogue GMPPCP [Guanosyl 5'-(beta,gamma-methylenediphosphonate)]: Variability of growth rates and the hydrolysis of GTP. *Biochemistry* **35**, 14331–14339.

Farrell, K. W., Jordan, M. A., Miller, H. P., and Wilson, L. (1987). Phase dynamics at microtubule ends – the coexistence of microtubule length changes and treadmilling. *J. Cell Biol.* **104**, 1035–1046.

Finer, J. T., Simmons, R. M., and Spudich, J. A. (1994). Single myosin molecule mechanics – piconewton forces and nanometer steps. *Nature* **368**, 113–119.

Fygenson, D. K., Flyvbjerg, H., Sneppen, K., Libchaber, A., and Leibler, S. (1995). Spontaneous nucleation of microtubules. *Phys. Rev. Lett.* **51**, 5058–5063.

Gardner, M. K., Hunt, A. J., Goodson, H. V., and Odde, D. J. (2008). Microtubule assembly dynamics: New insights at the nanoscale. *Curr. Opin. Cell Biol.* **20**, 64–70.

Gildersleeve, R. F., Cross, A. R., Cullen, K. E., Fagen, A. P., and Williams, R. C. (1992). Microtubules grow and shorten at intrinsically variable rates. *J. Biol. Chem.* **267**, 7995–8006.

Gittes, F., Mickey, B., Nettleton, J., and Howard, J. (1993). Flexural rigidity of microtubules and actin-filaments measured from thermal fluctuations in shape. *J. Cell Biol.* **120**, 923–934.

Gittes, F., and Schmidt, C. F. (1998a). Interference model for back-focal-plane displacement detection in optical tweezers. *Opt. Lett.* **23**, 7–9.

Gittes, F., and Schmidt, C. F. (1998b). Signals and noise in micromechanical measurements. In “Laser Tweezers in Cell Biology” (M. P. Sheetz, ed.), Vol. 55, pp. 129–156. Academic Press, San Diego.

Grishchuk, E. L., Molodtsov, M. I., Ataullakhanov, F. I., and McIntosh, J. R. (2005). Force production by disassembling microtubules. *Nature* **438**, 384–388.

Gupta, K. K., Paulson, B. A., Folker, E. S., Charlebois, B., Hunt, A. J., and Goodson, H. V. (2009). Minimal plus-end tracking unit of the cytoplasmic linker protein CLIP-170. *J. Biol. Chem.* **284**, 6735–6742.

Gustafsson, F. (1996). Determining the initial states in forward-backward filtering. *IEEE Trans. Signal Process.* **44**, 988–992.

Helenius, J., Brouhard, G., Kalaidzidis, Y., Diez, S., and Howard, J. (2006). The depolymerizing kinesin MCAK uses lattice diffusion to rapidly target microtubule ends. *Nature* **441**, 115–119.

Horio, T., and Hotani, H. (1986). Visualization of the dynamic instability of individual microtubules by dark-field microscopy. *Nature* **321**, 605–607.

Howard, J., and Hyman, A. A. (2009). Growth, fluctuation and switching at microtubule plus ends. *Nat. Rev. Mol. Cell Biol.* **10**, 569–574.

Hyman, A. A., Salser, S., Drechsel, D. N., Unwin, N., and Mitchison, T. J. (1992). Role of GTP hydrolysis in microtubule dynamics – information from a slowly hydrolyzable analog, GMPCPP. *Mol. Biol. Cell* **3**, 1155–1167.

Job, D., Valiron, O., and Oakley, B. (2003). Microtubule nucleation. *Curr. Opin. Cell Biol.* **15**, 111–117.

Jordan, M. A., Toso, R. J., Thrower, D., and Wilson, L. (1993). Mechanism of mitotic block and inhibition of cell-proliferation by taxol at low concentrations. *Proc. Natl. Acad. Sci. U.S.A.* **90**, 9552–9556.

Jordan, M. A., and Wilson, L. (2004). Microtubules as a target for anticancer drugs. *Nat. Rev. Cancer* **4**, 253–265.

Kerssemakers, J. W. J., Munteanu, E. L., Laan, L., Noetzel, T. L., Janson, M. E., and Dogterom, M. (2006). Assembly dynamics of microtubules at molecular resolution. *Nature* **442**, 709–712.

Khan, I. A., and Luduena, R. F. (1991). Possible regulation of the invitro assembly of bovine brain tubulin by the bovine thioredoxin system. *Biochim. Biophys. Acta* **1076**, 289–297.

Kikumoto, M., Kurachi, M., Tosa, V., and Tashiro, H. (2006). Flexural rigidity of individual microtubules measured by a buckling force with optical traps. *Biophys. J.* **90**, 1687–1696.

Kurachi, M., Hoshi, M., and Tashiro, H. (1995). Buckling of a single microtubule by optical trapping forces – direct measurement of microtubule rigidity. *Cell Motil. Cytoskeleton* **30**, 221–228.

Melki, R., Vainberg, I. E., Chow, R. L., and Cowan, N. J. (1993). Chaperonin-mediated folding of vertebrate actin-related protein and gamma-tubulin. *J. Cell Biol.* **122**, 1301–1310.

Mickey, B., and Howard, J. (1995). Rigidity of microtubules is increased by stabilizing agents. *J. Cell Biol.* **130**, 909–917.

Mitchison, T., and Kirschner, M. (1984). Dynamic instability of microtubule growth. *Nature* **312**, 237–242.

Moffitt, J. R., Chemla, Y. R., Smith, S. B., and Bustamante, C. (2008). Recent advances in optical tweezers. *Annu. Rev. Biochem.* **77**, 205–228.

Moores, C. A., Perderiset, M., Kappeler, C., Kain, S., Drummond, D., Perkins, S. J., Chelly, J., Cross, R., Houdusse, A., and Francis, F. (2006). Distinct roles of doublecortin modulating the microtubule cytoskeleton. *Embo J.* **25**, 4448–4457.

Odde, D. J., Buettnner, H. M., and Cassimeris, L. (1996). Spectral analysis of microtubule assembly dynamics. *Aiche J.* **42**, 1434–1442.

Oosawa, F. (1970). Size distribution of protein polymers. *J. Theor. Biol.* **27**, 69–86.

Pedigo, S., and Williams, R. C. (2002). Concentration dependence of variability in growth rates of microtubules. *Biophys. J.* **83**, 1809–1819.

Sandoval, I. V., and Weber, K. (1980). Guanosine 5'-(Alpha,Beta-Methylene)Triphosphate enhances specifically microtubule nucleation and stops the treadmill of tubulin protomers. *J. Biol. Chem.* **255**, 6966–6974.

Schek, H. T., Gardner, M. K., Cheng, J., Odde, D. J., and Hunt, A. J. (2007). Microtubule assembly dynamics at the nanoscale. *Curr. Biol.* **17**, 1445–1455.

Schek, H. T., and Hunt, A. J. (2005). Micropatterned structures for studying the mechanics of biological polymers. *Biomed. Microdevices* **7**, 41–46.

Schek, H. T., and Hunt, A. J. (2006). Optical tweezers. In “Encyclopedia of Medical Devices and Instrumentation” (J. G. Webster, ed.), Vol. 5, pp. 175–187. John Wiley & Sons, Hoboken, New Jersey.

Schiff, P. B., Fant, J., and Horwitz, S. B. (1979). Promotion of microtubule assembly invitro by taxol. *Nature* **277**, 665–667.

Slep, K. C., and Vale, R. D. (2007). Structural basis of microtubule plus end tracking by XMAP215, CLIP-170, and EB1. *Mol. Cell* **27**, 976–991.

Svoboda, K., Mitra, P. P., and Block, S. M. (1994). Fluctuation analysis of motor protein movement and single enzyme-kinetics. *Proc. Natl. Acad. Sci. U.S.A.* **91**, 11782–11786.

Svoboda, K., Schmidt, C. F., Schnapp, B. J., and Block, S. M. (1993). Direct observation of kinesin stepping by optical trapping interferometry. *Nature* **365**, 721–727.

Visscher, K., and Block, S. M. (1998). “Versatile Optical Traps with Feedback Control.” Academic Press Inc, San Diego.

Voter, W. A., and Erickson, H. P. (1984). The kinetics of microtubule assembly – evidence for a 2-stage nucleation mechanism. *J. Biol. Chem.* **259**, 430–438.

Walker, R. A., Obrien, E. T., Payer, N. K., Soboeiro, M. F., Voter, W. A., Erickson, H. P., and Salmon, E. D. (1988). Dynamic instability of individual microtubules analyzed by video light-microscopy – rate constants and transition frequencies. *J. Cell Biol.* **107**, 1437–1448.

Williams, R. C., and Rone, L. A. (1989). End-to-end joining of taxol-stabilized GDP-containing microtubules. *J. Biol. Chem.* **264**, 1663–1670.

Yamauchi, P. S., Flynn, G. C., Marsh, R. L., and Purich, D. L. (1993). Reduction in microtubule dynamics invitro by brain microtubule-associated proteins and by a microtubule-associated protein-2 2nd repeated sequence analog. *J. Neurochem.* **60**, 817–826.

CHAPTER 13

Microtubule Dynamics Reconstituted *In Vitro* and Imaged by Single-Molecule Fluorescence Microscopy

Christopher Gell^{*}, Volker Bormuth^{*}, Gary J. Brouhard[†], Daniel N. Cohen[‡], Stefan Diez^{*}, Claire T. Friel^{*}, Jonne Helenius[§], Bert Nitzsche^{*}, Heike Petzold^{*}, Jan Ribbe^{*}, Erik Schäffer[§], Jeffrey H. Stear[¶], Anastasiya Trushko^{*}, Vladimir Varga^{*}, Per O. Widlund^{*}, Marija Zanic^{*}, and Jonathon Howard^{*}

^{*}Max Planck Institute of Molecular Cell Biology & Genetics, 01307 Dresden, Germany

[†]Department of Biology, McGill University, Montréal, Québec, Canada H3A 1B1

[‡]Medical Scientist Training Program, Vanderbilt University, Nashville, Tennessee 37232

[§]Biotechnology Center (BIOTEC), TU Dresden, 01307 Dresden, Germany

[¶]Institute für Biologie, Humboldt Universität zu Berlin, 10115 Berlin, Germany

Abstract

- I. Introduction
- II. Single-Molecule TIRF Microscopy
 - A. TIRF Microscopy for Microtubule Assays
 - B. TIRF Theory
 - C. Two-Color TIRF Implementation
 - D. Using a TIRF Microscope—Practical Tips and Pointers
 - E. Considerations for Dynamic Microtubule Assays
- III. List of Reagents
- IV. Choice of Fluorophore/Protein Labeling
 - A. Common Labeling Strategies
 - B. Dye-Selection Considerations for Multicolor, Dynamic Microtubule Assays
- V. (Anti-)blinking/Photo-Toxicity/Photo-Bleaching Cocktails
 - A. Glucose Oxidase/Catalase with BME as an Oxygen Scavenging/Antifade System
 - B. Troubleshooting (Anti-)blinking/Photo-Toxicity/Photo-Bleaching Cocktails
 - C. Trolox as an Alternative Triplet-State Quencher
 - D. Effect of (Anti-)blinking/Photo-Toxicity/Photo-Bleaching Cocktails

- VI. Preparation of GMPCPP-Stabilized Microtubules
 - A. Single-Cycled Microtubules
 - B. Double-Cycled Microtubules
 - C. Preparation of Labeled Microtubules
 - D. General Information on Handling Microtubules/Tubulin
- VII. Glass Treatment and Sample Chamber Preparation
 - A. Safety
 - B. Key Equipment
 - C. Glass Cleaning and Surface Preparation
 - D. Glass Silanization
 - E. Sample Chamber Assembly and Use
- VIII. Binding of Microtubules and Passivation of Surfaces
 - A. Commonly Used Methods of Attachment
 - B. Typical Seed Binding/Surface Passivation Protocol
- IX. Dynamic Microtubule Assays
 - A. Protocol for Dynamic Microtubule Assay
 - B. Typical Reaction Solution
 - C. Considerations Regarding the Reaction Solution
 - D. Analysis of Dynamic Microtubule Assays

References

===== Abstract

In vitro assays that reconstitute the dynamic behavior of microtubules provide insight into the roles of microtubule-associated proteins (MAPs) in regulating the growth, shrinkage, and catastrophe of microtubules. The use of total internal reflection fluorescence microscopy with fluorescently labeled tubulin and MAPs has allowed us to study microtubule dynamics at the resolution of single molecules. In this chapter we present a practical overview of how these assays are performed in our laboratory: fluorescent labeling methods, strategies to prolong the time to photo-bleaching, preparation of stabilized microtubules, flow-cells, microtubule immobilization, and finally an overview of the workflow that we follow when performing the experiments. At all stages, we focus on practical tips and highlight potential stumbling blocks.

===== I. Introduction

Microtubules are highly dynamic polymers that undergo spontaneous transitions from growing to shrinking phases (Mitchison and Kirschner, 1984). This behavior, termed dynamic instability, is coupled to the hydrolysis of guanosine triphosphate (GTP) and is regulated by many proteins (Howard and Hyman, 2009), including depolymerizing kinesins (Helenius *et al.*, 2006; Varga *et al.*, 2009), polymerases (Brouhard *et al.*, 2008), and plus-tip proteins (Akhmanova and Steinmetz, 2008). The discovery of dynamic instability was contingent on the ability to visualize individual microtubules. Bulk assays such as turbidity, which detects only the total amount of polymer, are insensitive to the dramatic length changes that individual

microtubules undergo when a solution containing tubulin and GTP is under steady-state conditions (Mitchison and Kirschner, 1984).

With advances in fluorescence microscopy, especially the development of total internal reflection fluorescence (TIRF) microscopy (Axelrod, 2008; Axelrod *et al.*, 1984; Funatsu *et al.*, 1995) and the discovery of genetically encoded fluorescent proteins (Zhang *et al.*, 2002), the visualization of individual molecules is becoming routine. The principle underlying single-molecule fluorescence is visualization by localization. When a fluorophore is free in solution it diffuses very quickly ($\sim 100 \mu\text{m}^2/\text{s}$), and within the typical exposure time of a camera (0.1 s), the fluorophore will be “smeared out” over an area of several square microns, corresponding to many camera pixels, which are typically $\sim 0.01 \mu\text{m}^2$. However, when the molecule binds, for example to a microtubule, its rate of diffusion slows dramatically. All the fluorescence is now localized to a small number of pixels during the exposure time of the camera, giving a signal that exceeds the background, even if there are many fluorophores free in solution. TIRF microscopy is important because by exciting only those molecules near the surface where binding takes place, the background is reduced. However, other techniques that reduce the out-of-focus fluorescence, such as confocal microscopy, can also be used for single-molecule studies (Gell *et al.*, 2006).

Single-molecule fluorescence assays have provided many new insights into the movement of motor proteins. For example, the sizes of the steps taken by myosin-V along actin filaments (Yildiz *et al.*, 2003) and kinesin-1 along microtubules (Yildiz *et al.*, 2004) have been measured. Single-molecule assays have also provided new insights into the regulation of microtubule dynamics: kinesin-13 targets the microtubule end through diffusion on the lattice prior to capture at the end (Helenius *et al.*, 2006); XMAP-215 is a processive depolymerase that “surfs” on the growing end of a microtubule as it adds many tubulin dimers (Brouhard *et al.*, 2008); EB1 binds only transiently to the comet tail that it forms at the growing end of a microtubule (Bieling *et al.*, 2007).

The application of single-molecule techniques to study microtubule dynamics is technically much more challenging than its application to motor proteins. The reason is that motors move quickly, often with speeds on the order of $1 \mu\text{m/s}$, and therefore make many elementary steps in a second. By contrast, the dynamics of microtubules is slow. Growth is often only on the order of microns per minute, and the transitions from growth to shrinkage (catastrophe) and shrinkage to growth (rescue) take place at rates less than $1/\text{min}$. Thus, microtubule dynamics must be observed over time-scales of many minutes. This leads to several problems. The main one is that the fluorescent molecules will slowly accumulate on surfaces. Nonspecific binding to the chamber surfaces leads to an increase in the background, making detection of the fluorophores interacting specifically with the microtubules more difficult to observe. Furthermore, nonspecific binding leads to a reduction in the concentration of molecules in solution, causing an apparent decrease in activity. This chapter focuses on experimental procedures to reduce nonspecific binding to surfaces, as well as to increase the fluorescence lifetime of the fluorophores.

II. Single-Molecule TIRF Microscopy

Within the last decade, TIRF microscopy has emerged as a key tool in biophysics, particularly in single-molecule fluorescence studies (Gell *et al.*, 2006; Selvin and Ha, 2007). Incorporated into conventional fluorescence microscopes, TIRF allows imaging limited to a thin layer (~ 100 nm) above a glass substrate (for reviews see Axelrod *et al.*, 1984; Gell *et al.*, 2009; Thompson and Steele, 2007). This removes the distraction of out-of-focus fluorescent material, thereby providing sufficient signal-to-background to detect single molecules. Two methods to implement TIRF are commonly found in the literature: one uses a prism and the other a microscope objective as the condenser (Conibear and Bagshaw, 2000). In this section, we present an overview of the advantages of TIRF in the context of microtubule assays, provide a brief introduction to TIRF theory, and discuss its implementation in a multicolor objective-based system. Finally, we detail useful points to consider when using TIRF for dynamic microtubule studies.

A. TIRF Microscopy for Microtubule Assays

To study microtubule growth or shrinkage, and the mechanism by which microtubule-associated proteins (MAPs) enhance or inhibit growth or shrinkage (Brouhard *et al.*, 2008; Helenius *et al.*, 2006; Varga *et al.*, 2006, 2009), fluorescent microtubules (see Sections IV-VI) are immobilized (see Section VIII) onto glass surfaces (see Section VII and Fig. 1). Typically, high concentrations (100 nM-1 μ M) of MAPs and/or tubulin heterodimers are added to the solution, some proportion of which are fluorescent (see Section IX and Fig. 1). Because only the interactions of the MAP/tubulin with the microtubule are of interest, the microscope is focused on the stationary, surface-immobilized, microtubules. Fluorescence images are recorded, with typical exposure times of ~ 100 ms, over a period of time. Visualization of single molecules is mediated through their localization on the microtubules (as explained above), typically restricting them to a few pixels over the exposure time of each frame. In contrast, molecules not interacting with the microtubule have their signal spread over many pixels in a single frame (and also move out of focus) due to their comparatively rapid, three-dimensional diffusion in solution. In standard epifluorescence illumination, the large number of rapidly diffusing molecules in solution above the microtubules are illuminated and fluoresce, causing a high background signal. TIRF illumination allows a very thin layer (~ 100 nm) of solute above the glass surface to be exclusively illuminated. Thereby, fluorescent molecules that interact with the microtubules are excited efficiently. Molecules in the bulk solution reside only fleetingly within the illuminated layer and therefore contribute little to the detected fluorescence signal. This combination of restricted observation volume and localization of molecules at the microtubules allows us to visualize single fluorescent molecules.

B. TIRF Theory

In TIRF, fluorescent molecules are excited using an evanescent field generated by the total internal reflection (TIR) of a laser beam at the interface between a glass surface and an aqueous solution (Axelrod *et al.*, 1984), see Fig. 2.

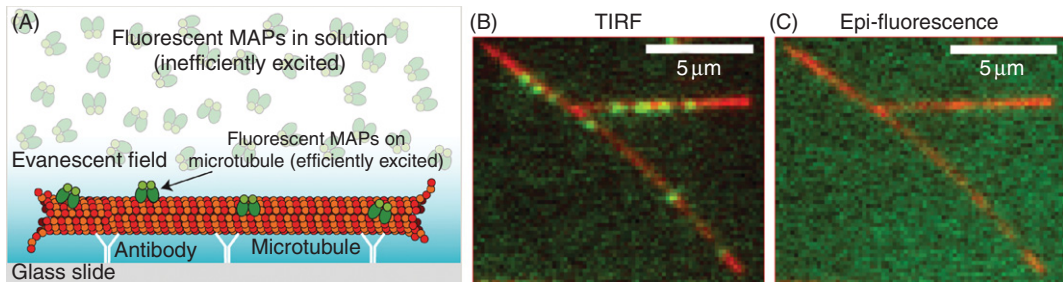


Fig. 1 (A) Schematic of the total internal reflection fluorescence (TIRF) experimental setup. Fluorescent-labeled microtubules (red) are immobilized onto glass surfaces using antibodies, fluorescent-microtubule-associated proteins (MAPs) (green), and/or fluorescent-tubulin (not shown) are added to the solution. The evanescent field for total internal reflection illumination is shown (blue). (B) and (C) Dual-color overlays of fluorescence micrographs of the same sample area. Different illuminations, TIRF (B) and epifluorescence (C), were used to excite enhanced green fluorescent protein-tagged (see Section IV) kinesin-1 (Leduc *et al.*, 2007). With TIRF illumination, the individual microtubule-interacting molecules are clearly visible. (See Plate no. 13 in the Color Plate Section.)

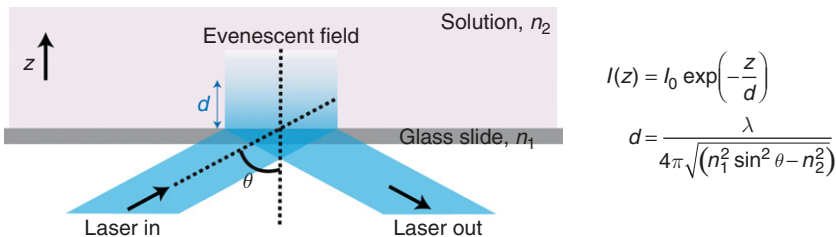


Fig. 2 Simplified optical geometry for total internal reflection evanescent wave generation, highlighting the key parameters (see text). The two equations describing the decay profile and penetration depth of the evanescent field are also shown.

The intensity of the evanescent field (I) decays exponentially in a direction (z) perpendicular to the glass surface and into the lower refractive index aqueous solution, with characteristic decay length (d , the distance at which the intensity has fallen e -fold). The decay length of the evanescent field, often called the penetration depth, is a function of the wavelength of light (λ), the refractive index of the glass (n_1), the average refractive index of the imaging solution (n_2), and the angle of incidence of the light (θ) (Gell *et al.*, 2009).

C. Two-Color TIRF Implementation

We achieve two-color TIRF in a through-the-objective-based configuration (Axelrod *et al.*, 1984; Conibear and Bagshaw, 2000; Gell *et al.*, 2006) installed into a standard inverted fluorescence microscope. A laser is focused onto the periphery of the back focal plane (BFP) of a high numerical aperture microscope objective (α Plan-Apochromat 100 \times , 1.46 NA, Carl Zeiss, Jena, Germany), as shown in Fig. 3. A narrow (<1 mm) collimated beam emerges from the objective, impinging on the coverglass/solution surface at an angle determined by the distance of the point of focus from the optical axis of the objective. The angle of incidence of the light at the interface can then be adjusted by translating the focused beam across

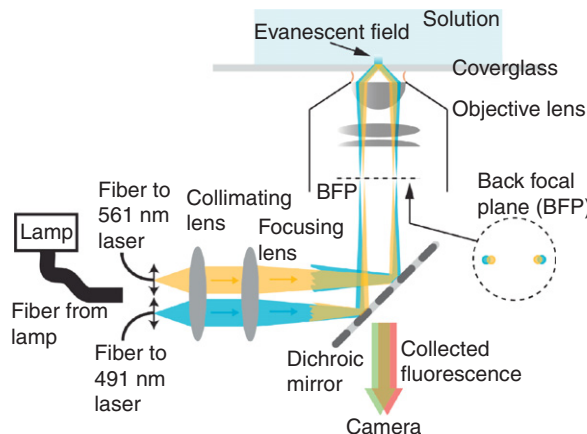


Fig. 3 Schematic of the layout of the two-color TIRF microscope used in our laboratory, see text for a description. (See Plate no. 14 in the Color Plate Section.)

the BFP. In our microscope, excitation light is provided using two lasers. One operates at a wavelength of 491 nm and the other at 561 nm (Cobolt Calypso and Jive, Cobolt, Sweden). The output from these lasers is coupled into two single-mode optical fibers (Oz Optics, Ottawa, Canada). The output ends of these fibers are mounted onto independent translation stages at the back port of an inverted microscope (Zeiss, Axiovert 200 M). Beams are collimated (lens, $f=80$ mm, 25-mm diameter) to a beam diameter of ~ 10 mm and focused (lens $f=120$ mm, 25-mm diameter) using a system based on a commercial condenser assembly (Visitron Systems, Puchheim, Germany). A dual-band polychroic mirror (zt488-491/561rdc, Chroma Tech. Corp., Bellows Falls VT, USA) then directs the light toward the BFP of the objective. This dual-fiber geometry allows the two lasers to be focused onto opposite sides of the back aperture of the objective. Importantly the incident angle, and therefore the penetration depth, as well as the focus, of each laser can be varied independently; this is in contrast to systems delivering multiple illumination wavelengths through a single fiber. Emitted fluorescence is collected by the same microscope objective and directed toward an electron multiplying charge-coupled device camera (Andor iXon+, Andor Tech., Belfast, UK). For simultaneous dual-color imaging, we use a beam splitter (W-View, Hamamatsu, Japan) in front of the camera that incorporates filters from Chroma Tech. Corp.

D. Using a TIRF Microscope—Practical Tips and Pointers

- For single-molecule imaging we typically use a laser beam power of ≈ 5 mW, measured as it exits the microscope objective.
- Temperature control: for dynamic microtubule assays we use an objective heater (#0280.004, with controller 37-2, Pecon GmbH, Erbach, Germany). We find this effectively regulates the temperature of the region of the sample around the objective focus.
- The epifluorescence arc-lamps on many microscopes generate considerable heat. They can significantly affect the temperature of the microscope, causing unwanted sample drift, but also heating the sample itself. Therefore, we mount our arc-lamp

off-scope and couple the light to the microscope through a large multimode optical fiber (see [Fig. 3](#)).

- Uniform illumination across the entire field of view (typically $\approx 80 \mu\text{m}^2$) is desirable. Two parameters affect this. Firstly, the divergence of the focused light in the objective BFP determines the illumination area at the coverglass surface; it should be adjusted for the field of view required. Secondly, interference with reflections of the laser light from the optical components and diffraction from dust on the surfaces of optical components (even when not in a conjugate plane) can cause fringes and nonuniform illumination. Therefore, keep your microscope clean, covered when not in use, and use good antireflection-coated filters and lenses.
- Accurate focusing on the BFP can be achieved by observing the transmitted beam emerging from the objective some meters away on the ceiling. Adjustment of the position of the focusing lens can then be performed.

E. Considerations for Dynamic Microtubule Assays

- Using a dual laser beam setup, with beam splitter, allows fluorescence to be collected simultaneously from two differently labeled proteins with single-molecule resolution. For dynamic growth assays, two lasers may not be necessary. Generally the microtubule extensions are very bright, due to the large number of incorporated fluorescent labels. Thus, a laser with a wavelength far from the excitation maximum of the tubulin–dye is usually sufficient to produce a detectable signal.
- The growing ends of dynamic microtubules are not fixed to the surface and can move outside the TIRF evanescent field. When possible, choose longer wavelengths and shallower angles of incidence of the TIRF laser to increase penetration depth. Some labs have employed methyl cellulose to reduce growing microtubule fluctuations ([Bieling *et al.*, 2007](#)).
- Chromatic aberrations both change the focus and distort recorded images. Therefore, it is essential to use an objective corrected at two wavelengths for chromatic aberration (an apochromat) when performing simultaneous dual-color TIRF imaging at two different wavelengths. This is necessary even when using a beam splitter such as the Hamamatsu W-View that incorporates some built-in correction.

III. List of Reagents

In this section, we present an alphabetical list of the reagents used throughout this chapter. We give details of product codes and manufacturers where possible, comment on storage and handling as well as details of preparation.

- Alexa Fluor 488 (Invitrogen, Molecular Probes, Karlsruhe, Germany, A30005), used for tubulin labeling (see [Hyman *et al.*, 1991](#)), we use the tetrafluorophenol conjugate.
- Antibeta-tubulin SAP4G5 (Sigma, Munich, Germany, T7816), typically a 1:50–1:200 dilution from the stock is used, in BRB80, stored at 4°C for several weeks.
- Antitetramethylrhodamine (Invitrogen, Molecular Probes, A6397), typically 10–20 µg/ml in BRB80, stored at 4°C, for several weeks.

- β -Mercaptoethanol (BME, Sigma, M3148), stored in \sim 100 μ l aliquots in small tubes at 4°C.
- BRB80 buffer (80 mM PIPES/KOH, pH 6.9, 1 mM ethylene glycol tetraacetic acid (EGTA), 1 mM MgCl₂). This buffer is commonly used to allow efficient polymerization of tubulin (Brinkley, 1997; Olmsted and Borisy, 1975; Weisenberg, 1972). We use KOH rather than NaOH because potassium is the main intracellular cation, and sodium ions enhance the hydrolysis of guanylyl-(alpha, beta)-methylene-diphosphonate (GMPCPP) in the microtubule lattice (Caplow *et al.*, 1994). Buffer is filtered (0.22 μ m vacuum filter), degassed, and the stock stored in 50 ml aliquots at -20°C.
- Bovine serum albumin (BSA, Sigma, A3059), stock solution is made at 10 mg/ml in BRB80, filtered, and the pH checked; solution is stored at 4°C for daily use for up to several months.
- Catalase (Sigma, C9322), stock solution is made at 1 mg/ml (4.2 uM) in BRB80, 10 μ l aliquots, snap-frozen in liquid nitrogen, stored at -20°C.
- Dichlorodimethylsilane (DDS, Aldrich, Munich, Germany, 440272), stored upright, in sealed container at 4°C—avoid agitating when handling.
- Dithiothreitol (DTT, Sigma, D0632). Aliquots stored at -20°C.
- EGTA (Sigma, E4378).
- Ethanol (Merck, Haar, Germany, 1.00983.2511).
- F127, Pluronic F127 (Sigma, P2443), stock solution of 1% F127 is dissolved in BRB80 overnight, filtered (0.22- μ m syringe filter), stored at 4°C.
- D-Glucose (Sigma, G7528) stock solution is made at 2 M in water, 10 μ l aliquots, stored at -20°C.
- Glucose oxidase (Sigma, G7016) stock solution is made at 2 mg/ml (12 uM) in BRB80, 10 μ l aliquots, snap-frozen in liquid nitrogen, stored at -20°C.
- guanylyl-(alpha, beta)-methylene-diphosphonate (GMPCPP) (Jena Biosciences Jena, Germany, #NU-405), 10 mM stock stored in 10 μ l aliquots at -80°C.
- Hydrogen peroxide (H₂O₂, 30%) (Sigma, 21676-3), stored at 4°C.
- Sulfuric acid (H₂SO₄, 97%) (Roth, Karlsruhe, Germany, X944.1).
- Magnesium chloride (MgCl₂, Merck, 1.05833.0250).
- Methanol (Merck, 1.06009.2511).
- Potassium hydroxide (KOH, 0.1 M, Sigma, P-6310). Add KOH slowly to BRB80 buffer to set the pH 6.9, the solution may warm.
- Neutravidin, 5–50 μ g/ml (Pierce, Rockford, IL, USA, 31000). Dissolve neutravidin at the required concentration in phosphate-buffered saline. It can be stored at 4°C for several weeks.
- PIPES (Sigma, P6757).
- Trichloroethylene (TCE, Sigma, 251402).
- Trolox (Sigma, 238813), see notes in text, Section V.
- Tubulin, unlabeled (purified from porcine brain, see Chapter 7 by Miller *et al.*, this volume).
- Tubulin, biotin labeled (Cytoskeleton Inc., Denver, CO, USA, T333-B)—for a labeling procedure (see Hyman *et al.*, 1991).
- Tubulin, fluorescent labeled (we label tubulin purified from porcine brain; see Chapter 7 by Miller *et al.*, this volume; Hyman *et al.*, 1991).
- TAMRA (Invitrogen, Molecular Probes, C1171), the succinimidyl ester conjugate is used for tubulin labeling (see Hyman *et al.*, 1991).
- Water, ultrapure (>18 M Ω /m).

IV. Choice of Fluorophore/Protein Labeling

The right choice of fluorescent label is important for the success of a dynamic microtubule experiment. It depends on the experimental approach, number of components in the assay, and available instrumentation. In this section, we highlight some of the considerations that affect the choice of labeling method and dye. We refer the reader to Bane *et al.* (this volume) and also the following papers (Gell *et al.*, 2006; Hunter *et al.*, 2003; Hyman *et al.*, 1991; Selvin and Ha, 2007) for more detailed information regarding labeling protocols.

A. Common Labeling Strategies

- *Chemical posttranslational dye labeling*

Typically amine or thiol-reactive dyes are used to covalently bind fluorophores to primary amines, the N-terminus, or cysteine groups of expressed proteins.

Advantages: Protein is expressed a single time and can be used for multiple labeling reactions with different dyes.

Disadvantages: Labeling conditions can be harsh; labeling site is often unspecific and unknown; labeling can occur at multiple sites, or not, in an uncontrolled manner; the protocol generally needs optimization for each biomolecule; thiol-labeling first requires the production of a cysteine-free mutant.

Successfully used: This method has been used successfully to label tubulin (e.g., Hyman *et al.*, 1991) and kinesin-1 (e.g., Mori *et al.*, 2007).

- *Fusions with intrinsically fluorescent proteins*

Make a fusion protein of green fluorescent protein (GFP) or a GFP-variant gene and the gene of interest.

Advantages: Excellent specificity; control over number of labels; defined stoichiometry; GFP derivatives available across the visible spectrum.

Disadvantages: Genetic modification can be time consuming; needs to be repeated if different fluorescent proteins (colors) are required; overexpression of some fusion proteins can fail; the photo-physical properties of GFP and its derivatives are not ideal (Dickson *et al.*, 1997); may alter protein activity.

Successfully used: We have used this method to label a variety of MAPs (Brouhard *et al.*, 2008; Helenius *et al.*, 2006; Varga *et al.*, 2006).

- *Fusions with SNAP-tag (or similar systems, e.g., HALO, ACP)*

*The SNAP-tag (New England Biolabs, Frankfurt am Main, Germany) is a small enzymatic protein that can be expressed as a fusion with the protein to be labeled, whose substrate can carry a dye that becomes covalently attached to the SNAP-tag (Gautier *et al.*, 2008).*

Advantages: After production of SNAP fusions, ready-to-use labeling substrates with a large range of chemical dyes are available; labeling is specific; protein is singly labeled or unlabeled; labeling is with dyes with optimized photo-physical properties.

Disadvantages: Initial genetic modification procedure can be a time-consuming process; requires a reliable overexpression system; may alter protein activity.

Successfully used: We have used this method to label kinesin-1 (unpublished).

Tip: *Whatever the choice of labeling protocol, it is essential to check that the activity of the labeled molecule is comparable to the wild type.*

Tip: We have experienced particular problems with some dyes (e.g., Atto 425) when labeling microtubules. Some dyes seem to stabilize the microtubules significantly, others prevent polymerization with labeled tubulin. Controls to check function should always be performed.

Tip: Fluorescent dye- or biotin-labeled tubulin is also commercially available (Cytoskeleton Inc.).

B. Dye-Selection Considerations for Multicolor, Dynamic Microtubule Assays

- *General considerations for single-molecule detection*

For single-molecule detection, look for dyes with high quantum yields and extinction coefficients at the laser wavelengths to be used. Note that literature values for these should be used only as a guide; the photo-physical properties of a dye will change depending on the molecule it is conjugated to and the solution used. Common dyes that have been used with success in the literature include TAMRA (Helenius *et al.*, 2006; Varga *et al.*, 2006), Cy dyes (Yildiz *et al.*, 2004), Alexa Fluor dyes (Bieling *et al.*, 2007), and various GFP fusions (Helenius *et al.*, 2006; Varga *et al.*, 2009).

- *Monitoring microtubule growth/shrinkage and a single MAP at single-molecule resolution*

Choose dyes with sufficiently separated fluorescence emission so that available emission filter sets can effectively separate the signals without overlap of one dye's fluorescence emission with the transmission range of the other dye's filter.

Choose a shorter wavelength dye for the MAP than the labeled microtubule: The emission curves of dyes typically have long tails toward longer wavelengths, but not to shorter wavelengths. As the signal from the microtubule will be bright, this could limit contrast in the single-molecule channel.

Choosing a shorter wavelength dye for the MAP, which is observed at the level of a single molecule using TIRF, generally means that the same laser can provide sufficient excitation of the growing/shrinking microtubule. This means that simultaneous dual-color experiments can be performed with a single laser and beam splitter.

- *Monitoring the behavior of two MAPs at single-molecule resolution*

Choose labels optimized for the two laser wavelengths, the filter sets, and the camera available.

Spectral overlap is less of an issue.

Microtubules should be either unlabeled or labeled with a third color (again choose a dye that does not overlap with the fluorescence spectrum of either MAP).

===== V. (Anti-)blinking/Photo-Toxicity/Photo-Bleaching Cocktails

Many fluorescent molecules used for single-molecule TIRF display unwanted blinking on the millisecond to second timescale, often, but not exclusively, due to the dye being excited into a triplet state (Aitken *et al.*, 2008; Rasnik *et al.*, 2006). Population of dye triplet states is also thought to be an important precursor to irreversible loss of fluorescence (photo-bleaching) (Aitken *et al.*, 2008; Rasnik

et al., 2006). Dye triplet states are effectively quenched by molecular oxygen, but the by-product of quenching is a singlet oxygen that is highly reactive and can induce oxidative damage to both dyes and proteins (Aitken *et al.*, 2008). Oxidation of dyes leads to photo-bleaching; oxidation of tubulin can, for example, cause the spontaneous breaking apart of microtubules (Guo *et al.*, 2006). The effects can be reduced, and concomitantly, the time-to-bleaching of fluorescent molecules can be prolonged, using enzymatic oxygen scavenger systems with additional triplet-state quenching chemicals. In this section, we detail the steps we typically take to reduce these effects in TIRF (and standard epifluorescence)-based microtubule assays in our laboratory.

A. Glucose Oxidase/Catalase with BME as an Oxygen Scavenging/Antifade System

D-Glucose is oxidized to gluconic acid by glucose oxidase, depleting oxygen in solution. This reaction generates hydrogen peroxide as by-product, which is degraded by the catalase in a second reaction step. BME in solution increases time-to-bleaching through triplet-state quenching as well as helping to maintain a protein-friendly reducing environment.

Include in the final reaction solution the following concentrations of components, typically in BRB80 buffer (see the reagent list in Section III, and the tips later, for further details of the reagents, their preparation, and use):

250 nM glucose oxidase in BRB80
64 nM catalase in BRB80
40 mM D-glucose in water
1% BME

Tip: *Store all components, separately, at -20°C in aliquots of 10 µl at a 100× concentration. Catalase and glucose oxidase are dissolved in BRB80 and snap frozen in liquid nitrogen. When thawed and stored on ice, aliquots will maintain activity for several hours. Once mixed together use the solution within 1 h, thereafter we have observed a loss of effectiveness. For consistency, do not refreeze thawed aliquots.*

Tip: *Add the glucose oxidase last and just before actually using the imaging buffer. This will initiate the first part of the reaction, which depletes the oxygen from solution.*

Tip: *DTT can be substituted for BME. Use a final DTT concentration of 10 mM. Note, however, BME and DTT have both been demonstrated to have negative effects on some dyes (Aitken *et al.*, 2008). For example, DTT appears to dramatically reduce the signal from the dye Alexa Fluor 488, but BME does not (Aitken *et al.*, 2008).*

B. Troubleshooting (Anti-)blinking/Photo-Toxicity/Photo-Bleaching Cocktails

If you observe significant bleaching or photo-induced damage of microtubules, check whether the glucose oxidase/catalase (GODCAT)/BME system works in a reference assay. We use a robust standard casein-gliding assay with kinesin-1 for this purpose (see Chapter 14 by Nitzsche *et al.*, this volume). Other points to consider are

1. GODCAT enzymes might adsorb to an incompletely blocked surface (see Section VIII and Chapter 28 by Bieling *et al.*, this volume), reducing their concentration.

2. BME (and DTT) activity decreases with exposure to air and can be a major reason for ineffective cocktails. Make small amounts (1–5 ml), aliquot to smaller sizes once, and store at 4°C in a desiccator. BME (and DTT) activity can be determined by assaying the amount of oxidized reagent using a spectrometer (Iyer and Klee, 1973; Mickey and Howard, 1995).
3. If the buffer that you use has a low buffering capacity and/or your imaging solution exchanges a lot of oxygen with the environment, pH can drop quite drastically over time due to production of gluconic acid from the oxidation of D-glucose by glucose oxidase (Selvin and Ha, 2007). In these cases, try to raise buffer capacity and/or reduce oxygen exchange with the environment.
4. The effectiveness of different oxygen scavenging/triplet quenching systems/dye systems is variable; it may be necessary to experiment to find the best cocktail for a given dye (see Aitken *et al.*, 2008; Rasnik *et al.*, 2006). We have found the protocols detailed here effective with TAMRA, GFP, RFP, Alexa 488, and Alexa 568.

C. Trolox as an Alternative Triplet-State Quencher

While BME (or DTT) has been a traditional component in many groups' oxygen scavenging/antiphoto-bleaching cocktails, it is known to cause slow blinking with some fluorescent dyes. Trolox (6-hydroxy-2,5,7,8-tetramethylchroman-2-carboxylic acid) has recently been characterized as an alternative triplet-state quencher (Aitken *et al.*, 2008; Rasnik *et al.*, 2006). In our assays, we keep BME present to maintain a reducing environment.

Include in the final reaction solution the following concentrations of components (see Section III, and the tips later, for further details of the reagents, their preparation and use):

250 nM glucose oxidase
 64 nM catalase
 40 mM D-glucose
 1% BME
 1 mM Trolox

Tip: 10 mM Trolox is dissolved for 1 h in the buffer that is used for imaging. This solution is then filtered (0.22-μm syringe filter) and the concentration checked using absorption at 290 nm and an extinction coefficient of 2350/M/cm. The pH should also be checked and adjusted to pH 6.9. The Trolox solution can then be stored at 4°C and used within 2 weeks.

D. Effect of (Anti-)blinking/Photo-Toxicity/Photo-Bleaching Cocktails

The effect of using different anti-bleaching and anti-photo-toxicity components is illustrated in Fig. 4. Single molecule fluorescence intensity trajectories were recorded from surface-immobilised Alexa Fluor 488 dye-labeled tubulin, using TIRF. An increase in the time-to-bleaching of the molecules is observed upon addition of the GODCAT/BME cocktail. However, blinking is induced by using BME alone as a triplet state quencher. The blinking is reduced when also using Trolox in the cocktail.

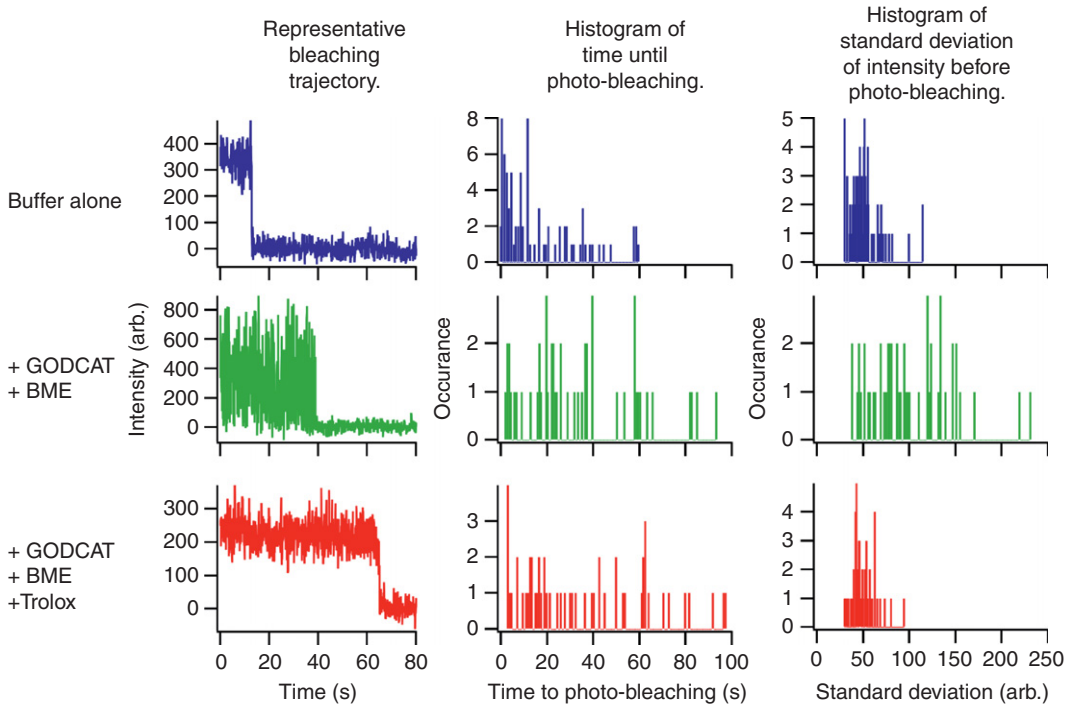


Fig. 4 The effectiveness of different cocktails is quantified by measuring the fluorescence versus time trajectories of single molecules. Here are shown example trajectories for single Alexa Fluor 488-labeled tubulin heterodimer immobilized on a glass slide and imaged using TIRF, histograms of the time until photo-bleaching from many such trajectories, and finally histograms of the standard deviation of the intensity from many single molecules before photo-bleaching occurs, each in buffer alone, with GODCAT + BME and with GODCAT + BME + Trolox. (See Plate no. 15 in the Color Plate Section.)

VI. Preparation of GMPCPP-Stabilized Microtubules

Stabilized microtubules for use as substrates for microtubule depolymerization assays, or as seeds upon which to nucleate the growth of microtubule extensions, are prepared by polymerization of tubulin in the presence of the slowly hydrolyzed GTP analogue, GMPCPP (Hyman *et al.*, 1992). The distribution of microtubule lengths obtained, and the propensity of the microtubules to spontaneously depolymerize, can be tailored by altering the concentration of tubulin used in the polymerization reaction and by additional cycles of polymerization, respectively.

A. Single-Cycled Microtubules

Step 1: For microtubules with an average length of $\sim 3.5 \mu\text{m}$ (suitable as seeds from which to grow extensions), the following mix is first incubated on ice for 5 min, then at 37°C for 30 min.

20 μM tubulin in BRB80
1 mM GMPCPP

Or, for microtubules with an average length of \sim 6.5 μ m (suitable as substrates for depolymerization assays), the following mix is first incubated on ice for 5 min, then at 37°C for 2 h.

2 μ M tubulin in BRB80
1 mM GMPCPP

Step 2: Spin microtubules in an ultracentrifuge (e.g., Beckman Airfuge, A95 rotor at 80,000 rpm/126,000 \times g) to remove unpolymerized tubulin, discard supernatant, and resuspend microtubule pellet in the required buffer (see Sections III and VIII).

Tip: *Single-cycled microtubules are made for immediate use. These microtubules are stable for several hours postpolymerization, depending on initial length. The stability of GMPCPP microtubules can be increased by a second cycle of polymerization—see below.*

Tip: *At 20°C the average rate of spontaneous depolymerization of single-cycled GMPCPP-stabilized microtubules immobilized on coverglass surfaces is in the range of 0.02–0.03 μ m/min.*

B. Double-Cycled Microtubules

To enhance the stability of microtubules, two cycles of polymerization in GMPCPP can be carried out (Caplow and Shanks, 1996). This results in an increased proportion of GMPCPP–tubulin relative to single-cycled microtubules by reducing the amount of nonexchanged guanosine diphosphate–tubulin present in the microtubule lattice; this is useful as short microtubule seeds will last longer in assays. This can also have important consequences when microtubules are used as substrates for depolymerization studies (Helenius *et al.*, 2006).

- **Cycle 1**

Step 1: For microtubules with an average length of \sim 3.5 μ m (suitable as seeds from which to grow extensions), the following mix is first incubated on ice for 5 min, then at 37°C for 30 min.

20 μ M tubulin in BRB80
1 mM GMPCPP

Step 2: To remove unpolymerized tubulin, spin incubation mix for 5 min in an ultracentrifuge (e.g., Beckman Airfuge, A95 rotor at 80,000 rpm/126,000 \times g) and discard the supernatant.

Step 3: Resuspend the microtubule pellet in BRB80. Choose a volume of buffer that will result in a tubulin concentration of 20 μ M after addition of GMPCPP in step 5 below (\sim 80% of the initial tubulin is routinely recovered after polymerization and resuspension).

Step 4: Incubate resuspended tubulin on ice for 20 min to depolymerize the microtubules.

- **Cycle 2**

Step 5: Add GMPCPP to the depolymerized tubulin to a concentration of 1 mM, resulting in a tubulin concentration of 20 μ M. Incubate on ice for 5 min, then at 37°C for 30 min.

Step 6: Spin microtubules for 5 min in an ultracentrifuge (e.g., Beckman Airfuge, A95 rotor at 80,000 rpm/126,000 \times g) and discard supernatant.

Step 7: The microtubule pellet should then be resuspended in the required buffer (see Sections III and IX). The volume of buffer used to resuspend the pellet can be chosen to give the required concentration of polymerized tubulin (~80% of the tubulin is routinely recovered from each cycle of polymerization and resuspension).

Tip: At 20°C the rate of spontaneous depolymerization of double-cycled GMPCPP-stabilized microtubules immobilized on coverglass surfaces is <0.01 $\mu\text{m}/\text{min}$.

Tip: Double-cycled microtubules can be stored for many months in liquid nitrogen by snap freezing immediately after resuspension. When required for use, they should be thawed by incubation at 37°C. It is best to store the microtubule samples in aliquots of ~100 μl or less so that they can be thawed rapidly (1–2 min). The ability to store microtubule seeds in this way can greatly reduce the day-to-day workload in performing dynamic microtubule assays.

Tip: The freeze–thaw process causes breakage of microtubules resulting in an average length of ~2 μm .

C. Preparation of Labeled Microtubules

A suitable proportion of dye-labeled tubulin can be used in the polymerization reaction to provide fluorescent microtubules. Biotinylated tubulin can be incorporated to bind microtubules to a neutravidin-coated surface (Section VIII). Labeled tubulin can be either prepared in-house (Hyman *et al.*, 1991) or purchased commercially (e.g., from Cytoskeleton Inc.).

- **Biotin-labeled microtubules:** To facilitate attachment to a neutravidin-coated surface, 10% biotin-labeled tubulin is combined with unlabeled tubulin in any of the above polymerization protocols.
- **Fluorescent microtubules:** To obtain fluorescent microtubules up to 25% TAMRA-labeled tubulin is combined with unlabeled tubulin in any of the above polymerization protocols.

Tip: To adjust the brightness of fluorescently labeled microtubules the ratio of labeled to unlabeled tubulin can be adjusted as required. We find that 5–25% fluorescent-labeled tubulin generally results in a good compromise between brightness and inhibition of the interaction of MAPs due to the presence of label.

D. General Information on Handling Microtubules/Tubulin

Tip: Unpolymerized tubulin is generally stored long-term at –80°C in small aliquots and kept on ice prior to use.

Tip: Microtubules should **NOT** be placed on ice as low temperatures cause rapid depolymerization.

Tip: If long microtubules (>10 μm) are required, a cut pipette tip (such that the opening of the tip has a larger diameter) should be used when resuspending the microtubule pellet to minimize shearing.

Tip: The concentration of polymerized tubulin in the resuspended microtubules can be determined by depolymerizing a small volume of the microtubule solution with 5× BRB80, 50 mM KCl, 5 mM CaCl_2 , and incubation on ice for 20 min. The

tubulin concentration is then determined by measuring the absorbance at 280 nm. The extinction coefficient for dimeric tubulin, calculated from the sequence of tubulin, including the contribution of two bound guanine nucleotides is 115,000/M/cm, assuming an approximate molecular weight of 100,000 g. Note that different labs tend to use different estimates for the extinction coefficient of tubulin.

===== VII. Glass Treatment and Sample Chamber Preparation

In this section, we describe the preparation and construction of sample chambers for studying microtubules in a single-molecule TIRF microscope. The aim is to produce clean, low-fluorescence glass surfaces, formed into simple flow cells, that allow convenient immobilization of microtubules or microtubule seeds and that can be effectively passivated to prevent unwanted nonspecific absorption (see Section VIII).

A. Safety

Many of the chemicals used here are potentially harmful, corrosive, or explosive. Particular care must be taken to familiarize yourself with the dangers, how to mitigate them, and how to deal with problems. All of these steps should be performed in a suitable fume hood.

B. Key Equipment

- 18 × 18 mm and 22 × 22 mm (0.17–0.19 mm thick) coverglass (e.g., Corning, No. 1½, 2870-18, and 2870-22), porcelain or polytetrafluoroethylene racks for coverglasses (e.g., Coverglass maxi-rack, Invitrogen, Molecular Probes, C24784)
- Hotplate, set to 60°C
- Fume hood, acid-resistant gloves, lab coat, eye protection, acid/chemical spill kit
- Acid-resistant tweezers, 1-ml “luer-lock” syringe, with long needle
- Several thick-walled, acid-/temperature-resistant glass containers (~250 ml volume, suitable to immerse coverglass racks)
- Measuring cylinder
- Ultrapure water (>18 MΩ/m), H₂SO₄ (97%), H₂O₂ (30%), DDS, TCE, methanol, ethanol, KOH
- Ultrasonic bath
- Clean nitrogen gas line for drying
- Coverglass holders for microscope
- Double-sided scotch tape (we use Scotch, “Double Face,” 136D MDEU)

C. Glass Cleaning and Surface Preparation

These steps result in clean, low-fluorescence glass surfaces with the correct reactivity to enable subsequent silanization, following the general approach of deCastro *et al.* (1999).

Precleaning.

1. Place coverglasses into racks, ensuring adjacent coverglasses cannot contact.
2. Sonicate for 15 min in a soap bath (2% Mucasol, 98% water); rinse in water for 1 min.

3. Bathe, sequentially, in acetone for 10 min, ethanol for 10 min, ultrapure water for 1 min.

“Piranha solution” cleaning to remove all organic matter. EXTREME CAUTION—VOLATILE AND CORROSIVE—RESEARCH THE PROPERTIES OF THIS SOLUTION CAREFULLY BEFORE USE.

1. Mix a sufficient volume of 30% H_2O_2 solution and H_2SO_4 at a ratio of 1:2 in a suitable container to fully immerse the precleaned coverglasses in their racks. Always add the peroxide to the acid, adding the peroxide slowly; note that if the peroxide concentration is greater than the acid an explosion could occur. The solution initially gets hot upon mixing, but the temperature should be maintained at 60°C throughout the cleaning process by additional heating. Prepare the solution just prior to use since it is only active for ~ 1 h.
2. Transfer precleaned coverglasses directly from the water to the Piranha solution. Bathe for 1 h at 60°C.
3. Transfer racks directly from the Piranha solution sequentially to 3 ultrapure water baths, bathing for 1 min each.

Bathe coverglasses in KOH solution to activate the OH groups on the glass surface for silanization.

1. Transfer racks from the third ultrapure water bath to a 0.1-M KOH bath for 15 min.
2. Transfer racks sequentially through two ultrapure water baths, bathing in each for 1 min.
3. Remove from water baths, dry coverglasses *completely* with clean nitrogen gas. Store in clean sealed glass containers.

Tip: *It is essential to prepare the coverglasses at all stages in as clean an environment as is possible; use an area dedicated to their preparation; dry slides away from any sources of dust; store the slide in double-sealed holders and bags; open the containers only briefly to remove slides.*

Tip: *For silanization (see below), use only freshly cleaned coverglass and silanize immediately after the slides have dried completely.*

Tip: *Clean glass surfaces are wetted by water. A test for cleanliness is to check whether a droplet of water spreads immediately over the complete coverglass. If a drop with a finite contact angle forms, the coverglasses are dirty! Clean glass surfaces have a high surface energy. Any dirt adsorption, in particular organic molecules (always present in ambient conditions, e.g., due to oil vapors of pumps and air conditioning), reduces the surface energy of glass and is thus energetically favorable, i.e., clean glass surfaces are an attractant for dirt. It is best to use clean surfaces right away or render them hydrophobic for storage (see below).*

Tip: *Dispose of piranha properly. Used solutions must not be stored in closed containers since gas formation continues and a closed container bares the risk of explosions.*

Tip: *Use a filter on the nitrogen gas line. Clean the nitrogen gun in acetone to remove oil.*

D. Glass Silanization

These steps functionalize cleaned glass surfaces with a hydrophobic silane that allows efficient passivation (see Section VIII). Silanization is performed with a 0.05% solution of DDS in TCE.

1. Add sufficient TCE to a clean glass container to immerse the cleaned coverglasses in their racks.
2. Add DDS (to a final concentration of 0.05%), stir while adding DDS to TCE.
3. Gently place the coverglasses in the TCE/DDS solution, bathe for 1 h.
4. Transfer the silanized glass, sequentially, through three methanol baths, placed in an ultrasonic bath for times of 5, 15, and 30 min.
5. Remove from the final methanol bath, dry coverglasses *completely* with clean nitrogen gas. Store in clean sealed glass containers.

Tip: We have found that DDS forms insoluble crystals during storage; avoid agitating the DDS in its bottle. Use a long needle and syringe to pierce the Teflon seal on the DDS bottle and draw off the required amount from the top. Add DDS via syringe under the TCE to avoid air contact. DDS vigorously reacts with water, resulting in crosslinking and crystal formation. Crystals, if present on coverglass surfaces, greatly reduce the surface's ability to be passivated. Store DDS under nitrogen or in a desiccator.

Tip: We store the silanized coverglasses at room temperature and find that they last for at least 1 month; hydrophobic, low-energy surfaces attract less dirt than clean glass surfaces and are thus more suitable for storage. Alternatively, storage under 0.22- μm filtered ethanol is possible.

Tip: The quality of the silanization can be checked by putting a water droplet (smaller than 2 mm—the capillary length of water) onto the glass surface and measuring its contact angle. The water contact angle should ideally be larger than 100°.

E. Sample Chamber Assembly and Use

These steps describe how we use a simple metal holder, one 18 \times 18 mm and one 22 \times 22 mm coverglass to make convenient, quick-to-construct sample chambers. We use small aluminum or brass holders designed to fit the microscope stage. The holder has a clear central aperture to allow approach of the microscope objective from underneath. The hydrophobic-rendered 22 \times 22 mm slide is clamped in the holder, then typically four strips of double-sided scotch tape are laid down to define three channels. The smaller 18 \times 18 mm slide is then pressed down onto the tape from the top. The depth of the channels is \sim 100 μm (Fig. 5).

Tip: Machine the holders as thin as possible; chamfer around the clear-aperture to allow access of the microscope objective to the outermost channels; do not place channels too close to the edges, else it may not be possible to image them with the microscope objective.

Tip: In place of double-sided tape, layers of Nescofilm (#2569.1, Bando Chemicals, Kobe, Japan) can be used to form the channels; further details can be found in Chapter 14 by Nitzsche *et al.*, this volume.

Tip: Using multiple layers of tape can increase the channel volume; this decreases the surface area-to-volume ratio of the channel, mitigating the effects of any undesirable surface binding.

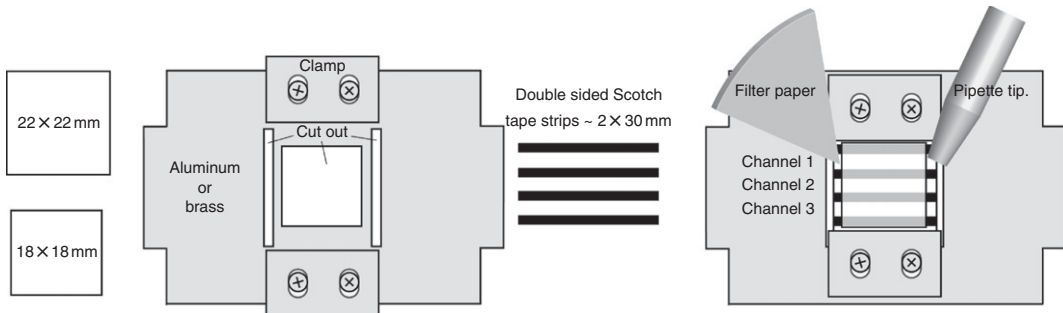


Fig. 5 Schematic of the sample holder design we used for microtubule assays. Channels defined by double-sided adhesive tape between hydrophobic-rendered coverglasses provide a convenient chamber in which to immobilize microtubules and to perfuse different solutions. Filter paper can be used to perfuse solutions, added at the opposite end of the channel using a pipette. In the case of hydrophobic channels, it may be necessary to introduce the first solution with the assistance of a vacuum line; filter paper is then used for subsequent perfusion steps.

Tip: *The flow profile in the channel is parabolic, thus there is slower movement of the solution near the channel walls. In order to exchange solution in the channels thoroughly, it is necessary to flow several channel volumes of solution.*

VIII. Binding of Microtubules and Passivation of Surfaces

Stabilized microtubules are bound to the surface *via* a spacer protein that attaches nonspecifically to the silanized coverglass surface, but specifically to the microtubule (see Fig. 1). The spacer protein holds the microtubule away from the surface, reducing unwanted surface interactions. Immobilized microtubules can be used as seeds from which to examine polymerization, substrates for depolymerization studies, and substrates for studying the mechanism of MAPs. The use of a spacer, in contrast to direct adsorption of the microtubule to the surface, ensures that the bottom surface of the microtubule is accessible and that the surface does not deform the microtubule. The spacer protein used depends on what microtubule/MAP property will be examined. One concern is microtubule-specific binding, i.e., that the surface should not bind the other components of the reaction mix used, including the additional tubulin used to grow extensions. In this section, we summarize different approaches to microtubule immobilization, highlighting their advantages and disadvantages for different types of assay. We then present a protocol for seed binding and subsequent passivation of the remaining surface.

A. Commonly Used Methods of Attachment

- Antitubulin antibody is used to bind to tubulin

The tubulin antibody binds nonspecifically to the surface, but specifically to the microtubule.

Advantages: No labeled tubulin required.

Disadvantages: Free tubulin can compete for binding and cause dissociation of the microtubule from the surface.

- Antifluorophore binding to labeled tubulin (Reuther *et al.*, 2006)

A useful method when a fluorophore such as TAMRA or Alexa488 is used to label the microtubule.

Advantages: Free tubulin (unlabeled or differently labeled) does not compete for binding; no direct contact with microtubule lattice.

Disadvantages: Binding dependent on labeling density of microtubule.

- Neutravidin binding to biotinylated tubulin

Advantages: Strong binding; free (unbiotinylated) tubulin does not compete for binding.

Disadvantages: Requires 5–10% biotinylated tubulin to be included in the microtubules, in addition to any other fluorescent labels that are used.

Tip: *The seeds should be bound tightly, but using the lowest possible surface density of attachment spacer, reducing any possible inhibition of normal binding of MAPs to the seeds.*

B. Typical Seed Binding/Surface Passivation Protocol

Step 1: The antibody/neutravidin is perfused into the hydrophobic-rendered glass flow-cell with the assistance of a vacuum (see Section VII) at the following range of concentrations:

Use one of

antibeta-tubulin SAP4G5 (typically a 1:50–1:200 dilution in BRB80)

antitetramethylrhodamine: 10–20 µg/ml (in BRB80)

neutravidin: 5–50 µg/ml (in BRB80)

Tip: *These stocks can be stored at 4°C for several weeks.*

Step 2: After 5-min incubation excess antibody/neutravidin is flushed out with ~5 channel volumes of BRB80.

Step 3: The remaining exposed surface is passivated in order to block any nonspecific surface binding using Pluronic F127. F127 is a tri-block copolymer consisting of two outer poly(ethylene oxide) (PEO)—also known as poly(ethylene glycol)—and an inner poly(propylene oxide) (PPO) blocks with 100 and 65 monomers, respectively. The PPO block is hydrophobic and strongly adsorbs onto the hydrophobic-rendered glass surface. The outer PEO parts form a polymer brush with approximately 10-nm thickness that is very effective in blocking protein adsorption in single-molecule experiments. Typically 1% Pluronic F127 in BRB80 is used.

Step 4: After 5 min incubation excess F127 is removed with ~10 channel volumes of BRB80.

Step 5: The channel is now ready for perfusion of solution containing prepared microtubules or microtubule seeds (see Section VI). The incubation time of microtubule seeds depends on the choice of immobilization method, microtubule seed, and antibody/neutravidin concentration, as well as the desired microtubule density in the channel. Typical times range from 5 to 15 min.

Tip: *The silanized coverglasses are hydrophobic. It is necessary to use a vacuum line to help draw in the first solution. After that, blotting/filter paper can be used. With care this can be done in situ on the microscope. Caution is needed not to introduce air bubbles into the channel.*

Tip: *The channels can dry out if left out on the bench for more than a few minutes. This can make it difficult to pull liquid through the channel ends and exposure to air will cause degradation of the microtubules. To avoid this, keep the sample chamber covered and either add additional BRB80 to the channel openings or keep a moist towel under the sample chamber. Chambers can be sealed to prevent evaporation using immersion oil.*

IX. Dynamic Microtubule Assays

In this section, we outline an assay that can be used to study the behavior of MAPs on dynamic microtubules. Firstly, we present the basic workflow for these types of assays and discuss the important components of the reaction mixture that will be perfused into the channel containing the microtubule seeds. Secondly, we discuss several important variables that must be considered and controlled for accurate experiments. Finally, we discuss the basic type of analysis carried out on these types of data (see elsewhere in this volume and [Bieling et al., 2007](#); [Brouhard et al., 2008](#), for additional information).

A. Protocol for Dynamic Microtubule Assay

Step 1: Prepare channels with fluorescently labeled GMPCPP-stabilized microtubule seeds bound to the surface (see Section [VIII](#)). Wash the channel with 5 channel volumes of BRB80.

Step 2: Place the holder on the microscope stage and bring the coverglass into contact with immersion oil on the objective. The objective is heated to the desired temperature (normally 35°C) by an objective heater (see Section [II](#)).

Step 3: Inject prewarmed reaction solution (see below) containing tubulin and/or a MAP of interest into the channel.

Step 4: Record a movie using TIRF illumination to visualize microtubule extensions growing from the seeds and/or the behavior of fluorescently labeled MAPs (see tips below).

B. Typical Reaction Solution

Prepare the reaction mixture including (1) antiblinking/photo-toxicity/photo-bleaching cocktail (see Section [V](#)); (2) the MAP of interest (if included), including any required nucleotide; (3) the following polymerization mix:

- tubulin (see notes for concentration and labeling ratio)
- 1 mM GTP
- 0.1 mg/ml BSA—providing additional blocking of nonspecific surface binding (competes with tubulin and MAPs for nonspecific binding sites).

C. Considerations Regarding the Reaction Solution

- Polymerization buffer

Typically the buffer for polymerization is BRB80 (Section [III](#)). Care should be taken if some of the components of the reaction solution are not predissolved in BRB80 buffer; in this case it is possible to use a suitable amount of more

concentrated buffer when mixing the reaction solution to keep the final concentration of PIPES at 80 mM.

- Ionic strength

MAPs differ in their requirements for the ionic strength of the reaction solution. The ionic strength can be increased by addition of KCl or decreased by using a lower concentration of PIPES. Note that changes in ionic strength also affect microtubule dynamics (Olmsted and Borisy, 1975); control experiments should always be carried out under identical buffer conditions.

- Tubulin concentration

In the absence of MAPs that promote microtubule growth, no growth of extensions will occur below $\sim 7\text{ }\mu\text{M}$ tubulin. At high ($\geq 15\text{ }\mu\text{M}$) tubulin concentrations spontaneous nucleation of microtubules can occur in the channel (Fygenson *et al.*, 1994).

- Ratio of fluorescent-labeled to unlabeled tubulin

The soluble tubulin introduced into the reaction chamber should not be 100% labeled. Despite the thin evanescent field from TIRF, the background fluorescence will become intolerable at micromolar concentrations of fluorescent tubulin. Therefore, a mixture of labeled and unlabeled tubulin must be used. Our experience suggests that a labeling ratio of 3–5% (3–5 fluorescent labels per 100 tubulin dimers) gives good signal to noise for the dynamic microtubule extensions.

- Ratio of fluorescent-labeled-to-unlabeled MAP

If single-molecule imaging of a MAP is desired, while investigating its effect on the microtubule dynamics, so-called “spiking” experiments can be performed (Varga *et al.*, 2009), where only a very small ratio of the MAP is labeled (see Sections II and IV). Typically the fluorescent-labeled MAP concentration should be kept below 1 nM, although the optimum concentration depends significantly on the particular characteristics of the MAP–microtubule interactions present.

Tip: *The key to obtaining reproducible growth rates in these experiments is the consistent handling of your tubulin. Each aliquot of tubulin must experience an identical procedure of thawing, incubation time on ice, lag time until use in the experiment. In addition, the concentration of tubulin should be precisely known and controlled for reproducibility.*

Tip: *When measuring microtubule growth rates at a constant concentration of tubulin, for example, generating growth versus concentration curves for MAPs such as XMAP215 (Brouhard *et al.*, 2008), it is recommended to “equilibrate” the channel with the appropriate concentration of soluble tubulin before each sample. This step ensures that the appropriate tubulin concentration is present in the channel upon addition of the protein of interest.*

Tip: *In the absence of MAPs we typically get a growth rate of 1.5 $\mu\text{m}/\text{min}$ with 10 μM tubulin at a temperature of 35°C. We find that time points taken at 5s intervals are ideal. Addition of MAPs can result in much higher growth rates ($>10\text{ }\mu\text{m}/\text{min}$). In this case, we use frame rates up to 10 Hz to ensure no events are missed during the time course.*

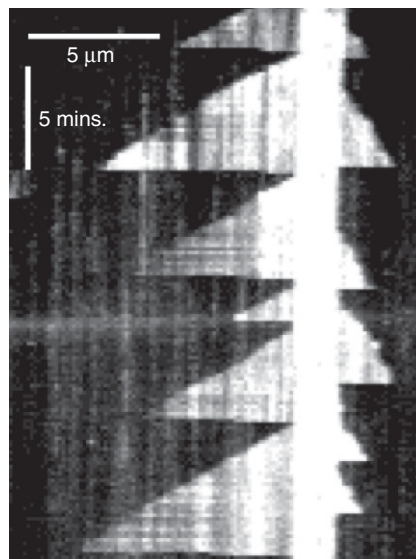


Fig. 6 Kymograph produced from a series of images, showing dynamic microtubule extensions growing from a GMPCPP stabilized seed. In the experiment 9.6 μ M unlabeled and 0.4 μ M Cy3-labeled tubulin was present in the channel, the objective was heated to 35°C, and TIRF images were recorded at 10-s intervals.

D. Analysis of Dynamic Microtubule Assays

The rate of extension of a growing microtubule tip can be determined through measurement of the microtubule length at different time points in a series of images recorded with TIRF illumination. However, care must be taken as thermal fluctuations will cause the ends of long microtubule extensions to move in and out of the TIRF evanescent field. This may affect the apparent measured extension size in an image. The intensity profile of the microtubule can be examined to determine if the tip has drifted out of the evanescent field. If a line scan along the microtubule shows an intensity profile that decreases exponentially, rather than decreasing abruptly, it is likely that the microtubule has bent upward and out of the field of view, making its true length impossible to measure. The dynamic properties can be determined using kymographs (see Fig. 6).

References

Aitken, C. E., Marshall, R. A., and Puglisi, J. D. (2008). An oxygen scavenging system for improvement of dye stability in single-molecule fluorescence experiments. *Biophys. J.* **94**, 1826–1835.

Akhmanova, A., and Steinmetz, M. O. (2008). Tracking the ends: A dynamic protein network controls the fate of microtubule tips. *Nat. Rev. Mol. Cell Biol.* **9**, 309–322.

Axelrod, D. (2008). Chapter 7: Total internal reflection fluorescence microscopy. *Methods Cell Biol.* **89**, 169–221.

Axelrod, D., Burghardt, T. P., and Thompson, N. L. (1984). Total internal-reflection fluorescence. *Annu. Rev. Biophys. Bioeng.* **13**, 247–268.

Bieling, P., Laan, L., Schek, H., Munteanu, E. L., Sandblad, L., Dogterom, M., Brunner, D., and Surrey, T. (2007). Reconstitution of a microtubule plus-end tracking system *in vitro*. *Nature* **450**, 1100–1105.

Brinkley, W. (1997). Microtubules: A brief historical perspective. *J. Struct. Biol.* **118**, 84–86.

Brouhard, G. J., Stear, J. H., Noetzel, T. L., Al-Bassam, J., Kinoshita, K., Harrison, S. C., Howard, J., and Hyman, A. A. (2008). XMAP215 is a processive microtubule polymerase. *Cell* **132**, 79–88.

Caplow, M., Ruhlen, R. L., and Shanks, J. (1994). The free energy for hydrolysis of a microtubule-bound nucleotide triphosphate is near zero: All of the free energy for hydrolysis is stored in the microtubule lattice. *J. Cell Biol.* **127**, 779–788.

Caplow, M., and Shanks, J. (1996). Evidence that a single monolayer tubulin-GTP cap is both necessary and sufficient to stabilize microtubules. *Mol. Biol. Cell* **7**, 663–675.

Conibear, P. B., and Bagshaw, C. R. (2000). A comparison of optical geometries for combined flash photolysis and total internal reflection fluorescence microscopy. *J. Microsc.* **200**, 218–229.

deCastro, M. J., Ho, C. H., and Stewart, R. J. (1999). Motility of dimeric ncd on a metal-chelating surfactant: Evidence that ncd is not processive. *Biochemistry* **38**, 5076–5081.

Dickson, R. M., Cubitt, A. B., Tsien, R. Y., and Moerner, W. E. (1997). On/off blinking and switching behaviour of single molecules of green fluorescent protein. *Nature* **388**, 355–358.

Funatsu, T., Harada, Y., Tokunaga, M., Saito, K., and Yanagida, T. (1995). Imaging of single fluorescent molecules and individual ATP turnovers by single myosin molecules in aqueous-solution. *Nature* **374**, 555–559.

Fygenson, D. K., Braun, E., and Libchaber, A. (1994). Phase diagram of microtubules. *Phys. Rev. E Stat. Phys. Plasmas Fluids Relat. Interdiscip. Topics* **50**, 1579–1588.

Gautier, A., Juillerat, A., Heinis, C., Correa, I. R., Jr., Kindermann, M., Beaufils, F., and Johnsson, K. (2008). An engineered protein tag for multiprotein labeling in living cells. *Chem. Biol.* **15**, 128–136.

Gell, C., Berndt, M., Enderlein, J., and Diez, S. (2009). TIRF microscopy evanescent field calibration using tilted fluorescent microtubules. *J. Microsc. (Oxford)* **234**, 38–46.

Gell, C., Brockwell, D. J., and Smith, D.A.M. (2006). “Handbook of Single Molecule Fluorescence Spectroscopy.” Oxford, UK, Oxford University Press.

Guo, H. L., Xu, C. H., Liu, C. X., Qu, E., Yuan, M., Li, Z. L., Cheng, B. Y., and Zhang, D. Z. (2006). Mechanism and dynamics of breakage of fluorescent microtubules. *Biophys. J.* **90**, 2093–2098.

Helenius, J., Brouhard, G., Kalaizididis, Y., Diez, S., and Howard, J. (2006). The depolymerizing kinesin MCAK uses lattice diffusion to rapidly target microtubule ends. *Nature* **441**, 115–119.

Howard, J., and Hyman, A. A. (2009). Growth, fluctuation and switching at microtubule plus ends. *Nat. Rev. Mol. Cell Biol.* **10**, 569–574.

Hunter, A. W., Caplow, M., Coy, D. L., Hancock, W. O., Diez, S., Wordeman, L., and Howard, J. (2003). The kinesin-related protein MCAK is a microtubule depolymerase that forms an ATP-hydrolyzing complex at microtubule ends. *Mol. Cell.* **11**, 445–457.

Hyman, A., Drechsel, D., Kellogg, D., Salser, S., Sawin, K., Steffen, P., Wordeman, L., and Mitchison, T. (1991). Preparation of modified tubulins. *Meth. Enzymol.* **196**, 478–485.

Hyman, A. A., Salser, S., Drechsel, D. N., Unwin, N., and Mitchison, T. J. (1992). Role of GTP hydrolysis in microtubule dynamics: Information from a slowly hydrolyzable analog, GMPCPP. *Mol. Biol. Cell* **3**, 1155–1167.

Iyer, K. S., and Klee, W. A. (1973). Direct spectrophotometric measurement of the rate of reduction of disulfide bonds. The reactivity of the disulfide bonds of bovine-lactalbumin. *J. Biol. Chem.* **248**, 707–710.

Leduc, C., Ruhnow, F., Howard, J., and Diez, S. (2007). Detection of fractional steps in cargo movement by the collective operation of kinesin-1 motors. *Proc. Natl. Acad. Sci. U.S.A.* **104**, 10847–10852.

Mickey, B., and Howard, J. (1995). Rigidity of microtubules is increased by stabilizing agents. *J. Cell Biol.* **130**, 909–917.

Mitchison, T., and Kirschner, M. (1984). Dynamic instability of microtubule growth. *Nature* **312**, 237–242.

Mori, T., Vale, R. D., and Tomishige, M. (2007). How kinesin waits between steps. *Nature* **450**, 750–754.

Olmsted, J. B., and Borisy, G. G. (1975). Ionic and nucleotide requirements for microtubule polymerization *in vitro*. *Biochemistry* **14**, 2996–3005.

Rasnik, I., McKinney, S. A., and Ha, T. (2006). Nonblinking and long-lasting single-molecule fluorescence imaging. *Nat. Methods* **3**, 891–893.

Reuther, C., Hajdo, L., Tucker, R., Kasprzak, A. A., and Diez, S. (2006). Biotemplated nanopatterning of planar surfaces with molecular motors. *Nano Lett.* **6**, 2177–2183.

Selvin, P. R., and Ha, T. (2007). “Single Molecule Techniques: A Laboratory Manual.” Cold Spring Harbor Laboratory Press, New York.

Thompson, N. L., and Steele, B. L. (2007). Total internal reflection with fluorescence correlation spectroscopy. *Nat. Protoc.* **2**, 878–890.

Varga, V., Helenius, J., Tanaka, K., Hyman, A. A., Tanaka, T. U., and Howard, J. (2006). Yeast kinesin-8 depolymerizes microtubules in a length-dependent manner. *Nat. Cell Biol.* **8**, 957–962.

Varga, V., Leduc, C., Bormuth, V., Diez, S., and Howard, J. (2009). Kinesin-8 motors act cooperatively to mediate length-dependent microtubule depolymerization. *Cell* **138**(6), 1174–1183.

Weisenberg, R. (1972). Microtubule formation *in-vitro* in solutions containing low calcium concentrations. *Science* **177**, 1104–1105.

Yildiz, A., Forkey, J. N., McKinney, S. A., Ha, T., Goldman, Y. E., and Selvin, P. R. (2003). Myosin V walks hand-over-hand: Single fluorophore imaging with 1.5-nm localization. *Science* **300**, 2061–2065.

Yildiz, A., Tomishige, M., Vale, R. D., and Selvin, P. R. (2004). Kinesin walks hand-over-hand. *Science* **303**, 676–678.

Zhang, J., Campbell, R. E., Ting, A. Y., and Tsien, R. Y. (2002). Creating new fluorescent probes for cell biology. *Nat. Rev. Mol. Cell Biol.* **3**, 906–918.

CHAPTER 14

Studying Kinesin Motors by Optical 3D-Nanometry in Gliding Motility Assays

Bert Nitzsche^{*}, Volker Bormuth^{*}, Corina Bräuer^{*}, Jonathon Howard^{*}, Leonid Ionov^{*}, Jacob Kerssemakers[†], Till Korten^{*}, Cecile Leduc[‡], Felix Ruhnau^{*}, and Stefan Diez^{*}

^{*}Max Planck Institute of Molecular Cell Biology and Genetics, 01307 Dresden, Germany

[†]Kavli Institute of Nanoscience, Delft University of Technology, 2628 CJ Delft, The Netherlands

[‡]Centre de Physique Moléculaire Optique et Hertzienne, Université Bordeaux 1, CNRS (UMR 5798), 33405 Talence cedex, France

Abstract

- I. Introduction
- II. Setup of Gliding Motility Assays
 - A. Surface Treatment and Flow-Chamber Preparation
 - B. Microtubule Preparation
 - C. Surface Immobilization of Motor Proteins
 - D. Attachment of Fluorescent Markers to Microtubules
 - E. Imaging of Microtubule Motility
- III. Analysis of Microtubule and Quantum Dot Movements
 - A. Quick Motility Evaluation in Two Dimensions
 - B. Nanometer Tracking in Two Dimensions
 - C. Resolving Nanometer Distances in the Third Dimension
- IV. Future Directions

Acknowledgments
Reagents
References

Abstract

Recent developments in optical microscopy and nanometer tracking have facilitated our understanding of microtubules and their associated proteins. Using fluorescence microscopy, dynamic interactions are now routinely observed *in vitro* on the

level of single molecules, mainly using a geometry in which labeled motors move on surface-immobilized microtubules. Yet, we think that the historically older gliding geometry, in which motor proteins bound to a substrate surface drive the motion microtubules, offers some unique advantages. (1) Motility can be precisely followed by coupling multiple fluorophores and/or single bright labels to the surface of microtubules without disturbing the activity of the motor proteins. (2) The number of motor proteins involved in active transport can be determined by several strategies. (3) Multimotor studies can be performed over a wide range of motor densities. These advantages allow for studying cooperativity of processive as well as non-processive motors. Moreover, the gliding geometry has proven to be most promising for nanotechnological applications of motor proteins operating in synthetic environments. In this chapter we review recent methods related to gliding motility assays in conjunction with 3D-nanometry. In particular, we aim to provide practical advice on how to set up gliding assays, how to acquire high-precision data from microtubules and attached quantum dots, and how to analyze data by 3D-nanometer tracking.

===== I. Introduction

Optically following the live action of motor proteins at work has been a long-standing goal of biologists. However, observing the motors directly using light microscopy is technically much more challenging than imaging the huge polymeric filaments of the cytoskeleton along which the motors move. Even the narrow, 6-nm wide actin filaments can be imaged by dark-field (Nagashima and Asakura, 1980) or epi-fluorescence (Yanagida *et al.*, 1984) microscopy. Historically, this facilitated the development of the so-called “upside-down” motility assays early on. In these “gliding” assays, the motors are bound to a planar substrate (usually a glass coverslip), and the movement of the filaments across the surface (Fig. 1) is followed by time-resolved microscopy (Kron and Spudich, 1986). By reducing the motor density on the surface, gliding assays even provide the possibility to obtain recordings from individual motor proteins (Howard *et al.*, 1989). Yet, it has always been an attractive idea to visualize the movement of the motors rather than that of the filaments. In order to do so “stepping” motility assays, in which the filaments are bound to the substrate and the motor movement along the immobilized filaments is imaged, have been developed. This was first done by binding the motors to large, micron-sized beads, which could be followed by video microscopy (Sheetz and Spudich, 1983; Spudich *et al.*, 1985; Yanagida *et al.*, 1984) or held in an optical trap (Rief *et al.*, 2000; Schnitzer *et al.*, 2000; Svoboda *et al.*, 1993). Later on, Funatsu *et al.* pushed the sensitivity of the fluorescence microscope to the limit of being able to visualize individual motor molecules labeled with the cyanine-based fluorophores (Funatsu *et al.*, 1995). Using total internal reflection fluorescence (TIRF) microscopy, the processive movement of individual kinesin-1 molecules along microtubules was visualized by labeling the motors with Cy3 (Vale *et al.*, 1996) or with the green fluorescent protein (GFP) (Pierce *et al.*, 1997). Since then, the number of single-molecule fluorescence measurements of kinesin and dynein motors interacting with microtubules has vastly expanded. Nowadays, not only the stepping of motors is observed in these assays, but also diffusion and (de)polymerizing activities of motors

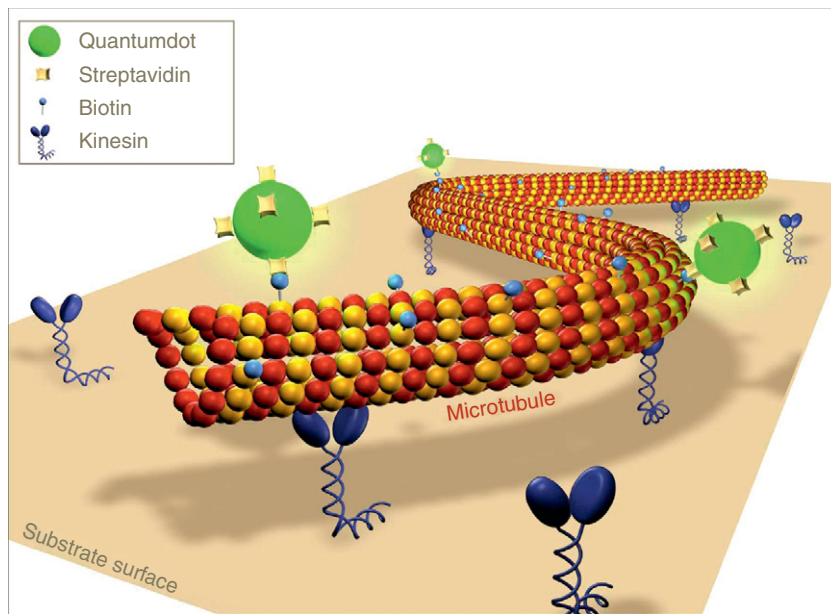


Fig. 1 Schematic diagram of a gliding motility assay in which reconstituted microtubules, tagged with semiconductor nanocrystals (quantum dots), are propelled over a kinesin-coated substrate surface. (See Plate no. 16 in the Color Plate Section.)

(and other microtubule-associated proteins) (Bieling *et al.*, 2007; Brouhard *et al.*, 2008; Fink *et al.*, 2009; Helenius *et al.*, 2006; Varga *et al.*, 2006, 2009).

Despite all the recent developments and groundbreaking results obtained in stepping motility assays, we think that there are still a number of compelling reasons to revisit the historically older gliding motility assays: (1) Fluorescently labeled filaments are bright objects that can be tracked with high precision. (2) Photostable optical reporters, such as quantum dots (QDs), can easily be attached to the filaments without interfering with the operation of individual motors. (3) Several strategies to determine the number of motors involved in transport are feasible. (4) The collective behavior involving multiple processive or nonprocessive motors can be studied over a wide range of motor densities. We will report methods and protocols that allow for experiments taking advantage of these benefits.

===== II. Setup of Gliding Motility Assays

When performing gliding motility assays, it is an essential prerequisite to immobilize the motor proteins on the surface in such a way that they lose as little activity as possible compared to a situation where they are free in solution or even to the *in vivo* situation. In particular, it is important to minimize the number of motors that only function partially, i.e., to avoid the existence of motors that bind rigorously to the filaments, unable to undergo their actual mechanochemical cycle. Along these lines, we regard the treatment of the surfaces and the method of motor

immobilization as the most critical steps in setting up a gliding motility assay. Unfortunately, there is no general protocol that works reliably with all types of motor proteins. Yet, there are certain concepts that, when adapted by some minor, but crucial, modifications, function with many different motor proteins. In the end, every gliding motility assay has to be optimized for the exact motor protein used, and evidence that the assay works is only provided by the facts that (1) the experiments are reproducible and (2) the gliding velocities are consistent with *in vivo* activity of the motor. Below we will list a number of example procedures and general hints on how to establish a “successful” gliding motility assay.

A. Surface Treatment and Flow-Chamber Preparation

Depending on the specific experiment, we routinely treat glass coverslips or silicon wafers with various cleaning and coating procedures to adjust the surface properties. The treated glass coverslips (for epi-fluorescence and TIRF measurements) or silicon wafers [for fluorescence-interference contrast (FLIC) measurements] then provide the surface of the flow chambers where the gliding motility experiments are performed in. Generally, surface preparation should be performed very carefully in a clean and dust-free environment to guarantee the reproducibility and the high quality of the experimental results.

Here we describe a simple, but effective, cleaning procedure (easy-clean), a method to passivate surfaces to prevent protein adsorption [based on polyethylene glycol (PEG)], a method to render surfaces highly hydrophobic (based on dichlorodimethylsilane), and an approach to generate surfaces, which gradually [in one dimension (1D)] change their capacity to bind proteins.

1. Easy-Clean Procedure

Load the glass coverslips or silicon wafer chips into porcelain or polytetrafluoroethylene (PTFE) racks. Place the racks into a glass container and fill with mucasol (1:20 dilution in deionized water) such that all coverslips/chips are completely covered. Sonicate (using Bransonic 2510, Branson, Danbury, CT, USA) for 15 min and rinse with deionized water for 2 min. Remove the water from the container using a (e.g., 1 ml) pipette tip connected to the vacuum line. Fill the container with ethanol, again immersing the coverslips/chips completely, sonicate for 10 min, and rinse with nanopure water for 2 min in the container. Take the racks out of the container and carefully blow dry the coverslips/chips using nitrogen.

When used under the microscope, these surfaces are mildly hydrophilic. Being usually devoid of any fluorescent particles, they are even suited for single-molecule fluorescence measurements.

Tip: We store the coverslips/chips (prepared by the easy-clean procedure as well as by the methods listed below) in a dry container, which is sealed such that no dust can get onto the surfaces.

2. Protein-Repelling Surfaces (Based on PEG-Silane)

To passivate surfaces, we use a procedure adapted from [Papra *et al.* \(2001\)](#) as follows: Load the glass coverslips or silicon wafer chips into porcelain or PTFE

racks. Place the racks into a glass container and fill with an ethanol/water mix (1:1). Sonicate for 5 min and rinse with deionized water for 2 min. Expose the coverslips to piranha-cleaning solution (60 ml sulfuric acid and 20 ml hydrogen peroxide; add the hydrogen peroxide last) for 10 min, rinse three times with nanopure water and sonicate in nanopure water for 10 min. After blow drying them using nitrogen, they are ready for the grafting of PEG. Incubate the coverslips/chips for 18 h at room temperature in 25 ml of toluene supplemented with 57.5 mg of 2-[methoxy (polyethyleneoxy)propyl]trimethoxysilane (PEG-silane, 90%) and 20 μ l HCl (37%). Ensure constant stirring and cover the container. In a subsequent cleaning procedure, rinse the coverslips/chips once in toluene, twice in ethanol, twice in nanopure water, and sonicate in nanopure water for 2 min.

Proteins will be repelled from a pegylated surface. That is why a substrate treated this way is suitable as a counterpart to the “imaging surface” of a flow chamber. If the nonimaged surface is pegylated, then all proteins of interest will interact with the “imaging surface” only.

3. Hydrophobic Surfaces (Based on Dichlorodimethylsilane)

This procedure is described in Chapter 13 by Gell *et al.*, this volume. We use hydrophobic surfaces to strongly adsorb antibodies (as adapter proteins for specific motor molecules) in combination with the possibility to block the rest of these surfaces against nonspecific protein binding by casein or Pluronics (see below).

4. Gradient Surfaces (Based on PEG)

Clean the highly polished silicon wafer chips (final chip size 50×10 mm, {100} orientation) in an ultrasonic bath with chloroform for 30 min. Place them in piranha-cleaning solution (see above) for 1 h and rinse several times with nanopure water. Spin-coat a thin layer (thickness 1.5 nm) of polyglycidylmethacrylate (PGMA, $M_n = 50,000$ g/mol, 0.02% in chloroform [we found this to work even better than using methylethylketone as solvent as reported previously (Ionov *et al.*, 2005)] on the chips. Spin-coat a thin film (thickness about 200 nm) of PEG-NH₂ (2% solution in chloroform, PEG-NH₂, $M_n = 5000$ g/mol, $M_w = 5400$ g/mol) on top and let the sample anneal for 1 h on a stage with a 1D temperature gradient (40–90°C along a length of 50 mm). Upon this heating step, the grafted PEG layer will form due to the chemical reaction between the terminal amino groups of the PEG and the epoxy groups of the PGMA. The temperature gradient translates to a gradient in the grafting density caused by the temperature dependence of the grafting kinetics. Remove ungrafted polymer using Soxhlet extraction in chloroform for 3 h [see also Ionov *et al.* (2005) for more details].

Such surfaces, which gradually change their protein-repelling properties (based on the PEG gradient) in 1D, can be applied for combinatorial and high-throughput investigations of proteins. When motor proteins are bound to such surfaces, they allow for probing the interactions of filaments with motors of different density on one sample surface, as well as for the sorting of filaments according to their length (Ionov *et al.*, 2005).

5. Flow-Chamber Preparation

The general procedure we use to assemble our flow chambers is described in Chapter 13 by Gell *et al.*, this volume. Apart from double-sided Scotch tape to confine the flow channels, we also use Parafilm or Nescofilm as an alternative. Flow-chamber assembly is then as follows: Cut the Para-/Nescofilm in stripes using a (razor) blade or a laser cutter (Speedy 100C 25W, Trotec, Marchtrenk, Austria). Place the prepared Para-/Nescofilm stripes on top of a 22 × 22 mm coverslip and cut off (using a razor blade) those parts of the stripes that protrude over the edges of the coverslip. Place the top coverslip (18 × 18 mm or silicon chip) in a central location on the stripes and transfer the assembly (22 × 22 coverslip facing down) to a heating plate with a temperature of $\approx 120^{\circ}\text{C}$ for Parafilm or $\approx 150^{\circ}\text{C}$ for Nescofilm. The two coverslips (or coverslip/silicon chip) will be firmly joined by the melting Para-/Nescofilm. This process can be well monitored by a change in the optical properties of the Para-/Nescofilm. Gently applying a bit of pressure to the top coverslip/chip during the melting process ensures a tight sealing and eliminates air bubbles that might have formed above or beneath the stripes. Without delay, place the flow chamber onto the surface of a metal (e.g., aluminum) block for fast cooling. Mounting the assembly in the appropriate holder (see also Chapter 13 by Gell *et al.*, this volume) is the last step before the channels (volume approximately 3 × 18 × 0.1 mm $\approx 5 \mu\text{l}$) of the flow chamber can be filled with solutions.

Tip: When using a pegylated coverslip (with an extremely hydrophilic surface) as one side of the flow chamber, double-sided Scotch tape and parafilm stripes frequently lift-off the pegylated surface and hence the channels become leaky. We therefore recommend using Nescofilm in conjunction with pegylated surfaces.

Tip: When assembling the flow chambers, take care to not expose bare surfaces to dust. Apply the same caution as during the surface preparation.

B. Microtubule Preparation

For gliding motility assays, microtubules are commonly reconstituted from purified tubulin. Thereby, their physical structure, including the number of protofilaments and the stiffness, strongly depends on the assembly conditions (Meurer-Grob *et al.*, 2001; Pierson *et al.*, 1978; Ray *et al.*, 1993). Below, we will describe the generation of stable (i.e., nondynamic) microtubules using the slowly hydrolyzable GTP-analogue GMP-CPP with/without further stabilization using Taxol. In order to allow for the attachment of streptavidin-coated QDs as fluorescent markers, part of the tubulin used in the polymerization reaction is biotinylated.

1. Biotinylated GMP-CPP Microtubules

Supplement 100 μl BRB80 (80 mM PIPES/KOH pH 6.9, 1 mM MgCl₂, 1 mM EGTA) by 2 μM tubulin, 4 mM MgCl₂, and 1 mM GMP-CPP. Tubulin may be a mixture of 5–50% fluorescently labeled (e.g., Alexa 488 or TAMRA), 2–50% biotinylated, and 50–93% unlabeled tubulin. (Note: Because very high tubulin labeling ratios can lead to artifacts in the interaction of motor proteins with the filaments, we never use more than 50% labeled tubulin in the polymerization reaction) Allow the microtubules to assemble for $\geq 2\text{ h}$ at 37°C . Centrifuge the

microtubule solution at $100,000 \times g$ for 5 min and resuspend in BRB80 (final tubulin concentrations 0.4–4 μM). For more details, see [Nitzsche *et al.* \(2008\)](#).

Tip: If the concentration of free tubulin is very low in the final solution (e.g., after centrifugation and dilution in high volumes), microtubules may depolymerize within a few hours. Performing the centrifugation step only shortly before using the microtubules greatly reduces this problem.

Tip: The stability of GMP-CPP microtubules can be quite variable due to residual GDP/GTP in the initial tubulin solution ([Caplow *et al.*, 1994](#); [Caplow and Shanks, 1996](#)). The durability of the microtubules can be greatly improved by an additional cycling step when preparing the tubulin solution (see Chapter 13 by Gell *et al.*, this volume).

Tip: More than 95% of the microtubules assembled in the presence of GMP-CPP consist of 14 super-twisted protofilaments ([Hyman *et al.*, 1995](#); [Meurer-Grob *et al.*, 2001](#)).

2. Biotinylated Double-Stabilized Microtubules

Prepare biotinylated microtubules using GMP-CPP (as described above). However, resuspending the microtubules after the centrifugation step, supplement the BRB80 with 10 μM Taxol and keep this amount of Taxol present in all subsequent solutions. Microtubules stabilized this way are stable for weeks at room temperature.

C. Surface Immobilization of Motor Proteins

We use two types of strategies to immobilize motor proteins on surfaces: non-specific and specific binding. In the simplest case (nonspecific binding) motor proteins are allowed to adsorb to surfaces precoated with other “space filling” proteins ([Howard *et al.*, 1993](#)). This nonspecific approach works for some kinesin motors (e.g., kinesin-1). For other motor proteins, however, procedures targeting specific sequences of the motor proteins can significantly improve the quality of motility assays. Thereby, bioactive linker molecules (e.g., specific antibodies or streptavidin) that are directed toward specified regions distal to the motor domain (e.g., purification tags, GFP or biotinylated sites) are first attached to the surface. After the rest of the surface is blocked by other space filling proteins (or polymers), the motor molecules can bind to the surface in a directed manner ([Crevenna *et al.*, 2008](#); [Kerssemakers *et al.*, 2006](#); [Leduc *et al.*, 2007](#)). Below we describe the immobilization of kinesin-1 motors using (1) nonspecific binding to casein-coated surfaces and (2) specific binding using penta-His antibodies against a tag sequence added to the tail of the kinesin-1 heavy chain.

1. Nonspecific Immobilization

Construct a flow chamber, using easy-clean glass coverslips, as described above. Flow in 0.5 mg/ml casein in BRB80 into one of the channels and let the surfaces incubate for 5 min. Replace the solution by 100 $\mu\text{g/ml}$ kinesin-1 in BRB80 supplemented with 10 μM to 1 mM ATP and 0.2 mg/ml casein and wait 5 min.

The actual gliding motility assay is then performed by perfusing a microtubule-containing “motility solution” [BRB80 augmented with microtubules, 10 μM to

1 mM ATP, 0.2 mg/ml casein, and an oxygen scavenger mix of 20 mM D-glucose, 0.02 mg/ml glucose oxidase, 0.008 mg/ml catalase, and 10 mM dithiothreitol (DTT) or 0.5% β -mercaptoethanol (BME)] into the flow chamber.

Tip: While casein has been reported to be a blocking agent which effectively prevents kinesin-1 from denaturing at the surface (Ozeki *et al.*, 2009), other proteins (e.g., BSA) may be more effective for other motors. However, even in cases where the surface blocking strategy is not based on casein, supplementing the ATP-containing motility solution with casein (\approx 0.2 mg/ml) often helps to achieve reliable motility.

Tip: Gradients in the density of motor proteins can be generated when motor proteins are nonspecifically adsorbed onto surfaces prepared with PEG gradients (see above).

2. Specific Immobilization (Via Antibodies)

Construct a flow chamber, using hydrophobic glass coverslips, as described above. Flow in penta-His antibodies in BRB80 (about 20 or 0.2 μ g/ml for high or low kinesin concentration assays, respectively). Wait 5 min. Perfuse 0.5 mg/ml casein in BRB80 to prevent nonspecific protein binding. Wait 5 min. Flow in 10 μ g/ml kinesin-1 (with a His-tag) in BRB80 supplemented with 0.2 mg/ml casein and 10 μ M to 1 mM ATP. Incubate for 5 min to bind the motors specifically to the antibodies by their His-tags. Similar to the procedure described above, the actual gliding motility assay is then performed by perfusing a microtubule-containing “motility solution” into the flow chamber [see also Leduc *et al.* (2007)].

Tip: The procedure described above is also applicable for flow chambers with easy-cleaned (see Section II.A) surfaces.

Tip: Make sure your antibody solution does not contain any contaminations that might block the surface of your flow chamber, thereby preventing effective adsorption of the antibodies.

Tip: Alternative to casein, Pluronic F127 (or similar copolymers) can be used to prevent nonspecific protein binding to hydrophobic surfaces (Crevenna *et al.*, 2008; Kerssemakers *et al.*, 2006). Note that Pluronics are applicable for passivation of hydrophobic surfaces only.

Tip: For other motors, sandwich-like, antibody-binding assays, providing longer and more flexible linkage between surface and motor proteins, might prove useful. For example, biotinylated anti-GFP antibodies (bound to surface-immobilized neutravidin) can be used to specifically bind GFP-tagged kinesin-8 motor proteins (Varga *et al.*, 2009). Similarly, surface-immobilized protein A can be used to bind an intermediate layer of (nonbiotinylated) anti-GFP antibodies.

Tip: Additional methods to specifically bind His-tagged motor proteins to surfaces, e.g., by nitrilotriacetic acid (NTA)-functionalized Pluronic (deCastro *et al.*, 1999) or NTA-PEG (Bieling *et al.*, 2008), have been reported in the literature.

D. Attachment of Fluorescent Markers to Microtubules

In order to study motor behavior in gliding assays, microtubule movement on motor-coated surfaces has to be measured with nanometer precision. For this purpose, fluorescence microscopy combined with nanometer tracking is well suited.

First, microtubules can be labeled with a multitude of fluorescent dyes along their lattices, making the contours of the filaments visible. Second, well-separated sub-resolution fluorescent emitters (such as QDs) can be coupled to microtubules. A combination of both labeling approaches can be applied to observe rotations of microtubules around their longitudinal axes (Nitzsche *et al.*, 2008).

1. Fluorescent Dyes

Fluorescent microtubules are most commonly generated by polymerizing tubulin heterodimers, a fraction of which are labeled with fluorescent dyes. The choice of fluorophores depends on several factors, such as emission and absorption spectra (especially when doing multicolor imaging), brightness, photostability, and compatibility with microtubule polymerization (see Chapter 13 by Gell *et al.*, this volume for details). Chemical coupling of fluorescent dyes to tubulin is commonly performed using succinimidyl chemistry. The procedure we are using is similar to that of Hyman *et al.* (1991). Besides, tubulin labeled with different dyes or bioactive small molecules (such as biotin) is commercially available.

2. Quantum Dots

QDs are fluorescent semiconductor nanocrystals that exhibit a number of superior optical properties compared to fluorescent dyes (Giepmans *et al.*, 2006; Resch-Genger *et al.*, 2008): (1) they emit at sharply defined wavelengths (dependent on their geometrical size), (2) their excitation spectrum is very broad (ranging from the UV up to closely below the emission wavelength), (3) they are very bright (due to their high extinction coefficients and quantum yields), and (4) their superior photostability guarantees long life-times in fluorescence imaging. These features make QDs ideally suited for high-precision nanometer tracking, in particular in multicolor applications. One drawback of the QDs is that they blink on various timescales (ranging from submilliseconds to many seconds). Although there is no way to eliminate blinking completely, it has been reported that the use of the reducing agents BME and DTT reduces blinking dramatically (Hohng and Ha, 2004). There are also recent reports about the synthesis of nonblinking QDs (Chen *et al.*, 2008; Mahler *et al.*, 2008; Wang *et al.*, 2009), though they are not commercially available.

QDs are available in a wide range of emission wavelengths. When choosing the right QDs, we find two considerations important: (1) to avoid crosstalk with the signal of the labeled microtubules, and (2) to optimize the emission intensity. Note that QDs emitting in the longer wavelength range (i.e., in the red spectrum) exhibit significantly higher extinction coefficients than those emitting at lower wavelengths. Red QDs are therefore better suited for nanometer tracking applications, where localization uncertainty scales with the inverse of the square root of the number of detected photons (Thompson *et al.*, 2002).

Labeling of microtubules with QDs is performed in the flow chamber (see following example): Wait 5 min after perfusion of the microtubule-containing motility solution (see Section II.C), in order to let microtubules bind to the motor-coated surfaces. Incubate the flow chamber with motility solution which, however, contains 2–50 pM streptavidin-conjugated QD 655 instead of microtubules. Wait 5 min. Wash

out QDs using 60–100 μ l of motility solution (without microtubules). At moderate labeling rates, i.e., when individual QDs are well separated in the optical microscope, there is no significant influence of the QDs on the gliding velocity of the microtubules.

Tip: When specifically immobilizing motors on the surface via antibodies, increased nonspecific binding of streptavidin-conjugated QDs to the surface might occur. In this case, try to keep the antibody concentration as low as possible. In particular, control the motor density on the surface via the antibody concentration rather than using high antibody concentrations in conjunction with variable motor concentrations.

Tip: According to the manufacturer's specifications, the casein we use may cause interference with the biotin–streptavidin system for it contains variable amounts of biotin. While we did not find this to be a critical issue in our assays, we precautiously store the QDs in their original stock solution (as purchased) and add them to the respective solution just before use.

Tip: It is also possible to bind QDs to microtubules in the test tube (Leduc *et al.*, 2007). However, when doing so, be aware that elevated concentrations of microtubules and QDs, high biotinylation rates of the microtubules, and/or long incubation times may lead to microtubule–microtubule cross-linking. In addition, free biotinylated tubulin may bind to and even saturate the streptavidin on the QDs.

E. Imaging of Microtubule Motility

In our standard setup for epi-fluorescence imaging, we acquire time-resolved movies of microtubule motility using an inverted fluorescence microscope (Axiovert 200M, Zeiss, Oberkochen, Germany) with a variety of optical objectives (e.g., 100 \times oil 1.3 NA, 63 \times water 1.2 NA, 40 \times oil 1.3 NA, Zeiss) in combination with an EMCCD camera (Ixon DV 897, Andor, Belfast, UK). Fluorescence excitation is achieved using either a mixed gas argon–krypton laser (Innova 70C Spectra; Coherent, Santa Clara, CA, USA) or a liquid-waveguide-coupled Lumen 200 metal arc lamp (Prior Scientific Instruments Ltd., Cambridge, UK). Image acquisition and basic data processing is done using a MetaMorph software package (Universal Imaging, Downingtown, PA, USA) controls. In the following, we describe modifications enabling dual-color TIRF and FLIC microscopy as well as a method to control the temperature of the gliding assay.

1. Total Internal Reflection Fluorescence Microscopy

TIRF microscopy allows for high-contrast imaging of fluorescent objects within the evanescent field near transparent substrate surfaces. The setup we are using consists of a commercially available TIRF slider and an alpha Plan-Apochromat 100 \times oil 1.46 NA DIC objective (both Zeiss).

2. Fluorescence-Interference Contrast Microscopy

FLIC microscopy can be employed to obtain nanometer height information of fluorescent objects above reflective surfaces. Direct and indirect light exciting a fluorophore in the vicinity of a reflective surface will self-interfere (as will the direct and indirect emission light) leading to a periodic modulation of the detected intensity

as function of object height above the surface (the “FLIC curve”) (Kerssemakers *et al.*, 2006; Lambacher and Fromherz, 1996). As a consequence of the interference, minimum intensity is observed directly on the reflecting surface while the first maximum is located about 100–150 nm above the surface. To apply FLIC microscopy to gliding motility assays, flow chambers have to be constructed such that the side toward the objective is transparent while the one distal to the objective is reflective—we use a glass coverslip and a silicon chip, respectively. The sample can be illuminated using a fluorescence lamp or a laser and imaging is performed “through” the flow chamber, using a water immersion objective, to minimize spherical aberrations. In order to acquire data in the sensitive range of the FLIC curve, i.e., in the range where the detected intensity varies strongly with distance above the surface, the silicon chips are featured with layers of transparent silicon oxide ranging in height from a few nm to about 80 nm. For an *in situ* calibration of the FLIC curve, silicon chips with varying heights of silicon oxide (Lambacher and Fromherz, 1996) or tilted microtubules can be used (Kerssemakers *et al.*, 2006) (see also Fig. 5 in Section III.C).

3. Dual-Color Imaging

For the simultaneous imaging of microtubules (e.g., labeled with green Alexa 488) and QDs (e.g., QD 655 emitting in the red at 655 nm), we use single-band excitation in the blue range of the spectrum of light. For detection, we separate the emission colors employing a spectral beam splitter (W-view A8509, Hamamatsu Photonics K. K., Hamamatsu City, Shizuoka Pref., Japan) mounted between the microscope and the camera. The exact specifications of the fluorescence filters in microscope and beam splitter will depend on the actual fluorophores and QDs used [see Nitzsche *et al.* (2008) for a specific example]. The signals of the two color-channels are then recorded on two different halves of the same CCD camera chip. In order to calibrate the dual-color overlay, we sparsely deposit multicolor tetraspeck fluorescent beads (0.2 μm diameter) onto the surface before the motor immobilization procedure. While an exact (hardware-based) alignment of the two color-channels is not possible due to perturbations in the optical paths, the multicolor beads can be used to generate a (software-based) offset map between the channels.

Tip: While laser illumination enables high excitation intensities within a narrow spectral band, it often comes with spatial inhomogeneities in the illumination over the field of view. These inhomogeneities result from the long coherence length of the laser light which causes unwanted interference effects in the imaging systems, mainly due to scattering. We therefore often perform our experiments using illumination by a metal arc-lamp, providing us with spatially homogeneous illumination yet at sufficient light intensity.

4. Temperature Control

To allow for highly reproducible measurements of gliding velocities, tightly controlling the temperature of the assays during imaging can be essential. The usual approach of heating the stage (and/or the objective) is rather slow and does not allow for cooling the sample. To overcome these drawbacks, we mount the flow chamber on a Peltier element connected to a heat sink. The Peltier element is powered by a remotely controllable, automated laboratory power supply (Elektro

Automatik EA-PS 3016-10B, Viersen, Germany). To change between heating and cooling, a computer-controlled polarity switch (constructed in-house) is employed for switching the polarity of the Peltier current. The temperature on the Peltier element is measured using a thermometer with analog readout capability (Physitemp BAT 10, Clifton, NJ, USA) and a tissue implantable thermocouple microprobe (Physitemp IT-23). Both the thermometer and the power supply are connected to the imaging computer via an analog I/O PCI card (DaqBoard/2000, IOtech, OH, USA-now Measurement Computing Corporation, Norton, MA, USA). Temperature control has been programmed in a journal within the imaging software (Metamorph, Universal Imaging Corp., Downingtown, PA, USA). Based on the temperature readout, the current necessary for the Peltier to reach the target temperature is calculated using the characteristic current-temperature relation of the Peltier element. However, if temperatures more than 10 K above or below room temperature are to be sustained for longer time periods, the power needs to be constantly adapted, to compensate for thermal power loss of the Peltier element. For this purpose an appropriate fine-tuning algorithm constantly checks whether the actual temperature is still within 0.2 K of the target temperature. If that is not the case and the temperature gradient is below 0.2 K/s, the algorithm adjusts the temperature the Peltier element is assumed to have at zero power (initially set to room temperature). That way, the temperature regulation is very robust not only against thermal power loss, but also against changes of ambient temperature and inaccuracies of the assumed characteristics of the Peltier element.

Our approach [for more details, see [Korten \(2009\)](#)] allows one to control the temperature of the sample in the range from -10 to 100°C with a response time of a few seconds. Like other methods, our setup shows defocusing upon temperature changes. However, the defocusing has turned out to be linear with temperature and is compensated for by adjusting the z-position of the microscope stage (motorized focus in the inverted Zeiss 200M) by 0.77 μm per 1 K temperature difference. While focus compensation is too slow for very fast temperature switches, the image is back in focus as soon as the temperature change slows down, making manual refocusing obsolete in most cases.

5. Practical Issues

1. Make sure the sample is tightly fixed on the microscope stage in order to avoid unwanted shifting in the field of view. If necessary, be creative to fix its position by additional means.
2. Thermal drift during imaging can be reduced significantly when allowing the flow chamber (including the sample holder) to thermally equilibrate for about 2 min before image acquisition (flow chamber already in contact with the immersion fluid, if nonair objectives are used).
3. Airflow in air-conditioned rooms can cause quite dramatic stage drift. A simple yet effective solution is to build a closed box (e.g., made of transparent polymethyl methacrylate) around the microscope.
4. To compensate for residual stage drift, bright fluorescent beads (e.g., tetraspeck beads) can be used as drift control in the sample. Ideally the signal of the beads should be much brighter than that of the fluorescent objects of interest. Otherwise, noise from bead tracking will significantly contribute to the localization error of the fluorescent objects of interest (see also [Section III.B](#)). If single beads are not

bright enough, the signal can be virtually improved by averaging the positions of multiple beads.

5. When imaging for a longer period of time, buffer will evaporate from the edges of the flow channels causing changes in buffer concentration and ionic strength. In order to avoid this, sealing the channel with vacuum grease or sigillum wax helps. If solutions within the flow chamber still need to be replaced during the experiment, an alternative is provided by placing some water-soaked cellulose towels beside the flow chamber and covering both with a small plastic box (like the lid of a pipette box).
6. Even without sophisticated microfluidic devices, solutions in flow channels can be exchanged keeping the sample in the very same field of view. The principle is that on the one side of the flow channel the desired solution is fed while the solution to be removed from the channel is sucked up with a piece of filter paper at the same time. With a steady hand and a bit of practice, this procedure works surprisingly well. When working carefully, the sample is only shifted by a few nanometers.
7. When exchanging solutions in the flow chamber during sample illumination, we sometimes observe a nonreversible slowdown of motility. We attribute this phenomenon to photo effects probably caused by oxygen which is introduced into the flow channels during buffer exchange. We avoid this problem by interrupting the illumination for the duration of the buffer exchange. Waiting for an additional 10–30 s seems to be sufficient time for the oxygen scavenger system to deplete the oxygen from solution.

III. Analysis of Microtubule and Quantum Dot Movements

Time-resolved image sequences of microtubules gliding on motor-coated surfaces contain valuable information about the activity of the motor proteins. In order to extract these data, a number of image-processing tools are available. We will describe the application of maximum intensity projections and kymographs as quick (and easy) evaluation methods to study motor trajectories and velocity. In order to resolve gliding parameters in the nanometer range (also allowing to search for stepwise motor movements), we use 2D tracking algorithms which involve sub-pixel fitting procedures. Moreover, we employ interference-based imaging methods to extend the nanometer tracking into the third dimension.

A. Quick Motility Evaluation in Two Dimensions

When aiming to quickly and efficiently determine a number of key motility parameters, such as the gliding velocities of microtubules, it is often sufficient to determine the position of the fluorescent objects with a precision in the order of the pixel size. Maximum intensity projections or kymographs—available in standard image acquisition and processing software packages such as ImageJ (public domain, Java-based project by Rasband, W., National Institutes of Health, USA, <http://rsbweb.nih.gov/ij/>) or Metamorph (Universal Imaging, Downingtown, PA, USA)—usually suffice for this purpose. While maximum projections can inherently provide data about multiple mobile objects within the field of view, they do not carry any

temporal information. Kymographs, on the other hand, are used to analyze the trajectories of single objects moving along a given path in a time-resolved manner.

1. Maximum Intensity Projections

Maximum (intensity) projections are images whose pixel values represent the maximum value of the respective pixel within a whole stack of images. For stacks of sequentially acquired images from the same field of view, a maximum projection therefore depicts the trajectories of the moving objects. Based upon this, the fastest way to obtain the velocities of gliding microtubules (Fig. 2A and D) is to measure their distances traveled in a maximum projection and divide this value by the time that passed between the acquisition of the first and last image in the stack. If the signal of a point source of light (like a microtubule-attached QD) is available, this can be directly used to measure the distance traveled by a microtubule (provided the QD is firmly attached to the microtubule ensuring there is no shift with respect to each other). If the whole microtubule is labeled by fluorescent dyes, a maximum projection will display the path of the microtubule plus its length. To then determine the velocity values correctly, the initial and final positions of either the leading or the trailing microtubule tip have to be visualized in the maximum projection. A very convenient way of doing so is a three-color overlay of (1) the first frame of the stack,

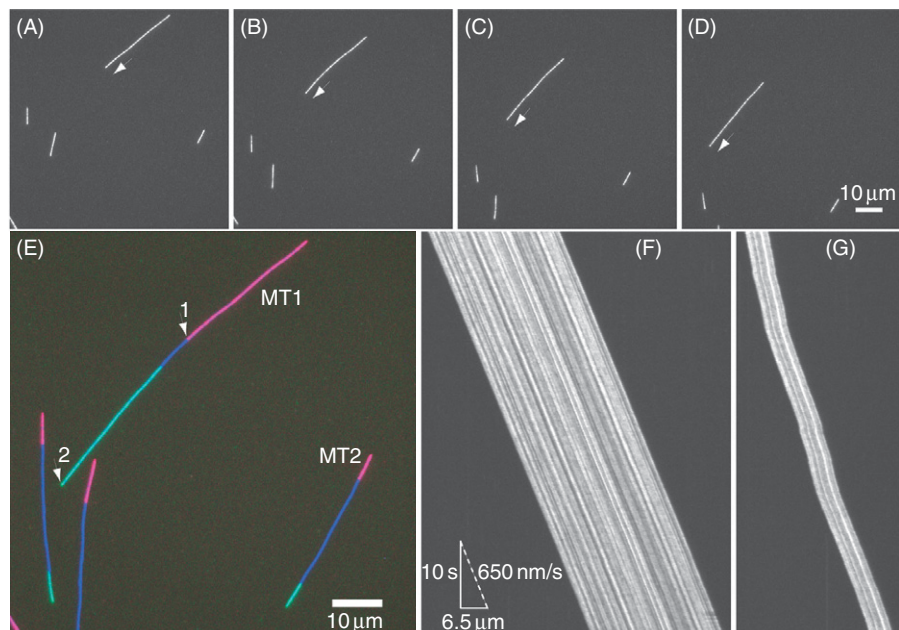


Fig. 2 Quick motility evaluation in two dimensions. (A–D) Fluorescence images of motile microtubules at 0 s (A), 20 s (B), 40 s (C), and 60 s (D). The arrows indicate the leading tip of one microtubule. Images are a subset from a continuously acquired movie (streaming mode over 60 s) with 10 frames per second. (E) Three-color overlay of first frame of the movie (red), last frame of the movie (green), and maximum projection of the path in between (blue). The distance traveled by the microtubule is measured between arrow 1 and 2. (F, G) Kymographs for microtubules MT1 moving with uniform velocity (F) and MT2 moving with nonuniform velocity (G). (See Plate no. 17 in the Color Plate Section.)

(2) the last frame of the stack, and (3) the maximum projection depicting the path in between (see Fig. 2E).

There are three major restrictions to maximum projections: (1) If a stack is very long or contains many moving objects, maximum projections can become quite crowded. (2) If the objects leave the field of view, no velocities can be measured. (3) If the objects move in an unsteady way, the obtained velocity values can be of questionable significance because the obtained velocities are average values over a certain time/distance.

2. Kymographs

Kymographs are space–time plots which display intensity values along a predefined path over time. Thus, in contrast to maximum projections, they can resolve time information. The cost is spatial information, which is reduced by projection from 2D to 1D. In order to measure velocities based upon kymographs, the path of the moving object has to be marked. A function within the data-processing software then generates the kymograph. Depending on the software either a direct measurement of velocities is possible or the lengths along the time and space axis have to be measured in order to calculate the velocities. While more labor intensive to generate, kymographs exhibit the major advantage of displaying the actual velocity (given by the slope of the kymograph) at a certain point in time or space (Fig. 2F and G).

B. Nanometer Tracking in Two Dimensions

Fluorescent objects with a size much smaller than the wavelength of light (and/or of known geometry) can be localized with much higher precision than the resolution of an optical microscope (usually about 200 nm for visible light) (Anderson *et al.*, 1992; Gelles *et al.*, 1988; Hua *et al.*, 1997; Yildiz *et al.*, 2003). We will describe a method to determine the position of single particles (QDs) and filaments (microtubules) using Gaussian-function-based models.

1. Tracking of Quantum Dots

QDs with a diameter of ≈ 20 nm appear as point sources of light; therefore, their intensity profile can be regarded identical to the Point-Spread-Function (PSF) of the imaging system. The PSF is well approximated by a 2D-Gaussian function (Cheezum *et al.*, 2001; Thompson *et al.*, 2002), and the localization of fluorescent particles by fitting the intensity profile to this model has become standard. When implementing this approach, one possibility is to fit intensity profiles of fluorescent particles to radially symmetric 2D-Gaussian functions with a fixed width corresponding to the dimension of the PSF [Eq. (1), σ fixed]. However, we found it important to also allow radially symmetric 2D-Gaussian functions with non-fixed widths [Eq. (1), σ not fixed] as well as elliptical 2D-Gaussian functions [Eq. (2) representing the probability density function of a bivariate normal distribution (Hogg and Craig, 1978)]. By allowing these additional degrees of freedom, fitting can accommodate slightly defocused images as well as particles with sizes large enough to increase the widths of their images beyond the width of the PSF (such as fluorescent beads in the 100-nm range). As a consequence, our fitting can readily be used to calculate precise intensity values corresponding to

the volumes under the 2D-Gaussian functions [e.g., for FLIC-based height measurements (see [Section III.C](#))].

$$I(x,y) = \frac{h}{2\pi\sigma^2} \cdot \exp\left[-\frac{(x-\hat{x})^2 + (y-\hat{y})^2}{2\sigma^2}\right] \quad (1)$$

$$I(x,y) = \frac{h}{2\pi\sigma_x\sigma_y\sqrt{1-\rho^2}} \cdot \exp \times \left[-\frac{1}{(1-\rho^2)} \left(\frac{(x-\hat{x})^2}{2\sigma_x^2} - \rho \frac{(x-\hat{x})(y-\hat{y})}{\sigma_x\sigma_y} + \frac{(y-\hat{y})^2}{2\sigma_y^2} \right) \right] \quad (2)$$

Here $I(x,y)$ denotes the value of the 2D-Gaussian function at position x, y ; h denotes the height of the Gaussian function; \hat{x}, \hat{y} denote the position of the center of the fitting function; for [Eq. \(1\)](#) σ denotes the width of the symmetric 2D-Gaussian function; for [Eq. \(2\)](#) σ_x, σ_y denote the widths of the elliptical Gaussian function in x - y directions (however, x - y directions are not generally coinciding with the two axes of the ellipse); and ρ denotes a correlation coefficient influencing orientation and shape of the Gaussian function—these parameters can be converted to (1) the actual widths of the Gaussian function along the major and minor axis of the ellipse and (2) to the angle between the major axis of the ellipse and the x -axis.

Using the described tracking approach for microtubule-attached QDs, we were able to resolve the 8-nm steps (see [Fig. 3B](#)) that kinesin-1 takes on the microtubule lattice, and even 4-nm steps of microtubules, which occur when microtubules are driven by two kinesin-1 motors in a gliding motility assay ([Leduc *et al.*, 2007](#)). In these experiments, we used the specific advantages of the gliding assay to count the number of (processive) motors acting on the microtubule. First, the GFP-labeled motors were well separated and could be identified as single molecules being colocalized with microtubules. Second, the microtubule itself indicated the number of motors involved in transport at very low motor density: the microtubule swiveled if only one motor was interacting with it. The transition to a nonswiveling state then corresponded to the case of two active motors.

2. Tracking of Microtubules

Compared to fluorescent objects with subresolution size in all dimensions, microtubules (densely labeled with fluorophores) create a much more complex intensity profile. Although subresolution-sized in their diameter, microtubules have a typical length of several microns. It is therefore practically impossible to fit the entire microtubule shape using a single fitting function. To tackle this problem, we have developed an algorithm that separates the filament into segments (see [Fig. 4](#)). The intensity profiles of the segments are then fitted to appropriate model functions (see [Fig. 3A](#)). The positions and orientations of the segments are finally combined and the contour of the microtubule is interpolated to create a continuous line between two end points. It has to be noted that the segments that include the microtubule ends have to be fitted to a different Gaussian-function-based model than the inner segments of the filament.

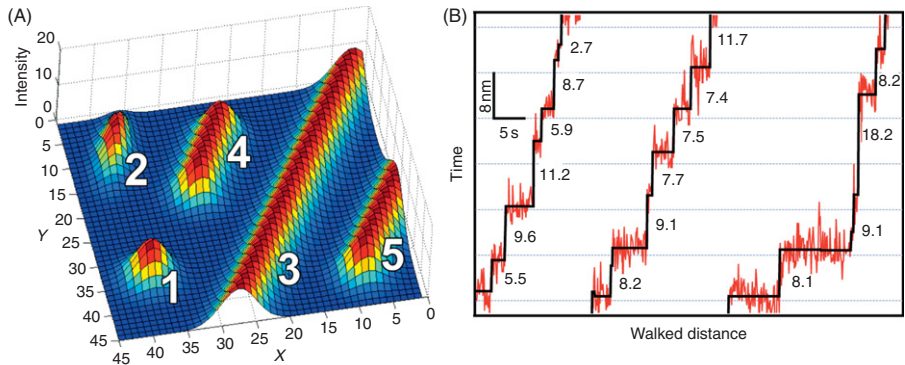


Fig. 3 Principle and application of 2D-tracking based on fitting intensity profiles to 2D-Gaussian models. (A) Intensity profiles of the models used to fit microtubule segments: (1) symmetric 2D-Gaussian function, (2) stretched 2D-Gaussian function, (3) short filament, (4) filament ridge, (5) end segment of filament. (B) 8-nm steps corresponding to the operation of a single kinesin-1 molecule on a microtubule. (See Plate no. 18 in the Color Plate Section.)

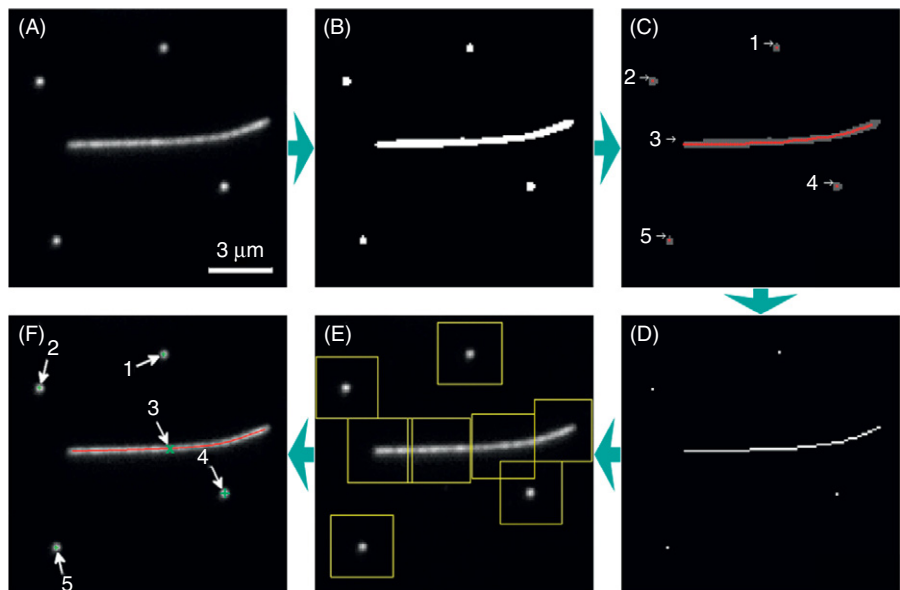


Fig. 4 General approach for tracking within a single frame. The grayscale image (A) is converted to a binary image (B) using an intensity threshold value. Objects are classified into particles (1, 2, 4, 5) and filaments (3) (C). A thinning algorithm (Lam *et al.*, 1992) is applied to calculate the skeleton of the image (D). The skeleton features are used to assign regions and appropriate fitting models to the particles and filament segments (E). Using estimated starting parameters, the regions are fitted separately, and for the filaments, the results are interpolated. The final tracking data are displayed in a graphical user interface: particle center (+), filament center (x), and filament contour (red line) (F). (See Plate no. 19 in the Color Plate Section.)

Tip: Microtubules can also be localized using 1D-Gaussian functions perpendicular to their longitudinal axis. However, we found that the orientation of the filaments had a high impact on the precision, which is not the case using the algorithm described above.

3. Implementation of the Tracking Routines

Our MatLab (The MathWorks, Natick, MA) based tracking algorithm (Ruhnow, in preparation) is designed to analyze large sets of data. The implementation is therefore entirely automated, however, still keeping the possibility to optionally adjust various parameters. In a first step, every frame is processed individually to determine the positions of all objects (see Fig. 4): (1) *Rough scanning*: Grayscale images are converted to binary images using predefined threshold values. Objects with intensity values above this threshold are classified as particles or filaments according to their area and shape. After applying a thinning algorithm (Lam *et al.*, 1992), different fitting regions and fitting models (according to Fig. 3) are assigned to the individual particles and filament segments. (2) *Fine scanning*: The regions are fitted with estimated starting parameters. The algorithm employs a nonlinear least-squares fitting routine (Coleman and Li, 1994; Moré, 1977) and estimates the error for each parameter. Overlaying regions (e.g., crossing microtubules) are combined and fitted using the sum of their initial models. (3) *Interpolating filament shape*: The contour between the two end points of a filament is derived using a spline interpolation based on the x–y positions and the orientation of the fitted filament segments.

In a second step, the fitted particle and filament positions from individual frames are connected into tracks using an adapted feature point tracking algorithm (Chetverikov and Verestóy, 1999). Thereby, a cost function for four subsequent frames is calculated and includes parameters like position, velocity, direction, intensity, or length. Particles and filaments, albeit processed simultaneously, are connected in separate tracks to preclude interference. Occlusions are handled with a post-processing step, where corresponding tracks are merged automatically. The final tracking results can be displayed in an overlay with the original images offering manual verification of the fitting. Tracks can be edited, merged, and analyzed using additional customized tools, including the possibility to relate the positions of the particles to the contours of the microtubules (Nitzsche *et al.*, 2008).

Precise tracking of the microtubules also provides an effective tool to determine the number of transporting motors at low to intermediate motor densities. The microtubules will be “pinpointed” by the active motors, resulting in reduced sideways fluctuations of the microtubule at the motor positions.

C. Resolving Nanometer Distances in the Third Dimension

When applying 2D-nanometer tracking to study the interaction of motor proteins with microtubules, the achieved understanding will always remain incomplete, because the molecules operate in 3D space. To complement 2D microscopic results with data from the third dimension, a number of approaches based on dual-focus imaging (Toprak *et al.*, 2007; Watanabe *et al.*, 2007) or split-image methods (Sun *et al.*, 2009; Yajima *et al.*, 2008) have recently been proposed and demonstrated. While these approaches are well capable of providing nanometer accuracy in the third dimension, they are technically demanding and require sophisticated microscope setups. In the following, we will describe an alternative, simple-to-implement, approach based on FLIC microscopy (Kerssemakers *et al.*, 2006; Lambacher and Fromherz, 1996), which relies on interference effects of excitation and emission light within a distance of about 1 μm from a reflecting surface. We will demonstrate this

method on the examples to measure the absolute height of gliding microtubules above the substrate surface (corresponding to the cargo-microtubule distance during active transport) and to observe rotations of gliding microtubules around their longitudinal axis (corresponding to helical paths of the motor proteins on the microtubule surface).

1. Measuring the Heights of Gliding Microtubules

The experimental setup to measure the heights of gliding, fluorescently labeled microtubules above a reflective surface is schematically depicted in Fig. 5. Interference effects lead to a vertical modulation of the detected emission intensity, which can be calibrated using tilted microtubules as nanoscopic rulers. When immobilized under a fixed tilt angle in a low concentration agarose gel, these microtubules exhibit a zebra-stripe intensity modulation when imaged on the camera chip (i.e., in the x - y plane). A side view onto the microtubules (obtained by z -plane sectioning) provides the tilt angle and allows for the precise determination of the FLIC curve. The height of moving microtubules can then be obtained by mapping their intensity onto the FLIC curve (Kerssemakers *et al.*, 2006).

Alternatively, an independent method to determine the height of gliding microtubules above a surface relies on thermally oxidized Si-wafers into which nonoverlapping patches (sizes approximately $10 \times 10 \mu\text{m}$) of different depths are etched [similar to Lambacher and Fromherz (1996)]. Microtubules moving over the SiO_2 steps will change their distance above the reflecting Si/SiO_2 interface and thus their intensity. Ratios of background-corrected fluorescence intensity values can then be obtained for each SiO_2 step. Because local intensity ratios—instead of absolute intensities—are derived here, the values are independent of spatial inhomogeneities in the illumination. The obtained data points for gliding microtubules as well as microtubules that are immobilized directly on the surface can be well fit by modified

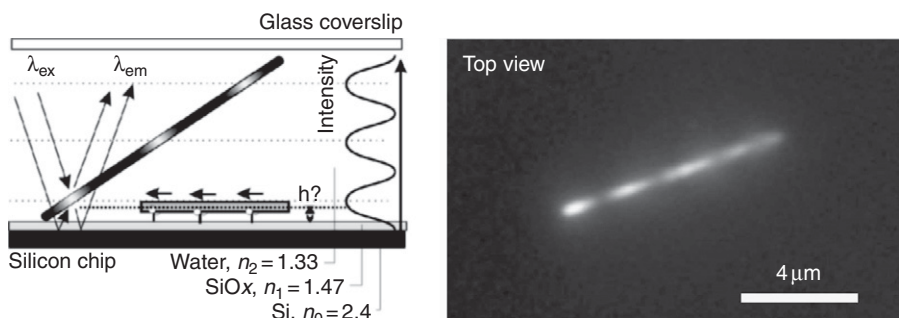


Fig. 5 Principle of quantitative FLIC microscopy on microtubules. Fluorescent, tilted microtubules close to a reflecting silicon surface (upon which a thin layer of silicon oxide has been thermally grown) are used as nanoscopic calibration rulers. Light with wavelength λ_{ex} may either excite the fluorophores in the microtubules directly or via the reflecting Si/SiO_2 interface. A similar light path exists for the light emitted by the fluorophores (λ_{em}). Thereby, the microtubules are illuminated and imaged from the glass side of a microscopic flow chamber in aqueous buffer. The height of moving microtubules can be obtained by mapping their intensity onto that of a fixed, tilted microtubule (left). Fluorescent image of a tilted microtubule as captured on the CCD camera chip (right).

FLIC curves. The lateral shift in the peaks of these curves then corresponds to the height difference between motile and surface-immobilized microtubules (Kerssemakers *et al.*, 2006).

2. Measuring Height Changes of Quantum Dots

When a fluorescent probe is being imaged by FLIC microscopy, the recorded intensity of the probe directly represents a measure of its height above the reflective surface. While it is difficult to judge the absolute height of such objects from individual images, changes in height (over time) can be easily visualized. Both maximum projections (Fig. 6A) and kymographs of FLIC movies provide a direct visual representation for the movement of mobile objects with nanometer sensitivity in the z -direction.

If nanometer sensitivity in all three dimensions is desired, the intensity information of the QDs (Fig. 6B) can be combined with the results from 2D-nanometer tracking. This way, we were able to characterize the pitch and orientation of the axial motion of microtubules in gliding assays (Nitzsche *et al.*, 2008).

IV. Future Directions

Studying the interactions of motor proteins with microtubules will continue to be an exciting field of biophysical research. In particular, investigations on cooperative motor effects will come more and more into focus. Gliding motility assays will be of great use in this research especially (1) when nonprocessive motors are to be investigated, (2) when the exact number of engaged motors needs to be known, (3) when microtubules are driven by a large number of motors (e.g., to study forces in motility systems using optical or magnetic tweezers), and (4) when motors of different directionality are to be combined on structured or unstructured motor surfaces. Moreover, gliding motility assays constitute the main framework for nanotechnological applications of biomolecular motors (Goel and Vogel, 2008; Hess and Vogel, 2001; van den Heuvel and Dekker, 2007). Reliable motility assays need to be developed for various synthetic environments. The described tracking

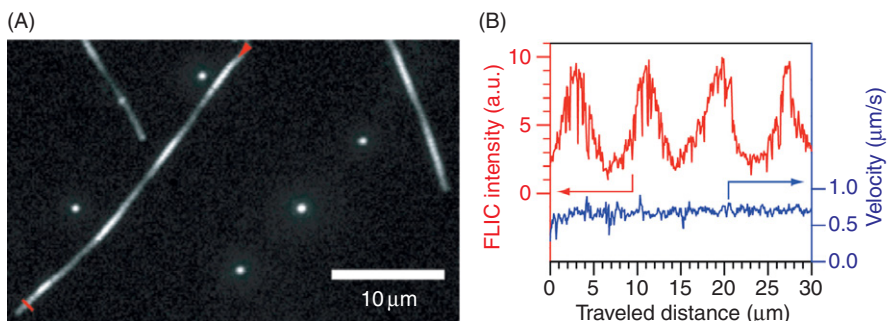


Fig. 6 Analyzing the axial rotation of gliding microtubules by following the up and down motion of the attached QDs. (A) Maximum projection of QD signal acquired at 10 frames per second. (B) FLIC intensity versus traveled distance of the QD obtained by nanometer tracking. Data correspond to part of the maximum projection marked by the red arrow and bar in (A). (See Plate no. 20 in the Color Plate Section.)

algorithms are readily applicable to molecular detection systems in which the velocity of gliding microtubules is used as readout parameter (Korten and Diez, 2008), or to novel surface imaging methods in which the intensity values of gliding microtubules can be used to probe nanometer-sized topographical surface features (Kerssemakers *et al.*, 2009). Similarly, the developed filament tracking routines will be of benefit in microtubule–microtubule sliding (Fink *et al.*, 2009) and depolymerization assays (Helenius *et al.*, 2006; Varga *et al.*, 2009).

Regarding the tracking precision, nanometer accuracy at an acquisition rate of 10 frames per second is easily possible with the described methods. However, when aiming for significantly faster imaging, the tracking precision is compromised with currently available probes. We therefore expect that the development of novel bright, nonblinking fluorescent probes as well as highly-scattering metal nanoparticles—all very well attachable to gliding microtubules—will contribute greatly to further improve the optical 3D-nanometry approaches.

===== Acknowledgments

The authors would like to thank all current and former members of the Howard and Diez laboratories for their tremendous efforts in helping to develop the described protocols. In addition, we thank Franziska Friedrich for the illustration of Fig. 1 as well as Marcus Braun and Gero Fink for valuable comments on the manuscript.

===== Reagents

- Alexa Fluor 488 5-TFP (Invitrogen Corporation, Carlsbad, CA, USA, #A30005).
- ATP (Roche Diagnostics GmbH, Mannheim, Germany, #10519979001).
- BME, β -mercaptoethanol (Sigma-Aldrich, St. Louis, MO, USA, #M6250); BME is kept in glass vials at 4°C for up to 1 month.
- BRB80 (80 mM PIPES, pH 6.9, with KOH, 1 mM EGTA, 1 mM MgCl₂).
- Casein (Sigma-Aldrich, St. Louis, MO, USA, #C7078); add 35 ml BRB80 to 1 g casein in a 50-ml centrifuge tube (e.g., Corning Inc., Corning, NY, USA, #430829). Place the Falcon tube in a rotating wheel at 4°C and allow the casein to dissolve overnight. Let the large precipitates sediment in the Falcon tube placed upright. Centrifuge the supernatant at 10,000 \times g at 4°C for 5 min. Filter the supernatant using a 0.2- μ m syringe filter. After adjusting the concentration to the desired value (e.g., 10 mg/ml), snap-freeze 40 μ l aliquots in liquid nitrogen, and store at -20°C.
- Catalase (Sigma-Aldrich, St. Louis, MO, USA, #C9322); stock solution is made at 2 mg/ml in BRB80, 10 μ l aliquots are snap-frozen in liquid nitrogen, and stored at -20°C.
- Chloroform (VWR International, West Chester, PA, USA, #1.02444).
- D-glucose (Sigma-Aldrich, St. Louis, MO, USA, #G-7528); stock solution is made at 2 M in water, 10 μ l aliquots are stored at -20°C.
- DTT, 1,4-Dithio-DL-threitol (Sigma-Aldrich, St. Louis, MO, USA, #43815); stock solution: 1 M in nanopure water, stored at -20°C.
- EGTA, ethylene glycol tetraacetic acid (Sigma-Aldrich, St. Louis, MO, USA, #E4378).

- Ethanol (VWR International, West Chester, PA, USA, #1.00983.2511).
- Glass coverslips (Corning Incorporated Life Sciences, Lowell, MA, USA, #2870-22 or #2870-18).
- Glucose oxidase (SERVA Electrophoresis GmbH, Heidelberg, Germany, #22778); stock solution is made at 20 mg/ml in BRB80; 10 μ l aliquots are snap-frozen in liquid nitrogen, and stored at -20°C .
- GMP-CPP (Jena Bioscience GmbH, Jena, Germany, #NU-405L).
- HCl (37%, Merck KGaA, Darmstadt, Germany, #100317).
- Hydrogen peroxide 30% (Sigma-Aldrich, St. Louis, MO, USA, #21.676-3).
- Kinesin-1; we use full-length *Drosophila* kinesin-1 that is purified by applying published protocols (Hancock and Howard, 1998).
- KOH-pellets (Merck KGaA, Darmstadt, Germany, #1.05012).
- MgCl₂ (VWR International, West Chester, PA, USA, #1.05833).
- Mucasol (VWR International, West Chester, PA, USA, #148-1111).
- Nescofilm (Carl Roth GmbH & Co. KG, Karlsruhe, Germany, #2569.1).
- Parafilm M (Pechiney Plastic Packaging, Menasha, WI, USA).
- PEG-NH₂ (M_n = 5000 g/mol, M_w = 5400 g/mol; Polymer Source Inc., Dorval, Quebec, Canada, #P2161-EGOCH3NH2).
- PEG-silane, 2-[Methoxy(polyethyleneoxy)propyl]trimethoxysilane [90% (ABCR GmbH & Co. KG, Karlsruhe, Germany, #AB111226, CAS 65994-07-2)].
- Penta-His antibodies (Qiagen Inc., Valencia, CA, USA, #34660).
- PGMA, Polyglycidylmethacrylate (M_n = 50,000 g/mol) was synthesized by free radical polymerization of glycidyl methacrylate (Sigma-Aldrich, St. Louis, MO, USA, #64161) as described previously (Ionov *et al.*, 2005).
- PIPES (Sigma-Aldrich, St. Louis, MO, USA, #80635).
- Pluronic F127 (Sigma-Aldrich, St. Louis, MO, USA, #P2443) stock solution is made at 1% in BRB80, filtered using a 0.2- μm syringe filter, and stored at 4°C .
- Qdots 655 (Invitrogen Corporation, Carlsbad, CA, USA, #Q10121MP).
- Sigillum Wax (Servoprax GmbH, Wesel, Germany, #A1 0303).
- Silicon wafer chips (50 \times 10 mm, {100} orientation; Semiconductor Processing Co, Boston, MA, USA or 10 \times 10 mm with oxide layers of \approx 30 nm, GESIM, Großerkmannsdorf, Germany).
- Sulfuric acid (Merck KGaA, Darmstadt, Germany, #1.00732.2500).
- TAMRA (Invitrogen Corporation, Carlsbad, CA, USA, #C1171).
- Taxol (Paclitaxel; Sigma-Aldrich, St. Louis, MO, USA, #T7191).
- Tetraspeck fluorescent microspheres (0.2 μm , #T7280, Invitrogen Corporation, Carlsbad, CA, USA).
- Toluene (Sigma-Aldrich, St. Louis, MO, USA, #34929).
- Tubulin, bovine (Cytoskeleton Inc., Denver, CO, USA; biotinylated #5.11.2147; unlabeled #5.11.2146; rhodamine labeled #5.11.2148).
- Tubulin, pig [tubulin is purified from pig brain as described in (Hunter *et al.*, 2003) and labeled (e.g., with TAMRA or Alexa Fluor 488) as described in Hyman *et al.* (1991)].
- Vacuum grease (High vacuum grease, Dow Corning Corporation, Midland, MI, USA).
- Water, nanopure ($>18\text{ M}\Omega\text{m}^{-1}$).

References

Anderson, C. M., Georgiou, G. N., Morrison, I. E., Stevenson, G. V., and Cherry, R. J. (1992). Tracking of cell surface receptors by fluorescence digital imaging microscopy using a charge-coupled device camera. Low-density lipoprotein and influenza virus receptor mobility at 4 degrees C. *J. Cell Sci.* **101** (Pt 2), 415–425.

Bieling, P., Laan, L., Schek, H., Munteanu, E. L., Sandblad, L., Dogterom, M., Brunner, D., and Surrey, T. (2007). Reconstitution of a microtubule plus-end tracking system in vitro. *Nature* **450**(7172), 1100–1105.

Bieling, P., Telley, I. A., Piehler, J., and Surrey, T. (2008). Processive kinesins require loose mechanical coupling for efficient collective motility. *Embo Rep.* **9**(11), 1121–1127.

Brouhard, G. J., Stear, J. H., Noetzel, T. L., Al-Bassam, J., Kinoshita, K., Harrison, S. C., Howard, J., and Hyman, A. A. (2008). XMAP215 is a processive microtubule polymerase. *Cell* **132**(1), 79–88.

Caplow, M., Ruhlen, R. L., and Shanks, J. (1994). The free-energy for hydrolysis of a microtubule-bound nucleotide triphosphate is near zero – all of the free-energy for hydrolysis is stored in the microtubule lattice. *J. Cell Biol.* **127**(3), 779–788.

Caplow, M., and Shanks, J. (1996). Evidence that a single monolayer tubulin-GTP cap is both necessary and sufficient to stabilize microtubules. *Mol. Biol. Cell.* **7**(4), 663–675.

Cheezum, M. K., Walker, W. F., and Guilford, W. H. (2001). Quantitative comparison of algorithms for tracking single fluorescent particles. *Biophys. J.* **81**(4), 2378–2388.

Chen, Y., Vela, J., Htoon, H., Casson, J. L., Werder, D. J., Bussian, D. A., Klimov, V. I., and Hollingsworth, J. A. (2008). "Giant" multishell CdSe nanocrystal quantum dots with suppressed blinking. *J. Am. Chem. Soc.* **130**(15), 5026–.

Chetverikov, D., and Verestóy, J. (1999). Feature point tracking for incomplete trajectories. *Computing* **62**(4), 321–338.

Coleman, T. F., and Li, Y. (1994). On the convergence of reflective newton methods for large-scale nonlinear minimization subject to bounds. *Math. Program* **67**(2), 189–224.

Crevenna, A. H., Madathil, S., Cohen, D. N., Wagenbach, M., Fahmy, K., and Howard, J. (2008). Secondary structure and compliance of a predicted flexible domain in Kinesin-1 necessary for cooperation of motors. *Biophys. J.* **95**(11), 5216–5227.

deCastro, M. J., Ho, C. H., and Stewart, R. J. (1999). Motility of dimeric ncd on a metal-chelating surfactant: Evidence that ncd is not processive. *Biochemistry* **38**(16), 5076–5081.

Fink, G., Hajdo, L., Skowronek, K. J., Reuther, C., Kasprzak, A. A., and Diez, S. (2009). The mitotic kinesin-14 Ncd drives directional microtubule-microtubule sliding. *Nat. Cell Biol.* **11**(6), 717–U747.

Funatsu, T., Harada, Y., Tokunaga, M., Saito, K., and Yanagida, T. (1995). Imaging of single fluorescent molecules and individual atp turnovers by single myosin molecules in aqueous-solution. *Nature* **374** (6522), 555–559.

Gelles, J., Schnapp, B. J., and Sheetz, M. P. (1988). Tracking kinesin-driven movements with nanometre-scale precision. *Nature* **331**(6155), 450–453.

Giepmans, B. N.G., Adams, S. R., Ellisman, M. H., and Tsien, R. Y. (2006). Review – The fluorescent toolbox for assessing protein location and function. *Science* **312**(5771), 217–224.

Goel, A., and Vogel, V. (2008). Harnessing biological motors to engineer systems for nanoscale transport and assembly. *Nat. Nanotechnol.* **3**(8), 465–475.

Hancock, W. O., and Howard, J. (1998). Processivity of the motor protein kinesin requires two heads. *J. Cell Biol.* **140**(6), 1395–1405.

Helenius, J., Brouhard, G., Kalaidzidis, Y., Diez, S., and Howard, J. (2006). The depolymerizing kinesin MCAK uses lattice diffusion to rapidly target microtubule ends. *Nature* **441**(7089), 115–119.

Hess, H., and Vogel, V. (2001). Molecular shuttles based on motor proteins: Active transport in synthetic environments. *J. Biotechnol.* **82**(1), 67–85.

Hogg, R. V., and Craig, A. T. (1978). "Introduction to Mathematical Statistics." 4th edn. Macmillan Publishing Co., Inc, New York.

Hohng, S., and Ha, T. (2004). Near-complete suppression of quantum dot blinking in ambient conditions. *J. Am. Chem. Soc.* **126**(5), 1324–1325.

Howard, J., Hudspeth, A. J., and Vale, R. D. (1989). Movement of microtubules by single kinesin molecules. *Nature* **342**(6246), 154–158.

Howard, J., Hunt, A., and Baek, S. (1993). Assay of microtubule movement driven by single kinesin molecules. *Meth. Cell Biol.* **39**, 137–147.

Hua, W., Young, E. C., Fleming, M. L., and Gelles, J. (1997). Coupling of kinesin steps to ATP hydrolysis. *Nature* **388**(6640), 390–393.

Hunter, A. W., Caplow, M., Coy, D. L., Hancock, W. O., Diez, S., Wordeman, L., and Howard, J. (2003). The kinesin-related protein MCAK is a microtubule depolymerase that forms an ATP-hydrolyzing complex at microtubule ends. *Mol. Cell* **11**(2), 445–457.

Hyman, A. A., Chretien, D., Arnal, I., and Wade, R. H. (1995). Structural changes accompanying GTP hydrolysis in microtubules: Information from a slowly hydrolyzable analogue guanylyl-(alpha,beta)-methylene-diphosphonate. *J. Cell Biol.* **128**(1-2), 117–125.

Hyman, A., Drechsel, D., Kellogg, D., Salser, S., Sawin, K., Steffen, P., Wordeman, L., and Mitchison, T. (1991). Preparation of modified tubulins. *Meth. Enzymol.* **196**, 478–485.

Ionov, L., Stamm, M., and Diez, S. (2005). Size sorting of protein assemblies using polymeric gradient surfaces. *Nano Lett.* **5**(10), 1910–1914.

Kerssemakers, J., Howard, J., Hess, H., and Diez, S. (2006). The distance that kinesin-1 holds its cargo from the microtubule surface measured by fluorescence interference contrast microscopy. *Proc. Natl. Acad. Sci. U.S.A.* **103**(43), 15812–15817.

Kerssemakers, J., Ionov, L., Queitsch, U., Luna, S., Hess, H., and Diez, S. (2009). 3D nanometer tracking of motile microtubules on reflective surfaces. *Small* **5**(15), 1732–1737.

Korten, T. (2009). “How Kinesin-1 Deals with Roadblocks: Biophysical Description and Nanotechnological Application”. Doctoral dissertation, TU Dresden, urn:nbn:de:bsz:14-qucosa-26443.

Korten, T., and Diez, S. (2008). Setting up roadblocks for kinesin-1: Mechanism for the selective speed control of cargo carrying microtubules. *Lab Chip* **8**(9), 1441–1447.

Kron, S. J., and Spudich, J. (1986). Fluorescent actin-filaments move on myosin fixed to a glass-surface. *Proc. Natl. Acad. Sci. U.S.A.* **83**(17), 6272–6276.

Lam, L., Lee, S. -W., and Suen, C. Y. (1992). Thinning methodologies – A comprehensive survey. *IEEE Trans. Pattern Anal. Mach. Intell.* **14**(9), 879.

Lambacher, A., and Fromherz, P. (1996). Fluorescence interference-contrast microscopy on oxidized silicon using a monomolecular dye layer. *Appl. Phys. A Mater. Sci. Process.* **63**(3), 207–216.

Leduc, C., Ruhnow, F., Howard, J., and Diez, S. (2007). Detection of fractional steps in cargo movement by the collective operation of kinesin-1 motors. *Proc. Natl. Acad. Sci. U.S.A.* **104**(26), 10847–10852.

Mahler, B., Spinicelli, P., Buil, S., Quelin, X., Hermier, J. P., and Dubertret, B. (2008). Towards non-blinking colloidal quantum dots. *Nat. Mater.* **7**(8), 659–664.

Meurer-Grob, P., Kasparian, J., and Wade, R. H. (2001). Microtubule structure at improved resolution. *Biochemistry* **40**(27), 8000–8008.

Moré, J. J. (1977). The Levenberg-Marquardt algorithm: Implementation and theory. In “Numerical Analysis” (Watson G. A. ed.), **Vol. Lecture Notes in Mathematics 630**, pp. 105–116. Springer, Berlin.

Nagashima, H., and Asakura, S. (1980). Dark-field light microscopic study of the flexibility of F-Actin complexes. *J. Mol. Biol.* **136**(2), 169–182.

Nitzsche, B., Ruhnow, F., and Diez, S. (2008). Quantum-dot-assisted characterization of microtubule rotations during cargo transport. *Nat. Nanotechnol.* **3**(9), 552–556.

Ozeki, T., Verma, V., Uppalapati, M., Suzuki, Y., Nakamura, M., Catchmark, J. M., and Hancock, W. O. (2009). Surface-bound casein modulates the adsorption and activity of kinesin on SiO₂ surfaces. *Biophys. J.* **96**(8), 3305–3318.

Papra, A., Gadegaard, N., and Larsen, N. B. (2001). Characterization of ultrathin poly(ethylene glycol) monolayers on silicon substrates. *Langmuir* **17**(5), 1457–1460.

Pierce, D. W., HomBooher, N., and Vale, R. D. (1997). Imaging individual green fluorescent proteins. *Nature* **388**(6640), 338–338.

Pierson, G. B., Burton, P. R., and Himes, R. H. (1978). Alterations in number of protofilaments in microtubules assembled in vitro. *J. Cell Biol.* **76**(1), 223–228.

Ray, S., Meyhofer, E., Milligan, R. A., and Howard, J. (1993). Kinesin follows the microtubule’s protofilament axis. *J. Cell Biol.* **121**(5), 1083–1093.

Resch-Genger, U., Grabolle, M., Cavaliere-Jaricot, S., Nitschke, R., and Nann, T. (2008). Quantum dots versus organic dyes as fluorescent labels. *Nat. Methods* **5**(9), 763–775.

Rief, M., Rock, R. S., Mehta, A. D., Mooseker, M. S., Cheney, R. E., and Spudich, J. A. (2000). Myosin-V stepping kinetics: A molecular model for processivity. *Proc. Natl. Acad. Sci. U.S.A.* **97**(17), 9482–9486.

Ruhnow, F. (in preparation).

Schnitzer, M. J., Visscher, K., and Block, S. M. (2000). Force production by single kinesin motors. *Nat. Cell Biol.* **2**(10), 718–723.

Sheetz, M. P., and Spudich, J. A. (1983). Movement of myosin-coated fluorescent beads on actin cables in vitro. *Nature* **303**(5912), 31–35.

Spudich, J. A., Kron, S. J., and Sheetz, M. P. (1985). Movement of myosin-coated beads on oriented filaments reconstituted from purified actin. *Nature* **315**(6020), 584–586.

Sun, Y., McKenna, J. D., Murray, J. M., Ostap, E. M., and Goldman, Y. E. (2009). Parallax: High accuracy three-dimensional single molecule tracking using split images. *Nano Lett.* **9**(7), 2676–2682.

Svoboda, K., Schmidt, C. F., Schnapp, B. J., and Block, S. M. (1993). Direct observation of kinesin stepping by optical trapping interferometry. *Nature* **365**(6448), 721–727.

Thompson, R. E., Larson, D. R., and Webb, W. W. (2002). Precise nanometer localization analysis for individual fluorescent probes. *Biophys. J.* **82**(5), 2775–2783.

Toprak, E., Balci, H., Blehm, B. H., and Selvin, P. R. (2007). Three-dimensional particle tracking via bifocal imaging. *Nano Lett.* **7**(7), 2043–2045.

Vale, R. D., Funatsu, T., Pierce, D. W., Romberg, L., Harada, Y., and Yanagida, T. (1996). Direct observation of single kinesin molecules moving along microtubules. *Nature* **380**(6573), 451–453.

van den Heuvel, M. G., and Dekker, C. (2007). Motor proteins at work for nanotechnology. *Science* **317**(5836), 333–336.

Varga, V., Helenius, J., Tanaka, K., Hyman, A. A., Tanaka, T. U., and Howard, J. (2006). Yeast kinesin-8 depolymerizes microtubules in a length-dependent manner. *Nat. Cell Biol.* **8**(9), 957–960.

Varga, V., Leduc, C., Bormuth, V., Diez, S., and Howard, J. (2009). Kinesin-8 motors act cooperatively to mediate length-dependent microtubule depolymerization. *Cell* **138**(6), 1174–1183.

Wang, X. Y., Ren, X. F., Kahlen, K., Hahn, M. A., Rajeswaran, M., Maccagnano-Zacher, S., Silcox, J., Cragg, G. E., Efros, A. L., and Krauss, T. D. (2009). Non-blinking semiconductor nanocrystals. *Nature* **459**(7247), 686–689.

Watanabe, T. M., Sato, T., Gonda, K., and Higuchi, H. (2007). Three-dimensional nanometry of vesicle transport in living cells using dual-focus imaging optics. *Biochem. Biophys. Res. Commun.* **359**(1), 1–7.

Yajima, J., Mizutani, K., and Nishizaka, T. (2008). A torque component present in mitotic kinesin Eg5 revealed by three-dimensional tracking. *Nat. Struct. Mol. Biol.* **15**(10), 1119–1121.

Yanagida, T., Nakase, M., Nishiyama, K., and Oosawa, F. (1984). Direct observation of motion of single F-Actin filaments in the presence of myosin. *Nature* **307**(5946), 58–60.

Yildiz, A., Forkey, J. N., McKinney, S. A., Ha, T., Goldman, Y. E., and Selvin, P. R. (2003). Myosin V walks hand-over-hand: Single fluorophore imaging with 1.5-nm localization. *Science* **300**(5628), 2061–2065.

SECTION III

Drugs

CHAPTER 15

Analysis of Tubulin Oligomers by Analytical Ultracentrifugation

John J. Correia

Department of Biochemistry, University of Mississippi Medical Center, Jackson, Mississippi 39216

Abstract

- I. Introduction
- II. Materials and Methods
 - A. Sample Equilibration, Buffer Composition, and Concerns for AUC Work
 - B. Filling Cells, Setting Up the Instrument, and Performing a Run
 - C. Data Analysis
- III. Results and Discussion
 - A. Tubulin Oligomers
 - B. Vinca Alkaloid-Induced Spirals
- IV. Summary

References

Abstract

This chapter describes the use of analytical ultracentrifugation in a Beckman XLA to study the self-association properties of tubulin and the interaction of tubulin with antimitotic drugs. Procedures for sample preparation, operation of the ultracentrifuge, and collection of data conform to standard modern methods. Analysis of sedimentation velocity data initially includes generation of $g(s)$ sedimentation coefficient distributions with DCDT⁺² and determination of weight average sedimentation coefficients S_w . S_w versus concentration data are then fit to isodesmic or indefinite assembly models to extract K_{iso} values, the association constant for each successive assembly step. Alternatively the raw data can also be analyzed by direct boundary analysis methods using the program Sedanal. Direct boundary analysis also extracts the K_{iso} value by fitting to the shape of the sedimentation boundary as a function of total concentration. While the fitting of weight average data as a function of protein or drug concentration to indefinite assembly models has been shown to be equivalent to direct boundary fitting of multiple data sets with Sedanal, direct

boundary fitting is preferred because it robustly identifies the presence of irreversible aggregation or mechanisms that are more complex.

===== I. Introduction

Analytical ultracentrifugation (AUC) has been a central technique in the development of our understanding of cytoskeletal components. Beginning in the 1970s with the discovery of isolation methods for tubulin and microtubules, numerous labs investigated the self-assembly properties of mammalian tubulin and its interaction with microtubule-associated proteins (MAPs). While many studies focused on assembly of microtubules by electron microscopy and turbidity approaches, investigations into the mode of association, stoichiometry, energetics, and thermodynamics of tubulin self-association were also explored in the Timasheff lab. These studies revealed the ability of tubulin to form indefinite spiral polymers and rings as a function of Mg^{+2} (Frigon and Timasheff, 1975a,b; Howard and Timasheff, 1986) and vinca alkaloid concentrations (Na and Timasheff, 1980, 1986). Detailed energetic and thermodynamic studies on families of vinca alkaloid derivatives have now also been performed (reviewed in Lobert and Correia, 2000; Lobert *et al.*, 1995, 1996, 1997, 1998a,b, 2000, 2007) and correlated with IC_{50} and clinical drug doses (Correia and Lobert, 2001, 2008; Lobert *et al.*, 2000, 2007). MAPs are also able to interact with tubulin heterodimers to make rings as demonstrated for both tau (Devred *et al.*, 2004; Dönges *et al.*, 1976) and MAP2 (Kirschner *et al.*, 1974; Marcum and Borisy, 1978a,b; Scheele and Bosiry, 1978; Valle and Borisy, 1978). More recently the hetero-interaction of tubulin with stathmin to make a 2:1 complex has been investigated by AUC approaches (Alday, 2009; Alday and Correia, 2009; Jourdain *et al.*, 1997, 2004; Chapter 23 by Devred *et al.*, this volume), while a surprisingly similar system involving interactions between actin and spire has also been studied (Bosch *et al.*, 2007). Finally, molecular motors that interact with microtubules have been extensively characterized by AUC methods (Cochran *et al.*, 2004; Correia *et al.*, 1995; Foster *et al.*, 1998; Mackey *et al.*, 2004; Rosenfeld *et al.*, 1996a,b, 2009). Here I present the methods we use to study tubulin self-association into small oligomers, focusing on experimental design, modeling, and data analysis.

===== II. Materials and Methods

A. Sample Equilibration, Buffer Composition, and Concerns for AUC Work

We will assume you have tubulin available in sufficient quantity and will only comment briefly where appropriate on isolation from brain (see Chapter 1 by Miller and Wilson, this volume, although we use glycerol preps), purification, or handling.

AUC data are typically collected in double beam mode with a reference sector (exceptions are the new FDS system (MacGregor *et al.*, 2004) and the pseudo absorbance mode (Kar *et al.*, 2000)). Thus, samples must be equilibrated so the reference blanks any buffer component signals. For rigorous thermodynamic work this means in the exhaustive dialysis tradition (Casassa and Eisenberg, 1964). However, tubulin is relatively unstable and prone to aggregation and must be

prepared quickly for AUC work. Thus, we prefer a G-50 fine spun column method (Penefsky, 1979; we refer to this as a Penefsky) that equilibrates the sample in a few minutes. Our typical buffers are 10–100 mM Pipes or Mes, 1–10 mM MgSO₄, 2 mM EGTA, 50 μM GXP, pH 6.5–7.5. In addition, while tubulin stability requires the presence of GXP, absorbance measurements in an XLA cannot be performed above ~100 μM GXP or AXP because of degraded signal to noise. Similar concerns apply to the use of mM concentrations of DTT or DTE, but this is mostly a problem with oxidized reducing agent and thus old buffer. Keeping reductant concentrations at 0.1 mM is typically sufficient for activity while avoiding baseline problems. (We prefer to use 1 mM TCEP since it has much less absorbance, is not oxidized by air, and demonstrates an absence of pH dependence, although reaction with protein can produce small baseline drifts that are most evident in equilibrium runs.)

1. Spun columns are prepared from pre-hydrated G-50 fine (stored cold in 0.01% NaAzide) and 5-ml syringes with a polyethylene frit placed in 15-ml polypropylene conical tubes. The resin typically is allowed to settle at the 5-ml line and then the column is gravity washed with at least three column volumes of the desired equilibration buffer. Columns can be made in advance and stored at 4° C as long as you keep the surfaced covered with buffer to avoid resin drying out. Just before use, allow all buffers to gravity flow through the column and pour off the flow through.
2. We store our PC-tubulin (~4–10 mg/ml) dropwise frozen in liquid N₂ and then keep at –80°C in plastic bottles. A sufficient weight of tubulin beads (often 2–3 beads ~0.2 g) is carefully poured into a 10-ml glass beaker and weighed. The beaker is placed in a shallow pool of room temperature water (in a plastic petri dish) and 0.3 ml of buffer is added to the beads to speed up thawing. When the beads thaw the beaker is moved to an ice bucket.
3. While the beads are thawing centrifuge the spun column and the 15-ml polypropylene conical tube in a table top clinical centrifuge at speed 5 (max speed 7) for 2 min at 4°C. (Older clinical centrifuges have a rheostat design and we set approximately half speed—the appropriate speed needs to be checked to ensure complete recovery of material without drying out the resin in the process (see Penefsky, 1979)).
4. Discard the flow through buffer and place the spun column in a dry 15-ml conical tube.
5. Slowly dropwise load the thawed PC-tubulin (or MAP or stathmin) onto the dried column, being sure not to squirt material down the sides before the gel re-swells. Centrifuge at speed 5 for 2 min. The column flow-through tubulin will be equilibrated in the chosen buffer. Repeat this step for buffers containing glycerol. (We recycle the G-50 by dumping the used resin in a 500-ml flask with water and 0.01% NaAzide until a sufficient quantity accumulates for refining and extensive washing with deionized water.)
6. Mix the flow-through tubulin well, dilute 10-fold (60/600 μl) and measure the OD at 278 nm blanking with the appropriate buffer. The tubulin concentration is 10× OD/1.2 in mg/ml or 10 times larger in μM (tubulin is a 100-KD heterodimer). The concentration recovered is typically >90% of the loaded material and will thus depend upon the weight of the original frozen beads thawed and the volume of the dilution buffer (Application of this technique to

other proteins (tau or MAP2) should work equally well, although you may need to use G-10 for proteins the size of stathmin to achieve recovery. For details see [Lobert and Correia, 2007](#).

7. A typical XLA 1.2-cm Beckman centerpiece holds ~450 μ l so we make up three samples of 500–600 μ l at the desired OD in 1.5-ml Eppendorf tubes. Label them A, B, C, lowest to highest concentration, to indicate which XLA cell to fill corresponding to which rotor hole the cell goes in. Mix each sample well by slight vortexing, followed by a brief 10-s spin in an Eppendorf bench top centrifuge (5415 R) to recover the full volume for cell filling. Note Beckman centerpieces come in 1.2- and 0.3-cm path lengths, so tubulin samples prepared at 0.1–5 mg/ml can be readily spun in an XLA ($\epsilon_{278\text{ nm}} = 1.2$) (see [Stafford \(2009\)](#) for a discussion of concerns for operation with interference optics).

B. Filling Cells, Setting Up the Instrument, and Performing a Run

1. Assemble three clean analytical cells being sure to torque at least three times to assure the desired tightness (125–150 depending upon the condition of your centerpieces). We use BD 1-ml tuberculin slip tip syringes fitted with a BD 24-gauge blunt tip syringe needle for cell filling. You can use the 27 G pointed needles that often come with these syringes if you can avoid scratching the surface of the centerpiece (can cause leaks) or the walls of the sector (can cause convection). With the filling holes up and screw ring facing toward you, fill the left side of each cell with reference buffer. While holding the cell in one hand with backlight to improve vision, fill to the very top leaving a small air bubble. (An alternative is to fill with a predetermined volume in both sectors, ~450 μ l.) Now fill each sample side going from lowest to highest concentrations, again filling to the top but not exceeding the height of the reference sector. Filling in this order allows you to fill all reference and sample sectors with a single syringe.
 - a. While new-generation centerpieces are being produced, current Beckman velocity centerpieces are rated at 42 K. Most old timers ignore these limits since we all use to spin them up to 60 K. But with time they will fail and crack, usually at the center rib. Camus (Durham, NH) produces SEDVEL50K and SEDVEL60K centerpieces that have a wider rib, thus providing more stability, while using less sample volume. The filling holes are also sculpted to not trap air and are thus easier to fill to the very top.
 - b. It has become more common to use a centerpiece with a channel between the reference and sample at the bottom of the sectors (also sold by Camus as meniscus matching cells, SedVel60-MM). At low speed (<10 K) this allows reference buffer to flow into the sample side causing perfect matching of the menisci. The run must be stopped and the cell shaken to mix the sample with this dilution buffer. The purpose of this is to avoid signal due to radial mismatch of buffer components. This is more critical with interference optics and not typically an issue with the XLA.
 - c. It has become common for users to under fill cells and thus have a meniscus at 6.1 cm rather than at 5.9 cm or less. While you save sample volume you also lose resolution because separation of zones is enhanced by longer sedimentation columns (recall the adage of a long, thin column in chromatographic separation). We strongly recommend maximum filling to

achieve the longest sedimentation distance and thus the highest resolution possible (Stafford, 2009).

2. Seal the cells (we use red polyethylene plastic sheets as gasket plugs, cut with an old style Beckman punchers on a block of wood) and align them in the rotor (sample A in hole 1, sample B in hole 2, etc.). Place the rotor and monochromator in the chamber, push the vacuum button, and allow the rotor to come to temperature equilibrium before starting the run (We leave the rotor and the monochromator in the chamber under vacuum all the time, and pre-equilibrate temperature to speed up the process. We also calibrate the temperature by the method of Liu and Stafford, 1995; a 20°C setting gives an actual temperature of 19.7°C in our XLA.)
3. The current Beckman software (ProteomeLab XL-A/XL-I) requires you to setup wavelength and radial data for each cell. We typically scan at 278 nm (the peak in a tubulin absorbance scan) from 5.8 to 7.2 cm collecting a single flash of the lamp at a spacing of 0.002 cm. The speed should be chosen to collect at least 50–75 useable scans prior to pelleting of the boundary. Select at least 99 scans per cell (for proper $c(s)$ analysis you want to pellet the smallest material) and the option stop XLA after last scan. Set up parameters and click on Start Methods Scan before the vacuum gets below 50 μm (The prohibition of running above 50 μm only applies to runs over 3 K and only with an analytical rotor. If you mistakenly click on Start Method Scan when the vacuum is below 50 μm the run will start regardless of temperature. You cannot just click on the vacuum button on the front panel and expect to achieve temperature and full vacuum in a reasonable time; the Start Method Scan button also turns on the diffusion pump, which is required to achieve full vacuum quickly).
 - a. We strongly recommend buying the Analytical Ultracentrifuge Service Manual for your XLA/XLI—this was part #679045 but may have changed with new software/firm ware versions. It is currently sold as a pdf and provides numerous tests and procedures useful for proper maintenance of your instrument, including how to calibrate wavelength and radial position, how to check lamp intensity, and how to calibrate delay times.
4. At temperature click on the start button on the front of the machine and watch the first few scans to be sure data are on scale and that there are no leaks. At the end of the run the data are compressed into a zip file to save disk space on the controller. These files should be transferred to another computer and stored in the folder format required for Sedanal analysis (Sedanal/User_Data/ProjectName/data/time) where date and time are in a six digit format (/012010/123000).
 - a. A proper signal-to-noise ratio requires a clean lamp. Cleaning the flash lamp should be something each lab knows how to do. Air or vacuum oil oxidizes on the lamp surface leaving a dark brown spot. This diminishes lamp intensity, especially in the lower UV (The newer monochrometer mount has threads that allow a window to screw into place to prevent vacuum oil deposits). On our machine a clean lamp provides 20,000 intensity at 230 nm, air versus air, while a drop in intensity below 3000–5000 significantly begins to degrade data quality. Depending upon your system you may need to clean the lamp a few times a week. We use toothpaste and a soft brush with a final series of rinsing with methanol.

b. Manual stopping of the run (rather than the stop XLA after last scan) often causes the wavelength drive to be fully extended making it difficult to mount the monochromator. To retract the wavelength drive piston you need to go to Service, Absorbance, Hardware Parameters, and reset the wavelength to 800 nm. This requires a “password” which you should get from your service rep.

C. Data Analysis

Here we present typical analysis of sedimentation velocity data from tubulin self-association studies. The wide size distributions along with the instability of tubulin make sedimentation velocity the preferred experimental method (see [Correia, 2000](#); [Sontag *et al.*, 2004](#)). Data should be initially processed by DCDT⁺² ([Philo, 2006](#)) to generate $g(s)$ distributions and weight average sedimentation coefficients, S_w . The Philo version of DCDT ([Stafford, 1992](#)) called DCDT⁺², is user friendly, if you wish an automated program that will select the number of scans, often from the middle of the run, to construct a $g(s)$. We prefer to do it manually and select scans as late in the run as possible to maximize resolution ([Fig. 1A](#)). There is a tutorial on the Stafford

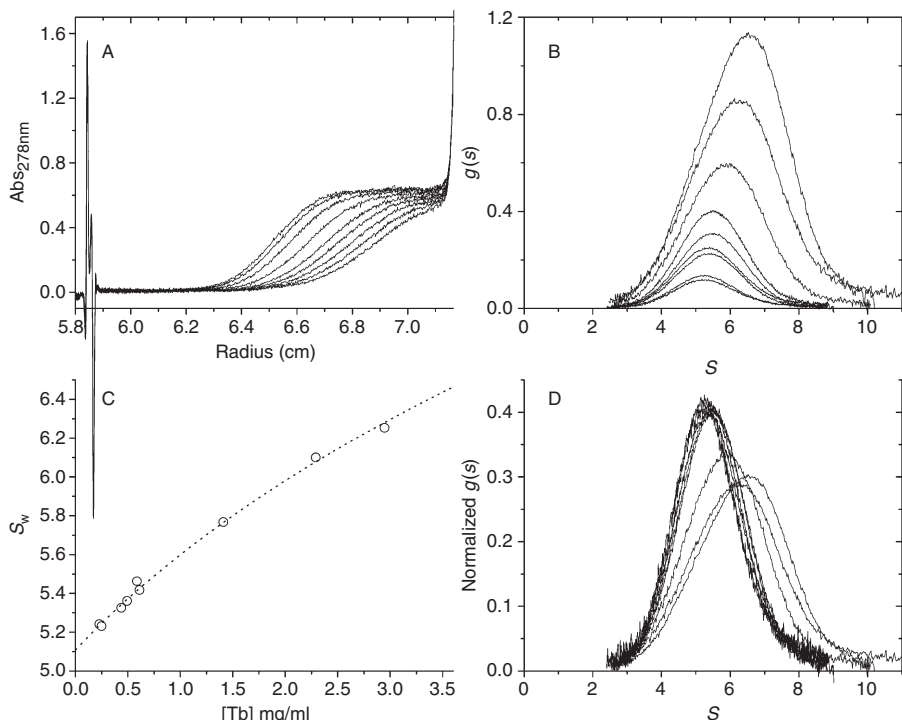


Fig. 1 DCDT⁺² analysis of sedimentation velocity data collected with PC-tubulin. (A) Plot of 9/18 scans typically used to generate a $g(s)$ from this type of data. (B) Plot of the $g(s)$ curves generated from nine samples run between 2 and 30 μM tubulin. The three samples above 1 mg/ml are corrected for path length to properly scale with the data collected in 1.2-cm path length centerpieces. (C) The data in panel B were analyzed to generate S_w values. These S_w data were then fit to an isodesmic model (...) corresponding to a K_{iso} values of $2.98 \times 10^4 \text{ M}^{-1}$. (D) The $g(s)$ data in panel B were normalized $g(s)/co$ to show the utility of plotting normalized $g(s)$ curves. Small shifts in size distributions are more apparent in this representation.

Web site that may be of use (<http://www.bbri.org/faculty/stafford/dcdt/dcdt.html>). Sedfit (Schuck, 2000) can also be used to generate $c(s)$ distributions and the S_w values produced with the integration function are equivalent to $g(s)$ derived values, that is, the information content is in the data not the analysis method (see Correia *et al.* (2005) for a detailed comparison of $g(s)$ and $c(s)$ analysis for isodesmic or indefinite assembly data. See the Sedfit Web site for information of the use of $c(s)$ at <http://www.analyticalultracentrifugation.com>) The central issue is making a plot of S_w versus protein (or drug) concentration to verify the trend of the data. A superposition of $g(s)$ plots will also shift to the right, to larger s values, as the concentration is increased. It is useful to plot the data as normalized $g(s)$ curves to enhance resolution (Stafford, 2009). (In DCDT⁺ this is done by pushing the Normalize button.) These representations ($g(s)$, S_w , and normalized $g(s)$) are shown in Fig. 1. Note we attempt to maintain a relatively constant “Peak broadening limit (kDa)” between data sets collected at different speeds because they have dramatically different size distributions. This helps to maintain a similar peak height to width character of the $g(s)$ plots and insure smoother appearing transitions as a function of protein or drug concentrations (Correia, 2000). A reasonable target value is 100–150 kDa, but appreciate this is not being used to extract molecular weights because it is an indefinite assembly mechanism; the goal is consistency of appearance and reasonable signal to noise in the family of $g(s)$ curves.

Direct boundary fitting is done with Sedanal (Correia *et al.*, 2005; Sontag *et al.*, 2004; Stafford and Sherwood, 2004). Data sets are preprocessed into bitmaps within the preprocess centrifuge data window (see the Sedanal Manual 5.03 for details, available at <http://rasmb.bbri.org/rasmb/.sedanal/>). Within the Fit preprocessed data window, data sets are selected along with the isodesmic model. Isodesmic data often require a large number of data points in the fitting, ~2400, and we need to vary the spacing so more points are located in the meniscus and the base regions that display the highest gradients (Fig. 2). The isodesmic fitting function must be instructed on how to relate N_i to s_i (Fig. 3; as described in Sontag *et al.* (2004)). These relationships were generated by Hydro calculations that built spiral polymers using a 42-bead model for the $\alpha\beta$ -tubulin heterodimer (see Sontag *et al.*, 2004 for details). To our knowledge this is the only software package that currently performs direct boundary fitting for isodesmic or indefinite association models as demonstrated by tubulin.

A final analysis issue concerns the importance of converting data to $S_{20,w}$ values. The data fitted in Fig. 1 is all expressed as S_{app} data. It does not matter that you convert; what matters is the ability to assign s_i values for each oligomer or each species. Those polynomials in Fig. 3 are expressed as s_i/s_1 so it works either way. However, Sedanal requires a density increment, which is typically entered as $(1-\nu\rho)$, where many investigators estimate $\nu\rho$ within Sedninterp using amino acid composition and buffer composition. Our lab measures density in an Anton Paar DMA 5000 at the experimental temperature, while the tubulin ν has been measured experimentally as well. The issue is Sedanal fits the experimental data without converting it to $S_{20,w}$ values but rather uses the actual experimental conditions. It is recommended you have $\nu\rho$ and extinction coefficient information (typically also from Sedninterp) available at the start of the fitting sessions.

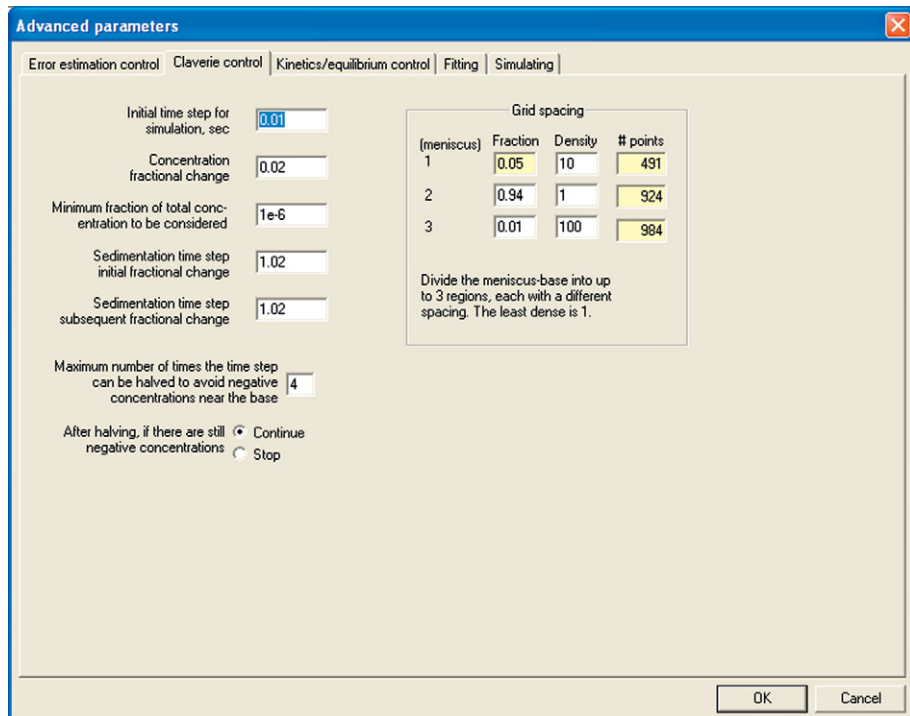


Fig. 2 The Claverie control options under the Advanced parameters window are displayed as a screen dump. Note the variation in the point density with more points at the meniscus and the base to deal with larger gradients.

III. Results and Discussion

A. Tubulin Oligomers

Self-association reactions require collecting data as a function of concentration. Figure 1 presents typical data collected on tubulin at 19.7°C in 80 mM Pipes, 1 mM MgSO₄, 2 mM EGTA, 0.1 mM TCEP, 50 μM GDP at pH 6.9 with 0.5% DMSO (data adapted from Alday and Correia, 2009). Figure 1A shows a subset of the 18 scans used to generate a typical $g(s)$ (range of Peak Broadening Limit values 117–129 kDa). Note the meniscus position at ~5.85 cm reveals a slight mismatch between sample and reference that for absorbance data does not impact the results; as discussed above, this longer column length maximizes resolution. A family of $g(s)$ curves is presented in Fig. 1B. Note the shift to higher s values and larger polymer sizes. Figure 1D displays the normalized $g(s)$ curves ($g(s)/co$) for the same data (Stafford, 2009). The shift in the distribution is more apparent even for the data below 1 mg/ml. This emphasizes the utility of using normalized plots. These $g(s)$ data were analyzed by DCDT⁺² and the weight average values S_w are plotted versus protein concentrations in Fig. 1C. (Note the data above 1 mg/ml corresponds to 1.7–3.5 OD and thus had to be collected in 3-mm centerpieces.) S_w data are fitted to an isodesmic model (see dotted line) where the S_i values correspond to a spiral

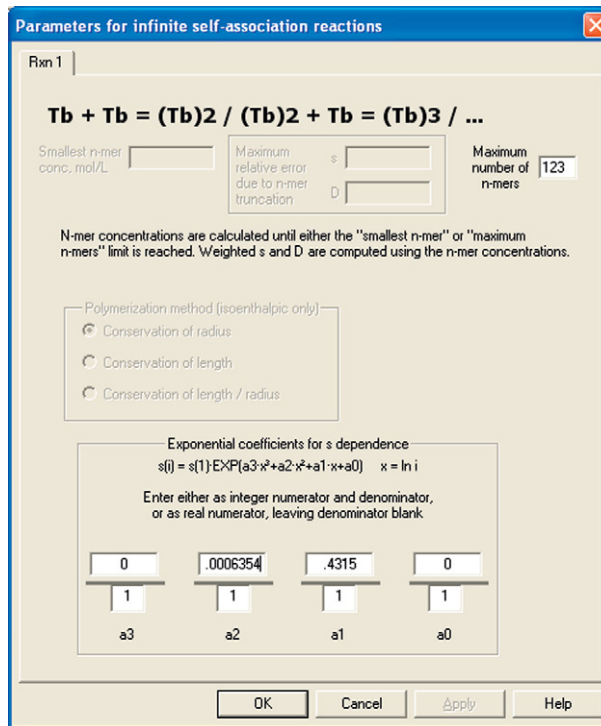


Fig. 3 The parameters for indefinite self-association reactions window. This option is visible when you select an isodesmic model. In this case you must select a function that defines the relationship between s_i and N_i (see Sontag *et al.*, 2004 for details).

polymer model derived from a 42-bead hydro model (Sontag *et al.*, 2004). The resulting K_{iso} value is $2.98 \times 10^4 \text{ M}^{-1}$ corresponding to a relatively weak indefinite association reaction under these conditions. K_{iso} is a strong function of Mg concentration, varying by an order of magnitude between 0 and 10 mM Mg (Frigon and Timasheff, 1975a,b; Sontag *et al.*, 2004). Figure 4 shows what this means in terms of polymer size distributions. Note the mass action dependence upon both Mg and protein concentration that shifts the distributions to larger oligomers.

The analysis of isodesmic sedimentation velocity data by direct boundary fitting requires the program Sedanal (Correia *et al.*, 2005; Sontag *et al.*, 2004). Data are preprocessed and then globally fit to an isodesmic model (selected from the “model to be fit” pull down list). Pairs of scans must be selected as with DCDT², to in part remove the systematic noise. However, for direct boundary fitting a wider range of scans can be chosen since the fitter is simulating data throughout the run, as dictated by the Claverie method; so comparisons to earlier data scans are convenient to do as well. The number of points required for these simulations tends to be large, >2400 , to avoid convergence errors, and it is best to use variable spacing of those points (see Fig. 2) with more point density at the base of the cell to deal with the steeper gradients. For an isodesmic model the user must also select the S_i versus N_i relationship (Fig. 3). The coefficients entered into the polynomial in Fig. 3 correspond to a 42-bead helical model as described by Sontag *et al.* (2004). An example of a direct

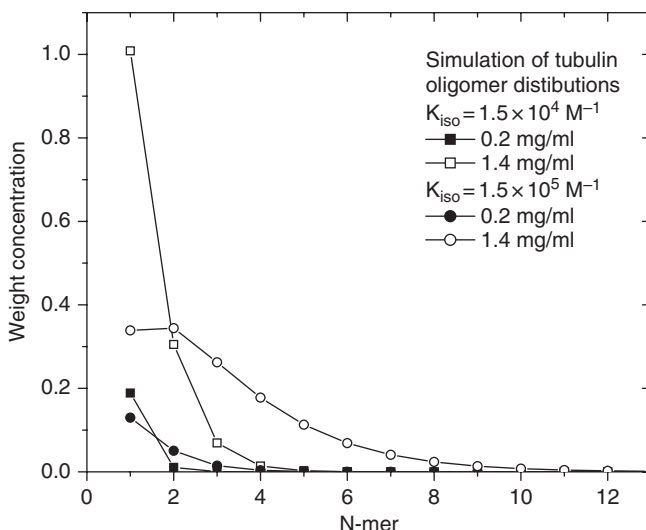


Fig. 4 Size distributions were simulated for various K_{iso} values corresponding to 0 and 10 mM Mg (Sontag *et al.*, 2004). The curves were generated at two protein concentrations corresponding to 2 and 14 μM total tubulin.

boundary fit of tubulin self-association data is shown in Fig. 5. This global fit of six data sets does a reasonable job of describing the shape of the sedimenting boundaries, although a few of the cells reveal systematic noise at the base. This is consistent with the presence of irreversible aggregates that are not involved in the isodesmic mechanism in some samples, but not all. This demonstrates the robust power of direct boundary fitting over S_w analysis (for a recent comparison of these approaches see Alday and Correia (2009)).

The presence of tubulin oligomers is generally not appreciated in the field with most investigators assuming 100% of free tubulin in solution is heterodimers. The nomenclature of the field is nonpolymerized tubulin, meaning the fraction not in microtubules, that is, the fraction that does not pellet in a preparative centrifuge. However, at the scale of small oligomers this is clearly not the case (Fig. 1). It has been known for some time that microtubule disassembly rates increase at higher Mg concentrations (O'Brien *et al.*, 1990). The molecular understanding of this is that oligomers are stabilized allowing dissociation in large steps. Stabilization of oligomers may also be related to the mechanism of action of microtubule destabilizing motors like MCAK (Desai *et al.*, 1999). Recently Hunt and coworkers used nm-resolution optical tweezers to study the step size during steady state microtubule dynamics and concluded only heterodimers were involved in assembly/disassembly excursions (see Chapter 12 by Charlebois *et al.*, this volume). These experiments were only done in 1-mM Mg conditions (the squares in Fig. 4), so a direct role for small oligomers in microtubule growth or shortening under other solution conditions may still be an open question. In the presence of XMAP215, microtubule growth has been shown to involve large excursions or steps consistent with MAPs nucleating or facilitating growth through interactions with oligomers (Kerssemakers *et al.*, 2006).

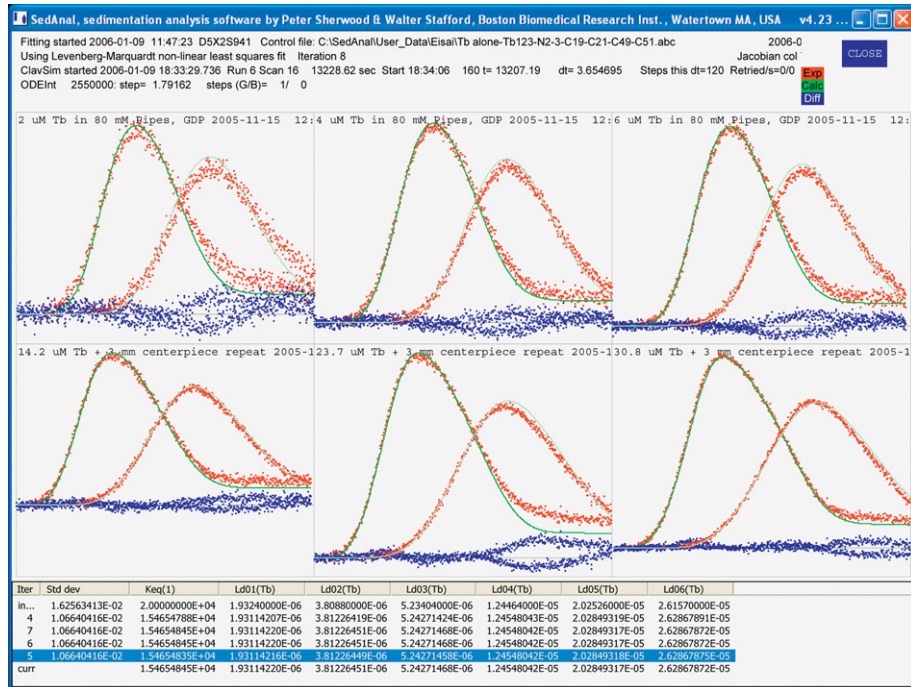


Fig. 5 An example of an isodesmic fit of tubulin self-association data with Sedanal. The data sets shown in this screen dump are a subset of the data shown in **Fig. 1**. Note data are analyzed as ΔC , or differences between scans, versus r to remove systematic optical noise. The systematic residuals observed near the base of some cells, but not all, indicates the presence of irreversible aggregates not accounted for in the indefinite assembly model.

B. Vinca Alkaloid-Induced Spirals

Similar methods have been used to study the induction of spirals by vinca alkaloids. Weight average analysis approaches have been extensively described (Lobert and Correia, 2000; Lobert *et al.*, 1997). The major difference is that the fitter input requires S_w , protein concentration in mg/ml and drug concentrations in μM for each data point. The extent of reaction is both protein and drug concentration dependent. Sample equilibration is again done by Penefsky at each drug concentration with the additional step of diluting the protein to the desired concentration prior to the drug equilibration step. Hence this requires two Penefsky steps. The ligand-induced indefinite $K_{2,\text{app}}$ value that applies to each sample can be expressed as

$$K_{2,\text{app}} = \frac{K_2}{\left(1 + \frac{1}{K_1[\text{Drug}]}\right)^2}$$

where K_1 describes the affinity for drug for tubulin heterodimers and K_2 is the indefinite association constant. Correia *et al.* (2005) describes the procedures required to fit these data with Sedanal. When collecting data at multiple drug concentrations, we fit each individual data set to extract the local $K_{2,\text{app}}$ value, that

is, an isodesmic model. Assumptions about the shape of the oligomers and the relationship between N_i and s_i still must be applied. These $K_{2,app}$ data are then plotted versus drug concentration and fit to the $K_{2,app}$ equation shown above to extract global K_1 , K_2 values. Recently, we (Alday and Correia, 2009) applied these methods to a new class of Halichondrin B analogs that only weakly induce oligomers. In this case runs were done as a function of protein concentration alone with a fixed excess drug concentration. These data were then globally analyzed by weight average and Sedanal approaches to extract a K_{iso} value under those conditions without extraction of K_1 or K_2 values. As described here, the direct boundary fitting method is more robust than the S_w fitting approach, although they generally agree within error (Alday and Correia, 2009).

IV. Summary

This chapter outlines a detailed description of how to prepare samples and set up the instrument to study tubulin self-association by AUC. The studies apply to tubulin alone or in the presence of antimitotic drugs. These same procedures also apply to hetero-interactions where tubulin is mixed with a regulatory protein, that is, a motor domain, stathmin, or tau. The major difference in approaches is the equilibration of both components prior to mixing, mixing over a reasonable stoichiometry, at least 1:4 to 4:1, and possibly collecting data at multiple wavelengths, especially if one component is labeled with a colored probe, that is, GFP (see Alday and Correia, 2009 for an example). Otherwise the analysis approach is similar and only differs in the model used to directly fit the boundary shapes. We have recently published tutorials on the use of Sedanal for self- and hetero-associating systems (see Correia and Stafford, 2009; Correia *et al.*, 2009).

References

Alday, P. H., and Correia, J. J. (2009). Macromolecular interaction of halichondrin B analogs Eribulin (E7389) and ER-076349 with tubulin by analytical ultracentrifugation. *Biochemistry*. **48**, 7927–7938.

Alday, P. H. (2009). Use of Fluorescently Labeled Proteins in Quantitative Sedimentation Velocity Studies of Heterogeneous Biomolecular Interactions. Ph.D. Thesis, University of Mississippi Medical Center, Jackson, MS.

Bosch, M., Le, K. H., Bugyi, B., Correia, J. J., Renault, L., and Carlier, M.-F. (2007). Analysis of the function of Spire in actin assembly and its synergy with formin and profilin. *Mol. Biol. Cell*. **28**, 555–568.

Casassa, E. F., and Eisenberg, H. (1964). Thermodynamic analysis of multicomponent solutions. *Adv. Protein Chem.* **19**, 287–395.

Cochran, J. C., Sontag, C. A., Maliga, Z., Kapoor, T. M., Correia, J. J., and Gilbert, S. P. (2004). Mechanistic analysis of the mitotic kinesin Eg5. *J. Biol. Chem.* **269**, 38861–38870.

Correia, J. J. (2000). The analysis of weight average sedimentation data. *Meth. Enzymol.* **321**, 81–100.

Correia, J. J., Alday, P. H., Sherwood, P., and Stafford, W. F. (2009). Effect of kinetics on sedimentation velocity profiles and the role of intermediates. In “Numerical Methods” (M. L. Johnson, ed.), Vol. 467, 135–161.

Correia, J. J., Gilbert, S. P., Moyer, M. L., and Johnson, K. A. (1995). Sedimentation studies on the kinesin head domain constructs K401, K366 and K341. *Biochemistry*. **34**, 4898–4907.

Correia, J. J., and Lobert, S. (2001). Physicochemical aspects of tubulin-interacting, antimitotic drugs. *Curr. Pharm. Design*. **7**(13), 1213–1228.

Correia, J. J., and Lobert, S. (2008). Molecular mechanisms of microtubule acting cancer drugs. In “Microtubule Targets in Cancer Therapy” (A. T. Fojo, ed.), pp. 21–46. Humana Press, Totowa, NJ.

Correia, J. J., Sontag, C. A., Stafford, W. F., and Sherwood, P. J. (2005). Models for direct boundary fitting of indefinite ligand-linked self-association. In “Analytical Ultracentrifugation: Techniques and Methods” (D. Scott, S. Harding and A. Rowe, eds.), pp. 51–63. Springer, Berlin.

Correia, J. J., and Stafford, W. F. (2009). Extracting equilibrium constants from kinetically limited reacting systems. In “Biothermodynamics”, Part A (M. L. Johnson, ed.), Vol 455, pp. 419–446. Academic Press, San Diego.

De Marco, V., de Marco, A., Correia, J. J., Goldie, K. N., and Hoenger, A. (2003). Dimerization properties of a *Xenopus Laevis* Kinesin-II C-terminal stalk fragment. *EMBO Reports*. **4**, 717–722.

Desai, A., Verma, S., Mitchison, T. J., and Walczak, C. E. (1999). Kin I kinesins are microtubule-destabilizing enzymes. *Cell*. **99**, 69–78.

Devred, F., Barbier, P., Douillard, S., Monasterio, O., Andreu, J. M., and Peyrot, V. (2004). Tau induces ring and microtubule formation from $\alpha\beta$ -Tubulin dimers under nonassembly conditions. *Biochemistry*. **43**, 10520–10531.

Dönges, K. H., Biedert, S., and Paweletz, N. (1976). Characterization of a 20S component in tubulin from mammalian brain. *Biochemistry*. **15**, 2995–2999.

Foster, K. A., Correia, J. J., and Gilbert, F. P. (1998). Equilibrium Binding Studies of Non-claret Disjunctional Protein (Ncd). *J. Biol. Chem.* **273**, 35307–35318.

Frigon, R. P., and Timasheff, S. N. (1975a). Magnesium-induced self-association of calf brain tubulin. I. Stoichiometry. *Biochemistry*. **14**, 4559–4566.

Frigon, R. P., and Timasheff, S. N. (1975b). Magnesium-induced self-association of calf brain tubulin. II. Thermodynamics. *Biochemistry*. **14**, 4567–4573.

Howard, W. D., and Timasheff, S. N. (1986). GDP state of tubulin: Stabilization of double rings. *Biochemistry*. **25**, 8292.

Jourdain, L., Curmi, P., Sobel, A., Pantaloni, D., and Carlier, M. F. (1997). Stathmin: A tubulin-sequestering protein which forms a ternary T2S complex with two tubulin molecules. *Biochemistry*. **36**, 10817–10821.

Jourdain, I., Lachkar, S., Charbaut, E., Gigant, B., Knossow, M., Sobel, A., and Curmi, P. A. (2004). A synergistic relationship between three regions of stathmin family proteins is required for the formation of a stable complex with tubulin. *Biochem. J.* **378**, 877–888.

Kar, S. R., Kingsbury, J. S., Lewis, M. S., Laue, T. M., and Schuck, P. (2000). Analysis of transport experiments using pseudo-absorbance data. *Anal. Biochem.* **285**, 135–142.

Kerssemakers, J. W., Munteanu, E. L., Laan, L., Noetzel, T. L., Janson, M. E., and Dogterom, M. (2006). Assembly dynamics of microtubules at molecular resolution. *Nature*. **442**, 709–712.

Kirschner, M. W., Williams, R. C., Weingarten, M., and Gerhart, J. C. (1974). Microtubules from mammalian brain: Some properties of their depolymerization products and a proposed mechanism of assembly and disassembly. *PNAS*. **71**, 1159–1163.

Liu, S., and Stafford, W. F. (1995). An optical thermometer for direct measurement of cell temperature in the Beckman instruments XL-A analytical ultracentrifuge. *Anal. Biochem.* **224**, 199–202.

Loibert, S., Boyd, C. A., and Correia, J. J. (1997). Divalent cation and ionic strength effects on vinca alkaloid-induced tubulin self-association. *Biophys. J.* **72**, 416–427.

Loibert, S., and Correia, J. J. (2000). Energetics of vinca alkaloid interactions with tubulin. *Meth. Enzymol.* **323**, 77–103.

Loibert, S., and Correia, J. J. (2007). Methods for studying vinca alkaloid interaction with tubulin. In “Microtubule Protocols” (J. Zhou, ed.), pp. 261–280, Chapter 18. Humana Press, Totowa, NJ.

Loibert, S., Fahy, J., Hill, B. T., Duflos, A., Entievant, C., and Correia, J. J. (2000). Vinca alkaloid-induced tubulin spiral formation correlates with cytotoxicity in the leukemic L1210 cell line. *Biochemistry*. **39**, 12053–12062.

Loibert, S., Frankfurter, A., and Correia, J. J. (1995). Binding of vinblastine to phosphocellulose-purified and $\alpha\beta$ -Class III tubulin: The role of nucleotides and β -tubulin isotypes. *Biochemistry*. **34**, 8050–8060.

Loibert, S., Frankfurter, A., and Correia, J. J. (1998a). The energetics of vinca alkaloid interactions with β -tubulin isotypes: Implications for drug efficacy and toxicity. *Cell Motil. Cytoskel.* **39**, 107–121.

Loibert, S., Ingram, J. W., and Correia, J. J. (2007). The thermodynamics of vinca alkaloid-induced tubulin spiral formation. *Biophys. Chem.*, Special Issue, Festschrift for Julian Sturtevant. **126**.

Loibert, S., Ingram, J. W., Hill, B. T., and Correia, J. J. (1998b). A comparison of thermodynamic parameters for vinorelbine- and vinflunine-induced tubulin self association by sedimentation velocity. *Mol. Pharmacol.* **53**, 908–915.

Lobert, S., Vulevic, B., and Correia, J. J. (1996). Interaction of vinca alkaloids with tubulin: A comparison of vinblastine, vincristine and vinorelbine. *Biochemistry*. **35**, 6806–6814.

MacGregor, I. K., Anderson, A. L., and Laue, T. M. (2004). Fluorescence detection for the XLI ultracentrifuge. *Biophys. Chem.* **108**, 165–185.

Mackey, A. T., Sontag, C. A., Satterwhite, L. L., Correia, J. J., and Gilbert, S. P. (2004). The ATPase mechanism behind the microtubule-based motility of GST-Kar3. *J. Biol. Chem.* **279**, 51354–51361.

Marcum, J. M., and Borisy, G. G. (1978a). Sedimentation velocity analyses of the effect of hydrostatic pressure on the 30 S microtubule protein oligomer. *J. Biol. Chem.* **253**(8), 2852–2857.

Marcum, J. M., and Borisy, G. G. (1978b). Characterization of microtubule protein oligomers by analytical ultracentrifugation. *J. Biol. Chem.* **253**(8), 2825–2833.

Na, G. C., and Timasheff, S. N. (1980). Stoichiometry of the vinblastine-induced self-association of calf brain tubulin. *Biochemistry*. **19**, 1347–1354.

Na, G. C., and Timasheff, S. N. (1986). Interaction of vinblastine with calf brain tubulin: Effects of magnesium ions. *Biochemistry*. **25**, 6222–6228.

O'Brien, E. T., Salmon, E. D., Walker, R. A., and Erickson, H. P. (1990). The effects of magnesium on dynamic instability of individual microtubules. *Biochemistry*. **29**, 6648–6656.

Penefsky, H. S. (1979). A centrifuged-column procedure for the measurement of ligand binding by beef heart F1. *Methods Enzymol.* **56**, 527–531.

Rosenfeld, S. S., Correia, J. J., Xing, J., Rener, B., and Cheung, H. C. (1996b). Structural studies of kinesin-nucleotide intermediates. *J. Biol. Chem.* **271**, 30212–30221.

Rosenfeld, S. S., Rener, B., Correia, J. J., Mayo, M. S., and Cheung, H. C. (1996a). Equilibrium studies of kinesin: Nucleotide intermediates. *J. Biol. Chem.* **271**, 9473–9482.

Rosenfeld, S. S., Van Duffelen, M., Behnke Parks, W. M., Beadle, C., Correia, J. J., and Xing, J. (2009). THE ATPase cycle of the mitotic motor CENP-E. *J. Biol. Chem.* **284**, 32858–32868.

Scheele, R. B., and Borisy, G. G. (1978). Electron microscopy of metal-shadowed and negatively stained microtubule protein. Structure of the 30 S oligomer. *J. Biol. Chem.* **253**, 2846–2851.

Schuck, P. (2000). Size-distribution analysis of macromolecules by sedimentation velocity ultracentrifugation and Lamm equation modeling. *Biophys. J.* **78**, 1606–1619.

Sontag, C. A., Stafford, W. F., and Correia, J. J. (2004). A comparison of weight average and direct boundary fitting of sedimentation velocity data for indefinite polymerizing systems. *Biophys. Chem.* **108**, 215–230.

Stafford, W. F. (1992). Boundary analysis in sedimentation transport experiments: A procedure for obtaining sedimentation coefficient distributions using the time derivative of the concentration profile. *Anal. Biochem.* **203**, 295–301.

Stafford, W. F. (2009). Protein–protein and ligand–protein interactions studied by analytical ultracentrifugation. In “Protein Structure, Stability, and Interactions” (J. W. Shriver, ed.), Vol. 490, pp. 83–113. Humana Press, Totowa NJ.

Stafford, W. F., and Sherwood, P. J. (2004). Analysis of heterologous interacting systems by sedimentation velocity: Curve fitting algorithms for estimation of sedimentation coefficients, equilibrium and rate constants. *Biophys. Chem.* **108**, 231–243.

Vallee, R. B., and Borisy, G. G. (1978). The non-tubulin component of microtubule protein oligomers. Effect on self-association and hydrodynamic properties. *J. Biol. Chem.* **253**(8), 2834–2845.

Vulevic, B., Lobert, S., and Correia, J. J. (1997). Role of guanine nucleotides in the vinca alkaloid-induced self association of tubulin: Effects of GMPCPP and GMPCP. *Biochemistry*. **36**, 12828–12835.